Thomas Dieing Olaf Hollricher Jan Toporski *Editors*

SPRINGER SERIES IN OPTICAL SCIENCES 158

Confocal Raman Microscopy



founded by H.K.V. Lotsch

Editor-in-Chief: W. T. Rhodes, Atlanta

Editorial Board: A. Adibi, Atlanta

T. Asakura, Sapporo

T. W. Hänsch, Garching

T. Kamiya, Tokyo

F. Krausz, Garching

B. Monemar, Linköping

H. Venghaus, Berlin

H. Weber, Berlin

H. Weinfurter, München

Springer Series in OPTICAL SCIENCES

The Springer Series in Optical Sciences, under the leadership of Editor-in-Chief William T. Rhodes, Georgia Institute of Technology, USA, provides an expanding selection of research monographs in all major areas of optics: lasers and quantum optics, ultrafast phenomena, optical spectroscopy techniques, optoelectronics, quantum information, information optics, applied laser technology, industrial applications, and other topics of contemporary interest.

With this broad coverage of topics, the series is of use to all research scientists and engineers who need up-to-date reference books.

The editors encourage prospective authors to correspond with them in advance of submitting a manuscript. Submission of manuscripts should be made to the Editor-in-Chief or one of the Editors. See also www.springer.com/series/624

Editor-in-Chief

William T. Rhodes

Georgia Institute of Technology School of Electrical and Computer Engineering Atlanta, GA 30332-0250, USA E-mail: bill.rhodes@ece.gatech.edu

Editorial Board

Ali Adibi

Georgia Institute of Technology School of Electrical and Computer Engineering Atlanta, GA 30332-0250, USA E-mail: adibi@ee.gatech.edu

Toshimitsu Asakura

Hokkai-Gakuen University Faculty of Engineering 1-1, Minami-26, Nishi 11, Chuo-ku Sapporo, Hokkaido 064-0926, Japan E-mail: asakura@eli.hokkai-s-u.ac.jp

Theodor W. Hänsch

Max-Planck-Institut für Quantenoptik Hans-Kopfermann-Straße 1 85748 Garching, Germany E-mail: t.w.haensch@physik.uni-muenchen.de

Takeshi Kamiya

Ministry of Education, Culture, Sports Science and Technology National Institution for Academic Degrees 3-29-1 Otsuka, Bunkyo-ku Tokyo 112-0012, Japan E-mail: kamiyatk@niad.ac.jp

Ferenc Krausz

Ludwig-Maximilians-Universität München Lehrstuhl für Experimentelle Physik Am Coulombwall 1 85748 Garching, Germany *and* Max-Planck-Institut für Quantenoptik

For further volumes: http://www.springer.com/series/624

Hans-Kopfermann-Straße 1 85748 Garching, Germany E-mail: ferenc.krausz@mpq.mpg.de

Bo Monemar

Department of Physics and Measurement Technology Materials Science Division Linköping University 58183 Linköping, Sweden E-mail: bom@ifm.liu.se

Herbert Venghaus

Fraunhofer Institut für Nachrichtentechnik Heinrich-Hertz-Institut Einsteinufer 37 10587 Berlin, Germany E-mail: venghaus@hhi.de

Horst Weber

Technische Universität Berlin Optisches Institut Straße des 17. Juni 135 10623 Berlin, Germany E-mail: weber@physik.tu-berlin.de

Harald Weinfurter

Ludwig-Maximilians-Universität München Sektion Physik Schellingstraße 4/III 80799 München, Germany E-mail: harald.weinfurter@physik.uni-muenchen.de Thomas Dieing Olaf Hollricher Jan Toporski

Editors

Confocal Raman Microscopy

With 155 Figures



Editors
Dr. Thomas Dieing
Applications & Support
WITec GmbH
Lise-Meitner-Strasse 6
89081 Ulm, Germany
thomas.dieing@witec.de

Dr. Jan Toporski Sales WITec GmbH Lise-Meitner-Strasse 6 89081 Ulm, Germany jan.toporski@witec.de Dr. Olaf Hollricher Research & Development WITec GmbH Lise-Meitner-Strasse 6 89081 Ulm, Germany olaf.hollricher@witec.de

Springer Series in Optical Sciences ISSN 0342-4111 e-ISSN 1556-1534 ISBN 978-3-642-12521-8 e-ISBN 978-3-642-12522-5 DOI 10.1007/978-3-642-12522-5 Springer Heidelberg Dordrecht London New York

Library of Congress Control Number: 2010932505

© Springer-Verlag Berlin Heidelberg 2010

This work is subject to copyright. All rights are reserved, whether the whole or part of the material is concerned, specifically the rights of translation, reprinting, reuse of illustrations, recitation, broadcasting, reproduction on microfilm or in any other way, and storage in data banks. Duplication of this publication or parts thereof is permitted only under the provisions of the German Copyright Law of September 9, 1965, in its current version, and permission for use must always be obtained from Springer. Violations are liable to prosecution under the German Copyright Law.

The use of general descriptive names, registered names, trademarks, etc. in this publication does not imply, even in the absence of a specific statement, that such names are exempt from the relevant protective laws and regulations and therefore free for general use.

Cover design: Integra Software Services Pvt. Ltd., Pondicherry

Printed on acid-free paper

Springer is part of Springer Science+Business Media (www.springer.com)

Preface

Readers of this book are aware that the theory of the Raman effect has been known for over 80 years, though routine Raman spectroscopy experiments were performed only after almost another half century of technological development. Since then, the analytical potential of this specific light-scattering effect has been explored for decades and resulted in a wealth of scientific publications. It took another major step in technical development toward the end of the second millennium that allowed the three-dimensional chemometric characterization of materials with high sensitivity and diffraction-limited resolution by combining confocal microscopy and Raman spectroscopy. With the inception of the resulting high-resolution confocal Raman microscopy as a novel analytical technique, new realms for the application of this method were defined and new research goals formulated. This has resulted in an expanding pool of experience and expertise.

The motivation to compile this book largely emerged from the observation that among the substantial portfolio of excellent publications of monographs on Raman spectroscopy, there are few dedicated to confocal Raman microscopy or even high-resolution confocal Raman imaging. Encouraged additionally by conversation and discussion with experts in the field of confocal Raman microscopy, we realized the demand for a reference work that condenses background information on physical, technical, hardware, and software aspects that serve as prerequisites for high-end analytical microscopy equipment. Equally important are comprehensive data evaluation methods to further and foster data processing, permitting advancement of research by simply providing tools to obtain novel results and make new discoveries.

The goal of this book therefore is to provide the best possible overview of the theoretical and practical facts and issues associated with confocal Raman microscopy. With the incorporation of over a dozen contributions from expert scientists and research groups spanning a wide range of applications in academic research as well as industry-driven research and development, this first edition of "confocal Raman microscopy" provides a comprehensive frame of reference for anyone involved in research employing confocal Raman microscopy. Aiming to keep pace with technological advancement, it is our intention to keep this book as up-to-date as possible

vi Preface

in order to provide our readership with the current state of the art in confocal Raman microscopy. We therefore welcome any constructive comments or suggestions for all future editions.

Ulm, Germany May 2010 Thomas Dieing Olaf Hollricher Jan Toporski

Contents

1	High	-Resolut	tion Optical and Confocal Microscopy	1					
	Olaf Hollricher and Wolfram Ibach								
	1.1		ction	1					
	1.2	Introduction to Theoretical Considerations in High-Resolution							
			copy	3					
	1.3		ection to Confocal Microscopy						
	1.4	Electro	Electromagnetic Scattering in Optical Systems						
	1.5	3D-Inte	3D-Intensity Distribution in the Focus						
		1.5.1	Large Aperture Angles	6					
		1.5.2	Transition to Small Aperture Angles	9					
	1.6	Theory	of Image Formation	11					
		1.6.1	Microscope	11					
		1.6.2	Confocal Microscope	12					
		1.6.3	Confocal Raman Microscope	12					
	1.7	Image 1	Formation for Light Scattering	13					
		1.7.1	Scattering Point	13					
		1.7.2	Reflection at a Mirror						
	1.8	Image 1	Formation for Raman Scattering	16					
		1.8.1	Raman Emitting Point						
		1.8.2	Raman Emission of a Layer	17					
	1.9	Pinhole	e Size	18					
	Refer	ences		20					
2	Intro	duction	to the Fundamentals of Raman Spectroscopy	21					
	Benja	amin Die	tzek, Dana Cialla, Michael Schmitt, and Jürgen Popp						
	2.1	Introduction							
	2.2		al Picture of Light Scattering						
		2.2.1	Frequency Dependence of Raman Scattering						
		2.2.2	Classical "Selection Rule" and Comparison to IR						
			Absorption	24					
		2.2.3	Scattered Raman Intensity						
		2.2.4	Shortfalls of the Classical Picture						

viii Contents

	2.3	Raman	Cross-Section Enhancement Mechanisms	
		2.3.1	Resonant Raman Scattering	28
		2.3.2	Advantages and Applications of Resonance	
			Raman Scattering	31
		2.3.3	Surface-Enhanced Raman Scattering	34
	Refer	ences		40
3	Ram	an Instr	umentation for Confocal Raman Microscopy	43
		Hollriche		
	3.1	Introdu	ection	43
	3.2		evelopment of Raman Microscopes	
	3.3		ality	
	3.4		thput of a Confocal Raman Microscope	
		3.4.1	Laser Wavelength	
		3.4.2	Excitation Power	
		3.4.3	Objective	
		3.4.4	Microscope Throughput	
		3.4.5	Coupling Between Microscope and Spectrometer	
		3.4.6	Spectrometer Throughput	
		3.4.7	Gratings	
		3.4.8	CCD Detector	
	3.5		sion	
4	Softv	vare Re	quirements and Data Analysis in Confocal	
			oscopy	61
			ng and Wolfram Ibach	
	4.1		iction	61
	4.2		ements for Data Acquisition Software	
		4.2.1	Data Acquisition	
		4.2.2	Correlation of Spatial and Spectral Data	
	4.3	Descri	ption of the Data Sets Acquired in Confocal	
		-	Microscopy	65
	4.4		ocessing of Raman Spectra	
		4.4.1	Cosmic Ray Removal	
		4.4.2	Smoothing	
		4.4.3	Background Substraction and Subtraction	
			of Reference Spectra	70
	4.5	Image	Generation	
		4.5.1	Univariate Image Generation	
		4.5.2	Multivariate Image Generation	
	4.6		Masks and Selective Average Calculation	
	4.7		nation of Single Spectra with Multi-spectral Data Sets	82
		4.7.1	Basis Spectra	83
		4.7.2	Fitting Procedure	83

Contents ix

	4.8 4.9	The Law of Numbers.	84 85							
	4.10 Refer		88 89							
	Refer	tenees	رن							
5	Nano-spectroscopy of Individual Carbon Nanotubes and Isolated									
	Grap	phene Sheets	91							
	Alain	Jungen								
	5.1	Introduction	91							
	5.2	Individual Carbon Nanotubes	92							
		5.2.1 Phonons	92							
		5.2.2 Theory	95							
		5.2.3 Experiment	96							
		1 2	98							
		5.2.5 Thermography								
	5.3	Isolated Graphene Sheets								
		5.3.1 Theory								
		5.3.2 Experiment								
		5.3.3 Charge Distributions								
	5.4	Conclusion								
	Refe	rences	08							
_	_									
6		an Spectroscopy and Confocal Raman Imaging in Mineralogy								
		Petrography	П							
		Fries and Andrew Steele								
	6.1	Introduction	11							
	6.2	Raman Spectroscopy and Imaging as a Mineralogy/Petrography	10							
		Tool								
		6.2.1 Working with Thin Sections								
		6.2.2 Control of Laser Power								
	6.3	"Raman Mineralogy" Using Imaging Raman Techniques 1								
		6.3.1 Mineral Phase Imaging								
		6.3.2 Crystallographic Orientation Imaging								
		6.3.3 Phase Composition Imaging								
	6.4	Examples of "Raman Petrography" Applications								
		6.4.1 Raman Analysis of Shocked Minerals								
		6.4.2 Contextual Imaging of Carbonaceous Materials								
		6.4.3 Fluid Inclusions								
		6.4.4 Ancient Terrestrial Carbonaceous Materials								
	6.5	Raman Mineralogy in Field Geology Studies								
		6.5.1 Extraterrestrial Exploration								
	6.6	Conclusion								
	Refer	rences	33							

x Contents

7			o-spectral Imaging of Cells and Intracellular Drug					
	Delivery Using Nanocarrier Systems							
	Miljković, Lara Milane, Amit Kale, Mansoor Amiji, Vladimir							
			Max Diem					
		,						
	7.1		ction					
	7.2							
		7.2.1	Data Acquisition					
		7.2.2	Introduction to Data Processing Methods					
		7.2.3	Experimental					
	7.3							
		7.3.1	Cell Imaging					
		7.3.2	Drug Delivery Systems					
	7.4		ion					
	Refe	rences						
8			nan Microscopy in Pharmaceutical Development 16:					
			efele and Kurt Paulus					
	8.1		etion					
		8.1.1	Vibrational Spectroscopy in Pharmaceutical					
			Development					
		8.1.2	Imaging in Pharmaceutical Development 169					
		8.1.3	Chemical Imaging in Pharmaceutical Development 172					
		8.1.4	Confocal Raman Microscopy in Pharmaceutical					
			Development					
	8.2		tions of Confocal Raman Microscopy in Pharmaceutical					
		Develop	oment					
		8.2.1	Practical Considerations					
		8.2.2	Investigation of Solid Dosage Forms by Chemical					
			Imaging					
	8.3	Conclus	sions					
	8.4	Materia	ls and Methods					
	Refe	rences						
9			ion of Therapeutic Coatings on Medical Devices 203					
		s Wormut						
			ound					
	9.2		Therapeutic Coatings					
		9.2.1	Coating Thickness					
		9.2.2	Swelling of Hydrophilic Gel Coatings					
	9.3		Therapeutic Coatings					
		9.3.1	Coating Morphology					
		9.3.2	Drug Mixed with Single Polymer: Morphology					
			and Elution					

Contents xi

		9.3.3	Drug Mixed with Two Polymers: Blending	216
		0.2.4	and Layering	
		9.3.4	Drug Mixed with Two Polymers: Exposure to Water	. 219
		9.3.5	Drug Mixed with Biodegradable Polymer: Drug Elution	220
		~	with Polymer Degradation	
	9.4		ry	
	Refer	rences		. 223
10	D	T	en of Diona Coll Walls	225
10		an 1mag urga Gier	ing of Plant Cell Walls	. 223
	10.1		ction	225
	10.1		ell Walls	
	10.2		Raman Spectroscopy of Plant Fibers	
	10.3		ell Wall Imaging by Confocal Raman Microscopy	
	10.4	10.4.1	· · · · · · · · · · · · · · · · ·	. 220
		10.4.1	in Wooden Cell Walls	220
		10.42		. 220
		10.4.2	Silica and Cell Wall Composition in Horsetail (E. hyemale)	222
	10.5	O411	(E. nyemaie)	
	10.5			
	10.6		and Methods	
	Refer	ences		. 233
11			nan Imaging of Polymeric Materials	. 237
	Ute S		Jörg Müller, and Joachim Koenen	
	11.1		ction	
	11.2		Imaging of Isotactic Polypropylene (iPP)	
	11.3	Raman	Imaging of Polymer Blends	. 244
		11.3.1	Raman Imaging of Thin Films of the Polymer Blend:	
			Polystyrene (PS)- Ethyl-Hexyl-Acrylate (EHA)	. 245
		11.3.2	Raman Imaging of Thin Films of the Polymer	
			Blend Ethyl-Hexyl-Acrylate (EHA)-Styrene-Butadiene	
			Rubber (SBR)	. 247
		11.3.3	Raman Imaging of Thin Films of the Polymer Blend	
			PS-EHA-SBR	. 249
	11.4	Polyme	r Coatings	. 251
		11.4.1	Acrylic Paints	. 251
		11.4.2	Adhesives	. 253
	11.5	Additiv	es in Polymer Matrices	. 253
	11.6		ry	
	Refer		······	
12	Stres	s Analys	is by Means of Raman Microscopy	. 259
	Thon	nas Werm	nelinger and Ralph Spolenak	
	12.1	Introdu	ction	. 259

xii Contents

	12.1.1	Theoretical Background	260
	12.1.2	Measuring in Conventional Back-Scattering	
		Configuration	261
	12.1.3	Off-Axis Raman Spectroscopy	263
	12.1.4	Stress Tensor Analysis in Back-Scattering	
		Raman Microscopy	266
12.2	Case St	rudies	268
	12.2.1	3D Raman Spectroscopy Measurements	268
	12.2.2	ZnO	271
	12.2.3	The Influence of Stress on the Peak Position	
		of Polymers	273
12.3	Discuss	sion	276
Refer	ences		277
Index			279

Contributors

Mansoor Amiji Department of Pharmaceutical Sciences and Center for Pharmaceutical Biotechnology and Nanomedicine, Northeastern University, Boston, MA 02115, USA, m.amiji@neu.edu

Tatyana Chernenko Department of Chemistry and Chemical Biology, Northeastern University, Boston, MA 02115, USA, nemosyne@gmail.com

Dana Cialla Institut für Physikalische Chemie, Friedrich-Schiller-Universität Jena, Helmholtzweg 4, D-07743 Jena, Germany, dana.cialla@uni-jena.de

Thomas Dieing Applications & Support, WITec GmbH, Lise-Meitner-Strasse 6, D-89081 Ulm, Germany, thomas.dieing@witec.de

Max Diem Department of Chemistry and Chemical Biology, Northeastern University, Boston, MA 02115, USA, m.diem@neu.edu

Benjamin Dietzek Institut für Physikalische Chemie, Friedrich-Schiller-Universität Jena, Helmholtzweg 4, D-07743 Jena, Germany; Institut für Photonische Technologien e.V., Albert-Einstein-Strasse 9, D-07745 Jena, Germany, benjamin.dietzek@uni-jena.de, benjamin.dietzek@ipht-jena.de

Marc Fries NASA Jet Propulsion Laboratory, 4800 Oak Grove Drive, Pasadena, CA 91001, USA, marc.d.fries@jpl.nasa.gov

Notburga Gierlinger Max-Planck-Institute of Colloids and Interfaces, Department of Biomaterials, Am Mühlenberg 1, D- 14476 Potsdam-Golm, Germany;

Johannes Kepler University, Institute of Polymer Science, Altenbergerstraße 69, A-4040 Linz, Austria, gierlinger@mpikg.mpg.de, notburga.gierlinger@jku.at

Thomas F. Haefele Novartis Pharma AG, Technical Research and Development, CH-4002 Basel, Switzerland, thomas.haefele@novartis.com, thaefele@hispeed.ch

Olaf Hollricher Research & Development, WITec GmbH, Lise-Meitner-Strasse 6, D-89081 Ulm, Germany, olaf.hollricher@witec.de

xiv Contributors

Wolfram Ibach WITec GmbH, Lise-Meitner-Strasse 6, D-89081 Ulm, Germany, wolfram.ibach@witec.de

Alain Jungen Micro and Nanosystems, ETH Zurich, Switzerland; Nicronex Consulting Ltd., Luxembourg, ajungen@ethz.ch, ajungen@nicronex.com

Amit Kale Department of Pharmaceutical Sciences and Center for Pharmaceutical Biotechnology and Nanomedicine, Northeastern University, Boston, MA 02115, USA, a.kale@neu.edu

Joachim Koenen WITec GmbH, Lise-Meitner-Strasse 6, D-89081 Ulm, Germany, joachim.koenen@witec.de

Christian Matthäus Department of Chemistry and Chemical Biology, Northeastern University, Boston, MA 02115, USA, c.matthaeus@yahoo.de

Lara Milane Department of Pharmaceutical Sciences and Center for Pharmaceutical Biotechnology and Nanomedicine, Northeastern University, Boston, MA 02115, USA, lara.milane@gmail.com

Miloš Miljković Department of Chemistry and Chemical Biology, Northeastern University, Boston, MA 02115, USA, milos.miljkovic@yahoo.com

Jörg Müller WITec GmbH, Lise-Meitner-Strasse 6, D-89081 Ulm, Germany, joerg.mueller@witec.de

Kurt Paulus Novartis Pharma AG, Technical Research and Development, CH-4002 Basel, Switzerland, kurt.paulus@novartis.com

Jürgen Popp Institut für Physikalische Chemie, Friedrich-Schiller-Universität Jena, Helmholtzweg 4, D-07743 Jena, Germany;

Institut für Photonische Technologien e.V., Albert-Einstein-Strasse 9, D-07745 Jena, Germany, juergen.popp@uni-jena.de, juergen.popp@ipht-jena.de

Luis Quintero College of Engineering, University of Puerto Rico, Mayagües, PR 00680, USA, luis.quintero@ece.uprm.edu

Ute Schmidt WITec GmbH, Lise-Meitner-Strasse 6, D-89081 Ulm, Germany, ute.schmidt@witec.de

Michael Schmitt Institut für Physikalische Chemie, Friedrich-Schiller-Universität Jena, Helmholtzweg 4, D-07743 Jena, Germany, michael.schmitt@uni-jena.de

Ralph Spolenak Laboratory of Nanometallurgy, Department of Materials, ETH Zurich, Switzerland, ralph.spolenak@mat.ethz.ch

Andrew Steele Geophysical Laboratory of the Carnegie Institution of Washington, 5251 Broad Branch Rd. NW, Washington, DC 20015, USA, asteele@ciw.edu

Vladimir Torchilin Department of Pharmaceutical Sciences and Center for Pharmaceutical Biotechnology and Nanomedicine, Northeastern University, Boston, MA 02115, USA, v.torchilin@neu.edu

Contributors xv

Thomas Wermelinger Laboratory of Nanometallurgy, Department of Materials, ETH Zurich, Switzerland;

Zürcher Hochschule für Angewandte Wissenschaften, Life Sciences and Facility Management, Einsiedlerstrasse 31, CH-8820 Wädenswil, Switzerland, thomas.wermelinger@mat.ethz.ch

Klaus Wormuth SurModics, Inc., 9924 West 74th St., Eden Prairie, MN 55344, USA, kwormuth@surmodics.com

Chapter 1 High-Resolution Optical and Confocal Microscopy

Olaf Hollricher and Wolfram Ibach

Abstract In this chapter, the theory of optical image formation in an optical microscope is described, and the difference between conventional and confocal microscopy is explained. The selection of the appropriate pinhole diameter is discussed in detail, as the pinhole diameter is crucial in obtaining the highest depth resolution as well as optimizing collection efficiency, because the Raman signal is typically very weak.

1.1 Introduction

More than 2000 years ago, Seneca¹ described the magnifying properties of water-filled glass spheres. Since that time, many researchers have known that all convex lenses can be used to magnify objects, but it took more than a millennium until further improvements led to the combination of several lenses to form an optical microscope. It is often said that Dutch spectacle maker Hans Janssen and his son Zacharias² were the first to develop the optical microscope by combining several lenses to form an optical microscope. It could, however, also have been the Dutch-German lens maker Hans Lippershey³ or even Galileo Galilei.⁴ Galileo combined a convex and a concave lens for his microscopes in 1609. Christiaan Huygens,⁵ also a Dutch scientist, developed the first achromatic objective in the late 17th century by combining two lenses of different kinds of glass, which was a big step forward.

Up to the 19th century, progress in quality and resolution was slow because microscopes were built using experience and trial and error, not using scientific knowledge.

¹ Lucius Annaeus Seneca the younger (* around 4 BC, † 65 AD).

² Zacharias Janssen (* around 1588, † around 1631).

³ Hans Lippershey (* around 1570, † September 1619).

⁴ Galileo Galilei (* 15.02.1564, † 08.01.1642).

⁵ Christiaan Huygens (* 14.04.1629, † 08.07.1695).

O. Hollricher and W. Ibach

Around 1873, Ernst Abbe,⁶ Prof. of Physics in Jena, Germany, developed his theory of optical image formation which was the basis of understanding the physics behind the optical microscope. His combined work with Carl Zeiss,⁷ who was a precision mechanic and Otto Schott,⁸ who had a PhD in chemistry and used his knowledge to develop glass with different optical properties, led to the development of the diffraction-limited optical microscope as it is known today. The resolution of the optical microscope remained nearly constant since the advent of Abbe's diffraction theory and is still about half of the wavelength of the excitation light.

During the 20th century, many new imaging techniques were introduced, such as fluorescence microscopy, interference microscopy, phase contrast, and dark-field illumination which made the optical microscope a powerful analytical tool, but the most important development of recent years is the confocal microscope.⁹

The principle underlying confocal imaging was patented by Marvin Minsky in 1957 (US patent 3013467), but it was not until the late 1980s that it became a standard technique. In confocal microscopy, a point-like light source (typically a laser) is focused onto the sample and the image of this spot is detected through a small pinhole in front of the detector. As the pinhole is located in the image plane of the microscope, the pinhole is confocal with the illuminating spot.

An image of the sample can only be obtained by either scanning the sample or the excitation spot point by point and line by line. This makes a confocal microscope much more complex than a conventional microscope, but the additional complexity is far outweighed by the advantage of having the detected light restricted to a small area around the focal point. Therefore, scattered light from above or below the focal point does not contribute to the image.

Although an increase in lateral resolution of a factor of ≈ 1.4 ($\sqrt{2}$) can be achieved by convolution of the excitation spot with the pinhole aperture, this resolution enhancement can only be achieved at a high price: the pinhole must be so small that 95% of the light is lost. The main advantage of confocal microscopy as compared to conventional microscopy is therefore the depth resolution and the much higher image contrast due to stray light suppression.

This chapter provides an introduction to the theory of confocal image formation. The first section describes the theory of image formation in an optical microscope and the differences between conventional and confocal microscopy are explained. The next section describes the choice of the appropriate pinhole diameter, suitable for highest depth and lateral resolution. Factors that need to be taken into account in order to achieve optimum results will also be explained.

⁶ Ernst Karl Abbe (* 23.1.1840, † 14.1.1905).

⁷ Carl Zeiss (* 11.9.1816, † 3.12.1888).

⁸ Otto Schott (* 17.12.1851, † 27.8.1935).

⁹ "Confocal" from "konfokal": (lat.) with equal focal points.

1.2 Introduction to Theoretical Considerations in High-Resolution Microscopy

All confocal imaging techniques, for example, confocal Raman microscopy or confocal two-photon microscopy are based on a point-to-point image formation. A detailed overview of these methods can be found in [1].

In this section, a theoretical background for this technique will be provided. The electromagnetic field distribution in the focus of an objective will be calculated, which is the starting point for the mathematical description of image formation. Furthermore, the fundamental difference between confocal microscopy and confocal Raman microscopy with its range of excitation possibilities will be discussed.

1.3 Introduction to Confocal Microscopy

In confocal microscopy, a point-like light source is focused with a lens or an objective onto a sample. The spatial extension of the focus spot on the sample is determined by the wavelength λ and the quality of the image formation. The image spot is then focused through the same (or a second) lens onto an aperture (pinhole) in front of a detector. The size of the pinhole is chosen so that only the central part of the focus can pass through the pinhole and reach the detector.

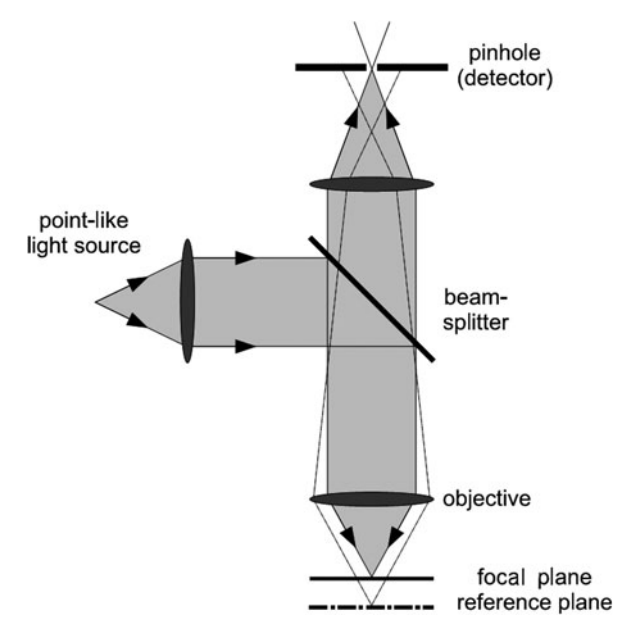


Fig. 1.1 Principal setup of a confocal microscope

One can see in Fig. 1.1 that rays that do not come from the focal plane will not be able to pass through the pinhole. From this simple geometric representation, two advantages of confocal microscopy can already be seen. First, through scanning of the sample with respect to the objective, a 3D image of the sample can be obtained. This is not possible in conventional microscopy. Second, only light from the focal plane will hit the detector. Therefore, image contrast is strongly enhanced.

Additionally, by choosing an appropriate pinhole diameter, the lateral resolution can be increased by up to a factor of $\sqrt{2}$.

1.4 Electromagnetic Scattering in Optical Systems

In this section, the basic principles necessary for calculating the field distribution in the focus are provided. A detailed discussion can be found in the articles of Wolf [2, 3]. Figure 1.2 shows the geometry used to illustrate this.

 S_0 is the origin of a monochromatic wave with frequency ω and S_1 its image obtained with geometric ray optics. The field distribution in the focus is described in the Cartesian coordinate system with origin in S_1 . Starting point is the Helmholtz equation

$$\Delta E + k^2 E = 0$$

which describes the space-dependent component of the electrical field:

$$\boldsymbol{E}(P,t) = \Re\left\{\boldsymbol{e}(P)\mathrm{e}^{-\mathrm{i}\omega t}\right\}$$

In general, the Helmholtz equation can be satisfied by

$$e(P) = \int_{-\infty-\infty}^{\infty} \int_{-\infty}^{\infty} e^{ik(s_x x + s_y y)} \left\{ U(s_x, s_y) e^{iks_z z} + V(s_x, s_y) e^{-iks_z z} \right\} ds_x ds_y \qquad (1.1)$$

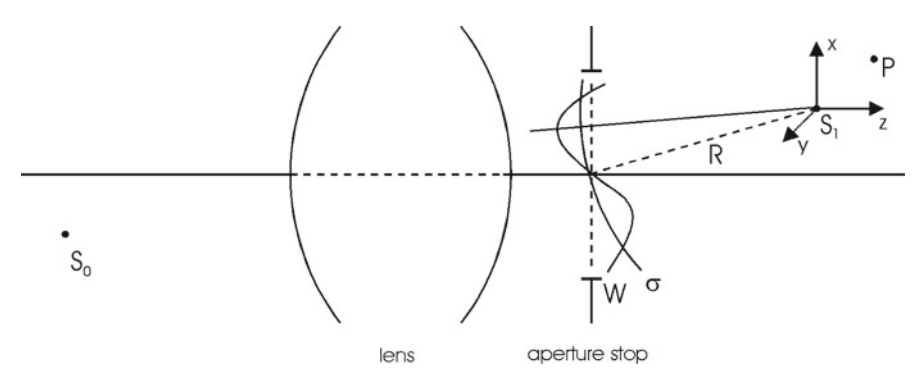


Fig. 1.2 Imaging geometry

where s_z is given by the condition $s_x^2 + s_y^2 + s_z^2 = 1$.

 $U(s_x, s_y)$ and $V(s_x, s_y)$ are arbitrary functions that have to fulfill the Kirchhoff boundary conditions. For the magnetic field

$$\boldsymbol{H}(P,t) = \Re\left\{\boldsymbol{h}(P)e^{-\mathrm{i}\omega t}\right\}$$

similar expressions can be found.

As described in [2], an approximate solution for the electrical field in the plane of the aperture can be found with the method of stationary phase. This leads to two general solutions:

$$e(P) = -\frac{\mathrm{i}k}{2\pi} \iint\limits_{\Omega} \frac{a(s_x, s_y)}{s_z} \mathrm{e}^{\mathrm{i}k\{\Phi(s_x, s_y) + s_x x + s_y y + s_z z\}} \mathrm{d}s_x \mathrm{d}s_y \tag{1.2}$$

$$\boldsymbol{h}(P) = -\frac{\mathrm{i}k}{2\pi} \iint_{\Omega} \frac{\boldsymbol{b}(s_x, s_y)}{s_z} \mathrm{e}^{\mathrm{i}k\{\Phi(s_x, s_y) + s_x x + s_y y + s_z z\}} \mathrm{d}s_x \mathrm{d}s_y$$
 (1.3)

Here, the functions $a(s_x, s_y)$, $b(s_x, s_y)$, and $\Phi(s_x, s_y)$ take the part of $U(s_x, s_y)$ and $V(s_x, s_y)$. These two functions have the following meaning.

The abberration function $\Phi(s_x, s_y)$ is a measure of how strongly the real wave front W deviates from the ideal spherical wave front σ . The factor $a(s_x, s_y)$ determines the amplitude of the field. In the geometrical optic, this is the intensity of the light beam. Along every beam $a(s_x, s_y)$ is independent of the position of the aperture.

All three numbers a, b, and Φ can be determined by ray-tracing algorithms.

Equations (1.2) and (1.3) represent the addition of planar waves inside the aperture. In contrast, using the Huygens – Fresnel principle one would add spherical waves.

1.5 3D-Intensity Distribution in the Focus

In the literature one can find two different descriptions for the field distribution in the focus. One describes the electrical field as a scalar and is correct only for small aperture angles. The vector description from Richards and Wolf [4] is more appropriate for the nature of light. Here, the field distribution is a function of the aperture angle α and therefore can also be applied to systems with large aperture angles.

If one compares small and large aperture angles one sees that the electrical energy density in the focal plane is no longer radially symmetric, but depends on the original polarization direction. Additionally, the energy density in the secondary maxima and minima gets larger.

1.5.1 Large Aperture Angles

For an abberration-free system $(\Phi(s_x, s_y) = 0)$, a system without wave front errors, all components of the electrical field in the focus can be derived from (1.2) and (1.3). To simplify the calculation the point S_0 (Fig. 1.2) is shifted to infinity. This point is the origin of an electrical field which is polarized in x-direction ($\phi_P = 0$). Therefore, the image of S_0 lies exactly in the focal plane of the lens S_1 . A change of the transmission of the lens due to its surface curvature, which could be calculated with the Fresnel formulas is neglected. Therefore, the surface curvature of the lens must be sufficiently small.

Because of the symmetry of the system, it is appropriate to change to spherical coordinates:

$$x = r_P \sin \theta_P \cos \phi_P$$
, $y = r_P \sin \theta_P \sin \phi_P$, $z = r_P \cos \theta_P$

The origin of the coordinate system is the geometrical focus point S_1 . We also change to so-called optical coordinates

$$u = kr_{\rm P}\cos\theta_{\rm P}\sin^2\alpha = kz\sin^2\alpha v = kr_{\rm P}\sin\theta_{\rm P}\sin\alpha = k\sqrt{x^2 + y^2}\sin\alpha$$
(1.4)

with

 $k=\frac{2\pi}{\lambda}$: absolute value of the wave vector $0^\circ < \alpha < 90^\circ$: half of the aperture angle

to eliminate the wavelength dependence. With these coordinates, the spatially dependent components of the electrical and magnetic fields can be written as

$$e_{x}(u, v) = -iA(I_{0} + I_{2}\cos 2\phi_{P})$$

$$e_{y}(u, v) = -iAI_{2}\sin 2\phi_{P}$$

$$e_{z}(u, v) = -2AI_{1}\cos \phi_{P}$$
(1.5)

$$h_{x}(u, v) = -iAI_{2}\sin 2\phi_{P} h_{y}(u, v) = -iA(I_{0} - I_{2}\cos 2\phi_{P}) h_{z}(u, v) = -2AI_{1}\sin \phi_{P}$$
(1.6)

Herein, I_0 , I_1 , and I_2 are defined over the integrals

$$I_{0}(u, v) = \int_{0}^{\alpha} \cos^{\frac{1}{2}} \theta \sin \theta (1 + \cos \theta) J_{0} \left(\frac{v \sin \theta}{\sin \alpha} \right) e^{iu \cos \theta / \sin^{2} \alpha} d\theta$$

$$I_{1}(u, v) = \int_{0}^{\alpha} \cos^{\frac{1}{2}} \theta \sin^{2} \theta J_{1} \left(\frac{v \sin \theta}{\sin \alpha} \right) e^{iu \cos \theta / \sin^{2} \alpha} d\theta$$

$$I_{2}(u, v) = \int_{0}^{\alpha} \cos^{\frac{1}{2}} \theta \sin \theta (1 - \cos \theta) J_{2} \left(\frac{v \sin \theta}{\sin \alpha} \right) e^{iu \cos \theta / \sin^{2} \alpha} d\theta$$

$$(1.7)$$

The parameter $A = \frac{kfl_0}{2} = \frac{\pi fl_0}{\lambda}$ is a constant containing the focal length f of the lens and the amplitude l_0 of the incoming light. The symbol J_n stands for the Bessel function of order n.

With these equations it is possible to calculate all properties that are important for microscopy. The electrical, magnetic, and total energy distribution have the forms

$$\langle w_{e}(u, v, \phi_{P}) \rangle = \frac{A^{2}}{16\pi} \left\{ |I_{0}|^{2} + 4|I_{1}|^{2} \cos^{2} \phi_{P} + |I_{2}|^{2} + 2 \cos 2\phi_{P} \Re(I_{0}I_{2}^{*}) \right\}$$

$$\langle w_{m}(u, v, \phi_{P}) \rangle = \frac{A^{2}}{16\pi} \left\{ |I_{0}|^{2} + 4|I_{1}|^{2} \sin^{2} \phi_{P} + |I_{2}|^{2} - 2 \cos 2\phi_{P} \Re(I_{0}I_{2}^{*}) \right\}$$

$$\langle w(u, v, \phi_{P}) \rangle = \frac{A^{2}}{8\pi} \left\{ |I_{0}|^{2} + 2|I_{1}|^{2} + |I_{2}|^{2} \right\}$$

$$(1.8)$$

As expected, the total energy density is independent of the angle ϕ_P . Not as obvious from the equations, but given by the symmetry of the arrangement is that the electrical energy distribution becomes the magnetic energy distribution when turned by 90° .

Also interesting is the Poynting 10 vector S that describes the energy flux density of the electromagnetic field in the propagation direction. Its time average can be calculated with the equations

$$\langle S_{x} \rangle = \frac{cA^{2}}{4\pi} \cos \phi_{P} \Im \{ I_{1} (I_{2}^{*} - I_{0}^{*}) \}$$

$$\langle S_{y} \rangle = \frac{cA^{2}}{4\pi} \sin \phi_{P} \Im \{ I_{1} (I_{2}^{*} - I_{0}^{*}) \}$$

$$\langle S_{z} \rangle = \frac{cA^{2}}{8\pi} \{ |I_{0}|^{2} - |I_{2}|^{2} \}$$

$$(1.9)$$

For the case of the electrical energy density (1.8) we will discuss what happens to the field distribution with increasing aperture angle. In Fig. 1.3 the electrical energy density is shown in the focal plane (u=0) for different aperture angles α as a function of the optical coordinate v. The case $\alpha=0^\circ$ corresponds to the case of Sect. 1.5.2, the transition to small aperture angles. For $\alpha=90^\circ$ the light comes from the complete half space. A cut through the center of the profile, as well as a 10-fold magnification is shown above and to the right of each graphic. The initial polarization of the electrical field is horizontal.

In Fig. 1.3 one can see that the electrical energy density drastically changes with increasing aperture angle. The width of the field distribution as a measure of the optical resolution becomes strongly anisotropic. In the cut through the center, parallel to the direction of polarization, one can see even for small aperture angles that the minima do not return to zero. The side maxima get larger with increasing aperture angle and reach a relative height of 4.3 % for $\alpha=90^\circ$. This is more than twice the value at $\alpha=0^\circ$ (1.8 %).

¹⁰ The Poynting vector was defined by John Henry Poynting.

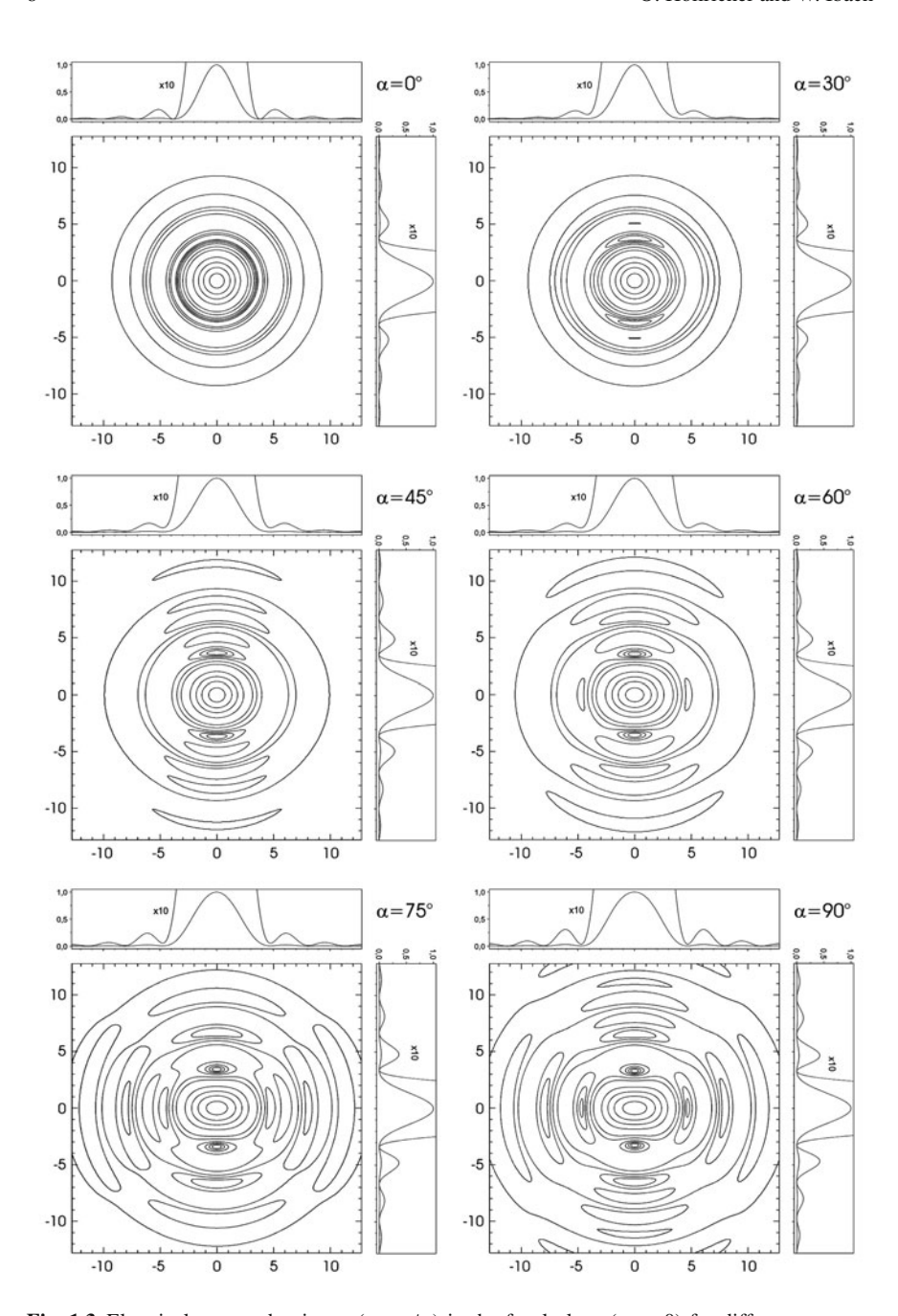


Fig. 1.3 Electrical energy density $w_e(u, v, \phi_P)$ in the focal plane (u = 0) for different aperture angles α as a function of v. The initial polarization of the electrical field is horizontal $(\phi_P = 0)$. The contour lines show the heights 0.002, 0.005, 0.01, 0.02, 0.05, 0.1, 0.3, 0.5, 0.7, and 0.9. A cut through the center of the profile and a 10-fold magnification are shown above and to the right of each graphic

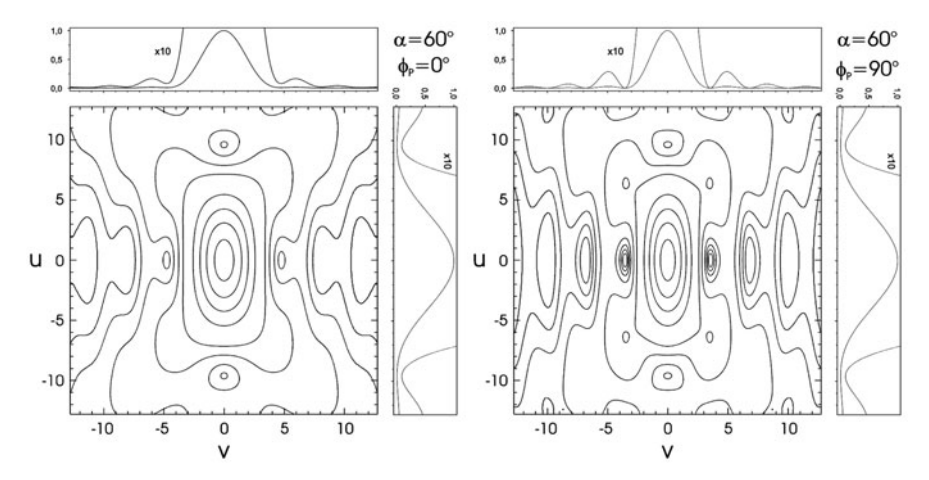


Fig. 1.4 A cut through the electrical energy density $w_e(u, v, \phi_P)$ for $\alpha = 60^\circ$. The optical coordinate u is plotted vertical, while the optical coordinate v is plotted horizontal. In the *left* image, the polarization of the electrical field is horizontal (in the image plane), while in the *right* image it is pointing out of the image plane. The contour lines show the heights 0.002, 0.005, 0.01, 0.02, 0.05, 0.1, 0.3, 0.5, 0.7, and 0.9

Figure 1.4 shows the field distribution in the axial direction. The figure shows a cut through the electrical field distribution w_e vertical to the focal plane. The position of the focusing lens would be above (or below) the figure. In the left image, the polarization of the electrical field is horizontal (in the image plane), while in the right image it is pointing out of the image plane.

Again one can see that the electrical energy distribution is highly anisotropic. Even in the axial direction the minima do not return to zero.

1.5.2 Transition to Small Aperture Angles

The theory in the last paragraph is appropriate to describe vector properties of light, but it is too complicated for a simple understanding. If one permits only small aperture angles I_1 and I_2 can be set zero, because for small x the relation $J_n(x) \sim x^n$ is fulfilled. Equations (1.5) and (1.6) simplify to

$$e_x = h_y = -iAI_0$$

$$e_y = e_z = h_x = h_z = 0$$

The initial polarization is preserved for small aperture angles. I_0 can be written so that the integral becomes independent of α

$$I_{0}(u, v) = \alpha^{2} e^{\frac{iu}{\alpha^{2}}} h(u, v)$$

$$h(u, v) = 2 \int_{0}^{1} \rho J_{0}(\rho v) e^{\frac{1}{2} iu\rho^{2}} d\rho$$
(1.10)

The function h(u, v) is called the 3D point spread function (PSF). It is normalized, so that h(0,0)=1. The PSF can be interpreted as a Greens function that describes the image of an infinitely small point. The approximation of small aperture angles simplifies the theoretical calculation, but is unfortunately coupled with a strong restriction. As a comparison, Fig. 1.5 shows the full width at half maximum (FWHM) of the electrical energy density at u=0 as a function of the aperture angle. The dashed line corresponds to the theory for small aperture angles, whereas the solid lines represent the correct theory for a cut parallel and vertical to the polarization direction. The width of the total energy density w (1.8) is shown as a dotted line. The total energy density w is better suitable for a comparison, because w is radially symmetric, as is the field distribution for small aperture angles.

As expected, all curves are equal for small aperture angles. With increasing α the difference between the curves becomes greater and greater. At an aperture angle of only $\alpha = 40^{\circ}$ the deviation between the curves is larger than 4%.

Oil- and water-immersion objectives cannot be adequately described by this theory, because their aperture angle is typically between 55° and 70° . For this case, the deviation of the FWHM is more than 10%.

In Fig. 1.5 one can also see that an increase in the aperture angle above 70° results in only a very small increase in resolution. A technical realization above this angle is therefore of little use.

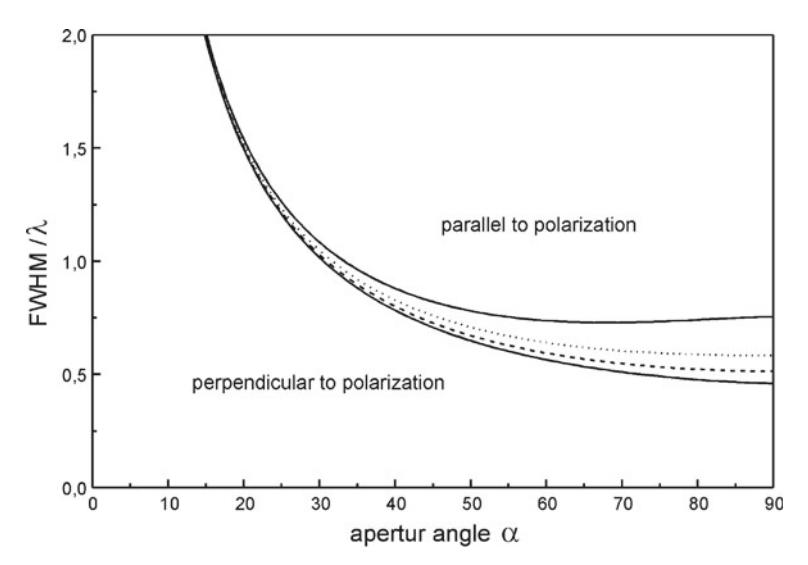


Fig. 1.5 Full width at half maximum (FWHM) of the field distribution in the focal plane; *solid lines*, electrical energy density; *dotted lines*, total energy density; and *dashed lines*, electrical or total energy density for small aperture angles

1.6 Theory of Image Formation

One of the most important properties of a confocal system is the point spread function (PSF), which is mainly determined by the microscope objective. This can be the electrical, magnetic, or total energy density in the focus. If a sample system couples only to the x-component of the electric field, the PSF of the excitation would only contain this component. The PSF of the detection can be different. This depends on the emitted light itself and on the properties of the detector. Of course it would be better if one could measure the PSF for every application. In this case, a deconvolution of the image would be possible without additional assumptions. In [5] a simple interferometric measurement setup is described that makes the measurement of the PSF possible. As a result, one not only finds the amplitude of the function h(u, v) but also the phase. The phase is especially important for a coherent image formation.

In the following paragraphs, h_1 stands for the PSF of the excitation and h_2 for the PSF of the detection. For simplification, both functions should be only scalar values. The modification of the light due to the sample can also be described by the scalar function $\tau(x, y, z)$. In general, τ is a complex function that influences the amplitude and phase of the electromagnetic field.

1.6.1 Microscope

The formation of the image in a microscope with point-like excitation and a large detector is far more complicated than the image formation in a confocal system (with a point-like detector). The reason is that the image formation is partially coherent. Both extremes can be mathematically described as follows:

$$I = |h_1|^2 \otimes |\tau|^2$$
 incoherent image formation (1.11)

$$I = |h_1 \otimes \tau|^2$$
 coherent image formation (1.12)

The difference between both cases is that for an incoherent image formation the intensities and for the coherent image formation the amplitudes have to be added. This difference can be illustrated with the following example. Consider the image formation of two points separated by the distance of the Rayleigh limit.¹¹

For the incoherent image formation, the two points are easily resolved (minimum). In the case of the coherent image formation, both points can no longer be separated (see Fig. 1.6).

¹¹ The Rayleigh criterion says that two points can be optically resolved if one point sits in the first minimum of the PSF of the second point.

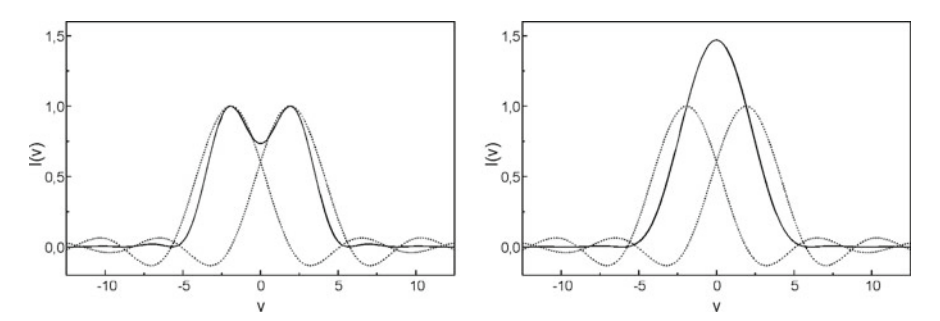


Fig. 1.6 Intensity distribution of two points that fulfill the Rayleigh criterion: *left*, incoherent image formation after (1.11); *right*, coherent image formation after (1.12)

The imaging quality of the detection described by function h_2 is not important here.

1.6.2 Confocal Microscope

Due to the point-like excitation and detection, the image formation in a confocal microscope must be described as coherent. This can be illustrated using the following equation after [6]:

$$I = \left| (h_1 h_2) \otimes \tau \right|^2 \tag{1.13}$$

The product $h_{\text{eff}} = h_1 h_2$ is called the effective PSF of the optical system. If one inserts the delta function $\delta(x)$ for τ , one gets the intensity point spread function. This function is plotted in Fig. 1.7 for a conventional and a confocal microscope. The FWHM differs roughly by a factor of $\sqrt{2}$.

1.6.3 Confocal Raman Microscope

The image formation of a confocal Raman microscope is strongly different from the case in Sect. 1.6.2. This is due to the nature of Raman scattering.

The Raman scattering is proportional to the excitation intensity $|h_1|^2$ and the Raman generation f(x, y, z). The resulting equation for the intensity distribution of the resulting image in a confocal Raman microscope is therefore [7]

$$I = |h_{\text{eff}}|^2 \otimes f \tag{1.14}$$

with

$$h_{\text{eff}} = h_1(u, v) h_2\left(\frac{u}{\beta}, \frac{v}{\beta}\right)$$
$$\beta = \frac{\lambda_2}{\lambda_1}$$

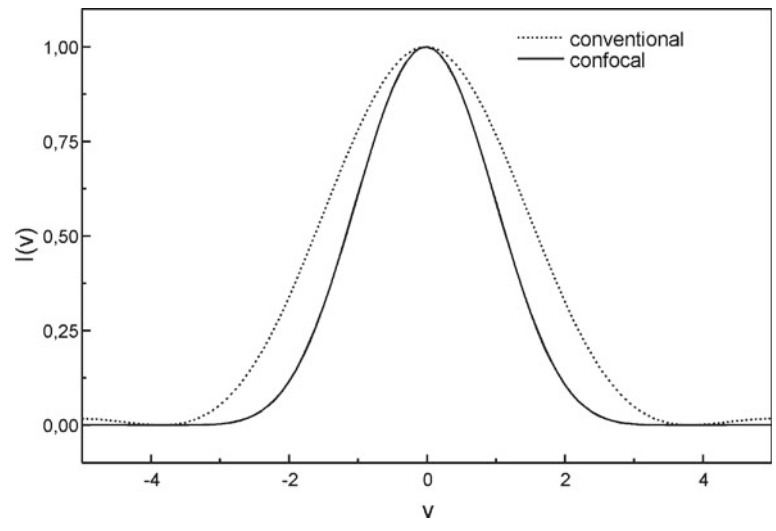


Fig. 1.7 Comparison of the intensity PSFs: $I_{\text{conventional}} = \left(\frac{2J_1(v)}{v}\right)^2$, $I_{\text{confocal}} = \left(\frac{2J_1(v)}{v}\right)^4$

The optical coordinates u and v refer to the wavelength λ_1 of the excitation light. This theory is not completely correct, because the wavelength of the Raman light has a certain frequency distribution and not only a single wavelength λ_2 . In principle, one must integrate over all Raman wavelengths. If the Raman wavelength is mostly distributed around a certain wavelength λ_x the error will be small if one replaces λ_2 with λ_x . A complete Raman spectrum is very complicated and for an exact solution the complete spectrum has to be taken into account.

1.7 Image Formation for Light Scattering

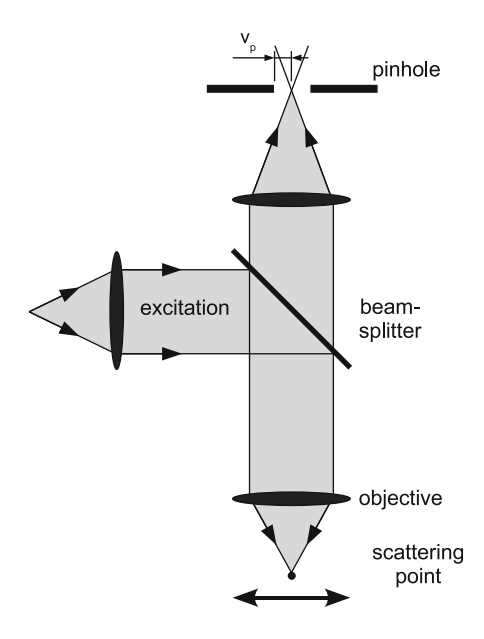
In the following two sections, the resolution of a confocal microscope as a function of pinhole size will be discussed. Since the achievable resolution strongly depends on the sample properties, these statements cannot be taken as valid in general but are true only under ideal conditions. For all calculations, the point spread function h(u, v) (1.10) was used.

1.7.1 Scattering Point

In the following, we consider the scenario of Fig. 1.8 in which a scattering point is scanned laterally across the excitation focus.

Up to now, all calculations have been performed for an infinitesimally small point detector. Now we replace this point detector with a real 2D detector of radius v_P .

Fig. 1.8 Confocal setup for a scattering point



This is the reason why the PSF h_2 in (1.15) has to be convolved with the detector function D to obtain the effective PSF for the detection.

Since we consider only a single scattering point in the object space, the convolution with the object itself is not necessary. After [8] we obtain the intensity distribution through

$$I = |h_1|^2 (|h_2|^2 \otimes D) \tag{1.15}$$

The FWHM of I(u = 0, v) is plotted in Fig. 1.9 as a function of the detector radius v_P . As can be seen, the detector radius should be below $v_P = 0.5$ for highest resolution. If the detector radius is larger than approximately $v_P = 4$, the resolution

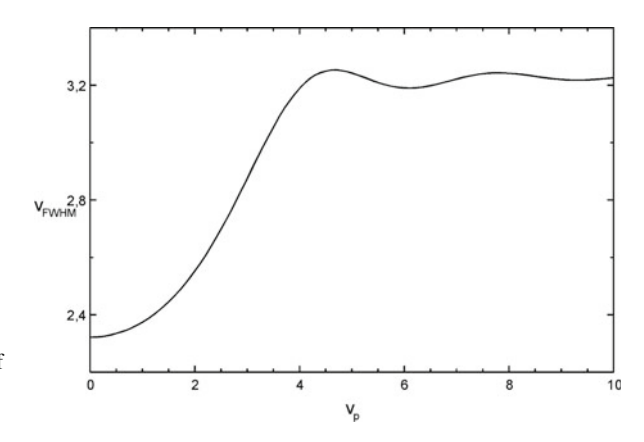


Fig. 1.9 Lateral resolution of a scattering point as a function of detector size v_P

will be the same as for conventional microscopy. Even in this case, stray light suppression remains as an advantage over conventional microscopy.

1.7.2 Reflection at a Mirror

The quality of the image can be easily checked by acquiring the signal while a mirror is scanned axially through the focus (Fig. 1.10).

Since the entire mirror plane reflects the light, the following integral [8] must be calculated:

$$I_{\text{plane}}(u) = \int_{0}^{v_p} |h(2u, v)|^2 v dv$$
 (1.16)

From Fig. 1.11 one can see that there is no loss in depth resolution up to a detector radius of $v_P = 2.5$. If the detector radius gets larger than $v_P = 3.5$ the depth resolution decreases linearly with increasing detector radius.

The depth resolution of a reflecting point shows a different behavior. For small detector radii, the resolution is worse than for a reflecting layer, but for larger radii the width becomes nearly constant. At $v_p = 10$, the depth resolution is no better than for a conventional microscope with point-like excitation, but if a homogeneous layer is investigated, no axial resolution is possible with a conventional microscope.

Since no lens abberrations are taken into account, (1.16) is symmetric to u = 0. In reality, the distribution usually looks different. There will be drastic deviations

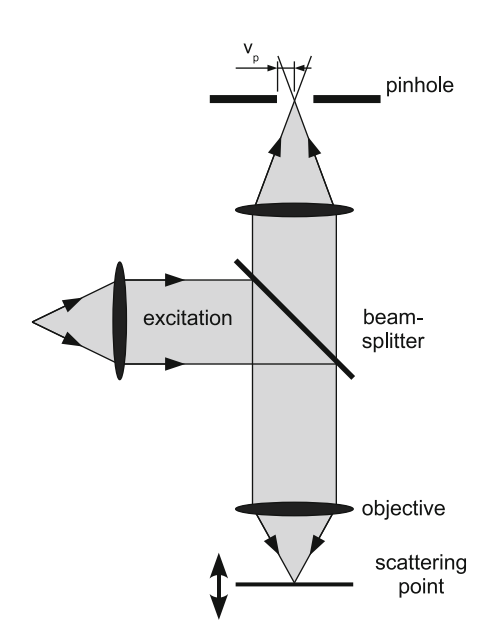
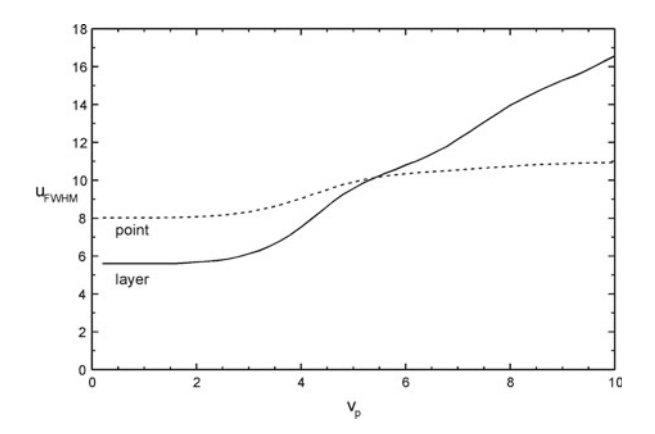


Fig. 1.10 Confocal setup for reflection at a mirror surface

Fig. 1.11 Comparison of the depth resolution for a point and a reflecting layer as a function of detector size v_P



if the setup is not optimized for the objective or the cover glass correction is not considered. An incorrect pinhole position is also immediately visible.

1.8 Image Formation for Raman Scattering

As discussed in Sect. 1.6.3, the image formation for Raman emissions is very different from the case of a scattering object. As an example, the resolution for a Raman emitting point and a Raman emitting layer will be calculated analogue to the last section.

1.8.1 Raman Emitting Point

Equation (1.14) is the basis for the curves shown in Fig. 1.12. v_P is the detector radius.

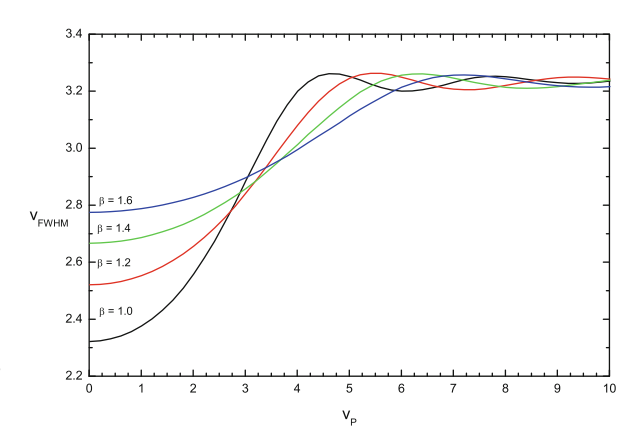


Fig. 1.12 Lateral resolution for a Raman emitting point as a function of detector size v_P for different β

The Raman emission wavelength is usually shifted by a certain factor relative to the excitation wavelength. This is taken into account by the parameter β , which is the ratio between the Raman and excitation wavelengths. For $\beta=1$ the resolution is the same as for a scattering point. With increasing shift of the Raman wavelength, the resolution decreases. If a small loss in resolution is accepted, one sees that the pinhole size should not be adjusted to the excitation, but to the Raman wavelength. If the wavelength shift is large, one should use a larger pinhole in order to avoid an unnecessary loss in signal.

For large pinhole sizes, all curves converge. Here again the case of a conventional microscope with point-like excitation is approached. In this case, the resolution is determined only by the excitation wavelength.

For 532 nm excitation, β is between 1 and 1.25, while for 785 nm excitation β can be as high as 1.4 (at 3600 rel. cm⁻¹).

1.8.2 Raman Emission of a Layer

The axial resolution at a Raman emitting layer differs strongly from the resolution at a reflecting surface. The reason is not mainly due to the wavelength shift but rather due to the incoherent image formation.

To calculate the axial point spread function $I_{CF}(u)$ of a Raman emitting layer in a confocal microscope, one must integrate over the intensity point spread function $I(u, v, \beta)$ (after [9]):

$$I_{\mathrm{CF}}(u) = \int_{0}^{\infty} I(u, v, \beta) v \mathrm{d}v$$

The best depth resolution achievable at a reflecting surface was u = 5.6, whereas the best depth resolution for a Raman emitting layer without a wavelength shift is only

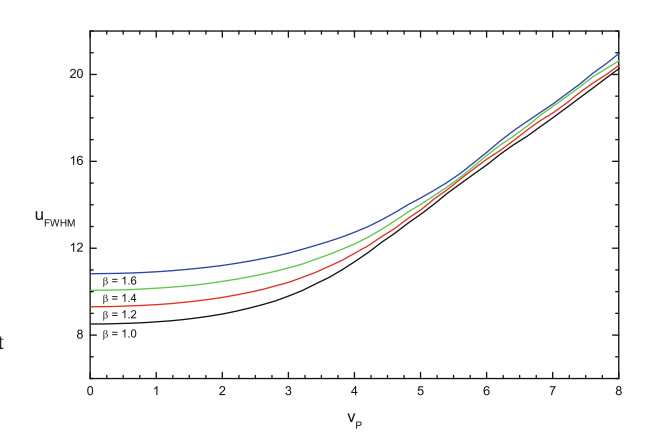


Fig. 1.13 Depth resolution at a Raman emitting layer for different β as a function of detector size v_P

u = 8.5 (Figs. 1.11 and 1.13). This becomes even worse with increasing wavelength shift β . Again, the detector size can be up to $v_P = 2.5$ without a loss in resolution.

1.9 Pinhole Size

Confocal microscopes typically have two output ports where one output port is equipped with an adjustable fiber coupler for multi-mode fibers or an adjustable pinhole. The core of the multi-mode fiber acts as a pinhole for confocal microscopy in the first case. The system needs to allow for lateral adjustment of the fiber so that maximum collection efficiency can be achieved.

The fiber additionally needs to be protected against mechanical strain and shielded from room light. With the fiber it is simple to direct the light to any detector, e.g., a PMT or a spectrometer.

The lateral position of the pinhole must be adjusted with micrometer precision (typical pinhole size 10– $100 \,\mu$ m) while the focus position is not very critical.

If ΔG is the object size and M the magnification of the objective, then the lateral image size is given by $\Delta B = \Delta G \cdot M$. But what about the axial magnification? From the image equation for thin lenses one gets the relation

$$|\Delta b| \approx |\Delta g| M^2$$

 $\Delta b \ll b$: image distance
 $\Delta g \ll g$: object distance (1.17)

Without the diffraction limit, an object of an axial extension of 200 nm would have a length of 2 mm in the image space at a magnification of M=100. Since the magnification M is quadratic in (1.17), the depth of focus is very high and the axial position of the pinhole is not critical.

The choice of the pinhole size is very important in Raman experiments. On one hand the signal should be as high as possible, while on the other hand the image should be confocal.

The size of the pinhole, in optical coordinates, should not exceed $v_{P_{\rm max}}=2.5$ to avoid a loss in z-resolution. To obtain the highest lateral resolution, the pinhole size should be below $v_{P_{\rm max}}=0.5$.

In practice, the pinhole size can be up to $v_{P_{\rm max}}=4$ without significantly changing depth resolution and up to $v_{P_{\rm max}}=2$ without significantly changing lateral resolution. As shown in Sect. 1.7.1, for $v_{P_{\rm max}}>4$, only the resolution of a conventional microscope remains.

For the experiment, the relation

$$\frac{M}{NA} \ge \frac{\pi d_0}{v_{P_{\max}} \lambda}$$

must be fulfilled, where M is the magnification, d_0 the diameter of the pinhole, and NA the numerical aperture of the objective. The left side of this equation is defined

by the objective and the beam path. In Table 1.1, the parameter $\frac{M}{NA}$ is calculated for several typical objectives.

Table 1.1 M/NA for different objective

Objective	10/0.25	20/0.4	40/0.6	60/0.8	100/0.9	100/1.25	100/1.4
M/NA	53	50	67	75	111	80	71

The right side of (1.9) is defined by the wavelength and the pinhole size itself (Table 1.2).

Table 1.2 $\frac{\pi d_0}{2.53}$ for typical wavelengths and pinhole sizes

2.070					
Wavelength (nm)	440	488	532	633	785
$d_0 = 10 \mu\text{m}$	29	26	24	20	16
$d_0 = 25 \mu\text{m}$	71	64	59	50	40
$d_0 = 50 \mu\text{m}$	142	129	118	99	80
$d_0 = 100 \mu \text{m}$	286	258	236	199	160
$d_0 = 200 \mu\text{m}$	571	515	472	397	320

With the help of these tables, the correct pinhole size can be determined for any experiment. If an objective with a magnification of $100\times$ and a numerical aperture of 0.9 is used at a wavelength of 633 nm, the optimum pinhole size would be 50 μ m for maximum depth resolution and 10 μ m for maximum lateral resolution.

In real experiments, one must usually find a compromise between resolution and collection efficiency. When a very small pinhole is used, the collection efficiency is strongly reduced. This is plotted in Fig. 1.14.

This graph shows the intensity on the detector as a function of pinhole size, normalized to the total intensity in the image plane (u = 0 in (1.16)). One can see that the collection efficiency is about 75% for maximum depth resolution ($v_P = 2.5$), but only 6% for maximum lateral resolution $v_P = 0.5$.

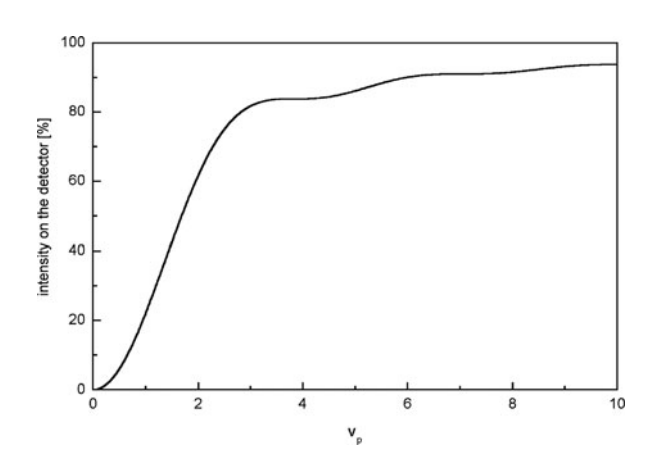


Fig. 1.14 Collection efficiency as a function of pinhole size normalized to the total power in the image plane

O. Hollricher and W. Ibach

For a scattering point (Sect. 1.7.1, $\beta=1$), the gain in resolution between using a pinhole size of $v_P=2.5$ and 0.5 is only about 16%, while for a Raman emitting sample with $\beta=1.2$ (Sect. 1.8.2) the gain in resolution is only about 8%, but for both cases the detected intensity is reduced by a factor of 12.5.

References

- J.B. Pawley, Handbook of Biological Confocal Microscopy, 2nd edn. (Plenum Press, New York, 1995)
- 2. E. Wolf, Proc. R. Soc. London A 253, 358 (1959)
- 3. E. Wolf, Proc. Phys. Soc. 74, 269 (1959)
- 4. B. Richards, E. Wolf, Proc. R. Soc. London A 253, 358 (1959)
- 5. R. Juškaitis, T. Wilson, J. Microsc. 189, 8 (January 1998)
- T. Wilson, Confocal Microscopy, Chap. IV.2. The imaging of simple objects (Academic, London, 1990) pp. 25–30
- 7. T. Wilson, *Confocal Microscopy*, Chap. IV.2. The imaging of simple objects (Academic, London, 1990) pp. 41–45
- 8. T. Wilson, A.R. Carlini, Opt. Lett. 12, 227 (April 1987)
- 9. C.J.R. Sheppard, M. Gu, Optik **86**(3), 104 (1990)

Chapter 2 Introduction to the Fundamentals of Raman Spectroscopy

Benjamin Dietzek, Dana Cialla, Michael Schmitt, and Jürgen Popp

Abstract The goal of this chapter is to provide a general introduction to the principles of Raman spectroscopy. The chapter will therefore begin with a theoretical description of the Raman effect, i.e., the classical electrodynamic treatment of Raman scattering, the discussion of the Raman intensities, and the quantum mechanical picture. Enhancement mechanisms for Raman microscopy will be discussed in the second part and resonant Raman as well as surface-enhanced Raman spectroscopy will then be explained in detail.

2.1 Introduction

During the last decade Raman spectroscopy has matured to become one of the most powerful techniques in analytical science due to its molecular sensitivity, its ease of implementation, and the fact that in contrast to IR absorption spectroscopy the presence of water is not hindering its applicability. The use of Raman spectroscopy originating in physics and chemistry has spread and now includes a variety of applications in biology and medicine revealing the molecular signature of diseases and individual bacteria, ultrafast spectroscopy to unravel the subpicosecond dynamics of structural rearrangements during chemical reaction and has reached for the stars – with the upcoming implementation of Raman spectrometers in the Mars missions of ESA and NASA [1]. Furthermore, latest developments have merged the chemical sensitivity and specificity of Raman scattering with the high spatial resolution of confocal microscopy yielding chemical images of a sample.

In this chapter, the fundamentals of Raman spectroscopy will be explained. First, we will discuss the classical picture of light scattering, which in the special case of inelastic scattering will correspond to Raman scattering. The classical discussion is followed by a quantum mechanical description of light scattering based on perturbation theory, and a description of effects, that enhances the weak Raman effect, like resonance Raman (RR) and surface-enhanced Raman scattering (SERS).

2.2 Classical Picture of Light Scattering

In this chapter, the classical picture of light scattering, i.e., the classical picture of interaction between an oscillating electromagnetic field and a molecular system, will be discussed. Generally, the primary incident electric field will disturb the electronic charge distribution in the molecule and thereby induce a dipole moment even in the case of an unpolar molecular system. The sum of the induced dipole moments will act as a macroscopic polarization, which represents the source for a secondary electric field irradiated by the molecules. This secondary field represents the scattered light. Within this quite general and qualitative framework it is clear that all scattering processes originate from the interaction of an electromagnetic field with the electronic subsystem of the sample. In order to understand how this interaction reveals information on the nuclear subsystem of the sample, i.e., structural information and normal coordinates, we will turn to a more quantitative yet still classical description of the matter – field interaction.

2.2.1 Frequency Dependence of Raman Scattering

This description starts with the formula for the induced dipole moment μ , which can be written as

$$\overrightarrow{\mu} = \widetilde{\alpha} \, \overrightarrow{E} \tag{2.1}$$

Here μ the molecular dipole induced by the external electric field E, which is characterized by its vector amplitude E_0 and its oscillation frequency ω_0 .¹ The real part of the field may thus be expressed as

$$\overrightarrow{E} = \overrightarrow{E}_0 \cdot \cos(\omega_0 t) \tag{2.2}$$

The proportionality factor between the external field and the induced dipole moment in (2.1) is the molecular polarizability, α , which is physically related to the extent to which the driving field is able to disturb the electron density of the sample out of its equilibrium configuration, i.e., the configuration in the absence of an external field.²

However, the polarizability of an electronic system is not a static quantity. Nuclear motion will modify the polarizability as the electron density adiabatically adjusts to the momentarily nuclear geometry to overall minimize the energy of the

¹ As in all practical modern applications of Raman scattering a laser is used as the excitation light source, the terms excitation light and laser light as well as excitation frequency, ω_0 , and laser frequency are used synonymously.

² We note that μ and E are vector quantities, while α represents a third-rank tensor. Keeping this in mind, vector notation is dropped from now on.

system. To formalize this effect, the polarizability is expanded into a Taylor series around the equilibrium nuclear geometry Q_0 , where Q represents the group of all individual normal modes q_0 .

$$\alpha = \alpha(Q) = \alpha_0 + \sum_{q=1}^{N} \left[\left(\frac{\partial \alpha}{\partial q} \right)_{q_0} \cdot q + \frac{1}{2} \left(\frac{\partial^2 \alpha}{\partial q \partial q'} \right)_{q_0 q'_0} \cdot q \cdot q' + O\left(q^3\right) \right]$$
(2.3)

In turn, oscillations with a characteristic frequency ω_q along each normal coordinate q can be excited, thus

$$q = q_0 \cdot \cos(w_q t) \tag{2.4}$$

Inserting (2.2) and (2.3) into (2.1) yields

$$\mu(t) = \left[\alpha_0 + \left(\frac{\partial \alpha}{\partial q}\right)_{q_0} \cdot q_0 \cdot \cos(\omega_q t)\right] \cdot E_0 \cdot \cos(\omega_0 t) \tag{2.5}$$

Here, without loss of generality, we reduced the sum over all normal modes to a representative mode q and further truncated the Taylor expansion in (2.3) after the term linear in the mode displacement. This approximation is referred to as electrical harmonic approximation. Using the trigonometric formula for the product of two cosine functions (2.5) can be re-written as

$$\mu(t) = \alpha_0 \cdot E_0 \cdot \cos(\omega_0 t) + \frac{1}{2} \left(\frac{\partial \alpha}{\partial q} \right)_{q_0} \cdot q_0 \cdot E_0 \cdot \cos\left[(\omega_0 - \omega_q) t \right]$$

$$+ \frac{1}{2} \left(\frac{\partial \alpha}{\partial q} \right)_{q_0} \cdot q_0 \cdot E_0 \cdot \cos\left[(\omega_0 + \omega_q) t \right]$$
(2.6)

This formula already constitutes the conceptual core of Raman scattering as a limiting case of general light scattering. As can be seen, the time-dependent induced dipole moment, which will act as a secondary source of (scattered) radiation, contains three distinct frequency terms:

- 1. The first one, $\alpha_0 \cdot E_0 \cdot \cos(\omega_0 t)$, oscillates at the same frequency as the incident radiation and thus will be responsible for scattered light at this frequency, i.e., elastic *Rayleigh scattering*. This term does not contain any information on the nuclear molecular degrees of freedom and is non-zero for all molecules due to the non-vanishing polarizability of the electronic molecular subsystem.
- 2. The second term in (2.6) oscillates with the difference between the laser and the molecular normal mode frequency. Hence, the radiation emitted by the induced

³ In the derivation presented here, molecular rotations are neglected as classical theory does not yield discrete excitation energies for molecular rotations.

dipole moment is red-shifted with respect to the excitation frequency. This term representing inelastic light scattering contains information about the molecular system via its dependence on ω_q . It is the source of the *Stokes scattering* that is usually presented as the Raman spectrum.

3. Finally, the time dependence of the third term is characterized by the sum $\omega_0 + \omega_q$. Thus, it represents a source for radiation, which is blue-shifted with respect to the laser frequency. This so-called anti-Stokes scattering is identical to the Stokes spectrum, but has a strongly reduced intensity due to the Boltzmann factor that describes the population of the thermally excited vibrational states.

2.2.2 Classical "Selection Rule" and Comparison to IR Absorption

In contrast to the elastic Rayleigh scattering, which classically depends on the equilibrium polarizability of the molecule, the inelastically scattered light stems from the non-zero derivative of the electronic polarizability at the equilibrium geometry along the qth normal coordinate, i.e., $\left(\frac{\partial \alpha}{\partial q}\right)_{q_0} \neq 0$. This relation provides an intuitive "selection rule" for Raman scattering of small molecules, which is useful in conceptually discriminating Raman scattering from infrared absorption.

Let us begin the discussion considering the symmetric stretching vibration of a homo-diatomic molecule, i.e., considering actually the only vibration of such molecule. Due to the symmetry of the system it does not have a permanent dipole moment in its equilibrium geometry. This zero-dipole moment is not changed upon small changes along the normal coordinate. Hence, the derivative of the dipole moment is zero and the vibration (see Fig. 2.1a) is not IR active.⁴

However, the polarizability of the molecule changes as a function of the nuclear displacement as can be qualitatively deduced from the limiting situations: ⁵ for zero internuclear distance the electron density resembles the density of a single atom, while at infinite internuclear distances the situation compares to two individual atoms of half mass. The latter having a larger polarizability than the former one. Thus, the polarizability can be expected to increase monotoneously along the normal coordinate and hence to have a non-zero derivative at the equilibrium position. In turn, the vibration is Raman active.

The situation is slightly more complex for the linear triatomic molecule considered in Fig. 2.1(b)–(d). In this case we shall consider the molecular dipole moment and polarizability in first–order approximation as the sum of bond dipole moments and bond polarizability, respectively. For the symmetric stretch vibration (Fig. 2.1b) the dipole moment changes as individual bonds are identical but opposite in sign yielding a constant dipole moment along the reaction coordinate. This results in

⁴ This is different for a hetero-diatomic molecule, which has a permanent dipole moment, whose derivative at the equilibrium position is non-zero.

⁵ For the derivation of a quantitative expression of the polarizability tensor the reader is referred to the section on the quantum mechanical picture of Raman scattering.

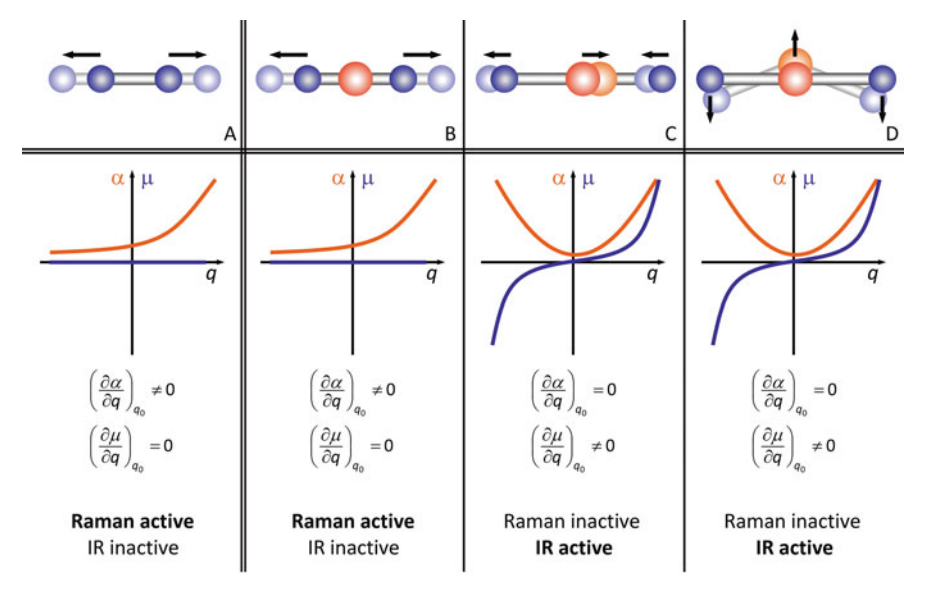


Fig. 2.1 The derivatives of polarizability (*red*) and dipole moment (*blue*) are schematically depicted for the normal modes of a two (a) and a three atomic molecule (b-d). Based on these intuitive considerations, conclusions on the IR and Raman activity of the modes can be drawn

no infrared absorption activity of this vibration. In contrast and according to the arguments presented for the homo-dinuclear molecule above, the molecular polarizability changes along the reaction coordinate giving rise to the Raman activity of this mode.

The situation is different for the antisymmetric stretching (Fig. 2.1c) and bending vibrations (Fig. 2.1d). In these cases it is obvious that the dipole moment will change sign, when the systems pass through the equilibrium configuration, thus $\left(\frac{\partial \alpha}{\partial q}\right)_{q_0} \neq 0$ and both vibrations are IR active. The changes of the polarizability along the mode are also non-zero but symmetric upon inversion of the sign of the reaction coordinate. Hence, the changes of the polarizability for small displacements can be approximated to be harmonic and $\left(\frac{\partial \alpha}{\partial q}\right)_{q_0} = 0$. Therefore, both the asymmetric stretch and the bending vibrations are Raman inactive. In principle, a similar conceptual approach of dissecting molecular dipoles and polarizabilities into bond dipoles and bond polarizabilities can be pursued for large molecules as well. However, this rapidly becomes cumbersome and is therefore not discussed further.

2.2.3 Scattered Raman Intensity

Having discussed the origin of the frequency dependence of the Raman spectrum and the classical "selection rules," we will now focus on a derivation of the

intensities observed in a Raman spectroscopic experiment. The considerations start from the oscillating induced dipole moment. For the simplicity of the discussion, we only consider the part of the dipole moment which oscillates at $\omega_0 - \omega_q$ and gives rise to the Stokes radiation:

$$\mu^{\text{Stokes}}(t) \propto \left(\frac{\partial \alpha}{\partial q}\right)_{q_0} \cdot q_0 \cdot E_0 \cdot \cos\left[(\omega_0 - \omega_q)t\right]$$
(2.7)

Each oscillating induced dipole serves as a Hertzian dipole, i.e., as an antenna emitting the secondary oscillation. The total power emitted by a Hertzian dipole is

$$P = \frac{|\ddot{\mu}|^2}{6\pi \cdot \varepsilon_0 \cdot c^3} = \frac{q_0^2}{12\pi \cdot \varepsilon_0 \cdot c^3} \cdot \left(\frac{\partial \alpha}{\partial q}\right)_{q_0}^2 \cdot \left(\omega_0 - \omega_q\right)^4 \cdot E_0^2 \tag{2.8}$$

In the second identity, a temporal average over the oscillating part of $|\ddot{\mu}|^2 \propto \cos^2(\omega t)$ has been performed. The scattered intensity observed in a Raman experiment is proportional to the overall power emitted by the induced dipole moment, hence

$$I_{\text{Stokes}} \propto \left(\frac{\partial \alpha}{\partial q}\right)_{q_0}^2 \cdot \left(\omega_0 - \omega_q\right)^4 \cdot E_0^2$$
 (2.9)

Equation (2.9), which together with (2.6) constitutes the central result of the classical discussion of Raman scattering, illustrates the dependence of the observed scattered intensity on molecular and experimental parameters. In order to be visible in a Raman spectrum, the molecular polarizability needs to change along the normal mode with a non-zero gradient at the equilibrium geometry. Thus, the gradient of the polarizability determines the Raman scattering intensity in contrast to the equilibrium polarizability, α_0 , which is roughly independent of the molecular species and influences the Rayleigh scattering term only. While $\left(\frac{\partial \alpha}{\partial q}\right)_{q_0}$ and ω_q provide molecular information about the system under study, ω_0 and E_0^2 are the experimental parameters that influence the intensities observed in the experiment. An increase of the laser power as well as the laser frequency will lead to more intense Raman scattering being observed.

Furthermore, (2.7) offers a roadway to the design of experiments with controlled Raman enhancement: resonance Raman spectroscopy and surface-enhanced Raman scattering. In resonance Raman scattering the laser frequency ω_0 is tuned into an electronic resonance of the system under study. The frequency dependence of $\left(\frac{\partial \alpha}{\partial q}\right)_{q_0}$, which becomes apparent only in a full quantum mechanical description of the molecular properties, then results in an increase of the scattered intensity and a reduction of spectral complexity compared to non-resonant Raman scattering. In

the case of surface-enhanced Raman scattering, the molecular species is brought into close contact with a metallic surface, which increases the Raman scattering cross-section by up to 15 orders of magnitude. As will be described in detail later, this effect is due to a combination of a field enhancement (E_0) and a chemical enhancement, which originates in surface-induced changes of the molecular polarizability.

2.2.4 Shortfalls of the Classical Picture

While the classical picture of light – matter interactions outlined above yields an intuitive understanding of the number of lines and line positions in a Raman spectrum and the relative amplitudes of Stokes and anti-Stokes lines, the non-quantized approach has some severe shortfalls. To give an obvious example, it does not provide any description for rotational Raman spectra for the simple reason that classical theory does not assign discrete frequencies to rotational transitions. Furthermore, a classical treatment does not offer a connection between the Raman scattering tensor $(\alpha_{ij})_k$ and the transition dipole moments, the molecular Hamiltonian and the frequency of the incident field. Thus, prominent and analytically important processes such as resonance Raman scattering and surface-enhanced Raman scattering are not explained within the classical theory. This information results naturally from a quantum mechanical perturbation theory approach to light – matter interactions and is considered in the following.

2.3 Raman Cross-Section Enhancement Mechanisms

The classical description of the scattered Raman intensity as presented in (2.9) provides an immediate starting point for the discussion of mechanisms to enhance the Raman scattering cross-section. As the enhancement of Raman scattering is of utmost importance for the detection of trace amounts of analytes abundant in biological samples [2, 3], contaminations found in products or pollutants in air [4, 5] or drinking water, the remainder of this chapter briefly introduces and discusses the two central and frequently used Raman enhancement mechanisms. The starting point of this discussion is (2.9), which reveals that the inelastically scattered intensity is proportional to the square of (i) the polarizability and (ii) the electric field. Consequently, the mechanisms routinely used to boost the Raman cross-section address these two entities and can be conceptually divided into resonance Raman scattering and surface-enhanced Raman scattering.

We will start the discussion reviewing the concepts of resonance Raman (RR) scattering and presenting two prominent applications from our group. Finally we will close this chapter by presenting the basics of surface-enhanced Raman scattering (SERS), surveying the variety of metallic substrates used in the application of SERS and highlight some biological applications of this intriguing technique.

2.3.1 Resonant Raman Scattering

In resonance Raman (RR) scattering the excitation wavelength is chosen to fall within an electronic absorption of the molecule under investigation (Fig. 2.2).

In this case and in contrast to non-resonant Raman scattering, not only inelastically scattered light but also fluorescence/luminescence is observed. As the cross-section for fluorescence is about six orders of magnitude larger than the resonance Raman cross-section the observation of Stokes scattered light is in many cases hampered by the presence of fluorescence. However, in cases of large fluorescence Stokes shifts (like in carbon nanotubes) or pre-resonant RR excitation wavelengths both processes can be observed. Another experimental approach to suppress fluorescence and obtain a pure RR signal is based on the different time dependences of both signals; while RR scattering originates from the excited-state wave packet prior to dephasing, it appears within a time window of roughly 20 fs after excitation. In contrast, typical fluorescence lifetimes are in the order of some hundred picosec-

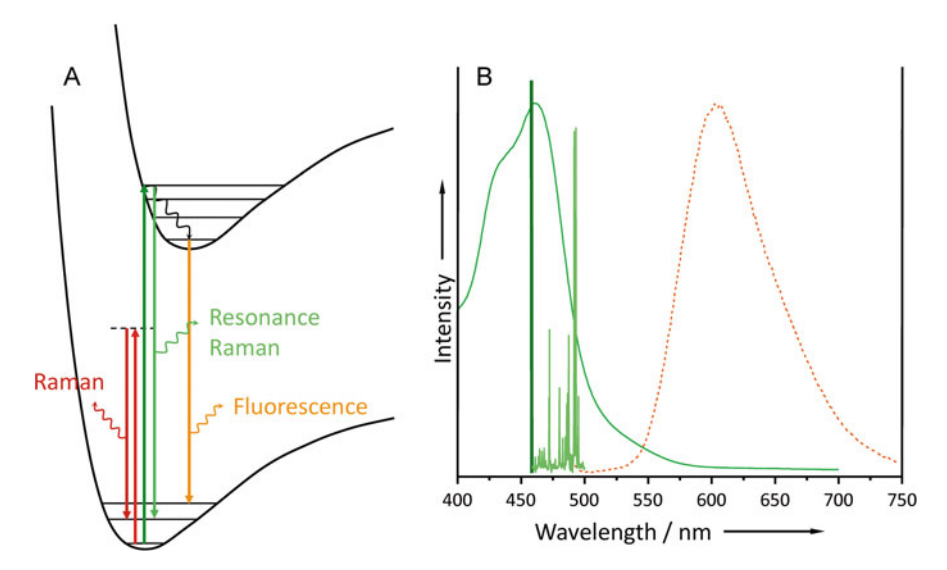


Fig. 2.2 (a) Energy level diagram and dipole transitions illustrating Raman, resonance Raman, and fluorescence. (b) Schematic comparison of absorption (*solid, green*) and emission spectrum (*dotted, red*) and a Raman spectrum excited in resonance (*light green*) with the ground-state absorption spectrum

⁶ It can be shown (see S. Mukamel, Principles of Nonlinear Optics and Spectroscopy, Oxford University Press (1995)) that in the case of no dephasing of the excited-state wavefunction RR scattering and fluorescence are identical. In the – in most experimental situations realistic – case of dephasing being present RR scattering is associated with the emission of the initial coherent excited-state wavefunction prior to dephasing, while fluorescence reflects the emission of the incoherent wavefunction after dephasing.

onds to nanoseconds. Hence, the use of an ultrafast Kerr shutter could enable the observation of the RR signal without emission contributions.

A more formalized description of RR scattering starts from (2.9) with the notion that the electric field is going to be treated classically, while the polarizability is given based on quantum mechanics and in particular perturbation theory [6]. In contrast to the notion in (2.9), it has to be kept in mind that α presents a complex-valued quantity. Thus within the quantum mechanical treatment, the absolute square of α enters the corresponding formula. As Raman scattering presents a two-photon process, second-order perturbation theory has to be applied. On this basis Kramer and Heisenberg (1925) and Dirac (1927) derived a quantum mechanical description of the molecular polarizability:

$$(\alpha_{\rho\sigma})_{fi} = \sum_{r} \left\{ \frac{\langle f | \mu_{\rho} | r \rangle \langle r | \mu_{\sigma} | i \rangle}{\hbar \omega_{ri} - \hbar \omega_{0} - i \Gamma_{r}} + \frac{\langle f | \mu_{\sigma} | r \rangle \langle r | \mu_{\rho} | i \rangle}{\hbar \omega_{rf} - \hbar \omega_{0} - i \Gamma_{r}} \right\}$$
(2.10)

In here, r and s denote the polarization of the incident and scattered light, respectively, while $|i\rangle$, $|r\rangle$, and $|f\rangle$ refer to the initial, intermediate, and final states of the Raman scattering process, ω_0 is the laser frequency, and ω_{ri} , ω_{rf} quantify the energetic differences between the respective states. The damping constant Γ_r has been introduced phenomenologically in order to mimic the homogeneous line widths of the respective band. While the first term in the sum represents the "intuitive" order of events within the scattering process, i.e., the "absorption" of a photon is followed by "emission" of the Stokes photon, the second term represents the reversed order of events, i.e., the Stokes photon is "emitted" prior to the interaction of the system with the pump, and formally follows from perturbation theory.

If – as in the case of RR scattering – the excitation wavelength is chosen to be resonant with a molecular electronic transition, the denominator of the first term becomes small and this term dominantly contributes to the molecular polarizability and thus to the observed Raman scattering. Under these circumstances, the polarizability is determined by the transition dipoles of the two transitions involved in the process and the lifetime of the intermediate state, which is inversely proportional to Γ . Hence, in electronic resonance

$$(\alpha_{\rho\sigma})_{fi} = \sum_{r} \left\{ \frac{\langle f | \mu_{\rho} | r \rangle \langle r | \mu_{\sigma} | i \rangle}{\hbar \omega_{ri} - \hbar \omega_{0} - i \Gamma_{r}} \right\}$$
(2.11)

This expression can be further simplified by invoking the Born – Oppenheimer approximation, i.e., factorization of the total wavefunctions $|i\rangle$, $|r\rangle$, and $|f\rangle$ into an electronic part $|\varepsilon_g\rangle$, $|\varepsilon_e\rangle$ and a vibrational wavefunction $|v_{i,f,r}\rangle$. Hence,

$$|i\rangle \approx |\varepsilon_g\rangle \cdot |v_i\rangle$$

$$|r\rangle \approx |\varepsilon_e\rangle \cdot |v_r\rangle$$

$$|f\rangle \approx |\varepsilon_g\rangle \cdot |v_f\rangle$$
(2.12)

Furthermore, the Herzberg – Teller and Condon approximations are invoked, which involve a Taylor expansion of the transition dipole moment as a function of the vibrational coordinates and a truncation of the expansion after the constant term. Hence, the transition dipole moment is assumed to be independent of nuclear displacement. Formally, the combination of both the Herzberg – Teller and the Condon approximations yields

$$\langle f | \mu_{\rho} | r \rangle = \langle v_{f} | \langle \varepsilon | \mu_{\rho} | \varepsilon' \rangle | v_{\varepsilon'} \rangle$$

$$\approx \overline{\mu_{\rho, \varepsilon \varepsilon'}^{(0)}}$$

$$\langle r | \mu_{\sigma} | i \rangle = \langle v_{\varepsilon'} | \langle \varepsilon' | \mu_{\sigma} | \varepsilon \rangle | v_{i} \rangle$$

$$\approx \overline{\mu_{\sigma, \varepsilon' \varepsilon}^{(0)}}$$
(2.13)

and hence the polarizability

$$(\alpha_{\rho\sigma})_{fi} = \sum_{\varepsilon'} \overline{\mu}_{\rho\varepsilon\varepsilon'}^{(0)} \overline{\mu}_{\rho\varepsilon'\varepsilon}^{(0)} \sum_{v_{\varepsilon'}} \frac{\langle v_f | v_{\varepsilon'} \rangle \langle v_{\varepsilon'} | v_i \rangle}{\hbar \omega_{ri} - \hbar \omega_0 - i \Gamma_{\varepsilon'v_{\varepsilon'}}}$$
(2.14)

as well as the vibronic part of the polarizability tensor, which we are concerned about in the context of Raman spectroscopy:

$$(\alpha_{\rho\sigma})_{fi} = \sum_{\epsilon'} \frac{\langle v_f | v_{\epsilon'} \rangle \langle v_{\epsilon'} | v_i \rangle}{\hbar \omega_{ri} - \hbar \omega_0 - i \Gamma_{\epsilon' v_{\epsilon'}}}$$
(2.15)

While (2.10), (2.11), (2.12), (2.13), (2.14), (2.15) allow an immediate grasp of the physics behind RR scattering, it is extremely cumbersome to evaluate the formulas quantitatively as the sum has to be performed over all possible, i.e., real and virtual, intermediate states. To obtain a description of the RR cross-section that is numerically easier to tackle, the Fourier transformation of the *sum-over-states* approach of Kramer, Heisenberg, and Dirac is reconsidered. This procedure yields the time-dependent description of RR scattering with

$$\left(\alpha_{\rho\sigma}\right)_{fi} = \frac{i}{\hbar} \int_{0}^{\infty} \langle v_f | v_i(t) \rangle e^{i(\omega_0 + \omega_i)t - \Gamma t} dt$$
 (2.16)

Equation (2.16) relates the RR scattering cross-section to the time-dependent overlap of the excited-state vibrational wavefunction $|v_i(t)\rangle$ with the final ground-state wavefunction $|v_f\rangle$. The time dependence of this quantity derives from the fact, that upon interaction with the electronically resonant pump photon, the initial ground-state wavefunction $|v_i\rangle$ is transferred to the electronically excited state. In this electronic potential $|v_i\rangle$ does not represent an eigenfunction of the Hamiltonian and consequently the propagation with the excited-state Hamiltonian \hat{H}_{ex} results in a

structural change of the wavefunction over time:

$$|v_i(t)\rangle = e^{\frac{i\hat{H}_{ex}t}{\hbar}} \left| v_i \right\rangle \tag{2.17}$$

It can be shown that $\langle v_f | v_i(t) \rangle$ and thus the RR cross-section is directly proportional to the displacement parameter Δ which is a measure of how far a molecule has to move in one state in order to reach the geometry of the other state.

Hence, those modes which undergo the largest geometry change upon electronic excitation are visible in the spectrum. These are the modes which are coupled to the absorption and show the steepest gradient at the Franck – Condon point of absorption. Thus, quantitative RR band analysis allows for the characterization of the excited-state geometry [7, 8], while non-resonant Raman scattering is limited to study ground-state structures of molecules.

Besides its intrinsic potential to study the structure of electronically excited states, RR scattering offers some further advantages in analytics as the resonance enhancement of the Raman cross-section boosts the intensity of the scattered light by up to eight orders of magnitude and consequently leads to a drastic improvement of the signal-to-noise ratio. Thus, the detection of analytes is possible in concentrations a couple of orders of magnitude lower than in non-resonant Raman scattering. Furthermore, only those modes are resonantly enhanced, that are coupled to the electronic excitation, which leads to a drastic reduction of the spectral complexity. Finally, RR offers advantages in studying mixtures of various analytes and chromophores as, by tuning the excitation wavelength into the absorption of a particular analyte, only the vibrational modes of this particular molecular system will become visible in the spectrum. The selective excitation of chromophores in RR scattering is furthermore of utmost advantage, when studying systems of more than a single chromophore in biological or biomimetic systems. It is not uncommon that chromophore-selective excitation is relevant for the biological/biomimetic function of a system. Therefore, it is extremely important to study the excited-state geometries and ultrafast initial dynamics of individual subunits of a larger system.

In conclusion, RR extends the potential of non-resonant Raman scattering to interrogate molecular structure to the study of excited-state structure and ultrafast sub-20 fs dynamics upon photoexcitation. Employing a pump wavelength within an electronic resonance of a molecular species boosts the Raman cross-section of the modes, which are coupled to the particular electronic transition. Thereby, the RR spectrum is less complex and concentration of analytes several orders of magnitude lower than compared to non-resonant Raman scattering can be detected.

2.3.2 Advantages and Applications of Resonance Raman Scattering

Since resonance Raman scattering occurs via enhanced scattering involving an excited electronic state, the technique can be used to gain information about the

molecular structure and dynamic of the excited electronic state. From the excitation profile (plot of intensity of resonantly enhanced modes vs. excitation wavelength) one can determine the strength of the interactions between the electronic excited state and the vibrational modes, the atomic displacement Δ between ground and excited state, and thus the change in bond length and bond angles when going from the ground to the excited state. From the overtone progression of totally symmetric vibrations, or combinations of them, the anharmonicity constant and harmonic frequencies of the appropriate vibrations can be calculated [9, 10]. However, resonance Raman spectroscopy is used not only because of its high power for photochemical analysis but rather because of its high sensitivity and selectivity. By electronic resonance enhancement the intensity of the scattered light can be increased by a factor of 10⁶ compared to non-resonant Raman excitation. This improves the signal-tonoise ratio and allows the detection of substances in solution at low concentrations $(10^{-3} - 10^{-5} \,\mathrm{M})$. As the enhancement results from a coupling of the vibrational modes (most of the time totally symmetric vibrational modes) to an electronically excited state, it is possible to exclusively select vibrational modes from certain chromophores by choosing an appropriate wavelength. Figure 2.3 illustrates this selectivity for guanosine-5'-monophosphate as an example.

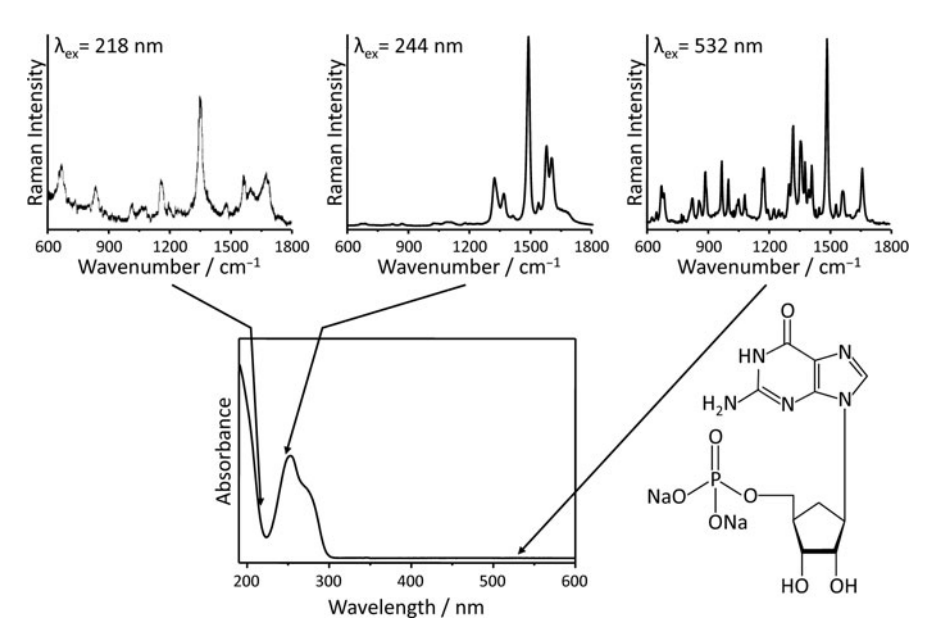


Fig. 2.3 Selectivity of resonance Raman spectroscopy. *Bottom*: UV/vis absorption spectrum of guanosine-5'-monophosphate (structure shown on the *right*). The *arrows* mark three different excitation wavelengths applied to record the Raman spectra. *Top*): the off-resonance Raman spectrum excited at 532 nm on the *right* and the resonance Raman spectra excited at 244 nm (*middle*) and 218 nm (*left*) involving two different electronic transitions (spectrum excited at 218 nm taken from [11])

By varying the Raman excitation wavelength to be resonant with different electronic transitions, selective excitation of different chromophores is possible. The off-resonance Raman spectrum excited at 532 nm (top right in Fig. 2.3) shows a very complex vibrational structure, since all Raman-active vibrations contribute to this spectrum. When exciting at 244 nm, only those vibrational bands are enhanced that couple to the $\pi - \pi^*$ transition centered around 253 nm. The spectrum is much simpler and special focus can be put selectively on those enhanced vibrations. A different enhancement pattern is found in the resonance Raman spectrum excited at 218 nm allowing one to investigate a different site within the molecule. This site specificity due to the application of different Raman excitation frequencies allows the study of smaller subunits in larger assemblies, as, e.g., probing the active center in proteins which is pivotal for the function of the respective molecules, or the selective excitation of macromolecules such as proteins or DNA in the presence of other molecules, as, e.g., in whole cells. The simplification of rich vibrational spectra from complex systems can also reduce the overlap of vibrational bands. When using excitation wavelengths in the deep UV (< 250 nm), fluorescence, which is often a problem in biological samples, is energetically far enough away from the scattered light and does not interfere with the Raman signal. This is illustrated in Fig. 2.4.

In case resonance Raman spectroscopy occurs via the same electronic excited states where the fluorescence emission originates (Fig. 2.4a), the Raman signals are often masked by the broad and featureless fluorescence spectra. This is especially the case when the Stokes shift, i.e., the energy difference between the absorption maximum and the fluorescence maximum, is only small (Fig. 2.4c). In UV resonance Raman spectroscopy, energy-rich UV light is used, so that higher electronic excited states are incorporated. Raman scattering occurs within the first few femtoseconds (10^{-15} s) directly from the high electronic state. The fluorescence process occurs only on a time scale of nanoseconds (10^{-9} s) and therefore the molecule can relax to the lowest excited electronic state via radiationless processes.

Since fluorescence occurs in most cases from the lowest energy excited state (Kasha's rule), the Raman and fluorescence signals are well separated on the energy scale as shown in Fig. 2.4b. The high sensitivity, selectivity, and the absence of interfering fluorescence brought forth various applications of the resonance Raman technique in biological, biochemical, and medicinal research in the last years. The techniques were successfully applied to study DNA conformation, native structures of proteins and peptides, the local environment of biological chromophores (such as hemoglobin, bacteriorhodopsin, carotinoids, just to name some of them [12–23]) in situ and in dilute aqueous solutions, and for the differentiation and identification of various bacteria, fungi, and algae [24–26].

Despite all the advantages experimental difficulties arise due to strong absorption of the excitation light which can cause thermal decomposition and unwanted photoreactions of the sample. Reabsorption of the scattered light makes a quantitative evaluation of the Raman intensity difficult and internal standards have to be used [27].

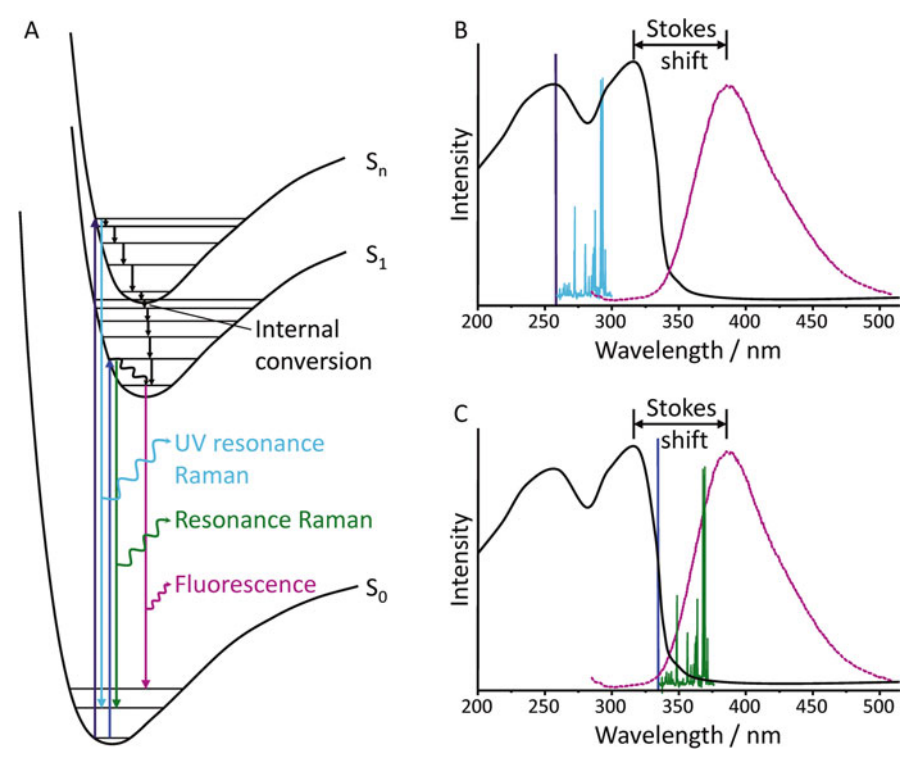


Fig. 2.4 Resonance Raman spectroscopy and fluorescence. (a) Energy level diagram (*dark blue arrows*: excitation, *light blue* and *green arrows*: Raman scattering, *pink*: fluorescence), (b) excitation to higher electronic states. Fluorescence and Raman signals do not interfere, (c) excitation at the high-wavelength edge of the absorption band. The Stokes shift is small and therefore the Raman and fluorescence signals overlap

2.3.3 Surface-Enhanced Raman Scattering

Since its first observation by Fleischmann and coworkers in 1974 [28], surface-enhanced Raman scattering (SERS) has matured into a widely used analytical tool in spectroscopy and microscopy [29, 30]. SERS was first observed for pyridine adsorbed on a silver electrode in an electrolyte cell. Subsequent experiments concluded an enhancement of the Raman scattering by roughly five orders of magnitude [31, 32].

Since SERS has been reported for molecules adsorbed on metallic structures formed of, e.g., silver, gold, aluminum, copper, palladium, and platinum [33, 34], an empirical correlation between the surface roughness of the metallic structure and the SERS enhancement has been established [30, 35, 36]. Especially adsorbance of a molecule on noble metal nanoparticles with strong surface curvature and roughness enhances its Raman scattering cross-section by up to 15 orders of magnitude. At the same time the complexity of the Raman spectrum is typically reduced down to

some prominent marker bands. Enhancement factors of up to 10^{15} ultimately allow for the detection of Raman signals from single molecules [37, 38] and sparked the use of SERS as an analytical tool in living-cell diagnostics [39, 40] and nanosensors [41, 42].

2.3.3.1 Enhancement Mechanisms

As discussed above, Raman scattering can be classically understood on the basis of induced dipole moments. Therefore, the Raman intensity corresponds to the total power emitted by such Hertzian dipole and is thus proportional to the square of the second time derivative of the induced dipole moment μ . μ itself is defined as product of the molecular polarizability α and the electromagnetic field of the incident laser beam E (see (2.1)). This gives rise to two complementary and multiplicative enhancement mechanisms, the interplay of which is still subject to discussions. The two conceptually distinct mechanisms, which are conventionally considered to account for the SERS effect, are (1) an electromagnetic mechanism for an enhancement of E and (2) a chemical mechanism for an enhancement of E:

1. Electromagnetic enhancement, which accounts for enhancement factors of up to 10¹¹, results from the excitation of localized surface plasmons within the metal nanoparticles which serve as SERS substrates. The metallic nanoparticles are smaller in size than the wavelength of the excitation light, i.e., typically sizes of up to 100 nm are used. Thus they act as dipoles, in a qualitative same way as the molecules in the Raman scattering process discussed above, and constitute the source for localized strong fields. The excited surface plasmons enhance both the local laser field experienced by a molecule, E₀, and the Stokes-shifted light scattered by the molecule. Thus, the nanoparticle acts as an antenna efficiently amplifying the Raman signal [43, 44].

The simplest formalized treatment of the electromagnetic mechanism involves the quasistatic treatment of an isolated metallic nanosphere (dielectric constant ε_i) embedded in a surrounding medium (dielectric constant ε_0). In Fig. 2.5 a schematic illustration is depicted. The incident laser light excites a plasmon on the surface of the nanoparticle.

The localized surface plasmon (LSP) resonance is characterized by the frequency, with which the plasmon oscillates locally on the surface of the nanoparticle. The nanoparticle itself acts as an antenna and the LSP irradiates a strong electromagnetic field \overrightarrow{E}_{LM} directly on the surface of the nanoparticle with a range of a few nanometers, which in the quasistatic approximation for an isolated nanosphere can be described as

$$E_{LM}^2 = E_0^2 |g|^2 \left(1 + 3\cos^2\theta \right) \tag{2.18}$$

wherein E_0 denotes the amplitude of the incident electromagnetic field and θ the angle relative to the applied field direction. The angle dependence encoded in (2.18) relates to the fact that in the approximation used the nanoparticle acts as

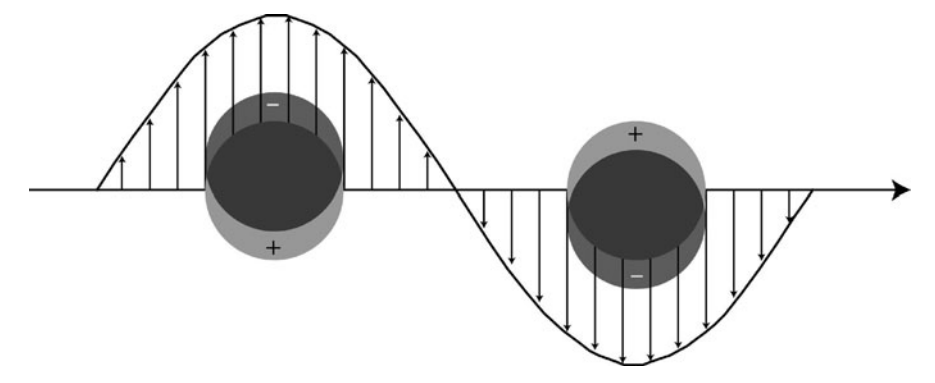


Fig. 2.5 Oscillation of free charges upon excitation of a localized surface plasmon in a metal nanoparticle. The *arrows* indicate the electric field

a Hertzian dipole and reflects the latter irradiation characteristics. The important factor $g=\frac{\varepsilon_i-\varepsilon_0}{\varepsilon_i+2\varepsilon_0}$ reveals that the strongest field enhancement, i.e., the largest values of E_{LM}^2 for a given experimental geometry, is observed if the plasmon resonance relation is met, i.e., $\Re(\varepsilon_i)\approx -2\varepsilon_0$ and $\Im(\varepsilon_i)<<1$. In theory, the proportionality between the field strengths of the LSP irradiation and the incoming field shows that extremely high Raman scattering intensities of molecules close to the surface can be achieved. However, an attempt to experimentally do so is often impractical due to burning of the sample [45, 46].

Not only the incident electric field is amplified by the LSP. Additionally, the Raman scattered light of analyte molecules in close proximity to the surface, \overrightarrow{E}_{Dip} , can be interacting with the induced electromagnetic field \overrightarrow{E}_{LM} on the nanoparticle surface and yields in \overrightarrow{E}_{SC} . Thus the SERS intensity is additionally enhanced by the contribution of \overrightarrow{E}_{Dip} and \overrightarrow{E}_{SC} [46]. See Fig. 2.6 for an illustration.

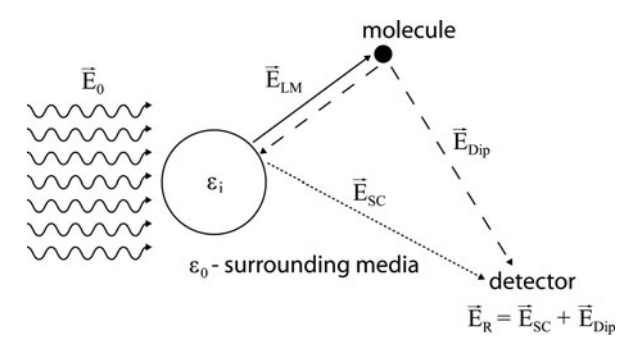


Fig. 2.6 Schematic illustration of the origin of electromagnetic enhancement of Raman scattering for molecules in close proximity to a nanoparticle surface

2. Chemical enhancement on the other hand can be understood as a surface-induced resonance Raman effect resulting from the chemisorption of a molecule on the metal surface. Due to chemisorption, the electronic structure of the substrate is disturbed allowing for a resonant excitation of a surface-induced electronically excited charge-transfer state. A simplified mechanism, as proposed in the literature [47, 48], is based on the formation of a surface complex upon chemisorption of a molecule on the metal layer. The formed surface complex is characterized by its charge-transfer character either transferring charge from the conduction band of the metal to unoccupied molecular orbitals or vice versa. In this context, chemical enhancement can thus be understood by a surface-induced resonance Raman effect along the lines discussed above in the general context of resonance Raman scattering.

Despite of the conceptual differences, an exact separation of the two distinct enhancement processes is extremely challenging and experimentally very difficult, as any parameter easily changed in the experimental design will have an influence on both mechanisms. A detailed understanding of the chemical enhancement and a reliable separation from purely electromagnetic enhancement is thus not only relevant for fundamental reasons but also crucial for the design of analytical tools. Since both enhancement mechanisms are multiplicative, unexpected chemical enhancements can easily lead to quantitatively and qualitatively wrong analytical conclusions. For the sake of simply increasing the Raman scattering cross-section, surface-enhanced resonance Raman scattering (SERRS) can be employed. Here, the excitation wavelength is not only in resonance with the surface plasmon absorption but more importantly also resonant to the electronic absorption of the adsorbed molecules. Thus, surface enhancement of the Raman signal appears combined with the adsorbate intrinsic enhancement of the scattering due to the dispersion of $\left(\frac{\partial \alpha}{\partial q}\right)_{q_0}$. As SERRS further enhances the scattering cross-section and thus allows for a lowering of the detection limit of a particular analyte, it has been implemented to study drug absorption and protein properties [49].

2.3.3.2 SERS-Active Substrates

Substrates used for SERS have to meet the following requirements aside from the plasmon resonance condition, i.e., $\Re(\varepsilon_i) \approx -2\varepsilon_0$ and $\Im(\varepsilon_i) << 1$, which is particularly well met for silver, gold, and copper when working with excitation in the visible spectral region: due to an increased field enhancement at strongly curved surfaces (lightning rod effect), the substrates should reveal sharp features or a significant nano-roughness. A different way of enhancing local fields is to place two (or more) nanoparticles/structures in close proximity, so that high fields are produced at the interface between the particles. Furthermore, in order to be applicable in bio-analytical chemistry, SERS substrates need to be (i) non-toxic and chemically compatible with the analytes or cells which are subject to detection, (ii) temporally stable, i.e., show no aggregation, which alters the enhancement during the

course of the experiment, (iii) reproducible, and (iv) ideally low cost and easily preparable.

Besides the conventional use of metal colloids, nanoparticles, and roughened surfaces, recent experimental efforts have been devoted to the design of highly reproducible SERS substrates with well-defined shapes and hence exactly controlled plasmonic properties. Pursuing this research goal, basically two independent experimental approaches have been followed: nanosphere lithography and electron beam lithography. *Nanosphere lithography* was pioneered by Fischer and Zingsheim, who demonstrated that a nanosphere containing solvent can be evaporated in a controlled way to form a dense monolayer on a substrate, which is subsequently used as a mask for a metal layer deposition. Van Duyne demonstrated the use of self-assembled sphere masks to produce highly organized particle arrays. Defect-free silver arrays of sizes up to $25\,\mu\text{m}^2$ have been reported, which revealed enhancement factors of more than 10^7 for benzenethiol on these arrays [50].

Metal deposition without removal of the nanospheres forms the basis of an approach conventionally referred to as films over nanospheres. Using the latter technique, substrates with enhancement factors of up to 10⁶ have been designed. The use of multilayer silver – gold films-over-nanosphere substrates allows to combine the high SERS enhancement typically observed for silver with the enhanced long-term stability typically associated with gold substrates [51, 52]. Electron beam lithography routinely produces highly reproducible patterns of a variety of materials. Structures that have been demonstrated in the literature include square and hexagonal arrays composed of ellipsoids, cylinders, and trigonal prisms as well as nanowires [53–58]. Another recently pursued approach in designing novel SERS materials, especially in connection with on-chip point-of-care protein diagnostics, is the use of enzymatic silver deposition. In this technique, a streptavidin peroxidase complex (SAPK) is coupled to a biotin-modified oligonucleotide immobilized on a glass surface due to the biotin - streptavidin interaction. The enzymatic silver deposition, which is caused by the enzymatic activity of the peroxidase, yields in the formation of nanostructures with sharp edges as depicted in Fig. 2.7 [59].

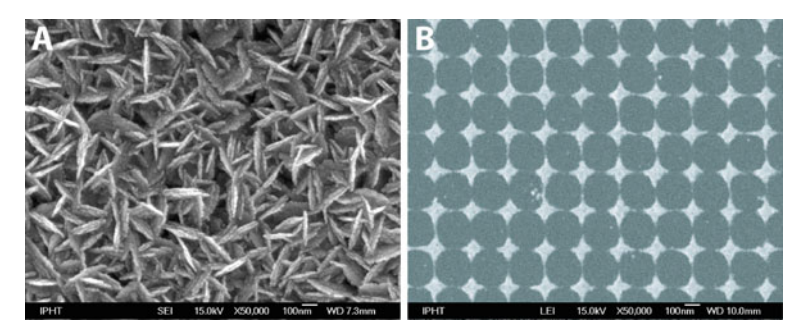


Fig. 2.7 Two examples of novel SERS substrates are depicted. (a) enzymatic grown metal particles and (b) substrates manufactured by electron beam lithography

2.3.3.3 Application of SERS

The significant enhancement of the scattering cross-section in SERS has sparked the use of SERS as an analytical tool.

First experiments demonstrate the capability of combining SERS with microfluidic devices in order to develop novel lab-on-a-chip devices. Popp and coworkers presented a proof of principle experiment for the application of a liquid/liquid microsegmented flow for serial high-throughput microanalytical systems with promising applications in clinical chemistry, pharmaceutical research, and analytical chemistry. They combined microspectral SERS analysis with reproducible sample volumes down to 180 nl and showed that their approach offers the capability of quantifying analytes by analyzing the SERS spectra [60, 61].

The combination of SERS spectroscopy readout and atomic force microscopy (AFM) or scanning tunneling microscopy (STM) yielded a novel microscopic technique called tip-enhanced Raman scattering (TERS) [62]. TERS combines the high spatial and topological resolution of AFM with the chemical sensitivity of Raman scattering. Employing a near-field optical effect, TERS is capable of resolving structures smaller than the diffraction limit of the laser light used. TERS investigations on the spectral composition of the surface of Staphylococcus epidermis quantified the nanoscale heterogeneity of the bacterial surface with spatial resolution as small, $50 \times 50 \,\mathrm{nm^2}$ [39, 40]. The chemical sensitive characterization of bacterial cell walls offers promising roadways to the design of novel drugs designed to selectively target a particular bacterium. Another recent highlight of TERS microspectroscopy was performed by Bailo and Deckert, who presented SERS spectra of a singlestranded RNA homopolymer of cytosine with a spatial resolution down to a couple of nucleobases [63]. Their experiment presents a benchmark in the application of TERS to directly monitor DNA transcription – a key process for the understanding of transcription errors and related diseases.

Another milestone in bringing TERS spectroscopy into the life science and in particular into the field of biomedical diagnostics has been recently presented by Deckert, Popp, and coworkers [64]. Their work revealed the high potential that lies in the combination of extremely high spatial resolution (20 nm) and chemical sensitivity intrinsic to TERS. Using the Raman enhancement on the tip surface the authors succeeded in recording Raman spectra of the surface of a single *Tobacco mosaic* virus. The recorded spectra were comparable to Raman spectra taken on bulk virus material and revealed the chemical composition – dominant contributions of RNA and proteins – of the virus. While the SERS-active tip interacts predominantly with the protein containing capsid, the range of the evanescent field of several nanometers allows for additional Raman bands of the RNA from the inside of the virus to be observed in the data. These results open new possibilities for the fast detection and identification of single virus particles, which is not achievable by conventional methods, and potentially study the interaction of viruses with cells and drugs.

Yet another intriguing application of SERS in analytical science shall be mentioned that has been presented by van Duyne and coworkers [65]. In their work SERS was used as the read-out mechanism to quantify the in vitro concentration

of glucose in solution within the clinically relevant concentration range of less than 10 mM. Their apparatus consisted of a roughened silver surface, which was modified with a hydrophilic partition layer. The latter was implemented to facilitate the preconcentration of glucose and various small analytes. The in vivo implementation of their glucose sensor allowed for online monitoring of the glucose level in anesthetized rats proving the capability of SERS-based devices to operate within a clinical procedure.

Finally, we want to mention an application that combines both Raman crosssection enhancement mechanisms discussed so far, i.e., the combination of resonance Raman and surface-enhanced Raman scattering, SERRS (surface-enhanced resonance Raman scattering), for DNA sequence analysis [49]. The basic concept in using SERRS for identification of specific DNA sequences is to couple the spectroscopic read-out with a biological essay. In this technique, the DNA fragment is chemically linked to a dye molecule which in turn is terminated to a noble metal surface by means of a covalently attached surface-seeking group. Hence, the dye, which might or might not be a fluorescent molecule, is covalently attached to the DNA fraction to be labeled and brought into close proximity of the noble metal surface. Therefore, characteristic Raman modes of the dye are enhanced. The biochemical essay ensures that the presence of a particular dye can be correlated with the presence of a particular DNA fragment and hence indirect DNA sensitivity is achieved. The dominant attractiveness of this technique is its high sensitivity in terms of absolute detection limits, which is reported to be in the range between 10^{-9} and 10^{-12} M, depending on the use of the particular SERRS marker and the metallic surface providing the Raman enhancement. Thus, the detection limit of SERRS in the DNA detection exceeds the sensitivity of a fluorescence read-out by roughly one to three orders of magnitude [49].

This brief and far-from-complete overview over recent applications and ongoing developments of surface-enhanced (resonance) Raman scattering demonstrates the enormous potential of Raman spectroscopy for biomedical analysis. Subsequent chapters in this book will provide further and more detailed insight into selected areas of Raman applications in the life science.

References

- 1. M. Schmitt, J. Popp, J. Raman Spectrosc. **37**(1–3), 20 (2006)
- 2. K.R. Ackermann, T. Henkel, J. Popp, ChemPhysChem 8(18), 2665 (2007)
- 3. K.R. Strehle, D. Cialla, P. Rösch, T. Henkel, K. M., J. Popp, Anal. Chem. 79(4), 1542 (2007)
- 4. P. Rösch, M. Harz, M. Schmitt, K.D. Peschke, O. Ronneberger, H. Burkhardt, H.W. Motzkus, M. Lankers, S. Hofer, H. Thiele, J. Popp, Appl. Environ. Microbiol. **71**(3), 1626 (2005)
- P. Rösch, M. Harz, K.D. Peschke, O. Ronneberger, H. Burkhardt, A. Schüle, G. Schmauz, M. Lankers, S. Hofer, H. Thiele, H.W. Motzkus, J. Popp, Anal. Chem. 78(7), 2163 (2006)
- B. Schrader (ed.), Infrared and Raman Spectroscopy, Methods and Applications, chap. Application of Non-classical Raman Spectroscopy, (Wiley-VCH, Weinheim, 1995), p. 465
- A.V. Szeghalmi, M. Erdmann, V. Engel, M. Schmitt, S. Amthor, V. Kriegisch, G. Noell, R. Stahl, C. Lambert, D. Leusser, D. Stalke, M. Zabel, J. Popp, J. Am. Chem. Soc. 126(25), 7834 (2004)

- 8. S. Lochbrunner, A. Szeghalmi, K. Stock, M. Schmitt, J. Chem. Phys. 122, 244315 (2005)
- 9. R.J.H. Clark, P.D. Mitchell, J. Am. Chem. Soc. 95(25), 8300 (1973)
- 10. W. Kiefer, H.J. Bernstein, J. Mol. Spectrosc. 43, 366 (1972)
- 11. S.P.A. Fodor, R.P. Rava, T.R. Hays, T.G. Spiro, J. Am. Chem. Soc. 107, 1520 (1985)
- 12. S.A. Asher, Anal. Chem. 65, A201 (1993)
- 13. J.M. Benevides, S.A. Overman, G.J.J. Thomas, J. Raman Spectrosc. 36, 279 (2005)
- 14. T. Egawa, S.R. Yeh, J. Inorg. Biochem. **99**(1), 72 (2005)
- 15. J.R. Kincaid, Porphyr. Handb. 7, 225 (2000)
- 16. J.R. Kincaid, K. Czarnecki, Compr. Coord. Chem. II 2, 131 (2004)
- 17. T. Kitagawa, Y. Miutani, Coord. Chem. Rev. **135/136**, 685 (1994)
- 18. T. Kitagawa, J. Porphyr. Phthalocyanines 6(4), 301 (2002)
- 19. R. Schweitzer-Stenner, J. Raman Spectrosc. 32(9), 711 (2001)
- T.G. Spiro, Biological Applications of Raman Spectroscopy, vol. 3, chap. Resonance Raman Spectra of Heme and Metalloproteins, (Wiley, New York, NY, 1987).
- 21. T.G. Spiro, C.A. Grygon, J. Mol. Struct. 173, 79 (1988)
- 22. G.J.J. Thomas, Annu. Rev. Biophys. Biomol. Struct. 28, 1 (1999)
- R. Withnall, Protein-Ligand Interactions, Structure and Spectroscopy: A Practical Approach, chap. Protein-Ligand Interactions Studied by Raman and Resonance Raman Spectroscopy, (Oxford University Press, Oxford, New York, 2001).
- K. Gaus, P. Rösch, R. Petry, K.D. Peschke, O. Ronneberger, H. Burkhardt, K. Baumann, J. Popp, Biopolymers 82(4), 286 (2006)
- 25. R.M. Jarvis, R.R. Goodacre, FEMS Microbiol. Lett. 232, 127 (2004)
- 26. E.C. Lopez-Diez, R. Goodacre, Anal. Chem. 76(3), 585 (2004)
- 27. Z.Q. Wen, S.A. Overman, G.J.J. Thomas, Biochemistry **36**, 7810 (1997)
- 28. M. Fleischmann, P.J. Hendra, A.J. McQuillan, Chem. Phys. Lett. **26**(2), 163 (1974)
- 29. R. Petry, M. Schmitt, J. Popp, ChemPhysChem 4(1), 14 (2003)
- K. Hering, D. Cialla, K. Ackermann, T. Dörfer, R. Möller, H. Schneidewind, R. Mattheis, W. Fritzsche, P. Rösch, J. Popp, Anal. Bioanal. Chem. 390(1), 113 (2008)
- 31. M.G. Albrecht, J.A. Creighton, J. Am. Chem. Soc. 99(15), 5215 (1977)
- 32. D.L. Jeanmaire, R.P. Van Duyne, J. Electroanal. Chem. Interfacial Electrochem. 84(1), 1 (1977)
- 33. M.J. Banholzer, J.E. Millstone, L. Qin, C.A. Mirkin, Chem. Soc. Rev. 37(5), 885 (2008)
- 34. B. Ren, G.K. Liu, X.B. Lian, Z.L. Yang, Z.Q. Tian, Anal. Bioanal. Chem. 388(1), 29 (2007)
- K. Kneipp, H. Kneipp, I. Itzkan, R.R. Dasari, M.S. Feld, J. Phys.: Condens. Matter 14(18), R597 (2002)
- 36. P.L. Stiles, J.A. Dieringer, N.C. Shah, R.P. Van Duyne, Annu. Rev. Anal. Chem. 1, 601 (2008)
- K. Kneipp, Y. Wang, H. Kneipp, L.T. Perelman, I. Itzkan, R.R. Dasari, M.S. Feld, Phys. Rev. Lett. 78(9), 1667 (1997)
- 38. S.M. Nie, S.R. Emery, Science **275**(5303), 1102 (1997)
- U. Neugebauer, P. Rösch, M. Schmitt, J. Popp, C. Julien, A. Rasmussen, C. Budich, V. Deckert, ChemPhysChem 7(7), 1428 (2006)
- U. Neugebauer, U. Schmid, K. Baumann, W. Ziebuhr, S. Kozitskaya, V. Deckert, M. Schmitt, J. Popp, ChemPhysChem 8(1), 124 (2007)
- 41. R. Gessner, P. Rösch, W. Kiefer, J. Popp, Biopolymers **67**(3), 327 (2002)
- R. Gessner, P. Rösch, R. Petry, M. Schmitt, M.A. Strehle, W. Kiefer, J. Popp, Analyst 129(12), 1193 (2004)
- 43. W.A. Murray, W.L. Barnes, Adv. Mater. 19(22), 3771 (2007)
- 44. K.A. Willets, R.P. Van Duyne, Annu. Rev. Phys. Chem. **58**, 267 (2007)
- 45. G.C. Schatz, R.P. Van Duyne, *Handbook of Vibrational Spectroscopy*, chap. Electromagnetic Mechanism of Surface-enhanced Spectroscopy, (Wiley Chichester, 2002), pp. 759–774
- 46. M. Kerker, D.S. Wang, H. Chew, Appl. Opt. 19(24), 4159 (1980)
- 47. J.F. Arenas, I. Lopez-Tocon, J.L. Castro, S.P. Centeno, M.R. Lopez-Ramirez, J.C. Otero, J. Raman Spectrosc. 36(6/7), 515 (2005)

- 48. A. Otto, J. Raman Spectrosc. **36**(6/7), 497 (2005)
- 49. D. Graham, K. Faulds, Chem. Soc. Rev. 37(5), 1042 (2008)
- A.J. Haes, C.L. Haynes, A.D. McFarland, G.C. Schatz, R.P. van Duyne, S. Zou, MRS Bull. 30(5), 368 (2005)
- X. Zhang, J. Zhao, A.V. Whitney, J.W. Elam, R.P. Van Duyne, J. Am. Chem. Soc. 128(31), 10304 (2006)
- 52. J. Stropp, G. Trachta, G. Brehm, S. Schneider, J. Raman Spectrosc. 34(1), 26 (2003)
- C.L. Haynes, A.D. McFarland, L. Zhao, R.P. Van Duyne, G.C. Schatz, L. Gunnarsson, J. Prikulis, B. Kasemo, M. Kaell, J. Phys. Chem. B 107(30), 7337 (2003)
- 54. G. Laurent, N. Felidj, J. Aubard, G. Levi, J.R. Krenn, A. Hohenau, G. Schider, A. Leitner, F.R. Aussenegg, J. Chem. Phys. 122(1), 011102/1 (2005)
- L. Billot, M. Lamy de la Chapelle, A.S. Grimault, A. Vial, D. Barchiesi, J.L. Bijeon, P.M. Adam, P. Royer, Chem. Phys. Lett. 422(4–6), 303 (2006)
- 56. K. Li, L. Clime, B. Cui, T. Veres, Nanotechnology 19(14), 145305/1 (2008)
- 57. D. Cialla, U. Hübner, H. Schneidewind, R. Möller, J. Popp, ChemPhysChem 9, 758 (2008)
- U. Hübner, R. Boucher, H. Schneidewind, D. Cialla, J. Popp, Microelectron. Eng. 85, 1792 (2008)
- 59. K.K. Hering, R. Möller, W. Fritzsche, J. Popp, ChemPhysChem 9(6), 867 (2008)
- K.R. Strehle, D. Cialla, P. Rösch, T. Henkel, M. Köhler, J. Popp, Anal. Chem. 79(4), 1542 (2007)
- 61. K.R. Ackermann, T. Henkel, J. Popp, ChemPhysChem 8(18), 2665 (2007)
- 62. E. Bailo, V. Deckert, Chem. Soc. Rev. 37(5), 921 (2008)
- 63. E. Bailo, V. Deckert, Angew. Chem. Int. Ed. 47(9), 1658 (2008)
- D. Cialla, T. Deckert-Gauding, C. Budich, M. Laue, R. Möller, D. Naumann, V. Deckert, J. Popp, J. Raman Spectrosc. 40(3), 240 (2008)
- C.L. Haynes, C.R. Yonzon, X. Zhang, R.P. Van Duyne, J. Raman Spectrosc. 36(6/7), 471 (2005)

Chapter 3 Raman Instrumentation for Confocal Raman Microscopy

Olaf Hollricher

Abstract Raman spectroscopy is a weak scattering technique in which typically less than one in a million excitation photons give rise to a single Raman photon. The situation is even more difficult in confocal Raman microscopy, as the detection volume is reduced by the small pinhole and thousands of spectra must be collected in a short period of time. Therefore, careful design of the excitation and detection optics as well as the appropriate choice of spectrometer and detector is important for successful experiments. As detectors and instrumentation in this field continue to quickly evolve, a snapshot of state-of-the-art Raman equipment and instrumentation will be provided.

3.1 Introduction

Raman scattering is typically a very weak effect due to the non-resonant interaction of the exciting photons with the molecules involved in the scattering process. Therefore, the number of Raman photons in a given measurement geometry is limited and any progress in technology that leads to a higher collection efficiency is very important.

Although the Raman effect was already discovered in 1928 by Chandrasekara Raman [1], who was awarded the Nobel Prize in Physics 2 years later, routine Raman spectroscopic experiments were not possible until the development of the laser in the 1960s [2].

In the 1970s and 1980s, the development of charge-coupled devices (CCDs) [3, 4] replaced photomultiplier tubes (PMTs) and enabled multi-channel detection. Willard S. Boyle and George E. Smith received the Nobel Prize in Physics in 2009 for the invention of the CCD camera.

As silicon detectors have a much higher quantum efficiency (QE) compared to PMTs in the visible and near-infrared regions of the spectrum and CCDs are available as linear detectors, this has reduced measurement times by at least three orders of magnitude. Before, the Raman band of interest had to be scanned across a PMT, a point detector only sensitive to a very narrow wavelength range selected by the exit slit of the spectrometer.

With the introduction of the CCD, the exit slit of the spectrometer could be replaced by a linear CCD detector, enabling the acquisition of 1000 channels (or more) at the same time.

3.2 The Development of Raman Microscopes

In the 1990s, companies first combined a Raman spectrometer with an optical microscope and established so-called micro-Raman spectroscopy. The microscope was used to focus the excitation light to a small spot a few micrometers in diameter to obtain a Raman spectrum from a microscopic area. For the first time, Raman spectra could be obtained from samples of only a few micrometers in diameter. The advantage of using a microscope objective instead of a simple lens is the high collection efficiency for the Raman signal due to the high NA¹ of the microscope objective. On the other hand, as one focuses the light to a microscopic spot, care must be taken to not heat the sample and thermally destroy it with an overly intense laser beam.

In a further approach, the micro-Raman instruments were equipped with stepper motor driven positioning stages to raster scan the sample and collect Raman spectra at a given number of sample positions. This technique, which was called Raman mapping, could be used to extract the relevant chemical information from each spectrum and to create a map of the distribution of the chemical components in a sample with a lateral resolution of a few micrometers.

As the acquisition of typical Raman spectra using these instruments could take several seconds integration time (or even much longer, depending on the required S/N ratio and scattering efficiency of the sample), general understanding was that this technique is very slow and creating a Raman map of a sample takes hours, if not days, to acquire [5]. If one uses an integration time of only 1 s/spectrum, a 60×60 -pixel Raman map takes $60 \times 60 = 3600 \, \text{s} = 1 \, \text{h}$ for the integration alone. Adding the time required to position the sample with a stepper motor stage, as well as the readout time for the CCD and the time for the backward scan, the total time required for this experiment can be easily twice as long. Keeping a system stable with an accuracy of better than 1 μ m over this timescale is already a challenge and a 60×60 -pixel map is only a very small image. A $200 \times 200 = 40,000$ spectra image under these conditions is virtually impossible if the integration time per spectrum is not dramatically lowered. If one wants to establish Raman imaging as a routine technique, the integration time per spectrum must be reduced to $100 \, \text{ms/spectrum}$ or even less.

Therefore, multiplex setups were developed to increase the acquisition speed similar to the transition from the single-point, zero dimensional PMT to the one dimensional CCD.

¹ Numerical aperture = sine of half of the acceptance angle of the objective.

Instead of illuminating a single point and scanning this point across the entire sample area, one idea is to illuminate a complete line and project this line onto the entrance slit of a spectrometer. Using an imaging spectrometer, the vertical axis of the CCD camera could be used for position information and the horizontal axis for energy dispersion. With this technique, one could acquire hundreds of spectra along the illuminated line at the same time. This technique is called "line imaging."

Another approach is to homogeneously illuminate the sample as a whole and acquire the desired spectral information without a spectrometer by sending the light through a (tunable) narrowband filter onto an imaging CCD. A single exposure collects the Raman light of the whole sample and scanning is no longer necessary. It is not possible to collect a complete Raman spectrum at every image point. Instead, the spectral information must be gained by taking several images at different filter passband positions. This technique is called "global imaging."

Although these techniques appear to increase detection speed through their multiplex advantages by several orders of magnitude, they have severe disadvantages that in most cases prevent their useful application.

One main disadvantage is that neither technique is confocal, so that there is either a slit instead of a round pinhole or no pinhole at all. "Confocal" is defined as "having the same focus" and describes an optical microscope in which the sample is illuminated with a point source and the image of this point is detected through a pinhole in front of the detector. The illuminating point source and the pinhole are both positioned in the same focal plane. An image of the sample is obtained either by scanning the laser focus point by point and line by line across the sample or by scanning the sample under the laser spot. As the signal is detected through a pinhole, only light originating from the focal plane can reach the detector. Light emitted above or below the focal plane is not in focus in the pinhole plane and therefore does not contribute to the image. The theory of confocal microscopy is described in Chap. 1.

3.3 Confocality

The natural enemy of Raman spectroscopy is fluorescence. As fluorescence is a resonant interaction of light with electronic sample states, the efficiency of fluorescence can easily be six orders of magnitude higher than that of the Raman interaction. If the sample shows fluorescence at the excitation wavelength used for Raman, in most cases the fluorescence intensity is so high that no Raman signal can be detected.

Therefore it is extremely important to reduce the fluorescence background as much as possible either by using an excitation wavelength at which the sample does not show fluorescence or by reducing the detection volume.

Unfortunately it is not always possible to find an excitation wavelength at which there is no fluorescence, because of the high efficiency of the fluorescence process compared to Raman scattering. In these cases, the confocal detection setup limits the collection of fluorescence to photons emitted from the focal plane. This dramatically

reduces the fluorescence background signal, so that in many cases Raman images can be obtained, where non-confocal techniques only detect fluorescence.

If the fluorescence is caused by impurities and not the sample itself, very often the fluorescence is bleached due to the high excitation intensity in the focal plane. In these cases, a confocal Raman image gives often very useful results, while nonconfocal techniques would still collect too much fluorescence from areas above and below the focal plane.

As the confocal detection principle limits the detected light to the focal plane, it also allows the analysis of transparent samples in 3D and an optical cross-section to be performed without cutting the sample in half. If the sample is a thin layer on top of a supporting substrate, only a confocal setup allows the separation of the signal from the sample from the background signal of the substrate. A less than 1 μm thin polymer sample on a cover glass (170 μm thickness) will give a more than 100 times smaller Raman signal than the glass substrate itself and can hardly be analyzed with a non-confocal technique.

Non-confocal techniques might have their niche applications, but the confocal setup is so far the most versatile technique that delivers the best results in terms of spatial resolution and background suppression.

3.4 Throughput of a Confocal Raman Microscope

It is extremely important to optimize the throughput of the confocal Raman microscope to allow confocal Raman imaging in reasonable amounts of time because the Raman signal is usually very weak. Figure 3.1 shows a sketch of a typical Raman microscope system consisting of an excitation laser, a microscope, and a spectrometer with CCD detector. Scanning movement of the sample is performed with a piezo-scanner which is very fast and extremely accurate when equipped with position sensors.

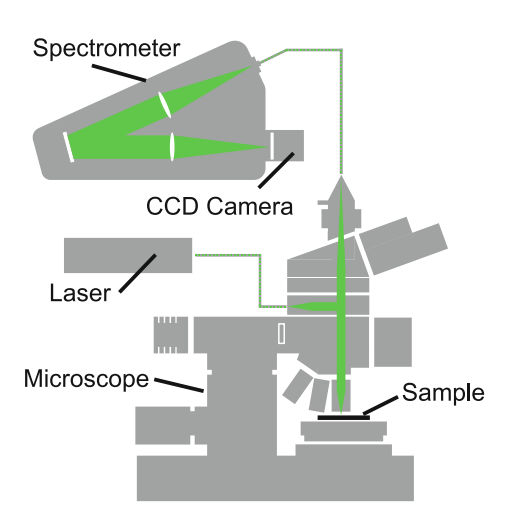


Fig. 3.1 Typical layout of a Raman microscope with a fiber-coupled laser source and spectrometer

To optimize the Raman signal, every part of the system must be optimized for the highest transmission and efficiency. It is very easy to lose an order of magnitude in sensitivity if the components are not properly chosen. If a single spectrum is desired, it is usually not important whether the necessary integration time is 1 or 10 s, but it makes a big difference if an image takes 15 min or 2.5 h.

In the following sections, points of specific importance are described.

3.4.1 Laser Wavelength

The Raman scattering intensity is proportional to v^4 , where v is the frequency of the exciting laser radiation. Excitation at 400 nm therefore leads to a 16 times higher Raman signal than excitation at 800 nm. On the other hand, many samples show strong fluorescence when excited in the UV or blue region of the spectrum and low fluorescence when excited in the red or NIR region of the spectrum.

The shorter the excitation wavelength, the higher the lateral resolution, because the resolution is given by $\Delta x = 0.61 \times \lambda/\text{NA}$, with Δx being the shortest distinguishable distance between two points, λ the wavelength, and NA the numerical aperture of the objective used. This relation also shows that the numerical aperture is equally important. Good objectives with a very high NA are easily available in the range from 400 to 900 nm. For UV wavelengths below 350 nm, Raman scattering is very high, but the number of available objectives is limited and their NA is typically very small. Also, sample damage due to the high photon energy is starting to be a problem. At long wavelengths, lateral resolution decreases and the Raman efficiency drops strongly, but fluorescence is less likely.

A laser suitable for Raman microscopy should

- have a Gaussian beam shape (single longitudinal mode, TEM00), so that it can be focused onto a diffraction-limited spot,
- be linearly polarized, to allow the observation of polarization-dependent sample properties,
- have a very narrow line shape of well below 1 cm⁻¹, to avoid broadening of the Raman lines,
- be very stable in frequency (variation $< 0.01 \, \mathrm{cm}^{-1}$), to allow stress measurements with high accuracy,
- be very stable in intensity (<1–2% power fluctuations), to allow accurate and comparable measurements of concentrations,

just to name a few of the essential properties.

3.4.2 Excitation Power

The Raman signal is proportional to the excitation power, but the excitation laser power should be chosen well below the point where absorption leads to thermal

decomposition of the sample. The acceptable laser power depends on laser wavelength, sample properties (absorption, thermal conductivity), and other imaging conditions (laser focus diameter, etc.). It can vary from a few microwatts to several hundred milliwatts. If the sample is transparent, the typically acceptable power for green excitation will be on the order of 10 mW for a 300 nm spot size.

3.4.3 Objective

To obtain the highest possible collection efficiency in combination with the best spatial resolution, one should use an objective with the highest numerical aperture applicable under the measurement conditions. One must also pay attention to the transmission characteristics of the microscope objective at the excitation wavelength. A good microscope objective might have 80–90% transmission at 500 nm wavelength, but only 40% or even less at 900 nm. The reason for this is that anti-reflection coatings that have less than 0.5% reflectivity in the visible can be far more reflective in the IR. This is particularly important as the light must pass through the objective twice.

The sample flatness needs to be considered as well when choosing the correct objective since a high NA objective will have a good depth resolution and collect from only a narrow height in the Z direction. This in turn means that a sample with a high topography will sometimes be in focus on the sample surface and sometimes not. In this case using an objective with a lower NA might be beneficial.

3.4.4 Microscope Throughput

The throughput of the microscope is as important as the throughput of the objective itself. The light must pass through the microscope twice, therefore the losses are squared. Fewer optical components with optimized throughput result in lower losses.

The laser beam is coupled into the microscope with a dichroic or holographical beam splitter. The reflectivity of this beam splitter should be as high as possible for the laser excitation wavelength, while its transmission for the Raman light should be high as well. With today's coating technology, dichroic filters are available that have a reflectivity >95% at the laser wavelength and at the same time a transmission of about 98% for the Stokes-shifted Raman light above approximately 150 cm⁻¹. If one needs to get closer to the Rayleigh line, holographic beam splitters must be used, but it is only a matter of time until coating technology will allow holographic filters to be completely replaced. Holographic filters will then only be needed if detection of the anti-Stokes Raman spectrum is necessary.

For efficient suppression of the Rayleigh line, an edge or notch filter which reduces the laser line intensity by six orders of magnitude while having a throughput of >95% for the Stokes-shifted Raman lines should be used.

3.4.5 Coupling Between Microscope and Spectrometer

It might sound trivial, but the optical coupling between microscope and spectrometer is extremely important because it has to serve several functions. The first obvious task is that it must couple the light effectively from the microscope into the spectrometer. If this is done with metallic mirrors that have 85% average reflectivity, after only four mirrors 50% of the signal is lost.

Additionally, the light must be coupled into the entrance slit of the spectrometer and its aperture must be transformed into the entrance aperture of the spectrometer. A higher divergence than the acceptance angle of the spectrometer will result in enormous losses; a smaller divergence will result in a reduced resolution because the grating is only partly illuminated.

For an effective confocal setup, the confocal pinhole size must be chosen according to the diameter of the point spread function on the image side of the objective. As an example, a $100 \times$ objective with NA = 0.9 at 633 nm excitation wavelength will produce a diffraction-limited airy disc of 43 μ m in the image plane. A confocal pinhole diameter of 50μ m will be in this case nearly ideal for maximum depth resolution and high collection efficiency. The illuminating NA in the image plane for the objective above is NA = 0.009 (0.9/100 = 0.009, because the product of magnification and NA is a constant (Étendue)²), while a typical $f = 300 \, \text{mm}$ spectrometer has an entrance aperture of NA = 0.125 (f/4).

To match the entrance aperture of the spectrometer, an additional intermediate magnification of $14 \times$ is needed which introduces losses and is subject to misalignment. A single multi-mode optical fiber with, in this case, $50 \, \mu m$ core diameter can be used to fulfill all these purposes. The fiber serves

- 1. as a pinhole, because only the core guides and transports the light,
- 2. as a light guide with extremely high efficiency (the only losses are 4% entrance and exit losses if non-coated entrance and exit surfaces are used),
- 3. as an entrance slit for the spectrometer, and
- 4. as an aperture matching device, because the exit aperture of the fiber (NA = 0.12) exactly matches that of the spectrometer, if a f/4 spectrometer is used.

3.4.6 Spectrometer Throughput

Most commercially available spectrometers have a throughput (including gratings) of only 30–35% (at 532 nm), although the gratings have an efficiency of up to 80%. This means that more than 50% of the light is lost in the coatings of the spectrometer mirrors. The reason for this is that most spectrometers are not optimized for

 $^{^2}$ The Étendue is a conserved quantity in optical systems. It basically characterizes how "spread out" the light is in area and angle.

the small frequency range of the Raman signal, but should work from UV to IR. Optimizing the spectrometer for the wavelength range of interest can therefore double the throughput [6].

3.4.7 Gratings

The grating in a spectrometer disperses the signal onto the CCD detector by deflecting each wavelength at a slightly different angle. The number of grooves per millimeter determines the dispersion characteristics. A high number of grooves/mm (lines/mm) results in a high dispersion and a high resolution, but also distributes the signal over a large number of CCD pixels. As, with very few exceptions, the narrowest lines of typical samples for confocal Raman microscopy have a width (FWHM = full width at half maximum) of not less than $2-3 \, \mathrm{cm}^{-1}$, a spectrometer with a resolution of about $1 \, \mathrm{cm}^{-1}$ is a good compromise.

It is useful to be able to switch between multiple gratings so that the user can use one grating with a dispersion that is matched to the detector size in order to ensure that the full Raman spectrum $(-100-3600\,\mathrm{cm}^{-1})$ is covered by the detector, as well as a high resolution grating that delivers approximately $1\,\mathrm{cm}^{-1}$ resolution.

To optimize the efficiency, gratings are typically "blazed" for a certain wavelength. This means that the grooves are angled so that the grating efficiency can reach 80% for the first diffraction order. The grating efficiency sets the upper limit of the throughput of the spectrometer. A typical grating efficiency for a 600 lines/mm grating with a blaze wavelength of 500 nm is shown in Fig. 3.2.

As can be seen, the grating efficiency peaks at the blaze wavelength and shows a strong drop-off with shorter wavelengths. With longer wavelengths, the falloff is less steep, but if this grating is used at 785 nm excitation, the efficiency is reduced by a factor of 2-3.

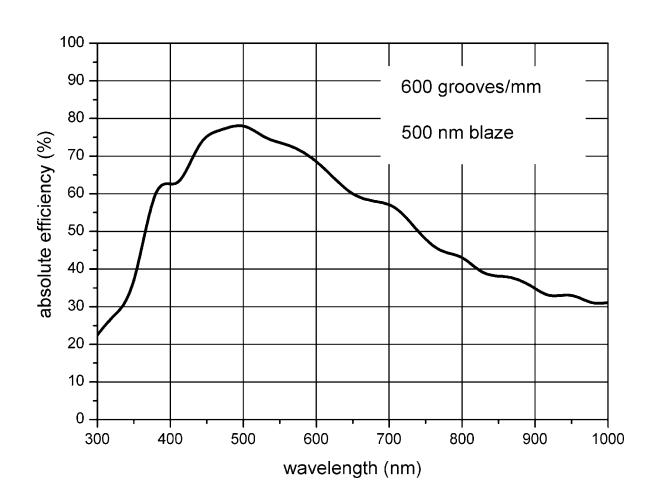


Fig. 3.2 Typical absolute reflection efficiency into the first order for unpolarized light of a 600 lines/mm grating blazed for 500 nm

3.4.8 CCD Detector

The detector is one of the key components of a Raman microscope and choosing the correct CCD strongly affects the performance of the instrument.

CCD cameras are available in a wide variety of detector sizes, uncooled or cooled, with Peltier or liquid nitrogen (LN) cooling, front- or back illuminated, as deep depletion models or with a UV coating, just to mention a few of the hundreds of variations.

A CCD (charge-coupled device) detector consists of an array of light-sensitive Si-photodiodes, each connected to a capacitor. In the photodiode, every detected photon creates an electron-hole pair which is separated by the internal electric field and the electrons are stored in the capacitor. A typical detector size for a spectroscopic detector is 1024×127 pixels (pixels per line \times pixels per column), with a pixel size of $26\,\mu m \times 26\,\mu m$.

The first important characteristic of the detector is its quantum efficiency (QE), which is the percentage of detected photons to total incoming photons. As the light-sensitive area of a CCD is partially blocked by electrical interconnection lines, the QE of a typical (front-illuminated) detector is about 45% at 500 nm. To increase the detection efficiency, many scientific detectors are available as back-illuminated devices, which means that they are etched to about 17 μ m thickness and the light is incident from the backside. With this technique and a proper anti-reflection (AR) coating, a QE of more than 90% can be achieved (at 500 nm).

A comparison of QE curves for typical front- and back-illuminated detectors is shown in Fig. 3.3.

The QE determines the signal that is detected in a Raman experiment. Equally important is the noise in the signal or the noise created in the detector itself, because the signal to noise ratio (S/N) determines the quality of a measurement.

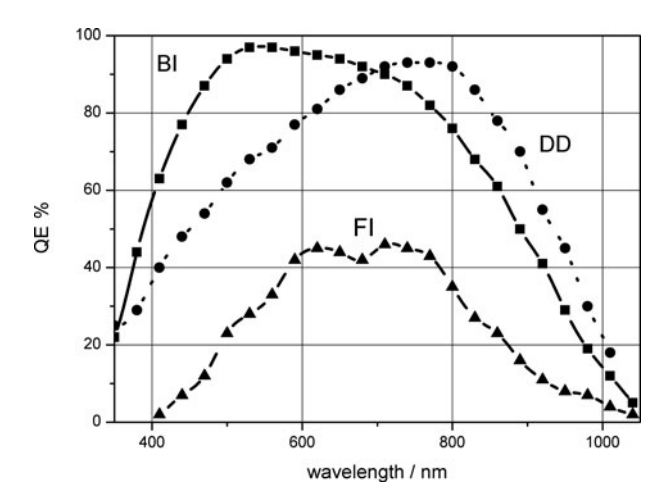


Fig. 3.3 Typical QE curves for back-illuminated (BI), back-illuminated deep-depletion (DD) and front-illuminated (FI) CCD detectors as a function of wavelength

The primary noise sources in a background-free measurement (no fluorescence or other background signal) are

- $\sigma_{\rm s}$ (shot noise) = $\sqrt{{\rm signal} (e-)}$
- σ_t (thermal noise) = $\sqrt{\sharp}$ of thermally created electrons
- σ_r (readout noise) = noise created by the readout amplifier during the amplification and digitization process

Ideally, the noise should be dominated by the shot noise of the signal itself. Every other noise source should be as small as possible.

Thermal noise is created by thermally excited carriers in the detector itself and can be strongly reduced by cooling the detector. At $-60\,^{\circ}$ C, the typical background signal due to thermally excited electrons is 0.01 electrons/pixel/s for a back-illuminated CCD. Therefore, thermal noise (which is the square root of the number of thermally created electrons) can be neglected up to integration times of a few minutes if the detector is kept at $-60\,^{\circ}$ C or below. As the integration times in a throughput optimized confocal Raman microscope are usually well below 1 s/spectrum, thermal noise is generally not a limiting factor.

A CCD temperature of -60 to $-70\,^{\circ}\text{C}$ is easily achieved with a good Peltier cooler, and more recently even $-90\,^{\circ}\text{C}$ has become possible, so that LN cooling is nearly obsolete.

More important is the readout noise of the readout amplifier in the detector itself. The readout noise is expressed in electrons and depends on the quality of the readout amplifier as well as the readout speed. For longer integration times (>50 ms), a slow readout amplifier is sufficient. A high-end 33-kHz readout amplifier produces a noise floor of less than four electrons. At 100-kHz readout speed, the readout noise of the best cameras is in the order of 10 electrons, while at 2.5-MHz readout speed it can easily be 35 electrons.

Using a 1024×127 -pixel detector with a 33-kHz readout amplifier, the minimum integration time will be about 32 ms (31 spectra/s). An image consisting of 256 lines with 256 spectra each (65,635 spectra) obtained with this integration time will take about 2100 s = 35 min acquisition time (retrace not counted). The noise of four electrons/pixel is equal to the shot noise of 16 electrons/pixel signal (18 photons/pixel signal at 90% QE).

If a 100-kHz readout amplifier is used, the minimum integration time is reduced from 32 to about 12 ms (83 spectra/s) and the image can be acquired in 790 s \approx 13 min, but the readout noise is then equal to the shot noise of a signal of 100 electrons/pixel (111 photons/pixel at 90% QE).

If a 2.5-MHz readout amplifier is used, the integration time can be further reduced to below 1 ms (1000 spectra/s) and the acquisition time can be as low as $65 \, \mathrm{s} \approx 1 \, \mathrm{min}$, but of course the available signal is reduced by a factor of 32 compared to the first and a factor of 12 compared to the second example due to the lower integration time per spectrum. The readout noise increases dramatically and now dominates the shot noise of every signal below 1225 electrons/pixel (1361 photons/pixel at 90% QE).

As one can see, especially at very short integration times (fast scanning), the readout noise starts to dominate all other noise sources and the signal is very often no longer shot noise limited.

The signal to noise ratio (S/N) for such CCD detectors can be calculated with

$$S/N = \frac{\text{Signal}}{\sqrt{\text{Signal} + \sigma_{\text{R}}^2 + \sigma_{\text{T}}^2}}$$
(3.1)

where σ_R is the readout noise and σ_T the thermal noise, which can be excluded in this case. If an experiment requires a S/N ratio of 10 at 32 ms integration time using the 33-kHz readout amplifier, this would mean a signal of 114 electrons/pixel (127 photons/pixel = 3969 photons/pixel/s) would be necessary. An ideal detector without any readout noise would achieve a S/N ratio of 10.68 (114/sqr(114)), so that the readout noise would only add 7% to the total noise.

At 12 ms integration time using the same conditions, the 100-kHz readout amplifier must be used and as the integration time is shorter, the signal is reduced by a factor of 2.7 (= 32 ms/12 ms). One would in this case detect only 43 electrons/pixel. This, together with a readout noise of 10 electrons for the 100-kHz readout amplifier, leads to a S/N ratio of 3.6 $\left(S/N = 43/\sqrt{10^2 + 43}\right)$. This signal is still detectable, but without readout noise the S/N ratio would be 6.6, which means that the S/N ratio is already reduced by a factor of nearly 2, just because of the readout noise.

At even shorter integration times, which means lower signal levels, things become even worse. At 1-ms integration time using the 2.5-MHz readout amplifier (35 electrons readout noise), the experiment would deliver only 3.56 electrons/pixel which leads to a S/N ratio of only 0.1 ($S/N = 3.56/\sqrt{35^2 + 3.56}$). Without readout noise, the S/N ratio would be 1.89, nearly a factor of 20 higher. A signal with a S/N ratio of 1.89 can be easily detected, while this cannot be said for a signal with a S/N ratio of only 0.1.

In the examples above, the digitization noise was neglected. After the readout amplification, the signal is digitized with typically 16-bit resolution in a scientific spectroscopic CCD. The A/D rate is expressed in electrons per A/D count and is usually chosen for maximum S/N without losing too much sensitivity. If a typical CCD has a saturation signal of 650,000 electrons/pixel, the amplification should be about 10 electrons/AD count (650,000/16 bit). Thus the "single bit uncertainty" or "digitization error" is also 10 electrons and is equal to the readout noise for a 100-kHz amplifier. This then already adds 41% ($1/\sqrt{1+1}=1.41$) to the readout noise, which means the readout noise is effectively $\sqrt{2}$ larger. Therefore, many CCDs have an additional amplifier with, e.g., 2x or 4x amplification before digitization, so that the noise added by digitization can be reduced (at the cost of dynamic range).

Ideally one would wish to have a detector that has 100% QE, no thermal noise, no readout noise, or any other noise source. This ideal detector would always be shot noise limited, which is as good as physics allows. A back-illuminated CCD with good cooling comes very close to this ideal detector if used with long integration times. In terms of QE and thermal noise one could already call it ideal.

Recent developments in CCD technology have led to a detector that comes even closer to what would be an ideal detector, at least in a certain wavelength range. This detector is called an EMCCD (electron-multiplying CCD).

3.4.8.1 EMCCD

An electron-multiplying CCD (EMCCD) is a normal CCD with an additional readout register that is driven with a much higher clock voltage than a normal CCD readout register. Due to this high clock voltage, electron multiplication through impact ionization is achieved with an adjustable total amplification of the signal of up to 1000 times. While shifting the carriers from pixel to pixel in the readout register, the probability for the generation of an excess carrier is extremely low (max. 1.0043), but as this process is repeated 1600 times, the total amplification can be as high as $1.0043^{1600} = 1000$. With this multiplication process, it is always possible to amplify the signal above the readout noise so that the S/N ratio is always limited by the Poisson noise of the signal, even if a very fast readout amplifier is used. The signal is then called shot noise limited.

As an example, a 1600×200 -pixel EMCCD with a 2.5-MHz readout amplifier can be read out in only 1.3 ms (= 760 spectra/s) without being limited by readout noise as in a normal CCD.

If the readout is restricted to a few lines of the CCD chip, even more than 1300 spectra/s are possible ($< 700 \,\mu s$ integration time/spectrum).

As demonstrated in the example above, the readout noise is only important for very low signals below a few hundred electrons per pixel, as is typical for short integration times. If the signal is not dominated by readout noise (large signal, long integration time), the "normal" readout register can be used and the EMCCD behaves like a state-of-the-art back-illuminated CCD.

Although an EMCCD camera is extremely sensitive and capable of detecting single photons, it cannot be used as a single photon detection device such as a photomultiplier because it lacks a discriminator. A certain number of generated carriers can originate from a different number of photons. This is taken into account in the so-called excess noise factor which adds a factor of 1.4 to the total noise of an EMCCD camera. Despite this factor, an EMCCD can still enhance the *S/N* ratio compared to a standard CCD, especially for very low signal levels and fast readouts.

Figure 3.4 shows the calculated *S/N* ratio versus signal (photons per pixel) for an EMCCD compared to a conventional CCD with 4, 10, and 35 electrons readout noise (33 kHz, 100 kHz, and 2.5 MHz readout speed). An excess noise factor of 1.4 was taken into account for the EMCCD. It was assumed that both cameras had 90% OE.

Figure 3.5 shows the improvement of the *S/N* ratio of an EMCCD compared to a normal CCD with 4, 10, and 35 electrons readout noise.

As one can see, the *S/N* ratio obtained with an EMCCD is improved for signal levels up to 18 (111; 1362) photons/pixel compared to a standard CCD with four (10; 35) electrons readout noise.

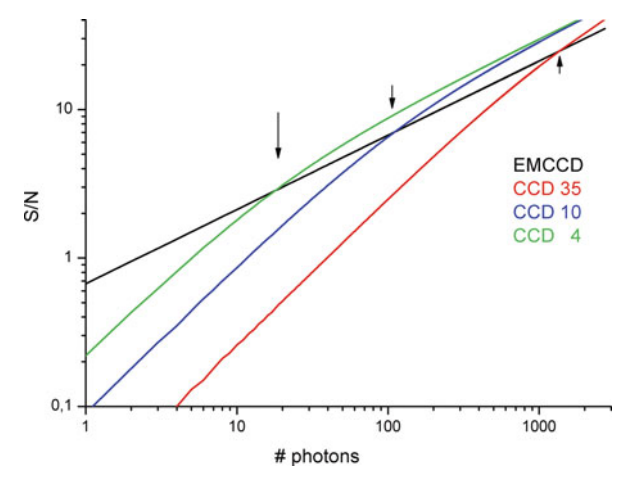


Fig. 3.4 Signal/noise ratio for a back-illuminated EMCCD detector compared to conventional back-illuminated CCD cameras with different readout noise levels (4, 10, and 35 electrons) as is typical for slow (33 kHz), medium (100 kHz), and fast (2.5 MHz) readout speeds as a function of photons per pixel. The *arrows* indicate the number of photons (18, 111, 1362) below which the *S/N* ratio of the EMCCD exceeds that of a conventional detector at the various readout noise levels

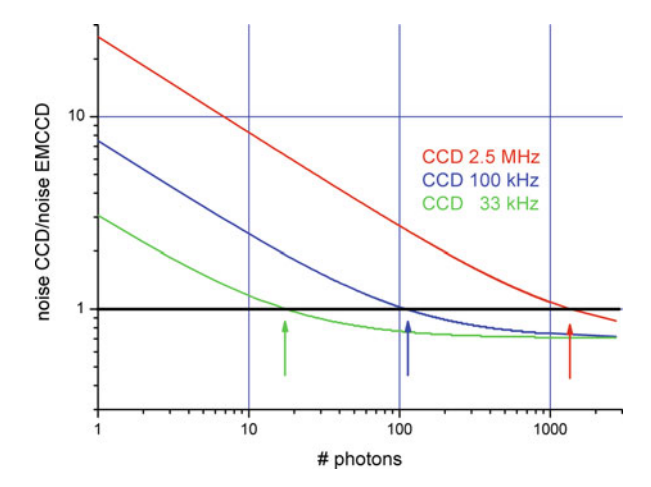


Fig. 3.5 Improvement of the *S/N* ratio for a back-illuminated EMCCD detector compared to conventional back-illuminated CCD cameras with different readout noise levels (4, 10, and 35 electrons) as is typical for slow (33 kHz), medium (100 kHz), and fast (2.5 MHz) readout speeds as a function of photons per pixel. The *arrows* indicate the number of photons (18, 111, 1362) below which the *S/N* ratio of the EMCCD exceeds that of a conventional detector at the various readout noise levels

A signal of 18 electrons or even less seems to be extremely small and that is certainly true if one is accustomed to working with single Raman spectra. As far as confocal Raman microscopy is concerned, things are different. Here, a large number of spectra (>10,000) are acquired and stored and similar spectra with a very low S/N ratio can be averaged to generate a single spectrum with a high S/N ratio. In

a confocal Raman measurement, even a *S/N* ratio of less than 0.1 in the individual spectra can be sufficient to identify unknown species if one knows which of the spectra have to be averaged or if multi-variate analysis methods are employed.

Example of an EMCCD Measurement

In order to illustrate the effect of the EMCCD gain, the following test was performed.

The sample for the tests presented here was an ultra-thin poly(methyl methacry-late) (PMMA) film spin-coated onto a glass substrate. The layer was scratched and the PMMA removed in some areas of the sample (in the center of the figures below). Here the height of the sample layer was determined by AFM to be 7.1 nm. Additionally, a needle-shaped contamination was found on the surface with a thickness of 4.2 nm. The origin and material composition of this contamination layer was not known initially, but could be determined by the confocal Raman measurements.

The results presented in Fig. 3.6 were obtained by acquiring 200×200 Raman spectra in a $50 \times 50 \,\mu\text{m}$ scan range and integrating the intensity of the CH stretching band of PMMA at around $3000 \, \text{cm}^{-1}$. Excitation power was $20 \, \text{mW}$ at $532 \, \text{nm}$ using a $100 \times$, NA = 0.9 objective.

Figure 3.6(a) was obtained with a standard back-illuminated (BI) CCD using a 62-kHz readout amplifier and 36 ms integration time per spectrum. With a little imagination, the scratch in the center of the image is barely visible, but the S/N ratio is much smaller than 1.

Figure 3.6(b) shows the same part of the sample imaged with an EMCCD with a gain of approximately 600. The image shows nearly the same S/N, but now the

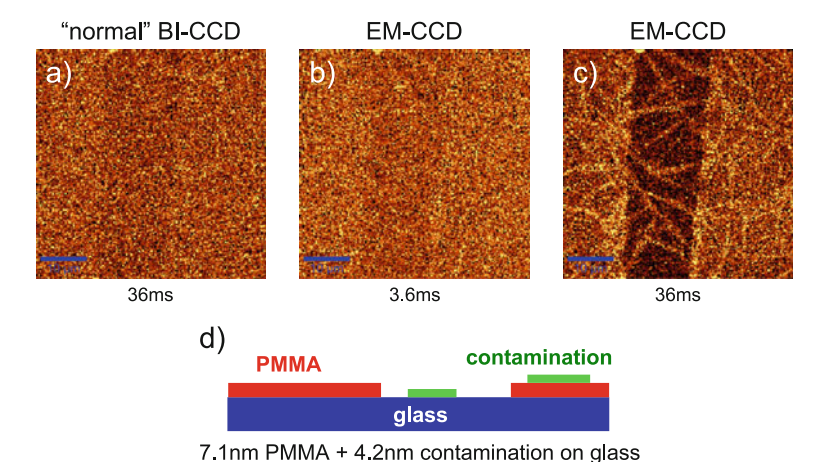


Fig. 3.6 Confocal Raman images of a 7.1-nm PMMA layer on glass obtained at the CH stretching band around $2950 \, \text{cm}^{-1}$: (a) back-illuminated CCD, (b, c) EMCCD. Scale bar: $10 \, \mu \text{m}$. (d) Schematic of the sample

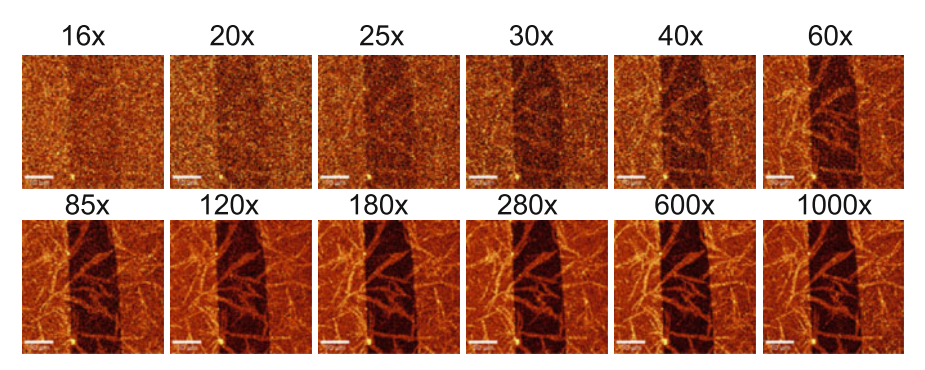


Fig. 3.7 Comparison of confocal Raman images acquired with different settings of the EMCCD gain

integration time was only 3.6 ms, 10 times faster than in Fig. 3.6(a). The complete image acquisition took 25 min for Fig. 3.6(a), but only 3.4 min for Fig. 3.6(b). Figure 3.6(c) was taken with the EMCCD, though now with the same integration time as in Fig. 3.6(a). One can clearly see not only the scratch but also the contamination in the form of a needle-like structure across the PMMA and glass surface which will be discussed later. Figure 3.6(d) shows a sketch of the sample.

For the next images, the sample was turned upside down and an oil-immersion objective with NA = 1.4 was used. The integration time was 7 ms/spectrum resulting in a total acquisition time of only 5.4 min (including 0.3 s/line for the back scan). Figure 3.7 shows 12 images acquired under the same conditions with different gain settings ranging from $16 \times$ to $1000 \times$.

Again, the signal around the CH stretching band was integrated to obtain the images. As one can see, the S/N ratio strongly increases up to a gain setting of about $200\times$. Above this, no further improvement in S/N is visible in the images.

In Fig. 3.8, the S/N ratio of the signal from the CH stretching band of the PMMA is plotted against the EMCCD gain. The standard deviation of the signal was interpreted as noise. As one can see, the signal increases up to a gain of $300\times$, which appears to be the optimum setting. Above this value, the S/N value slightly decreases again. Using the appropriate gain factor, the overall improvement is more than a factor of 5.

Due to the limited confocal depth resolution, none of the spectra obtained was a pure PMMA spectrum or a pure spectrum of the contamination layer. However, by averaging all spectra acquired in the area of the scratch with no contamination present, a pure glass spectrum was obtained. By subsequent subtraction of the glass spectrum from the PMMA spectrum as well as from the spectrum of the contamination, pure PMMA and contamination spectra could be calculated. These spectra were used for a basis analysis in which each measured spectrum is fitted as a linear combination of basic spectra [7, 8]. Using this technique, three images with the distribution of the three components (glass, PMMA, and contamination)

58 O. Hollricher

Fig. 3.8 *S/N* of the signal from the CH stretching band of PMMA plotted against the EMCCD gain

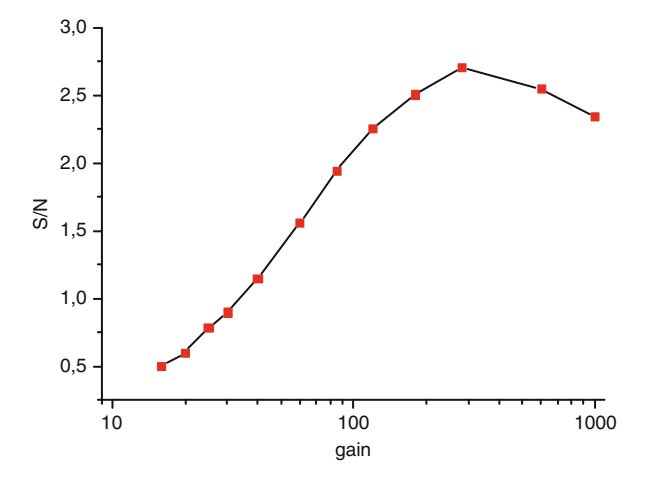
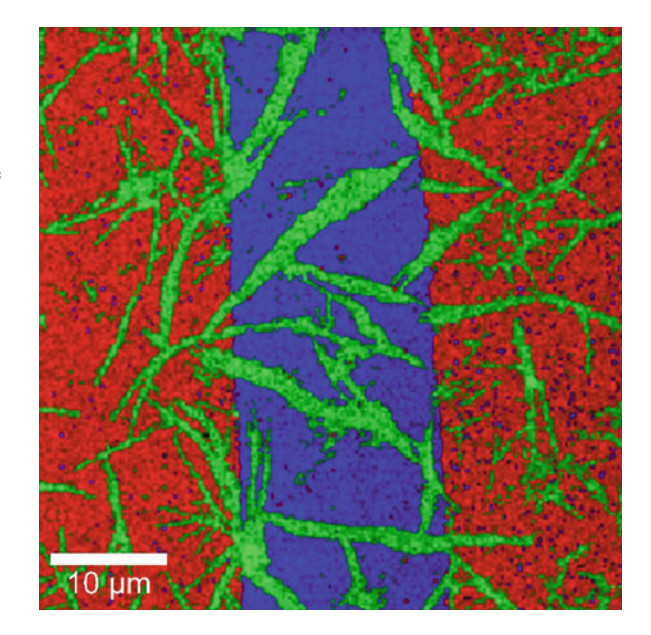


Fig. 3.9 Confocal Raman image of a 7.1-nm PMMA layer (red) and a 4.2-nm contamination layer (green) on glass (blue). 200x200 spectra, 7 ms integration time per spectrum. Total acquisition time: 5.4 min



could be obtained which were then color coded (blue = glass, red = PMMA, and green = contamination) to visualize their distribution (Fig. 3.9).

Figure 3.10 shows the spectra of the different components. From this, the green spectrum (contamination) could be easily identified as an alkane spectrum.

The sample was prepared for the AFM thickness investigation several weeks before the Raman measurement and stored in a polystyrene (PS) container. These PS containers are produced by injection molding and alkane is used to coat the mold for better separation. As the sample was stored (perhaps in a warm environment),

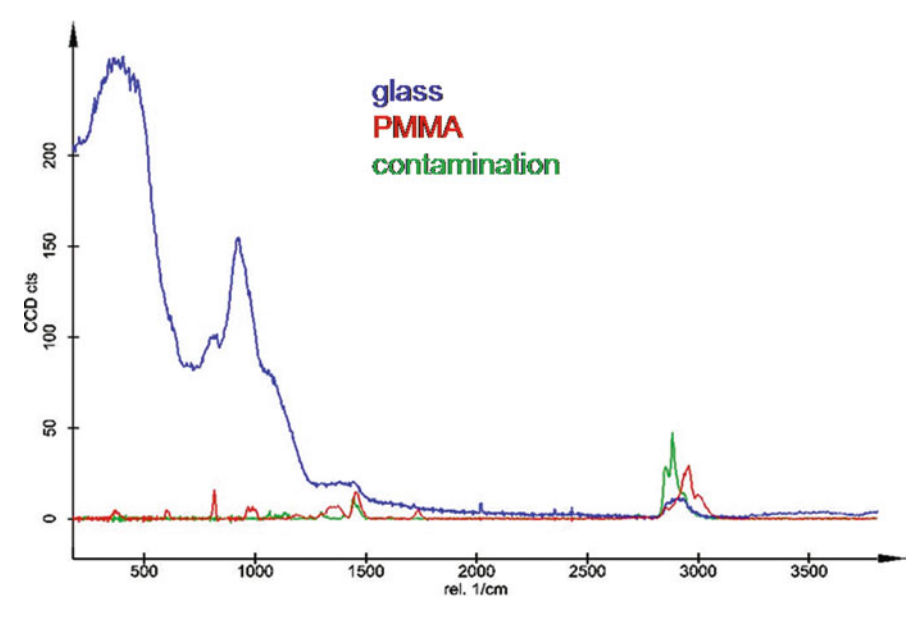


Fig. 3.10 Raman spectra as calculated from the Raman measurement in Fig. 3.9

part of the alkane evaporated and condensed onto the sample, which explains the needle-like structure and the fact that the coating also covers the scratch.

The maximum peak intensity of the PMMA band at 2950 cm⁻¹ in Fig. 3.10 is 28 counts. The signal integrated over the complete CH stretching region (about 330 cm⁻¹ or 150 pixels) is 1965 counts. The EM gain for this measurement was about 600×, so the 1965 counts correspond to only 98 electrons (109 photons) total. This corresponds to an average of 0.65 electrons (0.7 photons)/pixel and 1.4 photons maximum per CCD pixel in each spectrum recorded. This is possible because approximately 20,000 spectra were averaged to calculate the PMMA spectrum shown in Fig. 3.10, so the overall signal is 20,000 times greater. However, only spectra in which PMMA could be detected were taken. For this, the signal per spectrum must be strong enough to show the distribution of the PMMA in the Raman image, which enables one to select the correct spectra for averaging. As can be seen from Fig. 3.7, 0.7 photons/EMCCD pixel are more than enough to visualize the distribution of the PMMA layer in this example and to choose the appropriate spectra for the averaging process.

The result would have been even more impressive if a substrate with no background signal in the CH stretching regime would have been used. As can be seen from Fig. 3.10, the glass substrate has a small Raman band with about half of the signal of PMMA and about one-third of the alkane signal in exactly the same area. It is obvious that the confocality of the Raman system is crucial for investigating thin layers. Even with the best confocal setup, the information depth is at least 500 nm, which means that 500 nm of glass contributes to the Raman signal. As the Raman signal is proportional to the amount of material, a standard (non-confocal) setup

O. Hollricher

would have collected a glass signal more than 300 times greater (170 μm cover glass thickness), making detection of the thin coating layers impossible, even with much longer integration times.

3.5 Conclusion

Confocal Raman imaging is an extremely powerful technique that has applications in a variety of scientific fields. The confocality is important for the suppression of unwanted fluorescence background as well as backgrounds from substrates which may otherwise completely mask the signal of a thin coating layer. Good confocality additionally allows depth scans to be performed with a high level of depth resolution.

Because of the large number of spectra in an image, integration times per spectrum must be kept as short as possible. Therefore, the system as a whole should be optimized for the highest throughput to maximize the *S/N* ratio in the spectra obtained. The large number of spectra helps to obtain high-quality spectra even if a single spectrum might contain hardly any signal.

Using an EMCCD, the spectra can be kept nearly shot noise limited even at extremely low signal levels. The distribution of a 7.1-nm PMMA as well as a 4.2-nm alkane layer on a glass substrate could be easily detected and identified with an integration time of only 7 ms/spectrum. This reduced the overall acquisition time to a total of only 5.4 min for a 200×200 (= 40,000) spectra confocal Raman image. The diffraction-limited spatial resolution in this confocal image was 230 nm using a NA = 1.4 oil-immersion objective at 532 nm excitation. For very small signals that are dominated by the CCD's readout noise, the use of an EMCCD can improve the S/N ratio by a factor of more than 10 compared to the best available standard CCDs, while for larger signals the electron-multiplying circuit can simply be switched off and all properties of a standard (back-illuminated) CCD remain.

References

- 1. C. Raman, Indian J. Phys. 2, 387 (1928)
- 2. T. Maiman. U.S. Patent 3,353,115, 13 Apr 1961
- 3. W. Boyle, G. Smith, Bell Syst. Tech. J. 49, 587 (1970)
- S. Sze, Physics of Semiconductor Devices, (John Wiley & Sons, New York, Chichester, Brisbane, Toronto, Singapore, 1981), p. 407
- I. R. Lewis, H.G.M. Edwards (eds.), Handbook of Raman Spectroscopy (Dekker, New York, Basel 2001)
- 6. T. Dieing, O. Hollricher, Vib. Spectrosc. 48, 22 (2008)
- 7. U. Schmidt, S. Hild, O. Hollricher, Macromol. Symp. 230, 133 (2005)
- 8. U. Schmidt, W. Ibach, J. Mueller, O. Hollricher, SPIE Proc. 6616(1), 66160E (2007)

Chapter 4 Software Requirements and Data Analysis in Confocal Raman Microscopy

Thomas Dieing and Wolfram Ibach

Abstract In confocal Raman microscopy experiments, tens of thousands of spectra are commonly acquired in each measurement. Every spectrum carries a wealth of information on the material at the position where the spectrum is recorded. From each of these spectra the relevant information can be extracted to allow, i.e., the determination of the various phases present in the sample or variations in the strain state. For this purpose, the spectra need to be prepared (i.e., background subtraction) before the relevant information can be extracted using appropriate filters and algorithms. This information can then be visualized as an image, which can be further processed and exported for the presentation of the results of the experiment.

In this chapter, the requirements of the software in terms of handling the data streams and maintaining the spatial and spectral correlation between the spectra and the created images are illustrated. Spectral data processing features, simple and multi-variant algorithms for image creation as well as advanced data processing features are discussed.

4.1 Introduction

In the previous chapters the theoretical background as well as the instrumentation requirements for a confocal Raman microscope were illustrated. In addition to the hardware, software enabling the data handling and analysis plays a crucial role in enabling the acquisition and presentation of results of confocal Raman data.

Generally, the software included with commercially available confocal Raman microscopes facilitates data acquisition as well as data evaluation to varying degrees. Other software available on the market is purely focused on data evaluation.

The requirements for the software for data acquisition are described in Sect. 4.2 before a general description of the data sets acquired in confocal Raman microscopy experiments is presented in Sect. 4.3.

Once the data are acquired, it can be treated in various ways. In most cases, a preprocessing will first take place such as cosmic ray removal, background subtraction, or smoothing of the spectra. These are usually applied to both single spectra as well as multi-spectral data sets and are described in Sect. 4.4. Multi-spectral data sets are then commonly evaluated further to extract the information in a way that it can be displayed. For data sets originating from confocal Raman microscopy experiments, where at each image pixel a full spectrum was recorded, this evaluation will result in an image. This image generation can be performed using either single-variant or multi-variant methods. The resulting images and masks can then be evaluated further in combination with the multi-spectral data sets in order to obtain, for example, average spectra originating from certain areas on the sample. Combining the information contained in single spectra with the multi-spectral data sets allows further enhancement of the image contrast. These steps are described in Sects. 4.5–4.7. Combining the images generated allows the information contained in various images to be displayed in one multi-colored image (Sect. 4.8). From these images, phase separation and/or mixing can easily be identified.

In Sect. 4.9 it will be illustrated that even very noisy spectra acquired with extremely little signal can be treated through the described methods to extract the relevant information and obtain images with excellent contrast.

All the above-mentioned data processing techniques will be shown using a few sample systems which are introduced together with the acquisition parameters in Sect. 4.10.

4.2 Requirements for Data Acquisition Software

The requirements for any data acquisition software for confocal Raman microscopy are extensive. The main tasks can, however, be sorted into several groups, which will be described in the following.

4.2.1 Data Acquisition

4.2.1.1 Acquisition of Spectra

For the acquisition of spectral data the software must first read and store the data acquired by the spectroscopic CCD camera. While this may at first appear straightforward, it can already pose some significant challenges for the software.

Consider a spectroscopic CCD camera with 1600×200 pixels. Such cameras can be readout in a full vertical binning mode, by reading out only a certain region of interest or by reading out the entire chip as an image. The first cases, however, allow a significantly faster readout. A single spectrum readout from such a CCD camera will in this case consist of 2×1600 integer values (pixel number and intensity), which corresponds to a size of $2 \times 1600 \times 2$ bytes/integer = 6400 bytes per spectrum.

State-of-the-art CCD cameras such as EMCCDs can acquire single spectra in extremely short times (i.e., 0.76 ms has already been demonstrated [1]). This corresponds to more than 1300 spectra/s. The software must therefore be capable of handling this data stream of 1300 spectra/s \times 6400 bytes/spectrum \approx 7.9 MB/s. The challenge for the data acquisition software is that most modern cameras are connected to the PC via USB and thus the data stream needs to be handled by the

processor which at the same time needs to be able to manage all other tasks for the control of the microscope. Additionally, the data stream must be handled in a way that allows data acquisition without interruptions. If the software needs pauses after a certain number of acquired spectra to process and/or store the data, the advantage of the fast data acquisition is lost.

If the entire CCD chip of the camera must be readout (i.e., due to the necessity to acquire a reference, calibration spectrum with each spectrum recorded) the data stream would multiply by the vertical size of the chip (200 in the example above) thus lowering the maximum acquisition speed significantly.

An additional challenge for the software is memory space required by the spectra recorded. If, for example, a Raman image of 512×512 spectra is recorded, this results in a data amount of

$$512 \times 512$$
 spectra \times 6400 byte/spectrum = 1.56 GB

This is only the amount for one layer. Note also that once data processing starts, the data are typically transformed from integer to double precision to increase the accuracy of the calculations. This almost triples the storage space needed per spectrum. Luckily, however, such a high resolution is not always necessary and due to the time taken per Raman spectrum is often impractical. Therefore a resolution in the range of 150×150 pixels is generally sufficient.

Adding to the issue of memory space is that many analysis methods such as multivariate analysis require a substantial additional amount. Programmers must therefore balance computation time against available memory.

4.2.1.2 Control of the Microscope and Sample Positioning

In addition to the acquisition of the spectra discussed in the previous section, the software also needs to control all other parameters of the microscope. These are, but are not limited to, the control of the positioning of the grating within the spectrometer as well as the control over the position at which the spectra are recorded. The latter is done either by moving the sample through the focused laser spot or by moving the laser spot itself. In order to achieve high-resolution images it is necessary to perform this positioning with a high level of accuracy from both the control electronics as well as the controlling software. The software should also allow the acquisition of white light images at the position where measurements are taken. For high-resolution objectives, the field of view is sometimes small compared to the desired measurement area. In these cases it is advantageous if the software allows automated stitching of white light image in order to obtain an overview image.

4.2.2 Correlation of Spatial and Spectral Data

Apart from the above-discussed data acquisition, the software needs to establish correlations between and among the data acquired. For example, the software should

be capable of indicating where the spectra were recorded on the bitmap acquired from the white light image. Also, after the generation of a confocal Raman image though, i.e., an integral filter over a certain spectral region, the software needs to allow the display of the spectra at each position of the image by a simple mouse click to facilitate the analysis. Additionally, if spectra were taken with different gratings (and thus different spectral resolutions), the software needs to be able to correlate these spectra with each other. Figure 4.1 displays these correlations using the example of several measurements on a polymer blend sample (PS-PMMA on glass).

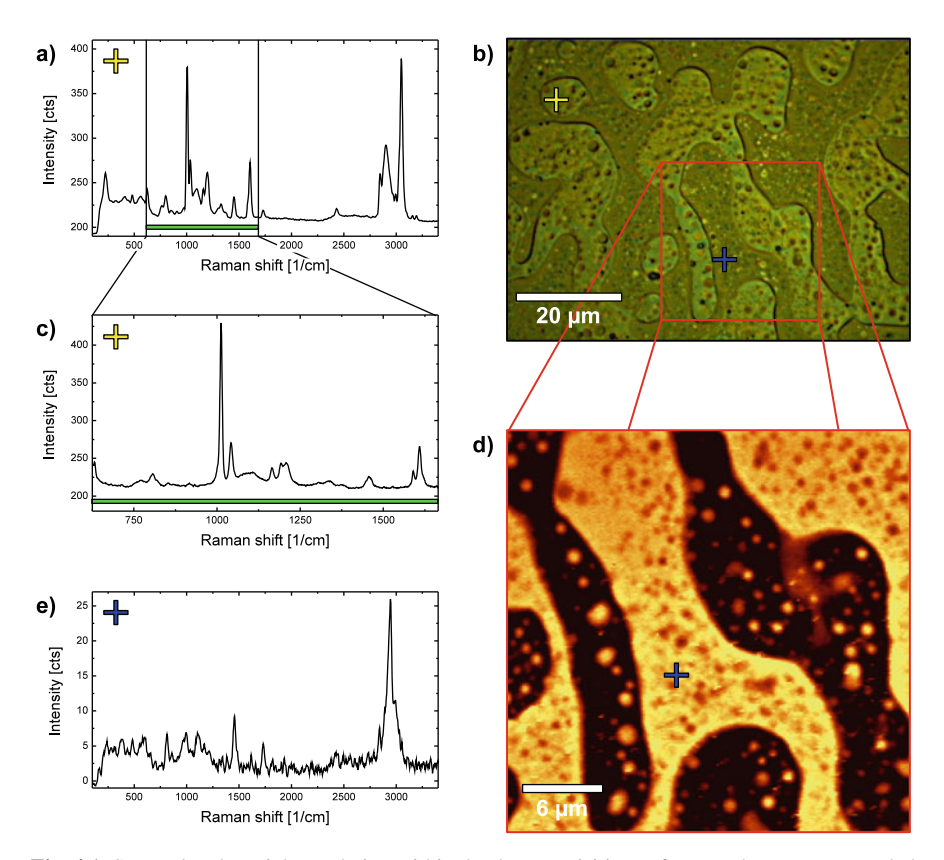


Fig. 4.1 Spectral and spatial correlation within the data acquisition software. The spectra recorded (**a**, **c**, **e**) are linked to the position where they are recorded as indicated by the *yellow* and *blue* crosses. The spatial correlation between the video image (**b**) and the confocal Raman image (**d**) is indicated by the *red box*. Additionally, the spectral axes are correlated for spectra recorded with different gratings as indicated by the *green* bar for a spectrum recorded using a 600 g/mm grating (**a**) and an 1800 g/mm grating (**c**). (**e**) One of the spectra recorded for the confocal Raman image (**d**) and its position correlation (*blue cross*) is shown

4.3 Description of the Data Sets Acquired in Confocal Raman Microscopy

Data acquired in confocal Raman measurements are generally five or even six dimensional. The dimensions are

- The spatial X, Y, and Z coordinates of the point where the spectrum was recorded (typically given in μ m).
- The spectral position given as the wave number (cm⁻¹), relative wave number (rel. cm⁻¹), or wavelength (typically given in nm).
- the intensity recorded at this spatial and spectral position (typically given in CCD counts or counts per second [cps]).
- Time may also be present as a sixth dimension.

Such a data set is sometimes referred to as a hyperspectral data set.

Individual spectra can of course be displayed in a straightforward way (intensity vs. spectral position) with the coordinates (and time if applicable) added in writing.

Displaying data sets containing more than one spectrum, however, becomes more complicated. Line scans (spectra collected along a single line) as well as time series (spectra recorded at the same position as a function of time) are sometimes displayed in a so-called waterfall display as shown in Fig. 4.2.

For confocal Raman image scans, an entire Raman spectrum is collected at every image point. A confocal Raman image scan consisting of 256×256 points will therefore contain $256 \times 256 = 65$, 536 individual spectra. One may distinguish between a single image scan, in which the spectra are recorded in one layer in three-dimensional space, and a multi-layered or stack scan, in which several parallel layers offset by a specific distance are recorded.

In either case, the information contained within each spectrum needs to be reduced to a single value, which will then determine the coloring of the pixel at this position (see also Sect. 4.5).

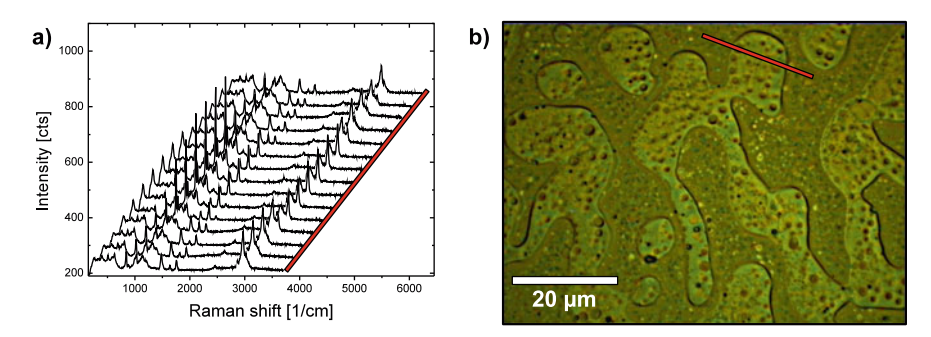


Fig. 4.2 Display of a line scan recorded along the line represented in *red* in the video image (b) in the form of a waterfall plot (a)

In the case of an image stack one can then display each layer of the stack individually or combine them with software in order to display the distribution in three dimensions. Some examples of this can be found in Chap. 12 by Thomas Wermelinger and Ralph Spolenak.

4.4 Pre-processing of Raman Spectra

Pre-processing of Raman spectra refers to the treatment of the Raman spectra before the generation of images or final presentation of the spectra. The steps described below are universal to spectra recorded and should generally be followed before any further processing.

4.4.1 Cosmic Ray Removal

Cosmic rays are high-energy particles from outer space which interact with atoms and molecules in the Earth's atmosphere. Due to their high energy, a large number (often called a shower) of particles are generated upon this impact which are mainly charged mesons. These quickly decay into muons. Due to their relativistic speeds (and thus the time dilation) some of these muons reach the surface of the Earth. Despite this exact reaction path, the term "cosmic ray" is also used (even if not 100% correct) for the muons interacting with devices on the Earth's surface and for simplicity, this term will be used in the following as well.

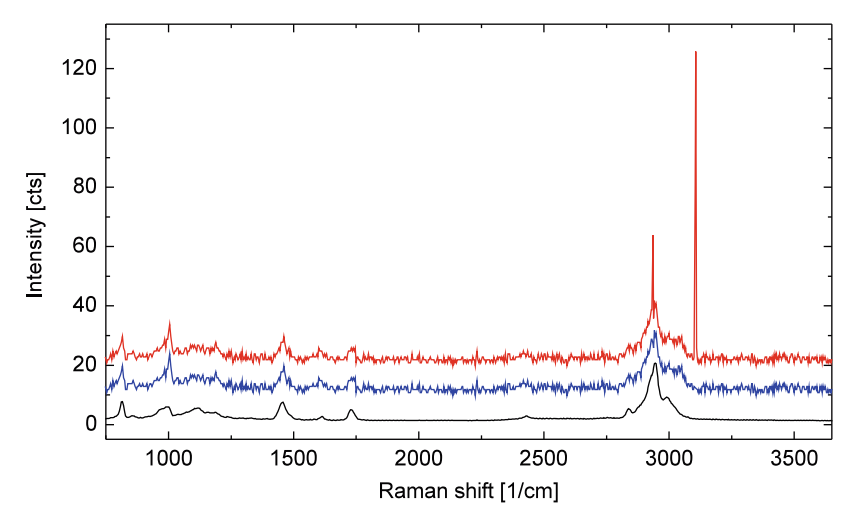


Fig. 4.3 Cosmic ray removal. The *red* spectrum was recorded with a short integration time and shows two cosmic rays near 3000 cm⁻¹. The *blue* spectrum is the same as the *red*, but after having undergone cosmic ray removal, and the *black* spectrum is the spectrum of this component (PMMA) recorded with a longer integration time for a better signal to noise ratio

If such a cosmic ray hits a CCD detector it will generate a false signal in the shape of a very sharp peak in the spectrum that is not related to the Raman signal. An example can be seen in red in Fig. 4.3.

Cosmic rays can be filtered out as shown in Fig. 4.3 and described below. There is, however, also the possibility to minimize the amount of cosmic rays recorded through the readout method of the CCD camera. As already described in Sect. 4.2.1.1, one method is the full vertical binning mode, which is the fastest readout method. In this case, all pixels are used even though typically only a few percent of the pixels are exposed to the Raman signal. If one limits the readout to the few lines in the detector at which the Raman photons hit the CCD camera, one typically excludes more than 90% of the pixels from the readout. This will of course reduce the probability of recording a cosmic ray. The disadvantages of this method is that it is a slower readout method and that during the readout, the light hitting the camera cannot be recorded. This method is therefore recommended for single spectra, whereas for Raman imaging it is not very suitable.

Once the spectra are recorded, various mathematical methods can be used to filter the cosmic rays from the spectra. In these, two principal approaches can be distinguished. These will be discussed in the following.

4.4.1.1 Spectral Cosmic Ray Removal

Filtering spectra in the spectral domain for cosmic rays has the advantage that this method works for true, one-shot exposures as well as for multiple accumulations, time series, or Raman image scans.

The principle of this method is that each pixel is compared to its adjacent pixels and if it exceeds a certain threshold, then it is identified as a cosmic ray. This method is heavily dependent on the size of the filter (= the number of adjacent pixels taken into account) and the threshold (or multiplicative factor). Therefore, any spectroscopic software should allow the adjustment of these values as well as the preview of the resulting spectrum to allow the user to select the correct parameters.

While this method can be problematic when using very sharp atomic emission lines, it works very well for Raman spectra in which (with only few exceptions) the natural line widths (FWHM) are typically $>3\,\mathrm{cm}^{-1}$. Additionally, Raman lines typically display a relative broad base of the peaks similar to Lorentzian curves. The Raman lines therefore have a certain rise, which is beneficial for this type of detection algorithm. It of course also depends on the spectral resolution of the spectrometer used.

Other methods for cosmic ray removal involving further computational methods are reviewed in the literature (i.e., [2]), but discussing these would exceed the scope of this chapter.

4.4.1.2 Temporal Cosmic Ray Removal

Removal of cosmic rays based on variations over time is also a very popular method. In this case spectra recorded one after another are compared and each pixel is compared to its variation in the time domain.

This method works well when evaluating single spectra with various acquisitions on the same position. It requires that there are only negligible changes from spectrum to spectrum. If the sample changes its spectral signature in a rapid way (for example, due to a chemical process taking place), the usage of this type of algorithm is problematic.

For confocal Raman imaging data sets, this method can also be applied. The user must be aware that in this case the spectra are recorded not only at different times but also at different spatial positions. In this case it additionally depends on the compositional variation of the sample compared to the resolution of the scan. If the changes from spectrum to spectrum are too dramatic, one faces again the problem that the algorithm might filter out real peaks.

4.4.2 Smoothing

Smoothing is a common practice used to reduce the noise potentially associated with a recorded spectrum.

Most smoothing algorithms rely on the fact that spectral data (in our case Raman) are assumed to vary somewhat gradually when going from spectral data point to data point, whereas noise associated with the spectrum typically changes very quickly. In this case, it can be useful to replace each value by a value calculated from the surrounding values in order to reduce the noise. Therefore, most filters for this purpose can be considered as low pass filters. Independent of the filter used, care must be taken in order to avoid alteration of the true Raman signal. Overly extensive smoothing, for example, will result in a "smearing" of the Raman peaks, thus altering their height and/or width. Additionally, small shoulder peaks might be lost.

The various filters which can be applied to the data essentially differ most significantly in the way that the replacement value is calculated. Most filters will allow the definition of how many values are taken into account around the value to be replaced. The software should allow the user a preview of the results in order to facilitate the choice of parameters.

The following filters are a typical selection of those used to smooth spectral data:

- 1. *Moving average* This filter is arguably the simplest filter for smoothing. For this filter a definable number of values to the left and right of the current value are averaged and the current value is replaced. Then this "window" moves to the next value and so on. For very slow changing signals (as might be the case in photoluminescence [PL]) this filter can be suitable.
- 2. Weighted average This filter differs from the Moving Average in that it does not take each value with the same weight, but multiplies each one with a binomial weighting factor or a Gaussian distribution. Table 4.1 shows the distribution of the binomial coefficients for the average calculation for various filter sizes. This filter ensures that the resulting value is closer to the real value as compared to the Moving Average filter even if the signal is changing more rapidly.

Table 112 Manifeld for the graph average inter					
Filter size	Range	Filter coefficients			
1	3	$\frac{1}{4}(1,2,1)$			
2	5	$\frac{1}{16}(1,4,6,4,1)$			
3	7	$\frac{1}{64}(1, 6, 15, 20, 15, 6, 1)$			
4	9	$\frac{1}{256}$ (1, 8, 28, 56, 70, 56, 28, 8, 1)			

Table 4.1 Matrices for the graph average filter

- 3. *Median* The median filter is generally less influenced by single data points that fall out of range of the "normal" signal. For example, if a cosmic ray is within the search window, the median filter will be less influenced by this than an average filter. This filter is a good choice for removing spikes in a line graph without heavy rounding of the edges of Raman peaks.
- 4. Savitzky Golay The Savitzky Golay filter (sometimes also known as DISPO (Digital Smoothing Polynomial) filter) essentially uses the surrounding values in a weighted way and fits a polynomial through these points in order to determine the "fitted" value at the current position. While the smoothing of this filter will not be as strong as, for example, a Moving Average filter, it will smooth the data considerably while largely maintaining the curve shape (peak width, peak intensities,...). A detailed discussion of the functionality as well as examples of this filter can be found in [3]. This filter has the additional advantage of allowing the calculation of the derivative of the spectrum, which can be useful for peak location (see black vertical lines in Fig. 4.4). Figure 4.4 shows an example of the usage of the Savitzky Golay filter. The use of this filter is especially recommended if the widths of the peaks in the spectrum are comparable.
- 5. Wavelet transformation techniques Wavelet transformation is a mathematical technique somewhat similar to Fourier transformation but with the advantage that both time and frequency information are maintained. Wavelets consist essentially of a family of basic functions which can be used to model the signal. Each level of the wavelet decomposition will result in an *approximation* and a *detail* result. The *approximation* result is then used as the basis for the next decomposition and this is repeated until a defined threshold. By using the correct combination of the *detail* results (one available per decomposition level) and the *approximation* result (only the last one is typically used here) one can perform the reconstruction (or inverse discrete wavelet transformation [IDWT]) to obtain a spectrum with either a strong noise reduction, a removed background or both. More detailed descriptions as well as some illustrative examples can be found in [4, 5].
- 6. *Maximum entropy filter* The maximum entropy method uses the fact that certain aspects of the instrument functionality are known. Through this, neighboring pixels in a spectrum are not statistically independent anymore and a filtering of these values is therefore possible.

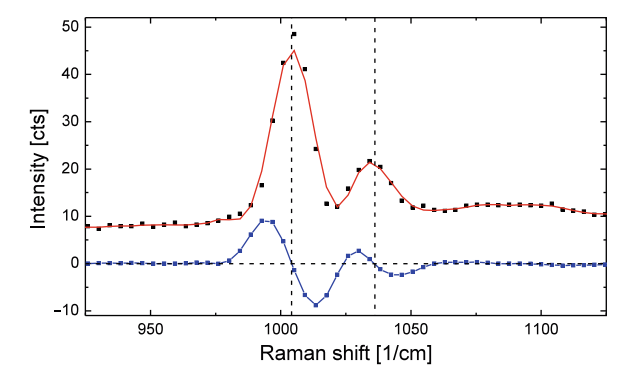


Fig. 4.4 Effect of the Savitzky – Golay filter. The *black points* in the top spectrum correspond to the data points recorded from the CCD camera (background subtracted) and the *red line* shows the spectrum after smoothing using the Savitzky – Golay filter. The *blue curve* in the bottom is the derivative of the spectrum obtained through the Savitzky – Golay filter

4.4.2.1 Smoothing in Raman Imaging

The filters discussed above can be applied to single spectra as well as to entire spectral data sets. In the case of Raman imaging, the experimenter can also take the spatial correlation between various spectra into account. In other words: for pure spectral filtering only the spectrally neighboring pixels are taken into account, whereas for Raman imaging, the spatially neighboring pixels may also be used. This is especially true for the case of the *Median* and *Average* filters.

Images generated from Raman data (see Sect. 4.5) can also be smoothed through filters and here Median and Average filters (in two dimensions) are the most prominent, but Fourier space filtering can also be employed.

4.4.3 Background Substraction and Subtraction of Reference Spectra

Any Raman spectra read from a CCD camera show some background signal. The sources of the background can be divided into two main categories, and the recommended removal of this background may differ somewhat. These two categories as well as the respective background removal are described below.

4.4.3.1 Background Originating from the CCD Camera

A CCD camera generally adds a DC voltage to the detected signal in order to ensure that the A/D converter, which converts the analog charge into a digital signal, will not receive a negative voltage due to noise. This results in a constant background of typically a few hundred to a few thousand CCD counts.

Most cameras additionally have a slight non-linear background due to inhomogeneities in the chip itself or a non-homogenous cooling of the CCD chip.

Removal of a Background Originating from the CCD Camera

The constant background originating from the CCD camera can be subtracted quite easily by subtracting the constant value added by the camera. One can, for example, find this value by averaging the part where the Raman edge filter is still blocking the signal but no Rayleigh peak is present.

The non-linear background of the CCD camera is best eliminated by the subtraction of a reference or a "dark" spectrum. A dark spectrum is ideally recorded using exactly the same integration parameters as were used for the recoding of the Raman spectrum. To minimize the noise of the "dark" spectrum, it is recommended to record it with the same integration time as the Raman spectrum, but to use many accumulations using this integration time. The software then needs to offer a simple functionality to calculate [Raman spectrum] – [dark spectrum]. However, the raw data should still be available to the user.

4.4.3.2 True Signal Background

There are very few "real-world" materials that will show a complete zero background in their Raman spectrum. Good confocality of the system, however, will largely reduce this background as described in the earlier chapters. Nevertheless, a remaining background such as fluorescence or some signal from the substrate often underlies the Raman spectrum.

Removal of Signal Background

There are several ways to subtract the background from the recorded spectrum. Some of the most prominent are

Single-pass polynomial background subtraction

For this type of background subtraction, a polynomial needs to be fitted to the spectrum and subtracted. Care must be taken to ensure, however, that the regions of the spectrum containing Raman peaks are not included in the values used to calculate the fit of the polynomial. This selection can either be done automatically through a peak recognition routine or manually through defining the regions in the spectrum where no peaks are present. The order of the polynomial is then the next variable which needs to be adjusted. Using a very high (i.e., ninth order) polynomial often fits the data well at first glace, but will often introduce "wave" -like artifact oscillations around the 0 value of the background. Using an order that is too low, on the other hand, might not allow the polynomial to follow the spectrum closely enough.

Moving average background subtraction

The calculation of the moving average was already described in Sect. 4.4.2. Using this method for background subtraction essentially calculates the moving average of definable regions, which should be the ones without Raman peaks. For the regions in which there are peaks, an interpolation between the points is calculated.

This resulting curve is then subtracted. Using this method, great care must be taken to ensure that no relevant information of the spectrum is altered.

Wavelet transformation techniques

The principles of wavelet transformation techniques have already been described in Sect. 4.4.2. Through the appropriate combination of the *detail* results (one available per decomposition level) and the *approximation* result (only the last one is typically used here) one can subtract the background. In this the *approximation* result is generally omitted from the reconstruction.

4.5 Image Generation

Confocal Raman imaging data sets (as described in Sect. 4.3) are typically five to six dimensional and thus the dimensionality needs to be reduced in order to display the information. As stated earlier, the dimensions are *X,Y,Z*, wave number, intensity, and time.

Considering a typical Raman image, which is a single scan along one plane, the dimensionality reduces to the two directions of the plane (let us assume X and Y for simplicity), the wave number and the intensity. While this is still a four-dimensional data set, we can in a quite straightforward way display the information from this.

For the image generation two main methods may be distinguished: univariate and multivariate analysis. The primary difference is that for a univariate analysis one spectrum at a time is evaluated and used for the generation of one data point per resulting image. Here the surrounding points also are considered for the value of the current pixel. In contrast to this all spectra in the data set play a role for each data point in the case of the multivariate data analysis. Typical univariate and multivariate methods will be described in the following sections.

4.5.1 Univariate Image Generation

As stated above, in univariate data analysis, each spectrum determines one value of the corresponding pixel in the image or the images. The value of these pixels can be determined by simple filters or by fitting procedures.

4.5.1.1 Simple Filters

Simple filters typically evaluate a certain part of the spectrum. Figure 4.5 shows an example of an integrated intensity (sum) filter evaluating the integrated intensity of various specific peaks found in the image scan of an oil – water – alkane immersion. The resulting images (Fig. 4.5c–e) show in more brightly colored areas the high intensities of these peaks and in darker colored areas the low intensities. Other types of filters can evaluate, for example, the peak width or the peak position and display this as an image.

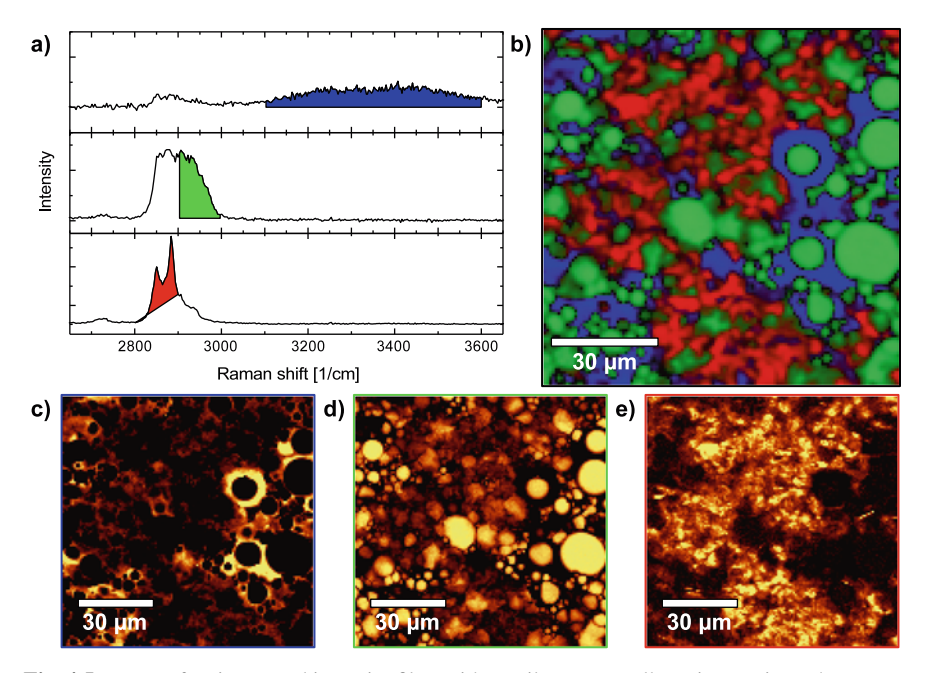


Fig. 4.5 Usage of an integrated intensity filter with an oil – water – alkane immersion. The spectra (a) are integrated in three different spectral areas. The water peak (*blue*) is evaluated without background subtraction and results in image (c). The oil peak is integrated as shown in *green* with the pixels adjacent to the higher wave number side of the peak used as the background level and results in image (d). The alkane is using pixels to the left and right of the integration area for background calculation (red) and results in image (e). Image (b) shows the combined image of (c), (d), and (e)

It should be noted that many of the filters used allow the extraction of a large amount of information from the data. However, there is also the danger of misinter-pretation. The list below shows some typical simple filters and their usage as well as considerations which should be taken into account to avoid misinterpretations.

• Integrated intensity filter (sum filter)

Information content:

A typical measure of the amount and scattering strength of a certain material within the focus.

Misinterpretation dangers:

- Other materials present in the sample might also have peaks at this position.
- The amount of material between the objective and the focal point might change and this would also have an influence on the absolute intensity of the peak.
- The polarization direction of the laser relative to the structure can also have an influence on this peak intensity.
- If the software does not provide good background subtraction methods, then changes in the background can influence the result.

• Peak width (i.e., FWHM)

Information content:

A measure of the crystallinity and the structural orientation relative to the polarization direction of the laser. Also, inhomogeneous peak broadening can occur in samples under stress for example.

Misinterpretation dangers:

- Non-resolved shoulder peaks can influence this result.
- If the software does not provide good background subtraction methods, then changes in the background can influence the result.
- Peak position (i.e., center of mass position)

Information content:

A measure for the strain within a material and for the general chemical neighborhood of the molecule

Misinterpretation dangers:

- Non-resolved shoulder peaks can influence this result
- If the software does not provide good background subtraction methods, then changes in the background can influence the result.

Simple filters have the advantage of being relatively low in processor load and thus they can be applied during ongoing data acquisition.

4.5.1.2 Fitting Filters

Fitting filters are a more sophisticated way of extracting the information required from the spectra. In this case the peaks of the spectra are fitted with polymeric or peak functions. Depending on the state (solid, liquid, or gas) and the environment of the molecules observed by Raman spectroscopy, the line shape of the emitted Raman line can lie anywhere between a Gaussian and a Lorentzian curve.

Voigt curves represent a convolution between Lorentzian and Gaussian curves and pseudo-Voigt curves are calculated by

$$m_u \times \text{Gauss} + (1 - m_u) \times \text{Lorentzian}$$

Here m_u is the profile shape factor. Pseudo-Voigt curves can be additionally differentiated in the degree of freedom of the FWHM (identical for Gauss and Lorenz or variable).

In addition to the above-discussed mixture of Lorentzian and Gaussian line profiles, the Raman curves may also be distorted by the local sample environment. Instrument functions will play an additional role. The change of the signal due to these instrument functions is heavily dependent on the microscope and spectrometer design [6] and it will depend on the instrument if this needs to be taken into account for peak fitting.

Filter	Information content		
Linear fit	SlopeOffset		
Quadratric fit	Peak positionCurvaturePeak intensity		
Gaussian fit	Peak positionWidthIntegrated intensityOffset		
Lorentzian fit	Peak positionWidthIntegrated intensityOffset		
Pseudo-Voigt fit	 Peak position Width (Gaussian and Lorentzian) Integrated intensity Offset Profile shape factor 		

Table 4.2 Fitting filters for spectral data

For these reasons, there is not one perfect peak function which can be used to perfectly match all Raman peaks. Table 4.2 shows some common fitting filters and which information can be obtained through them.

As can be seen from Table 4.2, all of the filters listed deliver more than one result per curve fitted. Therefore, the results after applying such filters to a confocal Raman image data set are multiple images as can be seen in Fig. 4.6. In addition to the results described in Table 4.2, the software should provide an error image in order to allow the user to quickly determine if the fitting error in a certain region is larger due to, for example, a line distortion. In Fig. 4.6 a confocal Raman image was recorded of a Vickers indent in Si and the resulting spectra were fitted using a Lorentzian function. The peak shift as well as the broadening can clearly be seen from the spectra (Fig. 4.6a) as well as from the images (Fig. 4.6b and c).

4.5.2 Multivariate Image Generation

As mentioned in a previous section, multivariate image generation uses the information of the entire hyperspectral data set for the determination of the value (and thus the color) of each image pixel. In the following the two most commonly used multivariate data analysis methods for the analysis of Raman spectra are presented. First the so-called Principal Component Analysis is discussed. This method is used not only for image generation but also for data reduction and distinction of sample properties based on the principal components.

The second method described is the *Cluster Analysis* which can be used for direct image generation or average calculation for further data analysis (see, for example, Sect. 4.7).

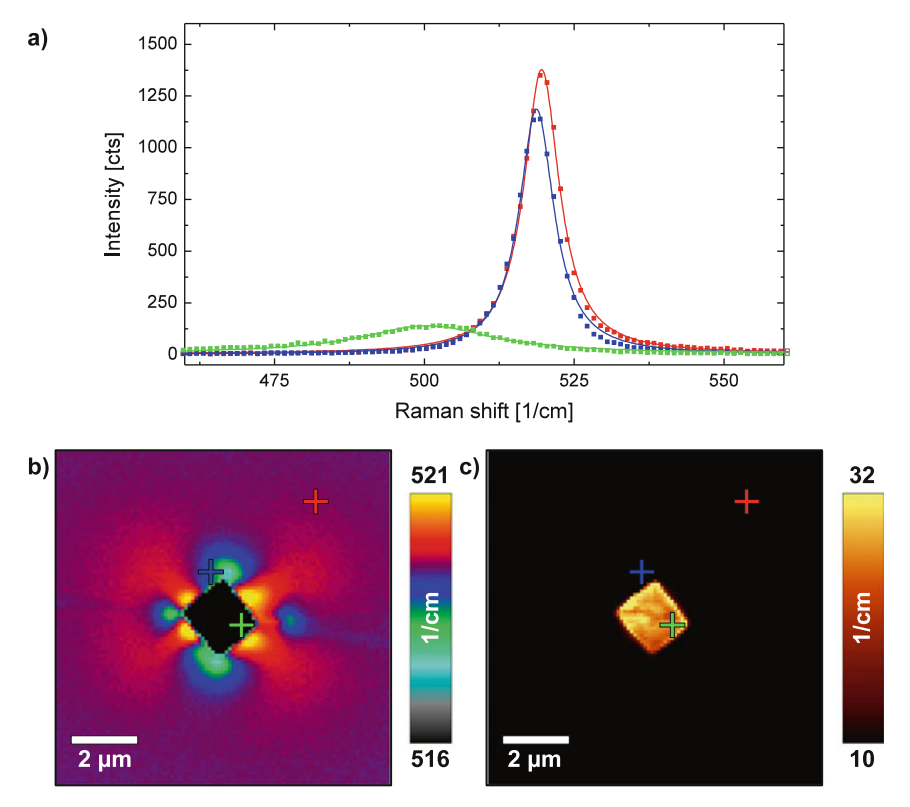


Fig. 4.6 Lorentzian fitting of first-order Si peaks around a Vickers indent. The spectra (a) are extracted from the points indicated by the corresponding colors in the images. (b) Shows the position of the first-order Si peaks and (c) shows the width of the line. Both are results from a Lorentzian fit

Vertex component analysis (VCA) is another multivariate method which finds the most dissimilar spectra in the data set as described in Chap. 7 by Christian Matthäus et al.

4.5.2.1 Principal Component Analysis

Principal component analysis (PCA) was first proposed in 1901 by Karl Pearson [7]. However, only the use of computers allowed its usage as we know it today due to the large computational effort required by the method. PCA is the underlying method for many other multivariate methods since it is very effective for data reduction. In this way a spectrum consisting of 1600 pixels and thus 1600 dimensions can often be reduced to approximately 4–6 dimensions. In some cases, this is then also the number of different components in the sample, since all the other spectra are a linear combination of the pure component spectra (see also Sect. 4.7).

In the following this reduction is explained in a greatly simplified way. The user is referred to, for example, [8, 9] for further reading and detailed explanation of the method.

Principal Function of the PCA

If we assume a single spectrum consisting of 1600 pixels, then this spectrum can be described as a single point in 1600-dimensional space. Each of the CCD pixels is one axis and the value recorded at this CCD pixel is the value along this axis. If we now look at a confocal Raman image, then we might have, for example, 150×150 (= 22,500) spectra and we will thus have 22,500 points in our 1600-dimensional space.

Now let us consider a Raman peak which is present in some of the spectra. As most Raman peaks are significantly wider than a single pixel (at least using the commonly used spectrometers and gratings) the pixels describing this peak are not statistically independent. Furthermore, most Raman spectra consist of more than one peak. Therefore the pixels which will increase if such a Raman spectrum is recorded are linked. In our 1600 dimensional space, this corresponds to a certain direction. Analyzing the entire data set will result in a variety of such directions. These directions describe a subspace in the 1600- dimensional space wherein all spectra can be found. These directions are orthogonal to each other, but cannot be identified as pure components, since, for example, they might point in the negative direction.

Each of those directions has a certain Eigenvalue associated with it and the value depends on the amount of variation within the data set explained by this direction. There is a strong spread in their value and some might be hundreds of times the value of others. Sorting them by value allows the quick determination of the relevant directions (= the principal components). If the sample consists, for example, of three components, then three principal components should describe the data set sufficiently, while the other directions should then only describe noise.

Noise and PCA

PCA can only work if the data set is not dominated by noise. Otherwise, even the principal components with the highest Eigenvalues will only describe noise. Figure 4.7 illustrates this for a simple two-dimensional example. Figure 4.7(a) shows a data set with two principal components PC_1 and PC_2 which perfectly describe the data set.

From the noise-dominated image in Fig. 4.7(b) it is obvious that no such principal components (or directions) can be defined, because for the noise-dominated data set all directions are equally good or bad.

Results from a PCA

Following the PCA, one can extract a variety of results. The most commonly used for the analysis of confocal Raman data are

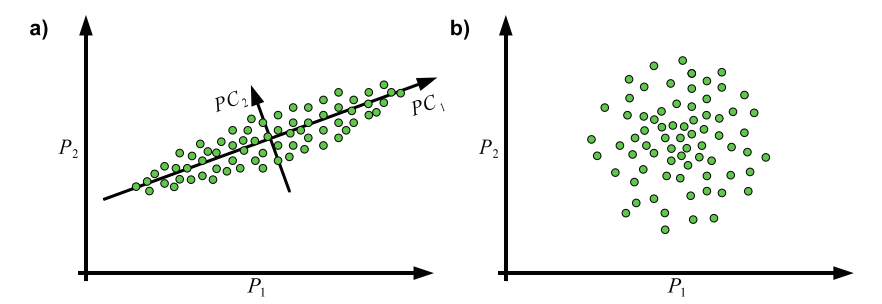


Fig. 4.7 Principal components of a typical two-dimensional data set (a) Noise-dominated data set in which principal components can no longer be found (b)

Reduced data set

Each of the 22,500 spectra used for the PCA is now described through principal components. As mentioned above a relatively small number of components is sufficient to describe the spectrum clearly. We can therefore export these "spectra of components" which now consist of only a few pixels instead of 1600 at each image pixel and use this for further investigation such as cluster analysis, which will then be much faster.

Images of the principal components

Each of the spectra used for the analysis can be described by a weighted combination of the principal components. If we now consider only one component, then this will result in one value per image pixel and we can of course display this, which then corresponds to the Raman image describing the abundance of a certain spectrum (direction) within the data set.

Reconstructed spectra from the principal components

If we calculate the spectra using, for example, only five components, then we will find spectra with much lower noise. Due to the fact that the noise is statistical and will not be described by one of the first approximately 20 directions, the noise will be reduced.

Please note here that this is only true if the spectra are recorded with a sufficient signal to noise ratio (S/N). For a S/N close to 1, no PCA is possible. In this case the noise would determine the "directions" of the principal components.

Cross correlation plots of various components

If we consider our spectra again and plot a point for each spectrum at a corresponding position in a coordinate system of principal component A vs. principal component B (or C, D, etc.) we can visualize the correlation between the components. We might have clearly separated point clusters, or we might have them aligned along a diagonal, for example.

4.5.2.2 Cluster Analysis

Cluster analysis applied to confocal Raman images is essentially the sorting of the tens of thousands of spectra in a data set according to their similarities. As a result one gets a certain number of areas or masks which indicate where the spectra belonging to the various clusters were acquired as well as the average spectra of each cluster. Other applications also include the identification of bacteria strands and even their position in their life cycle or the identification of pathogenic cells.

Cluster analysis has the advantage of being an automated and objective method to find similar regions in spectral data sets. It can, however, require significant processing power and time.

There are various ways of clustering the data and each has its advantages and disadvantages. In the following, some clustering principles are briefly introduced before two typical clustering methods as well as one variation are described. For detailed descriptions of cluster analysis, the reader is referred to the literature, for example, [9].

Distance Calculation in Cluster Analysis

As already introduced in Sect. 4.5.2.1, each spectrum can be seen as a single point in 1600 dimensional space (if the spectra contain 1600 pixels). For a confocal Raman image, this might be tens of thousands of points and the cluster analysis tries to group (or cluster) these points. The clustering is mainly dependent on the distance between the points. Spectra which differ significantly from each other will be further apart in the 1600-dimensional space than spectra that are similar or even close to identical. The distance therefore determines which spectrum belongs to which cluster.

There are various ways of defining the distance between the spectra. The Euclidean and the Manhattan distance calculations are but two examples of methods which work well for Raman imaging.

Care must be taken if some of the spectra in the data set contain a high fluorescence background, because depending on the distance calculation method, the fluorescence might have a quite strong influence on the clustering. The background of the spectra should in general be subtracted prior to cluster analysis.

Hierarchical Cluster Analysis

As indicated by the name, hierarchical cluster analysis creates a hierarchy of clusters. This hierarchy is often represented by a tree. In this analog, the trunk represents the main cluster containing all spectra. Following this, the clusters are split up into sub-clusters of various sizes (the branches) and these into further sub-clusters (smaller branches, then twigs, smaller twigs, etc.). The leaves are then the individual spectra in the data set.

In order to calculate the clusters one either starts at the base cluster and splits this up (divisive clustering) or with the individual spectra and merges them together (agglomerative clustering). Now the distance between the clusters must also be taken into account and there are again a variety of methods to calculate this distance such as the maximum distance between elements of each cluster, the minimum distance between elements of each cluster or the mean distance between elements of

each cluster. Once the cluster tree is calculated the height, or extraction level, must be defined and from this the masks and average spectra can be extracted.

While this method is almost completely unsupervised (with the exception of the extraction level) it requires a huge amount of processing power and/or time.

K-Means Cluster Analysis

The K-means cluster analysis is often assigned to the partial clustering methods. It differs from the hierarchical cluster analysis in that the number of clusters must be selected prior to the clustering. However, the method can also then be applied to the sub-clusters in order to sort them further into sub-clusters and thus generate a pseudo-hierarchical cluster tree as shown in Fig. 4.8. Here an oil – water – alkane immersion is first clustered into three clusters before the three clusters were again split up into sub-clusters. In this example one can clearly see the mixed phases which are partly due to edge effects and positions at which the laser spot hit the boundary between two phases. Note that water does not exist

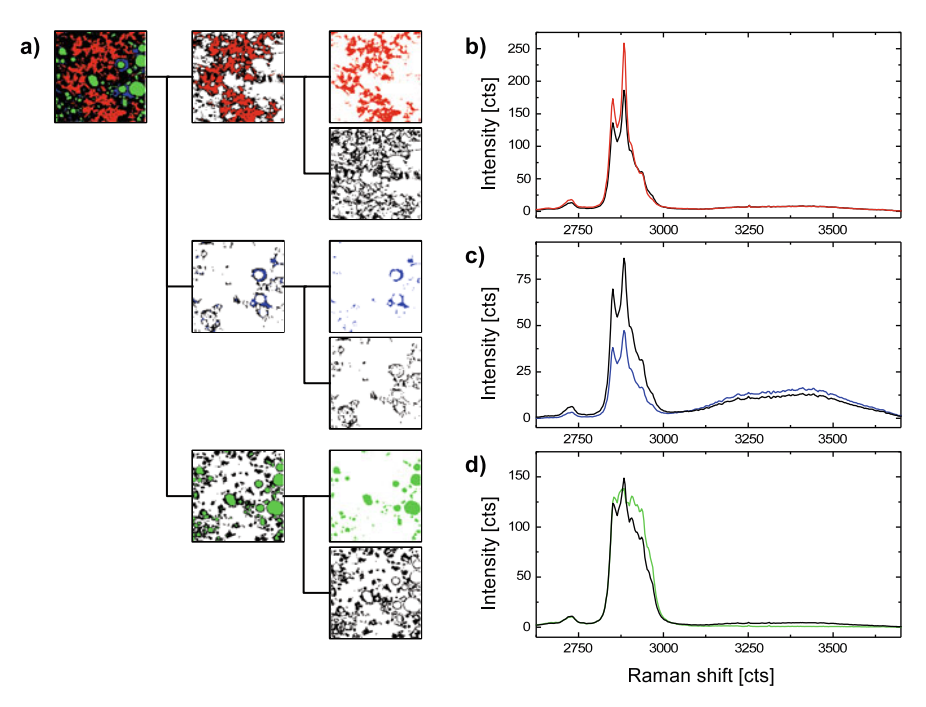


Fig. 4.8 *K*-means cluster analysis of an oil – water – alkane immersion. (a) Cluster tree with the root cluster on the *left*, the first level of clusters in the *middle*, and a further division into sub-clusters on the *right*. The sub-clusters each show a mixed phase marked in *black*. (b) Alkane spectrum (*red*) and the mixed phase (*black*) as extracted from the top two clusters. (c) Mixed alkane and water spectrum (*blue*) and the mixed phase (*black*) as extracted from the middle two clusters. The water phase does not exist as a pure phase in this sample. (d) Oil spectrum (*green*) and the mixed phase (*black*) as extracted from the bottom two clusters

as a pure component in this sample but is always to some degree mixed with the alkane.

Once the number of clusters (N) is defined for the K-means cluster analysis, the algorithm first defines N centers in the 1600 dimensional space and assigns each point (spectrum) the center closest to it. Then the centroid (one might also call it an average spectrum) for each group is computed. Following this the spectra are again sorted according to their distance to the calculated centroids and then the procedure is repeated. The algorithm is typically stopped once the assignment of the points (spectra) to their group ceases to change.

While this method needs somewhat more supervision than hierarchical clustering and is heavily dependent on the selection of the *N* initial centers, it requires much less processing power. For some commercial confocal Raman microscopes it can even be applied as an online evaluation tool during confocal Raman measurements with acquisition speeds of more than 600 spectra/s.

Fuzzy Clustering

In the hierarchical and *K*-means cluster algorithms, each spectrum either belongs to a cluster or does not. This is why the image outputs of these algorithms are binary masks (one for each cluster extracted).

In fuzzy clustering, the spectra can belong "to a certain degree" to a cluster. If a spectrum is located inside the cluster, then it belongs more to this cluster than one on the edge of it. Image outputs of this algorithm display this variation and are therefore not binary, but each pixel value typically has a value between 0 and 1 (or 100%).

This method instantly shows gradients in the images due to each pixel now having a certain probability of belonging to one cluster or another. One can also interpret this value as a measure of how well the spectrum fits to the corresponding cluster. However, the resulting clusters cannot be clustered further as is the case for classical *K*-means clustering.

4.6 Image Masks and Selective Average Calculation

In order to present the results of a confocal Raman imaging experiment, representative or average spectra found in the sample are typically shown. Extracting individual spectra from the data set is often undesirable, because these measurements typically display signal to noise (S/N) ratios which are unsuitable for presentation.

Therefore, averaging subsets of the data set is generally employed in order to calculate a smooth average spectrum. The definition of these subsets can be seen as binary images (masks) with the same pixel resolution as the recorded confocal Raman image. In these masks each pixel defines if the spectrum recorded at this position is used for the average calculation or not. This process is sometimes referred to as *selective average calculation*.

The definition of the masks can be performed in various ways:

Manual definition of the pixels

In order to define areas of interest manually, the user should be able to clearly identify those areas. This can be done through an integral filter and the resulting image. For example, the bright areas in Fig. 4.1 could be marked. The bright areas indicate a high PMMA content in this example and the mask could then be used to calculate the spectrum of PMMA with a good *S/N* ratio. The user should for this purpose be able to mark any arbitrary area within the image and define it as a mask.

While this method is very easy to implement, the major disadvantage is that it is quite subjective and the user can easily mark areas which contain a different spectrum. The average spectrum will then not be representative of the true single component. Additionally, it can be very laborious, if many small domains need to be marked.

Mask definition through calculation

Not all samples will have clearly defined areas of single components as is the case in the example shown in Fig. 4.1. It can therefore be desirable to use images with mathematical and logical operators in order to define the mask. One simple example is thresholding. In this, each pixel of the image is treated with a "<" or ">" operator in order to generate the mask. It might furthermore be desirable to combine these operations using a calculator style interface. The software needs to enable the user to preview the mask in order to facilitate the calculation. The masks generated in such a way can then be used again for selective average calculation.

This method facilitates significantly the marking of regions of interest in comparison to the manual definition described above. If various components show relatively strong intensities, it can become necessary to mathematically link several images in order to find a single component.

Cluster analysis

The cluster analysis typically generates binary masks as outputs in addition to the average spectra of the clusters. If the input to the cluster analysis is the result of a PCA, then the resulting spectra will be the averaged PCA spectra. One can therefore in this case use the mask output with the original hyperspectral data set to again calculate the selective average.

This method is certainly the most objective to find the masks. The only disadvantage in this method is that in the case of K-means cluster analysis, small clusters tend to be included in large ones and can be difficult to extract.

4.7 Combination of Single Spectra with Multi-spectral Data Sets

The fundamentals of image generation were described in the previous section. This section describes the generation of images based on the fitting of so-called "basis spectra" to the data set. This procedure produces images with much better contrast

than if only a small part of the spectrum is used (as is the case when using a sum filter, for example).

4.7.1 Basis Spectra

Basis spectra can be the spectra of the pure components present in the sample. This is the ideal case. Care must be taken, however, to record the spectra with exactly the same settings as used when the confocal Raman image was recorded. Typically the same integration time and many accumulations are chosen for this in order to obtain basis spectra with a good *S/N* ratio. An additional point which should be taken into consideration is whether the pure component can be present in the sample or if it might have undergone a chemical reaction to form a new component.

Quite often the pure spectra cannot (easily) be acquired from any arbitrary sample. In this case the basis spectra should be extracted from the scan. The selective averaging described in Sect. 4.6 is one method to perform this. Care must be taken to ensure that the spectra are pure and not mixed themselves. If they are mixed spectra, they need to be de-mixed because the fitting procedure will not work properly otherwise, as described in the following.

4.7.2 Fitting Procedure

The fitting procedure is essentially fitting each of the spectra recorded using the basis spectra. It tries to minimize the fitting error D described by the equation

$$D = \left(\overrightarrow{[\text{RecordedSpectrum}]} - a \times \overrightarrow{BS_A} - b \times \overrightarrow{BS_B} - c \times \overrightarrow{BS_C} - \cdots \right)^2 \quad (4.1)$$

by varying the weighting factors a, b, c, ... of the basis spectra \overrightarrow{BS} .

In order to improve such a fit, it is not advisable to use the entire recorded spectral range (i.e., from -100 to $3500\,\mathrm{cm}^{-1}$). The Rayleigh peak and common parts in the spectra (such as a glass substrate, for example) are best excluded from the fit. Additionally, parts of the spectra that do not contain Raman information should not be taken into account as they only contribute noise.

Following the fit of all the tens of thousands of spectra (using (4.1) for each spectrum recorded), the algorithm constructs one image for each basis spectrum showing the factors a, b, c, ... plus one image for the fitting error D.

Care must be taken in order to avoid using mixed spectra as the basis spectra. If such spectra are used the weighting factors can become negative, or if the fit is constrained to weighting factors greater than zero, the fit will not work properly.

Figure 4.9 shows an example of basis analysis. Here a thin layer of a PS-PMMA polymer blend was investigated with very short integration times (4.3 ms). The individual spectra were thus relatively noisy as can be seen from the red and blue spectra in Fig. 4.9(c) and (e).

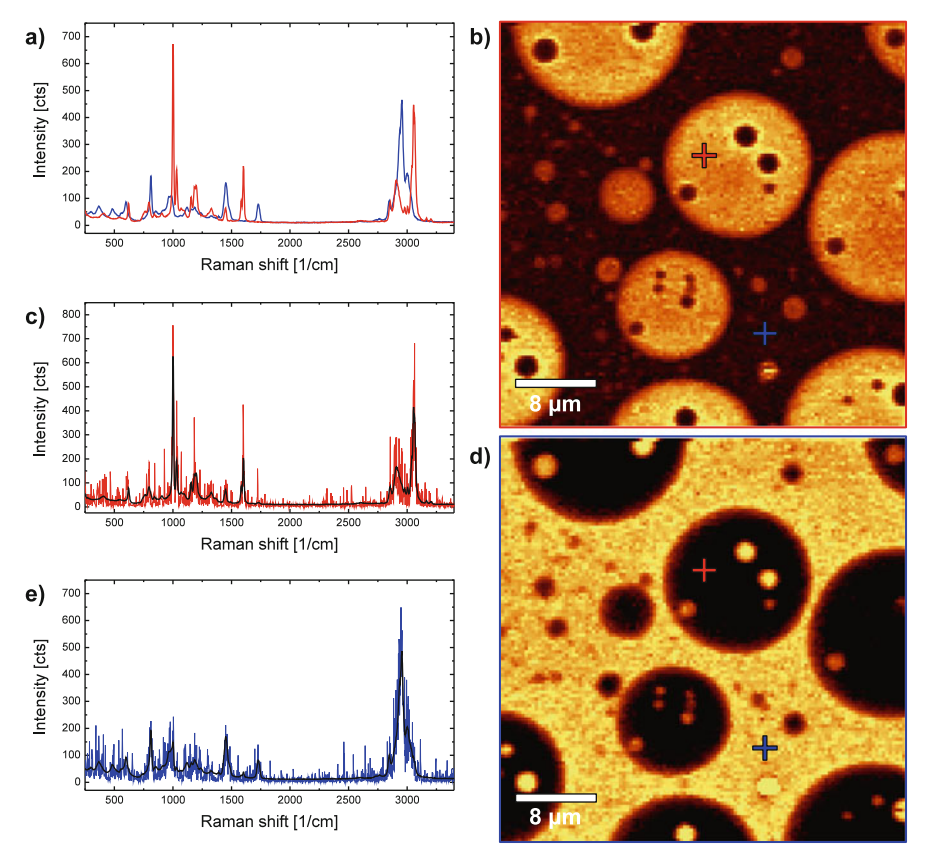


Fig. 4.9 Basis analysis of a PS-PMMA polymer blend. (a) Average spectra used for the fitting procedure. (c) and (e) Original spectra (red and blue, respectively) and fitted spectra (black) for PS (red) and PMMA (blue). The original spectra were recorded at the crosses indicated in the images on the right with the corresponding colors. (b) and (d) Resulting image showing the distribution of PS [b red frame] and PMMA [d blue frame] following the basis analysis. Brighter colors indicate a higher fitting factor and thus a higher signal intensity of the basis spectrum at the corresponding position

Using selectively averaged spectra with a good signal to noise ratio (see Fig. 4.9a) one can fit the individual, noisy spectra using the information contained within the entire spectral range. This results in a significant improvement of the S/N ratio and the contrast of the resulting images (see Fig. 4.9b and d).

4.8 Combination of Various Images

Following the generation of the images from the confocal Raman data, they need to be presented in a suitable way. If only the distribution of a single component or the shift of a Raman line need to be presented, then this is relatively straightforward.

However, if multiple images such as the results of the basis analysis need to be presented, the number of images can quickly become too large. It might be of additional interest to see if certain components are present as pure or mixed phases.

In such cases the combination of images is a good way to illustrate the distribution of components. In Fig. 4.5(b) the distribution of oil, water, and alkane is shown in green, blue, and red, respectively.

The color scales for each component are first adjusted, so that each component has an individual color scale (red, green, and blue (RGB) in this case). The images are then combined. One can combine the images by layering them and making the upper layers transparent depending on the value of each pixel. Another method is to combine the colored pixels in an additive way in order to illustrate the mixing of phases better. The colors are then combined and where, in the example above, water (blue) and alkane (red) are present, the resulting color is mixed (violet).

Note that the definition of the range of the color scale bar has a significant influence on the appearance of images and that care must be taken to choose appropriate settings.

4.9 The Law of Numbers

In this section a very noisy example data set is evaluated to illustrate the implementation and capability of the methods described above and show that even though the *S/N* ratio of the individual spectra is at first glance insufficient, the algorithms used can produce images and spectra of high quality.

The sample investigated was a PET-PMMA polymer blend spin coated onto a glass slide. The data were acquired in EMCCD mode and Fig. 4.10 shows an example of three of the 22,500 spectra recorded.

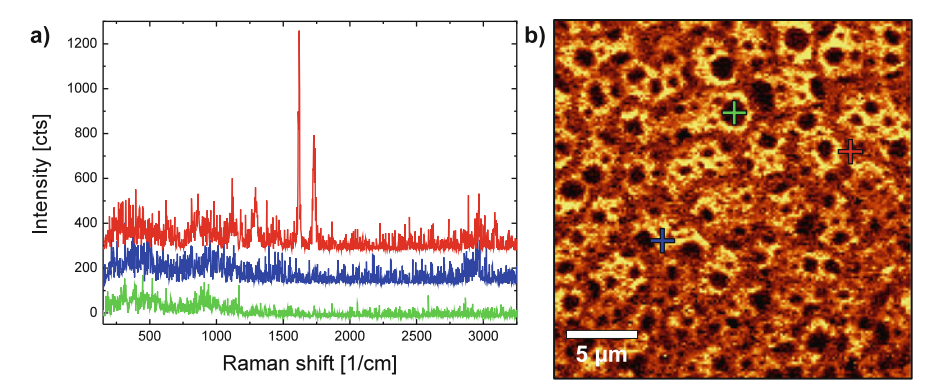


Fig. 4.10 Noisy PET-PMMA Raman image. The spectra (**a**) on the *left* show the three different components acquired at the positions marked in the image (**b**) with the corresponding colors (*green* = glass, *red* = PET, *blue* = PMMA). The image (**b**) on the *right* displays the distribution of PMMA in the sample as derived through a simple sum filter

The noise level in the spectra is significant and the S/N ratio is only slightly above 1. Even with this noise level, the sum filter applied to the CH-stretching region where PMMA shows a signal produces some image contrast as can be seen in Fig. 4.10(b).

Following cosmic ray removal and a background subtraction, a *K*-means cluster analysis was performed on the data set, resulting in three clusters. The average spectra of these clusters as well as the color–coded cluster map are shown in Fig. 4.11.

It can be clearly seen that the quality of the spectra as well as the spatial assignment of the pixels and thus the image contrast is dramatically improved. As can be seen from Fig. 4.11(a), all spectra still contain the glass background due to the limited depth resolution of the confocal setup and the thickness of the film (<<50 nm). It is additionally noticeable that the glass spectrum still shows a small peak in the CH-stretching region. This is due to edge effects of the clusters as already discussed in Sect. 4.5.2.2.

The spectra can now be de-mixed further by correct subtraction of the spectra from each other, which then results in the spectra shown in Fig. 4.12(c).

These spectra are used for the basis analysis and the resulting image for the PET and the PMMA is shown in Fig. 4.12(a) and (b), respectively. The scale bars to the right of image Fig. 4.12(a) and (b) indicate the fitting value. The glass background image (not shown here) now shows a homogenous distribution. Fig. 4.12(d) shows the combined image of the three components following basis analysis.

Figure 4.13 illustrates the effect on image contrast for the PMMA phase by simply displaying Figs 4.10(b) and 4.12(c) next to each other. The enhancement in image contrast due to the multivariate data methods and the de-mixing is clearly visible. This is especially apparent in the region where PET is located, the contrast is strongly enhanced.

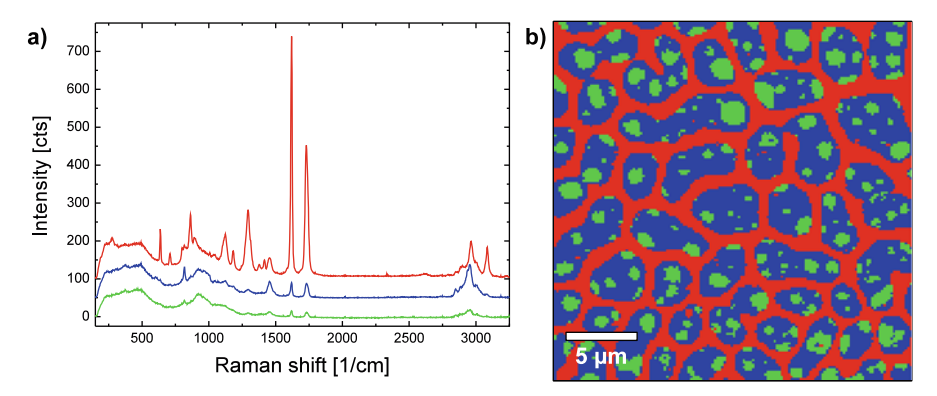


Fig. 4.11 PET-PMMA Raman image and spectra following K-means cluster analysis. The spectra on the *left* (**a**) show the average spectra of the three clusters (*green* = glass, red = PET, blue = PMMA) and the image on the right (**b**) shows the combined cluster map with the pixels color-coded as the spectra according to their cluster affiliation

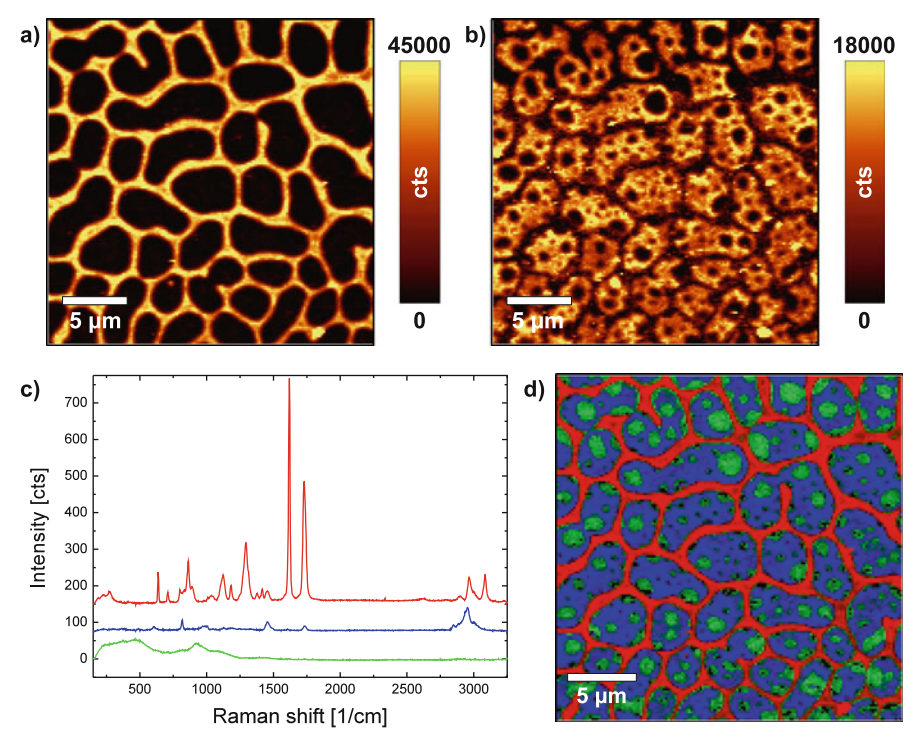


Fig. 4.12 The results of the basis analysis for PET (a) and PMMA (b), the de-mixed spectra used for the basis analysis (c) and the combined image of the three components (green = glass, red = PET, blue = PMMA)

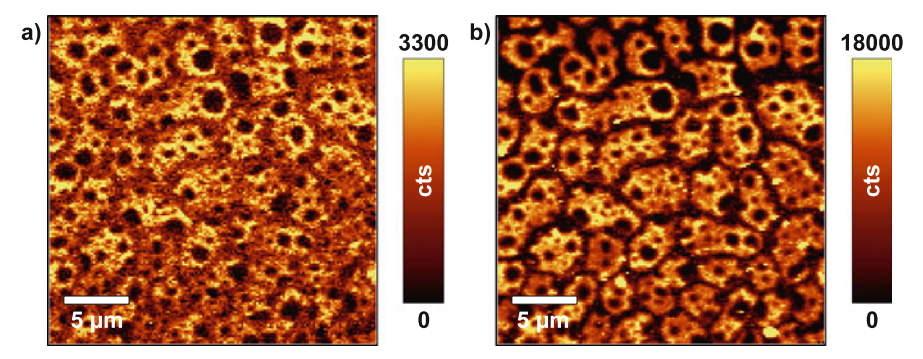


Fig. 4.13 Comparison of the image contrast before and after data evaluation. Image (a) was obtained through the sum filter and image (b) after basis analysis.

The scale bars on the right-hand side of the images are an additional indicator that the sum filter only uses the number of detected electrons¹ in the CH-stretching band, whereas the fitted image uses the photons in the entire spectral range, which is reflected in the higher scale bar values in Fig. 4.13(b).

This example demonstrates conclusively, that with a sufficiently large number of spectra (22,500 in this case), it is still possible to obtain a great amount of spectral and spatial information from the data sets by using multivariate methods and advanced data analysis algorithms, even though the individual spectra have a very low signal to noise ratio. However, the signals in the spectra still need to be sufficiently high to allow the cluster analysis to distinguish one cluster from another.

4.10 Materials and Methods

In order to illustrate the data processing of Raman spectra, a few example data sets were utilized throughout this chapter. The samples as well as the acquisition details will be explained in the following.

All data presented were recorded using an alpha300R confocal Raman microscope from WITec GmbH, a frequency-doubled Nd:YAG laser (532 nm) and a spectrometer equipped with a 600 g/mm and a 1800 g/mm grating as well as a backilluminated CCD camera. The samples were

- A PS-PMMA polymer blend either dropped onto or spin coated onto a glass slide
- A Si[100] wafer with an indent produced using a nano-indenter

Figure number	Sample description	Integration time [s]	Scan size [µm]	Scan resolution	Grating [g/mm]	Layer thickness
1	PS-PMMA	0.062	30 × 30	200×200	600	< 1μm
1	PS-PMMA	10×0.512	Single spectrum		600	$< 1 \mu m$
1	PS-PMMA	10×1.512	Single spectrum		1800	$< 1 \mu m$
2	PS-PMMA	5×0.512	22.4 (Line scan)	15	600	$< 1 \mu m$
3	PS-PMMA	0.062	Single spectrum		600	$< 1 \mu m$
4	PS-PMMA	0.062	(extracted) Single spectrum (extracted)		600	$<1\mu\text{m}$
5	O-A-W	0.017	100×100	128×128	600	N.A.
6	Si indent	0.069	10×10	100×100	1800	N.A.
8	O-A-W	0.017	100×100	128×128	600	N.A.
9	PS-PMMA	0.0043	40×40	120×120	600	$< 1 \mu m$
10–13	PET-PMMA	0.050	25×25	150×150	600	< 50 nm

Table 4.3 Experimental details for the example data sets

¹ Since this measurement is performed in EMCCD mode, the signal is strongly amplified and thus does not represent the number of photons.

- An oil alkane water (O A W) mix which was placed between two cover slips
- A PET-PMMA polymer blend spin coated on a glass slide

The objective used was either a $100 \times$ air objective with an NA of 0.9 or 0.95 or a $100 \times$ oil immersion objective with an NA of 1.25 (oil – alkane – water sample). Further experimental details can be found in Table 4.3.

References

- WITec GmbH. Ultrafast confocal raman imaging application examples. http://www.witec. de/en/download/Raman/UltrafastRaman.pdf (2008)
- L. Quintero, S. Hunt, M. Diem. Denoising of raman spectroscopy signals. Poster presented at the 2007 R2C Multi Spectral Discrimination Methods Conference (2007)
- 3. W.H. Press, S.A. Teukolsky, W.T. Vetterling, B.P. Flannery, *Numerical Recipes in C*, 2nd edn., chap. Savitzky-Golay Smoothing Filters, pp. 650–655, (The Press Syndicate of the University of Cambridge, 1999)
- 4. P. Ramos, I. Ruisánchez, J. Raman Spectrosc. 36, 848 (2005)
- G. Gaeta, C. Camerlingo, R. Ricio, G. Moro, M. Lepore, P. Indovina, Proc. SPIE 5687, 170 (2005)
- 6. T. Dieing, O. Hollricher, Vib. Spectrosc. 48, 22 (2008)
- 7. K. Pearson, Philos. Mag. 2(6), 559 (1901)
- 8. C. Bishop, Pattern Recognition and Machine Learning (Springer, New York, NY, 2007)
- 9. T. Hastie, R. Tibshirani, J. Friedman, *The Elements of Statistical Learning* (Springer, New York, NY, 2009)

Chapter 5 Nano-spectroscopy of Individual Carbon Nanotubes and Isolated Graphene Sheets

Alain Jungen

Abstract The following chapter will review the resonant Raman-active modes of single-walled carbon nanotubes emphasizing the diameter dependence of the radial breathing mode and selectivity of the optical transition energies (resonance). Thermal studies of individual freestanding single-walled carbon nanotubes showed a pronounced phonon softening. The second part of the chapter is devoted to Raman imaging of graphene. This particular type of carbon nanophase has become available only recently. The first Raman signatures of few-layer to single-layer graphene flakes could be obtained and compared with scanning probe microscopy. The effect of electrical charging (doping) on the Raman features is also demonstrated.

5.1 Introduction

Carbon is a unique element showing a variety of stable forms based on three different hybridizations of its atomic orbitals. Some of these forms are shown in Fig. 5.1.

Under ambient conditions, the layered structure of sp^2 hybridized graphite is the ground state phase for bulk carbon [1]. In addition to the diamond and graphite bulk phases, the discovery of fullerene triggered much of the recent interest in nanoscale phases of carbon [2].

Graphene is an atomically thin single sheet of sp^2 bonded carbon. It is the basic structural element of all other graphitic materials including graphite, carbon nanotubes, and fullerenes. Intrinsic graphene is a semi-metal and features a linear dispersion relation near the six corners of the 2D hexagonal Brillouin zone. This means that electrons and holes near these corners behave like relativistic particles [3].

A single-walled carbon nanotube (SWNT) can be conceptually considered as a seamless cylinder rolling up graphene with a size of a few nanometers in diameter and a length ranging from tens of nanometers to millimeters. For nanotubes there are many different types depending on the rolling direction of a sheet into a cylinder which then exhibits different diameters and properties [4, 5].

Single-walled nanotubes show different properties depending on their diameter and rolling direction. They are characterized by their chiral vector with indices n and m (see Fig. 5.2). This chiral vector determines whether a nanotube is

92 A. Jungen

Fig. 5.1 Different carbon allotropes with nanometer-scale phases ranging from 0D C60 fullerenes, 1D carbon nanotubes, 2D graphene, to 3D diamond and graphite

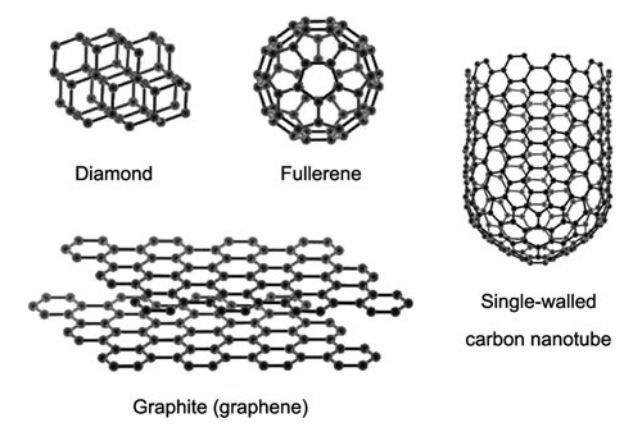
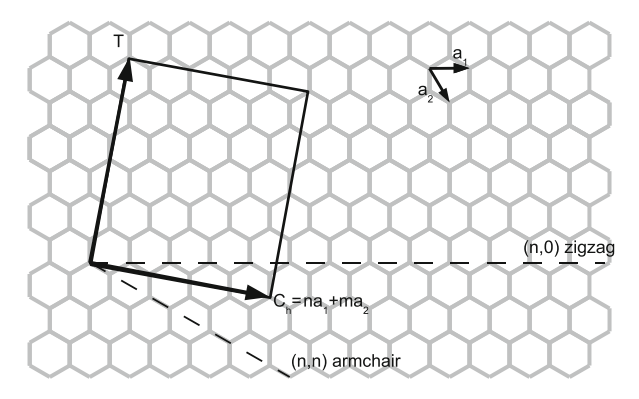


Fig. 5.2 The vector C_h describes how a sheet of graphene is rolled up to create a carbon nanotube [6]



semiconducting or metallic. If n = m, the nanotube is metallic; if n-m is a multiple of three, the nanotube is semiconducting with a small bandgap. Otherwise it has semiconducting properties with larger bandgaps.

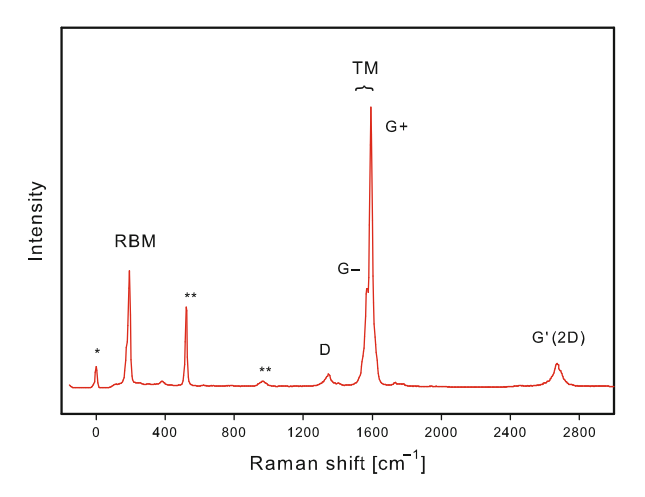
5.2 Individual Carbon Nanotubes

5.2.1 Phonons

Single-walled carbon nanotubes have several Raman-active vibrational modes; the exact number depends on the symmetry of the tube but is independent of its diameter. However, only four to five Raman bands are strongly resonance enhanced. Three of them are located around $1600\,\mathrm{cm}^{-1}$ and correspond to the characteristic G+, G-, and D-modes of the graphene sheet. As they are related to graphite they appear at similar frequencies in nanotubes.

The radial breathing mode (RBM), however, is specific to nanotubes and arises from a radial expansion and contraction of the entire tube. The phonon dispersion can be found theoretically by zone folding the graphene Brillouin zone.

Fig. 5.3 Typical Raman spectrum of an individual single-walled carbon nanotube recorded with a confocal micro-Raman spectroscope using a green 532 nm laser. The feature marked "*" is the attenuated elastically scattered Rayleigh line. Features marked "**" come from the Si support



However, this approach has some shortcomings, most notably for the acoustic modes. For example, the out-of-plane translation, an acoustic mode in graphene, transforms into the RBM in carbon nanotubes with non-zero frequency at the Γ -point.

A typical Raman spectrum of a single-walled carbon nanotube excited at $E_l = 2.33\,\mathrm{eV}$ is shown in Fig. 5.3. The low-frequency range of the RBM is between 80 and $350\,\mathrm{cm}^{-1}$, the intermediate range with the defect-induced vibration (D-mode), which involves phonons from the graphene K-point, lies between 1200 and $1400\,\mathrm{cm}^{-1}$, and the high-energy range from 1500 to $1600\,\mathrm{cm}^{-1}$ belongs to the tangential mode (TM). A fifth feature at twice the dispersive D-mode frequency, often referred to as the G'-mode, is being considered recently. It is not a defect-induced overtone of the D-mode but a double-resonant process crossing the Γ -point twice. In graphene its shape was found to depend on the number of individual graphene layers.

5.2.1.1 Radial Breathing Mode

In the RBM all carbon atoms move in phase in the radial direction creating a breathing-like vibration of the entire tube (see Fig. 5.4(a)). The force needed for a radial deformation of a nanotube increases as the diameter (and hence the circumference) decreases.

The expected dependence of the radial breathing mode frequency on diameter is

$$\omega_{\text{RBM}} = \frac{c_1}{d_t} + c_2 \tag{5.1}$$

with c_i being constants. Equation (5.1) was first introduced by Jishi et al. [7] and confirmed by many authors, each with slightly different c_i 's [8–11]. The range of proposed values differ by a few percent and translate into a similar uncertainty for d_t .

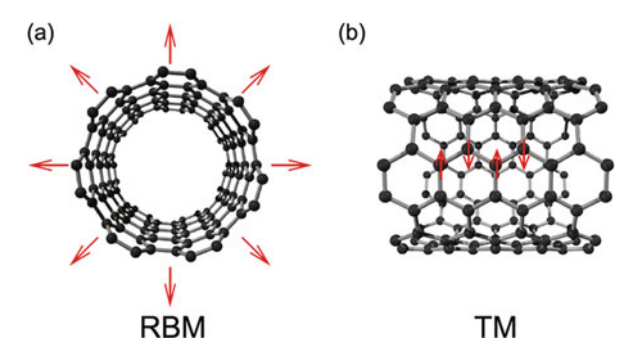


Fig. 5.4 Raman-active vibrational modes of carbon nanotubes. (a) The so-called radial breathing mode (RBM) is a prominent feature of the tubular nanostructure and not present in planar graphite. The Raman shift of the RBM is approximatively inversely proportional to the tube diameter. (b) An example of a tangential mode (TM). In analogy to graphitic Raman modes it is often also called G-mode or high-energy mode (HEM)

For isolated SWNTs, a quick and good diameter estimate can be made by considering $c_2 = 0$ and $c_1 = 229$ nm cm⁻¹ as reported by Popov et al. [12].

Various authors have measured their conversion parameters, for example, by fitting their data after having assigned the electronic transition energies (see Sect. 5.3.1).

5.2.1.2 Defect Mode

In order to understand a defect-enabled mode one has to consider the problem with visible Raman spectroscopy. As photons carry very little momentum, only scattering at the Γ -point (q=0) is allowed. If the process involves a non- Γ -point phonon, it takes a defect to elastically scatter back to Γ to compensate the gained momentum in a double-resonant process. This mechanism was explained by Thomsen et al. [13].

The D-mode in graphite is found at 1350 cm⁻¹ and is induced by disorder or defects. It is also described as a double Raman scattering in graphite. The intensity of the D-mode increases linearly with decreasing graphite crystallite size.

In carbon nanotubes, a Raman mode related to the graphite D-mode is also observed as shown in Fig. 5.3. The mechanism responsible for the laser-energy dependence is defect-induced, double-resonant Raman scattering. This mode is known to be dispersive $\omega = \omega(E_l)$ and peaks at 1345 cm⁻¹ when excited by a 532 nm green laser.

5.2.1.3 Tangential Mode

The high-energy vibrations in carbon nanotubes correspond to the graphene optical mode at $1580\,\mathrm{cm^{-1}}$. In contrast to the radial breathing mode, the carbon atoms vibrate tangentially to the tube wall as depicted in Fig. 5.4(b). A single Γ -point vibration of graphene transforms into a number of modes in carbon nanotubes due to the confinement of wave vectors along the circumference. The curvature of the

tube wall introduces a small softening of the in-plane force constants and makes the phonon frequencies slightly diameter dependent [14]. To a first approximation, however, rolling up the graphene sheet does not markedly soften the carbon bonds [15].

The Raman spectrum of the TM is, just like the RBM, specific to single-walled carbon nanotubes which allow their identification in a tube sample. Three to four close-by peaks appear with two dominant features at 1570 and 1593 cm⁻¹ and do not have a Lorentzian line shape. The 1582 cm⁻¹ position in SWNT corresponds often to a local minimum, allowing for a quick determination of the single-walled tube signature. Additionally, metallic SWNTs show a strong phonon softening of the longitudinal mode which is due to quantum confinement [16].

5.2.2 *Theory*

When the incident or scattered photons in the Raman process are in resonance with an electronic transition between the valance and conduction bands of the energy E_{ii} , the signal becomes very large as a result of the strong coupling between the electrons and phonons of the nanotube. This resonance enhancement allows the characterization of individual SWNTs with respect to electronic state, chirality, diameter, and conducting properties. As the RBM is characteristic for SWNTs, it can be used to determine their properties. The RBM integrated intensity $I(E_{\rm RBM})$ is a function of the laser excitation energy $E_{\rm L}$ and can be evaluated from the joint density of states according to the theory for incoherent light scattering

$$I(E_{\text{RBM}}) = \int \left| D(E) \frac{M_{\text{s}} M_{\text{ep}} M_{\text{i}}}{(E_{\text{L}} - E_{ii} - i\Gamma)(E_{\text{L}} - E_{\text{ph}} - E_{ii} - i\Gamma)} \right|^{2} dE$$
 (5.2)

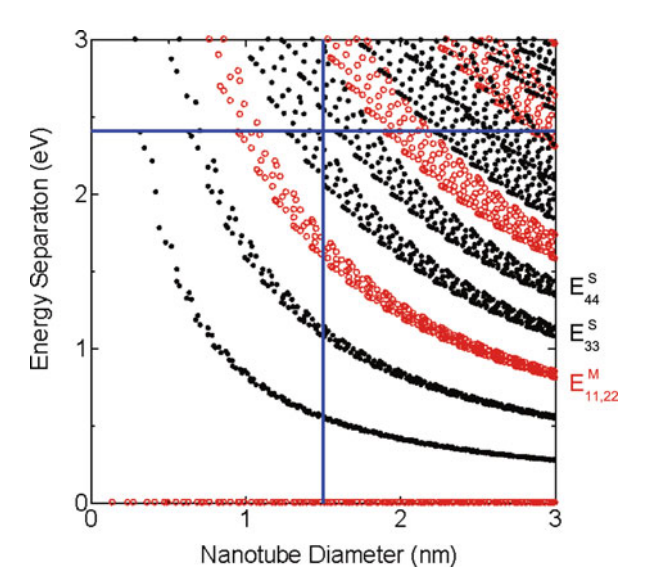


Fig. 5.5 Kataura plot

where Γ is the scattering process lifetime, $E_{\rm ph}$ the phonon energy, and M matrix elements for the scattering process. $M_{\rm i}$, $M_{\rm s}$ are the matrix elements for the electron-radiation interaction for the incoming and scattered, respectively, and $M_{\rm ep}$ is the electron-phonon interaction. The first and second factors in the denominator describe the resonance effect with incident and scattered light.

Figure 5.5 shows a so-called Kataura plot [17] relating the electrical transitions E_{ii} to the nanotube diameter. Branches shown in red refer to metallic tubes, whereas the semiconducting tubes' branches are shown in black. It can be seen that the electronic nature of 1.5 nm tubes probed by resonant Raman scattering using the 2.33 eV (532 nm) excitation is semiconducting. Both bands E_{33}^{S} and E_{44}^{S} are thus preferentially excited.

5.2.3 Experiment

Recent non-orthogonal tight-binding calculations extended the Kataura plot in the sense that maximum Raman intensities I_{ii} were calculated for every optical transition E_{ii} [12]. However, the intensity matching with measured data has been an experimental challenge. The Raman intensity, as well as the tube-dependent scattering efficiency, is dependent on the number of tubes under laser exposure. Furthermore, the orientation of the tubes with respect to the direction of the light polarization affects the Raman intensity [18]. Finally, their length and defects together with interactions with neighboring tubes can also affect the measured Raman intensity [19, 20]. This makes the tube-dependent Raman intensity measurement extremely difficult.

A statistical method is proposed for chirality assignment of a nanotube sample using a single laser line $E_{\rm L}$. Room temperature Raman spectra were recorded using a WITec CRM200 confocal Raman microscope using a frequency-doubled Nd:YAG green laser line (532 nm) delivered through a single mode fiber. This type of fiber supports only an single transversal mode which can be focussed to a diffraction-limited spot of about 400 nm (100× objective, NA=0.8). The backscattered light passed through a super-notch filter and focussed into a 50 μ m pinhole. The 300 mm spectrometer was equipped with a Peltier-cooled, back-illuminated charge-coupled device (CCD) camera. Precise positioning of the sample under the laser spot was achieved with piezoelectric actuators with a travel range of $200 \times 200 \times 20 \,\mu$ m³ in x, y, and z respectively. A total of 9600 spectra were obtained in six planar scans each collecting 40×40 spectra with an inter-spot distance of 1 μ m at a rate of 2 Hz. Sample preparation is described elsewhere [21, 22].

Figure 5.6 shows the raw data from the collected Raman spectra. RBM features were resolved by fitting each spectrum with Lorentzian lines in the range from 80 to 350 cm⁻¹. The intensities of the RBM modes were normalized with respect to the integrated intensities from the silicon support (LO phonon at 520 cm⁻¹). From this large amount of data a distinct picture of the Raman intensity distribution of the

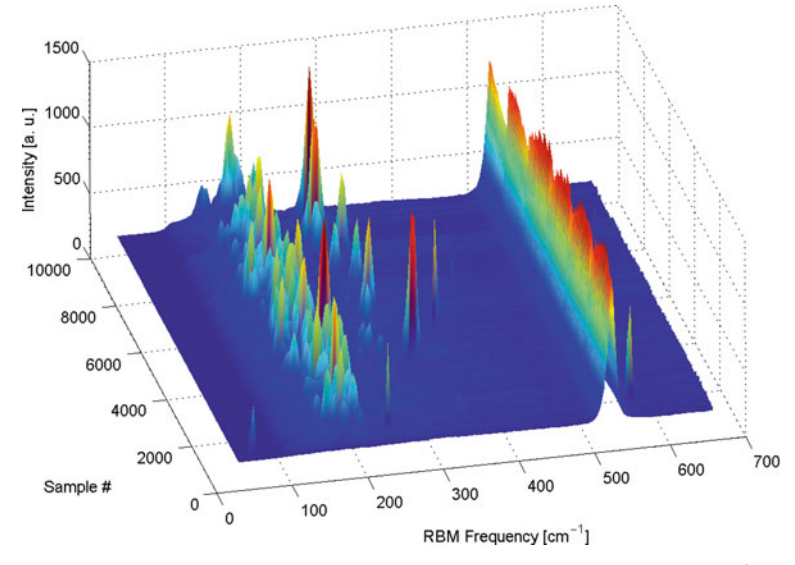


Fig. 5.6 Cascaded collected Raman spectra. The RBM is visible from 80 to $350 \, \text{cm}^{-1}$ while the LO phonon of the Si support appears at $520 \, \text{cm}^{-1}$

observed RBMs was obtained. This distribution was used to establish a histogram. The collected data were then compared to calculated optical transitions E_{ii} and maximum Raman intensities I_{ii} .

Figure 5.7(a) shows the optical transition energies as a function of the tube diameter (a close up of the Kataura plot from Fig. 5.5) as obtained from a non-orthogonal tight-binding model [24]. The tube diameter was calculated using (5.1) with $c_1 = 214 \, \mathrm{cm}^{-1}$ and $c_2 = 19 \, \mathrm{cm}^{-1}$. The position of the dots is indicated with respect to the excitation line of 2.33 eV (532 nm). The red dots correspond to SWNTs that have sufficient Raman efficiency at $E_{\rm L}$. Tubes lying close to the laser line but still shown in gray have a very weak intrinsic Raman intensity. They are omitted in Fig. 5.7(b) to avoid figure overloading.

Figure 5.7(b) shows the calculated I_{ii} and attenuated Raman intensities αI_{ii} of the selected SWNTs. The open dots are calculated maximum intensities. The filled dots were multiplied with a normal distribution function to model the distance (in electronvolt) to the laser line. The numbers in parenthesis indicate tube families (2n + m = constant).

Figure 5.7(c) shows the converted histogram from Fig. 5.6. The measured data (open circles) were corrected for sample population independence (filled circles). The intensity distribution shows a strong correlation with the attenuated data from Fig. 5.7(b). The pattern match is only valid for the attenuated data which emphasizes the importance of performing such an excitation-dependent correction.

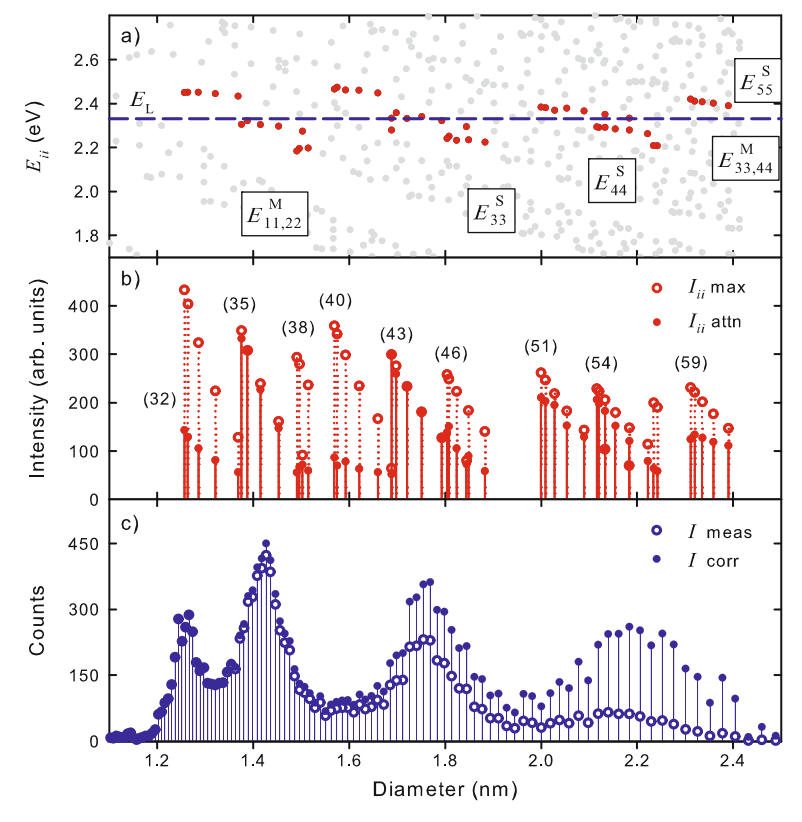


Fig. 5.7 (a) Optical transitions E_{ii} as a function of the tube diameter. (b) Calculated Raman intensities corresponding to the selected dots in (a). Numbers in parenthesis indicate tube families (2n + m). (c) Converted measured histogram. After [23]

5.2.4 Microscopy

This section describes the possibility to localize individual SWNTs grown between a support structure. SWNT bridges were synthesized by catalytic thermal CVD in a low-pressure furnace which can be operated down to a base pressure of 10^{-5} mbar. Prior to CVD growth, microchips were fabricated by surface micromachining of releasable 1.5 μ m thick poly-crystalline silicon (poly-Si) layers. After their release, the poly-Si layers were uniformly coated with a bimetallic thin film of 8 nm Al and 1 nm Ni. The film thickness was measured in situ by a quartz crystal microbalance. The chips were transferred in air and subjected to a hydrogen pre-treatment at 200 mbar and 850°C for 10 min to allow the reduction of nickel oxides and the formation of Ni islands. The latter serves as catalytic seeds for the growth of SWNTs under methane and hydrogen (3:1) at 200 mbar and 850°C during 15 min. Heating and cooling were performed under vacuum and the chamber was only opened after cooling to at least 250°C.

The samples were characterized by scanning electron microscopy (SEM, Zeiss Ultra 55 operated at 5 kV) and transmission electron microscopy (TEM, Philips CM200 microscope operated at 120 kV). Electron diffraction (ED) patterns were recorded on a Zeiss 912 Ω microscope at 60 kV. Raman spectra were recorded on a WITec CRM200. The details of the setup were already described in Sect. 5.2.3.

Figure 5.8 shows three suspended SWNTs across a trench defined by a tip pair at the technological limit for standard (surface micromachining) lithography.

The shape features alternating gap sizes between 12 and 2 μ m (Fig. 5.8b) to force SWNT growth only between the small gaps without the need of masking the catalyst [25]. Figure 5.8(c)1 shows a Raman image of the suspended SWNTs. The image was obtained by integrating the SWNT-specific Raman signatures, i.e., the radial breathing mode in the range from 80 to $350\,\mathrm{cm}^{-1}$ and the tangential (G) mode around $1592\,\mathrm{cm}^{-1}$ as shown in Fig. 5.8(d).

Raman scattering is resonant and at a fixed excitation energy of $2.33\,\text{eV}$ only two of the three crossing SWNTs could be seen at regular experimental conditions. Equation (5.1) was used to determine the diameter of one of the tubes to $1.43\,\mu\text{m}$, while for the other tube no RBM could be found. No defect-induced D-band signal

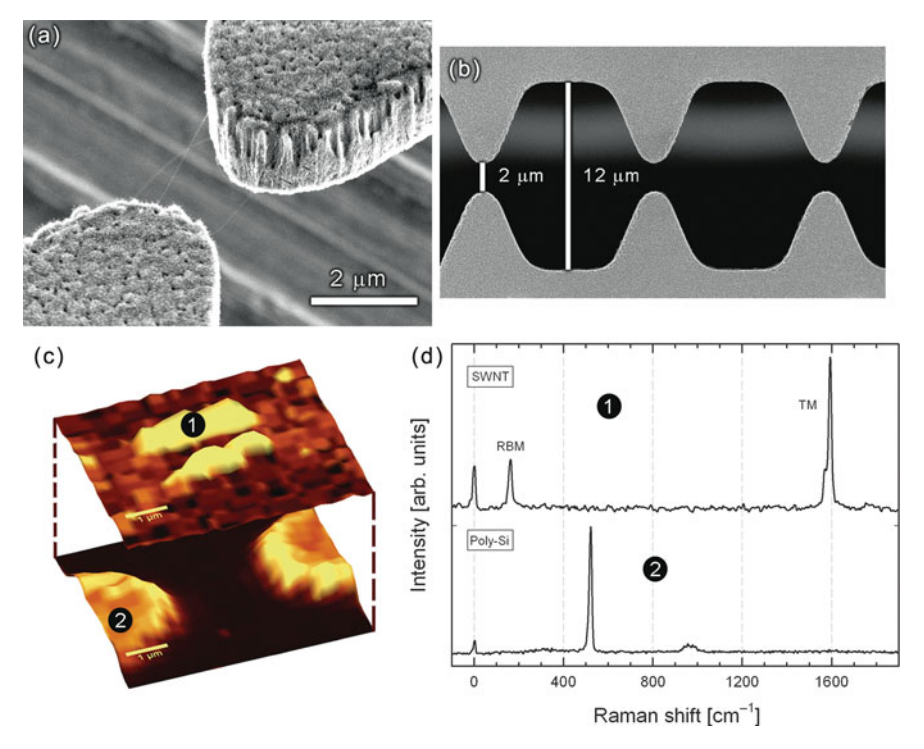


Fig. 5.8 (a) SEM image of three spanned SWNTs between a pair of closely spaced poly-Si tips. (b) Demagnified SEM from (a) to show the tip definition. (c) Raman image of the same tip pair as shown in (a). (d) Representative snapshots showing SWNT and poly-Si-specific phonon modes in the Raman shift. After [25]

at 1350 cm⁻¹ was observed, which is indicative for a good SWNT with high crystallinity. The Raman image in Fig. 5.8(c) 2 has been obtained by integrating over the longitudinal optical phonon mode of the poly-Si material. Both images can be overlayed as they picture the same structure. There is no doubt about the origin of the Raman features as the freestanding sample geometry does not suffer from any background signal.

5.2.5 Thermography

SWNTS have been proposed for applications in integrated circuits as transistors or interconnects [26, 27]. In other cases they were proposed as active elements in sensing applications based on their unique strain-dependent transport characteristics [28]. In all cases, knowledge about the influence of temperature onto their electro-mechanical properties is important to understand their overall behavior. Although several theoretical studies exist on the thermal properties of individual SWNTs [29], only few experimental investigations below room temperature are currently available.

Figure 5.9(a) shows a spatially resolved thermal image of a suspended SWNT. The figure shows that the freestanding nanotube is strongly influenced (heated) by the laser spot as a heat source. Laser intensities were varied from 0.5 to 7 mW corresponding to power densities of about 1.5 to 21 mW/ μ m² [30]. Figure 5.9(b) shows the thermal profile of the nanotube cross-section resolved by its phonon frequency which was characterized beforehand. It shows that for high laser intensities, the phonon softening is pronounced. A Gaussian intensity profile is observed along the cross-sectional direction (*Y*) of the tube indicating a correlation between the (Gaussian) profile of the laser spot and the SWNT as a point scatterer (considered of negligible width).

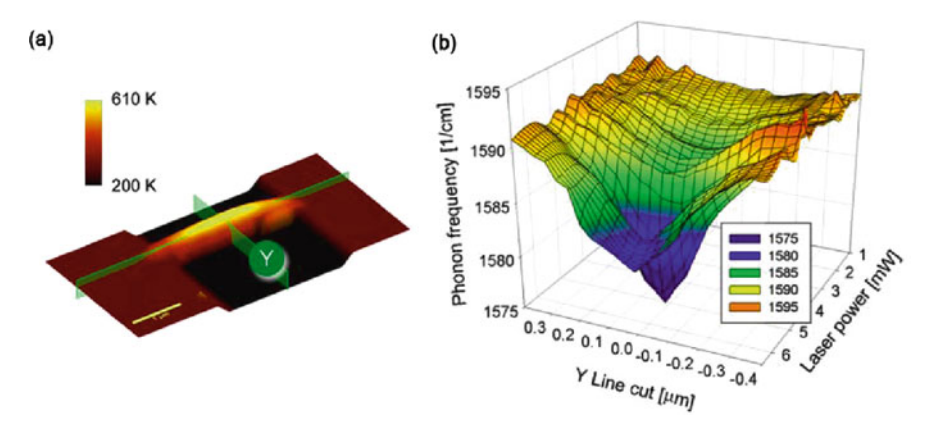


Fig. 5.9 (a) Raman thermal image of a single SWNT suspended between Si posts. (b) Phonon frequency of G-mode as a function of laser intensity scanned across the SWNT

5.3 Isolated Graphene Sheets

5.3.1 *Theory*

The energy dispersion for 2D graphene can be calculated using a tight-binding energy model. For a detailed calculation, the reader is referred to [4] and [31]. The result is

$$E_{\text{g2D}}^{\pm}(\mathbf{k}) = \frac{\epsilon_{\text{2p}} \pm \gamma_0 w(\mathbf{k})}{1 \mp s w(\mathbf{k})}$$
 (5.3)

where $E_{\rm g2D}$ is the 2D energy dispersion of graphite, $\epsilon_{\rm 2p}$ the site energy of the 2p atomic orbital, γ_0 the nearest-neighbor carbon–carbon interaction energy, and s the tight-binding overlap integral which is associated with the asymmetry between the valence and conduction bands in 2D graphite. E^+ and E^- correspond to the valence π and conduction π^* energy bands, respectively. The function w(k) in (5.3) is given by

$$w(\mathbf{k}) = \sqrt{1 + 4\cos\left(\frac{\sqrt{3}k_x a}{2}\right)\cos\left(\frac{k_y a}{2}\right) + 4\cos^2\left(\frac{k_y a}{2}\right)}$$
(5.4)

where a is the length of unit vector of graphene and k the wave vector. Equations (5.3) and (5.4) describe the energy dispersion of graphene which corresponds to the electronic properties of SWNTs. In Fig. 5.10 the electronic energy dispersion for 2D graphite is shown as a function of k in the hexagonal Brillouin zone.

The asymmetry of the conduction and valence bands is not important for the calculation of the energy difference of conduction and valence bands. Thus with s=0 and $\epsilon_{2p}=0$ the dispersion relation simplifies to

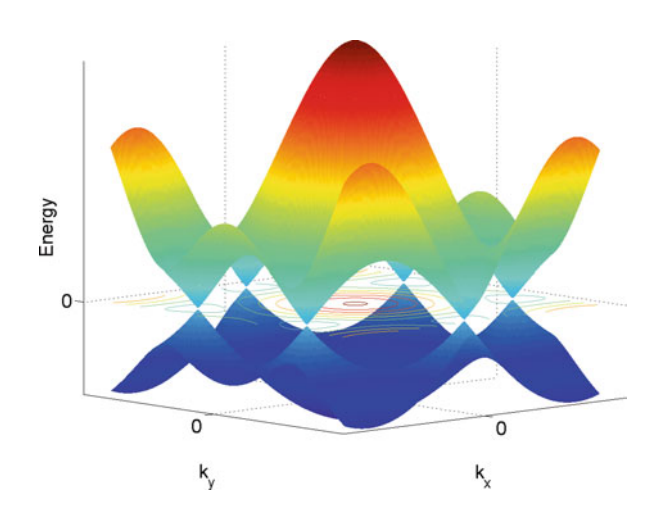


Fig. 5.10 Energy dispersion of π and π^* bands of graphene. The Fermi level is at E=0. Bands cross at the K-points. Data were computed using (5.3) and (5.4) and parameter values s=0.129, $\gamma_0=2.9$ eV

$$E_{\rm g2D}^{\pm} = \pm \gamma_0 \, w(\mathbf{k}) \tag{5.5}$$

Note that a simple way to get to the electronic properties of single-walled carbon nanotubes consists in starting from the graphene dispersion relation and applying a zone folding approximation between graphene π and π^* electronic states to calculate the band structure of tubes for any diameter and chirality [5]. Note also that the common π -orbital approach involves the assumption that the tight-binding approximation includes only the interaction of first-neighbor atom (nearest neighboring atom) [4].

5.3.2 Experiment

Only recently, single- and few-layer graphenes have been successfully transferred onto a substrate [32].

Transport measurements revealed a highly tunable 2D electron—hole gas with a linear energy dispersion around the Fermi energy embedded in a solid-state environment [33, 34]. Going to few-layer graphene, however, disturbs this unique system in such a way that the usual parabolic energy dispersion is recovered. The large structural anisotropy makes few-layer graphene therefore a promising candidate to study the rich physics at the crossover from bulk to purely 2D systems. Turning on the weak interlayer coupling while stacking a second layer onto a graphene sheet leads to a branching of the electronic bands and the phonon dispersion at the *K*-point. Double-resonant Raman scattering [35] which depends on electronic and vibrational properties turns out to be an ingenious tool to probe the lifting of that specific degeneracy.

The graphite films were prepared by mechanical exfoliation of highly oriented pyrolytic graphite (HOPG) and subsequent transfer to a highly doped Si wafer with a 300 nm SiO₂ (atomic oxidation process) cap layer.

The experimental setup for the confocal Raman measurement was identical to the one described in Sect. 5.2.3. With a very low incident power of 4–7 μ W, heating effects can be neglected.

The Raman spectrum of graphite has four prominent peaks (Fig. 5.11).

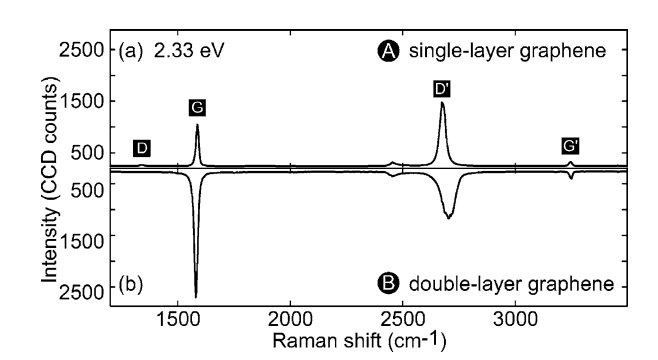
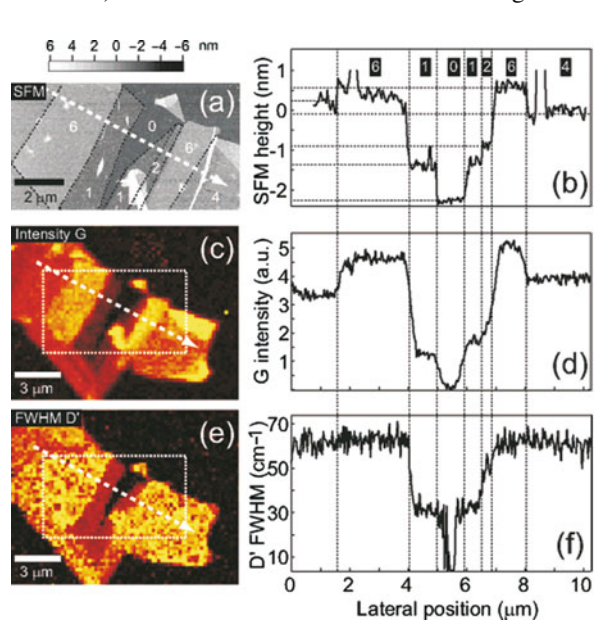


Fig. 5.11 Raman spectra of (a) single- and (b) double-layer graphene (collected at spots A and B, respectively, see Fig. 5.13b)

The peak around 1582 cm⁻¹, commonly called the G-line, is caused by the Raman-active E_{2g} phonon (in-plane optical mode), close to the Γ -point. The D-line around 1350 cm⁻¹ exhibits two remarkable features: its position shifts to higher frequencies with increasing incident laser excitation energies [36] and its relative signal strength (compared to the G-line) depends strongly on the amount of disorder in the graphitic material [36, 37]. The associated overtone D' around $2700 \,\mathrm{cm}^{-1}$ is pronounced even in the absence of a D-signal. Finally, the overtone of the G-line, the G'-line, is located at 3248 cm⁻¹, which is more than twice the energy of the G-line. The different experimental findings related to the dispersive D- and D'-bands could be explained by Thomsen and Reich within the framework of double-resonant Raman scattering [35]. The electronic and vibrational properties of graphite are dominated by the sp² nature of the strong intraplane covalent bonds. Raman spectra for multiple graphene layers can be compared qualitatively and quantitatively while investigating flakes with sections of various thicknesses. In Fig. 5.12(a), the scanning force microscopy (SFM) micrograph of a graphite flake with different layers is presented: the bare SiO₂ (indicated by "0") is surrounded by single-layer sections with steps of up to two, four, and six layers. The different step heights are clearly depicted in Fig. 5.12(b), where a cross-section of Fig. 5.12(a) (see white dashed arrow) is shown. By scanning the flake and collecting the complete Raman spectrum at every spot, we can subsequently filter specific spectral data for a spatially resolved data point and construct false-color 2D plots. In Fig. 5.12(c), the intensity of the G-peak is integrated from 1537 to 1622 cm⁻¹. We find a remarkable correlation with the SFM graph: brighter regions correspond to thicker sections.

The cross-section in Fig. 5.12(d) shows a steplike behavior, perfectly correlated with the topographical changes shown in Fig. 5.12(b). In Fig. 5.12(e), we plot the FWHM (full width at half maximum) of the D'-line. It shows the narrowing at the

Fig. 5.12 (a, b) SFM micrograph and cross-sectional plot (indicated with the white dashed arrow; lateral average over 400 nm) of a few-layer graphene flake with central sections down to a single layer. Raman maps (dashed square corresponding to the SFM image in (a)) showing (c) the integrated intensity of the G-line and (e) the FWHM of the D'-line. The related cross-sections (d, f) are aligned (vertical dashed lines) with the height trace



transition to a single layer (see, e.g., Fig. 5.11) and gives an evident contrast between single- and few-layer graphene sections. The two discrete levels in the FWHM of the D'-line shown in Fig. 5.12(f) related to a single layer ($\approx 30\,\mathrm{cm}^{-1}$) and two and more layers ($\approx 60\,\mathrm{cm}^{-1}$) suggest that the width of the D'-line can be used as an indicator for single-layer graphene. Raman spectroscopy can therefore be used to count the layers of a thin graphite stack and to discriminate between single and double layers. Combined with the double-resonant Raman scattering mechanism, an optical setup using light in the visible range turns out to be an alternative to scanning force microscopy, which requires stacking folds as height references.

Transport measurements show that the quality of the finite graphitic flakes on the silicon oxide matrix obtained with the technique explained above is remarkable: electronic mobilities up to $15,000\,\mathrm{cm^2}$ (Vs)⁻¹ were estimated from transport experiments. We also point out that Raman spectroscopy reveals quasi-defect-free graphitic sheets via the absence of a D-band signal. The appearance of the D-band can be related to the occurrence of defects and disorder. With confocal Raman imaging the spatial origin of the defects can be localized, which can have important consequences for the electronic properties [38]. By comparing the SFM micrograph in Fig. 5.13(c) with the Raman image of the integrated D-line (1300–1383 cm⁻¹)

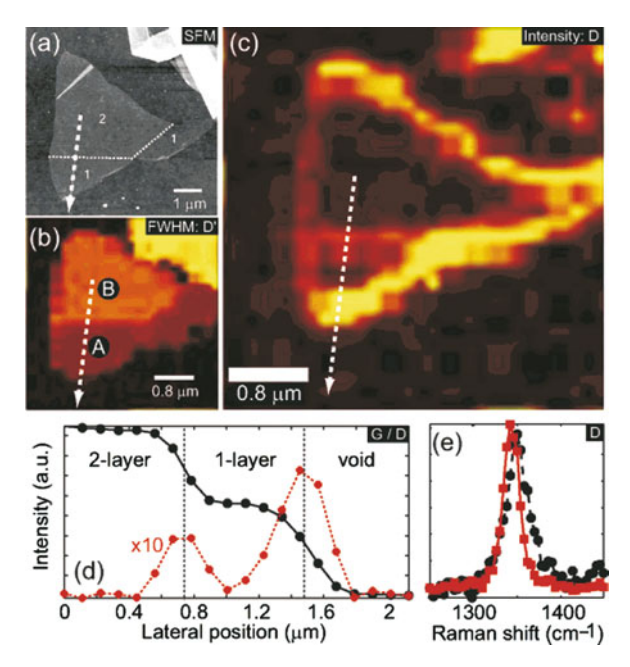


Fig. 5.13 (a) SFM micrograph of a graphitic flake consisting of one double- and two single-layer sections (*white dashed line* along the boundaries), highlighted in the Raman map (b) showing the FWHM of the D'-line. (c) Raman mapping of the integrated intensity of the D-line: a strong signal is detected along the edge of the flake and at the steps from double- to single-layer sections. (d) Raman cross-section (*white dashed arrow* in (c)): staircase behavior of the integrated intensity of the G-peak (*solid line*) and pronounced peaks at the steps for the integrated intensity of the D-line (*dashed line*). (e) Spatially averaged D-peak for the crossover from double to single layer (*black*) and from single layer to the SiO₂ substrate (*red*)

intensity in Fig. 5.13(c), it is obvious that the edges of the flake and also the borderline between sections of different heights contribute to the D-band signal, whereas the inner parts of the flakes do not. This is somewhat surprising because, for thinner flakes, the influence of a nearby substrate on the structural quality should be increasingly important.

In the cross-section in Fig. 5.13(d), one can clearly see that the D-line intensity is maximal at the section boundaries, which can be assigned to translational symmetry breaking or to defects. However, it should be emphasized that the D-line is still one order of magnitude smaller than the G-line. In Fig. 5.13(b), spatially averaged D-mode spectra from the two steps shown in Fig. 5.13(d) are presented. The frequency fits well into the linear dispersion relation of peak shift and excitation energy found in earlier experiments [36]. In addition, it is found that the peak is narrower and downshifted at the edge of the single layer, while it is somewhat broader and displays a shoulder at the crossover from the double to the single layer. In parts (a) and (b) of Fig. 5.11, the Raman spectra of the double- and single-layer graphene shown in Fig. 5.13(b) are compared and labeled A and B, respectively.

The Raman signal is significantly altered when peeling off the penultimate layer: the G-peak decreases strongly in intensity and shifts toward higher wave numbers. In connection with Fig. 5.12(b), we already stated that the integrated G-line signal is monotonically increasing with increasing flake thickness.

5.3.3 Charge Distributions

Electron-hole puddles in graphene have been predicted to be responsible for the finite conductance at vanishing average charge carrier density [39] and have recently been observed using a scanning single electron transistor [40]. Thus the identification of different doping domains might be desirable to investigate graphene devices.

Figure 5.14(a) and (b) shows Raman data for varying back-gate voltages $V_{\rm g}$, which by utilizing a simple capacitor model can be substituted by the electronhole concentration $n=\alpha(V_{\rm g}-V_{\rm g}^D)$. Here, $\alpha\approx7.2\times10^{10}\,{\rm cm}^{-2}/{\rm V}$ and $V_{\rm g}^D\approx2.5\,{\rm V}$ mark the charge neutrality point, which has been determined by transport measurements.

Figure 5.14(c) shows a significant difference between the G- and 2D-linewidths (FWHM). The G-phonon shows a rather strong change as a function of carrier density [42, 43] which is due to the fact that the Pauli exclusion principle prevents the phonon from decaying into an electron-hole pair for $|E_F| > \hbar \omega_G/2$, as illustrated in Fig. 5.14(d) [43]. The decay of the dispersive D-phonon with large wave vector q_D is unaffected by the Pauli exclusion principle for low doping in Fig. 5.14(e). It is expected that the 2D-linewidth stays constant up to a charging that corresponds to a Fermi level shift as large as the exciting laser energy $E_F \approx E_L$. This has a practical implication: since the peak width of the 2D-line, which has been recognized as the most striking feature to distinguish single-layer from few-layer graphene, is

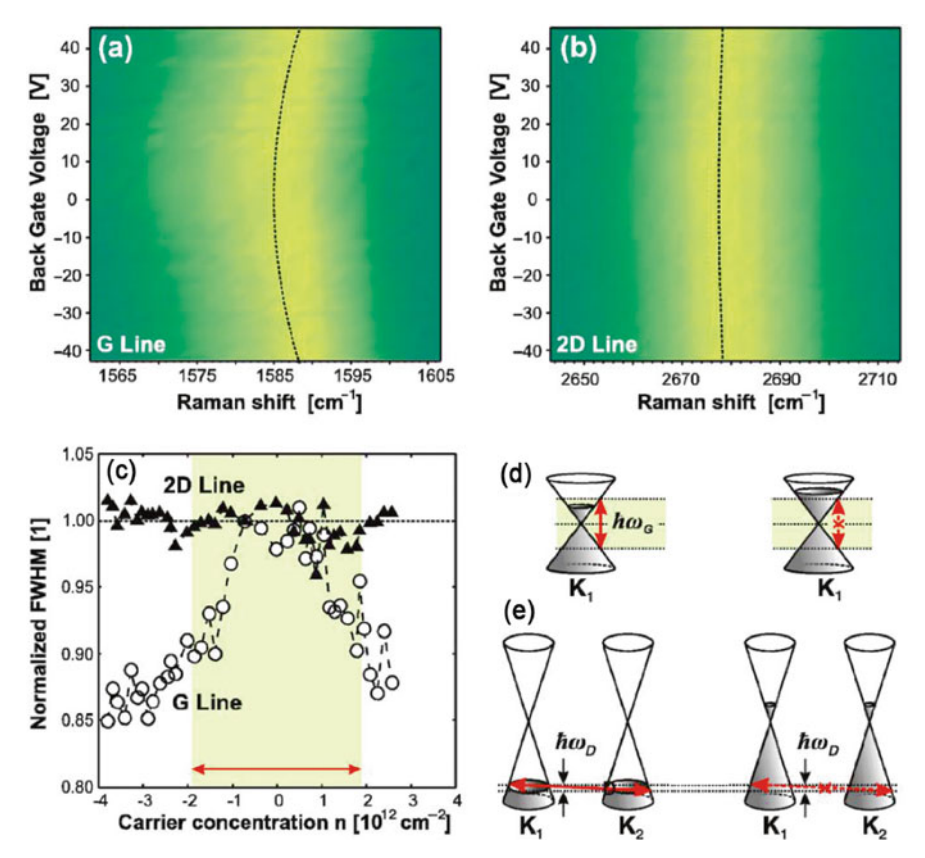


Fig. 5.14 (a) and (b) Maps of the G- and 2D-lines, respectively, as function of applied back-gate voltages are shown. (c) The normalize D-bandwidth (FWHM) of G and 2D as function of doping is shown. (d) and (e) Illustrations of the presence and absence of a phonon decay into an electron—hole pair, respectively, are shown. After [41]

insensitive to doping, it is a reliable-doping-independent measure for identifying single-layer graphene.

Raman microscopy sensing the doping-dependent G- and 2D-line shifts provides an interesting tool to investigate charge fluctuations and doping domains in graphene. Figure 5.15 shows the G- and 2D-peak positions and widths, their fluctuations and cross correlations of a graphene flake on a SiO_2 substrate. The RMS fluctuation of the G-peak is $3.3 \, \text{cm}^{-1}$ explaining the wide spread range of numbers reported in the literature [44–46].

The 2D-line is centered around 2679.4 cm⁻¹ and fluctuates about 0.9 cm⁻¹. The ratio of the fluctuations of the G- and 2D-line agrees well with the ratio of the doping-dependent G- and 2D-stiffening. Doped regions on the imaged flake can be observed. In the upper part of Fig. 5.15(c) and (d) one sees that toward the edges of the graphene sample charging is suppressed, whereas in the entire inner area significant charging is present. If one focuses on a quite uniform area it is found that

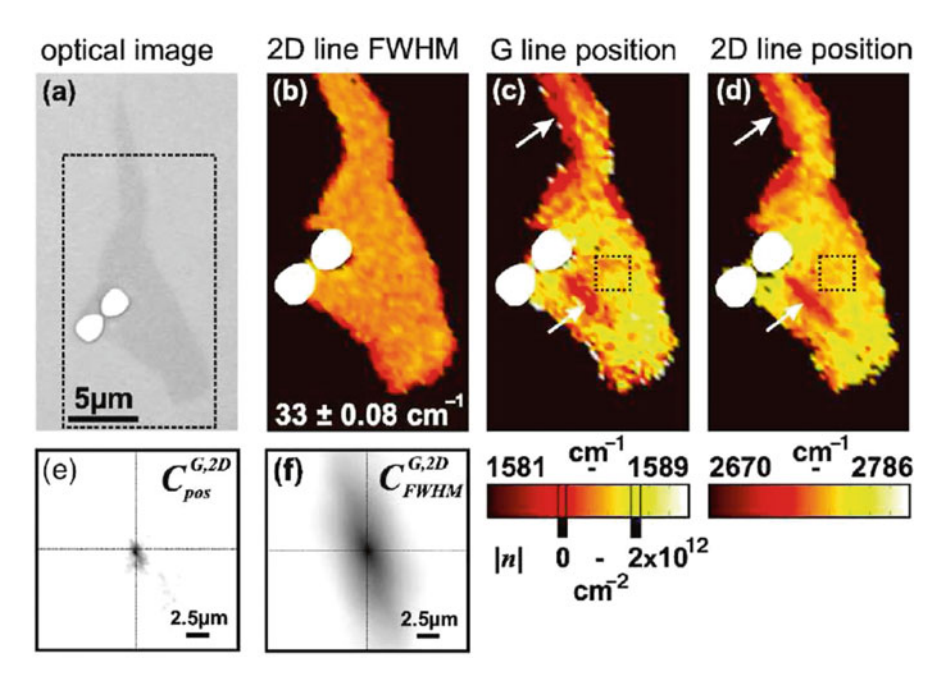


Fig. 5.15 (a) Green-filtered optical image (the two *white dots* are metal markers). (b) FWHM of the 2D-line. (c) and (d) show regions defined by the G- and 2D-peak positions, respectively. The *white arrows* mark correlated low doping areas, whereas the *dotted box* highlights a region with low charging fluctuations. (e, f) 2D cross correlation (adjusted) of the fluctuations of the G- and 2D-line positions (widths). After [41]

the G fluctuations are approximately $0.6\,\mathrm{cm}^{-1}$, which corresponds to $n=2.4\times10^{11}\,\mathrm{cm}^{-2}$.

Raman shifts of the G- and 2D-lines for charged graphene and spatial variations in the G- and 2D-peak positions can be attributed to different doping domains. In the low doping regime no clear distinction between electron and hole doping could be made since for both G- and 2D-lines, stiffening is observed. However, absolute doping fluctuations could be estimated.

5.4 Conclusion

Raman microscopy is a powerful tool with a very high sensitivity that allows the investigation of single-wall carbon nanotubes (SWNTs) as well as single sheets of graphene with sub-micrometer lateral resolution. With this technique it is easily possible to distinguish SWNTs from MWNTs, as well as to determine their diameter by analyzing the position of the radial breathing mode (RBM). It was demonstrated that due to the strong resonance enhancement of CNTs, even a single, freestanding SWNT could be imaged and its properties could be analyzed. By measuring the intensity and diameter of a large number of nanotubes that were excited with a

single excitation wavelength, the phonon scattering cross-section as a function of tube diameter could be derived.

Single graphene layers could be easily distinguished from two or more layers of graphene, because of their different Raman signature. In addition, the number of layers in a stack of graphene sheets has been correlated with the shape of a dispersive phonon mode enabling layer counting from Raman spectroscopy.

Raman microscopy could be even used to show that the edges of single graphene layers show different spectra than the layers themselves, which is most prominent in the defect (D-) band.

Finally, charging effects on doped graphene sheets could be visualized using Raman microscopy.

Acknowledgments The author wishes to thank in particular Dr. Christoph Stampfer and Prof. Christofer Hierold. Many of the results summarized in the present chapter have been achieved with the support and collaboration of numerous people. They are (in alphabetic order) Lukas Durer, Prof. Klaus Ensslin, Dr. Davy Graf, Thomas Helbling, Dr. Stephan Hofmann, Francoise Molitor, Matthias Muoth, Dr. Jannik Meyer, Simone Pisana, Prof. Valentin Popov, Dr. Stephan Stoll, and Dr. Ludger Wirtz.

Samples featuring individual nanotubes have been provided in collaboration with Nicronex Ltd., Luxembourg (www.nicronex.com).

References

- 1. J.D. Bernal, Proc. R. Soc. A 106, 749 (1924)
- 2. H.W. Kroto, J.R. Heath, S.C. O'Brien, R.F. Curl, R.E. Smalley, Nature 318, 162 (1985)
- 3. P. Avouris, Z. Chen, V. Perebeinos, Nature Nanotechnol. 2, 605 (2007)
- 4. S. Reich, C. Thomsen, J. Maultsch, Carbon Nanotubes: Basic Concepts and Physical Properties (Wiley-VCH, Weinheim, 2004)
- 5. M.S. Dresselhaus, G. Dresselhaus, P. Avouris, *Carbon Nanotubes: Synthesis, Structure, Properties and Applications* (Springer, Berlin, 2001)
- Adapted from http://en.wikipedia.org/wiki/Image:Types_of_Carbon_Nanotubes.png (2007)
- R.A. Jishi, L. Venkattaraman, M.S. Dresselhaus, G. Dresselhaus, Chem. Phys. Lett. 209, 77 (1993)
- S. Bandow, S. Asaka, Y. Saito, A.M. Rao, L. Grigorian, E. Richter, P.C. Eklund, Phys. Rev. Lett. 80, 3779 (1998)
- 9. J. Kuerti, G. Kresse, H. Kuzmany, Phys. Rev. B 85, 8869 (1998)
- 10. V.N. Popov, V.E.V. Doren, M. Balkanski, Phys. Rev. B **59**, 8355 (1999)
- 11. L. Henrard, E. Hernandez, P. Bernier, A. Rubio, Phys. Rev. B 60, 8521 (1999)
- 12. V.N. Popov, L. Henrard, P. Lambin, Phys. Rev. B **72**(3), 035436 (2005)
- 13. C. Thomsen, S. Reich, Phys. Rev. Lett. **85**, 5214 (2000)
- 14. O. Dubay, G. Kresse, Phys. Rev. B 67, 035401 (2003)
- B. Vigolo, A. Pénicaud, C. Coulon, C. Sauder, R. Pailler, C. Journet, P. Bernier, P. Poulin, Science 290, 1331 (2001)
- 16. O. Dubay, G. Kresse, H. Kuzmany, Phys. Rev. Lett. 88, 235506 (2002)
- H. Kataura, Y. Kumazawa, Y. Maniwa, I. Umezu, S. Suzuki, Y. Ohtsuka, Y. Achiba, Synth. Met. 103, 2555 (1999)
- 18. G.S. Duesberg, I. Loa, M. Burghard, K. Syassen, S. Roth, Phys. Rev. Lett. 85, 5436 (2000)

- 19. C. Fantini, A. Jorio, M. Souza, M.S. Strano, M.S. Dresselhaus, M.A. Pimenta, Phys. Rev. Lett. 93, 147406 (2004)
- A. Jorio, J.H. Hafner, C.M. Lieber, M. Hunter, T. McClure, G. Dresselhaus, M.S. Dresselhaus, Phys. Rev. Lett. 86, 1118 (2001)
- A. Jungen, C. Stampfer, J. Hoetzel, V. Bright, C. Hierold, Sens. Actuators A Phys. 130–131, 588 (2006)
- 22. J. Kong, H.T. Soh, A.M. Cassell, C.F. Quate, H.J. Dai, Nature 395, 878 (1998)
- A. Jungen, V.N. Popov, C. Stampfer, L. Durrer, S. Stoll, C. Hierold, Phys. Rev. B 75, 041405 (2007)
- 24. V.N. Popov, L. Henrard, P. Lambin, Phys. Rev. B **70**(11), 115407 (2004)
- A. Jungen, S. Hofmann, J.C. Meyer, C. Stampfer, S. Roth, J. Robertson, C. Hierold, J. Micromech. Microeng. 17, 603 (2007)
- 26. P. Avouris, J. Appenzeller, R. Martel, S.J. Wind, Proc. IEEE 91, 1772 (2003)
- A.P. Graham, G.S. Duesberg, R.V. Seidel, M. Liebau, E. Unger, W. Pamler, F. Kreupl, W. Hoenlein, Small 1, 382 (2005)
- 28. C. Stampfer, T. Helbling, D. Obergfell, B. Schoeberle, M.K. Tripp, A. Jungen, S. Roth, V.M. Bright, C. Hierold, Nanoletters 6, 233 (2006)
- D. Mann, Y.K. Kato, A. Kinkhabwala, E. Pop, J. Cao, X.R. Wang, L. Zhang, Q. Wang, J. Guo, H.J. Dai, Nature Nanotechnol. 2, 33 (2007)
- A. Jungen, J. Gauckler, C. Stampfer, L. Durrer, T. Helbling, C. Hierold, in *IEEE MEMS 08*, Tucson, AZ, USA, 2008, p. 733
- 31. R. Saito, G. Dresselhaus, M.S. Dresselhaus, Phys. Rev. B 61, 2981 (2000)
- K.S. Novoselov, A.K. Geim, S.V. Morozov, D. Jiang, Y. Zhang, S.V. Dubonos, I.V. Grigorieva, A.A. Firsov, Science 306, 666 (2004)
- K.S. Novoselov, A.K. Geim, S.V. Morozov, D. Jiang, M.I. Katsnelson, I.V. Grigorieva, S.V. Dubonos, A.A. Firsov, Science 438, 197 (2005)
- 34. Y. Zhang, Y.W. Tan, H.L. Stormer, P. Kim, Science **438**, 201 (2005)
- 35. C. Thomsen, S. Reich, Phys. Rev. Lett. **85**, 5214 (2000)
- 36. R. Vidano, D. Fischbach, L. Willis, T. Loehr, Solid State Commun. 39, 341 (1981)
- 37. F. Tuinstra, J.L. Koenig, J. Chem. Phys. **53**, 1126 (1970)
- 38. N. Peres, F. Guinea, A.C. Neto, Phys. Rev. B 73, 125411 (2006)
- 39. E.H. Hwang, S. Adam, S.D. Sarma, Phys. Rev. Lett. 98, 186806 (2007)
- J. Martin, N. Akerman, G. Ulbricht, T. Lohmann, J.H. Smet, K. von Klitzing, A. Yacoby, Nat. Phys. 4, 144 (2008)
- 41. C. Stampfer, F. Molitor, D. Graf, K. Ensslin, A. Jungen, C. Hierold, L. Wirtz, Appl. Phys. Lett. 91, 187401 (2007)
- 42. S. Pisana, M. Lazzeri, C. Casiraghi, K.S. Novoselov, A.K. Geim, A.C. Ferrari, F. Mauri, Nat. Mater. 6, 198 (2007)
- 43. J. Yan, Y. Zhang, P. Kim, A. Pinczuk, Phys. Rev. Lett. 98, 166802 (2007)
- 44. A.C. Ferrari, J.C. Meyer, V. Scardaci, C. Casiraghi, M. Lazzeri, F. Mauri, S. Piscanec, D. Jiang, K.S. Novoselov, S. Roth, A.K. Geim, Phys. Rev. Lett. 97, 187401 (2006)
- 45. D. Graf, F. Molitor, K. Ensslin, C. Stampfer, A. Jungen, C. Hierold, L. Wirtz, Nanoletters 7, 238 (2007)
- 46. A. Gupta, G. Chen, P. Joshi, S. Tadigadapa, P.C. Eklund, Nanoletters 6, 2667 (2006)

Chapter 6 Raman Spectroscopy and Confocal Raman Imaging in Mineralogy and Petrography

Marc Fries and Andrew Steele

Abstract Raman spectroscopy has long been used in geosciences and a wealth of data and publications are available. The majority of this information originates from point measurements using micro-Raman setups. With the application of confocal Raman imaging, additional analytical possibilities arise with respect to analyzing the three-dimensional spatial distribution of inorganic as well as organic phases on the centimeter to sub-micrometer scale. This chapter will highlight some of the key aspects experimenters should take into consideration when performing confocal Raman measurements as well as experimental results showing the insight gained into geological samples by the use of confocal Raman imaging.

6.1 Introduction

Raman spectroscopy is especially well suited for use in mineralogy and petrographic studies, as it provides non-destructive mineral identification very quickly and with excellent specificity. Additionally, it is sensitive to the presence and structure of carbonaceous phases that are difficult to characterize by optical microscopy or electron beam methods. Raman spectroscopy has the advantage over electron beam methods that Raman spectra can reveal the presence of a wide variety of mineral phases in a single spectrum of sub-micrometer resolution, as opposed to an electron beam that performs an elemental analysis that can include any or all phases within the excitation volume. The practical result of this is that a Raman spectrum can identify individual mineral phases in fine-grained clusters, while electron probe analysis only produces the bulk composition of the intermixed phases. With the relatively recent development of confocal Raman imaging, definitive petrography (the study of rocks in thin section) is now possible in fields of view ranging from tens of micrometers to centimeters across. Data gleaned in this way are used in turn for petrology studies (the study of the formation and alteration of rocks primarily through petrographic analysis). An additional benefit of the use of a visible light excitation laser is the interrogation of features that are buried in the interior of mineral grains, such as opaque and fluid inclusions. All of this can be done on either prepared thin sections or unprepared mineral surfaces, which places Raman spectroscopic techniques very prominently in a mineralogist's "tool kit" of analytical techniques.

6.2 Raman Spectroscopy and Imaging as a Mineralogy/Petrography Tool

Mineralogy and petrography techniques have traditionally relied heavily on optical microscopy, utilizing reflected, transmitted, and cross-polarized microscopy to identify minerals in thin section and describe their layout. The identities and textures of mineral phases are used to interpret the formation and subsequent alteration history of those minerals and their parent rock formation (Fig. 6.1). From there the investigator can draw conclusions about the history of the entire rock formation and its relationship to larger geologic units, thereby working with observations made under a microscope to draw insights on the creation, destruction, and movement of entire continents. In the case of fossilized materials, petrography is used to make fundamental descriptions of the evolution of life over geologic time as well as to discuss the very origin of life itself.

Raman spectroscopy is a very useful tool in petrographic analysis like these, as it can be used not only for mineral identification but also for investigation of carbonaceous matter in rocks. The study of carbonaceous material as a mineral phase in general is somewhat problematic. Under a microscope, condensed carbonaceous phases simply appear opaque. Electron beam techniques such as SEM or EDX, which are commonly used in mineralogical studies, are less sensitive to their presence and structure than phases composed of more massive elements. Some other techniques such as bulk chemical measurements require crushing and extraction, which produces useful information but destroys the fine mineralogical context needed to completely describe the origin and alteration history of the material. Raman spectra

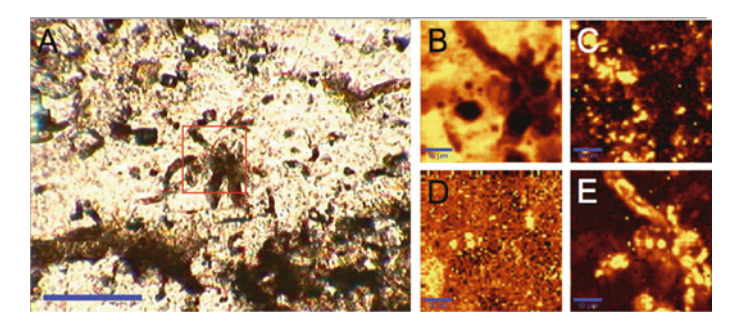


Fig. 6.1 Example of mineral phase mapping using Raman imaging in a thin section from the Strelley Pool formation. (a) Transmitted light image showing dark, filamentous features. A Raman image was collected in the *red box* and the *blue* scale bar is 80 μm in length. (b) Image of quartz within the *red box* in (a) showing the mineral matrix. Scale bar is 10 μm long. (c) Image of carbon, which somewhat surprisingly appears as a diffuse blebby phase and is not the primary constituent of the filaments. (d) Small pyrite grains (*yellow spots* to *right* and *left* of the image center). (e) Sulfate minerals that make up the filaments in this image, presumably formed by oxidation of pyrite grains in (d). Sample provided by M. Brasier and D. Wacey, of the Dept. of Earth Sciences, Oxford U., UK

are sensitive to the identity and structure of all known condensed carbon phases and are very specific in the identification of other mineral phases (Fig. 6.2). In addition, Raman imaging provides mapping of carbonaceous phases within the mineralogical context of their parent rock. For example, it allows an investigator to discern carbonaceous matter within primary fluid inclusions that formed as a rock first cooled from its parent melt from other carbonaceous matter found in late-phase alteration veins within the same rock. This distinction is especially important in the study of meteorites, where many features of the rock either could be an original feature of the meteorite or could possibly be the result of alteration after the meteorite fell to Earth.

The implementation of Raman spectroscopy is very straightforward, as very little sample preparation is necessary for a Raman measurement. Measurements can be performed on whole rocks placed under a microscope in the lab or on rock formations in situ by portable Raman instruments in field studies. Rocks are usually either ground to produce a flat surface for simple petrographic examination and Raman point measurement (such as in field studies), prepared as thin section for Raman imaging of fine details, or ground to a powder to perform point Raman analysis of a statistically relevant number of grains as a representative analysis of the host rock (but without the contextual information). Practically speaking, however, the most useful mineralogical/petrographic Raman measurements are done using imaging techniques on ground, otherwise smoothed, or polished surfaces both to maximize the signal quality and to remove surface weathering products from the rock. Unless, of course, the goal of the measurement is to examine surface weathering products!

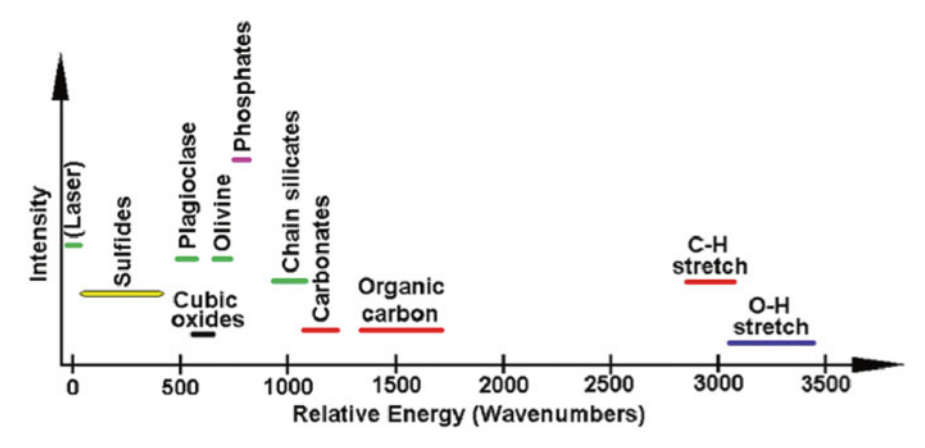


Fig. 6.2 Simplified diagram showing the general positions of prominent Raman peaks for a variety of common rock-forming minerals and compounds. Note that different families of minerals tend to have separate "fingerprint regions," and more importantly that many of these "fingerprint regions" can exist in a single spectrum without substantial overlap. This allows definitive mineral phase identification even in complex mineralogical mixtures

6.2.1 Working with Thin Sections

A typical petrographic thin section consists of a thin wafer of a rock sample that has been polished on both sides until transparent and is thin enough to reveal mineral birefringence in polarized light. The rock slice is affixed to a glass slide on one side and either sealed with a glass cover slip on the opposing face or left exposed. Confocal Raman spectroscopy is well suited for analysis of thin layers of material (i.e., [1]), as the excitation volume can be constrained in the *z*-axis to control signal input from polymer and glass layers, as well as the *x*- and *y*-axes to control and optimize image resolution. This allows collection of Raman spectra from selected mineral phases while rejecting spectral contributions from the glass slide, cover slip (if present), or bonding polymer. However, a number of considerations must be accounted for when working with thin sections.

- 1. Thin section surface irregularities and contamination: Depending on the minerals present in the thin section and the quality of preparation, some surface pits and irregularities may occur in the thin section surface. These typically occur in anisotropic phases such as pyroxenes and softer minerals such as clays. Surface roughness within these flaws can scatter the excitation beam somewhat, but the more important consideration is that polishing materials such as diamond paste and abrasive grains can become lodged in them. When collecting Raman spectra or images from near the surface of the thin section, these contaminants can be misinterpreted as materials native to the thin section rock. To avoid this error, examine the thin section in reflected light before analysis to familiarize yourself with the location and size of flaws. It can also be useful to create an image of the Rayleigh-scattered laser line itself, which serves as a monochromatic reflectivity image at the same resolution as calculated Raman images.
- 2. Mounting polymer permeation: Since mounting polymer started out as a liquid, expect to find it in every crack in the thin section mineral slab. This is especially true of thin sections made of friable materials, as these thin sections are often prepared using a vacuum impregnation method. Acquiring a reference spectrum of the polymer used to prepare the thin section under examination is a good idea. This spectrum can be used to differentiate mounting polymer from any organic compounds present in the thin section, usually by identifying spectral features in the C–H stretch mode region which is well removed from Raman modes of rock-forming minerals.
- 3. Minor polymer contribution through confocal "leaking": Confocal spectroscopy constrains light collection to within a narrow band very close to the instrument's focal plane, because light arising from either above or below the focal plane is rejected at the confocal aperture or pinhole. A small amount of light arising from directly along the axis of the excitation beam, however, may pass through the confocal aperture. Three conditions must be met for this to occur. First, the Raman signal of the interfering medium must be relatively strong, such as the C–H band stretch region of a thin section mounting polymer. Second, the

confocal aperture is relatively large (depending on the instrument and sample, roughly $\geq 50\,\mu\text{m}$). Finally, the excitation beam power is typically quite high, as the excited volume of material responsible for this light leak is smaller than the diameter of the excitation beam, and so the intensity of the interfering Raman signal is intrinsically small. This effect is usually a problem only for spectra collected fairly deep into a thin section such that the excitation volume is close to the lower mounting polymer layer. The result is that a minor C–H stretch mode Raman spectrum can appear in some spectra collected from a thin section and usually seen through large clear grains, which may lead to the mistaken conclusion that an aliphatic compound is present within the mineral phase.

- 4. Focus on the distal mineral surface: When viewing a thin section in transmitted light, it can be possible to focus on the mineral slab surface adjacent to the glass slide instead of the thin section surface, especially if the illumination source is intense. This is a minor problem, but can be rather embarrassing if you happen to be showing off your shiny new Raman spectrometer to a visitor at the time. The easy way around this is to focus on the thin section surface in reflected light when you start your work.
- 5. *Previous carbon coating*: Some thin sections, and especially those prepared out of rare materials such as meteorites, are examined with multiple methods in multiple laboratories. If the thin section has been examined using a vacuum electron probe technique such as scanning electron microscopy (SEM) or electron probe analysis, then it has probably been coated with an electrically conductive coating such as Au–Pd or carbon. These coatings can be "removed," but Raman spectroscopy is extraordinarily sensitive to the presence of carbon in particular. Previous Au–Pd coatings will appear as laser-reflective materials in cracks, low spots, and surface imperfections in the thin section. A carbon coating that has been "removed" will show up as an opaque or mildly transparent coating in the same surface imperfections but will yield a Raman spectrum consistent with that of glassy carbon. That is, the carbon G and D bands around 1590 and 1350 cm⁻¹, respectively (Tuinstra and Koenig [21]), will be broadened to the point that they overlap considerably. The optimal situation is to utilize Raman microscopy before applying techniques that may require elaborate sample preparation.
- 6. Surface alteration of soft carbonaceous phases during thin section preparation:
 Raman spectroscopy is extraordinarily sensitive to the structure of carbon. The actual interaction volume of the Raman excitation laser is very shallow in opaque phases to the point that it is comparable to the thickness of the surface layer disrupted by mechanical polishing. In other words, a Raman spectrum of a soft, opaque carbonaceous phase in a thin section is very likely only measuring the surface that has been mechanically abraded during polishing. Several researchers have noted this effect (i.e., [2]) and pointed out the importance of taking it into account when describing the structure of carbonaceous phases in thin section. To put it simply, do not accept measurements of carbon phase structure in thin section if the Raman measurement is made at the thin section surface, as that measurement is made only of the thin surface layer that has been disrupted

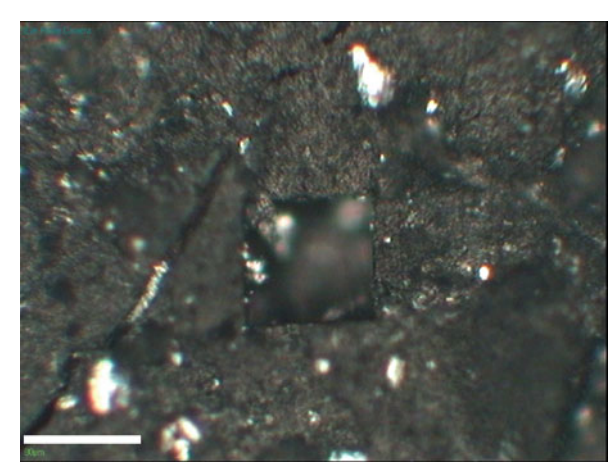
by polishing. Some researchers [2, 3] state that Raman measurements are best made on the contact between carbonaceous materials and any transparent mineral grain, on a surface that is embedded within the thin section and removed from the actual thin section surface. There is some room for argument as to whether or not this technique measures carbon structure that is truly representative of the carbonaceous material bulk structure, however. Whenever possible, it is advisable to work with both a thin section and fresh fracture surface of the same material. Raman images of the thin section can produce in situ maps of carbonaceous material to provide mineralogical context, and multiple spot Raman spectra of the same carbonaceous material on the fractured surface provide a statistically relevant set of spectra for interpretation of bulk microstructure of that same carbonaceous material in order to ascertain the extent of alteration of the carbon measured in thin section.

As long as these considerations are acknowledged and accounted for, none of the above should be a real obstacle to producing high-quality Raman images of samples in thin section.

6.2.2 Control of Laser Power

The signal intensity of Raman-scattered photons is commonly quoted to be around one one-millionth of the excitation laser strength, although in reality this value varies from mineral to mineral and from one Raman mode to another, as well as whether or not a particular mode undergoes resonant enhancement, etc. It is generally true, however, that the Raman effect is weak relative to the laser power used to observe it, and this leads to the very real possibility that a sample can be damaged by the excitation laser (Figs. 6.3 and 6.4).

Fig. 6.3 Laser beam damage in a fullerene soot. The square artifact in the center of the image is a hole that perfectly preserves the shape of a Raman image collected with an accidental "overdose" of laser power. A misread dial allowed approximately 50 times as much power as was intended, evaporating the carbonaceous material to leave a square hole and small, surviving silicate contaminants. The scale bar is 80 µm in length



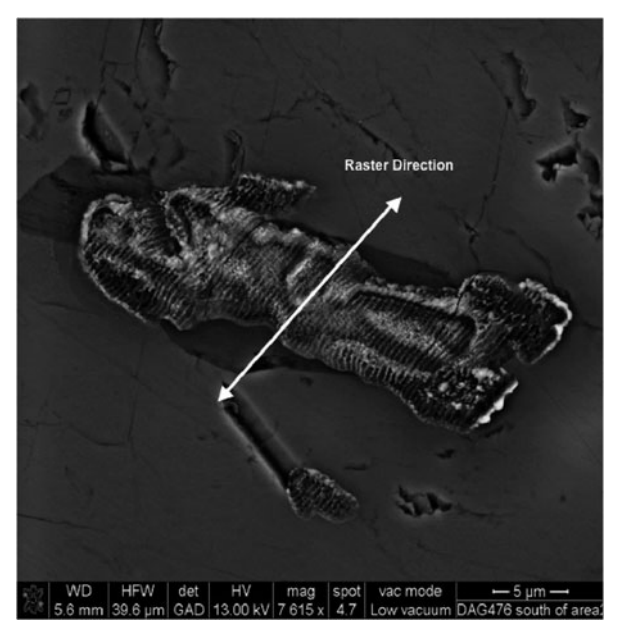


Fig. 6.4 Another one from the "What Not to Do" files, an SEM image showing laser damage in a chromite grain. A Raman image was collected using excessive laser power density with the raster direction proceeding along the axis indicated by the *white arrow*. The striation in the chromite grain is the result of damage incurred during repeated, parallel passes by the Raman excitation laser. Note that the opaque chromite grain absorbed sufficient laser power to damage the grain's surface, while the surrounding, transparent olivine was undamaged. This illustrates the dependence of laser power used to collect an image or spectrum on the nature of the material under investigation. Image collected by Dr. Edward Vicenzi, Smithsonian Institution, Washington, DC, USA

While many early papers described the laser power used in terms of output power at the laser itself, recent literature generally acknowledges the many factors involved and describes power in terms of power density (laser power per unit area) as measured at the laser spot focal plane. This is especially important considering that all Raman instruments feature some variability in total laser throughput due to scattering losses in the focusing optics as well as in the spot size at the focal plane. It is sufficient to describe the power density for a measurement simply by measuring the total laser power at the measurement focus and dividing by the calculated spot area, but there is room for improving upon this method. Laser power distribution at the measurement spot is not uniformly distributed, and there is a need at the time of this writing for establishment of a standard method of reporting laser power values that takes into consideration this and other parameters to include peak laser power for a given measurement spot. Beyond these considerations, for the application of "conventional" Raman spectroscopy (as opposed to resonantly enhanced methods described elsewhere), there are two primary considerations in managing laser power – the nature of the target material and the capabilities of the Raman device used.

6.2.2.1 Nature of the Sample

Understanding the nature of the sample is an important part of managing laser power. For example, a material that contains fine sulfides that are susceptible to oxidation on heating must be handled much more "lightly" than a sample composed entirely of transparent silicates. A mineral such as quartz or olivine, which exhibits very low absorption in visible light, can tolerate very high excitation beam flux without damage. Excitation in such a case occurs over a sample volume with a size and shape dependent on beam geometry, and thus on the optics of the instrument used. For opaque materials, such as chromite and reduced carbon, however, the excitation "volume" is practically a two-dimensional surface due to strong absorption of the beam at the mineral surface. Power density for such a case can become extraordinarily high since the power density formula's denominator (excitation area) becomes very small, thereby increasing the likelihood of damaging an opaque phase with what is a benign amount of laser power for transparent gains. Figure 6.4 illustrates this effect, showing small, opaque chromite grains that have been damaged by an excitation beam while surrounding, transparent olivine grains are unaffected.

The message here is that applied power density vs. acquisition time per pixel is one of the trade-offs applied to a measurement and that this factor should be applied with an understanding of the nature of the sample. This also serves to reinforce the notion that Raman imaging is best utilized in conjunction with optical petrography techniques that can provide the general information on sample character needed to select an appropriate amount of excitation laser power.

Other examples of minerals which are especially prone to laser damage include fine-grained minerals, sulfides, or samples embedded in an insulating medium such as aerogel. Fine-grained minerals will include some proportion of porosity and/or poorly ordered materials in its intergranular volume. Both of these impede thermal conduction, resulting in a material prone to laser heating damage. Many sulfides oxidize readily upon even mild heating, necessitating a Raman microscope with very high photon throughput combined with a very sensitive detector and low laser power density to produce a usable Raman spectrum without inflicting sample damage. A by-product of this fact is that Raman spectral standards of sulfide minerals currently are not as prevalent as spectra of more robust phases.

It is worth noting that cometary particles returned to Earth by the Stardust space-craft exhibit all three of the example features described in the previous paragraph. Most of them are fine grained, they contain fine sulfide grains [4], and in their unprocessed form they are contained in an aerogel insulating medium. Raman measurements of Stardust particles focus on analysis of carbonaceous phases as a result, as these phases typically show strong Raman spectral features and are reasonably resistant to heating damage [5–7], although a limited number of measurements have been performed on other phases [8]. This author determined that fine sulfides fired into aerogel using a light gas gun converted readily to oxides under laser power density of only $33 \,\mu\text{W/cm}^2$ [Fries, unpublished data], which made this phase extraordinarily difficult to analyze safely. Stardust samples are generally examined following

removal from the aerogel capture medium [9] followed by curatorial processing such as gold foil mounting or ultramicrotoming. The authors also utilized an empirical method for determining the upper threshold of allowable power density for Stardust-like samples using fine, meteoritic sulfide particles. Troilite (FeS) particles were scraped off a slab of the Toluca iron meteorite and pressed onto gold foil just as the Stardust particles were. Sub-micrometer particles were examined over long integration times under increasing laser power to identify the power level where magnetite first started to appear due to heating in air, as seen in the appearance of the strong 670 cm⁻¹ Raman peak for magnetite.

6.2.2.2 Raman Instrument Parameters

Due to variation in instrument design and laser spot geometry, it is advisable not to rely on power settings reported in literature but rather to perform this type of preparation using the actual instrument to be used in the analysis. As far as Raman instruments are concerned, there are a few important avenues available for control of sample damage. These are optimizing instrument efficiency/detector sensitivity and the effective control of applied power. For laboratory instruments, modern commercial devices include high-throughput instruments and options for high-sensitivity detectors. Beyond the choice of instrument and detector, the primary factor in instrument design is arguably the choice between fiber-based and fiber-less Raman systems. A system that uses fiber optic cables as the confocal pinhole and for light transmission to the detector is capable of very high resolution imaging with good fluorescence suppression capability, but at the expense of Raman signal throughput due to the small core diameter of the fiber (typically 25–100 µm). The absorption within the fiber itself is measured in dB/km and thus negligible. Conversely, instruments with large pinholes generally allow more light to reach the detector, but at the expense of depth resolution and fluorescence rejection. In any event, laser power applied to a sample must be carefully applied to prevent damage, and the best means to address it is by a careful set of heating trials using minerals that each investigator intends to analyze, using the same instrument to be used in the analysis. Differences in signal throughput, sensitivity, excitation beam shape, and other factors between instruments demand that a set of trials are done on the actual instrument in use and that any such measurements done on similar instruments should be used only as broad guidelines and only if necessary.

6.3 "Raman Mineralogy" Using Imaging Raman Techniques

Petrography, at its core, is the study of minerals in thin sections. This means that a petrographer interprets the identity of each mineral in a rock and draws conclusions on the formation and alteration history of the rock and its parent formation from the setting and identity of the suite of minerals present. Imaging Raman spectroscopy is especially well suited to this task, as it can be used not only to identify the minerals

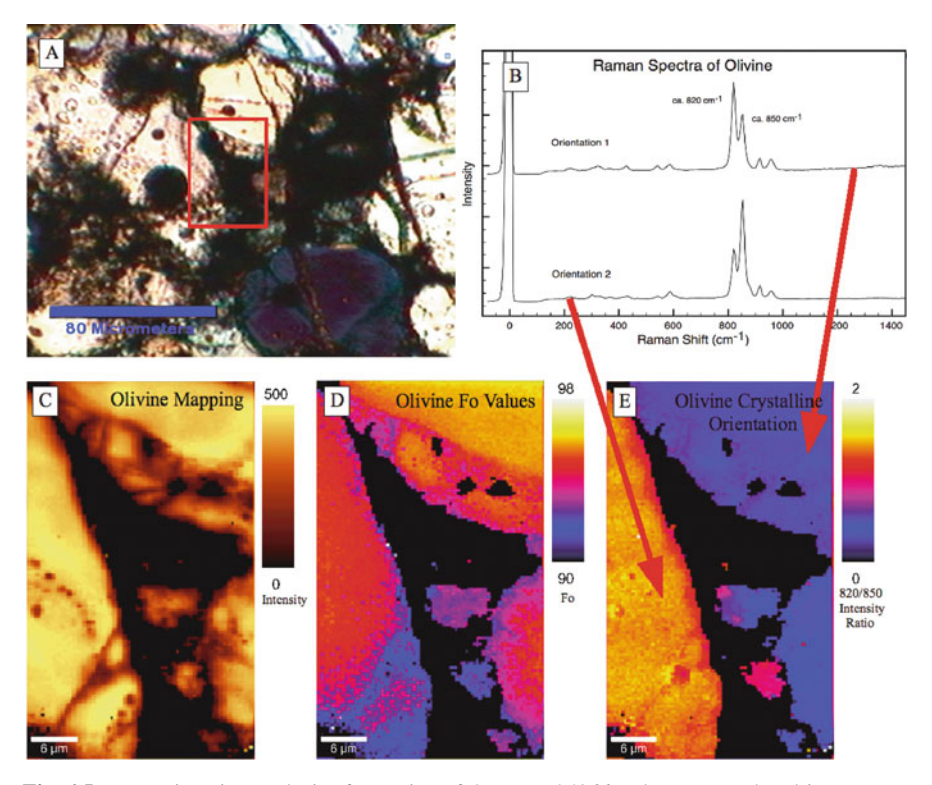


Fig. 6.5 Raman imaging analysis of a portion of the *QUE 94366* carbonaceous chondrite, a meteorite found in Antarctica. (a) shows a transmitted light microscopy image with the *red box* highlighting the area examined using Raman imaging. (b) shows two Raman spectra of olivine within the scan area, showing the variation in peak intensity arising from changes in crystalline orientation relative to the polarization plane of the excitation beam. (c) is an image of intensity of a Gaussian fit to the \approx 850 cm⁻¹ Raman peak of olivine, showing the location of olivine within the scan area. (d) shows olivine iron content in terms of Fo (Fosterite) number, showing sub-micron variation in iron content in this phase. (e) is an image of the ratio between \approx 820 and \approx 850 cm⁻¹ Raman peak intensities, indicating crystalline orientation of the various grains. Note that the small grains in the lower center of the image are revealed to be polycrystalline or separate from the larger grains. Also notice that variations in iron content exist within single grains, as shown by comparing (d) and (e)

but also to map their appearance in a thin section (as in Fig. 6.2). Fine details such as crystallographic orientation, overall water content, presence of aqueous alteration products, compositional variation can also be identified and separately mapped (i.e., Fig. 6.5) to highlight and interpret them.

6.3.1 Mineral Phase Imaging

Raman spectroscopy of minerals produces information on the identification of condensed phases with the exceptions of metals and of phases that fluoresce strongly under the excitation beam. A very wide variety of phases produce reasonable Raman spectra to include transparent, opaque, and metallic phases (to include sulfides). To illustrate the broad range of mineral species that can be identified using Raman spectroscopy, note that the freely available RRUFF online Raman database contains over 2000 distinct mineral spectra [10]. Raman spectra can also contain information on a mineral phase's chemical composition [11, 12], latent strain (i.e., [13, 14]), crystalline orientation [12, 15], grain size [16, 17], thermal history in some [18, 19] and are very sensitive to the presence and structure of carbon [20–22].

With the advent of Raman imaging, that information can be expanded from a point measurement to images of petrographic thin sections or even unprepared rock, presented in terms of mineral phase maps or images of mineral properties (Fig. 6.6).

Where electron probe or SEM/EDS imaging produces maps of mineral elemental composition that can identify, for example, an SiO₂ phase, Raman imaging of the same phase can generate maps of quartz, coesite, tridymite, cristobalite, lechatlierite, or silicate glass and place that phase in a mineralogic context. Each pixel in such a Raman image can be as small as hundreds of nanometers across, depending on the instrument, which is a finer resolution than that featured by many analytical techniques commonly employed in mineralogy/petrography. Additionally, each Raman spectrum can contain Raman spectral lines of several mineral phases and by (a happy) coincidence most common rock types generate lines that do not interfere spectrally with those of other phases. For example, have a look at Fig. 6.7.

The mineralogy at the rim of a meteorite chondrule shown there is too fine grained to completely characterize the minerals present using optical petrography techniques. Raman imaging reveals the various phases present and is used to produce very finely detailed images of each of them, regardless of whether they are

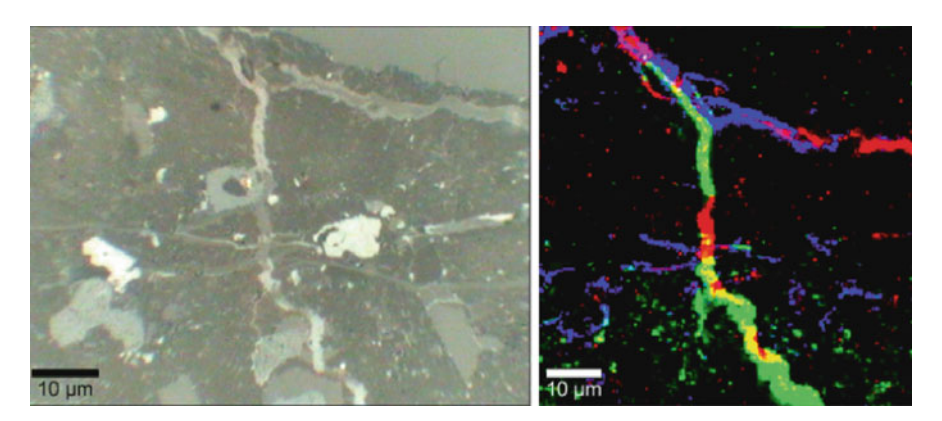


Fig. 6.6 Alteration vein in the *MIL 03346* martian meteorite. *Left*: reflected light image of a polished thin section. *Right*: Raman image with mineral phases highlighted. *Red* is jarosite, *green* is goethite, and *blue* are clay minerals. Isotopic analysis of these phases show that they are martian in origin, which provides researchers with samples of martian aqueous alteration products for study [from Vicenzi et al. 2007]

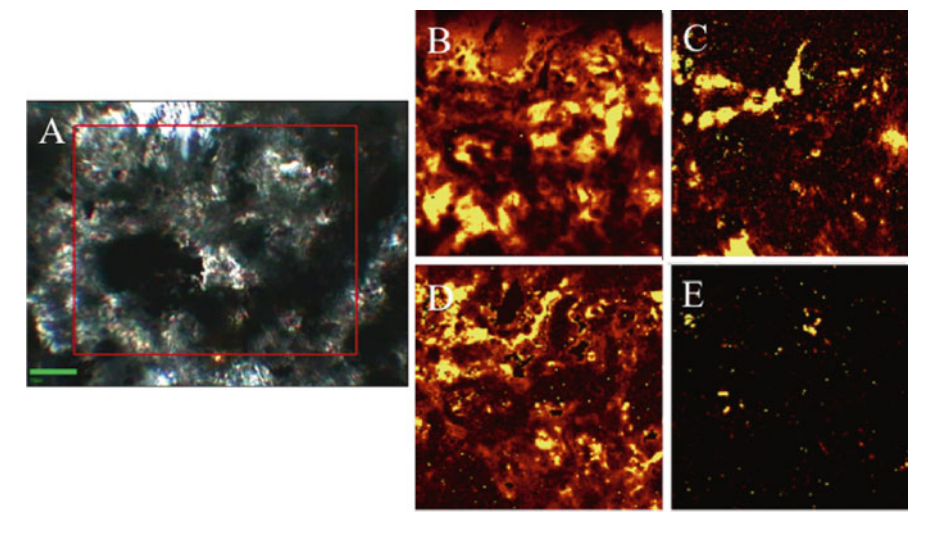


Fig. 6.7 Identification of individual mineral phases in a complex, fine-grained mixture. (a) Transmitted light microscopy image of the fine-grained rim on a chondrule in the *QUE 94366* CV-type carbonaceous chondrite. A Raman image was collected approximately within the *red square*, and the scale bar is $10\,\mu$ m long. (b) Image of the olivine within the scanned area, as seen from the intensity of the $820\,\mathrm{cm^{-1}}$ olivine peak. (c) Pyroxenes within the scan, as measured using the intensity of the $\approx 1010\,\mathrm{cm^{-1}}$ peak. (d) Macromolecular carbon as seen from the intensity of the $\approx 1580\,\mathrm{cm^{-1}}$ G band. (e) Whitlockite, an anhydrous phosphate mineral. These phases are distinguished by Raman spectral features on a scale that is impractical for standard petrographic analysis

transparent silicates or opaque carbonaceous material. This capability allows not only mineralogy by Raman spectroscopy but also petrography by Raman imaging. In other words, a bulk rock can be identified through identification and morphology characterization of its constituent minerals through Raman imaging.

6.3.2 Crystallographic Orientation Imaging

Fundamentally, Raman spectroscopy works by exciting vibrations in the crystal matrix of a target material using an excitation laser. Some of these vibrations propagate along a particular crystallographic direction or directions such that they propagate asymmetrically through the crystallographic unit cell. In this case, changing the vector of the excitation beam relative to the vibration propagation vector will diminish the likelihood of exciting that particular vibrational mode. The practical effect of this feature is that the same mineral phase in different crystallographic orientations can exhibit a peak or peaks with variable intensity. Raman imaging can reveal the orientation of these grains by generating a calculated image of the ratio of the intensity of an orientation-dependent Raman peak to another peak in the same mineral that is relatively invariant in intensity (Fig. 6.8). This calculation has the added benefit of normalizing the image to remove relative phase spectrum

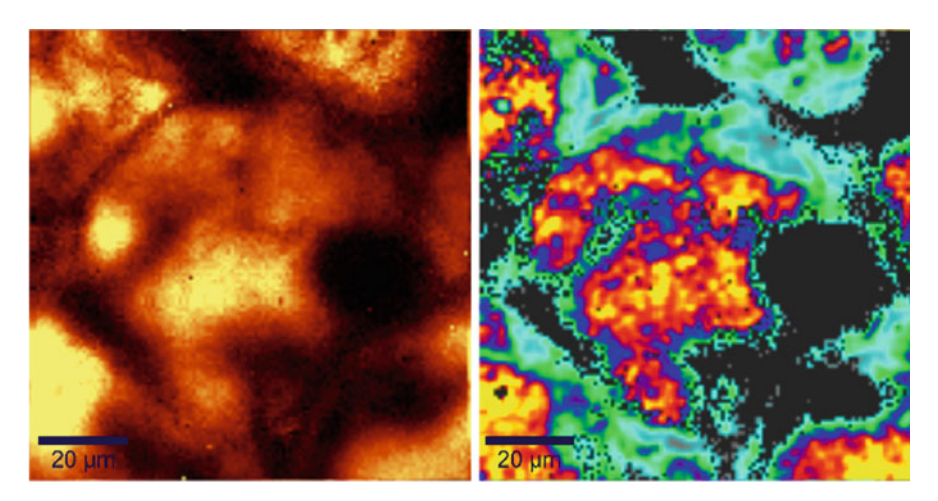


Fig. 6.8 *Left image*: image of quartz from a thin section of the Rhynie chert. *Right image*: dimensionless quartz grain orientation image assembled by calculating the relative intensity variation of the 132 cm⁻¹ quartz peak relative to the 466 cm⁻¹ peak. The 132 cm⁻¹ peak varies in intensity with change in orientation to the excitation beam but the 466 cm⁻¹ does not. Expressing the image as a ratio removes intensity variation due to local quartz abundance and other effects. Sample provided by M. Schweizer, Oxford U., UK

intensity from consideration. The resulting image reveals the orientation of all the grains of a particular phase in a scan field, which allows measurement of grain size as well as providing more detail in the determination of petrographic phase relationships.

The example shown in Fig. 6.8 shows quartz grains in the early Devonian Rhynie chert imaged using the ratio of the 128 cm⁻¹ peak intensity to that of the 465 cm⁻¹ Raman peak. The peak at 128 cm⁻¹ is sensitive to crystalline orientation, allowing the calculation of this image. Many minerals exhibit Raman peaks with orientation-sensitive peak intensity and so this technique can be widely applied.

6.3.3 Phase Composition Imaging

Variations in the crystalline unit cell dimensions of a phase are the basis for measurement of phase composition variation, as well as for latent strain. In the case of phase composition, variations in unit cell parameters arise from substitution of one atom for another. A good example of this phenomenon is the replacement of iron with magnesium (or vice versa, depending on the mechanism at work) in the case of the fayalite (Fe₂SiO₄)/forsterite (Mg₂SiO₄) solid solution (Fig. 6.5d). The Raman spectra of these phases are similar and are dominated by symmetric and antisymmetric SiO₄ tetrahedra vibrational modes, with a continuous shift to higher wave numbers concurrent with replacement of iron with magnesium (or vice versa, if that is the way you would prefer to look at it!). This feature is useful for spot Raman analysis, but is especially informative in the form of calculated Raman images of

mineral composition. This analysis must be performed with a pair of caveats in place, namely

- (1) latent crystal strain can also produce a Raman peak shift and must be considered and
- (2) Raman peak shift is a function of atomic replacement, but it is not necessarily specific as to which atom is substituted.

As an example of the latter, some olivine grains in extraterrestrial samples are known to feature enhanced manganese up to several weight percent (LIME or low-iron manganese-enriched olivine; [23]). An elemental analysis technique such as electron probe analysis is necessary to discern this effect from iron/magnesium variation, but in any event the shift of Raman peaks in olivine can be used to produce images of Fe-content variation. In the case of olivine composition, LIME olivines are uncommon and are only known to occur in unequilibrated, ancient meteoritic materials, so are not usually a consideration. Other minerals such as the pyroxene family, however, feature cation substitution by a range of elements to include iron, calcium, aluminum, magnesium, chromium, and others and so elemental substitution is much more difficult to deconvolute from Raman spectra alone. Some researchers have addressed this effect, however, and produced systematic trends using natural samples [11, 24].

In the case of latent crystal strain, this effect usually shows a pronounced anisotropy relative to the original shock propagation vector and is revealed in Raman images as a deviation in a single direction across several grains. Compositional changes, in contrast, usually vary radially through individual grains to produce mantle-and-rim microstructure or some other texture, which is clearly tied to grain morphology. Latent strain effects in natural samples are typically rare, as most lithologies which show strain effects (i.e., \approx metamorphic rocks which have experienced plastic flow) are exposed to elevated temperatures at the same time and small-scale strain tends to be reduced or eliminated through annealing. Shocked material such as those associated with terrestrial impact events, however, can exhibit latent strain arising from the impact shock itself, and potentially with associated phase changes, which may or may not revert to low-pressure phases upon post-shock relaxation/annealing.

6.4 Examples of "Raman Petrography" Applications

6.4.1 Raman Analysis of Shocked Minerals

In nature, the most pronounced example of shock processing is seen in impactaltered mineralogy. Examples of shock processing are seen in terrestrial impact craters and materials ejected from craters, meteorites which have experienced impact shock prior to falling to Earth, and terrestrial explosion crater materials such as those found in and around nuclear test pits. The shock in more materials is so intense, such as examples from the ureilite meteorites [25] and terrestrial impact craters such as the Popigai impact structure [26], that graphite or other carbon precursors has been transformed to diamond. Other researchers have noted the presence of a high-pressure form of rutile (TiO₂) [27], known as alpha-PbO₂-structured TiO₂ in the Ries crater in Germany [28], the Chesapeake impact structure [29], and in shocked grains associated with the Australasian tektite field [30]. These mineral phases are relatively stable following their shock-induced phase change, as is the SiO₂ polymorph coesite [31–33], and may be signatures of impact processing. Some shock-derived phases, however, are strongly metastable at room temperature and pressure and can revert to an ambient-stable phase upon heating with the excitation laser.

Collecting Raman images of shocked samples is difficult and requires careful characterization of the power output of the instrument. Even then, the signal/noise ratio of data in the resulting images is often quite low out of necessity to prevent damaging the sample with excessive laser power. Even so, images of the petrography of shock-formed phases can be useful, such as that of coesite from the Ries crater breccia shown in Fig. 6.9. In addition shock-processed samples tend to luminesce under the excitation beam, as they typically contain a high defect density. Nonetheless, the spectra in Fig. 6.9 are sufficient to identify coesite and the image is of sufficient quality to characterize its morphology.

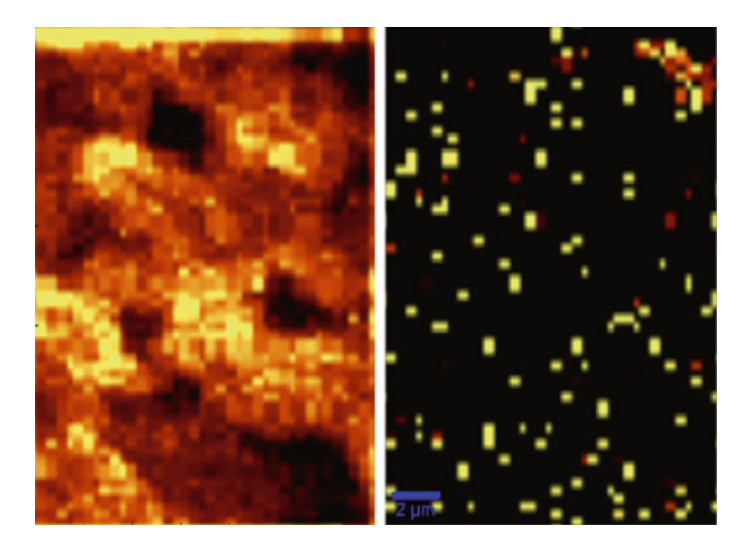


Fig. 6.9 Coesite in impact suevite from the Ries meteorite impact crater, Germany. *Left image*: silicate glass. *Right image*: small bleb of coesite in the upper right-hand corner co-located with "hole" in the glass image on the *left*. Note that the noisy image is caused by the low excitation power used to preserve this metastable phase combined with the inherent luminescence of shocked materials. Even with this limitation, however, both the placement and identity of coesite are identifiable

6.4.2 Contextual Imaging of Carbonaceous Materials

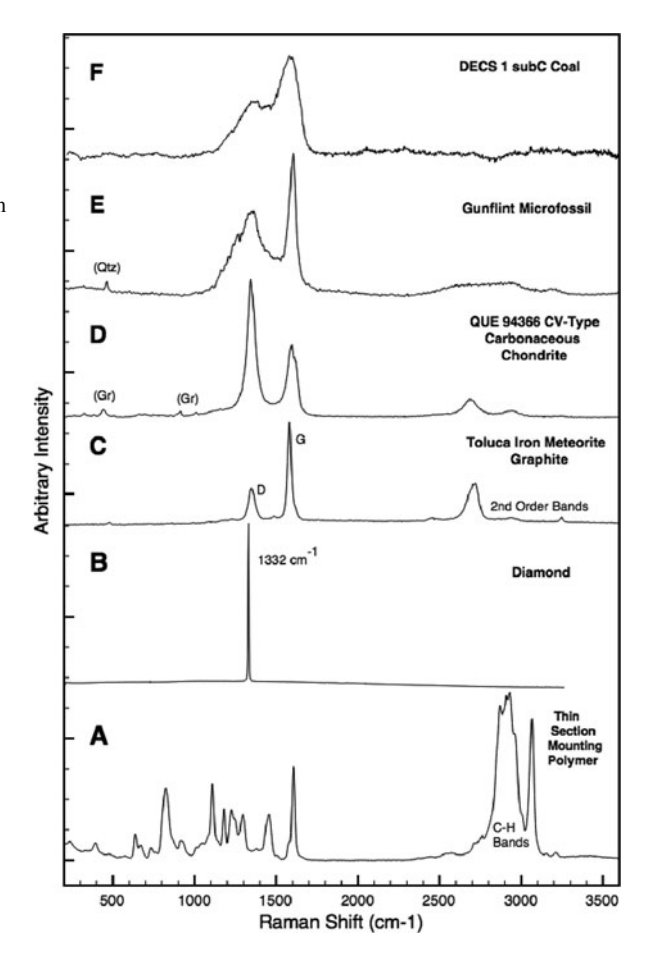
Raman spectroscopy of condensed carbon phases such as diamond, kerogen, polymers, and macromolecular carbon (MMC, i.e., condensed, reduced carbon spanning a wide range of crystalline order) in general is a topic of special interest when working with minerals. For one thing, the spectrum of all of these phases is particularly intense compared to silicates, allowing for the detection of very small amounts of material. Additionally, other analytical methods commonly used in mineralogy and petrography, such as x-ray diffraction (XRD), are not especially sensitive to poorly ordered carbonaceous materials such as kerogen and macromolecular carbon. Raman imaging allows placement of these phases in a mineralogical context, which is a unique analytical capability. Furthermore, Raman spectra of carbonaceous phases are very sensitive to their degree of crystallographic order, which allows conclusions to be drawn on the thermal history and formation conditions of these phases [18, 34, 35].

The Raman spectrum of MMC exhibits three principal features, namely the "disordered" or D band around 1350 cm⁻¹, the "graphitic" or G band around 1580 cm⁻¹ [21, 36, 37], and a series of second-order Raman modes found in the vicinity of 2700 cm⁻¹ [38] (Fig. 6.10).

Figure 6.10(a) shows a typical thin section mounting polymer, with its prominent C-H bands revealing the aliphatic nature of this compound. Note that this spectrum is immediately distinct from the reduced carbon phases here, which allows for definitive discrimination between mounting polymer and native carbon species in a thin section. In Fig. 6.10(b) a single-crystal diamond spectrum is displayed showing the distinct, very intense, and sharp 1332 cm⁻¹ Raman peak whereas in Fig. 6.10(c) graphite from the Toluca iron meteorite as an example of highly crystalline, graphitic carbon is shown. As visible in this figure, the primary Raman modes of high-aromaticity condensed carbon are labeled the D ("disordered") band, the G ("graphitic") band, and the various additive and multiplicative second-order bands. Crystalline graphite can be devoid of a D band, but this example has been polished (see text). Figure 6.10(d) shows carbon from a chondrule in the *QUE 94366* CV-type carbonaceous chondrite. This example has been processed at high temperature but apparently not for as long as the Toluca example. The peaks are narrow, which indicates relatively small distribution of graphitic crystallite sizes, but the D band is intense relative to the G band, indicating an overall disordered structure. Minor grossite (Gr) is present in this spectrum. In Fig. 6.10(e) an example of kerogenous material from the Gunflint microfossil is displayed. The G band is relatively narrow and intense indicating growth of a small size distribution of graphitic domains under thermal metamorphism, and the complex shape of the D band may indicate a wide range of disordered conformations arising from heteroatom enrichment. Finally Fig. 6.10(f) shows the subbituminous (C) coal DECS 1 from the US DOE Coal Sample Bank and Database, an example of a poorly ordered coal. Broad D and G bands indicate a poorly ordered structure overall.

In some earlier literature, the G band is referred to as the "ordered" or O band. Tuinstra and Koenig [21] were the first to point out that the mean crystalline domain

Fig. 6.10 Comparison of the Raman spectra of a few carbon phases. (a) A typical thin section mounting polymer. (b) Single-crystal diamond spectrum. (c) Graphite from the Toluca iron meteorite. (d) Carbon from a chondrule in the OUE 94366 CV-type carbonaceous chondrite. (e) Kerogenous material from the Gunflint microfossil. (f) Subbituminous (C) coal DECS 1 from the US DOE Coal Sample Bank and Database



size is proportional to the D/G band intensity ratio, with refinement by Knight and White [39], followed by Matthews et al. [40] that accounts for variation due to laser excitation wavelength. Raman spectra of carbon phases are unusual in two aspects. For one, there is a measurable shift in the D band Raman mode peak position with excitation wavelength [40, 41]. This shift is highly unusual, as Raman modes are essentially energy loss from an incident photon due to crystalline vibrational modes of specific energy and so typically occur at the same Raman shift regardless of excitation wavelength. For the other aspect, the second-order Raman modes commonly seen in condensed carbon are unusual in that most mineral species exhibit first-order modes only.

As a mineralogical phase, condensed carbon covers a range of structures ranging from diamond with its sp³-hybridized molecular orbitals and face-centered cubic structure [20] to graphite, which is composed entirely of sp²-hybridized carbon arranged in a hexagonal lattice. Between these end members (and, arguably, a third end member composed of crystalline aliphatic polymer), condensed carbon spans

an infinitely variable degree of crystalline order, ranging from amorphous soot to poorly ordered kerogens and mildly heated condensed carbon, through a continuum of crystalline ordering up to single-crystal graphite. Much of the naturally occurring carbon found as a mineralogical phase appears somewhere along this continuum. Generally speaking, MMC found in rocks either precipitates from hydrothermal systems [42], precipitates from mantle-derived fluids and in some pegmatites [43, 44] or accumulates from organic matter (many references, e.g., [45]), then undergoes metamorphism along with its parent rock. Steele et al. [43] note an abiogenic MMC formation mechanism from condensation of mantle-derived volatiles in both terrestrial and martian rocks, implying that this is a common process in rocky bodies large enough to support both carbon-containing volatiles at depth and intrusive volcanism. The MMC becomes systematically more crystalline under heat and pressure while losing volatiles (which is why coal seams can contain pockets of methane and/or carbon dioxide), reaching a fully graphitized form above 400°C according to Landis [46] and at eclogite facies (500°C and 20 kbar) according to Beyssac et al. [47]. Extensive graphitization is also noted in carbonaceous materials metamorphosed to granulite [8] and greenschist facies [48]. During metamorphism, trends are seen in both G and D band peak center position (i.e., [49]), G and D band width [50], as well as D/G intensity and area ratios [48]. Wopenka and Pasteris [1993] report trends in the intensity of the first overtone of the D band as well, which they define as the "S" peak [50]. Trends are also seen with respect to the La (i.e., crystallite length in the direction parallel to the graphite basal plane) grain size measurement defined by Tuinstra and Koenig [21] as well, where greater thermal treatment generally leads to larger La grain size. Generally speaking, increasing thermal metamorphism leads to greater crystallization (graphitization), which drives the G band center toward $\approx 1582 \, \mathrm{cm}^{-1}$, G band width toward a instrument-limited low value, the D band toward a value that depends on the excitation wavelength [40], and the D/G intensity and area ratios toward zero. Unfortunately, deconvolution of the D band can produce large fitting errors without resorting to fitting the band to multiple peaks, especially for relatively amorphous materials, thus complicating the use of D band features as a function of carbon metamorphism. By contrast, use of the G band is relatively straightforward as long as the D' band at 1610 cm⁻¹ when that band is prominent. Much of the information to be found in a Raman spectrum of carbon can be expressed with a G band position vs. G band width (FWHM) graph, which reveals a trend of graphitization grade as well as a distinct portion of the graph around 1582 and $\approx 20 \,\mathrm{cm}^{-1}$ FWHM, respectively, that indicates material featuring graphitic domains that are large with respect to the excitation beam.

One form of poorly ordered carbon, "glassy carbon" [51, 52], exhibits little or no long-range crystallographic ordering but, according to the nomenclature committee of the International Union of Pure and Applied Chemistry (IUPAC), is not truly amorphous, as it exhibits consistent short-range ordering and contains few or no dangling bonds [53]. While glassy carbon is best known as a synthetic phase, it is worthy of mention in a mineralogical context because other studies [47] show that any carbonaceous material arising from organic compounds can show resistance to graphitization even at high temperature. The mechanism at work is the

same in both synthetic and naturally occurring phases. Apparently, graphitization is impeded by the presence of a significant atomic percent of heteroatoms such as O, N, and possibly S, leading to a chemically heterogenous, carbonaceous phase which resists metamorphism. This problematic twist means that heteroatom content complicates the analysis of the metamorphic history of MMC. It may be possible to tightly constrain the age and thermal history of a carbonaceous phase if both the crystalline structure and heteroatom content are known, and this topic is ripe for further scientific investigation.

6.4.3 Fluid Inclusions

Fluid inclusions are exactly what they sound like – small pockets of fluid within a mineral grain. They hold special importance in the study of minerals because they represent samples of volatile compounds in the formation of environment and subsequent metamorphism. The study of volatiles in deeply emplaced rocks such as peridotites, for example, provides information about the melting points and physical behavior of rocks in the deeper parts of the Earth's crust or even the mantle (review by Anderson [54]). Fluid inclusions include two general types – primary and secondary inclusions.

Primary inclusions are essentially trapped pockets of fluid within grains that date to the original crystallization of the host phase. They commonly contain multiple phases, including glass, and are concentrated in elements that feature poor solubility in the parent mineral. Basically, primary fluid inclusions are formed as the surrounding grain solidifies and rejects incompatible elements, which concentrate as droplets and are frozen in place. These inclusions tend to have "fluid-like" shapes with droplet-like morphology or possibly reverse crystal morphology that mirrors the crystal shape of the surrounding mineral and tend to occur alone or in small groups removed from the edges of their parent grain (e.g., [55]). Sometimes, primary fluid inclusions in minerals that form at high temperature and pressure will contain vapor bubbles in them caused by shrinkage of the parent mineral during cooling. These vapor bubbles can sometimes contain a relative vacuum due to this shrinkage, as improbably as that may seem.

Secondary fluid inclusions are often found lying in a plane or along a line within a mineral grain. These inclusions form when the parent grain cracks while still at relatively high pressure and/or temperature in the presence of volatiles. The volatiles percolate into the crack and form pockets while the parent grain "heals" itself through grain regrowth. The resulting trains of inclusions include material present after the rock has already crystallized from its parent melt, and their contents provide insight into the metamorphic history of the parent rock. There is extensive literature on the analysis and interpretation of fluid inclusions (e.g., [55, 56]) and for the purposes of this chapter it is sufficient to simply point this out and comment that Raman spectroscopy and confocal Raman imaging is especially well suited to fluid inclusion analysis (see [57] for a review). A visible light Raman excitation beam can probe the contents of fluid inclusions within transparent grains such as olivine,

pyroxenes, and quartz without exposing the inclusion at the thin section surface [58]. This allows for direct measurement of the content of the fluid phase, and virtually eliminates the possibility of contamination if the sample preparation and Raman analysis are done carefully.

Raman analysis of fluid inclusions has been performed on meteorites in one chrondritic setting. To date, two chondrites – the Monahans and Zag ordinary chondrites – have been found to contain halite/sylvite grains with trapped brine inclusions. The parent salt grains are often a brilliant purple color due to irradiation, indicating that these grains are very old [59, 60]. This is a remarkable find, as up to this point no fluid-filled inclusions had been conclusively proven in any type of meteorite. The existence of fluid inclusions in Monahans and Zag showed that liquids could exist at least for a short time on smaller asteroidal bodies.

6.4.4 Ancient Terrestrial Carbonaceous Materials

The topic of Raman imaging of ancient carbonaceous materials, either fossiliferous or just purportedly so, is an expansive topic that can warrant its own chapter. Much of the study of ancient carbonaceous materials has fixated on assigning an age to the earliest life on Earth, perhaps to the detriment of studies of the actual environmental conditions present when these formations – and perhaps life itself – came into being. Nonetheless, much research into ancient carbonaceous materials features Raman spectroscopy and Raman mapping or imaging. Some researchers have made the claim that some particular carbonaceous material is biogenic based on Raman spectra [61] while others have claimed otherwise [62] and even demonstrated that this is not tenable due to lack of sufficient differentiability between biogenic and abiogenic carbonaceous materials, especially for ancient materials that have experienced extensive metamorphism [42, 63]. Uncertainties arise in the interpretation of this information both in how it pertains to the genesis of the carbonaceous material and in the petrologic history of its host formation. This uncertainty is magnified with increasing age of the material, as both chemical degradation and thermal metamorphism add ambiguity to both the origins of the carbonaceous material and its host rock. There is no doubt that considerable information can be gleaned on the structure of carbonaceous materials using Raman spectroscopy, and that such information tied with spatial context through Raman imaging gives a tremendous amount of information about the nature of a given carbonaceous material and its microenvironment (Fig. 6.11).

Some work has been done in describing fossil carbonaceous material relative to coal, which is fairly well understood, with the result that Nestler et al. [64] described Permian fossilized tree fern materials as having reached anthracite rank during metamorphism.

6.5 Raman Mineralogy in Field Geology Studies

With the development of small, reasonably sensitive spectrograph/detector combinations, miniature solid-state lasers, and field-ruggedized computers, portable

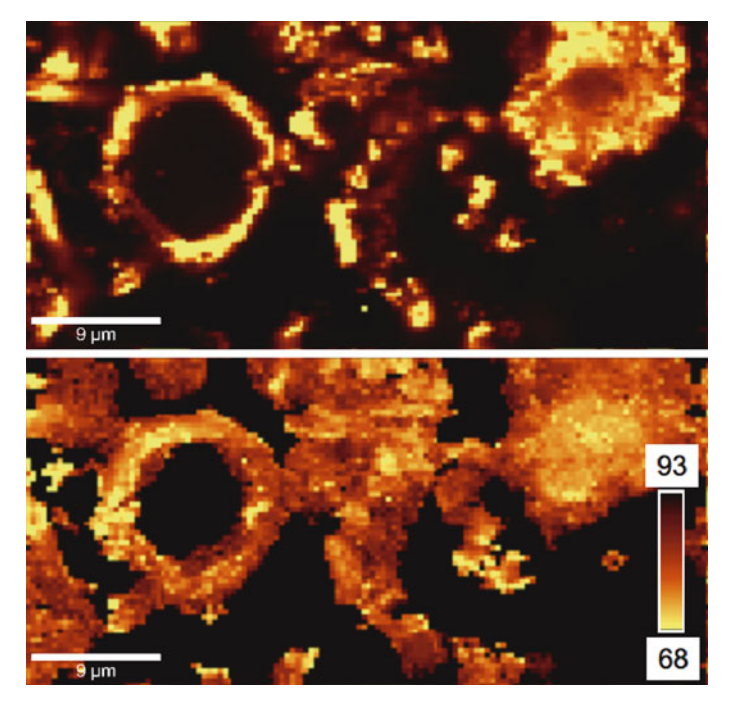


Fig. 6.11 Raman image of kerogenous material from the Precambrian Gunflint chert. The *upper image* is made from the intensity of a Gaussian fit to the G band of carbonaceous material in the chert. The matrix (not shown here) is quartz, as is befitting a chert. The *lower image* is calculated to show the graphitic domain size in the α crystallographic direction, or L_{α} (Matthews et al. [40]), regardless of G band intensity. The scale bar shows L_{α} in angstroms, and the lighter colored areas of the image represent relatively fine-grained carbonaceous material. This effectively reveals sub-micron variation in kerogen structure, which most likely represents metamorphosed remnants of structure from the organic matter precursor. Sample provided by M. Schweizer, Oxford U., UK

Raman spectroscopy devices are now commercially available. Several of these instruments are hand held, allowing the user to analyze the mineralogy and biological status of outcrops and other samples under their native environmental conditions [65]. Most instruments are even specially designed for performing field mineralogy, and many allow the user to match spectra with any database to include mineral spectral libraries. Some of the pioneers in this application brought full-sized Raman instruments designed for laboratory use into remote field locations [66] for both mineralogy and astrobiological studies. Modern field Raman instruments are capable of identifying most mineral species, but current available models typically cannot query C–H and O–H stretch modes at high Raman shift and are limited to interrogating relatively robust mineral species due to their intense laser flux. The high laser power density required for field Raman is a consequence of the un-cooled, relatively insensitive detectors that are required for small, battery powered instruments. Future technology improvements in the areas of battery efficiency and/or

132 M. Fries and A. Steele

detector sensitivity may allow for low power density laser sources that will expand the range of mineral phases identifiable using hand-held Raman instruments. At present, the capability to easily collect Raman spectra in a field environment is a powerful mineralogy tool. In the future, instruments will undoubtedly improve on this capability, perhaps to include Raman imaging capabilities.

6.5.1 Extraterrestrial Exploration

At the time of this writing, no Raman spectrometer has flown on a space exploration mission. While Raman is obviously of very little utility for flyby or orbiter missions (a laser powerful enough to produce a Raman signal observable from orbit would produce an impressive network of glassy sidewalks as a by-product!), small Raman spectrometers would be extraordinarily useful for both manned and unmanned landed missions [67, 68]. In pursuit of this, a miniature Raman instrument is currently under development for the European Space Agency's (ESA) ExoMars rover mission [69]. The goal of this mission is to search for life and/or evidence of past life on the martian surface using a variety of instruments. Such an instrument would have to be sufficiently sensitive to collect spectra at low laser power density values in order to detect organic compounds, and both the instrumental parameters and final instrument manifest for the mission are undecided at present. A Raman instrument called the Mars multibeam Raman spectrometer (MMRS; [70-72]) was also one of the instruments developed for use on NASA's MER rovers (Mars Exploration Rovers, "spirit" and "opportunity") that are actively exploring the martian surface at the time of this writing. Ultimately, however, the MMRS was passed over for other instruments.

A Raman device in general, utilized on a robotic rover/lander or as a hand tool for astronauts, has the advantages of producing very fast identification of mineralogy as well as the potential to directly identify the presence of some organic compounds, or at least point out the presence of a wide variety of carbonaceous phases that may be consistent with evidence of extinct life. As such, Raman spectroscopy is particularly well suited to science priorities identified for exploration of Mars [67]. Rapid mineralogy investigations possible using Raman spectroscopy methods are of particular interest in exploration of the Moon, asteroids, and possibly comets as well. What about using a Raman instrument on Venus, however? Since any venusian mission would be sharply constrained in mission duration (due to the destructively high temperature), sample handling, and other factors, some researchers point to the speed and relative simplicity of Raman analysis as advantages for mineralogy studies on our sister planet. Significant obstacles exist in the form of atmospheric scatter and absorption in both the excitation beam and Raman signal, the difficulty of collecting a signal through hot optics, and other problems associated with operating in the 92 MPa pressure and \approx 460°C conditions on the venusian surface [73]. Raman spectroscopy may be especially well suited to this environment, however, as its rapid acquisition speed should allow the analysis of a large number of samples, and work

has been done on analyzing Venus-specific mineralogy in particular [74]. Work with pulsed Raman systems at a distance through a simulated venusian atmosphere has also produced usable spectra [75]. While this application is intriguing, significant technical challenges must be overcome to make it practical.

A Raman device in general, utilized on a robotic rover/lander or as a hand tool for astronauts, has the advantages of producing very fast identification of mineralogy as well as the potential to directly identify the presence of some organic compounds, or at least point out the presence of a wide variety of carbonaceous phases that may be consistent with evidence of extinct life.

6.6 Conclusion

For future applications it is reasonable to expect that technological advancements will deliver improvements in detector sensitivity, power supply efficiency, computing power, more compact lasers, and who knows what all else as time passes. Future generations of hand-held Raman systems can conceivably include hand-held instruments for astronauts' use on the lunar, martian, or other planetary surfaces. Such an instrument could provide a rapid mineralogical assessment of rocks and outcrops and could serve as a first-pass tool for astrobiological analysis. Rock targets identified as interesting by a quick, hand-held Raman analysis would conceivably be returned to a laboratory for in-depth study, perhaps to include Raman imaging for petrographic and petrologic analysis. Given present capabilities and future possibilities, it is easy to envision a not-so-distant future where field scientists wield small, powerful Raman instruments as a matter of course both on this planet and others.

References

- 1. A. Macdonald, A. Vaughan, P. Wyeth, J. Raman Spectrosc. 36, 185 (2005)
- 2. J. Pasteris, Appl. Spectrosc. **43**, 567–570 (1989)
- A. El Goresy, P. Gillet, S. Mostefaoui, M. Chen, V. Masaitis, Lunar and Planetary Science 33 XXXIII (Houston, Texas, 2002), p. 1031
- 4. M. Zolensky, . co authors, Science **314**, 1735 (2006)
- 5. D. Fischbach, Carbon 3, 342 (1965)
- 6. H. Murty, D. Biederman, E. Heintz, Carbon 7, 667 (1969)
- 7. H. Murty, D. Biederman, E. Heintz, Carbon **7**, 683 (1969)
- 8. B. Wopenka, G. Matrajt, S. Bajt, Lunar and Planetary Science XXXIX **39** (Houston, Texas, 2008), p. 1827
- 9. D. Brownlee, et al., Science 314, 1711 (2006)
- R. Downs, Program and Abstracts of the 19th General Meeting of the International Mineralogical Association in Kobe, Japan O03–13, 2006
- 11. A. Wang, B. Jolliff, L. Haskin, K. Kuebler, K. Viskupic, Am. Mineral. 86, 790 (2001)
- 12. M. Fries, A. Steele, Lunar and Planetary Science XXXVIII 38 (Houston, Texas, 2007), p. 2195
- 13. S. Prawer, K. Nugent, Diamond Relat. Mater. 7, 215 (1998)
- L. Wong, C. Wong, J. Liu, D. Sohn, L. Chan, L. Hsia, H. Zang, Z. Ni, Z. Shen, Jpn. J. Appl. Phys. 44, 7922 (2005)
- H. Ishibashi, M. Arakawa, S. Ohi, J. Yamamoto, A. Miyake, H. Kagi, J. Raman Spectrosc. 39, 1653 (2008)

134 M. Fries and A. Steele

16. A. Wang, Lunar and Planetary Science Conference XXX 15 (Houston, Texas, 1999), p. 1644

- 17. M. Salis, P. Ricci, A. Anedda, J. Raman Spectrosc. 40, 64 (2009)
- 18. O. Beyssac, L. Bollinger, J. Avouac, G. B., Earth Planet. Sci. Lett. 225, 233 (2004)
- G. Cody, C. Alexander, H. Yabuta, A. Kilcoyne, T. Araki, H. Ade, P. Dera, M. Fogel, B. Militzer, B. Mysen, Earth Planet. Sci. Lett. 272, 446 (2008)
- 20. S. Solin, A. Ramdas, Phys. Rev. B 1, 1687 (1970)
- 21. F. Tuinstra, J. Koenig, J. Chem. Phys. 53, 1126 (1970)
- 22. J. Koenig, Appl. Spectrosc. Rev. 4, 233 (1971)
- 23. K. Klöck, W. adn Thomas, D. McKay, H. Palme, Nature 339, 126–128 (1989)
- A. Wang, L. Haskin, B. Jolliff, K. Kuebler, Lunar and Planetary Science Conference XXXI 16 (Houston, Texas, 2000)
- 25. C. Goodrich, Meteoritics **27**, 327 (1992)
- 26. V. Masaitis, M. Mikhailov, T. Selivanovskaya, Meteoritics 7, 39 (1972)
- 27. L. Gerward, J. Olsen, J. Appl. Cryst. 30, 259 (1997)
- A. El Goresy, M. Chen, P. Gillet, L. Dubrovinsky, G. Graup, R. Ahuja, Earth Planet. Sci. Lett. 192, 485 (2001)
- 29. J. Jackson, J. Horton, I. Chou, H. Belkin, Am. Mineral. 91, 604 (2006)
- 30. B. Glass, M. Fries, Meteorit. Planet. Sci. 43, 1487 (2008)
- 31. L. Coes, Science 118, 131 (1953)
- 32. H. Boyer, D. Smith, C. Chopin, B. Lasnier, Phys. Chem. Miner. 12, 45 (1985)
- 33. V. Stähle, R. Altherr, M. Koch, L. Nasdala, Contrib. Mineral. Petrogr. 155, 457 (2007)
- 34. J. Pasteris, B. Wopenka, Can. Mineral. 29, 1 (1991)
- 35. T. Yui, E. Huang, J. Xu, J. Metamorph. Geol. 14, 115 (1996)
- 36. C. Castiglioni, C. Mapelli, F. Negri, G. Zerbi, J. Chem. Phys. 114, 963 (2001)
- 37. S. Reich, C. Thomsen, Philos Trans. R. Soc. Lond. A 362, 2271 (2004)
- 38. R. Nemanich, S. Solin, Phys. Rev. B 20, 392 (1979)
- 39. D. Knight, W. White, J. Mater. Res. 4, 385 (1989)
- 40. M. Matthews, M. Pimenta, G. Dresselhaus, M. Dresselhaus, M. Endo, Phys. Rev. B **59**, R6585 (1999)
- 41. A. Sood, R. Gupta, S. Asher, J. Appl. Phys. **90**, 4494 (2001)
- 42. J. Pasteris, B. Wopenka, Astrobiology 3, 727 (2003)
- 43. A. Steele, M. Fries, H. Amundsen, B. Mysen, M. Fogel, M. Schweizer, N. Boctor, Meteorit. Planet. Sci. 42, 1549 (2007)
- T. Tsunogae, M. Santosh, J. Dubessy, Y. Osanai, M. Owada, T. Hokada, T. Toyoshima, in Geodynamic Evolution of East Antarctica: A key of th East-West Gondwana Connection, vol. 308, ed. by M. Satish Kumar, Y. Motoyoshi, Y. Osanai, Y. Hiroi, K. Shiraishi (Geological Society, London, 2008) p. 317
- 45. W. Francis, Coal: Its Formation and Composition (Edward Arnold (Ed.) Ltd., London, 1954)
- 46. C. Landis, Contrib. Mineral. Petrol. **30**, 34 (1971)
- 47. O. Beyssac, F. Brunet, J.P. Petitet, B. Goffe, J.N. Rouzaud, Eur. J. Mineral. 15, 937–951 (2003)
- 48. M. Tice, B. Bostick, D. Lowe, Geology 32, 37 (2004)
- O. Beyssac, J.N. Rouzaud, B. Goffe, F. Brunet, C. Chopin, Contrib. Mineral. Petrol. 143, 19 (2002)
- 50. B. Wopenka, J. Pasteris, Am. Mineral. **78**, 533 (1993)
- 51. R. Franklin, Proc. R. Soc. Lond. A 209, 196 (1951)
- 52. P. Harris, Philos. Mag. 84(29), 3159 (2004)
- 53. E. Fitzer, K.H. Kochling, H. Boehm, H. Marsh, Pure Appl. Chem. **67**, 473 (1995)
- 54. T. Anderson, E.R. Neumann, Lithos 55, 1 (2001)
- 55. E. Roedder, in *Fluid Inclusions*, ed. by P.E. Ribbe. Reviews in Mineralogy, vol. 12. (Mineralogical Society of America, Chantilly USA, 1984)
- 56. L. Diamond, Lithos 55, 69 (2001)
- 57. E. Burke, Lithos **55**, 139 (2001)
- 58. J. Dubessey, B. Poty, C. Ramboz, Eur. J. Mineral. 1, 517 (1989)

- M. Zolensky, R. Bodnar, D. Bogard, D. Garrison, E. Gibson, L. Nyquist, Y. Reese, C.Y. Shih, H. Wiesmann, Science 285, 1377 (1999)
- 60. A. Rubin, M. Zolensky, R. Bodnar, Meteorit. Planet. Sci. 37, 125 (2002)
- 61. W. Schopf, A. Kudryavtsev, D. Agresti, T. Wdowiak, A. Czaja, Nature 416, 73 (2002)
- M. Brasier, O. Green, A. Jephcoat, A. Kleppe, M. van Kranendonk, J. Lindsay, A. Steele, N. Grassineau, Nature 416, 76 (2002)
- 63. J. Pasteris, B. Wopenka, Nature **420**, 476 (2002)
- 64. K. Nester, D. Dietrich, K. Witke, R. Rößler, G. Marx, J. Mol. Struct. 661-662, 357-362 (2003)
- 65. J. Jehlička, P. Vítek, H. Edwards, M. Heagraves, T. Capoun, Spectrochim. Acta A (2008)
- 66. D. Wynn-Willams, H. Edwards, Icarus **144**, 486 (2000)
- 67. A. Ellery, D. Wynn-Williams, Astrobiology 3, 565 (2003)
- 68. N. Tarcea, T. Frosch, P. Rösch, M. Hilchenbach, T. Stuffler, S. Hofer, H. Thiele, R. Hochenleitner, J. Popp, Space Sci. Rev. 135, 281 (2008)
- 69. I. Escudero-Sanz, B. Ahlers, G. Courreges-Lacoste, Opt. Eng. 47, 033001 (2008)
- A. Wang, L. Haskin, A. Lane, T. Wdowiak, S. Squyres, R. Wilson, L. Hovland, K. Manatt, N. Raouf, C. Smith, J. Geophys. Res. Planets 108, 5.1 (2003)
- 71. A. Wang, K. Kuebler, B. Jolliff, L. Haskin, J. Raman Spectrosc. 35, 504 (2004)
- S. Sharma, A. Wang, L. Haskin, Lunar and Planetary Science Conference XXXVI 36 (Houston, Texas, 2005)
- 73. K. Lodders, B. Fegley Jr., *The Planetary Scientist's Companion* (Oxford University Press, New York, 1998)
- 74. A. Wang, Planetary raman spectroscopic study for understanding venus evolution history. Venus Geochemistry: Progress, Prospects, and New Missions, Abstract No. 2003 (2009)
- S. Clegg, J. Barefield, R. Wiens, C. Quick, S. Sharma, A. Misra, M. Dyar, M. McCanta, L. Elkins-Tanton. Venus geochemical analysis by remote raman-laser induced breakdown spectroscopy (raman-libs). Venus Geochemistry: Progress, Prospects, and New Missions, Abstract No. 2013 (2009)

Chapter 7 Raman Micro-spectral Imaging of Cells and Intracellular Drug Delivery Using Nanocarrier Systems

Christian Matthäus, Tatyana Chernenko, Luis Quintero, Miloš Miljković, Lara Milane, Amit Kale, Mansoor Amiji, Vladimir Torchilin, and Max Diem

Abstract Raman spectroscopy in combination with optical microscopy provides a new non-invasive method to examine and image cellular processes. Based on the spectral parameters of a cell's components it is possible to image cellular organelles, such as the nucleus, chromatin, mitochondria, or lipid bodies, at the resolution of conventional microscopy. Several multivariate or spectral de-mixing algorithms, for example, hierarchical cluster analysis or orthogonal subspace projection, may be used to reconstruct an image of a cell. The non-invasive character of the technique as well as the associated chemical information may offer advantages over other imaging techniques such as fluorescence microscopy. Currently of particular interest are the uptake and intracellular fate of various pharmaceutical nanocarriers, which are widely used for drug delivery purposes, including intracellular drug and gene delivery. We have imaged the uptake and distribution patterns of several carrier systems over time. In order to distinguish the species of interest from their cellular environment spectroscopically, the carrier particles or the drug load itself may be labeled with deuterium. The first part of the chapter will briefly introduce the concept of Raman imaging in combination with multivariate data analysis on some simple cell models, after which the results of the uptake studies are discussed.

7.1 Introduction

Microscopic imaging of cells and their substructures by various optical techniques is an extensively studied subject within cellular biology. Apart from conventional optical microscopy, there are numerous imaging techniques based on light absorption, emission, and scattering effects. Most prominent are fluorescence imaging techniques, for example, epifluorescence and confocal fluorescence microscopy. It is very common to employ lasers as an excitation source – especially in the case

of non-linear techniques such as two-photon microscopy (TPM), second- and third-generation imaging (SHIM, THIM), or fluorescence correlation and fluorescence resonance energy transfer microscopy (FCM, FRET) [1–4].

Raman microscopy is a non-invasive imaging technique that combines vibrational spectroscopy with optical imaging. It has the intrinsic advantage of directly investigating molecular compositions and structures without introducing any external labels or dyes. Fluorescence techniques based on autofluorescence or fluorescent labels introduced either chemically, genetically (such as green fluorescence protein labeling), or through antibodies often suffer from fast photobleaching, and the associated protocols are often rather invasive. The interference of relatively bulky fluorophores with the biological activity of a labeled substance is also a much contented topic. With the development of Raman microscopes, it is now possible to image cells with subcellular resolution based on differences in chemical composition or protein conformation, which are reflected in the spectral features of the various cellular components. It has been demonstrated that Raman microscopy can be utilized to observe the metabolic activity of single living cells – such as NADPH-oxidase activity inside granulocytes, which is important for the initiation of the immune response [5, 6], lipid body accumulation around phagosomes in leukocytes [7], and hemoglobin oxidation/heme aggregation in erythrocytes [8]. The degeneration of proteins during necrosis may be monitored by changes in the appearance of Raman spectra [9]. There also have been efforts to introduce Raman labels, i.e., molecules that have a high Raman scattering cross-section, to detect cellular enzymes and receptors [10].

In terms of imaging cellular components, two main approaches have been pursued. In several cases the distribution of a species can be monitored directly, meaning that the species of interest has characteristic Raman peaks, which are sufficiently different from the spectroscopic features of the general protein/lipid environment of a cell. Reasonable contrast can be achieved by plotting DNA band intensities to image chromatin or the nucleus [11–13]. Sometimes it is possible to observe resonance Raman effects, provided that the system of interest and the employed laser frequency allow for such excitation. For example, resonance Raman effects in cells have been reported for certain cytochromes [14], hemozoin formation in red blood cells infected with malaria [8, 15], and photodynamic agents that are being explored for use in tumor therapy [16, 17]. Resonance Raman signals usually dominate over the spectra from cell proteins. Plotting peak intensities and peak positions can be referred to as univariate imaging.

Raman spectra reflect the biochemical composition within the focal volume, which is determined by the diffraction limit of the applied laser light. As a result, the observed Raman spectra are the superposition of band intensities and shapes, originating from different biochemical components. However, due to the interactions of the components, the observed spectra are never a pure superposition of component spectra. In order to extract the relevant spectroscopic information, several multivariate methods based on similarity comparisons may be applied. A common method employed for spectral imaging is hierarchical cluster analysis (HCA)

[18, 19]. In principle, the algorithm searches for the most similar spectra within a data set by calculating the vector product for each individual spectrum with every other spectrum in the data set. The most similar spectra are then grouped together into separate clusters. More recently, methods based on vertex component analysis (VCA) have been introduced [20, 21]. In contrast to HCA, this algorithm searches for the most dissimilar spectra in a data set and expresses all other spectra as mixtures of the most dissimilar spectra. Both algorithms will be briefly described in the Sect. 7.2. In the following discussion, the concept of Raman imaging in combination with multivariate data analysis will be introduced for several types of common cell lines.

Apart from imaging subcellular features, Raman microscopy may provide an opportunity to follow the uptake of molecules in cultured cells. Controlled by diffusion, endocytosis, and various transport mechanisms, a range of molecules such as polypeptides and carbohydrates may pass the membrane. This uptake may be facilitated by "active transport," where molecules are pumped in and out of a cell in an energy-dependent manner, or by "passive transport," which relies on gradientdriven diffusion. Provided that the uptake is sufficiently large, it may be possible to observe optical signals of the targeted molecules. One major advantage of Raman imaging is the high spectral information content. This allows an interpretation of the chemical integrity (modification) and physical integrity (conformational change) of a substance. Many substances are metabolized inside the cell such that the structure of the product differs from that of the original compound. Often, these chemicals are either activated or deactivated due to metabolic transformation. Raman spectra provide important experimental evidence about the extent and type of metabolic transformations that a compound encounters after cellular internalization. Also of interest are conformational changes of active compounds, such as the conformational change of a peptide at a receptor binding site. Numerous spectroscopic data of solution studies can be found in the literature. Raman microscopy allows the comparison of data measured on isolated structures in solution to data acquired from dynamic experiments conducted inside a living cell.

Increasingly popular in pharmaceutical sciences is the concept of active drug delivery systems that can encapsulate and release a payload within the intracellular environment of target (disease) cells with minimal accumulation in non-target (healthy) cells [22]. Many pharmacologically active compounds have low solubility and thus low bioavailability within diseased tissue. If a compound is fairly soluble in water, it often cannot pass through the cell membrane due to low lipophilicity. Many bioactive compounds do not have amphiphilic properties, meaning that they are both sufficiently hydrophilic as well as lipophilic, which would allow passage through the membrane barrier by diffusion. In order to bypass this problem, small particle-based drug delivery systems have been introduced. Currently there are various types of delivery systems under investigation. However, in principle these systems are nanoscale structures that can encapsulate or protect the bioactive species of interest. In order to distinguish the species of interest from their cellular environment, the carrier particles or the drug load itself may be labeled with deuterium.

7.2 Method

7.2.1 Data Acquisition

Raman spectra were acquired using a CRM200 confocal Raman microscope (WITec GmbH, Ulm, Germany). Excitation (ca. 30 mW each at 488, 514.5, or 632.8 nm) is provided by an air-cooled Ar ion or a HeNe laser (Melles Griot, Model 05-LHP-532 and 928). Exciting laser radiation is coupled into the microscope through a wavelength-specific single-mode optical fiber. The incident laser beam is collimated via an achromatic lens and passes a holographic band-pass filter, before it is focused onto the sample through the microscope objective. A Nikon Fluor $(60\times/1.00 \, \text{NA}, \, \text{WD} = 2.0 \, \text{mm})$ water-immersion objective was used in the studies reported here. Most images presented were recorded at a resolution or step size of 500 nm with 500 ms exposure time using the 488 nm excitation line.

Fluorescence measurements were performed on the same instrument also using the 488 nm excitation. For a comparison of mitochondrial distribution observed through Raman and fluorescence imaging, the cells were first scanned to collect the Raman spectra. Subsequently, Mitotracker^(R) stain was carefully added and the fluorescence emission of the cell was rescanned at significantly lower laser power with a dwell time of $100 \, \text{ms}$ per data point. Data were exported from the WITec software as ASCII files into our off-line data processing software. One of these ASCII files is a composite file consisting of 1024 intensity points for each of n spectra, where n is the product of the x- and y-dimensions of the data set (or the x- and z- or the y- and z- data sets for depth profile scans). The other ASCII file is a one-dimensional vector of the wavenumber shifts for each of the 1024 intensity points (see below).

7.2.2 Introduction to Data Processing Methods

A number of mathematical methods have been introduced to exploit hyperspectral data sets for imaging applications. Very common are cluster analysis techniques, which sort the spectra of a data set into different groups or subsets according to their similarity. There are partial clustering algorithms, such as k-means and fuzzy c-means clustering and hierarchical clustering methods. Especially hierarchical clustering has found widespread applications to image Raman data sets of various biological and medicinal samples such as tissue biopsies [23–25].

Another possible approach to analyze data cubes that consist of a large number of spectra is hyperspectral unmixing [20]. In spectral unmixing the spectra from individual pixels are decomposed into several constituent spectra and fractions that indicate to what extent each constituent spectrum contributes to the spectrum in each pixel. By plotting the fractions of the constituent spectra, also called endmembers, the abundances of each endmember can be imaged. Several decomposition algorithms, for example, orthogonal subspace projection and vertex component analysis,

have been developed [21, 26]. So far, hyperspectral unmixing has mainly been employed to data sets of remote sensing techniques in geology, agriculture, and ecology.

Spectral data hypercubes, produced by raster scanning the sample through the focal point of the Raman microscope, were analyzed using software written in-house in the MATLAB^(R) (TheMathWorks, Inc., Natick, MA) environment. Before analysis, the raw data cubes were processed to remove cosmic ray artifacts and to present each spectrum of the data set as a vector with linear wavenumber increments. Both these aspects will be discussed in Sect. 7.2.2.1 entitled Data Pre-processing, whereas the multivariate analytical methods will be presented in Sect. 7.2.2.2.

7.2.2.1 Data Pre-processing

Raman data collected using CCD detectors are frequently contaminated by sharp spikes generally attributed to cosmic rays impinging on the detector array. Depending on their angle of incidence, they produce large spurious intensities (often larger than 100,000 counts) at a few adjacent detector diodes. We have used a combination of spatial and frequency filtering methods to remove these spikes in the raw data sets. Spatial filtering, i.e., comparing the spectrum of a given pixel to the spectra of eight adjacent pixels, is particularly useful, since it is highly unlikely that the eight surrounding pixels exhibit a spike at the same wavenumber, since the surrounding pixels were acquired at very different points in time. Contaminated spectral intensity points were corrected using the average of the eight surrounding intensities at the same wavenumber.

Most multivariate methods of data analysis require that each spectrum is represented as a linear vector of equidistant data points. However, in a Czerny – Turner monochromator, the dispersion $d\lambda/d\beta$ in the exit plane changes with the cosine of the diffracted angle β and therefore, varies over the dimension of the CCD detector. For 488 nm excitation and a 600/mm grating, for example, the spectral bandpass varies from about 5.5 cm⁻¹/pixel at about 200 cm⁻¹ to about 3.3 cm⁻¹/pixel at 4500 cm⁻¹. Thus, it is necessary to linearize the data before further analysis. The cosmic ray corrected data cubes were linearized as follows. A vector was created with a fixed, preset wavenumber interval, typically 2 or 4 cm⁻¹. The MATLAB interpolation function was then used to interpolate the intensities at the nonequidistant wavenumber points to those at the fixed integer increments. At this point, the data cube was stored as a three-dimensional matrix in MATLAB 8-byte floating point format. However, the length of each spectral vector after linearization is no longer 1024 points, but is given by the difference of the highest and lowest wavenumber point on the array, divided by the wavenumber increment selected $(2 \text{ or } 4 \text{ cm}^{-1})$. The number of points in each vector is henceforth referred to as N.

7.2.2.2 Multivariate Data Analysis

In this section, we discuss the two methods of multivariate data analysis used in this research. The two methods are quite different and can be used to visualize different aspects in a data set. One of these methods, hierarchical cluster analysis

(HCA), is an unsupervised method that clusters data by their similarity. To this end, spectral distances are calculated and spectra are assigned to clusters based on these distances. Vertex component analysis (VCA), on the other hand, is a method that expresses all spectra in a data set as linear combinations of the most dissimilar spectra. Both methods have distinct advantages and disadvantages and may be used to determine different features in a data set.

Hierarchical Cluster Analysis (HCA)

HCA is a powerful method for data segmentation based on local decision criteria. These criteria are based on finding the smallest "distances" between items such as spectra, where the term "distances" may imply Euclidean or Mahalanobis distances, or correlation coefficients (vide infra). HCA is, per se, not an imaging method, but can be used to construct pseudo-color maps from hyperspectral data sets derived from cells or tissue sections. Later in this chapter, high-spatial resolution maps of individual cells will be presented that are based on hierarchical clustering.

HCA starts by computation of the spectral correlation matrix, C, according to

$$C = S^T S (7.1)$$

or

$$C_{ij} = \sum S^{i}(\nu_{N})S^{j}(\nu_{N}), N = 1...n$$
 (7.2)

The C matrix is a $(n \cdot n)$ matrix (n is the number of spectra in the data set) in which the off-diagonal terms C_{ij} are the correlation between spectra i and j, summed over all data points of the spectral vector $S(v_N)$.

The correlation matrix is subsequently searched for the two most similar spectra coefficients, i.e., two spectra i and j for which the correlation coefficient C_{ij} is closest to unity. Hereafter, these two spectra are merged into a new object, and the correlation coefficient of this new object and all other spectra is recalculated. In this process, the dimensionality of the correlation matrix is reduced by one.

The process of merging is repeated, but the items to be merged may be spectra or spectra and merged objects. In the merging process, a membership list is kept that accounts for all individual spectra that are eventually merged into a cluster. We have used Ward's algorithm for the process of merging of spectra and the repeated calculation of the correlation matrix. Once all spectra are merged into a few clusters, color codes are assigned to each cluster. The coordinates from which a spectrum was collected are indicated in this color. In this way, pseudo-color maps are obtained that are based entirely on spectral similarities. Mean cluster spectra may be calculated that represent the chemical composition of all spectra in a cluster.

HCA assigns cluster membership on a yes/no basis: a spectrum either is a member of a cluster or is not. This assignment is based strictly on similarity and requires no fitting to any reference spectra. HCA has been used to produce pseudo-color maps of human cells imaged by confocal Raman microscopy with a spatial resolution of better than 500 nm. HCA was able to distinguish cellular regions that were

associated with the cytoplasm, mitochondria, nucleus, and nucleolus. The spectral differences observed between these subcellular organelles are miniscule; yet HCA was able to group the spectra by small, recurring differences. Subsequent inspection of the mean cluster spectra can often shed light on the spectral differences between the clusters.

The disadvantage of HCA is that the correlation matrix C is of dimension n^2 ; thus, if a 100×100 point map is collected, C is of dimension $10,000 \times 10,000$. Thus, the memory requirements and the time necessary for searching this matrix are enormous. Typical execution times for a 100×100 pixel map are about 3 h, using fast 64-bit processors running under Windows XP64, and 8 Gbyte of RAM.

Vertex Component Analysis (VCA)

VCA uses a completely different approach to reduce the dimensionality of data. Each spectrum is represented as a vector in N-dimensional space, where N, as defined before, is the number of color elements in each vector. This representation may not be too obvious to spectroscopists; thus, it will be elaborated upon in some detail. Imagine that a spectrum is recorded at two frequencies, or channels, v_1 and v_2 only. Thus, each spectrum can be decomposed into intensities along the two channels v_1 and v_2 as shown in Fig. 7.1, panel (a). If two spectra are identical, they will have two identical vectors; two spectra having the same "composition" but different total intensities will have parallel vectors. Figure 7.1, panel (b), shows different spectra in two-channel space; their vectors fall on a line as indicated.

For spectra composed of three channels or frequencies, a quiver of vectors is obtained whose endpoints lie on a triangle, as shown in Fig. 7.1, panel (c). For four-dimensional spectra, the endpoints of the vectors lie in a tetrahedron. In general, the progression from point to line to triangle to tetrahedron, etc., is known in geometry as a simplex. A simplex describes a p-dimensional hull, or polytop, that possesses p+1 corners.

The principle behind VCA is the assumption that the most extreme vectors in the original representation are "pure component spectra," or endmembers. These

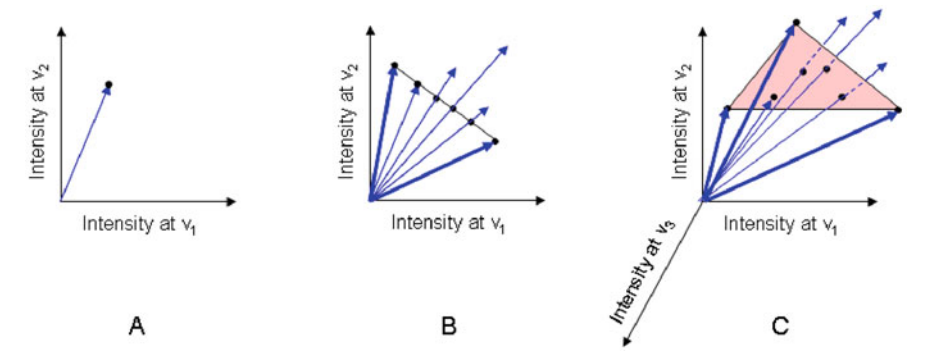


Fig. 7.1 Schematic presentation of a simplex: (a) represents the resulting vector for a spectrum recorded at two frequencies. (b) shows different spectra in two-channel space; all vectors fall on a line. (c) illustrates the vector space for three channels, the vector endpoints lie in a triangle

endmembers are indicated in Fig. 7.1, panels (b) and (c) as the heavy vectors pointing to the ends of the line, or the corners of the triangle, respectively. VCA proceeds from the original dimensionality (in our case $N \approx 1000$, the number of color points in each Raman spectrum) and reduces the dimensionality step-by-step by a process known as "orthogonal subspace projection." In each of these steps, the problem is reduced from a p-simplex to a (p-1)-simplex. The process is terminated when the number of endmembers reaches a pre-determined level. This "spectral unmixing" described so far does not necessarily find the true spectral basis sets. For example, in a map of a human cell VCA will not necessarily produce a pure spectrum of DNA, since no pixel in the sample is due to pure DNA (DNA is always associated with histone proteins). Thus, the best one can do with VCA is the decomposition of the spectra into a few basis spectra, or endmembers, which represent the degree to which spectra can be unmixed. We found that for cells contained in an aqueous environment, one endmember spectrum is always that of pure water (which is truly an endmember). Other endmembers will contain the most significant spectral features of the remainder of the cell. In the examples to be discussed below, the features of water + protein and the features of phospholipids are found prominently in the endmember spectra. VCA images are reconstructed by coding up to three abundance matrices for each pixel point as RGB maps and superimposing these maps.

7.2.3 Experimental

7.2.3.1 Cell Culture Protocols

Human HeLa and MCF-7 cells (cell line CCL-2 and HTB-22, ATCC, Manassas, VA) were grown in 75-cm³ culture flasks (Fisher Scientific, Loughborough, Leicestershire, UK) with 15 mL of Eagle's minimum essentials medium (MEM, ATCC) and 10% fetal bovine serum (ATCC) at 37°C and 5% CO2. Cells were seeded onto and allowed to attach to polished CaF2 substrates (Wilmad LabGlass, Buena, NJ), which were chosen to avoid background scattering that is observed from regular glass windows. The CaF2 substrates were removed from the culture medium after 12–24 h, and the cells were fixed in a 10% phosphate-buffered formalin solution (Sigma-Aldrich, St. Louis, MO) and washed in phosphate-buffered saline. For Raman and fluorescence measurements, the CaF2 windows with the attached and fixed HeLa cells were submerged in buffer solution during the measurement.

Fluorescence staining for mitochondrial distribution was carried out by adding Mitotracker^(R) Green FM (Invitrogen, Carlsbad, CA) to a final concentration of 200 nM. Fluorescence images were collected at 20 min after the stain was added.

7.2.3.2 Nanoparticle Preparation

Liposomes

1,2-Distearoyl- d_{70} -sn-glycero-3-phosphocholine (DSPC- d_{70}) was obtained from Avanti Polar Lipids, Inc. (Alabaster, AL). Plain liposomes were prepared from

DSPC- d_{70} by the lipid film hydration method [27, 28]. The dried lipid film prepared from the chloroform solution of DSPC- d_{70} was hydrated and vortexed with HEPES buffered saline (HBS), pH 7.4, at DSPC- d_{70} concentration of 1.6 mM. The resulting liposomes were sized through doublestacked 200 nm pore size polycarbonate membranes (Nucleopore) using a hand-held extruder (Avanti). The liposome size was monitored by using a Coulter N4 MD submicron particle size analyzer (Coulter Electronics).

TATp-Liposomes

Purified TATp was received from Tufts University Core Facility (Boston, MA). For preparing TATp-liposomes, TATp-PEG₃₄₀₀-PE was added to the lipid film. The hydration and sizing of TATp-liposomes were done as described above. TATp-PEG₃₄₀₀-PE was prepared by reacting TATp with p-nitrophenyl carbonyl-PEG₃₄₀₀-DOPE (pNP-PEG-PE) [29].

PEO-PCL-Particles

PCL/Pluronic^(R) F 108 blend nanoparticles were prepared using solvent displacement in an acetone/water system as previously described [30]. The nanoparticles were loaded with ceramide at 20% w/w. The deuterated ceramide N-palmitoyl- (d_{31}) -D-erythro-sphingosine was provided by Avanti Polar Lipids, Inc. (Alabaster, AL).

7.3 Results

7.3.1 Cell Imaging

A eukaryotic cell consists of 60–70% water and roughly 30% of bioorganic molecules such as proteins, DNA, RNA or nucleic acids, polysaccharides, lipids, and some inorganic salts and other small molecules. Most of the dried cell mass consists of proteins (60%) and nucleic acids (25%) [31]. Figure 7.2 shows the Raman spectra of individual cellular components.

The spectra A and B are examples of a typical α -helical and β -sheet protein, C and D show the spectra of DNA and RNA, and E and F are spectra of common phospholipids and lipids. All spectra have very pronounced intensities in the C–H stretching region from 2800 to 3100 cm⁻¹ and from 750 to 1800 cm⁻¹ often referred to as the fingerprint region. The characteristics of the Raman spectra of cellular components have been well described [31–34] and the main assignments are listed in Table 7.1.

Figure 7.3(a) below is a microscopic picture of a HeLa cell, an epithelial adenocarcinoma cell from a cervical cancer cell line.

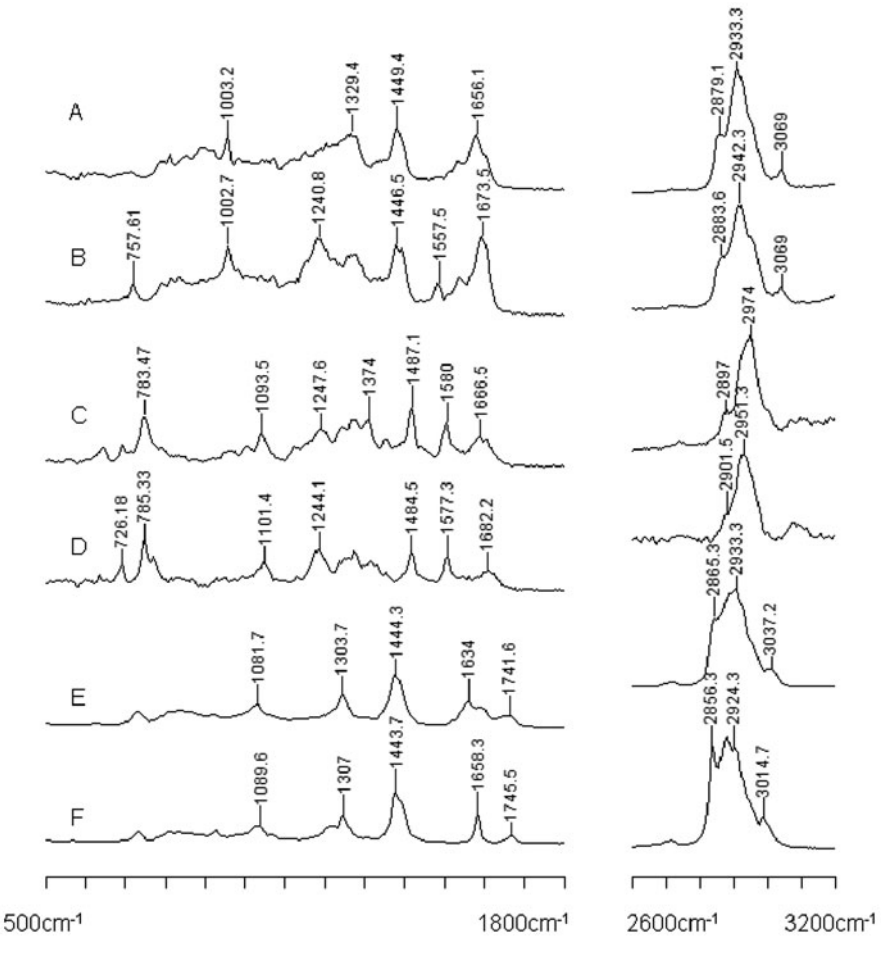


Fig. 7.2 Raman spectra of cellular components: (a) A spectrum of albumin, a typical α -helical protein (b) A spectrum of γ -globulin, a protein rich in β -sheet structure. (c) and (d) Raman spectra of DNA and RNA, respectively. (e) and (f) The spectra of a phospholipid (phosphatidylethanolamine) and a typical lipid (1,2-dioleoyl-3-trimethylammonium-propane (chloride salt)). All spectra were acquired using a 514.5 nm excitation

Figure 7.3(b) is a univariate Raman image of that cell constructed from the scattering intensities of the C–H stretching vibrations. The image reflects different protein densities or water content within the cell. Figure 7.3(c) and (d) shows the results of the data processing algorithms based on hierarchical cluster and vertex component analysis, respectively. Easily discerned is the nucleus as well as different structures within the cytoplasm. Figure 7.3(e) is a fluorescence image of the cell after adding a rhodamine derivative dye (Mitotracker Green^(R)) that accumulates inside mitochondria showing the distribution. Mitochondrial aggregation is the highest in the perinuclear region and adopts tubular structures in the outer regions of the

		<u> </u>
Vibrational mode	Frequency cm ⁻¹	Description
C–H stretching	2800-3020	C–H stretching mode
C=O stretching	1745	C=O stretching, ester group of lipids and phos- pholipids
Amide I	1655	C=O stretching mode, peptide linkage
DNA/RNA	1570-1580	C=C stretching, purine bases
CH ₂ and CH ₃	1425–1475	Anti-symmetric methyl and methylene deforma- tions, peptide side chains, phospholipids, lipids
Amide III	1260–1350	Coupled C-H, N-H deformation modes, peptide backbone
PO ₂ -	1095	Symmetric stretching mode of phosphate esters, DNA, RNA, phospholipids
Phenylalanine	1002	Symmetric stretching (ring breathing) mode of phenyl group
DNA/RNA	785	Pyrimidine ring breathing

Table 7.1 Assignment of predominant bands in the Raman spectra of cellular components

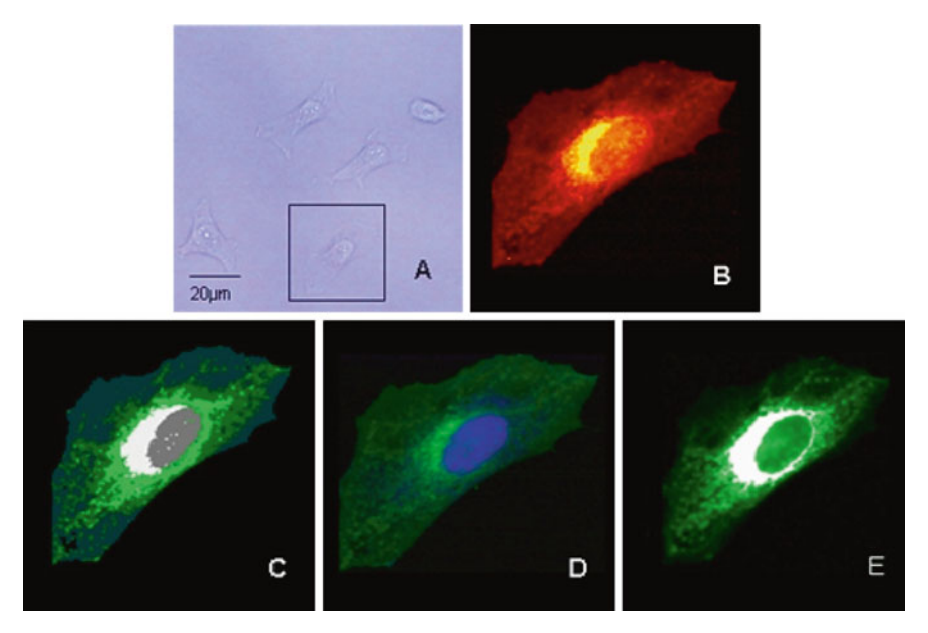


Fig. 7.3 Raman images of a HeLa cell: (a) is a microscopic picture. (b) shows a Raman image based on the C–H stretching intensities. (c) is a false color representation of an HCA calculation. (d) Abundance map generated by a VCA algorithm and (e) shows a fluorescence image after adding a mitochondria-specific rhodamine dye (Mitotracker green^(R)). Both mathematical algorithms reveal the location of the nucleus as well as the distribution of the mitochondria and are consistent with the fluorescence image. The spatial resolution or step size was approximately 300 nm

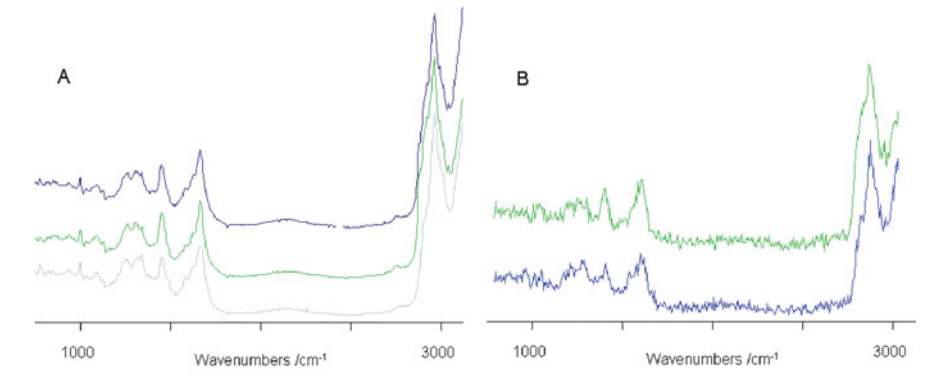


Fig. 7.4 (a) Mean cluster average spectra from the HCA results shown in Fig. 7.3(c). *Gray trace*: nuclear region; *light green*: mitochondria-rich region; *blue*: cytoplasm. (b) Raman endmember spectra from the VCA image in Fig. 7.3(d). *Blue trace*: nuclear spectrum; *light green trace*: mitochondria distribution in the cytoplasm

cytoplasm. It is well known that mitochondria are morphologically heterogeneous within cells [35]. The fluorescence image correlates very well with the outcome of the HCA and VCA, whereas the VCA algorithm seems to result in better spatial resolution. The correlation of mitochondria-specific stains and images generated from HCA and VCA was found to be very reproducible and may be reliable without counterstaining for every experiment [19, 36].

The Raman spectra associated with the pseudo-color images Fig. 7.3(c) and (d) are plotted in Fig. 7.4.

Figure 7.4(a) shows the mean cluster spectra resulting from the HCA and Fig. 7.4(b) shows the endmember spectra of the VCA algorithm. The colors of the individual spectra correspond to the colors in the images. The greatest contrast between the spectra is apparent within the C–H stretching region from 2800 to $3100\,\mathrm{cm^{-1}}$. The C–H band of the mean cluster spectrum from the nucleus is more narrow compared with the bands from the cytoplasm and has a distinct shoulder at around $2880\,\mathrm{cm^{-1}}$, whereas the slope of the spectra from the cytoplasm has more, but less distinct features. There are also many noticeable differences in the finger-print region of the spectra below $1800\,\mathrm{cm^{-1}}$. For HCA, minute differences are very reproducible when results from several cells are compared [19]. The signal-to-noise ratio of the mean cluster spectra is, of course, extremely high given the large number of individual spectra averaged over (ranging from several hundreds to several thousands). The endmember spectra of the VCA have the quality of single-point spectra. However, spectral differences can be easily recognized.

Figures 7.5 and 7.7 show examples of Raman intensity, HCA, and VCA generated images for two other cell types. Figure 7.5(b), (c), and (d) is an image of a MCF-7 cell, an epithelial cell from a breast cancer cell line. Figure 7.7(b), (c), and (d) shows a germ-line cell from a mouse. The morphology of the MCF-7 cells is different from the morphology of the HeLa cells although the nuclei and the cytoplasm are similar in size. The cell here has two large nucleoli, which are also typical

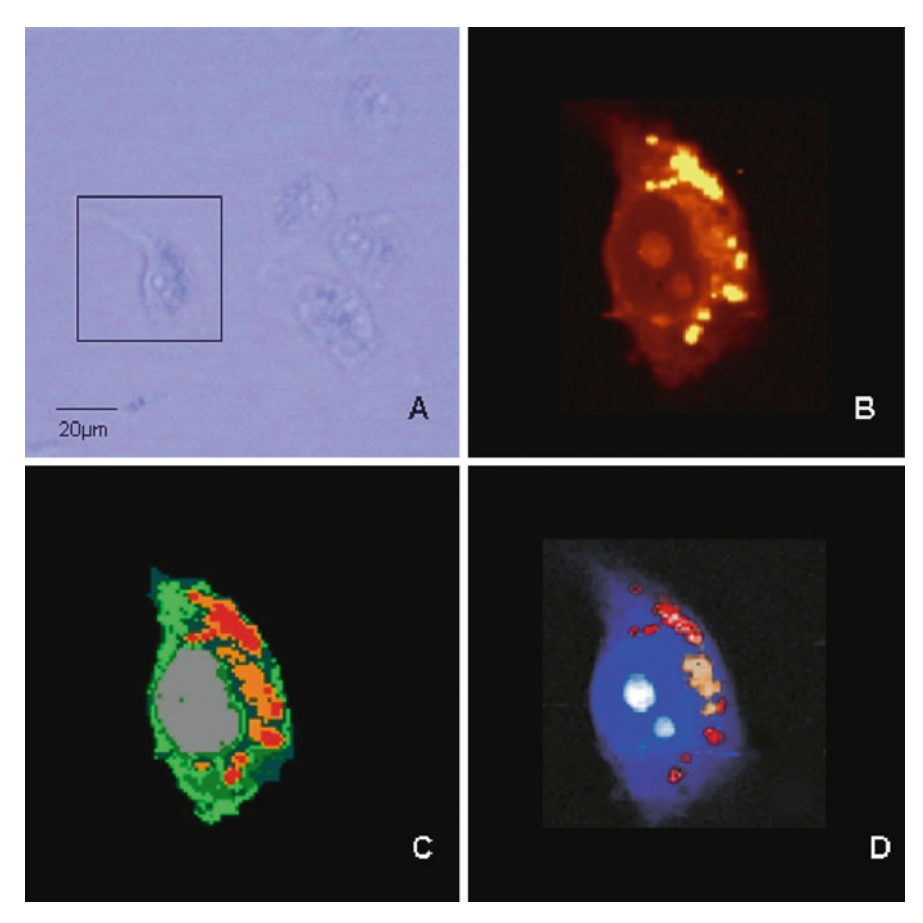


Fig. 7.5 Raman images of an MCF-7 cell: (a) A microscopic picture, (b) Raman map reconstructed from the scattering intensities of the C–H stretching vibrations. (c) and (d) The results of multivariate data analysis algorithms HCA and VCA, respectively, are shown. The HCA algorithm depicts the nucleus and differentiates regions in the cytoplasm. The VCA calculation resulted in discrimination between the cell body and the lipid-rich regions in the cytoplasm

for HeLa cells. However, MCF-7 cells appear to have relatively large vesicle-like inclusions, which can be noticed as dark spots in the optical image (Fig. 7.5a) and very bright areas in the Raman image (Fig. 7.5b).

The HCA algorithm again easily distinguishes the nucleus and several regions in the cytoplasm including the above-mentioned very bright spots of high Raman intensity. The associated Raman spectra are plotted in Fig. 7.6(a). The mean cluster spectra of the nucleus and from the cytoplasm are again very similar to the mean cluster spectra from nucleus and cytoplasm of the HeLa cells. The light green and green regions are again likely to be associated with the distribution of mitochondria. Very different spectral features can be noticed for the spectra from the red and orange regions that correlate very well with the areas that show the vesicle-like

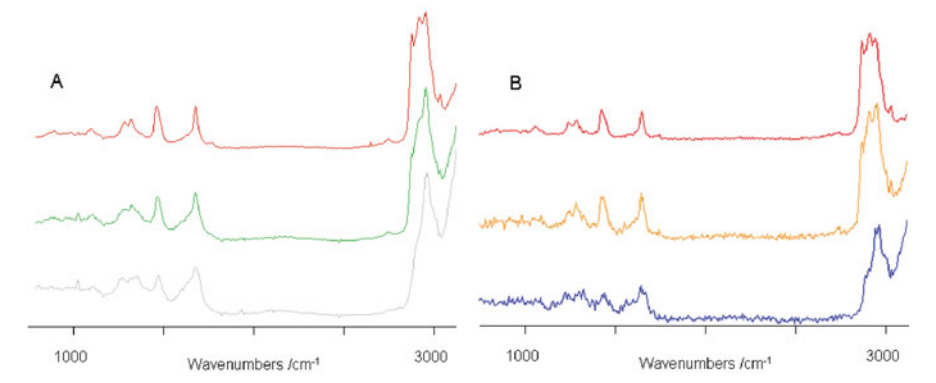


Fig. 7.6 (a) Mean cluster average spectra from the HCA results shown in Fig. 7.5(c). *Gray trace*: nuclear region; *light green*: mitochondria-rich region; *blue*: cytoplasm. (b) Raman endmember spectra from the VCA image in Fig. 7.5(d). *Blue trace*: nuclear spectrum; *orange and red trace*: lipid- or phospholipid-rich region in the cytoplasm

inclusions with high scattering intensities. Comparing these spectra with the lipid and phospholipid spectra from Fig. 7.2 it is obvious that the regions are of high lipid or phospholipid content. It is most likely that these vesicle-like inclusions represent a combination of endosomes, lysosomes, transport vesicles, and metabolic intermediates.

Applying the VCA algorithm to the data set of the MCF-7 cell resulted in three distinct endmembers, which are plotted in Fig. 7.6(b). The blue endmember is again a typical protein spectrum. The red endmember shows typical lipid features and the orange endmember appears as a superposition of spectral characteristics of proteins and lipids. The abundances of the endmembers are shown in Fig. 7.5(d). The images reconstructed from both algorithms are in very good agreement. Interestingly, the algorithm did not discriminate the regions with high mitochondria concentration. This was found to be typical for data sets from this particular cell type and is perhaps due to the high lipid content in these cells. The distinct spectral features of the alkane side chains may obscure the spectral contrast between the regions of high and low mitochondria concentration.

Figure 7.7(a) shows the picture of a mouse oocyte. Oocytes are germ-line cells (egg cells) at a specific developmental stage within the reproductive track. Oocytes undergo several stages of maturation before being ready for fertilization. Their morphology is very different from the morphology of any somatic cell. The chromatin is arranged in a germinal vesicle and the cytoplasm is very proliferative and rich in nourishing proteins. Mouse oocytes are usually 80–100 μm in diameter, which can be a time challenging size for Raman data acquisition with good signal-to-noise ratio at the best possible spatial resolution. The HCA and VCA algorithms again readily find three different kinds of spectra, which are plotted in Fig. 7.8(a) and (b). The associated cluster and abundance maps are displayed in Fig. 7.7(c) and (d) in the accustomed fashion. The overall protein matrix is shown in blue. Spectra with significant lipid or phospholipid contributions are in red and reveal most likely

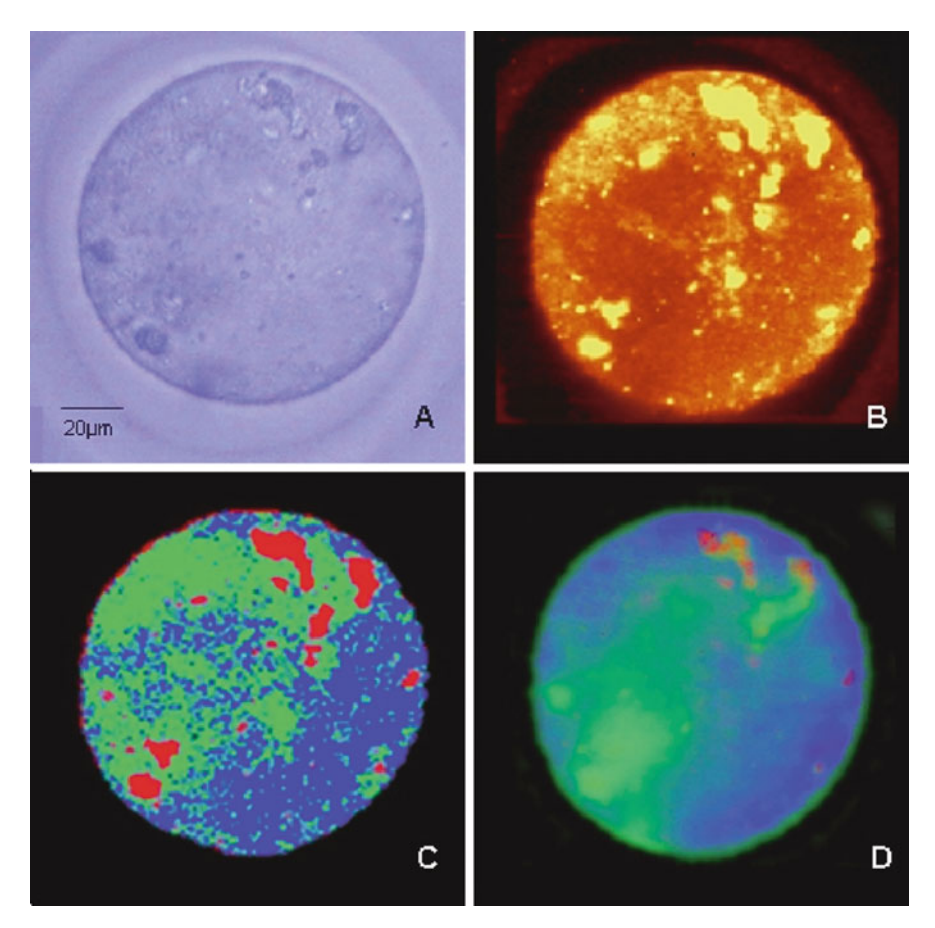


Fig. 7.7 Raman images of a mouse oocyte cell: (a) A microscopic picture, (b) reconstructed image from the scattering intensities of the C–H stretching vibrations. (c) and (d) The results of multivariate data analysis algorithms HCA and VCA, respectively, are shown. The algorithms discriminate between lipid-rich regions shown in *red*, likely to be associated with smooth-surfaced endoplasmic reticulum and different protein compositions in the cytoplasm

complexes of smooth-surfaced endoplasmic reticulum (SER) as commonly found in these cells [37]. The green regions and spectra are presumably again related to the distribution of mitochondria that are very abundant to support nourishing processes. The distribution patterns of the green areas agree very well with distribution patterns of mitochondria found in oocytes [38]. Mitochondrial distribution is known to be related to oocyte health and is an indicator for pre-implantation viability [38].

In general, the imaging results for the three cell types presented here are very satisfying. The images based simply on the Raman intensities show great resolution (Fig. 7.7b) and can certainly rival optical images from light microscopy. Very interesting is the quality of the images generated from the multivariate data analysis algorithms. For the distribution of mitochondria, for example, we were able

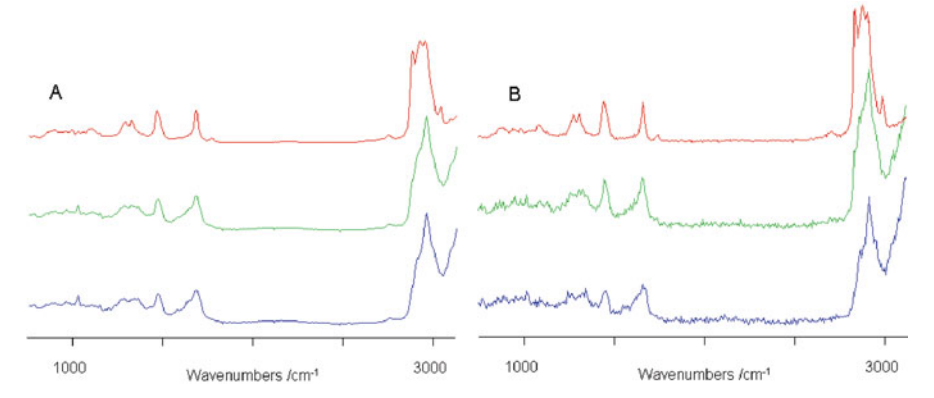


Fig. 7.8 (a) Mean cluster average spectra from the HCA results shown in Fig. 7.7(c). *Blue trace*: cytoplasm; *light green*: cytoplasm; *red*: lipid-rich regions. (b) Raman endmember spectra from the VCA image in Fig. 7.7(d). *Blue trace*: cytoplasm; *green trace*: cytoplasm; *red trace*: lipid- or phospholipid-rich regions

to demonstrate that it is possible to correlate the outcome of these algorithms with organelle-specific stains. Imaging the mitochondrial distribution can provide crucial information in experiments monitoring drug response to compounds that trigger apoptosis. For the cell types shown here, the HCA and VCA algorithms delivered similar insight about the cell morphologies, whereas the VCA apparently resulted in slightly better spatial resolution.

7.3.2 Drug Delivery Systems

Many biologically active compounds that may have the potential to be used as therapeutic agents exhibit low efficiency in in vivo experiments due to low bioavailability at the site of action [39, 40]. Apart from physiological reasons, such as metabolic changes before the compound reaches its target organ or tissue, physical properties (for instance, solubility, hydrophobicity, or the pKa value) may hinder the desired activity of a drug. In many treatments, especially in cancer therapy, the active compound has to pass through the cellular membrane to reach its site of action inside the cells of the diseased/target tissue. Furthermore, once inside the cell a compound may be recognized as foreign and be degraded by lysosomal pathways. To overcome these problems, it would be beneficial to deliver the active compound to the actual site of action, not only to the target tissue but also to the cellular organelles where bioactivity/effect is greatest [22]. Possible intracellular targets are the nucleus for gene therapy [39, 41–43], mitochondria for pro-apoptotic therapy [42, 44], or lysosomes for the therapy of lysosomal storage diseases. Cellular and subcelluar targeting could increase the efficiency of a drug while decreasing the magnitude and occurrence of side effects.

Such considerations have led to the development of so-called drug delivery systems. Extensive research exploring possible chemical structures of drug delivery systems has been performed. Many of these structures are small self-assembling systems that form nanoscale vesicles. These nanoparticles can enclose various compounds and can be designed such that release does not take place before the delivery system has reached its target site. Among the most popular self-assembling nanocarriers are lipid bilayer structures or liposomes, amphiphilic molecules that form micelles and particles composed of biodegradable polymers. To support cell membrane penetration, organelle specificity, or to bypass lysosomal degradation, the surface of these particles may be modified with antibodies, cell penetrating peptides, or the particles may be constructed from molecules that are pH sensitive and thus release their drug load after entering a low pH environment, such as that of a cancer cell.

So far, the most common approach to image nanoparticle uptake and subcellular distribution is to add a small percentage of a fluorophore to the particles [22, 40]. In principle, this method provides important insight and information about cellular uptake and distribution patterns. However, if the fluorescent labels are not covalently bound to the nanoparticle constituents, the fluorophore may diffuse out of the particles and subsequently show a different distribution that does not correlate with the distribution of the nanocarriers. Although fluorescent labels are widely used in biological applications, fluorophores are generally bulky compounds and the extent of fluorophore interference with the innate activity of drug is a topic surrounded by much contention. If the fluorophore is covalently attached to the nanoparticles' component molecules, it may alter the chemical properties and biological behavior of the core material. Alternative techniques for cellular imaging and trafficking would be invaluable in verifying the results of fluorescent imaging and to compensate for the aforementioned pitfalls of common fluorescent labeling. In the following sections we are introducing the results of intracellular uptake and trafficking kinetics of drug delivery systems using the spectral information of Raman image acquisition.

7.3.2.1 Liposomes

As mentioned before, one of the promising delivery systems are liposome-based structures. Liposomes are constructed from self-assembling phospholipid molecules that consist of hydrophobic alkane chains and a hydrophilic head group. The molecules form a membrane-like bilayer where the hydrophobic parts point toward each other. The size of these spherical bilayers can vary from around 50 nm up to a micron. The feasibility of liposomes as drug delivery systems has been repeatedly demonstrated [45–47]. Although important information regarding the uptake kinetics of liposomes by cells as well as their intracellular distribution and degradation is obtained by applying various techniques, such as small-angle X-ray spectroscopy [47], fluorescence microscopy [40], flow cytometry, and spectral bio-imaging [48], many issues related to the fine mechanisms of the liposome/cell interaction remain unresolved.

In order to distinguish the phospholipids of the liposomes from those naturally occurring in intracellular membranes, the hydrogen atoms of the alkyl side chains were exchanged with deuterium. As long as the deuterium is covalently bound to the molecule of interest, its chemical properties remain unaltered. This approach may generally serve as a non-invasive labeling technique to study the uptake and intracellular fate of pharmacologically active compounds. The scattering intensities of C–D vibrations are usually very pronounced and shifted away from the C–H intensities by around $800\,\mathrm{cm}^{-1}$ into a spectral region where neither proteins nor nucleic acids have any spectral features, thus providing high sensitivity because of the absence of spectral overlap.

Figure 7.9 shows a Raman spectrum of liposomes composed of deuterated 1, 2-distearoyl- d_{70} -sn-glycero-3-phosphocholine (DSPC- d_{70}) in an aqueous environment. The spectrum is clearly dominated by the scattering intensities of the C–D vibrations of the aliphatic side chains between 2000 and 2310 cm⁻¹. All other peaks in the region between 650 and 1800 cm⁻¹ are of lower intensity. The C–H stretches of the un-deuterated bonds of the phosphoester residue appear between 2800 and 3020 cm⁻¹. Spectra of pure vesicles in water were acquired as single position spectra at 2 s exposure.

Figure 7.10 shows Raman images of MCF-7 cells incubated with DSPC-*d*₇₀ liposomes for 12 h at a concentration of 2 mg/mL. The pictures in the first column (A1–A3) are Raman images based on the C–H stretching intensities, reflecting different density or water content within the cells. Nucleus and nucleoli can be well distinguished from the cytoplasm. Again, the very bright areas within the cytoplasm correspond to small vesicle structures found to be typical for this particular cell type. The images from the second column (B1–B3) were constructed from the abundances of the three most dissimilar spectra or endmembers found by the VCA algorithm. The endmember spectra are shown in column 3 (C1–C3). The green endmembers

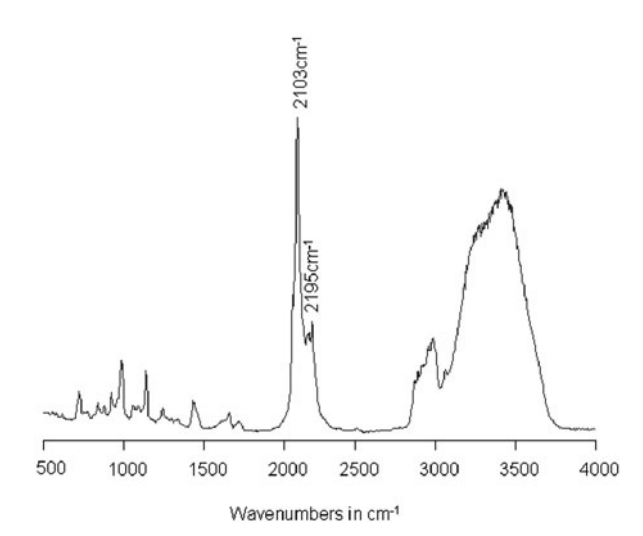


Fig. 7.9 Raman spectrum of DSPC- d_{70} -based liposomes in aqueous environment

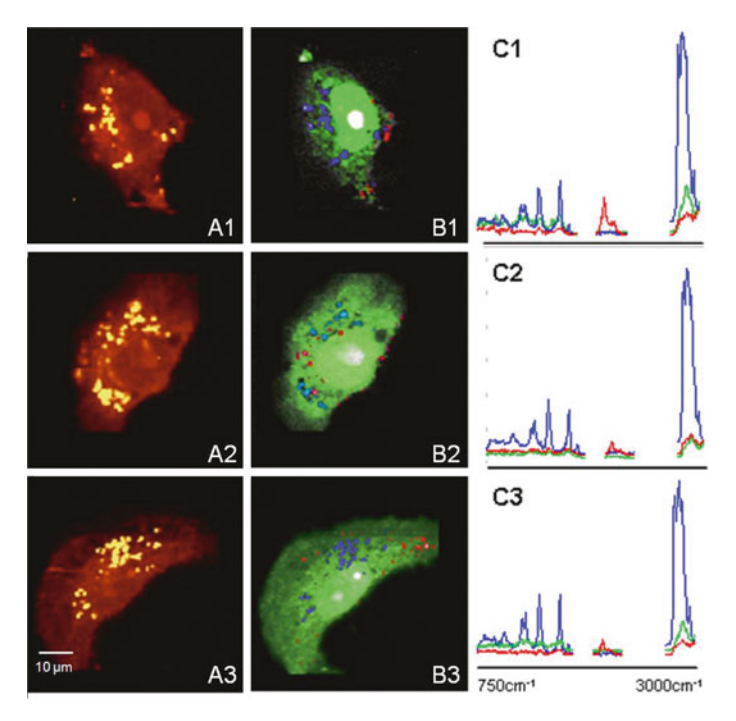


Fig. 7.10 Raman and VCA images of MCF-7 cells incubated with DSPC- d_{70} liposomes for 12 h: (a) images in the first column were reconstructed from the C-H stretching intensities, (b) the images in the second column were generated using the VCA algorithm for the spectral regions of 750–1800, 2000–2300, and $2800-3100\,\mathrm{cm}^{-1}$. (c) The third column shows the corresponding endmember spectra. The abundances plotted in *red* show the distribution of the liposomes, *blue* are lipid-rich regions, *green* is for proteins

show the typical protein features as discussed in the previous section. By plotting the abundances, the cell bodies are beautifully constructed.

The blue endmembers show very typical features of lipids or phospholipids, which show the distribution of the small vesicles. The red endmembers are very similar to the spectra of the deuterated liposomes and therefore reveal the distribution of the liposomes inside the cells.

It can be clearly seen that after 12 h of incubation time a significant amount of liposomes has entered the cells. It appears that they aggregate as small droplet-like inclusions (probable endosomes), which can be found all over the cell body. The size of these aggregates is about 1–2 µm or smaller. It is known that liposomal nanoparticles enter the cell via macropinocytosis [22, 49], which can be followed by secondary endocytosis and could lead to aggregation on the micrometer scale. However, Rayleigh scattering of very small particles can lead to spots of apparent size larger than the effective one. Thus, some of the observed spots may in reality be smaller than the theoretical spatial resolution. Twelve hours of incubation time was needed in order to reproducibly detect liposomal inclusions in most of

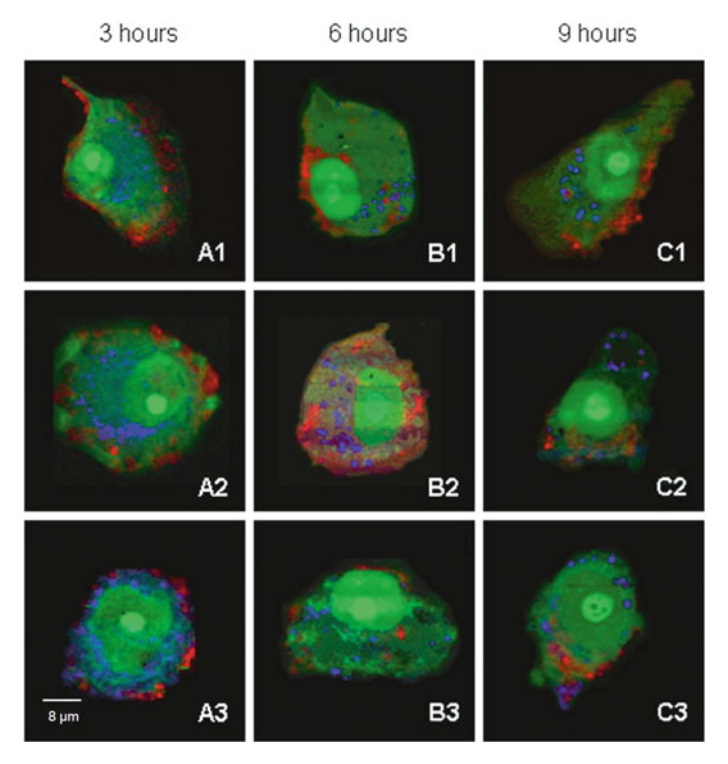


Fig. 7.11 VCA generated images of MCF-7 cells incubated with TATp-modified DSPC- d_{70} liposomes for 3, 6, and 9 h (color coding as in Fig. 7.10). The abundances of the modified liposomes are shown in *red*. The corresponding endmember spectra are shown in Fig. 7.12

the cells. After 6 h, very few cells showed inclusions. It is reasonable to assume that between 6 and 12 h the amount of uptake increases linearly before it reaches a plateau. Interestingly, longer incubation times up to 24 h did not result in significantly more inclusions. However, the longer the incubation time, the more inclusions were found in the perinuclear region rather than around the cell peripheries [50]. For every incubation time approximately 10 cells were imaged.

In order to enhance the uptake, liposomes were modified with a cell-penetrating peptide, derived from a trans-activating transcriptional activator (TATp) peptide from HIV. Carrier systems modified with the TAT peptide are currently considered very promising for drug delivery systems. Figure 7.11 shows the VCA images of MCF-7 cells that were incubated with TATp-modified DSPC- d_{70} liposomes for 3, 6, and 9 h.

As in the previous images, the protein distribution is plotted in green; regions rich in lipids or phospholipids are plotted in blue and the localization of the liposomes are depicted in red. Very obvious is the tremendous enhancement of the uptake efficiency. Not only is the amount of liposomes that penetrate the membranes increased but also the necessary incubation times are significantly reduced. After 3 h large

aggregates can be seen around the edges of the cells. Another 3 h of incubation lead to the penetration of the whole cell body, and after 9 h the liposome concentration appears to be largest in the perinuclear region. Due to the enhancement in uptake, the translocation of the liposomes inside the cell bodies can be clearly followed.

Comparing the endmembers associated with the individual incubation times shown in Fig. 7.12, it is of interest to notice that the endmembers from the cells incubated for 3 h show the distinct features of the protein, lipid, and liposome components, whereas the blue endmember spectra associated with the lipid-rich regions for the 6 and 9 h incubations show significant contributions from the C–D vibrations of the liposome phospholipids. Currently, it is not known what the long-term fate of the phospholipids introduced by the uptake of liposome structures is. Even though active intracellular fusion processes of lipids from nanoparticles are entropically unfavored, model studies have shown that lipid transfer between membrane vesicles is generally possible [51–53]. It is conceivable that over time phospholipids from liposomes become incorporated into intracellular membranes.

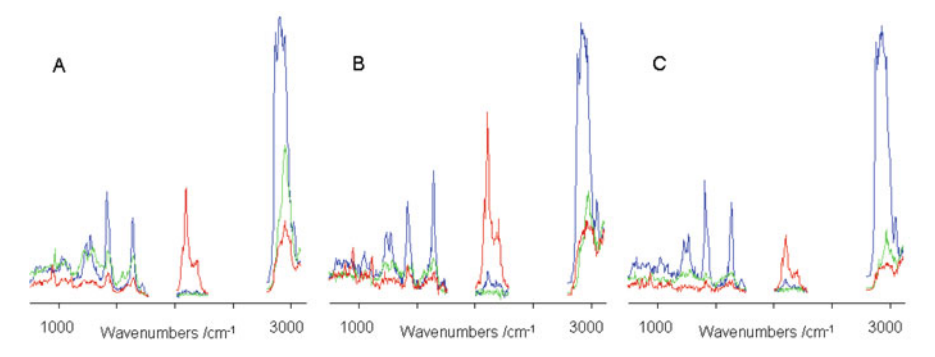


Fig. 7.12 VCA endmember spectra from cells incubated with TATp-modified DSPC- d_{70} liposomes for (a) 3, (b) 6, and (c) 9 h. The corresponding abundances are shown in Fig. 7.11

7.3.2.2 Biodegradable Polymeric Nanocarriers

Under physiological conditions a number of polymers get degraded, usually by hydrolysis, and therefore offer a variety of biomedical applications. Several biodegradable polymers have been tested as platforms for nano-sized carrier systems. Apart from applications as nanocarriers, biodegradable polymers may serve as coatings for cardiovascular stent implants or as aerosol particles for intrapulmonary drug delivery [54–56]. Among the most popular polymers, which have been approved by the American Food and Drug Administration (FDA) for therapeutic devices, are particles based on poly(ethylene glycol) (PEG) also called poly(ethylene oxide), (PEO), poly(D,L-lactic-glycolic acid) (PLGA), and poly (ε -caprolactone) (PCL). Employing solvent displacement methods in an organic solvent/water system, the polymers assemble into nano-sized particles, which can subsequently be loaded with smaller molecules.

The particles used in the studies described here were composed of a PEO-PCL polymer blend. To further test the capability of Raman microscopy to follow the uptake of deuterated species, a set of experiments was performed in which the actual payload of the carrier system was deuterated. As a biologically active species, a compound of the ceramide family was selected. Ceramides are known to act as second messenger signaling molecules involved in differentiation, proliferation, and apoptosis [57]. Endogenous ceramide (synthesized by sphingomyelin hydrolysis or by de novo synthesis) elicits a response to extracellular stimuli such as irradiation and chemotherapeutic agents [57, 58]. Ceramides contribute to the apoptotic pathway through the activation of apoptotic inducers, the creation of protein permeable channels in the mitochondria outer membrane and the clustering of CD95 (death receptor) in cell membranes [57, 59]. The molecule chosen here was *N*-palmitoyl- d_{31} -D-erythro-sphingosine (C16- d_{31} ceramide), in which the fatty-acid side chain was fully deuterated.

Figure 7.13 shows the Raman spectra of the plain PEO-PCL nanoparticles, the C16- d_{31} ceramide, and the particles loaded with 20% w/w ceramide.

All spectra are dominated by the C–H stretching intensities between 2800 and 3100 cm⁻¹. The C–D stretching vibrations of the deuterated alkyl side chain are shifted to 2030 and 2230 cm⁻¹. The spectrum of the loaded particles can be seen as a superposition of the ceramide and the PEO-PCL spectrum.

Figure 7.14 shows the VCA images of HeLa cells treated with C16- d_{31} ceramide-loaded PEO-PCL nanoparticles for 7 and 14 h. Again, the abundances of the three most dissimilar endmembers were used to reconstruct the images. The distribution of the endmembers resembling protein spectra are plotted in blue, the endmembers that contain the C–D intensities from the deuterated alkyl chains of the ceramide are in red. The third endmembers are plotted in green and are likely to correlate with the regions where a high concentration of mitochondria is expected. Similar to the

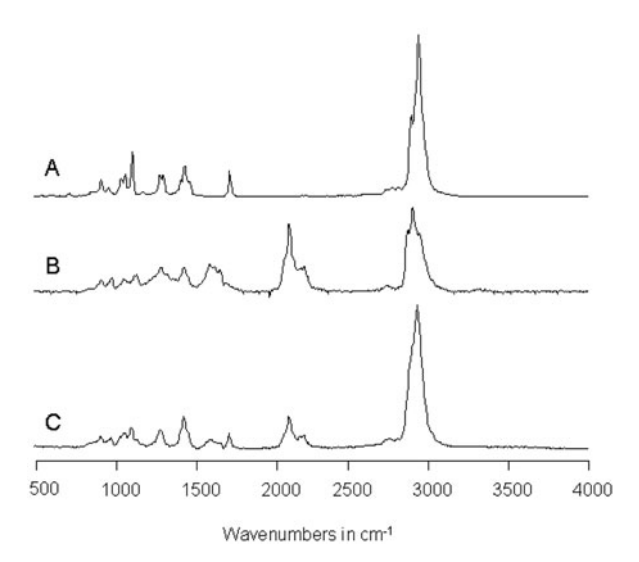


Fig. 7.13 Raman spectra of the plain poly(ethylene oxide)-modified poly(epsilon-caprolactone) (PEO-PCL) nanoparticles (**a**), the C16- d_{31} ceramide (**b**), and the particles loaded with 20% of the ceramide (**c**)

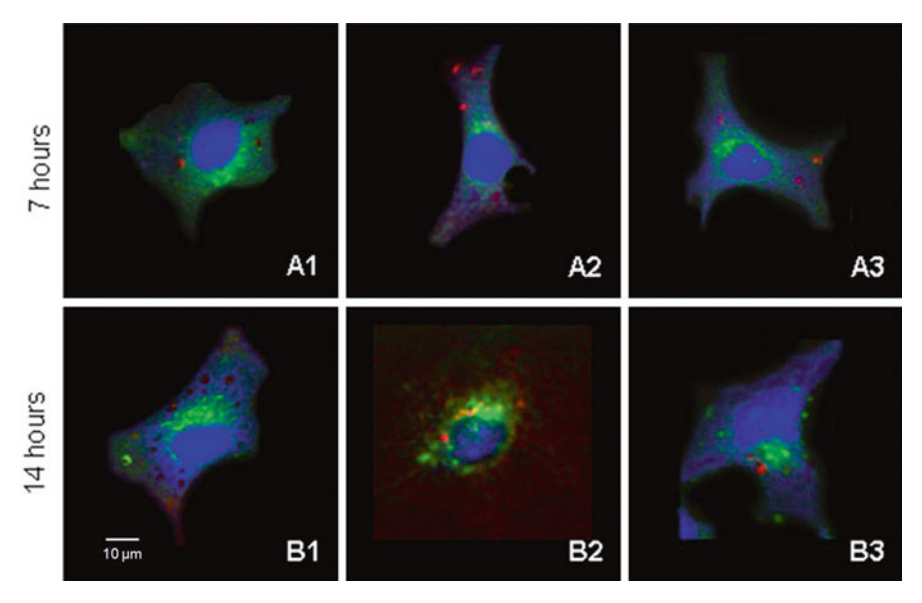


Fig. 7.14 VCA images of HeLa cells treated with C16- d_{31} ceramide-loaded poly(ethylene oxide)-modified poly(epsilon-caprolactone) (PEO-PCL) nanoparticles for 7 and 14 h. The distribution of the deuterated ceramide is shown in *red*

liposomes, the PEO-PCL particles appear as small aggregates, which are present within the cytoplasm after 7 h of incubation. Apart from the bright red spots one can notice areas of a darker red color that seem less dense. Spectra from both regions along with an enhanced image of cell C are shown in Fig. 7.15.

The spectrum from the bright red aggregates still exhibits spectral features associated with the PEO-PCL particles, since the shape of the C–H stretching band is very similar and the peak of the ester linkage of the PCL is obviously present. The spectra from the dark red regions, on the other hand, do not show these features. The ceramide molecules are still associated with the nanoparticles in the bright regions and but have dissociated from the nanocarrier in the dark red regions. The C–D intensities of the dark red regions rather overlay with spectral features from proteins. Thus, either the ceramide diffused out of the particles or the particles/polymers have already been transformed through cellular metabolism. Little is known about the lifetime of these particles inside the cytoplasm. However, one can notice a very fine distribution of the ceramide within the cytoplasm. It does not seem likely that the molecules originate from the aggregates shown in bright red.

Consistent with the liposome experiments, incubation times were selected such that most of the cells had incorporated significant amounts of nanoparticles, which was apparent after 7 h. Incubation for another 7 h did not result in significant additional uptake. Images for 14 h of incubation are shown in the second row in Fig. 7.14. Similar to the results for 7 h, the C–D intensities are associated either with spectral features from the nanoparticles or with spectral features from proteins. It is possible

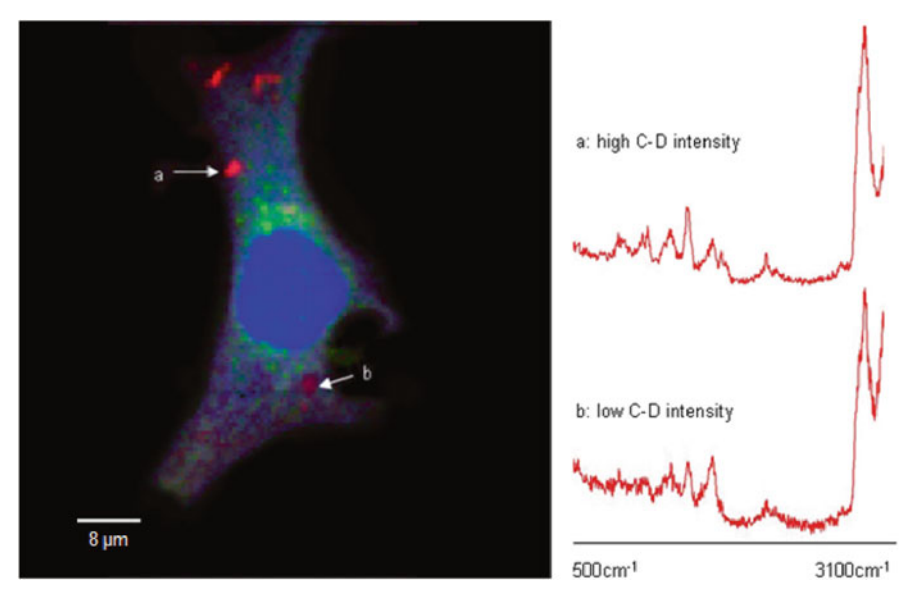


Fig. 7.15 VCA image of a HeLa cell incubated with C16- d_{70} ceramide-loaded poly(ethylene oxide)-modified poly(epsilon-caprolactone) (PEO-PCL) particles and Raman spectra with high and low C–D stretching intensities. The spectra from the *bright red regions* (**a**) still show spectral features of the PEO-PCL particles, whereas the spectra from the *dark red regions* (**b**) have typical protein features indicating a dissociation of the deuterated ceramide from the nanoparticles

that the upper limit of the uptake processes is regulated by how much each individual cell is able to tolerate. It is not possible to say at this point, whether the limitation is set by the amount of nanoparticles, by the amount of ceramide, or by other factors such as particle size or shape. With respect to the amount of uptake, the results from the experiments with the PEO-PCL nanoparticles are similar to the results from the liposome study. In both cases a certain level or limit was reached after approximately 7 h for the PEO-PCL particles and 12 h for the liposomes. Although it is difficult to quantify the amount of particles that are taken up, it seems that fewer of the PEO-PCL particles get into the cell, but they tend to form larger aggregates. The time frame of 7 h was apparently sufficient for the cells to metabolize some of the polymeric nanoparticles, whereas the liposomes were stable and showed only translation to the perinuclear region. The experiments with the TATp-modified liposomes indicated clearly that the phospholipids from the liposomes fuse with intracellular membranes. Perhaps very long incubation times with the non-modified liposomes would show the same result. Thus the fate of the delivery systems based on liposomes and polymeric nanoparticles is completely different. By comparing the incubation times needed to reach a level of saturation, it is possible to conclude that the PEO-PCL particles are taken up faster, by about a factor of 2, than the non-modified liposomes.

7.4 Discussion

The results presented here show the great potential of Raman microscopy for cell imaging applications. In terms of spatial resolution, the images can clearly rival conventional optical microscopy yet with the benefit of adding compositional information. Perhaps the greatest advantage of the technique is that main cellular features or organelles, such as the nucleus, nucleoli, mitochondria, or lipid-rich regions, can be visualized without any external labels. Although fluorescence staining protocols are widespread and well established in biology, they are often laborious and difficult to reproduce. Multiple staining procedures may be needed to image more than one feature. As demonstrated here, Raman microscopy in combination with multivariate data analysis offers an interesting alternative for label-free non-invasive imaging. The employed methods have, by no means, been exhausted. Different spectral regions may be more sensitive to different types of organelles, and different algorithms may extract different spectral information. To correlate the outcome of multivariate data analysis with well-established staining techniques is an ongoing effort in our research.

The results of the HCA and VCA algorithms are highly intriguing. Both algorithms recognize main morphological features in all three cell types presented here. As mentioned before, HCA leads to very good signal-to-noise ratios in the mean cluster spectra. Although HCA is computationally expensive, for very noisy data sets the method may be preferable over the VCA algorithm. VCA, on the other hand, is faster and results in better image contrast because the algorithm does not average over neighboring pixels. Depending on the nature of the data set one or the other method may be favorable.

For the uptake experiments of the nanocarrier systems, the VCA generally gave better results. Since the particle aggregates for the non-modified liposomes and the PCL particles are rather small, only a few pixels have the associated spectral features (in this case the C–D stretching intensities); these were usually missed by the HCA. For VCA to work well, distinct spectral contrast is needed. Since the C–D stretching modes do not overlay with any other Raman bands, sufficiently high sensitivity was achieved.

The outcome of the uptake experiments is very encouraging. The main emphasis of the model studies presented here was to show that Raman microscopy may serve as a new imaging modality to follow the uptake and intracellular fate of biologically interesting compounds. The experiments show that the technique certainly has enough sensitivity. It was possible to image the uptake of liposome-based systems as well as drug-loaded polymeric nanocarriers. For the latter, the dissociation of the active compound was successfully monitored. Especially the concept of deuterium labeling is very promising. In principle, any organic molecule may be labeled with deuterium. Provided that enough of the substance of interest gets incorporated into the cell body, Raman microscopy may offer plenty of possibilities to non-invasively study uptake mechanisms, efficiencies, and metabolic transformations of various compounds on cells grown in in vitro cell cultures.

Acknowledgments We would like to thank Judy Newmark and Carol Warner for their inspirations and help with the oocyte images. Partial support for this research was provided by the NIH (Grant No. CA 090346 to M.D.). Funding from the IGERT nanomedicine education program (to T.C. and L.M.) is gratefully acknowledged.

References

- K. Schenke-Layland, I. Riemann, O. Damour, U. Stock, K. König, Adv. Drug Deliv. Rev. 58(7), 878 (2006)
- 2. K. König, J. Microsc. 200(2), 83 (2000)
- 3. A. García-Sáez, P. Schwille, Appl. Microbiol. Biotechnol. 76(2), 257 (2007)
- 4. T. Kohl, P. Schwille, Adv. Biochem. Eng. Biotechnol. 95, 107 (2005)
- N. Sijtsema, A. Tibbe, I. Segers-Nolten, A. Verhoeven, R. Weening, J. Greve, C. Otto, Biophys. J. 78(5), 2606 (2000)
- 6. C. Otto, N. Sijtsema, J. Greve, Eur. Biophys. J. 27(6), 582 (1998)
- H.J. van Manen, Y. Kraan, D. Roos, C. Otto, Proc. Natl. Acad. Sci. USA 102(29), 10159 (2005)
- 8. B. Wood, L. Hammer, L. Davis, D. McNaughton, J. Biomed. Opt. 10(1), 014005 (2005)
- 9. S. Verrier, I. Notingher, J. Polak, L.L. Hench, Biopolymers 74(1-2), 157 (2004)
- K. Nithipatikom, M.J. McCoy, S. Hawi, K. Nakamoto, F. Adar, W. Campbell, Anal. Biochem. 322, 198 (2003)
- N. Uzunbajakava, A. Lenferink, Y. Kraan, E. Volokhina, G. Vrensen, J. Greve, C. Otto, Biophys. J. 84(6), 3968 (2003)
- 12. N. Uzunbajakava, C. Otto, Opt. Lett. **2073–2075**(28), 21 (2003)
- C. Matthäus, S. Boydston-White, M. Miljković, M. Romeo, M. Diem, Appl. Spectrosc. 60(1), 1 (2006)
- 14. N. Sijtsema, C. Otto, G. Segers-Nolten, A. Verhoeven, J. Greve, Biophys. J. 74(6), 3250 (1998)
- 15. B. Wood, D. McNaughton, Expert Rev. Proteomics 3, 525 (2006)
- A. Feofanov, A. Grinchine, L. Shitova, T. Karmakova, R. Yakubovskaya, M. Egret-Charlier, P. Vigny, Biophys. J. 78(1), 499 (2000)
- S. Arzhantsev, A. Chikishev, N. Koroteev, J. Greeve, C. Otto, N. Sijtsema, J. Raman Spectrosc. 30, 205 (1999)
- 18. C. Krafft, T. Knetschke, R. Funk, R. Salzer, Anal. Chem. 78(13), 4424 (2006)
- 19. C. Matthäus, T. Chernenko, J. Newmark, C. Warner, M. Diem, Biophys. J. 93(2), 668 (2007)
- 20. N. Keshava, Lincoln Lab. J. 14(1), 55 (2003)
- 21. J. Nascimento, J. Bioucas Dias, IEEE Trans. Geosci. Remote Sens. 43(4), 898 (2005)
- 22. V. Torchilin, Annu. Rev. Biomed. Eng. 8, 343 (2006)
- C. Krafft, M. Kirsch, C. Beleites, G. Schackert, R. Salzer, Anal. Bioanal. Chem. 389(4), 1133 (2007)
- B. de Jong, T. Schut, K. Maquelin, T. van der Kwast, C. Bangma, D. Kok, G. Puppels, Anal. Chem. 78(22), 7761 (2006)
- C. Krishna, G. Sockalingum, R. Bhat, L. Venteo, P. Kushtagi, M. Pluot, M. Manfait, Anal. Bioanal. Chem. 387(5), 1649 (2007)
- 26. C. Chang, IEEE Trans. Geosci. Remote Sens. **43**(3), 502 (2005)
- 27. S. Dipali, S. Kulkarni, G. Betageri, J. Pharm. Pharmacol. 48(11), 1112 (1996)
- 28. W. Liang, T. Levchenko, V. Torchilin, J. Microencapsul. 21, 151 (2004)
- V. Torchilin, T. Levchenko, A. Lukyanov, B. Kwah, A. Klibanov, R. Rammohan, G. Samokhin, K. Whiteman, Biochim. Biophys. Acta 1511, 397 (2001)
- 30. D. Shenoy, M. Amiji, Int. J. Pharm. **293**(1–2), 261 (2005)
- 31. D. Naumann, Appl. Spectrosc. Rev. **36**(2–3), 239 (2001)
- 32. T. Spiro, *Biological Applications of Raman Spectroscopy*, vol. 1 (Wiley, New York, Chichester Brisbane, Toronto, Singapore, 1987)

- 33. C. Yu, E. Gestl, K. Eckert, D. Allara, J. Irudayaraj, Cancer Detect. Prev. 30(6), 515 (2006)
- 34. K. Short, S. Carpenter, J. Freyer, J. Mourant, Biophys. J. 88(6), 4274 (2005)
- 35. T. Collins, M. Bootman, J. Exp. Biol. 206(12), 1993 (2003)
- C. Matthäus, T. Chernenko, L. Quintero, L. Milane, A. Kale, M. Amiji, V. Torchilin, M. Diem, *Biophotonics: Photonic Solutions for Better Health Care*, chap. Raman microscopic imaging of cells and applications monitoring the uptake of drug delivery systems (SPIE, Strasbourg, France, 2008).
- 37. J. van Blerkom, Reproduction 128, 269 (2004)
- C. Warner, J. Newmark, M. Comiskey, S. De Fazio, D. O'Malley, M. Rajadhyaksha,
 D. Townsend, S. McKnight, B. Roysam, P. Dwyer, C. DiMarzio, Reprod. Fertil. Dev. 16, 729 (2004)
- 39. V. Torchilin, Eur. J. Pharm. Sci. 11(Supplement 2), S81 (2000)
- 40. V. Torchilin, Adv. Drug Deliv. Rev. **57**(1), 95 (2005)
- 41. C. Plank, W. Zauner, E. Wagner, Adv. Drug Deliv. Rev. 34(1), 21 (1998)
- 42. G. Kaul, M. Amiji, Pharm. Res. 22(6), 951 (2005)
- 43. J. Panyam, V. Labhasetwar, Adv. Drug Deliv. Rev. **55**(3), 329 (2003)
- 44. J. Chawla, M. Amiji, Int. J. Pharm. **249**(1–2), 127 (2002)
- 45. V. Torchilin, Nat. Rev. Drug Discov. 4, 145 (2005)
- L. Serpe, M. Guido, R. Canaparo, E. Muntoni, R. Cavalli, P. Panzanelli, C. Della Pepal, A. Bargoni, A. Mauro, M. Gasco, M. Eandi, G. Zara, J. Nanosci. Nanotechnol. 6(9–10), 3062 (2006)
- 47. N. Rao, V. Gopal, Biosci. Rep. 26(4), 301 (2006)
- 48. U. Huth, R. Schubert, R. Peschka-Süss, J. Control. Release 110(3), 490 (2006)
- 49. J. Wadia, R. Stan, S. Dowdy, Nat. Med. 10(3), 310 (2004)
- 50. C. Matthäus, A. Kale, T. Chernenko, V. Torchilin, M. Diem, Mol. Pharm. 5(2), 287 (2008)
- 51. J. Kristl, B. Volk, P. Ahlin, K. Gombac, M. Sentjurc, Int. J. Pharm. 256, 133 (2003)
- 52. J. Wojewodzka, G. Pazdzior, M. Langner, Chem. Phys. Lipids 135(2), 181 (2005)
- C. Palmerini, C. Cametti, S. Sennato, D. Gaudino, E. Carlini, F. Bordi, G. Arienti, J. Membr. Biol. 211, 185 (2006)
- 54. E. Kang, J. Robinson, K. Park, J. Cheng, J. Control. Release 122(3), 261 (2007)
- 55. A. Belu, C. Mahoney, K. Wormuth, J. Control. Release **126**(2), 111 (2008)
- D. Edwards, J. Hanes, G. Caponetti, J. Hrkach, A. Ben-Jebria, M. Eskew, J. Mintzes,
 D. Deaver, N. Lotan, R. Langer, Science 276(5320), 1868 (1997)
- 57. L. Siskind, J. Bioenerg. Biomembr. **37**(3), 143 (2005)
- 58. A. Struckhoff, R. Bittman, M. Burow, S. Clejan, S. Elliott, T. Hammond, Y. Tang, B. Beckman, J. Pharmacol. Exp. Ther. **309**(2), 523 (2004)
- 59. E. Gulbins, H. Grassmé, Biochim. Biophys. Acta 1585(2-3), 139 (2002)

Chapter 8 Confocal Raman Microscopy in Pharmaceutical Development

Thomas F. Haefele and Kurt Paulus

Abstract There is a wide range of applications of confocal Raman microscopy in pharmaceutical development. It is a powerful tool to probe the distribution of components within a formulation, to characterize homogeneity of pharmaceutical samples, to determine solid state of drug substances and excipients and to characterize contaminations and foreign particulates. The information obtained by confocal Raman microscopy is extremely useful, sometimes even crucial, for drug substance design, for the development of solid and liquid formulations, as a tool for process analytics and for patent infringements and counterfeit analysis. In this chapter, those aspects and applications will be presented, focusing on solid drug formulations. This chapter will also reveal the advantages and demonstrate the synergies of Raman mapping as compared to similar imaging methods such as SEM/EDX, NIR and MIR imaging.

8.1 Introduction

Pharmaceutical development links research and production. It starts with the takeover of a lead compound (the drug) from research and continues until the final drug product is launched on the market. It comprises all steps necessary to deliver a safe, effective and economic drug to the patient. Until the launch of a pharmaceutical product, extensive efforts are required to explore its toxicology, to develop a vehicle for drug delivery, to generate clinical data on safety and efficacy and to invent robust processes to manufacture the drug and the drug product. Everything needs to fulfil regulatory requirements for a successful registration. There is a wide range of applications of chemical imaging (CI) in pharmaceutical development. CI is powerful to probe the distribution of components within a formulation, to characterize homogeneity of pharmaceutical samples, to determine solid state of drug substances and excipients and to characterize contaminations and foreign particulates. The information obtained by chemical imaging, in particular by confocal Raman microscopy, is essential, sometimes even crucial, for drug substance design, for the development of solid and liquid formulations, as a tool to assure process quality and for counterfeit analysis. Complex systems from the submicron up to the macroscale can be investigated. Especially in combination, chemical imaging

methods exhibit their full potential and the information obtained is very complementary. The more methods employed, the more comprehensively a system is described.

Raman spectroscopy is successfully applied for a manifold of tasks in the whole process of drug discovery and drug development. In this chapter we will focus on the applications of confocal Raman microscopy for the technical aspects of drug development. Usages of Raman technology to investigate biomedical tissue or cells, either in vivo or ex vivo, will not be reviewed. For implementations of Raman spectroscopy in this field we would like to refer to other literature [1, 2].

By far the most commonly employed and most compliant dosage forms today are solid oral dosage forms (e.g. tablets). On the other hand, synthetic chemical molecules of limited molecular weight (typically smaller than 1000 g mol⁻¹) depict the main class of active pharmaceutical ingredients (API). Biological APIs, such as proteins, antibodies and enzymes, are contained only in a minor part of marketed products.

In this chapter we will describe the application of confocal Raman microscopy to characterize solid dosage forms of small synthetic APIs, not only due to their importance and predominance but also due to other aspects: when investigated with Raman spectroscopy both solid materials and small synthetic molecules yield more information (sharper and stronger signals) and are simpler to investigate compared to liquids and large biological molecules. We elucidate relevant aspects and applications of chemical imaging. Also we will discuss advantages and demonstrate the synergies of complementary imaging methods when applied in combination. The content of this chapter is relating to industrial applications and much of the data and figures presented are from investigations of IP (intellectual property)-protected specimens. Comprehensive descriptions and details of samples can thus not be given, structural and spectral features not be presented.

8.1.1 Vibrational Spectroscopy in Pharmaceutical Development

8.1.1.1 Analytical Requirements

When a lead compound is handed over from research to development, often only the molecular structure and a limited number of physical parameters are known (besides, of course, biomedical target and mode of action). In technical development, first an efficient and economic synthesis pathway for the drug substance needs to be discovered or optimized and the reactions required need to be upscaled to production scale. The output of such processes should be not only chemically pure substances but also materials possessing optimized physical and physicochemical properties. Particle size, particle shape and most importantly solid state (polymorphism and salt form) need to be optimized according to specific needs. A tailormade particle design is the base for a stable drug product formulation as well as reproducible pharmacology.

In parallel to drug substance development, drug product development takes place. A route of administration and a suitable dosage form need to be defined and tested, formulation processes need to be optimized and scaled up.

All these steps require substantial analytical support. Especially the release of materials for clinical testing requires extensive analysis. The workhorse for routine analytics is liquid chromatography, but the list of methods to fully characterize a material and prove its safety is very long. Almost every producer of analytical equipment has invented some kind of more or less significant applications of his technology for the (once) sound and solvent cash cow – pharmaceutical industry. Thus any available analytical method is somewhere employed in pharmaceutical development, either in-house or externally.

Apart from release of clinical material the most critical analytical challenge is the characterization of the solid state of the active pharmaceutical ingredients. Polymorphism is the ability of a compound to crystallize as more than one distinct crystal species. This means that different polymorphic forms (or polymorphs) have different arrangements or conformations of the molecules in the crystal lattice. Solvates, also known as pseudopolymorphs, are crystal forms having either stoichiometric or nonstoichiometric amounts of a solvent incorporated in the crystal lattice. If the incorporated solvent is water, the solvate is commonly known as a hydrate. If a solid does not possess a distinguishable crystal lattice and the molecular arrangement of molecules is disordered, it is considered amorphous. The amorphous state is structurally similar to the liquid state [3–5].

Polymorphic forms of a drug substance can have different chemical, physical and physicotechnical properties. Differences can occur, e.g. in

- Packing properties (density, refractive index, conductivity, hygroscopicity)
- Thermodynamic properties (melting point, heat capacity, vapor pressure, solubility)
- Kinetic properties (dissolution rate, stability)
- Surface properties (surface free energy, interfacial tension, shape, morphology)
- Mechanical properties (compactibility, tensile strength)

These properties can have a direct effect on the ability to process and manufacture the drug substance and the drug product. Polymorphism further has pharmacological implications due to altered effectiveness and suitability for a particular formulation. Finally, polymorphism also effects regulatory approval and intellectual property issues. Thus, polymorphism of an active pharmaceutical ingredient (API) can affect the quality, safety, efficacy and developability of a drug product and is therefore of fundamental importance in pharmaceutical industry [6, 7].

In addition to polymorphic modifications a drug substance can be crystallized in different salt forms. Any drug substance can be classified as either an acid or a base because the drug substance possesses the ability to react with other, stronger acids or bases. As such, the drug substance also would possess the ability to exist as an ionic species when dissolved in suitable fluid media. If an API is crystallized together with an appropriate counterion, a salt can be generated.

There is a wide range of cationic as well as anionic counterions available. Screening of the best available and crystallizable salt is performed routinely with every novel chemical entity. Similar to polymorphism, salt forms are varying from each other in the degree of solubility and many other physical and chemical factors, as denoted for polymorphs. If the characteristics of the free acid or free base are found to be not acceptable an appropriate salt form might provide improved aqueous solubility, dissolution rate, hygroscopicity, chemical stability, melting point or mechanical properties of a drug substance. There are a number of methods that can be used to characterize polymorphs and salt forms of a drug substance. X-ray powder diffraction (XRPD) is regarded as the gold standard for solid-state analysis. Other methods include thermal analysis (e.g. differential scanning calorimetry (DSC) and thermal gravimetric analysis (TGA)), hot-stage microscopy, solid-state nuclear magnetic resonance spectroscopy (ssNMR) and last but not least vibrational spectroscopy.

8.1.1.2 Infrared Spectroscopy

Vibrational spectroscopy is in any case one of the more significant classes of analytical methods used in pharmaceutical development. Not only solid-state analysis but also a wealth of other applications is feasible. Mid-infrared (IR) spectroscopy is very commonly employed to prove chemical identity and to characterize solid state. Even though IR spectroscopy is simple to perform and cheap to acquire, it normally yields only limited information and additional analytical methods are required as a backup.

Near-infrared (NIR) spectroscopy is gaining much of importance in recent years, mainly driven by the initiative of the International Conference on Harmonization (ICH) for Quality by Design (QbD) [8] and by the US Food and Drug Administration (FDA) Guidance on Process Analytical Technology (PAT) [9]. Scientific process understanding shall support innovation and efficiency in pharmaceutical development, manufacturing and quality assurance. NIR is thus employed throughout processing and manufacturing to monitor quality as well as performance parameters in production-based systems. Not only NIR spectroscopy but also NIR imaging using a microscope-mounted focal plane array (FPA) detector is employed. Both quantitative and qualitative analyses are feasible and NIR can also be deployed in-line of a production line [10].

Terahertz (THz) spectroscopy and terahertz imaging evolved only very recently. They make use of THz frequencies, which lie in between microwaves and near-infrared. Complementary to the other vibrational spectroscopy methods, terahertz spectroscopy also allows the characterization of solid states [11, 12]. The development of terahertz chemical imaging is still in its infancy. Due to the intrinsic limitation of chemical information obtained it is mainly employed to investigate tablet integrity as well as coating uniformity and thickness [13]. It is also reported that THz imaging was successfully employed to investigate the spatial distribution of excipients on tablet surfaces [14].

8.1.1.3 Raman Spectroscopy

The applications of Raman spectroscopy in the pharmaceutical environment are discussed more in detail. Raman spectroscopy is applied routinely to resolve a wide range of tasks. Due to the easy or even needless sample preparation, as well as the ability to measure in aqueous environment, it is a very important technology [2]. Its main application is within solid-state analysis. Apart from XRPD, DSC and TGA, Raman spectroscopy is the most beneficial tool to characterize polymorphic forms. Vibrations originating from the crystal lattice (phonons) and from the carbon backbone yield much stronger signals in Raman compared to IR and NIR spectroscopy. In addition, the low wavenumber region, where most of the relevant vibrational information on the solid state is contained, is easily accessible by Raman. Specially designed spectrometers allow the registration of Raman spectra down to 50 rel. cm⁻¹.

Due to the ability of small-volume sampling, speed of data acquisition, finger-printing capabilities and automated high-throughput analysis of multi-well plates, Raman spectroscopy is routinely used for polymorph and salt screening [15, 16].

Due to these high-throughput screening (HTS) capabilities, Raman spectroscopy is also implemented to support structure elucidation in combinatorial and parallel-synthesis technologies. Because of the intrinsic lack of structural information it is only complement to backup IR. Asymmetrical functional groups with a large dipole moment do not yield strong signals in Raman spectroscopy in contrast to IR [17].

Market approval of a new drug product requires extensive testing of product stability. Ageing and stressing under defined conditions of temperature and humidity for long time periods are inevitable. Owing to the HTS potential Raman spectroscopy is also routinely employed for stability screening of drug products [18–21].

Raman is also employed as PAT technology. Being insensitive to aqueous solvents Raman spectroscopy is an appropriate tool for reaction monitoring. Glass signals do not interfere and thus direct product analysis in vials and process quality control using fibre probes is feasible [22, 23].

Non-invasive in nature and easy and fast to perform, Raman spectroscopy is also a suitable tool for counterfeit identification. Counterfeits generally either do not contain any API or contain a different API. Raman allows distinguishing between genuine and counterfeit product either by identification of the ingredients or even by investigation of (fake) packaging [24].

8.1.2 Imaging in Pharmaceutical Development

8.1.2.1 Light Microscopy

Microscopes of almost any kind are in use within pharmaceutical development. Depending on the probe or radiation deployed, visual investigations can be performed from the macroscale down to a few nanometres. Often not only surfaces

can be visualized but also information can be gained from the inner structure of a specimen. The most commonly employed microscopes are light microscopes. Available in various setups almost only the financial budget limits the resolution and available methods. Simple stereomicroscopes are very prominent and abundant tools to get a rough idea of visual appearance of any kind of sample. More advanced light microscopes for material testing are less often encountered in pharmaceutical laboratories. Both upright stands and inverse systems with optical beam paths for incident and transmitted light are in use. In combination with motorized sample stages and image analysis, automated investigations of large numbers of samples or large sample areas are feasible [25, 26].

Apart from simple bright-field microscopy by far the most important illumination technique is polarized light microscopy. It is usually performed with a polarizing element below the sample to produce plane polarized light and an analyser that is set to give total extinction of the background and thus to detect any birefringence. Polarized light microscopy can distinguish between isotropic and anisotropic materials. Isotropic materials (e.g. gases, liquids, unstressed glasses) demonstrate the same optical properties in all directions. Anisotropic materials, in contrast, have optical properties that vary with the orientation of incident light with the crystallographic axes. They demonstrate a range of refractive indices depending both on the propagation direction of light through the substance and on the vibrational plane coordinates [27, 28].

Polarized light microscopy is very efficient to investigate particle shape, particle size and in combination with image analysis also particle size distribution. But in the latter case, a $\lambda/4$ filter must be used, to change the character of polarization of light from linear to circular and thus to avoid an extinction of particles caused by 90° crossed polarizers. In addition to the ability to detect any birefringence it is very powerful in exploring crystal growth and crystallinity in general. In combination with a hot-stage, temperature-dependent phase transformations can be observed. Not only melting points but also eventual solid-state transformations can be followed [29, 30].

Contrasting methods commonly employed in biological sciences such as phase contrast or differential interference contrast (DIC) to visualize thin low-contrast structures such as cells are required for creams and ointments to increase the contrast of the border of emulsion droplets. Histological approaches to increase contrast (e.g. staining) are uncommon for investigation of pharmaceutical materials by light microscopy.

Fluorescence microscopy in contrast, another typical tool from biological sciences, is a very valuable tool also in pharmaceutical material sciences. Many APIs exhibit autofluorescence due to functional groups. Polymeric and inorganic excipients not uncommonly reveal also an intrinsic fluorescence. Even though the emission wavelengths are very unspecific and difficult to assign, valuable information can be obtained on the homogeneity and uniformity of a mixture [31–33].

An interesting approach to further investigate the structure of a dosage form as well as its dissolution behaviour is the substitution of the API with a model fluorescent dye. In this way, distribution of the API in the formulation and the release of the API from the formulation can be simulated [34].

Time-dependent disintegration of tablets is a further area, in which light microscopy can be applied. The understanding of such complex dissolution reactions is crucial for method development. This has been shown recently by investigating drug release of osmotic depot systems by stereo-light microscopy [35].

8.1.2.2 Electron Microscopy

Electron microscopy is evenly used to probe visual appearance of pharmaceutical samples. Most advantageous is scanning electron microscopy (SEM), which is routinely employed for drug substance analysis. Extremely high resolutions down to a few nanometres and a very flexible field of view make it a very powerful tool. Transmission electron microscopy (TEM) is rarely employed, mainly due to the demanding sample preparation and limited sample contrast. But when highest resolution for investigation of finest nanostructures is required, TEM is the most powerful method.

When a material is probed using a focused electron beam various types of radiation are produced. These secondary radiations can be registered using different detectors to gain characteristic information on the specimen under investigation.

Most commonly secondary electrons (SE) are detected leading to a large depth of field, which yields a characteristic 3D appearance useful for understanding the sample's surface structure. SE imaging is used to obtain surface information for a qualitative description of the sample: surface defects, porosity and the 3D structure can be evaluated.

The intensity of backscattered electrons (BSE) is strongly related to the atomic number of the specimen. Thus, BSE images can provide a certain material contrast.

Other resulting types of signals are, e.g. X-rays or cathode luminescence, which will be partly discussed later on [36].

An SEM setup does not necessarily need to be bulky in space and fill a whole room. Today, also transportable bench-top systems are available, still offering acceptable resolution. This allows on-site inspection of analytes at the production site.

High-resolution SEM usually requires high vacuum and coating of the samples surface with a thin carbon or metal film to prevent electric charging of the sample. As a consequence, liquid samples, biological cells and living tissue will be denatured or disintegrated. Recently, new types of detectors, e.g. inlens detectors, have evolved. Optimally localized in the gun they require only low voltages and not necessarily a sputtering of the sample to gain reasonable results.

SEM is ideally suited to characterize the morphology and the homogeneity of a sample. Particle sizing and determination of particle size distribution are an easy task as well. An experienced operator can deduce a multitude of characteristics of a sample just by obtaining and interpreting meaningful scanning electron micrographs [37–40].

8.1.2.3 Further Microscopic Methods

Atomic force microscopy (AFM) is best employed to resolve submicrometre structures. From an atomic force microscopist's point of view, a tablet needs thus to be considered a very large body. Lateral dimensions of primary particles of solid dosage forms are typically in a size range of 0.01–0.1 mm. Even after tabletting the surface roughness of pharmaceutical solid samples can be of considerable height differences. The lateral scan range (the field of view) and the vertical range of the cantilever might thus be too limited to investigate "macroscopic" specimens like a tablet. If the system is adapted to the analyte or vice versa, decent information on surface topography can be obtained. The application of nano-particles is very unusual up to now but is increasing and thus also the need for AFM will be enhanced [41, 42].

Other approaches have been taken to circumvent the hindrance of oversized roughness height. The combination of an AFM with an ultramicrotome has provided very interesting results. Sequential trimming of a specimen surface with an ultramicrotome followed by characterization by an AFM of each section allows insights into the sample. Reassembling the obtained *z*-stacks and rendering them allows the generation of the specimens 3D structure [43].

AFM is applied not only to characterize topography and surface roughness but also to investigate mechanical properties of surfaces. Recording force – distance curves allows information on adhesion, elasticity or friction [44, 45]. Nanomechanical measurements were successfully applied to quantitatively distinguish amorphous and crystalline domains through local Young's modulus measurements [46].

Further imaging methods popular in conventional materials testing are, e.g. X-ray microtomography (XMT) and acoustical imaging. XMT uses X-rays to create cross-sections of a 3D-object, which can be rendered to recreate a 3D model of a body. X-rays can be used to see inside a sample based upon material density differences [47, 48]. Acoustical imaging employs ultrahigh-frequency ultrasound. The transmitted or reflected echo of the ultrasound reflects changes of the impedance due to varying material density [49]. Both methods are non-destructively and penetrate solid materials allowing the visualization of internal features, including defects such as cracks, delaminations and voids. Due to the limited spatial resolution, applications in pharmaceutical development are scarce.

8.1.3 Chemical Imaging in Pharmaceutical Development

Imagine watching a movie without the ability to hear or see. Seeing only screenplay without sound, or vice versa, communicates limited information of the message the director of the film or actors may want to transport. Understanding the seen or heard more than anything will be a matter of interpretation, only the combination of both senses would allow enjoying and comprehending the full experience. Spectroscopic investigations yield chemical and physical information; microscopy on the other hand delivers spatial information. In analogy to the above, the merger of both,

spectroscopy with microscopy, must be very powerful. In fact, many methods of microspectroscopy have evolved in the last decades. The approach has originated either from the spectroscopy side by spatially focusing and rastering the exciting radiation (e.g. time-of-flight secondary ion mass spectroscopy, TOF-SIMS) or from the microscopy side by extracting physicochemical information from secondary signals (e.g. X-ray quanta from SEM). In contrast to fluorescence microscopy no marker needs to be introduced into the system under investigation. Chemical imaging (CI) probes intrinsic properties of a molecule or atom, often in a non-invasive way. Spatially resolved chemical information delivers a wealth of new information, not accessible otherwise. Furthermore, an image can often reveal more information than any table or numerical result. A colour-coded distribution map of a system can be very straightforward to elucidate the complexity of the system. Just like adding additional senses to a living organism, the combination of several types of detectors in one and the same imaging system strongly enhances the analytical capability (e.g. FTIR and Raman in a light microscope). If such a combination in the same system is not feasible, then the sequential investigation of the same area using different chemical imaging methods can be considered an alternative approach. The more complementary methods are applied to investigate an analyte, the more information is obtained and the more comprehensive the analyte is characterized [50–53].

Chemical imaging is new to pharmaceutical development and not yet routinely employed. Sizeable investments and lack of request from health authorities have impeded the wide proliferation of CI technologies in pharmaceutical industry, even though a wealth of applications exist, which allow new insights into old challenges. The assessment of visual appearance as well as chemical and physical nature is feasible in one step. Particle size, particle size distribution (PSD), morphology and particle shape are delivered by microscopy [54]. Combined spectroscopy techniques as described above resolve spatially the chemical identity of ingredients (structure and/or elements) as well as their solid state (polymorphism, crystallinity, etc.). Supplementary information regarding mechanical properties such as adhesion, elasticity and stiffness can also be made available. Possible foreign particulates can easily be detected and identified. Content uniformity, sample homogeneity and spatial distribution of components are important information, required for all pharmaceutical products. The chemical compatibility of actives and excipients after stressing at increased temperature and humidity can be resolved and ageing effects detected. The information obtained by chemical imaging technologies allows improved and accelerated drug product design and can proof novel drug delivery concepts.

There is some controversy as to when to denominate a method "imaging" or "mapping". We will refer to the term imaging whenever a technology yields an image, no matter if the image was produced by point mapping, line scanning or global illumination [55].

Of the available CI technologies we would like to introduce the following, relevant to pharmaceutical sciences.

Energy-dispersive X-ray spectroscopy (EDX) is generally performed in conjunction with a scanning electron microscope (SEM). When irradiating a sample in the SEM with an electron beam, several types of secondary radiation are

produced. Secondary electrons and backscattered electrons are used for generating SEM images as described above. X-rays are another type of radiation that is generated. When a high-energy electron beam hits an atom in its ground state, an electron in an inner shell might be excited and ejected, creating an electron vacancy in the shell. This vacancy is immediately filled by an electron from a higher energy shell. The resulting potential energy is released as a discrete X-ray quant, characteristic for the potential difference between higher energy to a lower energy electron shell. Thus, the X-rays detected are characteristic of the atomic structure of the element from which they were emitted; this allows the elemental composition of the specimen to be measured qualitatively and quantitatively, if the roughness of the sample surface is low. Theoretically, all elements with at least one p-shell electron (starting from ⁵Boron) are suitable for EDX analysis. Practically, however, reasonable signals are achieved starting from ⁸Oxygen [56]. Modern SEMs allow a spatial resolution down to a few nanometres. For EDX this resolution can hardly be achieved, mostly due to limited acquisition times. Generally, an EDX map consists of a much lower number of pixels than a typical SEM image. EDX is typically employed for characterization of polished metallic surfaces or minerals, but it can be very useful also for the analysis of drug products [57, 58]. Pharmaceutical samples unfortunately rarely exhibit flat planes or polished surfaces, further limiting resolution and making quantitative analysis difficult. Flat surfaces to improve resolution for EDX mapping can be prepared, for example, by microtomy. The vast majority of pharmaceutical actives and excipients is of organic nature, thus contains carbon, hydrogen and oxygen atoms. A discrimination of components is difficult because no intrinsic marker, e.g. a more exotic element, is present. EDX mapping thus only allows substantial spatial discrimination of ingredients if at least one component includes a different element, e.g. sulphur, phosphorous or chlorine. If such an element is present in the API or any of the excipients, the distribution within pharmaceutical systems can easily be characterized. SEM generally requires sputtering of the sample surface with a thin conducting layer of typically carbon, platinum or gold. Improper choice of the sputtering material can limit spectral resolution of EDX due to overlapping peaks of the coating material. Thus, the optimal material to improve surface conductivity is a layer of carbon which does not disturb the emission of the X-ray signals of the analyte.

EDX mapping is a widely underestimated method and very complementary to vibrational microspectroscopy. Due to the widespread availability in pharmaceutical laboratories, it should be applied much more often [59–61].

A method related to EDX is X-ray fluorescence (XRF). Similar to EDX, electrons from the inner orbitals of an atom are expelled due to bombardment with an irradiation, creating an electron vacancy which is refilled by an electron from higher energy orbitals. Again, the energy released is detected as an X-ray quant characteristic for the electron configuration of the element. In XRF a high-energy X-ray beam is employed as primary irradiation in contrast to an electron beam in EDX. The term fluorescence is applied to phenomena in which the absorption of higher energy radiation results in the re-emission of lower energy radiation. Due the incorporation of an X-ray source, the irradiating beam is less focused than an

electron beam in SEM. The spatial resolution in XRF is best around $10\,\mu m$, about 1000 times worse compared to EDX. Another drawback is that elements can only be detected starting from the third period (sodium and heavier). On the other hand, a major advantage is that XRF can be operated under atmospheric pressure and is thus less invasive than high-vacuum EDX. It is therefore better suited to investigate virtu, archeological samples and specimens from forensic science. In addition, XRF is also employed for elemental analysis of metals, glasses and ceramics [62–64].

Time-of-flight secondary ion mass spectroscopy (TOF-SIMS) is another method which can be employed for chemical imaging. It uses a focused, pulsed primary ion beam (typically Cs, Ga, Au or Bi dimers or trimers, SF₅ or C₆₀) to produce secondary molecular ions from the surface monolayer of a sample. The ejected secondary ions are collected and their mass is determined by measuring the exact time at which they reach the detector. Because it is possible to measure the time-of-flight on a scale of nano-seconds, it is possible to produce a very high mass resolution down to 0.001 atomic mass units (amu) at a range of typically 0-10.000 amu. The limit of detection can be as low as part, per billion although TOF-SIMS generally does not allow fully quantitative analysis. The ion beam can be scanned over a sample to produce maps at submicrometre resolution. TOF-SIMS is a highly surfacesensitive method being able to detect molecules within a depth of a few angstrom. The invasive nature of the primary ion beam can be used to generate depth profiles by removal of surface monolayers by sputtering under the ion beam. TOF-SIMS is useful to determine the elemental, isotopic or molecular composition of the surface [65]. TOF-SIMS is best used to probe flat surfaces. Microscopically rough materials such as pharmaceutical products need to be trimmed first. Due to the high vacuum required in the analytical chamber, only solid samples can be investigated. Charging of non- or poorly conducting sample surfaces due to the irradiating ions may inhibit analysis, even though charge compensation is applied. Even though complex and cost intensive, TOF-SIMS provides unique information on composition of molecular components up to several thousands of daltons and is well complementary to other imaging methods. Several successful applications in pharmaceutical sciences have been reported [66–69].

Apart from spatially resolved X-ray spectroscopy to probe elemental configuration and mass spectroscopy to probe molecular composition, vibrational spectroscopy is most commonly used for chemical imaging. Efficient midinfrared spectral imaging (MIRSI) requires a focal plane array (FPA) detector, single nitrogen-cooled MCT (mercury-cadmium-telluride) detectors would require immense time spans to generate a map. An FPA detector is a device at the focal plane of the lens consisting of a rectangular array of light-sensing pixels. In contrast to a charge coupled device (CCD) sensitive to visible light, an FPA is sensitive in the infrared spectrum. MIRSI employs attenuated total reflectance (ATR) objectives made from either a germanium or a diamond crystal. ATR allows direct examination without further preparation. A beam of infrared light is passed through the ATR crystal in such a way that it reflects at least once off the internal surface in contact with the sample. This reflection forms the evanescent wave, which extends into the

sample, typically a few micrometres. The beam is then collected by a detector as it exits the crystal. Transmission mode and diffuse reflection are normally not suitable for MIRSI. The image resolution is actually limited to 64×64 or 128×128 pixels. Also the field of view (FOV) is inflexible and defined by the ATR lens employed. MIRSI allows fast acquisition of chemical images at spatial resolutions of only a few micrometres. The chemical information obtained is generally very specific and significant [10, 70]. A prerequisite for MIRSI is thus to have a flat surface, i.e. trimming of a sample is often required. Physical contact of the ATR crystal might induce sample damage. Furthermore, the bent shape of the ATR crystal can lead to optical aberrations. Only few applications of MIRSI within pharmaceutical development are reported in literature, e.g. [71–76].

More convenient and more commonly employed is near-infrared spectral imaging (NIRSI), also employing a FPA detector, enabling thousands of spectra to be acquired simultaneously. NIRSI is operated either in transmission or in diffuse reflection mode. ATR is not required. In diffuse reflection, the primary radiation is scattered by interaction with the sample and the reflected light is recorded by the detector. The NIR radiation can penetrate considerably into the specimens. NIRSI is much easier to perform than MIRSI but the spectra obtained lack specificity. Both NIRSI and MIRSI are generally good for differentiating solvates and pseudopolymorphs. Because NIRSI primarily probes broadened combination and overtone bands, it lacks specificity to discriminate true polymorphs. Similar to mid-infrared, FOV, pixel resolution and spatial resolution are defined by the lens and the FPA and cannot be changed flexibly. Flat surfaces are advantageous for NIRSI as well, and sample trimming may be required. Except for sample heating NIRSI is fully non-destructive. Various NIRSI applications are reported in the literature, e.g. [77–79]; the recent review of Gendrin et al. provides a comprehensive overview [10].

8.1.4 Confocal Raman Microscopy in Pharmaceutical Development

Theory, device setup, advantages and limitations of confocal Raman microscopy (CRM) are discussed elsewhere in this book. We will thus only give an overview of the applications of CRM in pharmaceutical development reported in literature.

The first application of CRM to map pharmaceuticals appeared in 1999 [80]. It entails the mapping of a binary solid dispersion (API and polymer) prepared through melt extrusion. Although rather old by now, this publication illustrates well, what CRM is best used for. The goals of this study reflect the main applications of CRM in pharma development today: physical state of the drug, stability of the formulation as well as content uniformity and homogeneity. Compared to recent instrumentation, the technology that the authors had at hand seems very basic [40]. A map of $45 \times 25 \,\mu\text{m}^2$ consisting of only 200 measurements is very rough compared to around 10,000-100,000 spectra of today's Raman images. Even though much higher resolution is available, also today the interpretation of chemical images is difficult

and can be ambiguous. The authors of the 1999 publication seemed very keen to conclude that the solid dispersion investigated was homogeneously distributed. Nonetheless, this article is extraordinary due to the fact that a semi-solid dosage form is investigated and not a common solid dosage form, such as a tablet, which is in general easier to characterize.

In the same year, a short conference contribution appeared in which confocal Raman imaging was employed to study the structural ordering and the micron-scaled homogeneity of biopolymers for pharmaceutical applications. Unfortunately, no experimental details are given [81]. A very fascinating result was reported in another publication, where CRM was applied to generate a 3D visualization of a three-component salt [82]. Kador et al. (2001) report on the complementarity of various chemical imaging methods. NIRSI and CRM were employed sequentially to describe an entire formulation at exactly the same area. This chemical image fusion approach could remove ambiguity from the data obtained by the two separate techniques. It was also found that CRM is most suitable to detect the active and inorganic constituents whereas NIRSI is best to characterize carbohydrates [83].

By far the most common application of CRM is the imaging of solid dosage forms to prove content uniformity. Tablets generally are ideal to be investigated by CRM. API and excipients often exhibit major spectral differences. Primary particles used for granulation are typically in a size range from 1 to 100 µm. These dimensions are also found as individual component domains in tablets. As described elsewhere in this volume, the resolution of CRM just perfectly fits these requirements. Domains and boundaries can be visualized at full resolution. If the CRM system allows large area mapping, even entire tablets (up to centimetres) can be characterized regarding content uniformity. Starting from the year 2000 several reports have appeared where the spatial distribution and identification of individual components within a tablet were investigated [84–86]. The complexity of the systems regarding number of components and similarity is varying significantly. Simple twocomponent systems are investigated, but also systems with up to five different tablet ingredients were discriminated [78, 87]. Concentrations of the API below 1% wt/wt are detectable [88]. Also, discrimination of particulate polymorphic impurities in tablets of only 0.05% wt/wt was described. This is very astounding because this reflects a much better limit of detection (LOD) than, e.g. powder XRD (PXRD) [77]. The ability not only to probe content uniformity but also to verify the solid state of the active component makes CRM an extremely powerful tool. Mechanical stress during processing (granulation and tabletting) similar as ageing at elevated temperatures and/or humidity can affect the solid state of the active, which is, of course, highly undesirable. Surface amorphization, e.g. can affect considerably the bioavailability of a dosage form.

Other important dosage forms where CRM can show its full potential are powder inhalation formulations. These formulations normally consist of small API particles below $10\,\mu m$ dispersed with a carrier excipient. Flight and release properties are often improved by particle design and eventually by addition of lubricants. Of course, agglomeration of API particles or demixing of the dispersion is very undesirable and may strongly affect the efficiency of the formulation. CRM can either be

applied to study the original bulk dispersion or also deposits on cascade impactors, which simulate the different regions within the pulmonary tract. Characterization of component distribution and deposition of powder inhalation formulations by CRM has been successfully demonstrated in the literature with various components and inhaler systems [89, 90].

Two out of three compounds in the drug discovery pipelines in pharmaceutical companies have a solubility in water of less than 100 µg/ml and may thus be termed insoluble or practically insoluble. Semi-solid dosage forms for oral or topical administration (application to body surfaces), e.g. solid dispersions or solid microemulsion preconcentrates, may help to overcome this challenge by stabilizing a specific form of an API, which is generally thermodynamically less favourable but more soluble. Semi-solid dosage forms filled into hard gelatine capsules are thus employed in pharmaceutical sciences to improve solubility, leading to an improved bioavailability while decreasing variability and reducing food effect [91]. CRM was successfully applied to probe uniformity and distribution as well as solid state within the formulation. Generally the systems under investigation consist of the API dispersed in one dispersing agent [80, 92]. The preparation method of the dispersions can affect the solid state. Results showed the presence of different polymorphic forms as well as an amorphous form [93]. Recently, the fine structure of solid microemulsion preconcentrates was resolved. It was found that the preconcentrates are two-phase systems, where clusters of crystalline polyethylene glycol form the solid structure and the liquid microemulsion preconcentrate is dispersed in between as a separate phase. The drug remained dissolved in the liquid phase even at increased concentrations. Solid dispersions, in contrast, could stabilize a dissolved state of the API only to a certain concentration. Increasing the amount of API leads to a precipitation of API in a crystalline state [40].

Depot systems for intramuscular application or stents for applications in blood vessels generally consist of a biodegradable polymeric matrix, in which the API is dispersed either in particulate form or molecularly. Upon administration in the body the polymer matrix is slowly hydrated and degraded releasing the active component. Depot systems are optimized for a steady long acting release over weeks and months. Bursts in release are strongly unwanted. Content uniformity, accurate particle size distribution and defined solid states are a prerequisite to achieve this effect. CRM can resolve any of these challenges. Either in original state or after weeks of hydration, coherent results can be generated.

Homogeneity regarding API concentration as well as effect of drug elution on coating morphology was recently investigated with stents. Effects such as appearance of particulate structures, segregation of API to the outer surfaces and drug/polymer demixing could be observed by CRM and other chemical imaging methods [66]. Although developed over a decade ago there are still only a limited number of reports discussing the application of CRM in pharmaceutical development. There might be two reasons for this: first, only the major pharmaceutical companies can afford chemical imaging facilities, and, second, the pharmaceutical industry is very much restricted due to intellectual property reasons and reports thus are scarce. At least also health authorities have now discovered the value of

confocal Raman microscopy and the wealth of information available generated by this technique [94]. A boost of chemical imaging might therefore be expected to happen within pharmaceutical development [95].

8.2 Applications of Confocal Raman Microscopy in Pharmaceutical Development

8.2.1 Practical Considerations

Confocal Raman microscopy is perfectly suited to characterize pharmaceutical specimen. At the same time, pharmaceutical specimens represent ideal samples for maximum performance of a CRM system for several reasons:

Most pharmaceutical samples consist of white powders. Visible light can therefore be applied to probe the specimens without risk of absorption, followed by sample heating and degradation. Visible radiation, e.g. green light, yields good optical resolution, acceptable Raman intensities and normal optics and detectors can be used, fluorescence is rarely a problem.

Synthetic APIs typically weigh less than 1000 g/mol and consist of a distinct carbon backbone, typically with aromatic and non-saturated functional groups. They yield very strong and very sharp Raman signals, normally of several times higher intensity and less broad than the signals of (polymeric) excipients. Smallest variations in the carbon backbone and the crystal lattice yield spectral variation. Thus polymorphic forms and solvates can generally easily be discriminated by CRM. Biomolecules and biopolymers, e.g. RNA, oligopeptides and proteins are much more demanding with respect to experimental parameters and yield weaker and broader signals. Fortunately for the analyst, biomolecules still account only for a small part of pharmaceutical API.

Due to regulatory requirements, pharmaceutical substances are of very high purity. In addition, reference material of various polymorphic forms and salt forms are available due to the respective screening programs. Molecular structure, solid state, solvent content, crystallinity and particle size are generally known of every component in the system under investigation. It is thus possible to obtain reference spectra from pure, clearly defined material at high spectral resolution. These reference spectra are very valuable for multivariate data analysis, e.g. as basis spectra for classical least squares (CLS) algorithms. CLS can improve the LOD and noise levels and it is considered as the most credible data processing algorithm in comparison to principal component analysis, cluster analysis or multivariate curve resolution [86, 96].

As mentioned earlier, the size range of pharmaceutical samples is just right for a modern CRM. Primary particles are usually $1-100\,\mu\text{m}$, granules are typically a few hundred micrometres whereas a tablet measures millimetres to centimetres. A CRM equipped with a state-of-the-art Piezo-drive scan stage is excellent for imaging at highest spatial submicron resolution with FOV of a few hundred micrometres.

Attachment of an additional motorized scan stage allows generating large area mappings of entire macro-objects. Thus, overview images of a full body can be generated followed by high-resolution images of areas of interest at a much smaller scale.

8.2.1.1 Critical Parameters

Even though analytes and analytical technology match very well, there are certain restrictions to be considered. Certain critical parameters need to be adjusted carefully.

The irradiating laser wavelength and laser power are the most determining factors and need to be tuned to maximize Raman signal levels, yet must exclude absorption by the sample followed by degradation at the same time. A sample can decompose, undergo a phase transition or simply heat up and emit longer wavelength radiation when absorbing energy. The sample's electronic absorption spectrum has a strong effect on the probability that the sample will absorb energy. A hot sample emits black-body radiation. Thus, for samples that absorb radiation at the laser wavelength, the operator must be careful when selecting the appropriate laser power to maximize the S/N and minimize black-body radiation caused by sample heating. If the sample absorbs too strongly, a change of laser wavelength is required [97, 98]. Defocusing, change of lens to a lower magnification and NA or cooling of the sample using a cryogenic stage decrease the probability of sample degradation additionally [99].

Although mentioned as the issue number one in every textbook on Raman spectroscopy [100], to our experience fluorescence noise due to improper choice of laser wavelength is only a minor problem when conducting confocal Raman microscopy of pharmaceuticals. Even when using a green laser at 532 nm, only a very low percentage of pharmaceutical samples exhibit intrinsic fluorescence, mostly originating from celluloses and polymeric excipients; intrinsic fluorescence of APIs is very seldom. Fluorescence can either be removed through photobleaching or be eliminated by data treatment. Polynomial baseline correction or inclusion of extracted fluorescence signal as additional basis spectra during data processing using classical least squares allows removal of such noise. This offers the advantage that components can be localized also according to their fluorescent trace and not only due to the Raman signal. An elegant and efficient way to remove fluorescence (as well as to improve S/N) is to employ a numerical method based on wavelet transforms to process data. Wavelet transforms can be suitable to suppress noncorrelated noise and background signals. The Raman spectrum is decomposed by wavelet transform into "frequency components". The low-frequency (fluorescence, background) and the high-frequency data sets (noise, spikes and "cosmic rays") are rejected and the remaining sets are reconstructed to yield an improved Raman spectrum [101–104].

Another decisive component of a CRM is the objective lens. The numerical aperture (NA) of the lens defines the spatial resolution as well as the collection efficiency. Thus, a maximum NA is desirable. High NA means applying an oil-immersion

objective or objectives with very short working distance. For non-invasive investigation of rough solids, however, a long working distance non-immersed objective is required. Hence, a compromise needs to be made. Of high importance is also the focal depth of a lens, a measurement of the space in which an object can be displayed at acceptable sharpness. If flat polished surfaces are under investigation, this parameter will not be of interest. Should samples exhibit very rough and curved surfaces it will be difficult to get all objects within the FOV in focus. Due to the fact that CRM is performed confocally, all objects not in focus (above or below the focus plane) will not yield Raman signals. If very uneven specimens need to be characterized, objective lenses with a lower magnification and lower NA and a large pinhole are required.

Alternatively, sample preparation to generate flat surfaces is a solution. Tablets, e.g. can be treated employing a tablet mill or a microtome equipped with a steel or glass knife. For the investigation of powders and microscopic particles it is recommended to embed the materials in a non-fluorescent resin. The resin blocks with embedded particles can be cut with a glass or diamond knife of a microtome to generate blockfaces with flat surfaces. Embedding and sectioning yield an additional advantage: the inside of a specimen is revealed and can be imaged as cross-section of the sample.

Measurement time is limited in an industrial environment. A maximized cost – benefit ratio thus often defines the quality of results. Modern CRM allows the generation of low-resolution maps (e.g. 10,000 pixels per image) with limited information contents within a few minutes. Higher quality images of 50,000–100,000 pixels per image may require measurement time of an hour or more. Already at a pixel number of 40,000, images of acceptable smoothness and graininess are achieved. If acquisition time is not a limiting factor, the number of pixels per image might be limited by the performance of the computer employed for data processing. Data treatment such as noise removal demands considerable computing power.

Even though the spot size of the laser, and thus the optical resolution, is diffraction limited, the image quality can be improved considerably through oversampling. Oversampling means imaging at increments considerably smaller than the "theoretical" optical resolution. If the step size of a scanner is chosen at a value of 5-10 times smaller than the laser spot size, chemical images at very high resolutions can be achieved [105]. This is illustrated with a CRM image and a corresponding SEM image of a two-component inhalation particle in Fig. 8.1. The particles' shape was optimized to yield better flight properties and a very low bulk density. The lateral resolution R_L of confocal Raman microscopy is diffraction limited and approximated by the irradiating wavelength multiplied by 0.61 and divided by the numerical aperture NA of the lens. For very small pinholes, the resolution can be further improved by a factor of $1/\sqrt{2}$ [106]. The theoretical lateral resolution of the example in Fig. 8.1 (λ 532 nm, NA 0.75) is thus equal to 284 nm. Oversampling at a step size of 32 nm has resulted in an image where this theoretical spatial resolution has been at least levelled. A nanoscopic non-homogeneous distribution of component A (in red) and component B (in green) is visible.

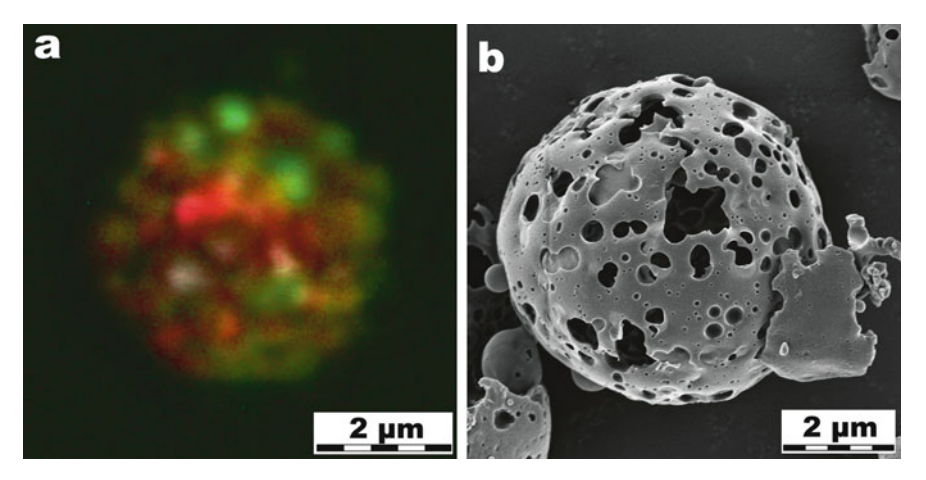


Fig. 8.1 Confocal Raman microscopic image (a) and a corresponding yet not colocalized SEM image (b) of inhalation particles with optimized flight properties, consisting of two components. Component A is visualized in *red* whereas component B is represented in *green*. A submicron resolution is achieved by CRM. SEM further visualizes the nanoscopic morphology. CRM data were obtained using a WITec CRM200 equipped with a 63 × lens (NA 0.75) and a Nd:YAG laser (532 nm at 50 mW) at a pixel number of 62,500 and an integration time of 40 ms per pixel

8.2.1.2 Limitations

CRM being a spectroscopic imaging method also entails various limiting aspects innate to spectroscopy or microscopy.

Typical for imaging methods, CRM does not allow bulk analysis of an entire lot. Generally only confined areas are investigated and a finite number of images are acquired. Sampling is thus critical. Areas under investigation need to be representative of the entire sample, which further needs to be representative of the whole lot. The higher the number of images acquired the more significant the results [100].

Also, spatial quantization is difficult. The 2D chemical images underestimate the size of spheres and overestimate the size of cubes [87].

Further, the interpretation of microscopic and spectroscopic data and judging of data quality requires substantial expertise and experience on the user side. The representation of microscopic results is often subjective. Reviewers therefore often "blame" (the of course respectable) microscopy to be an "art" rather than science. Quantitative results are difficult to achieve in Raman spectroscopy. Even though Raman intensity is directly proportional to the concentration of the scattering species several effects falsify any attempt to deduce quantitative output. Raman intensity and thus also LOD are very specific to every kind of substance and may differ greatly. A dissolved plasticizer is much more difficult to detect than any particulate pharmaceutical active. Intensities of Raman bands further depend on the intensity and wavelength of irradiation as well as state of polarization of the irradiating light and of the collection optics [98]. Variation of focus due to topography effects and resulting beam geometry at the sample further affect signal intensity. The Raman spectrum of the sample is also affected by the transmission characteristics of the sample matrix or the sample container [97, 107]. When characterizing solids,

varying packing densities (intrinsic for polymorphs!) and particle size strongly affect signal strength [108, 109]. At best semi-quantitative output can be generated regarding composition. Only relative assumptions of concentrations are possible. When studying a series of related samples with different relative concentrations, CRM can be used to elucidate trends.

In confocal Raman microscopy, where the irradiating laser spot is often smaller than the particle under investigation, an additional effect can occur. Already in very early publications, C.V. Raman mentioned the polarization of inelastic scattering [110, 111]. The Raman spectrum depends on the orientation of the crystallographic axes with respect to the direction and polarization of both the excitation and the scattered light [112–114]. Intensities of Raman bands may vary dramatically depending on the angle between polarizability tensor of a specific molecular vibration and the exciting source (Fig. 8.2).

In widefield Raman microscopy and FT-Raman spectroscopy this effect is often negligible since the optical resolution of typically several hundreds of micrometres is much larger than the irradiated crystal species and thus averaged spectra are collected. In contrast, confocal Raman microscopy allows a spatial resolution down to the optical limit of diffraction. It is therefore easily feasible to image single particles.

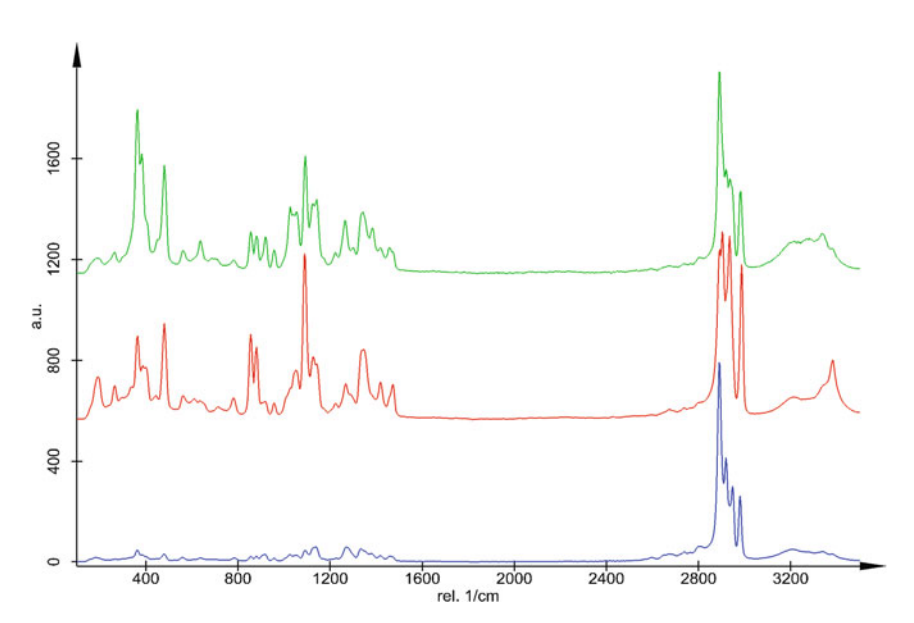


Fig. 8.2 Raman spectra of α -lactose monohydrate with spectral dissimilarities due to different angles between crystallographic axes of underlying single particles and incident light. Throughout the whole spectral range, peak intensities are varying. In addition, certain vibrations are fully annihilated or strongly amplified due to varying spatial orientation of the imaged crystalline particles

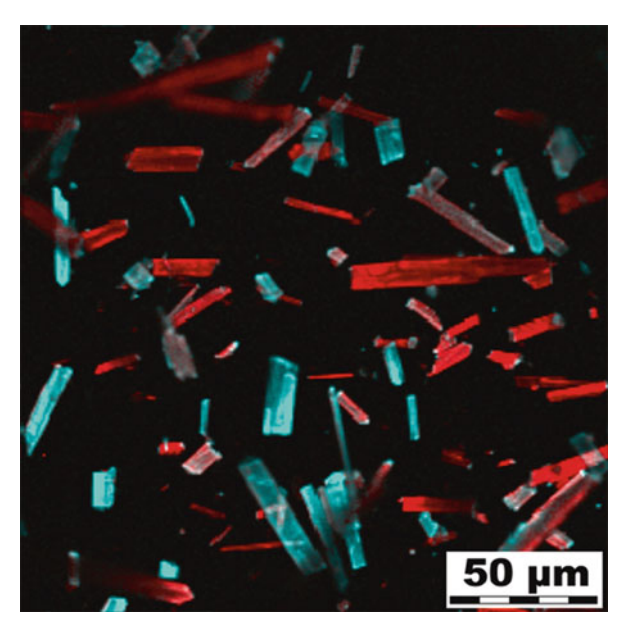


Fig. 8.3 Confocal Raman microscopic image of lath-shaped API particles. Particles are all of identical chemical and physical states but can be discriminated according to spatial orientation: horizontally oriented particles in red; vertically oriented particles in cyan. Data were obtained using a WITec CRM200 equipped with a $40 \times lens$ (NA 0.60) and a Nd:YAG laser (532 nm at 50 mW) at a pixel number of 62,500 and an integration time of 20 ms per pixel

Raman spectra obtained with CRM can thus reveal substantial differences in peak intensities due to unequal orientations of single crystals. A discrimination of single particles is possible due to different spatial orientation (Fig. 8.3).

Since a complete extinguishment of certain vibrations is possible, the erroneous conclusion might be drawn that observed spectral differences are due to, e.g. polymorphism. Varying band intensities can make it difficult to get qualitative information on polymorphism.

On the other hand, the polarization effects also yield valuable additional information. Reports in the literature show that polarized micro Raman spectroscopy has successfully been employed to study molecular orientation distributions of various materials, including ceramics and inorganics [115, 116], polymer films [117], liquid crystals [118, 119] or biological polymers [81]. Such polarization effects are very pronounced with small synthetic API crystals, containing aromatic structures allowing pi-stacking. Excipients, which are often of polymeric nature (PEG, cellulose, PVP, etc.) or occur in an amorphous state, exhibit this phenomenon rarely. Data processing of hyperspectral data cubes by classical least squares algorithms using base spectra, which include polarization information, can improve the fit quality considerably and can also improve image resolution.

In a recent study in our laboratories, single pellets for modified release were tested regarding internal structure, long-term stability and drug release. Modified release pellets consist of an inert carbohydrate-based core on which an API layer is applied through a spray drying process. Finally, the pellets are coated with a film for

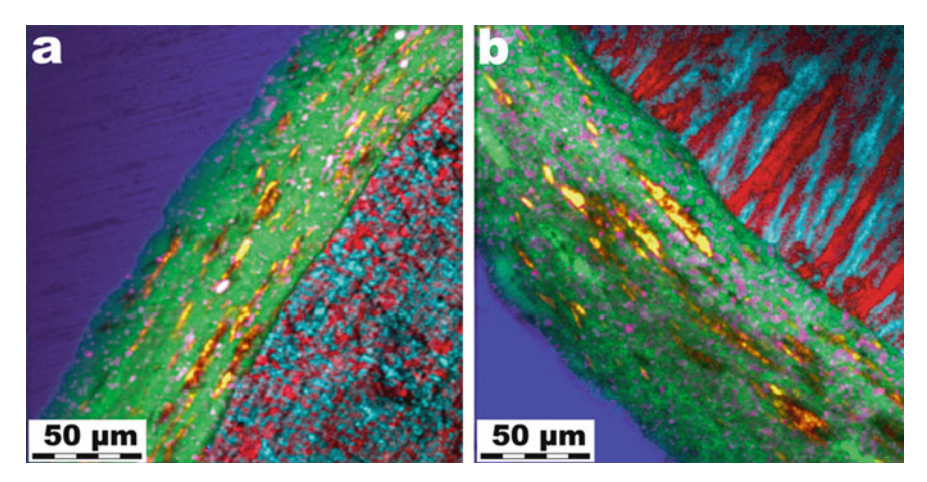


Fig. 8.4 Confocal Raman microscopic images of two types of modified release pellets. The APIs in both pellets were resolved according to spatial orientation of the single crystals (visualized in red and cyan). In image (a), the internal structure of the API layer indicates a concentric layered growth of the phase during spray drying. On the other hand, the API in image (b) has (re-)crystallized in a perpendicular star-like manner, even though spray dried and thus applied layer by layer. Pellets were embedded in a resin (visualized in blue) and cut equatorially using a microtome. The film coat consists of organic (green) and inorganic components (purple and orange). The internal structure of the coating indicates a concentric onion-like growth. Data were obtained using a WITec CRM200 equipped with a $20 \times lens$ (NA 0.40) and a Nd:YAG laser (532 nm at 50 mW) at a pixel number of 62,500 and an integration time of 20 ms per pixel

sustained release [60, 120]. One interesting aspect was found when inspecting two types of modified release pellets by CRM (Fig. 8.4). Both types were processed and prepared exactly the same way, but two different API were applied. The APIs in both pellets were resolved according to spatial orientation of the single crystals (visualized in red and cyan). The outer coating consists of organic (green) and inorganic components (purple, orange) whereas the resin used for embedding is visualized in blue.

In Fig. 8.4(a), the internal structure of the API layer indicates a concentric layered growth of the phase after spray drying, as can be expected. Interestingly, even though spray dried and thus applied layer by layer, the API crystals in the second type of pellets have arranged in a perpendicular, star-like manner. The second API thus appears to have dried and crystallized much slower, allowing rearranging its secondary structure. Possibly, the first solidification of the API has resulted in an amorphous phase, which subsequently has transformed over time in a more stable, crystalline form. This information was only achievable due to the ability to discriminate crystalline species according to their spatial orientation.

8.2.2 Investigation of Solid Dosage Forms by Chemical Imaging

8.2.2.1 Product Homogeneity

Long acting release (LAR) depots generally consist of an API dispersed within a biodegradable matrix. The drug is slowly released as the matrix degrades, primarily

through hydrolysis. LAR depot injections maintain all of the clinical and pharmacological characteristics of the immediate-release dosage form, with the added feature of slow release from the site of injection, reducing the need for frequent administration. With its specific pharmacokinetic profile, LAR depots can be administered, e.g. once a month instead of three times a day, strongly enhancing patient compliance [121]. Long-acting release depot injections have demonstrated their clinical and economic value on the market [122, 123].

Although these systems have achieved a high level of success, some unmet technical challenges remain, amongst others the ease of reconstitution and injection of the depot injections. Surface properties and internal structure can be tailored through preparation methods as well as composition of biodegradable matrix. Analytical methods, however, are required to attest the required structure. A non-homogeneous drug distribution can lead to a retarded or accelerated release (e.g. a burst). Many studies have investigated the detailed structure of LAR depots and the relationship to drug release. To achieve this goal, techniques providing spatially resolved information such as scanning electron microscopy or confocal microscopy were used [124]. However, most of the studies were performed with model compounds, such as fluorescent dyes, or were focusing on drug release and burst [125].

CRM and EDX allow the investigation of real samples, e.g. for clinical testing, and are not restricted to model compounds. They allow detailed information of the spatial drug distribution within the depots by making use of the chemical contrast of API and matrix. Both methods are excellent tools which help in optimizing processes to produce ideal LAR depots. Figure 8.5(a) shows an SEM image of typical LAR depots. Even though surface roughness can be estimated, no information is available on the inner structure. Embedding in a resin followed by trimming with a microtome discloses this information. Several kinds of depots, prepared by different processes, were investigated by EDX and CRM. In Fig. 8.5(b) and Fig. 8.5(c), two SEM images of blockfaces are overlaid by EDX mappings of the API. The API in this example contains a unique element and can thus be discriminated from the matrix and embedding resin.

CRM further allows the location of biodegradable matrix (green) and the resin used for embedding (blue, Fig. 8.5d and e). The resolution is more than sufficient to clearly visualize the basically homogeneous distribution of the API (colour-coded red), even though primary API particles are smaller than five microns. By interpreting data from both methods, SEM and CRM, additionally a core-shell structure can be assigned to one sort of the depots (Fig. 8.5c and e). They possess a much thicker shell of pure matrix material than the other depots (Fig. 8.5b and d). This information on the internal structure was very important to improve process to obtain LAR depots of optimized release as well as syringeability.

Solid oral dosage forms often feature a coating on top of the tablet core. On one hand this might be motivated by marketing purposes where colour coatings are applied to foster branding and make tablets visually more attractive. On the other hand, coatings may also improve compliance by making a tablet smoother and easier to swallow or to mask an unpleasant taste. Coatings often also have a pharmacological function. Functional coatings are, e.g. used to modify the release or to improve

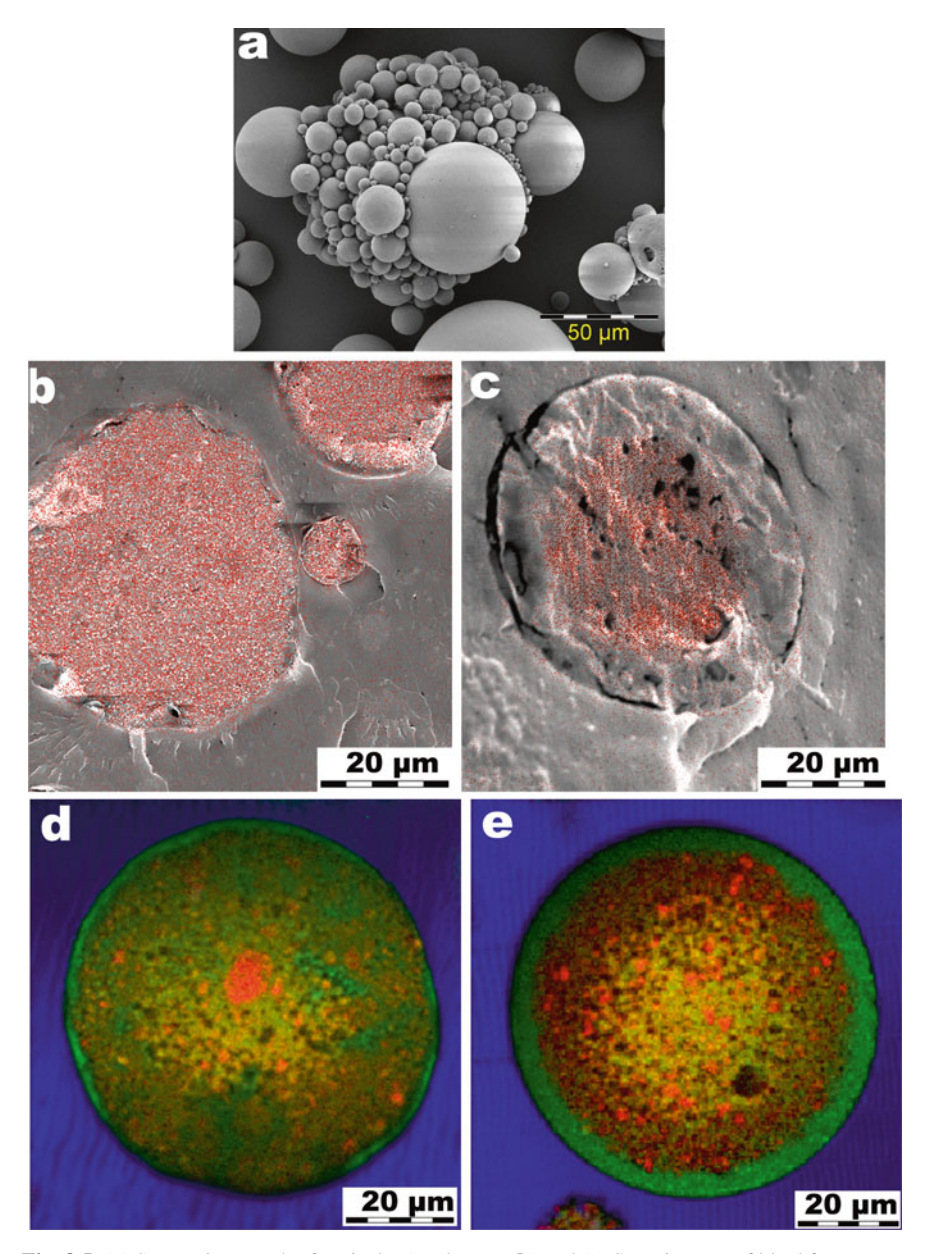


Fig. 8.5 (a) SEM micrograph of typical LAR depots; (b) and (c) SEM images of blockfaces overlaid by EDX map; (d) and (e) CRM mappings of similar blockfaces of corresponding depots. The API (in *red*) is homogeneously distributed within the biodegradable matrix (*green*) but the depots in (c) and (e) possess a much thicker shell of pure matrix material than the depots in (b) and (d). Depots were embedded in a resin (visualized in *blue*) and cut equatorially using a microtome. CRM data were obtained using a WITec CRM200 equipped with a 40 × lens (NA 0.40) and a Nd:YAG laser (532 nm at 20 mW) at a pixel number of 62,500 (5d) respectively 40,000 (5e) and an integration time of 100 ms per pixel

the stability of a formulation [126–128]. The solubility of a functional coating can be tailored by variation of the mixture, e.g. hydrophobic agents, hydrophilic agents and plasticizers [129–131].

On an industrial scale, the smallest alteration of a process may have dramatic effects on the output. A change of the quality of an ingredient, exchange of equipment or modification of reaction parameters can affect the product. In many cases the cause of altered product quality cannot be elucidated by simple means. An extensive root-cause analysis might be required to identify the reasons. Chemical imaging can be a powerful tool to fulfil such tasks. Dissolution testing of a tablet lot has revealed a modified release, compared to regular tablet lots. After inspection with various methods, CRM could resolve the cause. The tablet coating, which controls the release, exhibited inhomogeneities (Fig. 8.6).

On a microscopic level, a layering of the three coating components, separated from each other, could be visualized. The root cause was a coagulation of the coating solution during the spray drying process. Elucidation of the root cause with any other method than chemical imaging would have been very difficult.

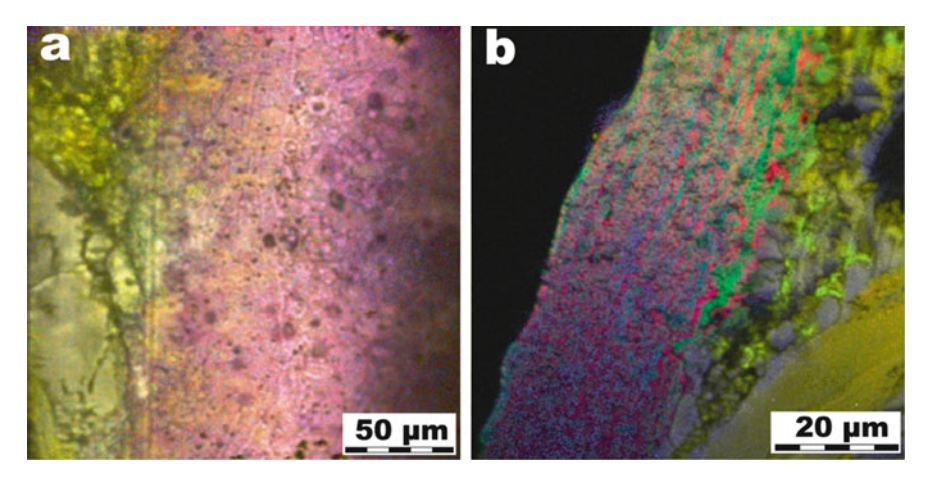


Fig. 8.6 CRM images of tablet coatings. The tablets were cut using a scalpel. The coating consists of a hydrophobic coating agent (red), a hydrophilic coating agent (green) and a plasticizer (blue). Tablet core ingredients are not discriminated but entire core is visualized in yellow. The regular tablet coating in (a) appears homogeneous with occasional air bubbles. The coating of the tablet lot showing anomalous dissolution behaviour in (b) exhibits a layered, phase-separated structure. Data were obtained using a WITec CRM200 equipped with $20 \times (a)$ and $63 \times (b)$ lenses (NA 0.40, respectively 0.75) and a Nd:YAG laser (532 nm at 50 mW) at a pixel number of 62,500 and an integration time of 50 ms per pixel

8.2.2.2 Content Uniformity

One alternative to oral dosage forms is administration through the respiratory tract via inhalation. Inhalation provides an excellent delivery route for the treatment of both pulmonary and non-pulmonary conditions. Delivering medications via inhalation generally requires smaller doses, offers a rapid onset of drug action and reduces adverse effects compared with other routes of administration [132].

Nebulizers, metered dose inhalers (MDI) and dry powder inhalers (DPI) have been competing on the market for many years. DPIs in general are easier to use and cause fewer irritant effects than the pressurized MDIs, in which a drug/propellant mixture is stored in solution in a pressurized canister. DPIs involve micronized powder, often packaged in single dose quantities in packs. Dry powder inhalers have therefore a considerably longer shelf life compared to MDIs containing drug solutions [133].

When the lung is the target for the aerosol (because the intent is either to treat the lung surface or to get the drug into the blood through the capillaries via the alveoli), the inhaled aerosol must consist of particles in a certain size range. The size, where drug particles can efficiently be adsorbed, ranges from 0.1 to 5 μ m. Larger particles tend to simply land in the mouth and throat and do not make it into the lung. Smaller particles tend to get inhaled and may immediately be exhaled.

In many DPIs, much larger carrier particles are used as bulking agent and to aid in powder uptake from the device during inhalation. These carriers are often sugar particles, typically $50\text{--}100\,\mu\text{m}$ in diameter. The much smaller drug particles attach to these excipient particles. The increased aerodynamic forces on the carrier/drug agglomerates improve entrainment of the small drug particles upon inhalation. In addition easier filling of small individual powder doses is allowed. Upon inhalation, the powder is broken up into its constituent particles with the aid of turbulence or mechanical devices such as screens or spinning surfaces on which particle agglomerates impact, releasing the small, individual drug powder particles into the air to be inhaled into the lung. The sugar particles are intended to be left behind in the device and in the mouth/throat region.

Sometimes an additional lubricant is included in the DPI formulation. The lubricant is meant to form a film on the other particles' surfaces and is supposed to avoid agglomeration and to ease the release of the API particles from the carriers [134, 135].

One of the main challenges in commercial research and development is the production of such micronized API particles on a large scale. Crystallization of such small API particles is rarely feasible, thus comminution, e.g. by milling is required. Milling may lead to solid-state transformations or amorphization of the drug particles. As mentioned before, the solid state of an API is crucial for its bioavailability [136].

Even though the composition of a DPI formulation is rather simple, a homogeneous distribution of the active and the carrier particles is required. Demixing or agglomeration is strongly unfavourable. Micronized API particles should be statistically distributed and sticking to larger carrier particles.

Chemical imaging is well suited to characterize formulation for dry powder inhalers. SEM can quickly resolve morphology, particle size distribution and detect possible agglomerates. CRM in addition is capable of probing solid state and content uniformity, which is illustrated in Fig. 8.7.

SEM was applied to confirm a uniform content and particle size distribution. CRM was further applied to probe several different approaches to prepare DPI mixtures. The powder formulation in (b) appears to consist of homogeneously

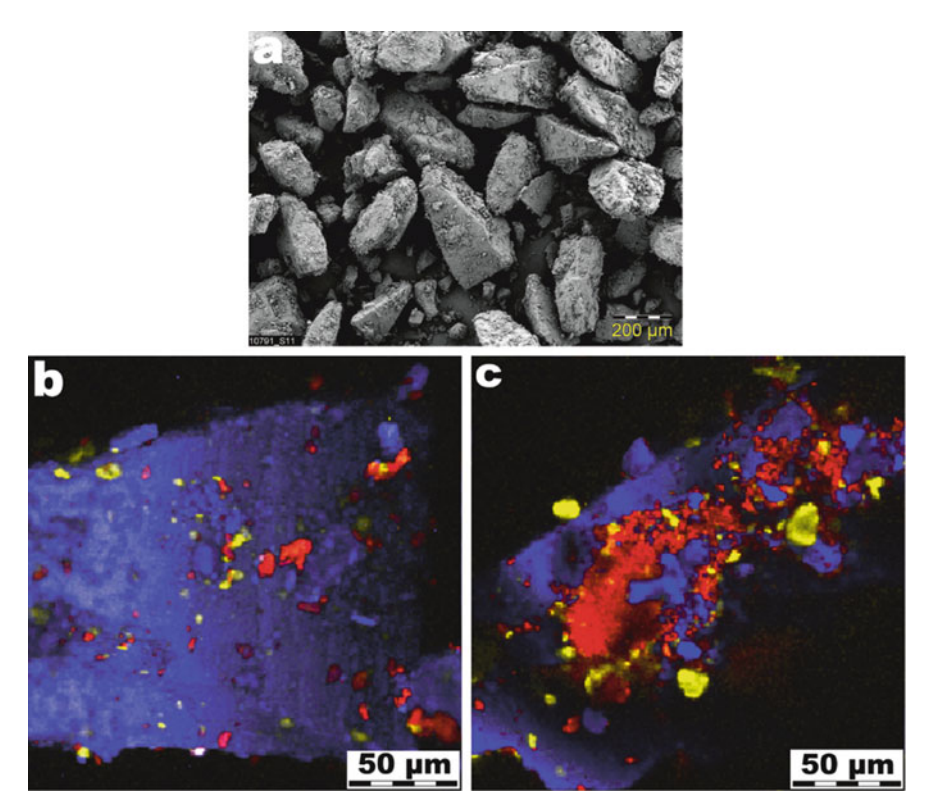


Fig. 8.7 (a) SEM image of a dry powder inhaler formulation consisting of large carrier particles on which micronized API powder is absorbed. (b) and (c) CRM images of similar DPI mixture. API particles are visualized in red, lubricant in yellow and the carrier particles in blue. CRM image (b) was obtained using a WITec CRM200 equipped with a $20 \times lens$ (NA 0.40) and a Nd:YAG laser (532 nm at 50 mW) at a pixel number of 40,000 and an integration time of 200 ms per pixel. 7c was obtained using a WITec CRM200 equipped with a $63 \times lens$ (NA 0.75) and a HeNe laser (633 nm at 35 mW) at a pixel number of 40,000 and an integration time of 150 ms per pixel

distributed API (visualized in red) and lubricant particles (in yellow) on carriers (in blue). Micronized particles are not agglomerated. Even the lubricant film on the carrier is detectable. In contrast, the formulation in (c) cannot be denoted optimal. In this formulation, the API tends to be strongly agglomerated. A homogeneous statistical distribution is not the case, such a formulation cannot yield an efficient delivery of the drug. No unwanted polymorphic forms or other solid-state variation could be confirmed in any of the formulations.

Tablets are the most popular dosage form in use today. About two-thirds of all prescriptions are dispensed as solid dosage forms, and half of these are compressed tablets, as they are easy and convenient to apply. A tablet can be formulated to deliver an accurate dosage to a specific site; it is usually taken orally, but can be administered sublingually, rectally or intravaginally.

Some APIs may be tableted as pure substances, although this is rarely the case; most formulations include excipients. These are inert ingredients, which either

enhance the therapeutic effect or are necessary to construct the tablet. The filler is a bulking agent, providing a quantity of material which can accurately be formed into a tablet. Binders hold the ingredients together so that they can form a tablet. Lubricants are added to reduce the friction between the tablet and the punches so that the tablet compression and ejection processes are smooth. Disintegrants are used to promote wetting and swelling of the tablet so that it breaks up in the gastrointestinal tract. Additional ingredients may also be added such as colouring agents, flavouring agents, and coating agents.

Crucial in the manufacturing process of tablets is content uniformity. To ensure that the appropriate amount of active ingredient is equal in each tablet, it is a prerequisite that the ingredients are well mixed. Powders that can be mixed well do not require granulation and can be directly compressed into tablets. If a sufficiently homogenous mix of the components cannot be obtained by simple mixing, the ingredients must be granulated prior to compression to assure an even distribution of the active compound in the final tablet. Two basic techniques are used to prepare powders for granulation into a tablet: wet granulation and dry granulation.

In a wet granulation process, a liquid binder or adhesive is added to the powder mixture. The amount of binder needs to be adjusted properly, over wetting will cause the granules to be too hard whereas under wetting will cause them to be too soft and friable. Once the solvent evaporates the wet mass has formed densely held agglomerates. Finally, the agglomerates are milled, which results in formation of granules.

Dry granulation is employed when the product to be granulated may be sensitive to moisture and heat. The dry mixture is compacted and densified in a press followed by milling. It requires drugs or excipients with cohesive properties. Dry granulation often produces a higher percentage of non-compacted products, which can compromise the quality or create yield problems for the tablet [137–139].

Compressed tablets are exerted to great pressures in order to compact the material. These mechanical stresses can affect the solid state of ingredients. Polymorphic forms of the drug substance can undergo phase conversion when exposed to manufacturing processes, such as compaction, drying and milling. Exposure to environmental conditions such as humidity and temperature can also induce polymorph conversion. Tabletting can also yield amorphization, e.g. at the tablet surface. Any alteration in solid state of course also affects the dissolution behaviour and thus the bioavailability of the drug.

Chemical imaging is suitable to probe both content uniformity and analysis of chemical and physical states. Figure 8.8 shows chemical images of a sectioned tablet. The tablet contains an API (visualized in red), a filler (in cyan), a disintegrant (in blue) and a lubricant (in yellow).

All four tablet components can be identified and discriminated. Large area mapping provides information on content uniformity whereas high-resolution images provide details on the fine structure within the tablet. The solid state of the API can be analysed and confirmed by either method, large area scan or high-resolution image. The FOV is too limited to conclude upon content uniformity but the high-resolution structure can be elucidated. The tablet was trimmed using a microtome to obtain a flat surface.

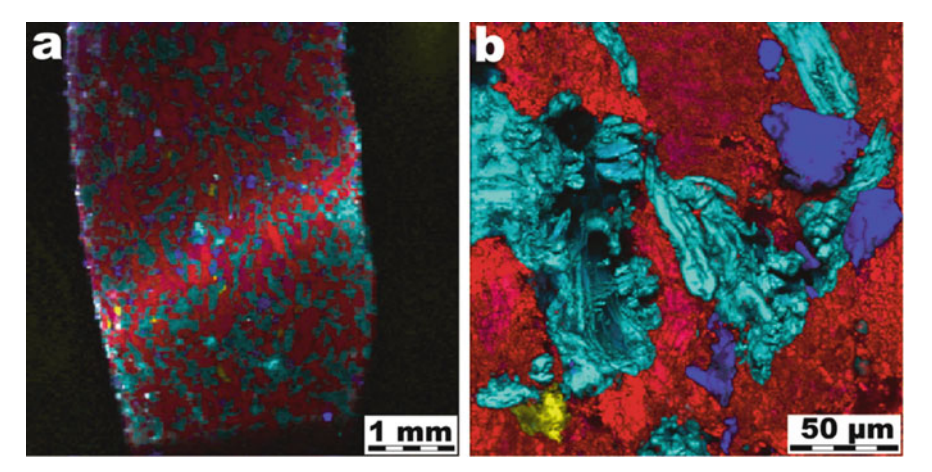


Fig. 8.8 (a) CRM large area imaging of a tablet section. The tablet contains an API (in red), a filler (in cyan), a disintegrant (in blue) and a lubricant (in yellow). A homogeneous distribution and PSD of the components can be confirmed. The sample was partly tilted during acquisition resulting in partly defocused areas. (b) CRM high-resolution imaging of a section of the same tablet lot as in (a). Data in (a) were obtained using a WITec alpha700 equipped with a $40 \times lens$ (NA 0.6) and a Nd:YAG laser (532 nm at 50 mW) at a pixel number of 22,500 and an integration time of 30 ms per pixel. Data in (b) were obtained using a WITec CRM200 equipped with a $63 \times lens$ (NA 0.75) and a Nd:YAG laser (532 nm at 50 mW) at a pixel number of 122,500 and an integration time of 20 ms per pixel

Tablets can also be inspected using SEM and EDX. Even though most pharmaceutical ingredients contain C, H and O, it is feasible that components can be identified and discriminated according to exceptional elements. In Fig. 8.9, an SEM image (a) and the corresponding EDX map (b) are presented of the surface of another tablet. Four unique elements are contained within the tablet. The element visualized in red is only present in the API; the element visualized in green belongs to the filler; the element visualized in yellow to the glidant, whereas the element

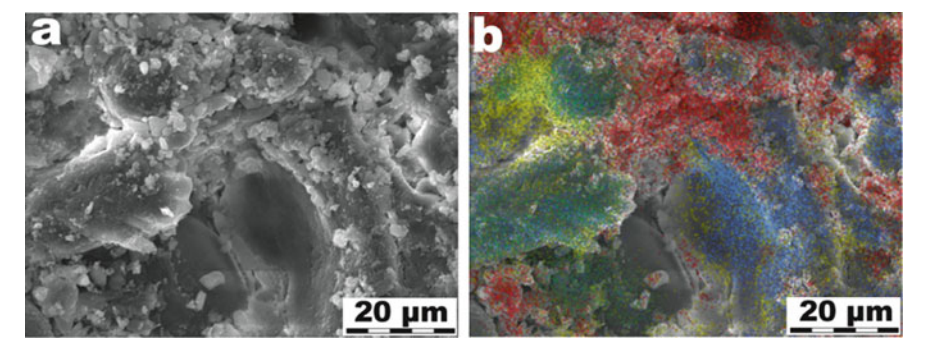


Fig. 8.9 SEM image (**a**) and corresponding EDX mapping (**b**) of a tablet surface. Four unique elements are present within the tablet. The element visualized in *red* is only present in the API; the element visualized in *green* belongs to the filler; the element visualized in *yellow* belongs to the glidant, whereas the element in *blue* is present in filler as well as in glidant. Identification of particles of interest according to the elemental composition at high spatial resolutions is feasible

in blue is present in filler as well as in glidant. SEM allows inspecting smallest particles and their morphology. EDX can be used to identify particles and domains according to their elemental fingerprint.

8.2.2.3 Solid-State Analysis

In the last section we have elucidated the possibility that an API can undergo a solid-state conversion during processing, e.g. granulation or tabletting. Mechanical stress, increased humidity or temperature can affect the integrity of dosage forms. CRM is an excellent tool to investigate such solid-state transformations. In Fig. 8.10 an image of a tablet surface containing API and four excipients is presented. It was found that the API is present not only in crystalline state but also in amorphous state. The crystalline form was detected only as discrete particles on the surface. The remainder of the API presented at the surface had transformed into an amorphous phase during tabletting.

Crystalline API is visualized in red, amorphous API in green, binder in cyan, disintegrant in blue, lubricant in yellow and glidant in purple.

Not only final products can be investigated, also before and after processing steps CRM can be employed to control quality of a product. In Fig. 8.11 an image of a granule after wet granulation is presented. Even though only one specific polymorphic form was deployed in the initial powder blend, a mixture of two polymorphic forms was detected after wet granulation. The initial polymorph

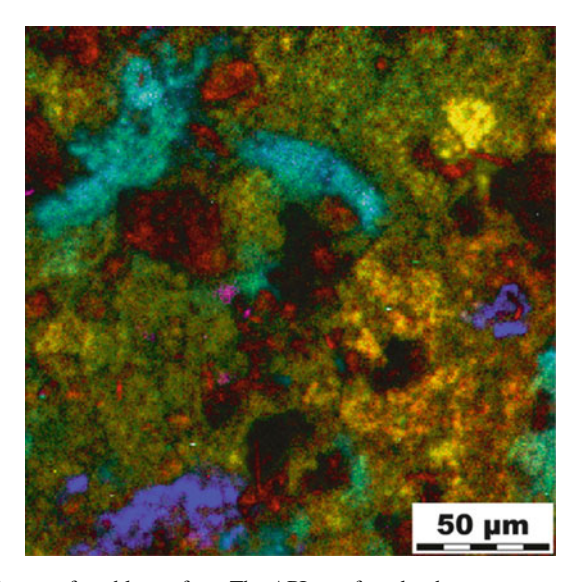


Fig. 8.10 CRM image of a tablet surface. The API was found to be present not only in crystalline (*red*) but also in amorphous state (in *green*). The excipients included are as follows: binder in *cyan*, disintegrant in *blue*, lubricant in *yellow* and glidant in *purple*. Data were obtained using a WITec CRM200 equipped with a lens (NA 0.40) and a Nd: YAG laser (532 nm at 33 mW) at a pixel number of 90,000 and an integration time of 100 ms per pixel

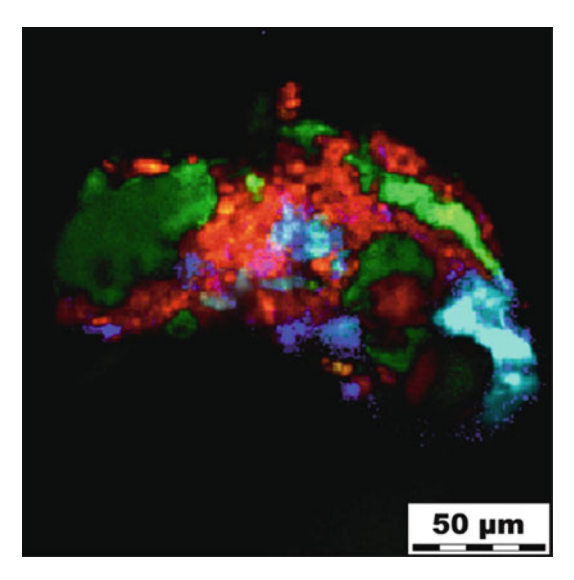


Fig. 8.11 CRM image of a granule after wet granulation. Two polymorphic forms of the API are found. The initial polymorph (in red) has partly transformed into a second polymorphic form (in cyan) during wet granulation. Filler is visualized in green and the disintegrant in blue. Data were obtained using a WITec CRM200 equipped with a $20 \times lens$ (NA 0.40) and a Nd: YAG laser (532 nm at 33 mW) at a pixel number of 40,000 and an integration time of 20 ms per pixel

(visualized in red) must have partially converted into another polymorphic form (in cyan) due to processing. The filler is visualized in green and the disintegrant in blue.

The stability and shelf life of dosage forms are routinely tested at defined temperatures and humidity for extended periods of time. Chemical incompatibilities of API and ingredients might lead to reactions or degradations. CRM is commonly employed to investigate effects of stressing and ageing. Initial samples are compared with samples from specific intervals. Figure 8.12 depicts a rare case where a solid-state reaction has taken place. Only from inspection by stereomicroscopy it was obvious that some transformation must have occurred. The originally smooth surface had transformed and become rough and brittle. Investigation of tablets before and after stressing has resulted in a very interesting conclusion. Initially the API was present solely as a Ca salt (visualized in red) together with four excipients: acidulant (in green), filler (in blue), binder (in cyan) and lubricant (in yellow). After stressing the situation had changed: the API was found in the aged tablets only as free base. No more Ca salt was detectable. Astonishingly, an additional component was found in the tablet, which was identified with reference spectra: a calcium salt of the acidulant (visualized in purple).

This finding has led to the conclusion that the API must have reacted with the acidulant and a cation transfer must have occurred. The initial Ca salt form of the

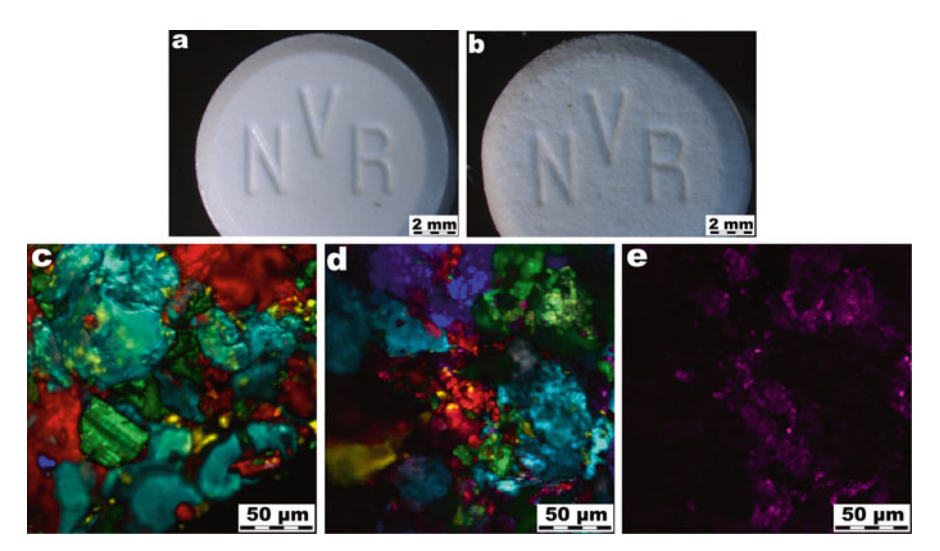


Fig. 8.12 Stereomicroscopic image of a tablet illustrating the initial appearance. Image (**b**) visualizes the alterations that occurred during stressing at increased temperatures and humidity for a certain point in time. The surface of the tablet has become much rougher and the texture more brittle. (**c**) CRM image of an initial smooth tablet surface. The API is present as a calcium salt. The acidulant is visualized in *green*, the filler in *blue*, the binder in *cyan* and the lubricant in *yellow*. Image (**d**) represents a CRM image of the rough surface of a stressed tablet. Acidulant, filler, binder and lubricant are still present but the API is now found as free base; no more API-Ca salt is present. In addition a further component was detected which could be identified as the calcium salt of the acidulant, visualized in *purple* in (**e**). CRM data were obtained using a WITec CRM200 equipped with a 20 × lens (NA 0.40) and a Nd:YAG laser (532 nm at 50 mW) at a pixel number of (**c**) 62,500 and (**d** or **e**) 40,000 and an integration time of 50 ms per pixel

API was hydrated. During the solid-state reaction with the acidulant the crystal water was released and the free water had soaked the tablet, leading to an increased surface roughness. The reaction is denoted as follows:

$$[API][Ca]^* \times H_2O + [Acidulant][H]_2 \rightarrow [API][H]_2 + [Acidulant][Ca]^+ \times H_2O$$

$$(8.1)$$

Confocal Raman microscopy is extremely powerful in discriminating solid states. Even when substances are chemically identical or very closely related, the Raman spectrum normally shows sufficient spectral dissimilarities due to different solid states to discern them unequivocally. Figure 8.13 represents a CRM image of a physical mixture of six closely related APIs.

This physical mixture was prepared as proof that CRM is suitable to discriminate a co-complex of two APIs (APII and API2) and the pure non-complexed forms of API1 and API2. To further complicate things, other solid-state forms of API1 and API2 were added. Even though very closely chemically related, the six compounds were easily discriminated by CRM. Co-complex and single API particles showed sufficiently different spectral features to distinguish them.

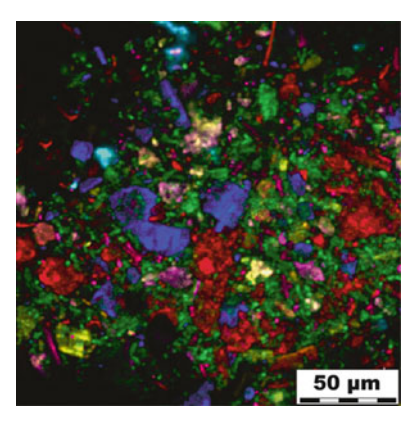


Fig. 8.13 CRM image of a physical mixture of six closely related APIs: a co-complex of two APIs (API1 and API2) in red, a salt form of API1 in blue, the free acid form of API1 in green, a salt form of API2 in purple, the free acid form of API2 in yellow and finally an ester form of API2 in cyan. Even though very close chemical relationships exist, the six compounds can be discriminated by CRM. See main text body. Data were obtained using a WITec CRM200 equipped with a $20 \times lens$ (NA 0.40) and a Nd:YAG laser (532 nm at 50 mW) at a pixel number of 16,000 and an integration time of 50 ms per point

8.2.2.4 Foreign Particulates

In general, pharmaceutical products are required to be essentially free of visible foreign particles; limits on the number of subvisible particles are allowed. The FDA requires that contamination problems are fully investigated in a timely fashion. Identification of small particle contamination is thus of key importance in the development of pharmaceutical products and formulations for regulatory compliance [140].

There are two general types of contaminants, product-related and foreign material. Ingredients may coagulate or precipitate, thus forming solid particles or degradation of any component might be the origin of any product-related contaminant. Particles of external origin may be derived from the product container or packaging material. These types of particles include glass, rubber, aluminium, plastics and paper. Contamination can also result from the manufacture of the product; examples of these include charred product, detergents and lubricant oils. Metal and metal corrosion, Teflon, graphite and rubber particles are indications of tank, filter or equipment failure. Environmental contaminants such as fibres and skin cells are also detected. The most common contaminants in pharmaceuticals are cellulose (cotton and paper) fibres, synthetic fibres, silicone, plastics, rubber, metal particles and corrosion products, glass particles and char particles [141].

Microscopical analysis is particularly well suited to the analysis of particulate contamination because the particles are usually too small to be analysed using conventional methods. Size, shape and surfaces of a foreign body can be described with simple light microscopy. Often more powerful methods are required, allowing information on the identity of the material to be obtained. Chemical imaging is highly suitable to resolve such tasks. EDX is especially valuable in the analysis and comparison of glass and metallic fragments. Vibrational microspectroscopy is

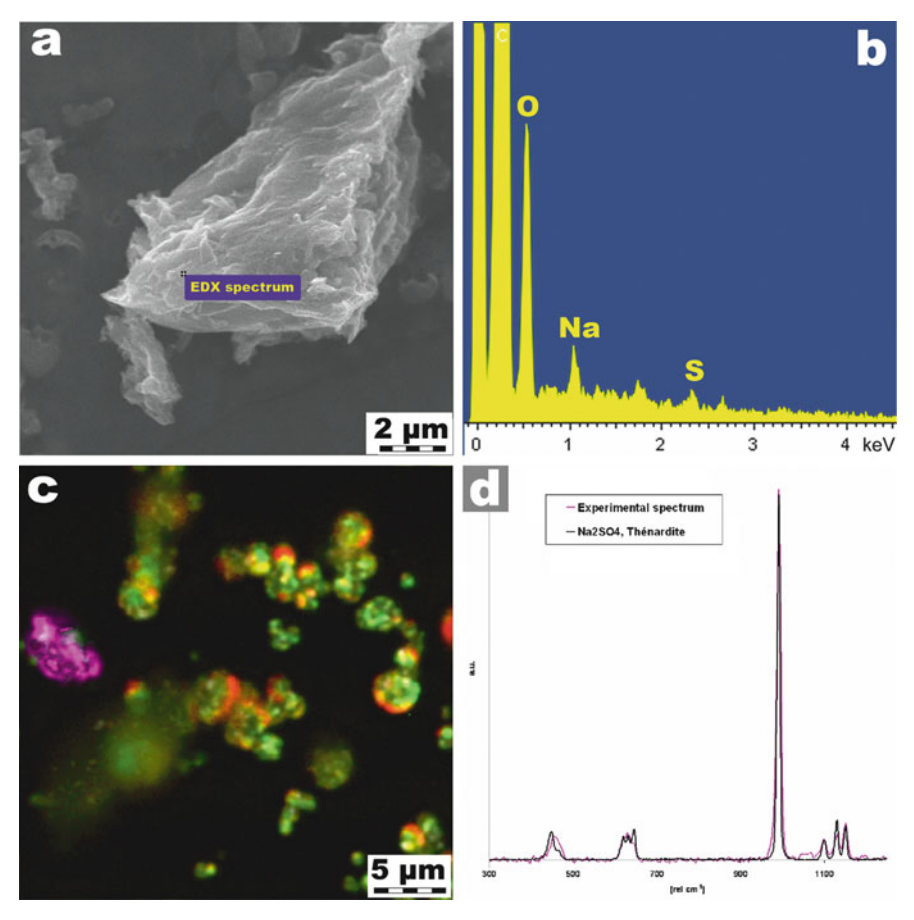


Fig. 8.14 A contaminant, foreign in particle size and shape, was found in a powder mixture as can be seen in the SEM image in (a). An EDX spectrum was acquired on one of these particles. Elemental analysis has disclosed the presence of sodium, oxygen and sulphur within the contaminant as presented in (b). Further analysis by CRM has similarly resolved such particulates, visualized in *pink* in (c). Comparison of the obtained Raman spectra with reference spectra has led to the solution sodium sulphate, presented in (d). CRM data were obtained using a WITec CRM200 equipped with a $63 \times lens$ (NA 0.75) and a Nd: YAG laser (532 nm at 50 mW) at a pixel number of 62,500 and an integration time of 50 ms per pixel

similarly powerful for identification of small particles, especially those of an organic nature [142–144].

The potential chemical imaging is illustrated in Fig. 8.14. Foreign particulates were found within a solid powder mixture. The contaminants were different from the rest of the powder particles in particle size and shape. EDX elemental analysis of one of these particles has disclosed the presence of sodium, oxygen and sulphur within the contaminant. Further analysis of the contaminants by CRM and comparison of the obtained Raman spectra with reference spectra from a database has resolved the identity. The foreign particulates were made from non-critical anhydrous sodium sulphate, a by-product of a preparation process.

8.3 Conclusions

Health authorities are encouraging the pharmaceutical industry to adopt the use of a quality by design (QbD) approach, where quality is designed into the product rather than quality being tested in the product. The concept of QbD, which can be applied during development, manufacturing and life cycle management, is based on the idea that processes are understood thoroughly.

One approach towards successful ObD is the implementation of chemical imaging methods within the development cycle. CI, in particular confocal Raman microscopy, provides valuable information on pharmaceutical samples. Various aspects of a product can be characterized by chemical imaging, such as visual appearance (morphology, particle size, particle size distribution and surface roughness), content uniformity (composition, distribution and homogeneity), chemical identity (structure and stability) and physical state (solid state, polymorphism, crystallinity and phase transformations). Especially the combination of several CI methods is highly valuable. Due to their complementary nature with different spatial resolutions and different types of chemical information provided, intrinsic advantages of every method accumulate and limitations are decreased. Chemical imaging can be applied not only for product development, product design, process validation, process quality control, life cycle management but also for counterfeit and generics analysis. Solid as well as liquid and semi-liquid dosage forms can be probed; single components, e.g. pure drug substance, as well as complex formulations can be investigated from a nanoscopic resolution up to the macroscopic regime.

Several successful applications of confocal Raman microscopy and energy-dispersive X-ray analysis implemented for the characterization of pharmaceutical solid dosage forms were presented in this chapter. Content uniformity, solid-state analysis or contaminant analysis are easy tasks for CI, especially if methods are applied in combination. The complementarity of CRM together with EDX is apparent.

8.4 Materials and Methods

Confocal Raman microscopy was performed using a WITec CRM200 (WITec GmbH, Ulm, Germany) equipped with a Nd:YAG laser (532 nm at 50 mW) and a HeNe laser (633 nm at 35 mW). Three LD Plan-Neofluar[®] lenses were employed, namely $20 \times (NA~0.40)$, $40 \times (NA~0.60)$ and $63 \times (NA~0.75)$, Carl Zeiss MicroImaging GmbH, Jena, Germany).

Alternatively, a WITec Alpha700 (WITec GmbH, Ulm, Germany) equipped with a $40 \times \text{Plan}$ ELWD lens (NA 0.6, Nikon GmbH, Düsseldorf, Germany) and a Nd:YAG laser (532 nm at 50 mW) was employed.

SEM investigations were performed using a FESEM Supra 40 microscope from Zeiss (Carl Zeiss NTS GmbH, Oberkochen, Germany).

EDX data were obtained using a INCA 300 detector (Oxford Instruments, Abingdon, UK) attached to a JEOL JSM 6040LV (JEOL Inc., Peabody, USA). The Si(Li)

detector consisted of a $30\,\mathrm{mm}^2$ detecting crystal and was mounted at a takeoff angle of 35° and at $10\,\mathrm{mm}$ working distance. Mappings were registered at a spatial resolution of 256×256 spectra and a spectral range of 0–20 keV at frame rates of $26.7\,\mathrm{s}$.

Stereomicroscopy was executed using a SteREO Discovery.V12 with PlanApo S 0.63 × objective (both Carl Zeiss MicroImaging GmbH, Göttingen, Germany).

Blockfaces and tablet sections were prepared using glass knifes and/or a histo diamond knife (Diatome AG, Biel, Switzerland) attached to a Leica EM UC6 ultramicrotome (Leica Microsystems GmbH, Wetzlar, Germany).

Acknowledgments We would like to thank Dirk Märtin for his assistance with scanning electron microscopy and energy-dispersive X-ray spectroscopy.

References

- E. Pivonka, J. Chambers, P. Griffiths, Applications of Vibrational Spectroscopy in Pharmaceutical Research and Development (Wiley, Chichester, 2007)
- 2. S. Sasic, Pharmaceutical Applications of Raman Spectroscopy (Wiley, Chichester, 2008)
- R. Hilfiker, F. Blatter, M. von Raumer, Relevance of Solid-State Properties for Pharmaceutical Products in Polymorphism in the Pharmaceutical Industry (Wiley, Weinheim, 2006), pp. 1–19
- 4. W. McCrone, Phys. Chem. Org. Solid State 2, 725–767 (1965)
- 5. D. Giron, Am. Pharm. Rev. 11, 66 (2008)
- 6. D. Giron, M. Mutz, S. Garnier, J. Therm. Anal. Calorim. 77, 709 (2004)
- 7. G. Chawla, A. Bansal, Curr. Res. Inf. Pharm. Sci. 5, 9 (2004)
- 8. http://www.ich.org/LOB/media/MEDIA3096.pdf
- 9. http://www.fda.gov/cder/guidance/6419fnl.pdf
- 10. C. Gendrin, Y. Roggo, C. Collet, J. Pharm. Biomed. Anal 48, 533 (2008)
- J. Zeitler, D. Newnham, P. Taday, T. Threlfall, R. Lancaster, R. Berg, C. Strachan, M. Pepper, K. Gordon, T. Rades, J. Pharm. Sci. 95, 2486 (2006)
- 12. P. Taday, Philos Trans. R. Soc. Lond. A 362, 351 (2004)
- J. Spencer, Z. Gao, T. Moore, L. Buhse, P. Taday, D. Newnham, Y. Shen, A. Portieri, A. Husain, J. Pharm. Sci. 97, 1543 (2008)
- 14. Y. Shen, P. Taday, D. Newnham, M. Pepper, Semicond. Sci. Technol. 20, S254 (2005)
- 15. T. Kojima, S. Onoue, N. Murase, F. Katoh, T. Mano, Y. Matsuda, Pharm. Res. 23, 806 (2006)
- 16. C. Anderton, Pharm. Rev. 7, 42 (2004)
- S. Moss, G. Bovermann, R. Denay, J. France, C. Guenat, L. Oberer, M. Ponelle, H. Schröder, Chimia 61, 346 (2007)
- S. Bell, J. Beattie, J. McGarvey, K. Peters, N. Sirimuthu, S. Speers, J. Raman Spectrosc. 35, 409 (2004)
- K. Chan, O. Fleming, S. Kazarian, D. Vassou, G. Chryssikos, V. Gionis, J. Raman Spectrosc. 35, 353 (2004)
- 20. L. Taylor, F. Langkilde, J. Pharm. Sci. 89, 1342 (2000)
- 21. M. Auer, U. Griesser, J. Sawatzki, J. Mol. Struct. 661–662, 307 (2003)
- V. Tumuluri, M. Kemper, I. Lewis, S. Prodduturi, S. Majumdar, B. Avery, M. Repka, Int. J. Pharm. 357, 77 (2008)
- 23. G. Walker, S. Bell, M. Vann, D. Jones, G. Andrews, Chem. Eng. Sci. 62, 3832 (2007)
- M. de Veji, P. Vandenabeele, K. Alter Hall, F. Fernandez, M. Green, N. White, A. Dondorp, P. Newton, L. Moens, J. Raman Spectrosc. 38, 181 (2007)
- 25. K. Sugano, T. Kato, K. Suzuki, K. Keiko, T. Sujaku, T. Mano, J. Pharm. Sci. 95, 2115 (2006)
- 26. E. Brewer, A. Ramsland, J. Pharm. Sci. 84, 499 (1995)

- 27. J. Heath, Dictionary of Microscopy (Wiley, Chichester, 2005)
- 28. D. Murphy, Fundamentals of Light Microscopy and Electronic Imaging (Wiley, Chichester, 2001)
- 29. I. Vitez, A. Newman, M. Davidovich, C. Kiesnowski, Thermochim. Acta 324, 187 (1998)
- D. Berry, C. Seaton, W. Clegg, R. Harrington, S. Coles, P. Horton, M. Hursthouse, R. Storey, W. Jones, T. Friscic, N. Blagden, Cryst. Growth Des. 8, 1697 (2008)
- 31. S. Pygall, J. Whetstone, P. Timmins, C. Melia, Adv. Drug Deliv. Rev. 59, 1434 (2007)
- 32. B. Jovice, P. Kamali-Zare, H. Brismar, L. Bergstroem, Langmuir 24, 11096 (2008)
- 33. R. Ortiz, J. Au, Z. Lu, Y. Gan, M. Wientjes, AAPS J. 9, E241 (2007)
- 34. C. Berkland, K. Kim, D. Pack, Pharm. Res. **20**, 1055 (2003)
- 35. V. Malaterre, J. Ogorka, R. Gurny, N. Loggia, K. Paulus, Eur. J. Pharm. Biopharm. (submitted)
- G.I. Goldstein, D.E. Newbury, P. Echlin, D.C. Joy, C. Fiori, E. Lifshin, Scanning Electron Microscopy and X-ray Microanalysis (Plenum Press, New York, NY, 1981)
- D. Murphy, F. Rodriguez-Cintron, B. Langevin, R. Kelly, N. Rodriguez-Hornedo, Int. J. Pharm. 246, 121 (2002)
- P. Mura, M. Faucci, A. Manderioli, G. Bramanti, L. Ceccarelli, J. Pharm. Biomed. Anal. 18, 151 (1998)
- 39. D. Bozic, R. Dreu, F. Vrecer, Int. J. Pharm. 357, 44 (2008)
- 40. L. Ping, S. Hynes, T. Haefele, M. Pudipeddi, A. Royce, A. Serajuddin, J. Pharm. Sci. (in print)
- 41. T. Li, K. Park, Pharm. Res. 15, 1222 (1998)
- 42. L. Sipos, A. Som, R. Faust, R. Richard, M. Schwarz, S. Ranade, M. Boden, K. Chan, Biomacromolecules 6, 2570 (2005)
- 43. A. Efimov, A. Tonevitsky, M. Dittrich, N. Matsko, J. Microsc. 226, 207 (2007)
- 44. L. Harding, M. Reading, D. Craig, J. Pharm. Sci. 97, 2768 (2008)
- 45. U. Sindel, I. Zimmermann, Powder Technol. 117, 247 (2001)
- 46. S. Ward, M. Perkins, J. Zhang, C. Roberts, C. Madden, S. Luk, N. Patel, S. Ebbens, Pharm. Res. 22, 1195 (2005)
- 47. V. Busignies, B. Leclerc, P. Porion, P. Evesque, G. Couarraze, P. Tchoreloff, Eur. J. Pharm. Biopharm. **64**, 38 (2006)
- 48. C. Wua, B. Hancock, A. Mills, A. Bentham, S. Best, J. Elliott, Powder Technol. 181, 121 (2008)
- L. Kessler, Acoustic Microscopy, Metals Handbook (ASM International, Ohio, 1989), pp. 465–482
- M. Nelson, C. Zugates, P. Treado, G. Casuccio, D. Exline, S. Schlaegle, Aerosol Sci. Technol. 34, 108 (2001)
- A. Apeldoorn, Y. Aksenov, M. Stigter, I. Hofland, J. Bruijn, H. Koerten, C. Otto, J. Greve, C. Blitterswijk, J.R. Soc. Interface 2, 39 (2005)
- 52. P. Bergese, I. Alessandri, I. Colombo, N. Coceani, L. Depero, Compos. Part A 36, 443 (2005)
- 53. D. Volodkin, A. Petrov, M. Prevot, G. Sukhorukov, Langmuir 20, 3398 (2004)
- 54. H. Lange, Chem. Ing. Tech. 9, 1091 (1993)
- 55. D. Clark, M. Henson, F. LaPlant, S. Šašić, L. Zhang, in *Pharmaceutical Applications of Chemical Mapping and Imaging* (J.M. Chalmers, P.R. Griffiths (Eds.)) in "Handbook of Vibrational Spectroscopy" vol. 1 (Wiley, New York, Chichester, Brisbane, Toronto, Singapore, 2007), pp. 309–335
- A. Garratt-Reed, Energy Dispersive X-Ray Analysis (BIOS Scientific Publishers, Oxford, 2003)
- 57. A. Kenda, O. Eibl, P. Pongratz, Micron **30**, 85 (1999)
- 58. J. Bovin, Micron Microsc. Acta 23, 143 (1992)
- 59. K. Paulus, Proc. 31st Micr. Conf. (DGE, Dresden, 2003)
- 60. S. Ensslin, K. Moll, K. Paulus, C. Mäder, J. Control Release 128, 149 (2008)
- 61. P. Nevsten, P. Borgquist, A. Axelsson, L. Wallenberg, Int. J. Pharm. 290, 109 (2005)
- 62. S. Fitzgerald, Spectrosc. Eur. 17, 24 (2005)

- 63. T. Miller, G. Havrilla, Powder Diffraction 20, 15 (2005)
- 64. B. Beckhoff, B. Kanngiesser, N. Langhoff, R. Wedell, H. Wolff, *Handbook of Practical X-Ray Fluorescence Analysis* (Springer, Berlin, 2006)
- 65. A. Benninghoven, Angew. Chem. Int. 33, 1023 (1994)
- 66. A. Belu, C. Mahoney, K. Wormuth, J. Control Release 126, 111 (2008)
- 67. A. Belu, D. Graham, D. Castner, Biomaterials 24, 3635 (2003)
- 68. N. Winograd, Appl. Surf. Sci 203-204, 13 (2003)
- 69. A. Belu, M. Davies, J. Newton, N. Patel, Anal. Chem. 72, 5625 (2000)
- 70. N. Harrick, *Internal Reflection Spectroscopy* (Wiley, Chichester, 1967)
- 71. K.L.A. Chan, S.V. Hammond, S.G. Kazarian, Anal. Chem. 75, 2140 (2003)
- 72. C. Krafft, D. Codrich, G. Pelizzo, V. Sergo, Analyst 133, 361 (2008)
- 73. G. Reich, Pharm. Ind. **64**, 870 (2002)
- 74. Y. Roggo, A. Edmond, P. Chalus, M. Ulmschneider, Anal. Chim. Acta 535, 79 (2005)
- C. Ricci, L. Nyadong, F. Fernandez, P. Newton, S. Kazarian, Anal. Bioanal. Chem. 387, 551 (2007)
- C. Ricci, C. Eliasson, N. Macleod, P. Newton, P. Matousek, S. Kazarian, Anal. Bioanal. Chem. 389, 1525 (2007)
- 77. M. Henson, L. Zhang, Appl. Spectrosc. 60, 1247 (2006)
- 78. S. Sasic, Appl. Spectrosc. 6, 239 (2007)
- 79. G. Reich, Adv. Drug Delir. Rev. **57**, 1109 (2005)
- 80. J. Breitenbach, W. Schrof, J. Neumann, Pharm. Res. 16, 1109 (1999)
- 81. I. Chourpa, P. Carpentier, P. Maingault, P. Dubois, SPIE 3608, 48 (1999)
- 82. L. Kador, T. Schittkowski, M. Bauer, Y. Fan, Appl. Opt. 40, 4965 (2001)
- 83. F. Clarke, M. Jamieson, D. Clark, S. Hammond, R. Jee, A. Moffat, Anal. Chem. **73**, 2213 (2001)
- 84. H. Boyer, J. Oswalt, Analusis 28, 3 (2000)
- 85. P. Treado, M. Nelson, Pract. Spectrosc. 28, 191 (2001)
- 86. L. Zhang, M. Henson, S. Sekulic, Anal. Chim. Acta **545**, 262 (2005)
- 87. D. Clark, S. Sasic, Cytometry A 69A, 815 (2006)
- 88. S. Sasic, Pharm. Res. **24**, 58 (2007)
- 89. D. Fraser Steele, P. Young, R. Price, T. Smith, S. Edge, D. Lewis, AAPS J. 6, Article 32 (2004)
- 90. A. Theophilus, A. Moore, D. Prima, S. Rossomanno, B. Whitcher, H. Chrystyn, Int. J. Pharm. 313, 14 (2006)
- 91. A. Serajuddin, P. Li, T. Haefele, Am. Pharm. Rev. 11, 34 (2008)
- A. Docoslis, K. Huszarik, G. Papageorgiou, D. Bikiaris, A. Stergiou, E. Georgarakis, AAPS J. 9, Article 43, E361 (2007)
- 93. G. Papageorgiu, D. Bikiaris, E. Karavas, S. Politis, A. Docoslis, Y. Park, A. Stergiou, E. Georgarakis, AAPS J. 8, Article 71, E623 (2006)
- 94. W. Doub, W. Adams, J. Spencer, L. Buhse, M. Nelson, P. Treado, Pharm. Res. 24, 934 (2007)
- 95. C. in *Revealing Chemistry Through Advanced Chemical Imaging*. Visualizing Chemistry: The Progress and Promise of Advanced Chemical Imaging (National Academies Press, Washington, 2006)
- 96. H. Martens, T. Naes, *Multivariate Calibration* (Wiley, New York, NY, 1992)
- 97. B. Bowie, D. Chase, I. Lewis, P. Griffiths, Handb. Vib. Spectrosc. 3, 2355 (2002)
- 98. J. Thomas, P. Buzzini, G. Massonnet, B. Reedy, C. Roux, Forensic Sci. Int. 152, 189 (2005)
- 99. P. Hendra, Int. J. Vib. Spectrosc. 4, 2 (2000)
- 100. C. McGoverin, T. Rades, K. Gordon, J. Pharm. Sci. 97, 4598 (2008)
- C. Camerlinge, F. Zenone, G. Gaeta, R. Riccio, M. Lepore, Meas. Sci. Technol. 17, 298 (2006)
- 102. P. Ramos, I. Ruisanchez, J. Raman. Spectrosc. 36, 848 (2005)
- 103. T. Cai, D. Zhang, D. Ben-Amotz, Appl. Spectrosc. 55, 1124 (2001)
- 104. F. Ehrentreich, L. Sümmchen, Anal. Chem. **73**, 4364 (2001)

- F. Adar, E. Lee, S. Mamedov, A. Whitley, Spectrosc. Suppl.: Raman June vol. 1–3, 38–43 (2006)
- 106. http://www.olympusfluoview.com/theory/resolutionintro.html
- 107. N. Everall, J. Lumsdon, Vib. Spectrosc. 2, 257 (1991)
- 108. M. Pellow-Jarmann, P. Hendra, R. Lehnert, Vib. Spectrosc. 12, 257 (1996)
- T.R.M. De Beer, W.R.G. Baeyens, Y. Vander Heyden, J.P. Remon, C. Vervaet, F. Verpoort, Eur. J. Pharm. Sci. 30, 229 (2007)
- 110. C. Raman, K. Krishnan, Nature 121, 501 (1928)
- 111. C.V. Raman, K.S. Krishnan, Nature 122, 169 (1928)
- 112. R. Snyder, J. Mol. Spectrosc. 37, 353 (1971)
- 113. D. Bower, J. Polym. Sci. 10, 2135 (1972)
- 114. C. Bremard, P. Dhamelincourt, J. Laureyns, G. Turrell, Appl. Spectrosc. 39, 1036 (1985)
- 115. X. Zhang, Y. Liu, S. Chen, J. Raman Spectrosc. 36, 1101 (2005)
- M. Bickermann, B. Epelbaum, P. Heimann, Z. Herro, A. Winnacker, Appl. Phys. Lett. 86, 131904 (2005)
- 117. M. Tanaka, R. Young, J. Mater. Sci 41, 963 (2006)
- 118. W. Jones, D. Thomas, D. Thomas, G. Williams, J. Mol. Struct. 708, 145 (2004)
- 119. P. Camorani, M. Fontana, Mol. Cryst. Liq. Cryst. 465, 143 (2007)
- S. Ensslin, K.P. Moll, T. Haefele-Racin, K. Mäder, Pharmaceutical Research 26, 1534–1543, (2009)
- 121. http://www.sandostatin.com
- 122. R. Langer, Nature **392**, 5 (1988)
- 123. M. van de Weert, W. Hennink, W. Jiskoot, Pharm. Res. 17, 1159 (2000)
- 124. A. Messaritaki, S. Black, C. van der Walle, S. Rigby, J. Control Release 108, 271 (2005)
- 125. S. Mao, J. Xu, C. Cai, O. Germershaus, A. Schaper, T. Kissel, Int. J. Pharm. 334, 137 (2007)
- 126. F. Sadeghi, J.L. Ford, M.H. Rubinstein, Drug Dev. Ind. Pharm. 27, 419–430 (2001)
- 127. K. Goracinova, L. Klisarova, A. Simov, Drug Dev. Ind. Pharm. 22, 255-262 (1996)
- 128. S. Lin, Curr. Ther. Res. Clin. 41, 564–573 (1987)
- 129. R. Rowe, J. Pharm. Pharmacol. 38, 214-215 (1986)
- 130. M. Saettone, G. Perini, P. Rijli, Int. J. Pharm. 126, 83 (1995)
- 131. M. Beck, I. Tomka, Macromolecules **29**, 8759 (1996)
- 132. J. Rau, Respir. care **50**, 367 (2005)
- 133. G. Crompton, J. Aerosol Med. 4, 151 (1991)
- A. Hickey, Pharmaceutical Inhalation Aerosol Technology (Marcel Dekker, New York, NY, 2004)
- 135. W.H. Finlay, *The Mechanics of Inhaled Pharmaceutical Aerosols: An Introduction* (Academic Press, London, 2001)
- 136. D. Wieckhusen, Chimia **60**, 598 (2006)
- 137. L. Augsburger, S. Hoag, *Pharmaceutical Dosage Forms: Tablets* (Informa HealthCare, London, 2008)
- M. Rubinstein, J. Wells, *Pharmaceutical Technology: Tableting Technology* (Ellis Horwood, Chichester, 1993)
- 139. D. Parikh, *Handbook of Pharmaceutical Granulation Technology* (Informa HealthCare, London, 2005)
- 140. K. Steffens, Pharma. Ind. 52, 1412 (1990)
- 141. G. Shearer, The Microscope **51**, 3 (2003)
- 142. X. Cao, Z. Wen, A. Vance, G. Torraca, G. Li, W. Jing, P. Masatani, C. Yee, Microsc. Microanal. 14, 1608 (2008)
- 143. M. Lankers, J. Munhall, O. Valet, Microsc. Microanal. 14, 1612 (2008)
- 144. J. Blanchard, J. Coleman, C. D'Abreu Hayling, R. Ghaderi, B. Haeberlin, J. Hart, S. Jensen, R. Malcolmson, S. Mittelman, L. Nagao, S. Sekulic, C. Snodgrass-Pilla, M. Sundahl, G. Thompson, R. Wolff, Pharm. Res. 21, 2137 (2004)

Chapter 9 Characterization of Therapeutic Coatings on Medical Devices

Klaus Wormuth

Abstract Therapeutic coatings on medical devices such as catheters, guide wires, and stents improve biocompatibility by favorably altering the chemical nature of the device/tissue or device/blood interface. Such coatings often minimize tissue damage (reduce friction), decrease chances for blood clot formation (prevent platelet adsorption), and improve the healing response (deliver drugs). Confocal Raman microscopy provides valuable information about biomedical coatings by, for example, facilitating the measurement of the thickness and swelling of frictionreducing hydrogel coatings on catheters and by determining the distribution of drug within a polymer-based drug-eluting coatings on stents. This chapter explores the application of Raman microscopy to the imaging of thin coatings of cross-linked poly(vinyl pyrrolidone) gels, parylene films, mixtures of dexamethasone with various polymethacrylates, and mixtures of rapamycin with hydrolysable (biodegradable) poly(lactide-co-glycolide) polymers. Raman microscopy measures the thickness and swelling of coatings, reveals the degree of mixing of drug and polymer, senses the hydrolysis of biodegradable polymers, and determines the polymorphic forms of drug present within thin therapeutic coatings on medical devices.

9.1 Background

The introduction of synthetic or modified natural materials ("biomaterials") into the human body for the treatment, augmentation, or replacement of tissue or organs presents significant challenges. First, the biomaterial must retain "biofunctionality" in the aggressive chemical, enzymatic, and mechanical stress environments within the human body. Second, the biomaterial must exhibit "biocompatibility" and thus not induce allergic, toxic, or carcinogenic reactions or create blood clots. Ideal biocompatibility means the body "accepts" the biomaterial: the surface of the implanted material induces the same biochemical reactions induced by tissues in the body [1, 2]. Unfortunately, most implanted materials react non-ideally with the body, inducing a cascade of biochemical processes. Tissues surrounding an implant often react as if an injury or infection had occurred, and inflammation cells attack the implant. In the typical positive scenario, biocompatibility occurs through creation of

204 K. Wormuth

a thin layer of fibrotic (scar) tissue without inflammation cells which encapsulates the implant and prevents further biochemical reactions [3].

The nature of the outer surface of the biomaterial influences the types of proteins which initially adsorb onto the implant surface and thus influences cellular responses to the implant. Both surface chemistry (charge, polarity, hydrophilicity) and surface morphology (roughness, mechanical compliance) play a role in cell-biomaterial interactions. In general, hydrophilic surfaces are more biocompatible than hydrophobic surfaces [1]. Surface modification of biomaterials through application of "therapeutic coatings," coatings, which induce beneficial healing effects, is one approach for improving the biocompatibility of medical devices.

Therapeutic coatings for medical devices fall into two categories: passive and active. Upon coating a hydrophobic material with a hydrophilic gel, "passive" therapeutic effects occur as the medical device surface now presents the surrounding tissue with a soft, porous, hydrophilic surface filled with body fluids. In the case of temporary use medical devices such as catheters or guide wires, hydrophilic gels improve the ability to maneuver the device through arteries by providing a slippery low friction and non-thrombogenic surface between the device and the blood vessel walls. In the case of implanted devices, healthy tissue often grows into hydrophilic gels [1].

"Active" therapeutic coatings result from binding biochemically active materials (proteins, biopolymers) onto surfaces, which hopefully induce the biochemical reactions to favor biocompatibility [2]. Another type of active therapeutic coating controls the release of a drug into the tissue surrounding a device with the goal of inducing the proper healing responses in a localized area around the device [4]. Local drug delivery (with controlled release) offers significant advantages over systemic drug delivery (injections or tablets) by maintaining drug dosage within the therapeutic window and reducing toxic side effects (Fig. 9.1). One highly successful example of an active therapeutic coating on a medical device is the "drug-eluting stent" [4].

One option in the treatment of atherosclerosis of the heart involves implantation of a stent (Fig. 9.2), a wire mesh, which when inserted into a blood vessel opens blockages and restores blood flow, while mechanically preventing the recollapse of the vessel. In some cases, stent implantation causes tissue damage and induces formation of excess scar tissue, which results in re-blockage of the artery

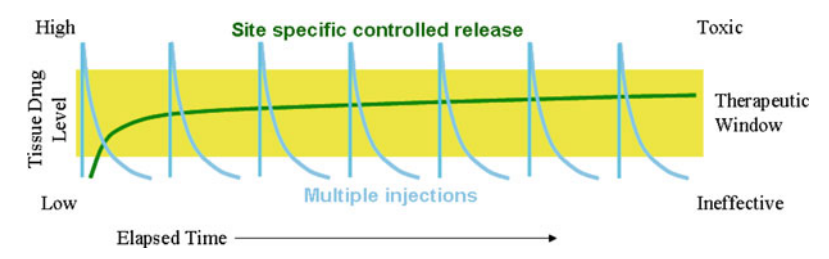


Fig. 9.1 Schematic illustration of drug level in tissue as a function of time. Comparison of multiple injections (*blue*) with site-specific controlled drug delivery (*green*)



Fig. 9.2 Brightfield microscopy image of drug-eluting stent (8-mm long Cordis Cypher stent)

(restenosis). Through delivery of an antiproliferative drug, such as rapamycin from a drug-eluting stent (a stent coated with a thin polymer coating containing drug), restenosis events are significantly reduced [4]. Formulation of drug-eluting coatings remains a challenge since the coating must be thin and conformal, the polymer matrix must be tailored to incorporate high concentrations of drug and to control the rate or release (elution) of the drug, and the coating must withstand the severe deformations of the stent wires, which occur upon insertion of the stent into the blood vessel. Once the drug has eluted, the healing process should result in encapsulation of the stent wires into healthy tissue within the walls of the blood vessel.

Critical to the development of a successful therapeutic coating is a thorough physical and chemical characterization of the coating prior to implantation (in vitro), along with characterization of the interaction of the coated medical device with tissue after implantation in the body (in vivo). For hydrophilic gel coatings, questions arise as to the coating thickness, uniformity of thickness, and degree of swelling. For drug-eluting coatings, additional questions arise as to the homogeneity of mixing of drug and polymer, the polymorphic form of the drug present, and the mechanisms by which the drug elutes from the polymer. As highlighted in this chapter, confocal Raman microscopy provides some insights and answers to these questions.

9.2 Passive Therapeutic Coatings

9.2.1 Coating Thickness

Coating thickness is sometimes surprisingly difficult to accurately measure. Coating durability, degree of swelling, and biochemical efficacy often correlate with coating thickness. From experience, various methods successfully measure coating thickness, but each method exhibits advantages and disadvantages. Confocal Raman microscopy provides one useful in situ method for the measurement of coating thickness.

Creation of a sharp step between coated and uncoated regions allows the step height (coating thickness) to be measured by electron microscopy, interferometry, or atomic force microscopy (AFM) methods. While creation of a clean, sharp step is sometimes possible via scraping or cryo-fracture, the method requires coatings with poor adhesion to the substrate or coatings, which have significantly different 206 K. Wormuth

mechanical properties compared to the substrate such that the coating partially cracks off the substrate and creates a step between coated and uncoated regions. However, the method does destroy the sample, and sampling—the ability to measure coating thickness at many locations to gain statistical confidence—is problematic.

If the refractive index of the coating differs significantly from that of the substrate (for example, polymer coatings on metal or glass), interferometric methods sometimes successfully measure coating thickness. In certain cases, the interference fringes created by light interacting with the air/coating interface and the coating/substrate interface may allow creation of images of the distribution of coating thickness over a region with nanometer vertical resolution (z) and optical resolution in x–y [5]. In commercially available instruments, the refractive index difference between substrate and coating must be significant (greater than about 0.5) and the coating must be thicker than 1 or 2 μ m for the method to be successful.

Confocal Raman microscopy also allows measurement of coating thickness of polymers on various substrates. For example, consider a coating of dry hydrophilic polymer (cross-linked poly(vinyl pyrrolidone)) on glass. A cross-sectional image created by mapping the intensity of the polymer Raman bands (carbon–hydrogen stretch region where air and glass exhibit no signal) indicates regions where polymer coating is present versus regions where polymer was scraped off the glass (no Raman signal) (Fig. 9.3). Note that the image was created using a

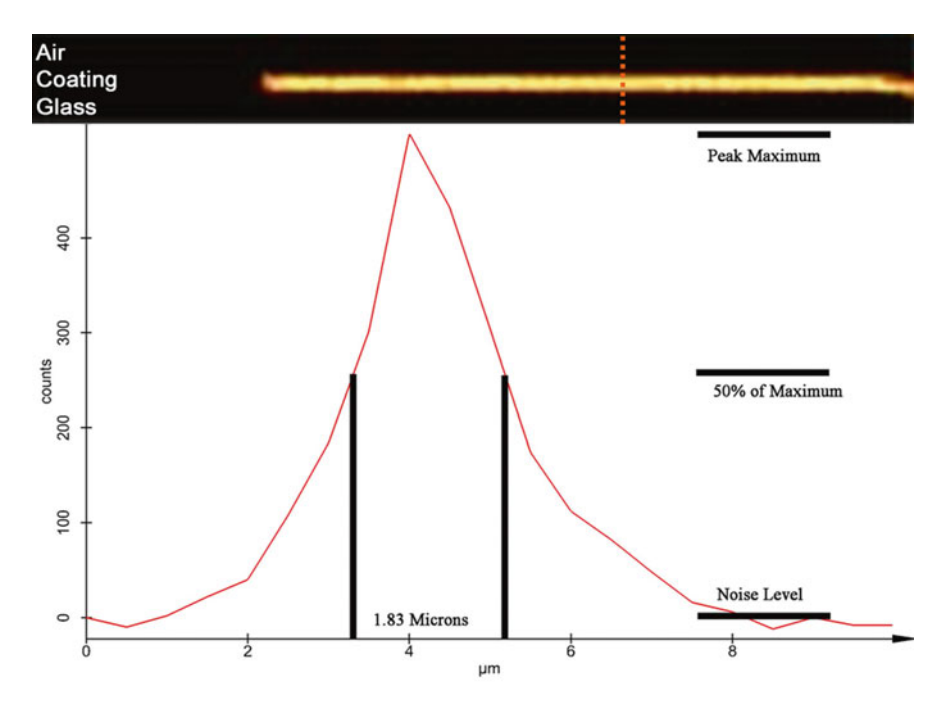


Fig. 9.3 *Top*: Raman microscopy cross-section image of poly(vinyl pyrrolidone) hydrogel coating on glass. *Bottom*: profile of Raman signal intensity (2800–3100 cm⁻¹ band) through coating along path indicated by *dashed red line*

 $100 \times$ microscope objective with a numerical aperture (NA) of 0.90 without application of immersion oil (dry). A plot of the integrated intensity as a function of vertical (z) distance over one section of this image shows a peaked curve (Fig. 9.3). Upon using the assumption that the actual interface appears at 50% of the maximum Raman intensity, the coating thickness in this region is determined to be about $1.8 \,\mu$ m (Fig. 9.3).

The 50% maximum intensity method is applied with the assumption that the vertical resolution at each interface in the confocal Raman measurement is at best about $0.5 \,\mu\text{m}$ but likely poorer [6, 7]. Despite the resolution limitations, the thickness measured by confocal Raman microscopy compares favorably with the values obtained in the AFM and interferometric methods, for both the coatings shown in Fig. 9.3 also for a similar sample with a slightly thicker coating (Table 9.1).

Especially for thicker samples, use of a dry microscope objective becomes problematic. Spherical aberrations occur at the interfaces between the microscope objective, air, and the sample, which compress the vertical axis in the measurement and result in significantly smaller values of coating thickness compared to those obtained from other methods [6, 7]. However, use of oil-immersion fluid to reduce spherical aberration is not practical for the polymer coatings examined here, since the coatings absorb immersion oil. Another way to approximately correct for spherical aberrations is to multiply the vertical scale of the confocal Raman measurement by the refractive index of the polymer (1.53 for poly(vinyl pyrrolidone)). For the coatings examined above, the "corrected" thickness values appear somewhat greater than those obtained with the AFM and interferometry methods, but still within the estimated resolution limits of the Raman method (Table 9.1).

Vapor deposition of parylene, a hydrophobic barrier polymer used in medical device applications, creates coatings of extremely uniform thickness [8]. Knowledge of the mass of coating applied, the density of the coating (1.283 g/cm³), and the dimensions of the substrate allow calculation of the expected coating thickness. For two significantly different coating weights applied to silicon wafers, the AFM and interferometry methods show general agreement with the calculated value of the coating thickness (Table 9.2). However, the Raman intensity method (50% of maximum) yields much smaller thickness values compared to calculated AFM and

Table 9.1 Coating thickness of poly(vinyl pyrrolidone) hydrogels on glass (μm)

Sample	AFM-step	I-step	I-thickness	Raman	Raman*
1	2.2	2.2	2.3	1.8	2.7
2	2.5	2.5	2.9	2.1	3.1

AFM-step = atomic force microscopy, height of step between coated and uncoated

I-step = interferometry, height of step between coated and uncoated
 I-thickness = interferometry thickness method (subtraction of fringes at interfaces)

Raman = 50% intensity method shown in Fig. 9.3, $100 \times$ dry objective (NA = 0.90)

Raman* = Raman value multiplied by refractive index of polymer (1.53)

208 K. Wormuth

		<u> </u>	1 /		(1	
Sample	Calculated	AFM-step	I-step	I-thickness	Raman	Raman*
Wafer 1	1.7	1.6	1.5	1.9	1.0	1.7
Wafer 2	5.5	**	4.9	5.2	2.8	4.6

Table 9.2 Coating thickness of parylene on silicon wafer (μm)

Abbreviations and descriptions as per Table 9.1

Average of five measurements per sample

interferometry results (Table 9.2). Here especially, correction for spherical aberrations by multiplication of the thickness value by the refractive index for parylene (1.66) results in coating thickness values, which compare favorably with the calculated values (Table 9.2).

For a set of even thicker coatings of poly(ethyl methacrylate) polymer (refractive index = 1.485) on steel substrates, the Raman and interferometry measurements correlate linearly, but again the Raman measurements (dry objective) underestimate the coating thickness significantly (Fig. 9.4).

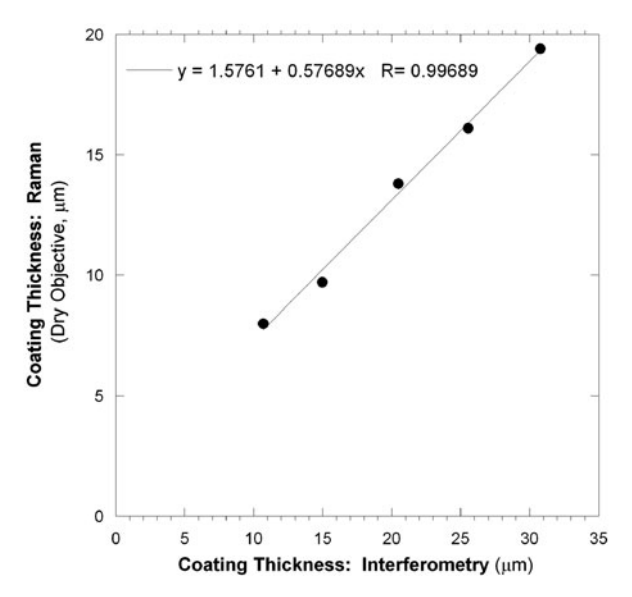


Fig. 9.4 Correlation of coating thickness as measured by Raman microscopy with coating thickness as measured by interferometry (thickness method) for coatings of poly(ethyl methacrylate) on steel

9.2.2 Swelling of Hydrophilic Gel Coatings

While use of an oil-immersion object to reduce spherical aberrations is not practical due to oil absorption, use of a water-immersion objective on cross-linked

^{*} Raman value multiplied by the refractive index of parylene (1.66)

^{**} Too thick to measure with AFM

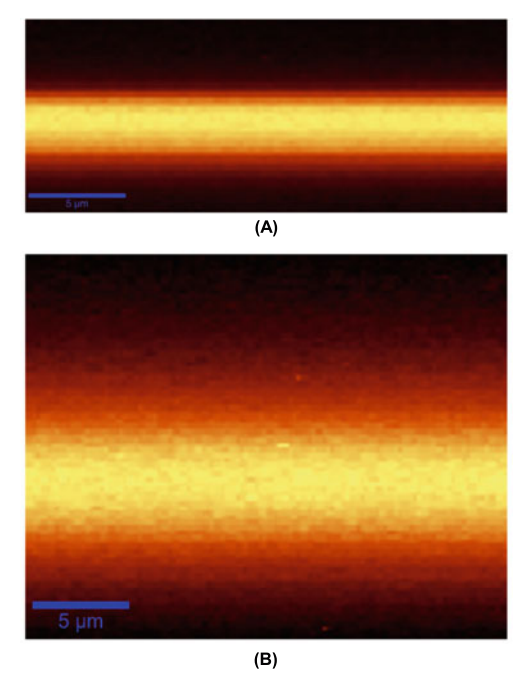


Fig. 9.5 (a) Raman microscopy cross-sectional image of a dry poly(vinyl pyrrolidone) coating on glass as imaged with a $100\times$ dry objective (NA = 0.90). (b) Raman microscopy cross-sectional image of a wet poly(vinyl pyrrolidone) coating on glass as imaged with a $60\times$ water-immersion objective (NA = 1.00)

hydrophilic gel coatings not only results in a reduction of spherical aberrations but also allows measurement of the water swelling behavior of a gel coating. Two different cross-linked poly(vinyl pyrrolidone) coating formulations on glass were imaged dry (dry objective $100\times$, NA = 0.90) and wet with water (water-immersion objective $60\times$, NA = 1.00). Upon soaking, the Raman signal from the coating (CH-stretch) decreases due to dilution of the coating with water, and the Raman signal extends much farther above the glass surface indicating the gel is swollen (Fig. 9.5).

From these images, thickness values were calculated, and the swelling ratio (wet thickness/dry thickness) estimated (Table 9.3). Formula 1 appears to be more cross-linked (swells less) than Formula 2 (Table 9.3).

Table 9.3 Swelling of poly(vinyl pyrrolidone) hydrogels

Formula	Thickness dry (µm)	Thickness wet (µm)	Swelling ratio
1	4.9	8.3	1.7
2	1.8	5.5	3.0

210 K. Wormuth

9.3 Active Therapeutic Coatings

9.3.1 Coating Morphology

The passive therapeutic coatings discussed above usually contain one type of cross-linked hydrophilic polymer. On the other hand, active therapeutic coatings for drug delivery are often blends of drug(s) with hydrophobic polymer(s). Coatings of drugs alone usually exhibit little mechanical strength and often release drug too quickly, but upon blending with polymers, good mechanical strength and controlled release of the drug are possible. Upon optimization of the drug–polymer interaction, the polymer should slow the diffusion of water into the coating and thus slow the diffusion of drug out of the coating.

Upon blending multiple ingredients, coating morphology (microstructure) becomes important. The degree of dispersion of drug within the coating influences the mechanical strength of the coating: coarse dispersion of drug likely yields weaker coatings since the drug itself exhibits little mechanical strength. Note that with fine dispersion, drugs may act as plasticizers [9].

The morphology of the coating also strongly influences the mechanisms and rate of drug elution. If the polymer provides a diffusional barrier to the drug, as the degree of mixing between drug and polymer increases, the rate of drug elution should slow. However, not only is mixing critical but also important is the physical form (polymorphic form) the drug assumes within the coating. Drugs may exist in various polymorphs: a non-crystalline (glassy) amorphous form, various crystalline forms with different crystal lattice spacings, or in a crystalline form incorporating some solvent or water (solvate or hydrate) [10]. These drug polymorphs may dissolve at different rates and thus influence the overall elution rate [10].

In particular, drug in the glassy amorphous form exhibits unique properties. Upon cooling molten liquid drug at a high cooling rate, a supercooled liquid may form, which upon further cooling freezes into a metastable glass (at a glass transition temperature). At lower rates of cooling, the drug will crystallize. Compared to the crystalline state, amorphous drug exhibits higher internal energy and thus may exhibit greater rates of dissolution, greater solubility, and greater bioavailability [10, 11]. However, the amorphous drug may also exhibit greater chemical reactivity along with a tendency to spontaneously crystallize [10, 11].

Recent work indicates that polymers can stabilize the amorphous state of a drug, but that the stabilization is kinetic rather than thermodynamic [12, 13]. The inherent solubility of drug in polymer is usually low, but significant supersaturation is possible in some cases. Polymers reduce molecular mobility and thus increase the kinetic barriers to crystallization [12, 13]. Note that an amorphous drug/polymer mixture might be a molecular "solution" of drug in polymer, but could be a dispersion of amorphous drug domains in polymer. In x-ray diffraction, amorphous drug and polymers appear as a background signal without sharp spectral features, which complicates separation of the components in a mixture. However, in Raman microscopy, amorphous drug, crystalline drug, and polymers often exhibit spectra

with unique spectral features, which allow separation of the signals and hence the corresponding components in the sample.

As demonstrated below, confocal Raman microscopy helps to answer the pharmaceutics questions regarding drug polymorph form within drug/polymer coatings. Raman microscopy shows the degree of mixing of drug within polymer matrices, and Raman spectra often uniquely fingerprint the polymorphic forms of drugs within coatings.

9.3.2 Drug Mixed with Single Polymer: Morphology and Elution

In an effort to better understand the relationships between the drug morphology (degree of mixing, polymorphs) and elution behavior, the steroid dexamethasone was mixed with a series of polymers whereby the hydrophobic nature of the polymer was systematically varied. Upon increasing the alkyl chain length of poly(alkyl methacrylate) polymers, the polymer becomes more hydrophobic. A series of poly(alkyl methacrylate) polymers ranging from poly(ethyl methacrylate) (alkyl chain length = 2) to poly(octadecyl methacrylate) (alkyl chain length = 18) were mixed with dexamethasone at 5, 15, and 33 wt% concentration and spray coated onto stents from solutions in the solvent tetrahydrofuran (THF).

At first the coatings were observed with an optical microscope under white light illumination. Using different modes (brightfield, darkfield, and polarized light), regions of clear and cloudy coating were identified, and the presence and frequency of birefringent (crystalline) regions qualitatively noted. The resulting "morphology map" plots the relationship between formulation variables (dexamethasone concentration and polymer type) and the observations from optical microscopy (Fig. 9.6).

Overall, the morphology map indicates that upon increasing dexamethasone concentration and/or increasing the alkyl chain length of the polymer, the appearance of the stent coatings progresses from clear to cloudy to birefringent (Fig. 9.6). In other words, drug/polymer miscibility decreases at higher drug concentrations and with more hydrophobic polymers.

Optical microscopy provides a low resolution overview of coating morphology, but Raman microscopy probes the nature of the clear/cloudy/birefringent morphologies at higher spatial resolution. Cross-sectional Raman images perpendicular to the stent wire allow mapping of the distribution of the ingredients in the stent coatings from the outer coating/air surface down to the inner coating/metal wire (stent) surface.

The micro-Raman spectrum obtained at a particular pixel in a Raman image of a stent coating contains information on the local composition of drug and polymer at that spatial location, along with information on the polymorphic form of the drug present. While the spectra of crystalline dexamethasone and, for example, poly(butyl methacrylate) polymer differ significantly with some unique peaks (Fig. 9.7), the spectra of the two polymorphs of dexamethasone (amorphous and crystalline) differ only subtly with no unique peaks (Fig. 9.8).

212 K. Wormuth

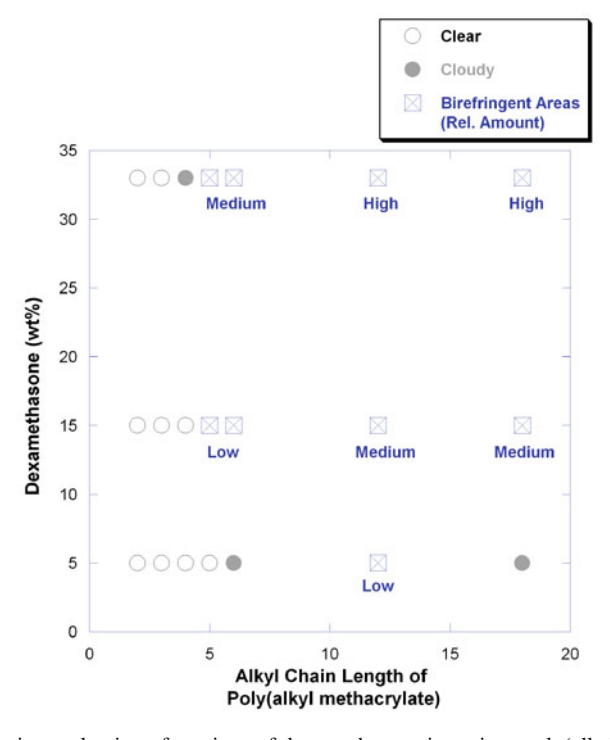


Fig. 9.6 Qualitative evaluation of coatings of dexamethasone in various poly(alkyl methacrylate) on stents via optical microscopy. Observations of clear, cloudy, and birefringence coatings as a function of dexamethasone concentration and alkyl chain length (carbon number) of the poly(alkyl methacrylate)

Thus, independent images of polymer, amorphous drug, and crystalline drug cannot be generated by simple peak integration. In the following, an augmented classical least squares method (aCLS) was applied to the full Raman spectral data set in order to deconvolute the image data into separate images of the distribution of the amorphous and crystalline polymorphs of dexamethasone within the polymer matrix [14].

Raman microscopic images were taken of the stent coatings prepared along the formulation path at fixed 33 wt% dexamethasone, but with varying alkyl chain length of the poly(alkyl methacrylate) (Fig. 9.6). Along this formulation path, the coating appearance transitions from clear to cloudy to birefringent (Fig. 9.6). Raman microscopy of the clear coatings at alkyl chain length of two or three carbons shows homogeneous mixing of amorphous drug within polymer. However, at an alkyl chain length of four carbons (poly(butyl methacrylate), PBMA), cloudiness appears and Raman microscopy indicates some segregation of amorphous drug and PBMA (Fig. 9.9).

This figure shows a cross-sectional image of the coating on a stent. Top of image shows air (dark, no Raman signal), middle of image shows coating (brightly

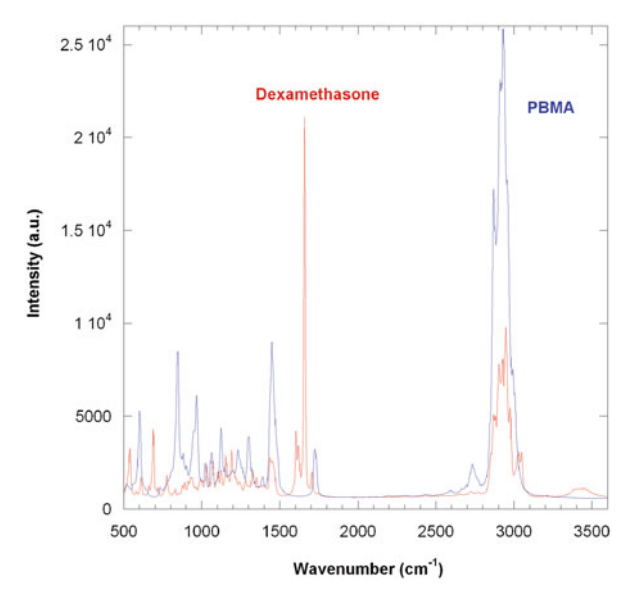
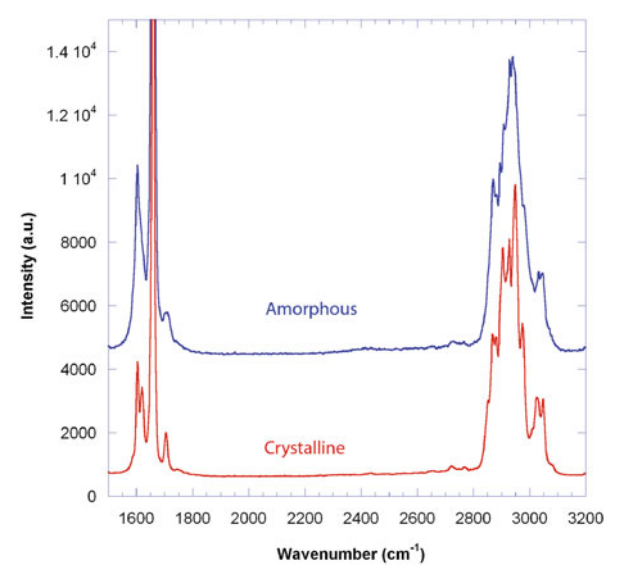


Fig. 9.7 Comparison of the Raman spectra of crystalline dexamethasone (red) and poly(butyl methacrylate), PBMA (blue)



 ${f Fig.~9.8}$ Comparison of the Raman spectra of amorphous (blue) and crystalline (red) dexamethasone

214 K. Wormuth



Fig. 9.9 Raman microscopic cross-sectional image of coating of 33 wt% dexamethasone in poly(butyl methacrylate) on stent. Red = amorphous dexamethasone, green = poly(butyl methacrylate). image dimension = $100 \times 10 \, \mu \text{m}$

colored), and bottom shows stent metal (dark, no Raman signal). In Fig. 9.9, two images are overlaid: an image of the Raman signal intensity from amorphous dexamethasone (color-coded red) and the image of Raman signal intensity from PBMA polymer (color-coded green). Raman signal intensity is proportional to concentration [15]. Thus, yellow regions (red plus green) are mixtures of dexameth-sone plus PBMA: yellow-green regions are relatively richer in PBMA and orange-yellow regions are relatively richer in dexamethasone (Fig. 9.9). From multiple observations, the regions of cloudier coating in optical microscopy correlate with regions of increased dexamethasone signal in Raman microscopy. While the Raman results indicate some segregation of amorphous dexamethasone into cloudy regions, the aCLS routine applied to the image data did not detect crystalline dexamethasone. Note that in optical microscopy the cloudy regions often appear bluish, which is indicative of scattering from small particulates. The cloudy regions may contain a dispersion of nano-sized amorphous domains or perhaps contain nano-sized crystalline domains below the detection limit of the Raman method.

Upon further increasing alkyl chain length to six (poly(hexyl methacrylate), PHMA) the morphology map indicates a significant transition to a "medium" amount of birefringence (Fig. 9.6). The birefringence likely arises from regions of crystalline drug within the coating. Two regions with birefringence were identified with the optical microscope and imaged with the Raman microscope.

In the Raman microscopic images of the two regions (Fig. 9.10), the Raman signal intensities are associated with three colors: red associated with amorphous drug, green associated with crystalline drug, and blue associated with polymer. The Raman images of the PHMA coatings show regions of crystalline drug (green),

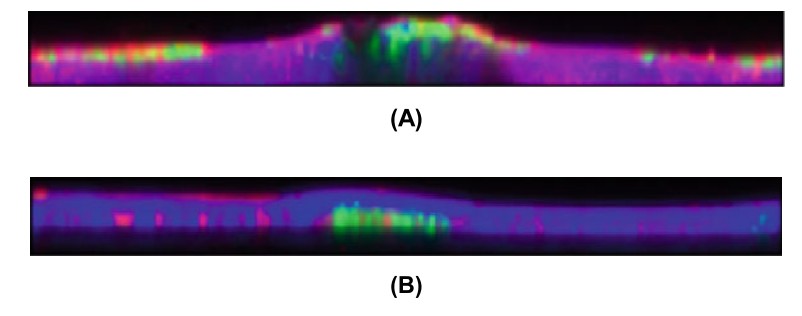


Fig. 9.10 Raman microscopic cross-sectional images of two different birefringent regions of coating of 33 wt% dexamethasone in poly(hexyl methacrylate) on stent. (a) Crystals near outer coating surface: red = amorphous dexamethasone, green = crystalline dexamethasone, blue = poly(hexyl methacrylate). (b) Crystals near inner stent surface: red = amorphous dexamethasone, green = crystalline dexamethasone, Blue = poly(hexyl methacrylate). Image dimension = $100 \times 10 \,\mu m$

which correlate with the birefringence observed in optical microscopy (Fig. 9.10). Note, however, that the Raman images distinguish two types of crystalline behavior: crystalline drug present at the outer coating/air surface (Fig. 9.10a) or crystalline drug present at the inner coating/metal surface (Fig. 9.10b). Certainly the two types of crystals will elute differently, since "crystal A" is not covered by a polymer diffusional layer, whereas "crystal B" is.

For the region with crystalline drug near the outer coating/air surface, a bulge appears in the coating. At the bulge, the laser light in the Raman experiment is scattered strongly by the crystals, light does not penetrate below the crystals, and thus the interior region under the crystals appears dark (no Raman signal). On both sides of the bulge in the coating the coating is transparent, and lavender (purple)-colored regions indicate significant mixing of amorphous drug (red) with polymer (blue) along with some additional surface segregation of drug into amorphous (orange-red) and crystalline (green) phases.

For the region with crystalline drug near the inner coating/metal interface, a smaller bulge also appears over the crystalline region, and amorphous drug is mixed into the surrounding polymer, along with some surface segregation of amorphous drug present at both the inner and outer surfaces (Fig. 9.10). These images from confocal Raman microscopy yield microstructural information rich in detail, showing the spatial relationships between polymer and the amorphous and crystalline drug regions.

The microstructure revealed by Raman microscopy does correlate with drug elution. Along the path with fixed 33 wt% dexamethasone, upon increasing the alkyl chain length, the overall elution rate increases (Fig. 9.11).

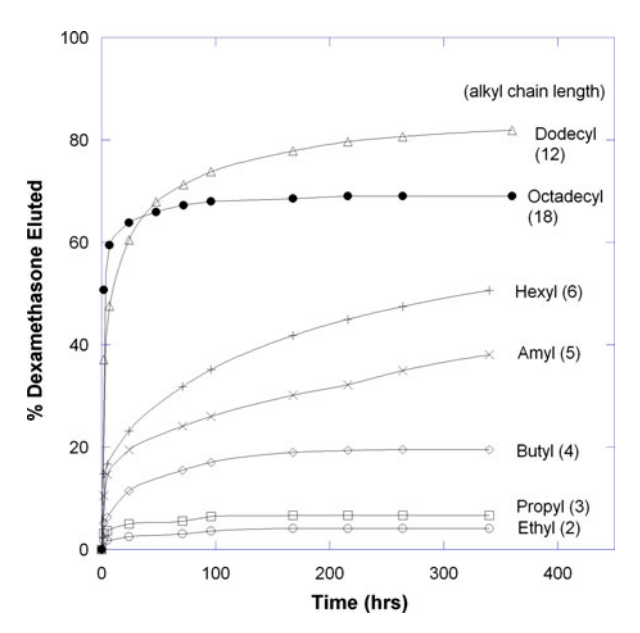


Fig. 9.11 Amount of dexamethasone eluted as a function of time for coatings of 33 wt% dexamethsone in various poly(alkyl methacrylates) on stents

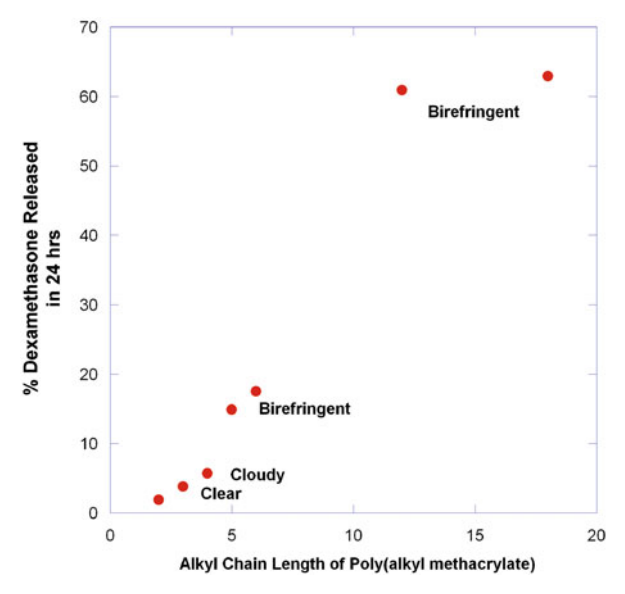


Fig. 9.12 Percent of dexamethasone eluted in the first 24 h ("burst") from coatings of 33 wt% dexamethasone in various poly(alkyl methacrylates) on stents as a function of the alkyl chain length (carbon number) of the polymer

Note that two components of the elution curves are important: the initial amount of drug released in the first 24 h ("burst") and the rate of release of drug thereafter. The burst increases significantly as amorphous drug crystallizes and separates (demixes) from the polymer, and the polymer is less able to provide a diffusional barrier to the drug (Fig. 9.12).

After the initial burst, the slopes of the elution curves generally increase as alkyl chain length is increased, indicative of increasing diffusivity of the drug within the polymer matrix (Fig. 9.11). Indeed, with increasing alkyl chain length the glass transition temperature decreases systematically for these poly(alkyl methacrylates) and thus the free volume within the polymers increases, which is the likely origin of the increase in elution rate [16]. Note the exception of poly(octadecyl methacrylate). In this case, the octadecyl side chains are now long enough to crystallize and thus inhibit drug diffusion (Fig. 9.11).

9.3.3 Drug Mixed with Two Polymers: Blending and Layering

In some cases, performance advantages occur upon blending or layering polymers. A reinforced polymer matrix results upon mixing a rubbery polymer with a brittle polymer. A less sticky coating surface results upon layering a non-sticky polymer over the top of a sticky polymer. When mixing drug into blended or layered polymers, various "phases" are possible: amorphous drug mixed into the first polymer or amorphous drug mixed into the second polymer or separate phases of pure drug in crystalline or amorphous form. Raman microscopy allows determination of the

partitioning of amorphous drug between multiple polymers or the distribution of drug between layers of polymers.

Consider mixtures of dexamethasone blended into poly(butyl methacrylate) (PBMA), a hard polymer with a high glass transition temperature, and poly(dodecyl methacrylate) (PDMA), a soft polymer with a low glass transition temperature. At a weight ratio of 43.5/43.5/13 of dexamethasone/PBMA/PDMA, a thick layer of coating solution in THF was cast onto a glass slide and allowed to dry slowly with the goal of creating relatively large regions of phase separation. A Raman microscopic planar image of the coating shows round domains of PDMA (blue) dispersed in a continuum of amorphous dexamethasone (red) mixed with PBMA (green) which appears yellow-green and orange (Fig. 9.13). Note that upon closer inspection, some small regions of PDMA mixed with amorphous dexamethasone (purple) appear within the predominantly PDMA (blue) regions (Fig. 9.13).

Integration of the micro-Raman spectra over the imaged regions clearly shows the strong preferential partitioning of amorphous dexamethasone into the PBMA-rich phase: The strong dexamethasone Raman peak at 1660 cm⁻¹ appears substantially larger in the PBMA-rich regions than in the PDMA-rich regions (Fig. 9.14).

Compared to the slowly drying cast film examined above, a much faster drying process occurs upon spray coating a stent, since multiple thin layers of dried spray droplets are sequentially applied to build up a thick coating. Upon first spray coating the same formulation as discussed above, dexamethasone/PBMA/PDMA, onto a stent, and then overcoating with PBMA alone, a highly microstructured coating is created (Fig. 9.15). With the same color coding as noted above (amorphous dexamethasone = red, PBMA = green, PDMA = blue), the two-layer coating exhibits three distinct microstructures: a green PBMA-rich layer at the top outer surface of the coating, a yellow-orange PBMA plus dexamethasone layer at the base of the coating, along with blue PDMA-rich blobs dispersed throughout the coating. Surprisingly, the PDMA blobs also appear in the outer PBMA-rich layer, indicating

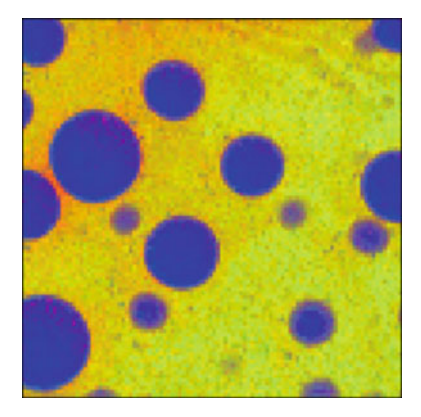


Fig. 9.13 Raman microscopic image of a 43.5/43.5/13 by weight coating of dexamethasone/PBMA/PDMA cast onto glass. Planar image of coating, parallel to glass substrate. Red = amorphous dexamethsone, green = PBMA, blue = PDMA. Image dimension = $100 \times 100 \, \mu \text{m}$

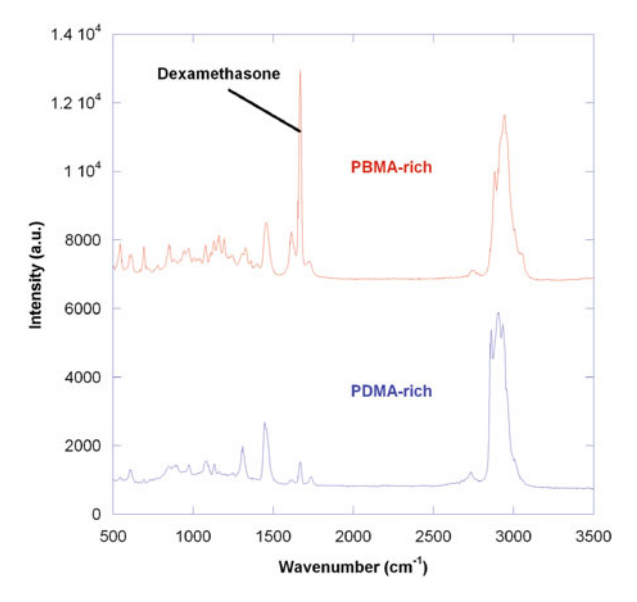


Fig. 9.14 Average micro-Raman spectra obtained for regions rich in PBMA and for regions rich in PDMA from the Raman microscopic image shown in Fig. 9.13

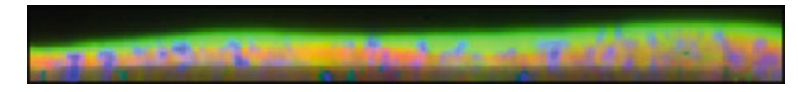


Fig. 9.15 Raman microscopic cross-sectional image of twolayer coating on stent. *Bottom coating layer*: 43.5/43.5/13 wt% dexamethasone/PBMA/PDMA; *top coating layer*: 100 wt% PBMA; red = 20 amorphous dexamethasone, green = PBMA, blue = PDMA; image dimension $= 120 \times 12$ µm

some intermixing between the bottom dexamethasone/PBMA/PDMA layer and the top PBMA layer (Fig. 9.15). The spray coating exhibits similar phase separation to that found in the cast films, albeit at a smaller length scale: small domains of PDMA-rich regions dispersed within a continuum rich in both PBMA and dexamethasone. In addition to the amorphous regions discussed above, a few birefringent regions were found in the stent coatings of dexamethasone/PBMA/PDMA overcoated with PBMA. One of these birefringent regions was imaged in order to determine the distribution of amorphous and crystalline drug within the PBMA/PDMA blend. Since it is difficult to simultaneously overlay images of all four components, three images were created for comparison purposes: a first image showing the relationship of the two drug forms (Fig. 9.16a), a second image showing the relationship of the two polymers (Fig. 9.16b), and a third image showing the relationships between amorphous drug and the two polymers (Fig. 9.16c).

Clearly the first two images show that amorphous and crystalline drug sharply segregate and that the two polymers sharply segregate into blobs and layers (Fig. 9.16). Around the crystalline region, the Raman microscopic images reveal

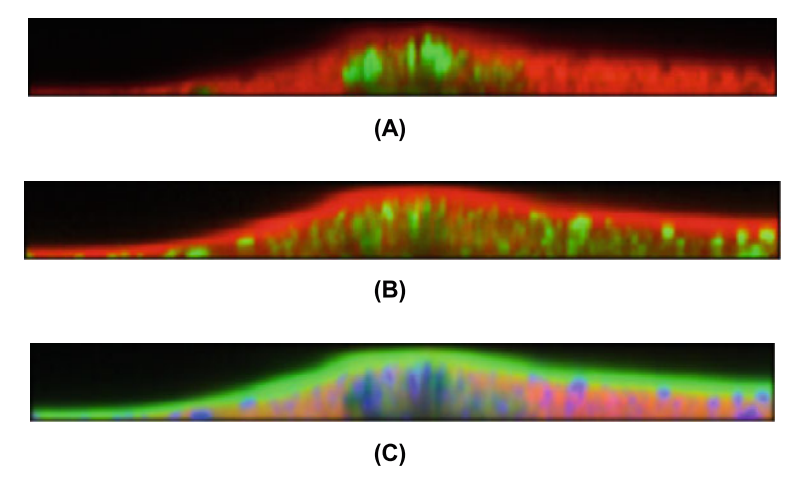


Fig. 9.16 Raman microscopic cross-sectional images of two-layer coating on stent. *Bottom coating layer*: 43.5/43.5/13 wt% dexamethasone/PBMA/PDMA; *top coating layer*: 100 wt% PBMA; (a) red = amorphous dexamethasone, green = crystalline dexamethasone; (b) red = PBMA, green = PDMA; (c) red = amorphous dexamethasone, green = PBMA, green = PDMA; image dimensions = $120 \times 12 \, \mu m$

a microstructure similar to that found in Fig. 9.15: a PBMA-rich layer (green) on top of a PBMA plus dexamethasone layer (yellow-orange), along with dispersed PDMA-rich blobs (blue) (Fig. 9.16). As found within the drug/single polymer mixtures, in the drug/multiple polymer mixtures birefringence is correlated with crystalline regions which appear within bumps (thicker regions) in the coating.

From the comparison of Fig. 9.16(a) and (b), it appears that the crystals formed in regions richer in PDMA than PBMA. As implied in all the results from both cast films and spray coatings, and also in the morphology map of dexamethasone in single polymers, dexamethasone appears much less "soluble" in PDMA than PBMA, and thus dexamethsone likely crystallizes (separates out) at much lower concentrations in PDMA than in PBMA. And, as discussed in the next section, if the drug becomes mobile, regions of PDMA could act as nucleation sites for the transition from amorphous to crystalline dexamethasone.

9.3.4 Drug Mixed with Two Polymers: Exposure to Water

Spin coatings of dexamethasone/PBMA/PDMA on silicon wafers also create the same morphology observed in cast coatings on glass: round PDMA-rich regions dispersed in PBMA plus dexamethasone. However, in spin coatings the size of the PDMA-rich regions is smaller and the overall coating thinner than found for the cast film coatings. In an effort to better understand the early stages of the drug elution process, a spin coating of dexamethasone/PBMA/PDMA was submerged in water and imaged using a water-immersion objective. A first Raman image shows the relationship of the two drug forms (Fig. 9.17a), and a second Raman image shows the relationship of the two polymers (Fig. 9.17b).

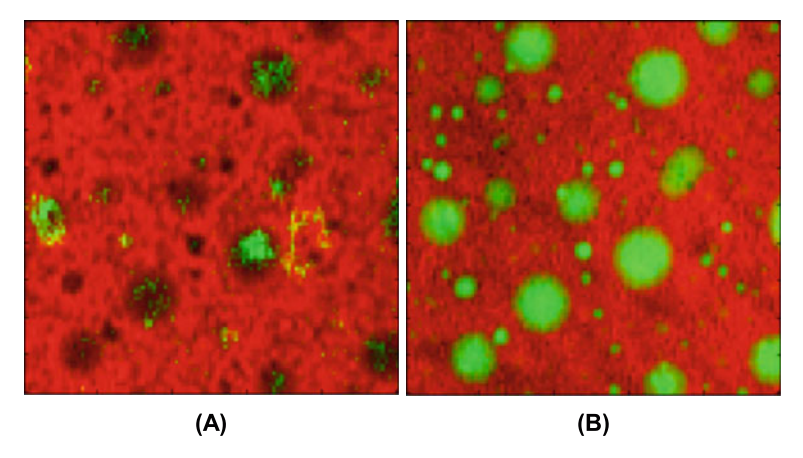


Fig. 9.17 Raman microscopic images of a 43.5/43.5/13 by weight coating of dexamethasone/PBMA/PDMA. Spin coating on silicon wafer soaked for 1 h in water and imaged with water-immersion objective. Planar image of coating, parallel to wafer substrate. (a) Red = amorphous dexamethasone, green = crystalline dexamethasone. (b) Red = PBMA, green = PDMA. Image dimensions = 25 × 25 μ m

Small crystals of drug appeared in the coating upon exposure to water for about 1 h (Fig. 9.17). However, as Raman microscopy shows, the crystals appear non-uniformly over the coating surface: most of the crystals formed in locations which were PDMA rich (Fig. 9.17). Apparently, even though a much higher concentration of amorphous dexamethasone mixes with PBMA than with PDMA, the amorphous dexamethasone present in PDMA-rich regions is less stable upon exposure to water and crystallizes readily upon exposure to water for relatively short periods of time. Water is a strong plasticizer and only small amounts of water are required to reduce the glass transition temperature of an amorphous drug or polymer [10].

In summary, for coatings of dexamethasone in PBMA/PDMA blends, dexamethasone appears much more miscible with PBMA than PDMA. Upon mixing dexamethasone in both PBMA and PDMA simultaneously, dexamethasone preferentially partitions into PBMA at a relatively high concentration compared to PDMA (Fig. 9.14). Following exposure of these mixtures to water, crystals of dexamethsone nucleate within PDMA-rich regions (Fig. 9.17).

9.3.5 Drug Mixed with Biodegradable Polymer: Drug Elution with Polymer Degradation

In some cases, the interaction between human tissue and metal yields better biocompatibility than the interaction between tissue and polymer. "Biodegradable" polymers coated onto stents initially control the elution of drug and then erode away, leaving a bare metal surface. Biodegradation occurs through hydrolysis or enzymatic degradation which breaks the polymer into small molecular fragments [17]. Here a common biodegradable polymer, poly (D,L lactide-co-glycolide) or PLGA was mixed with a high concentration (50 wt%) of the drug rapamycin, spray coated onto stents, and the coated stents soaked in buffer at 37°C. Note that a recently published study on similar mixtures compared the results of x-ray photoelectron spectroscopy (XPS) and time-of-flight secondary ion mass spectrometry (ToF-SIMS) with results from Raman microscopy [18].

Prior to soaking, the 50/50 rapamycin/PGLA coating appeared somewhat cloudy, and cross-sectional Raman microscopic images show some segregation of amorphous rapamycin from the PLGA polymer, with no crystalline rapamycin present (Fig. 9.18). After soaking in buffer for 10 days, chemical analysis of the drug content of the buffer indicated that more than 50% of the drug eluted from the coating. Raman microscopy confirms the chemical analysis: after soaking for 10 days, the average Raman signal due to rapamycin decreases substantially compared to the average signal found prior to soaking, over the regions of the coating imaged with Raman microscopy (Fig. 9.19).

However, Raman microscopic images indicate that the elution is non-uniform: after soaking, the coating exhibits significant non-uniformities in the distribution of the remaining amorphous rapamycin (Fig. 9.18). Note that the rapamycin does not crystallize during elution and that no pores or voids appear in the coatings. Upon soaking, not only does drug elute by diffusion, but water also penetrates into the coating. The addition of water likely reduces the glass transition temperature of the PLGA, which perhaps allows "healing" of the polymer as drug elutes.

Comparison of the Raman images before and after soaking for 10 days suggests that some decrease in coating thickness occurs (Fig. 9.18). The thickness decrease could be due to biodegradation of PLGA, but is more likely due to elution of significant volumes of rapamycin. After soaking for an additional 22 days (total of 32 days), coating thickness continues to decrease. However, the average Raman spectrum over imaged regions of the coating shows no evidence for chemical changes in the PLGA polymer (Fig. 9.20). Upon hydrolysis, the molecular weight of the polymer remaining in the coating probably decreases [17, 19]. The Raman spectrum of PLGA will change with changes in the copolymer composition and polymer crystallinity, but is not sensitive to changes in molecular weight [20]. Comparison of the Raman spectrum of the coating after soaking for 32 days with

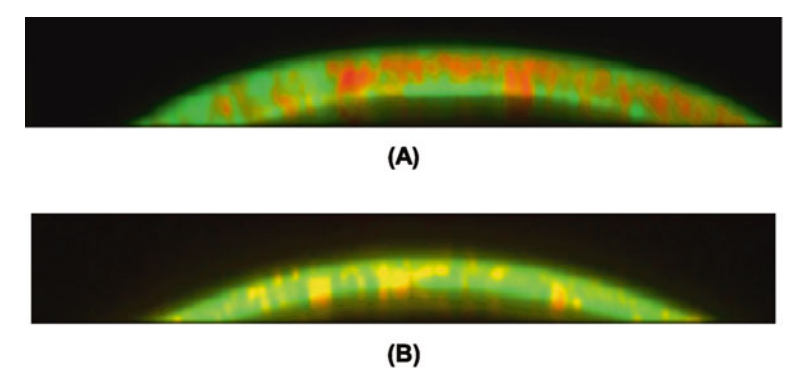


Fig. 9.18 Raman microscopic cross-sectional images of 50 wt% rapamycin in PLGA coated onto a stent. (a) Prior to soaking in buffer. (b) After soaking in buffer for 10 days at 37°C. Image dimensions = $70 \times 30 \ \mu m$

222 K. Wormuth

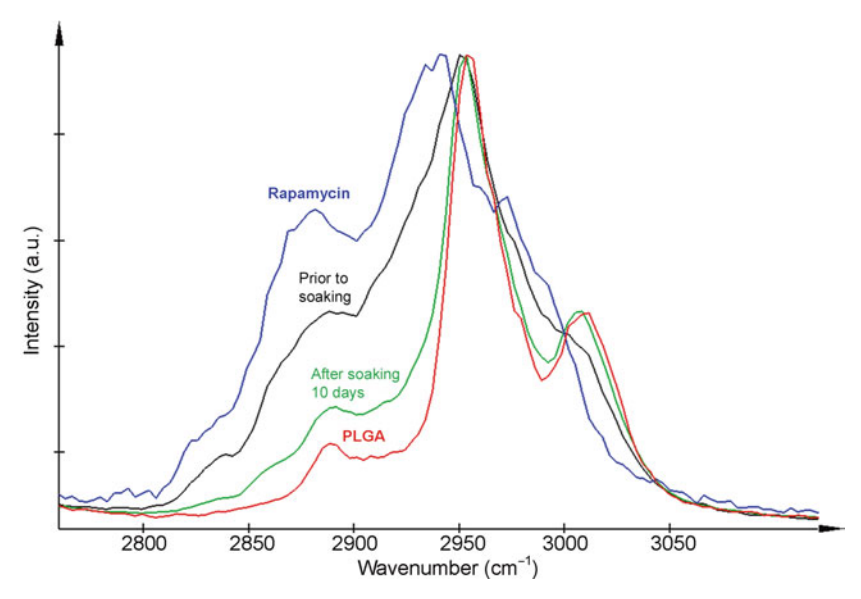


Fig. 9.19 Average micro-Raman spectra over the regions imaged in Fig. 9.18. Comparison of the spectra of coatings of 50 wt% rapamycin in PLGA prior to soaking and after soaking for 10 days with the spectra of rapamycin and PLGA standards

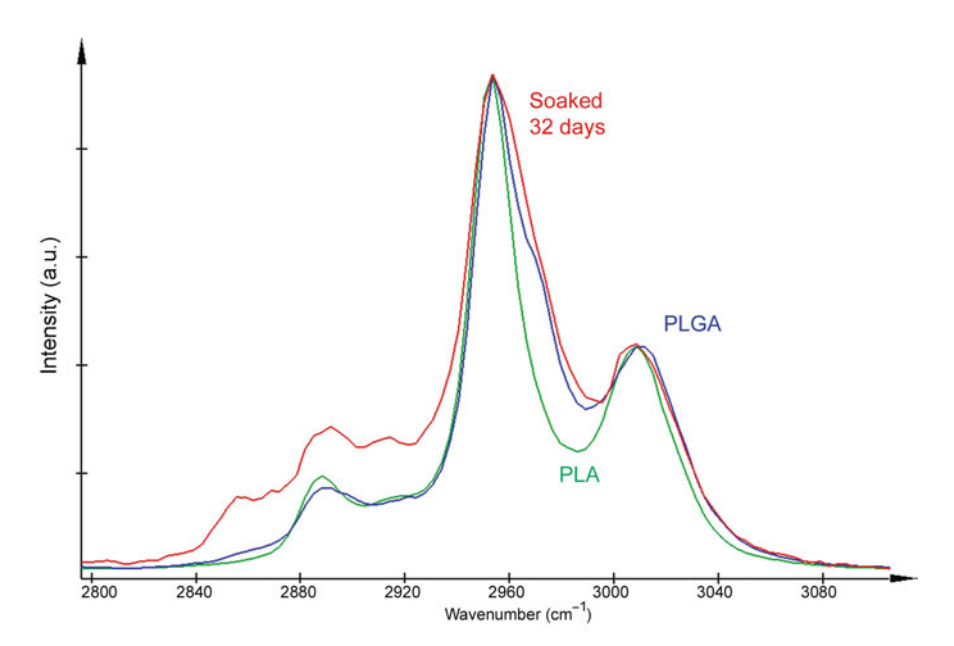


Fig. 9.20 Comparison of the Raman spectra of PLA and PLGA standards with the average micro-Raman spectra over an imaged region of a stent coating (50 wt% rapamycin in PLGA coating on stent soaked in buffer for 32 days at 37°C)

the spectra of PLGA polymer (50/50 lactide/glycolide) and poly(D,L lactide) (100/0 lactide/glycolide) suggests no preferential hydrolysis of glycolide or lactide.

9.4 Summary

In many cases, therapeutic coatings on medical devices provide significant clinical benefits by mediating device/tissue and device/blood interactions. In the development of therapeutic coatings, significant challenges arise in meeting biocompatibility, durability, and other performance criteria. As shown in this chapter, confocal Raman microscopy of therapeutic coatings yields important information on the coating thickness, degree of swelling, degree of dispersion of drug, and the polymorphic forms of drugs present within the coatings. Such information helps in the elucidation of the mechanisms by which hydrophilic gel coatings swell, reduce surface friction, and increase blood compatibility. This further helps in the elucidation of the mechanisms by which drug elutes from coatings on stents and how biodegradable coatings on stents erode with time. In particular, confocal Raman microscopy allows characterization of the materials science and pharmaceutics aspects of the amorphous form of drugs. Drug in amorphous form presents both benefits and challenges and is difficult to characterize with methods other than confocal Raman microscopy.

References

- B. Ratner, A. Hoffman, F. Schoen, J. Lemons, Biomaterials Science: An Introduction to Materials in Medicine, 2nd edn. (Academic, San Diego, London, 2004)
- 2. B. Ratner, S. Bryant, Annu. Rev. Biomed. Eng. 6, 41 (2004)
- 3. D. Klee, H. Höcker, Adv. Polym. Sci. 149, 1 (1999)
- P. Serruys, A. Gershlick, Handbook of Drug-Eluting Stents (Taylor & Francis, London, New York, NY, 2005)
- 5. G.H. Kim, S.W. Kim, Appl. Opt. 38, 5968 (1999)
- 6. N. Everall, Spectroscopy 19, 22 (2004)
- 7. T. Bridges, M. Houlne, J. Harris, Anal. Chem. 76, 576 (2004)
- 8. J. Fortin, T. Lu, *Chemical Vapor Deposition Polymerization* (Kluwer Academic, Dordrecht, 2003)
- 9. F. Siepmann, V.L. Brun, J. Siepmann, J. Control. Release 115, 298 (2006)
- 10. R. Hilfiker, Polymorphism in the Pharmaceutical Industry (Wiley-VCH, Weinheim, 2006)
- 11. B. Hancock, G. Zografi, J. Pharm. Sci. 86, 1 (1997)
- 12. H. Konno, L. Taylor, J. Pharm. Sci. 95, 2692 (2006)
- 13. P. Marsac, S. Shamblin, L. Taylor, Pharm. Res. 23, 2417 (2006)
- 14. D. Haaland, E. Thomas, Anal. Chem. 60, 1193 (1988)
- 15. M. Pelletier, Appl. Spectrosc. **57**, 20A (2003)
- 16. M. Beiner, K. Schröter, E. Hempel, S. Reissig, E. Donth, Macromolecules 32, 6278 (1999)
- 17. J. Anderson, M. Shive, Adv. Drug Deliv. Rev. 28, 5 (1997)
- 18. A. Belu, C. Mahoney, K. Wormuth, J. Control. Release 126, 111 (2008)
- 19. A. Hausberger, P. DeLuca, J. Pharm. Biomed. Anal. 13, 747 (1995)
- 20. G. Kister, G. Cassanas, M. Vert, Polymer 39, 3335 (1998)

Chapter 10 Raman Imaging of Plant Cell Walls

Notburga Gierlinger

Abstract To gain a better understanding of plant cell walls, several microscopic and chemical methods have been used for their analysis in recent years. However, a knowledge gap exists about the location, quantity, and structural arrangement of molecules on the micrometer scale within the native cell wall. Advances in confocal Raman microscopy and imaging have tackled this problem in a non-invasive way and provide chemical and structural information in situ with a high spatial resolution ($<0.5 \ \mu m$).

Examples of high-resolution Raman imaging on wood cells are given, showing that changes in polymer chemistry and orientation can be followed within and between different cell wall layers. In horsetail (*Equisetum hyemale* [E. Hyemale]) tissue, in addition to the mapping of plant cell wall polymers, the distribution of amorphous silica is investigated. Area scans from a cross-section are included as well as a depth profiling within a silica-rich knob on the outer stem wall.

10.1 Introduction

To gain a better understanding of plant cell walls several microscopic and chemical methods have been applied during the last years. However, a knowledge gap exists concerning the location, quantity, and structural arrangement of molecules on the microlevel in the native cell wall. Advances in confocal Raman microscopy and the imaging approach have tackled this problem in a non-invasive way and provide chemical and structural information in-situ with a high spatial resolution ($<0.5\mu$ m). Examples of high-resolution Raman imaging are given on wood cells, showing that changes in polymer chemistry and orientation can be followed within and between different cell wall layers. Chemical images are based on the changes of the integral intensity or band width of Raman bands attributed to specific plant cell wall polymers and cellulose orientation. In addition to the mapping of the plant cell wall polymers, the distribution of amorphous silica is followed and chemical imaging based on a partial least square fit with model spectra (basis analysis) is shown in horsetail tissue (*Equisetum hyemale*).

10.2 Plant Cell Walls

Plant cell walls are complex and dynamic structures and determine cell and plant shape [1]. Built up by incorporation of photosynthetically fixed carbon they represent the most abundant source of terrestrial biomass and renewable energy. Furthermore they are of practical importance for human and animal nutrition and as a source of natural fibers for textiles, materials, and paper products. The understanding of plant cell walls is thus of high interest for many practical applications, from both the scientific and biomimetic view, as nature has evolved a big pool of plant cell walls differing in properties according to the desired needs. On a broad view two types of cell walls can be distinguished: primary walls are deposited during cell growth and secondary cell walls after cell growth has ceased. Primary cell walls need to be both mechanically stable and sufficiently extensible to permit cell expansion while avoiding the rupture of cells under their turgor pressure and consist mainly of polysaccharides that can be broadly classified as celluloses, hemicelluloses, and pectins. The latter two classes of cell wall components are often referred to as matrix polysaccharides. Secondary cell walls are deposited after the cessation of cell growth and confer mechanical stability upon specialized cell types such as xylem elements and sclerenchyma cells. These walls represent composites of celluloses and hemicelluloses and are often impregnated with lignins, an aromatic system composed of phenylpropane units [2–4]. Crystals of cellulose form the microfibrillar foundation in all plant cell walls. Although native cellulose, termed cellulose I, has been one of the most studied subject in polymer science, the biosynthesis and ultrastructure of cellulose are not yet completely resolved [5-8]. The deceptive simplicity of the repeating β -1–4 linking cellobiose unit is not indicative of the complex arrangement of amorphous and crystalline regions at the fibril and fiber level. Within the plant cell wall cellulose is embedded in the matrix polymers, which play an important role in the development of the cell wall [9, 10] as well as for its final properties. The polysaccharidic matrix polymers, the hemicelluloses, and the pectins comprise a variety of different chemical configurations as well as the lignin, the polyphenolic incrusting polymer in secondary plant cell walls.

Furthermore the secondary plant cell wall of wood consists of different sublayers (S1, S2, and S3) formed at different periods during cell differentiation [11]. The S2 layer is the thickest (75–85% of the total thickness of the cell wall) and most important for mechanical stability [12]. Between adjacent cells, a middle lamella layer attached to the primary cell wall ensures the adhesion of a cell to its neighbors. The chemical composition of the cell wall and the alignment of the cellulose microfibrils in the different sublayers show significant inter- and intraspecies variability and determine the different cell wall properties [13].

Most traditional chemical analyses of plant cell walls are destructive, since they require disintegration of the plant tissue. But the functional characteristics of cell walls depend not only on the composition of the cell wall polymers but also on the fine details of their macromolecular structure and conformation and on their highly ordered architecture at scales from a few nanometers to several microns. Much of this fine detail is lost when cell wall polymers are fractionated and/or solubilized

to be examined by the classical chemical techniques. In addition, sample isolation difficulties arise when small cell wall areas or single layers are of interest, since they have to be carefully excised.

The combination of Raman and infrared spectroscopy with microscopy has developed as an important set of tools in plant cell wall research [14–22], as they allow to acquire information concerning the molecular structure and composition in a native state. Raman microspectroscopy has the advantage that spectra can be acquired on aqueous, thicker yet not opaque samples with a higher spatial resolution. But the impedance of sample autofluorescence, which may hinder the analysis or constrain the quality of the spectra, limited applications on plant tissues, until the development of the NIR-FT (near-infrared Fourier-transformed)-Raman technique [23]. For mapping and imaging of whole plant organs (seeds, fruits, leaves) the lateral resolution (10 μ m) of the NIR-FT technique is adequate [24–26], whereas for investigations on the lower hierarchical level of cells and cell walls the high resolution gained with a visible laser-based system is needed.

10.3 Micro-Raman Spectroscopy of Plant Fibers

Raman applications on plants began with the investigation of cellulose [27–29]. During the last decade micro-Raman spectroscopy was successfully applied to investigate non-destructively different types of natural cellulosic plant fibers, e.g., flax [19, 30–34], cotton [31, 35], jute, ramie, kapok, sisal, and coconut fibers [31]. Studies comprise general characterization of fibers [19, 31] as well as analysis of the molecular changes during mechanical processing [36], tensile deformation [37, 38], and chemical treatments [32]. Furthermore the preferential orientation of the functional groups of plant polymers was derived from the response of the relative intensities of characteristic bands with changing polarization of the incident exciting radiation relative to the fiber axis [20, 29]. In plant fibers the intensity of most of the Raman bands assigned to cellulose is strongly dependent on its preferential orientation along the fiber in relation to the polarization direction of the incident exciting radiation. By investigating polarization-dependent spectral changes on a fiber with known parallel cellulose microfibril orientation, interpretation and calibration regarding cellulose orientation can be derived for unknown samples and imaging results. Ramie (Boehmeria nivea) represents such a model system, as it is composed of almost pure cellulose oriented parallel along the fiber axis. Spectral changes in dependence of the angles of the incident laser polarization were investigated. The most pronounced changes are found for the bands at 1097 and 2898 cm⁻¹ (Fig. 10.1). These are assigned to $\nu_s(C-O-C)$, mainly related to $\beta(1\rightarrow 4)$ glycosidic linkages of the cellulose skeletons, and ν (CH) and ν _s(CH₂) modes of the glucopyranose rings and to the methylene groups of the glucopyranose side chain, respectively [39, 40]. The effect of orientation has to be taken into account in the data analysis, when spectra of native plant cell walls are acquired with polarized laser irradiation; this is also true for Raman imaging experiments.

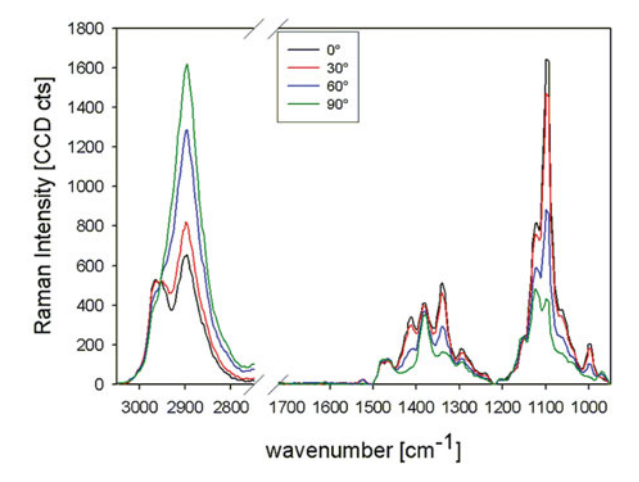


Fig. 10.1 Baseline-corrected Raman spectra acquired from a ramie fiber with different polarization directions of the incident laser: 0° (parallel to the fiber), 30° , 60° , and 90° (perpendicular to the fiber)

10.4 Plant Cell Wall Imaging by Confocal Raman Microscopy

One of the first Raman imaging studies in plant research was carried out on flax stem tissue [19]. Using the NIR-FT-Raman technique area maps were collected in 6–10 µm steps and chemical profiles calculated by integration over specific spectral regions. By this method no information was gained at the cellular level, yet the distribution of the major components (cellulose, lignin, non-cellulosic polysaccharides) was demonstrated for different anatomical tissue types (epidermal tissue, bast, fibers, and core) [19]. To investigate changes at the hierarchical level of individual cells and/or cell wall layers, a higher spatial resolution is necessary and, as a consequence, the application of visible laser excitation is preferential. In the last years the potential of Raman imaging was demonstrated on wood cell walls [41–43]. A 785 nm near-IR laser-based Raman system was applied to study beech cell walls [43], but also confocal Raman microscopes with 633 nm [41] and 532 nm [42] visible laser excitation wavelengths were used to investigate the wooden cell walls with sub-micron spatial resolution.

10.4.1 Imaging Cellulose Orientation and Lignin Distribution in Wooden Cell Walls

Wooden cell walls consist of 40–50% cellulose, associated with a mixture of hemicelluloses (20–30%), lignin (20–35%), extractives (2–20%), and ash (0.2–3%) [11, 12]. In order to interpret the Raman spectrum of such a multi-component material, not only the contribution of each component needs to be identified, individual Raman bands need to be assigned to component-specific moieties and/or functional

groups. Most of black spruce (*Picea mariana*) Raman features could be assigned to cellulose and lignin, however, contributions of hemicelluloses occurred at similar wavenumbers to cellulose and could not be clearly distinguished [44].

As an example of imaging of wooden cell walls, the reaction wood of a tropical wood species (*Laetia procera*) was chosen, because of a highly specialized, non-uniform cell wall structure. Reaction wood in general is of interest as these tissues are able to generate tensile stresses of up to 70 MPa, which are able to pull leaning stems and branches upward [45, 46]. It is still much debated how the mechanism works, consequently this special plant cell wall composition and structure have been of considerable research interest for decades [47–49].

After imaging a sample area of interest, Raman images can be calculated by integrating over bands assigned to, e.g., lignin to visualize its distribution within the cell wall [41, 42]. By integrating from 1545 to 1698 cm⁻¹ areas with high lignin content show high intensity (bright yellow, Fig. 10.2a). The compound middle lamella and the cell corners, which glue the wood fibers together, are confirmed as highly lignified areas. The secondary cell wall is intermediately lignified and an unusual layered structure with changing lignin incrustation is visualized (Fig. 10.2a).

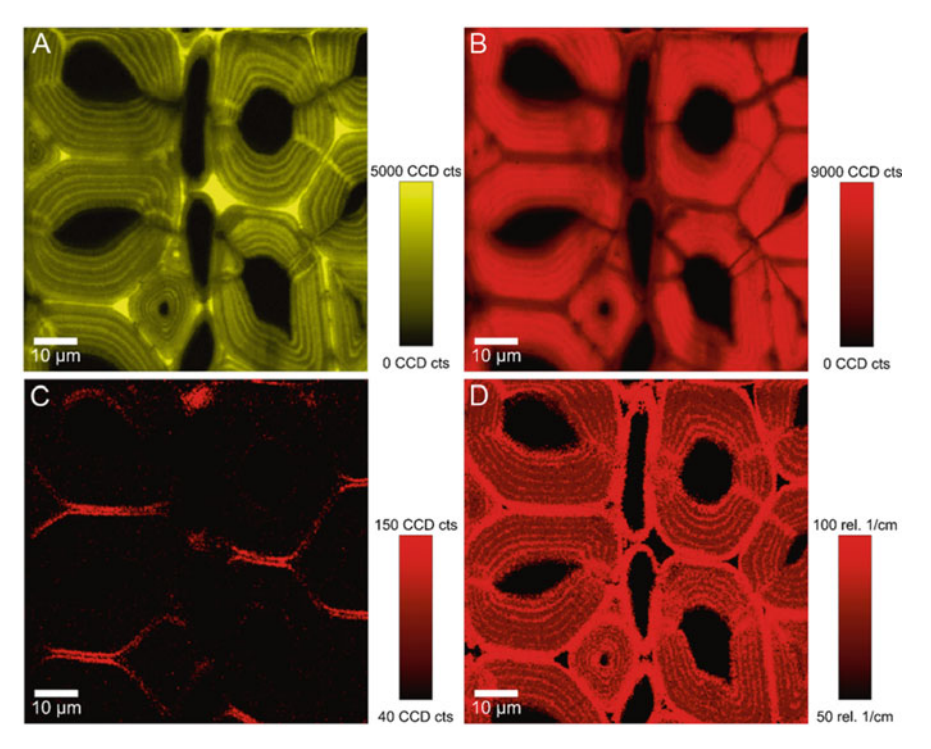


Fig. 10.2 Raman images ($80 \,\mu\text{m} \times 80 \,\mu\text{m}$) of a cross-section of tension wood of *L. procera* calculated by integrating from 1545 to $1698 \, \text{cm}^{-1}$ (**a**, lignin), from 2774 to $3026 \, \text{cm}^{-1}$ (**b**, cellulose amount and orientation parallel along the fiber), and from $1067 \, \text{to} 1106 \, \text{cm}^{-1}$ to accentuate the orientation-sensitive cellulose band at $1097 \, \text{cm}^{-1}$ (**c**, cellulose oriented with a high angle in respect to the fiber) and the band width at 50% height of the CH-stretching region (**d**, $2823-2917 \, \text{cm}^{-1}$)

Integrating over the $\nu(CH)$ and $\nu_s(CH_2)$ modes from 2774 to 3026 cm⁻¹ reflects cellulose amount and/or orientation (Fig. 10.2b) and gives a contrary picture: highest intensity in the secondary cell wall, low between the cells, and no clear layering. By restricting the integration to the very orientation-sensitive band at 1097 cm⁻¹, two 1-μm thick layers are emphasized in the laser polarization orientation (Fig. 10.2c). Within this region of high intensity the cellulose is supposed to be not oriented parallel along the fiber axis, but with a high angle in respect to the fiber axis. The spectral explanation is that in the investigated cross-section if cellulose is aligned parallel to the fiber axis the ν_s (C–O–C) is low, as excitation is perpendicular to the backbone. When cellulose is aligned with a high angle in respect to the fiber axis, the C-O-C linkage becomes more parallel aligned and therefore the signal is enhanced in the laser polarization direction (Fig. 10.2c). Besides images based on changes of integrated band intensities, also the change in band width can be used to detect and follow molecular changes at the cell wall level (Fig. 10.2d). For the CHstretching region (2773–3044 cm⁻¹), images reflect mainly changes in the cellulose orientation (Fig. 10.2d). Only the 2898 cm⁻¹ band of the overlapping CH-stretching bands raises with changes in orientation and thus also the doublet widths changes in dependence of the orientation (Fig. 10.1). In the cross-section the band width is decreasing (signal intensity increasing), when the cellulose is aligned parallel along the fiber. In this situation the side chain methylene groups are perpendicularly arranged with respect to the cellulose molecule and in plane with the incident light.

When polarized laser light is used in combination with Raman imaging care has to be taken to interpret every intensity change by concentration differences of the cell wall polymers, as changes in the orientation of the molecules may also affect intensity. This may complicate data interpretation, but on the other hand provides insights into changes of orientation of the molecule within the sample [42, 50]. In wood the angle of the cellulose microfibrils in respect to the cell axis is termed microfibril angle (MFA) and of great importance as it was demonstrated to be closely related to the mechanical properties [48, 49].

One major advantage of the imaging approach presented here is that verification of the interpretation (orientation or concentration effect) of imaging results as well as detailed insights can be gained by extracting average spectra of defined areas. So, one has not to rely solely on imaging results, like, for example, in staining experiments or fast imaging approaches based on the intensity of only one wavelength. Another big advantage is that the image calculation can reveal changes in chemistry and/or orientation at a high spatial resolution. These changes are often not even visible in the light microscopic images and it would be impossible to place the laser beam accurately on such small regions of interest to resolve these changes. By extracting the spectra after image calculation the spectral information can be gained accurately from very small, defined regions for detailed investigation.

Regions of interest for extracting average spectra can be selected by hand or defined by intensity thresholds based on the calculated chemical images (Fig. 10.2a–d). By selecting a threshold for the lignin intensity above 5000, for example, solely the cell corners are selected (upper picture, Fig. 10.3a) and an average spectrum of the cell corner is calculated (upper black line, Fig. 10.3a).

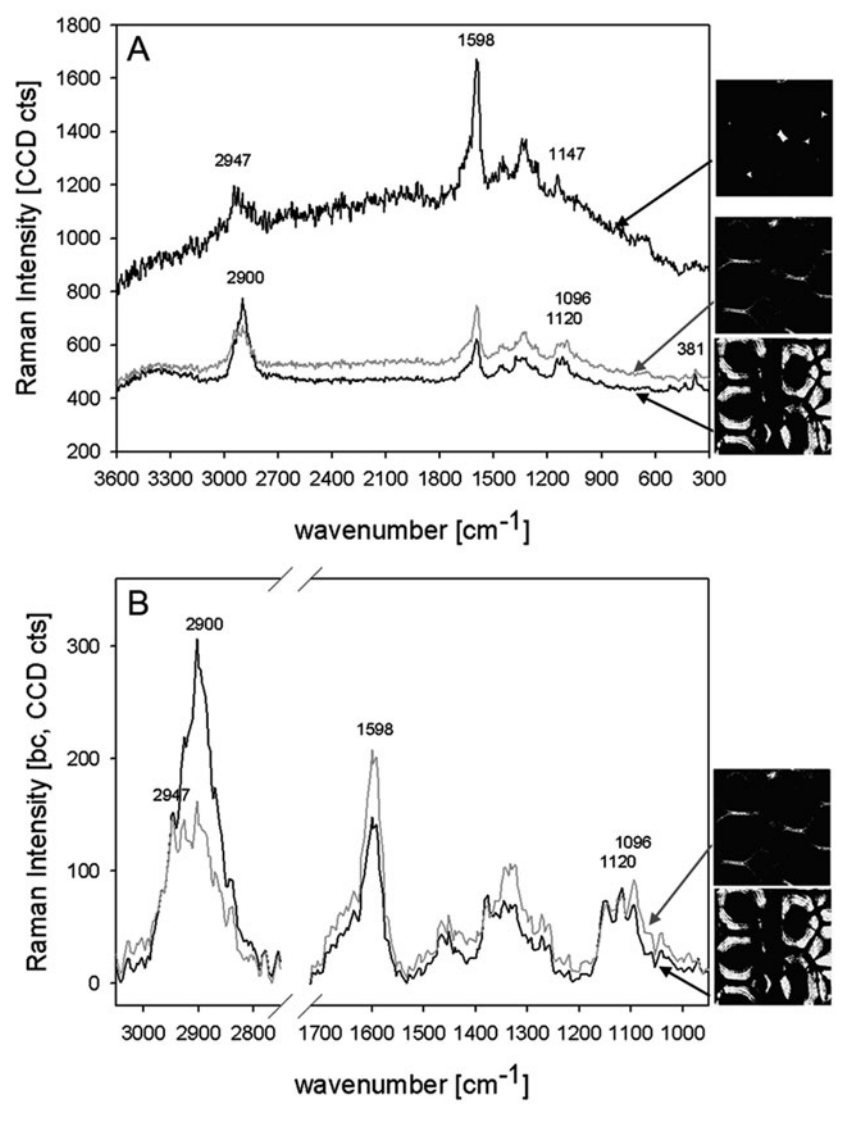


Fig. 10.3 Extracted average spectra of *L. procera* Raman images (Fig. 10.2) of (**a**) the cell corner (integral intensity of the band at 1598 cm $^{-1} > 5000$, *white area* in the *upper image* and *upper black line*) and two regions differing in orientation within the secondary cell wall (integral intensity of $1096 \, \mathrm{cm}^{-1}$ band > 100, *middle image* and *gray line*; integral intensity of $2900 \, \mathrm{cm}^{-1}$ band > 7000, *bottom image* and *black line*) and (**b**) a zoom into regions of interest of the baseline-corrected secondary cell wall spectra

The cell corner spectrum reflects only lignin characteristic bands and suggests that lignin is the main compound in these areas. Besides, it also shows that lignin causes a high level of background fluorescence, which can disguise small contributions to the Raman spectrum of other polymers present in small amounts, e.g., pectin. In the spectra extracted from the secondary cell walls, the aromatic-stretching vibration of lignin at 1598 cm⁻¹ is much smaller and fluorescence reduced (spectra on the bottom, Fig. 10.3a). In these spectra characteristic cellulose bands can be found, e.g., at 1096 and 1122 cm⁻¹. The two spectra were extracted from zones identified by the imaging approach to differ in cellulose orientation. A zoom in of the CH-stretching region and the fingerprint region bands confirms the opposite trend of the band at 2900 and 1097 cm⁻¹ and thus the interpretation as changes of orientation (Fig. 10.3b).

Besides revealing molecular changes within the cell wall layers, the high spatial resolution of confocal Raman microscopy enabled also the characterization of accessory compounds within the lumen of single cells, e.g., lipid droplets in the xylem of trees [51] or spherical storage compounds in wood parenchyma cells [42].

10.4.2 Silica and Cell Wall Composition in Horsetail (E. hyemale)

Minerals and inorganic substances in plants are normally determined as the residues remaining after all the combustible material has been burned off (fully oxidized) and subsumed as ash content. Regrettably, this method does not result in detailed information on the kind of inorganic components. Confocal Raman microscopy studies allow the identification, characterization, and spatial localization of inorganic substances in fossil [52–54] and living plants in situ [55–58]. Recent Raman imaging studies were carried out on horsetail samples (E. hyemale) [59, 60]. Another common name of the plant is "scouring rush", a reference to its early use for cleaning pots made possible by its high accumulation of silica up to 25% dry weight [61]. Aspects of processes regarding silica deposition, its association with other biomolecules, as well as the chemical composition of the outer strengthening tissue still remain unclear, questions which were addressed by Raman imaging [59, 60]. Basis analysis (partial least square fit based on model spectra) was performed in this study, besides the visualization of differences in chemical composition by calculating the integral intensity of selected bands [59]. Average spectra extracted from defined regions of different chemical images seemed to represent almost pure cellulose (hemicellulose), pectin, and amorphous silica features and were thus seen as appropriate to be used as model spectra for these compounds. Concluding that the Equisetum plant cell walls consist mainly of these compounds, every Raman spectrum in the acquired Raman images is a linear superposition (S) of the spectra of the single compounds. By having the model spectra (basis spectra, B_k) of the single compounds, it is possible to estimate the weighting factor a_k by the least squares fit $(S = \sum a_k B_k)$. The weighting factor a_k is proportional to the

quantity of the component k in the material and stored in an image. Color coding and combining the different weighting factor images lead to a complete summarizing image of the distribution of the model compounds. The distribution of cellulose, pectin, and silica is visualized within one image for every investigated tissue region (Fig. 10.4a–d). Silica accumulation is color-coded blue and confirmed in the knob region (Fig. 10.4a) as well as in a small layer below the cuticula besides the knob region (Fig. 10.4d). In addition it becomes clear that in the epidermal layer below the knob, silica is still detectable in combination with cellulose/hemicellulose, whereas the pectin amount seems to be decreased (Fig. 10.4a, pink color). This is in contrast to the epidermal layer besides the knob where pectin plays the main role (Fig. 10.4d, green). In the epidermis only a small cellulose-rich inner ring (red) is found, which becomes continuously thicker inward and the pectin more and more restricted to the cell corners (Fig. 10.4d). Within the hypodermal

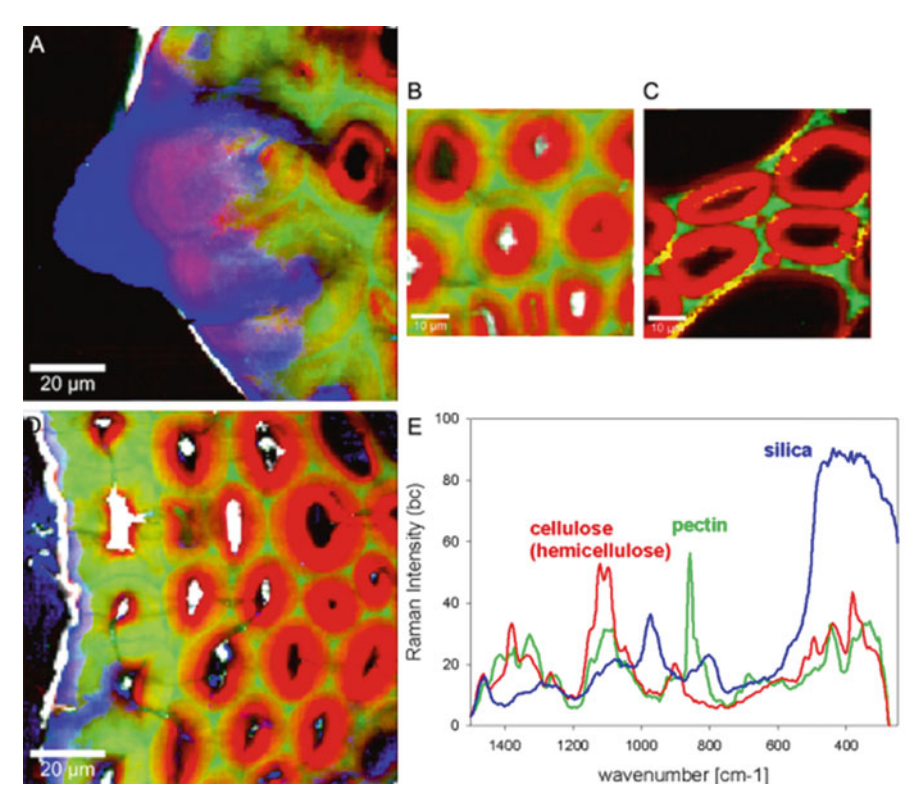


Fig. 10.4 Combined color images (**a–d**) from *E. hyemale* derived from a basis analysis (partial least square fit) with average spectra (**e**) extracted from defined regions representing mainly amorphous silica, pectin, and cellulose. *Blue* represents high weighting factor and consequently content for silica, *green* for pectin, and *red* for cellulose (hemicellulose). The *white color* shows the cuticular layer and deposits within some lumens of the cells not further investigated [59]

sterome the two-layered structure with a pectinized outer ring and an inner ring with highly oriented cellulose comes out (Fig. 10.4b). Further inward uniform pure cellulose/hemicellulose fibers are found and the pectin is restricted to the CC and middle lamella (Fig. 10.4c).

In the spectrum extracted from the knob region (Fig. 10.4e, blue spectrum) as a main contribution a broad band below $500\,\mathrm{cm^{-1}}$, attributed to amorphous silica, and a band at $976\,\mathrm{cm^{-1}}$, assigned to silanol groups, were found. From this, we concluded that these protrusions were almost pure amorphous, hydrated silica. No silanol group vibration was detected in the silicified epidermal layer below and an association with cell wall polymers was indicated.

10.5 Outlook

The potential of confocal Raman microscopy/imaging for non-destructive in situ investigation of plant cell walls has already been demonstrated on various plant tissues. The high spatial resolution allows detection of changes in the cell wall polymer composition and/or orientation on the cell and cell wall level. The Raman imaging approach allows acquiring spectra with short integration time (0.2-2 s), which minimizes problems with sample degradation. The signal to noise ratio of the spectra is sufficient to visualize chemical and orientational changes not visible in the light optical micrographs. The extraction of average spectra with a better signal to noise ratio from the identified areas of interest can support image interpretation and reveal more details. Conclusions about all cell components can be derived nondestructively at once and in context with structure. This major advantage and potential also comprises a drawback as highly overlapping bands are sometimes difficult to interpret and conclusions on components with minor amount may be ambiguous. Nevertheless, more experiments on other cell wall variants and selective chemical treatment as well as the combination with other methods (e.g., antibody probes) will improve our understanding of the generated Raman spectra in future.

10.6 Material and Methods

The Raman mapping experiments shown in this book chapter were done with a confocal Raman microscope (CRM200, WITec, Ulm, Germany) described in detail together with the sample preparation and data analysis in [42, 59].

Acknowledgments R. Nöske (Potsdam University, Department of Chemistry) is thanked for providing the horsetail sample, B. Clair (Universite Montpellier) for the tropical wood sample, and I. Burgert, O. Paris, and P. Fratzl (Max Planck Institute of Colloids and Interfaces, Department Biomaterials, Potsdam) for enabling the work. The author acknowledges the APART program of the Austrian Academy of Sciences and the Max Planck Society for funding.

References

- 1. C. Martin, K. Bhatt, K. Baumann, Curr. Opin. Plant Biol. 4(6), 540 (2001)
- A. Boudet, The Plant Cell Wall Annual Plant Reviews (Blackwell, CRC Press, 2003), chap. Towards an understanding of the supramolecular organization of the lignified wall, pp. 155–178
- 3. M. Jarvis, M. McCann, Plant Physiol. Biochem. **38**(1/2), 1 (2000)
- 4. M. O'Neill, W. York, *The Plant Cell Wall Annual Plant Reviews* (Blackwell, CRC Press, 2003), chap. The composition and structure of plant primary cell walls, pp. 1–44
- 5. A. O'Sullivan, Cellulose 4(3), 173 (1997)
- 6. R. Atalla, *MIE Bioforum* (UNI Publisher Co, Japan, 1999), chap. The structure of native celluloses, and the origin of their variability
- 7. R. Brown, I. Saxena, Plant Physiol. Biochem. **38**(1–2), 57 (2000)
- 8. D. Klemm, B. Heublein, H. Fink, A. Bohn, Angew. Chem. Int. Ed. 44(22), 3358 (2005)
- 9. R. Atalla, J. Hackney, I. Uhlin, N. Thompson, Int. J. Biol. Macromol. 15(2), 109 (1993)
- 10. S. Fry, J. Exp. Bot. 40(1), 1 (1989)
- 11. C. Plomion, G. Leprovost, A. Stokes, Plant Physiol. 127, 1513 (2001)
- D. Fengel, G. Wegener, Wood: Chemistry, Ultrastructure, Reactions (Walter de Gruyter & Co., Berlin, 1989)
- 13. J. Barnett, V. Bonham, Biol. Rev. **79**(2), 461 (2004)
- M. McCann, M. Hammouri, R. Wilson, P. Belton, K. Roberts, Plant Physiol. 100 100, 1940 (1992)
- M. McCann, M. Bush, D. Milionia, P. Sadoa, N. Stacey, G. Catchpole, M. Defernez, N. Carpita, H. Hoft, P. Ulvskov, R. Wilson, K. Roberts, Phytochemistry 57, 811 (2001)
- M. Kacuráková, P. Capeka, V. Sasinková, N. Wellner, A. Ebringerova, Carbohydr. Polym. 43, 195 (2000)
- 17. D. Stewart, Appl. Spectrosc. **50**(3), 357 (1996)
- 18. C. Séné, M. McCann, R. Wilson, R. Crinter, Plant Physiol. 106, 1623 (1994)
- 19. D. Himmelsbach, S. Khahili, D. Akin, Vib. Spectrosc. 19, 361 (1999)
- 20. R. Atalla, U. Agarwal, Science 227, 636 (1985)
- G. Toole, M. Kacurakova, A. Smith, K. Waldron, R. Wilson, Carbohydr. Res. 339(3), 629 (2004)
- 22. V. Morris, S. Ring, A. MacDougall, R. Wilson, *The Plant Cell Wall Annual Plant Reviews* (Blackwell, 2003), chap. Biophysical characterisation of plant cell walls, pp. 55–91
- 23. B. Schrader, A. Hoffmann, A. Simon, J. Sawatzki, Vib. Spectrosc. 1(3), 239 (1991)
- 24. M. Baranska, H. Schulz, P. Rösch, M. Strehle, J. Popp, Analyst 129(10), 926 (2004)
- 25. R. Baranski, M. Baranska, H. Schulz, Planta 222(3), 448 (2005)
- 26. M. Baranska, H. Schulz, E. Joubert, M. Manley, Anal. Chem. 78(22), 7716 (2006)
- 27. R. Atalla, J. Ranua, E. Malcolm, Tappi J. 67(2), 96 (1984)
- 28. J. Wiley, R. Atalla, Carbohydr. Res. **160**, 113 (1987)
- 29. R. Atalla, R. Whitmore, C. Heimbach, Macromolecules 13(6), 1717 (1980)
- 30. S. Fischer, K. Schenzel, K. Fischer, W. Diepenbrock, Macromol. Symp. 223, 41 (2005)
- H. Edwards, D. Farwell, D. Webster, Spectrochim. Acta Part A Mol. Biomol. Spectrosc. 53(13), 2383 (1997)
- A. Jähn, M. Schröder, M. Füting, K. Schenzel, W. Diepenbrock, Spectrochim. Acta Part A Mol. Biomol. Spectrosc. 58, 2271 (2002)
- 33. P. Peetla, K. Schenzel, W. Diepenbrock, Appl. Spectrosc. **60**(6), 682 (2006)
- 34. W. Morrison, D. Himmelsbach, D. Akin, J. Evans, J. Agric. Food Chem. 51(9), 2565 (2003)
- 35. Y. Liu, S. Kokot, T. Sambi, Analyst 123(4), 633 (1998)
- 36. B. Schrader, H. Klump, K. Schenzel, H. Schulz, J. Mol. Struct. **509**, 201 (1999)
- N. Gierlinger, M. Schwanninger, A. Reinecke, I. Burgert, Biomacromolecules 7(7), 2077 (2006)

N. Gierlinger

- 38. S. Eichhorn, J. Sirichaisit, R. Young, J. Mater. Sci. 36, 3129 (2001)
- 39. J. Wiley, R. Atalla, Carbohydr. Res. **160**, 113 (1987)
- H. Edwards, D. Farwell, D. Webster, Spectrochim. Acta Part A Mol. Biomol. Spectrosc. 53(13), 2383 (1997)
- 41. U. Agarwal, Planta 224(5), 1141 (2006)
- 42. N. Gierlinger, M. Schwanninger, Plant Physiol. **140**(4), 1246 (2006)
- 43. T. Röder, G. Koch, H. Sixta, Holzforschung **58**, 480 (2004)
- 44. U. Agarwal, S. Ralph, Appl. Spectrosc. **51**(11), 1648 (1997)
- J. Barnett, G. Jeronimidis, Wood Quality and Its Biological Basis (Blackwell Scientific, Oxford, 2003), chap. Reaction Wood, p. 226
- 46. T. Okuyama, H. Yamamoto, M. Yoshida, Y. Hattori, R. Archer, Ann. Sci. For. 51, 291 (1994)
- 47. W. Côté, A. Day, *Cellular Ultrastructure of Woody Plants* (Syracuse University Press: Syracuse, 1965), chap. Anatomy and Ultrastructue of Reaction Wood, pp. 391–418
- 48. N. Nishikubo, T. Awano, A. Banasiak, V. Bourquin, F. Ibatullin, R. Funada, H. Brumer, T. Teeri, T. Hayashi, B. Sundberg, E. Mellerowicz, Plant Cell Physiol. **48**(6), 843 (2007)
- 49. H. Yamamoto, M. Yoshida, T. Okuyama, Planta **216**(2), 280 (2002)
- 50. N. Gierlinger, I. Burgert, N Z J. For. Sci. **36**(1), 60 (2006)
- 51. P. Rösch, H. Schneider, U. Zimmermann, W. Kiefer, J. Popp, Biopolymers 74(1-2), 151 (2004)
- 52. D. Dietrich, K. Witke, R. Rossler, G. Marx, Appl. Surf. Sci. 179(1-4), 230 (2001)
- K. Witke, J. Gotze, R. Rossler, D. Dietrich, G. Marx, Spectrochim. Acta Part A Mol. Biomol. Spectrosc. 60(12), 2903 (2004)
- J. Nowak, M. Florek, W. Kwiatek, J. Lekki, P. Chevallier, E.Z.N. Mestres, E. Dutkiewicz,
 A. Kuczumow, Mater. Sci. Eng. C Biomim. Supramol. Syst. 25(2), 119 (2005)
- A. Macnish, D. Irving, D. Joyce, V. Vithanage, A. Wearing, R. Webb, R. Frost, Aust. J. Bot. 51, 565 (2003)
- 56. L. Prinsloo, W. du Plooy, C. van der Merwe, J. Raman Spectrosc. 35(7), 561 (2004)
- 57. D. Dietrich, S. Hemeltjen, N. Meyer, E. Baucker, G. Ruhle, O. Wienhaus, G. Marx, Anal. Bioanal. Chem. **374**(4), 749 (2002)
- 58. D. Dietrich, S. Hinke, W. Baumann, R. Fehlhaber, E. Baucher, G. Ruhle, O. Wienhaus, G. Marx, Anal. Bioanal. Chem. **376**(3), 399 (2003)
- 59. N. Gierlinger, L. Sapei, O. Paris, Planta **227**(5), 969 (2008)
- L. Sapei, N. Gierlinger, J. Hartmann, R. Nöske, P. Strauch, O. Paris, Anal. Bioanal. Chem. 389, 1249 (2007)
- 61. T. Timell, Sven. Papperstidn. 67(9), 356 (1964)

Chapter 11 Confocal Raman Imaging of Polymeric Materials

Ute Schmidt, Jörg Müller, and Joachim Koenen

Abstract Polymers play an essential role in modern materials science. Due to the wide variety of mechanical and chemical properties of polymers, they are used in almost every field of application and are still a dynamic area in the development of new materials with demanding requirements. Raman spectroscopy is one of the standard characterization techniques used to uniquely determine the chemical composition of a polymer. Modern materials, however, are generally heterogeneous, in which various chemical components or polymorphs of the same chemical species can be present in a very small sample volume. For the analysis of such heterogeneous materials, the combination of Raman spectroscopy with confocal microscopy delivers information about the spatial distribution of the various chemical species with a resolution down to 200 nm. The aim of this contribution is to demonstrate the power of confocal Raman imaging for the characterization of heterogeneous polymeric materials. The first section will deal with polymorphs of polypropylene in polymer films, followed by the nondestructive analysis of polymer blends. A later section will deal with multi-layer polymer coatings and paints and finally various additives to polymer matrices will be discussed.

11.1 Introduction

The characterization of heterogeneous systems on the microscopic scale continues to grow in importance and to impact key applications in the fields of materials science, nanotechnology, and catalysis. The development of advanced polymeric materials for applications such as these requires detailed information about their physical and chemical properties on the nanometer scale. However, some details about the phase separation process in polymers are difficult to study with conventional characterization techniques due to the inability of these methods to chemically differentiate materials with sufficient spatial resolution and without damage, staining, or preferential solvent washing. One technique that has been used successfully in the characterization of heterogeneity in polymers is atomic force microscopy (AFM) [1–4]. AFM can provide spatial information along and perpendicular to the surface of a polymer film with a resolution on the order of 1 nm. The most commonly used AFM imaging mode for polymers is the intermittent contact mode also known as AC

mode or tapping mode [5]. In this AFM imaging mode the cantilever is oscillated at its resonance frequency and the topography of the surface is scanned by keeping the oscillation damping constant. A phase image can be recorded simultaneously with the surface topography. In this image, the phase shift between the free oscillation of the cantilever in air and the oscillation while the tip is in contact with the surface is recorded [6]. Since the phase shift depends as much on the viscoelastic properties of the sample as on the adhesive potential between sample and tip, the phase image outlines domains of varying material contrast without describing the nature of the material properties [7–11]. Nevertheless, phase images are often used to characterize polymers at high resolution [12, 13]. If a composite material consists of compounds with similar mechanical properties, a clear assignment of the phases to the corresponding materials by AFM is quite challenging. To discriminate between materials with similar mechanical properties, additional spectroscopic information is useful. On the macroscopic scale, Raman spectroscopy has become widely used for the characterization of chemical and structural features of polymeric materials [14]. The tremendous value of the Raman effect lies in the fact that the difference in energy between the elastically scattered photons and the Raman-shifted photons is caused by the excitation or annihilation of a specific molecular vibration. This energy shift is characteristic for the type and coordination of the molecules involved in the scattering process. Raman spectra provide qualitative and quantitative information about various polymer features [15–17] such as

- chemical nature: structural units, type and degree of branching, end groups, additives
- conformational order: physical arrangement of the polymer chain
- state of order: crystalline, mesomorphous, and amorphous phases
- orientation: type and degree of polymer chain and side group alignment in anisotropic materials.

However, in most spectroscopy setups the spatial resolution is very poor because the excitation laser spot diameter is on the order of 100 µm. Optical microscopy, on the other hand, is capable of providing spatial resolution down to 200 nm using visible light excitation. In a confocal microscope, the light from the sample is detected through a pinhole at the back focal plane of the microscope, giving rise to depth resolution and a strongly reduced background signal [18]. By combining a highthroughput confocal microscope with an extremely sensitive Raman spectroscopy system, it is possible to obtain Raman spectra from extremely small sample volumes down to 0.004 μ m³ as will be shown later. To collect high-resolution Raman images, the sample is scanned point by point and line by line through the excitation focus [18]. Thus, the confocal Raman microscope (CRM) combines the chemical sensitivity of Raman spectroscopy and the high resolution of confocal microscopy, providing an ideal tool for the characterization of materials in the sub-micrometer range. To achieve the highest resolution, the CRM can be extended with AFM capabilities which enable the user to link the chemical information obtained by confocal Raman spectroscopy with the ultra-high spatial and topographical information acquired by AFM.

The Raman experiments presented in this chapter were performed with a WITec alpha300RA (combined Raman-AFM) using green excitation (532 nm) and a $100 \times$, NA=0.9, objective. The AFM measurements were done using the same instrument in AFM-AC mode.

11.2 Raman Imaging of Isotactic Polypropylene (iPP)

Polypropylene (PP) is a thermoplastic polymer synthesized from the monomer propylene with the chemical formulas shown in Fig. 11.1. Its dual functionality as plastic and fiber leads to its varied fields of application. As a plastic it is used as reusable containers, stationary plastic parts, laboratory equipment, automotive components, banknotes, etc. As a fiber, polypropylene is used to make ropes, unwoven textiles, packaging materials, etc. The large number of end use applications for PP is due to the ability to tailor grades with specific molecular properties and additives during its manufacturing processes.

The characterization of the morphology of polypropylene fibers in complex structures remains a focus of ongoing research. The crystallinity and the extent of orientation of molecular chains are two of the most important morphological characteristics of the fiber structure that influence the final properties. Raman spectroscopy is one of the many methods used to characterize the microstructure of a semicrystalline polymer. It provides the capability to probe the conformational states of polymer chains in its micro-environment [19–21]. Differences in the Raman spectrum of chains in non-crystalline regions with conformational irregularities or nonhelical conformations can be expected [22–25]. A theoretical determination of the vibrational Raman bands of helical polypropylene chains can be found in [26, 27], whereas stress-induced deformations of polypropylene chains are reported in [28] and [29]. The structure of a polymer is given by its particular structural arrangement [30]. In isotactic polypropylene, a crystallizable polymer, the structural arrangement

$$CH_3$$
 (a)

U. Schmidt et al.

is given by the arrangement of crystalline and amorphous domains. The formation of crystalline and amorphous domains is influenced by the crystallization conditions. Crystallization from the unstressed melt results in a randomly nucleated spherulitic structure, whereas crystallization which occurs in an extensional flow field (e.g., during the extrusion process) results in a row-nucleated structure. Depending on the extrusion conditions, bundles of oriented fibers can be formed.

To determine a correlation between the orientation of lamellar rows of isotactic polypropylene and Raman spectra, a uniaxially drawn isotactic polypropylene film (OPP) with a thickness of 50 μ m was investigated using polarized Raman spectroscopy. High-resolution atomic force microscopy measurements on such films show a highly oriented fibrillar structure, which is oriented in parallel to the extrusion direction [31]. On this highly oriented isotactic polypropylene film, polarization-dependent Raman spectra were recorded. Figure 11.2 shows a schematic of the four different geometries in which Raman spectra were recorded.

The polarized Raman spectra from the OPP film are presented in Figs. 11.3 and 11.4. The spectra result from one sample position. A half-wave plate was used to rotate the polarization of the incident laser light either parallel or perpendicular to the fiber, whereas the scattered light passed through an analyzer either parallel or perpendicular to the polarization direction of the incident laser light. All recorded Raman spectra were normalized to the bands at 1435 and 1457 cm⁻¹, which are not polarization dependent. These bands are assigned to methyl group deformations in isotactic polypropylene and show an additional splitting only at very low temperatures [19].

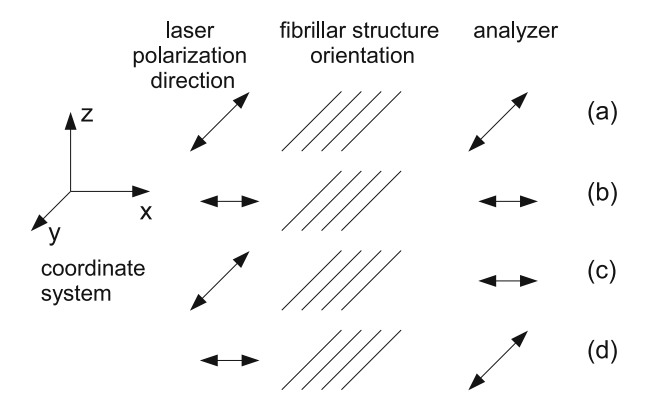
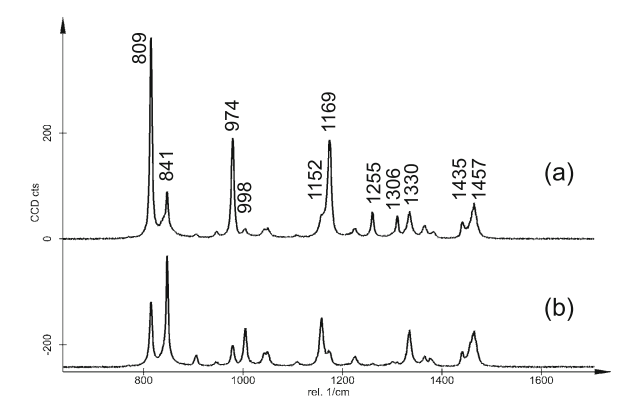


Fig. 11.2 Schematics of the scattering geometry defined in the above-shown coordinate system, the incident laser propagates in z-direction. By using a half-wave plate the incident laser light can be polarizes in x- or y-direction. The scattered light is analyzed either in parallel or in perpendicular to the polarization direction of the incident laser light. The four possible combinations with respect to the orientation of a 1D structure is presented: incident light polarization and analyzer oriented in parallel with the 1D structure (**a**), incident light polarization and analyzer oriented perpendicular to the 1D structure (**b**), and polarization direction of laser and analyzer arranged perpendicular to each other in the two possible arrangements with the 1D structure (**c**, **d**)

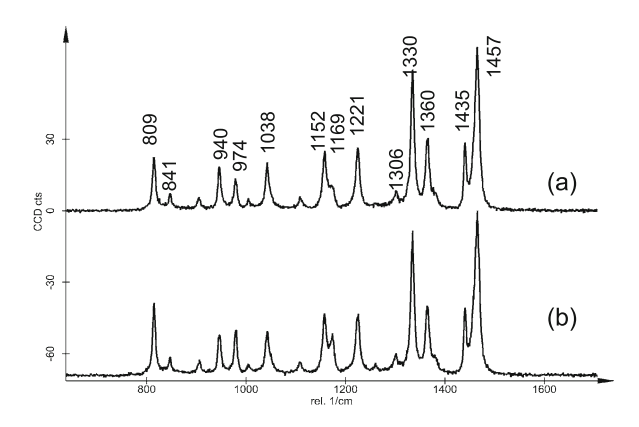
Fig. 11.3 Polarization-dependent Raman spectra of uniaxial isotactic polypropylene: polarization direction of laser, fiber, and analyzer oriented in parallel (a), and polarization direction of laser and analyzer oriented perpendicular to the iPP fibers (b)



The spectra shown in Fig. 11.3 are recorded in the configuration in which the polarization direction of the incident and scattered laser light is in the same direction, whereas in Fig. 11.4 the spectra recorded in the crossed orientation of laser polarization direction and analyzer are presented. The two later configurations show only minor differences in Raman band intensities as reported before by [20] and [32]. Fiber orientation and laser polarization-dependent changes can be clearly observed in the spectra shown in Fig. 11.3. The Raman bands at 809, 841 and 1152, 1169 cm⁻¹ are the most characteristic of a directional ordering of the polymer chains in isotactic polypropylene. Based on normal mode calculations it has been shown that these bands in solid state are associated with the helical chain structure [33, 34].

Considering the above-described polarization dependency of Raman spectra recorded from highly oriented isotactic polypropylene, Raman imaging of polypropylene provides information about the structural arrangement of ordered and disordered polymer chains. Figure 11.5 shows a Raman image of biaxially oriented polypropylene (BOPP). A 2D array of 100×50 single Raman spectra was recorded from a surface area of $50 \times 30 \ \mu m^2$ using a frequency doubled Nd:YAG

Fig. 11.4 Polarization-dependent Raman spectra of uniaxial isotactic polypropylene: polarization direction of laser and fiber oriented in parallel with analyzer perpendicular (a) and polarization direction of laser perpendicular and analyzer oriented in parallel to the fiber orientation (b)



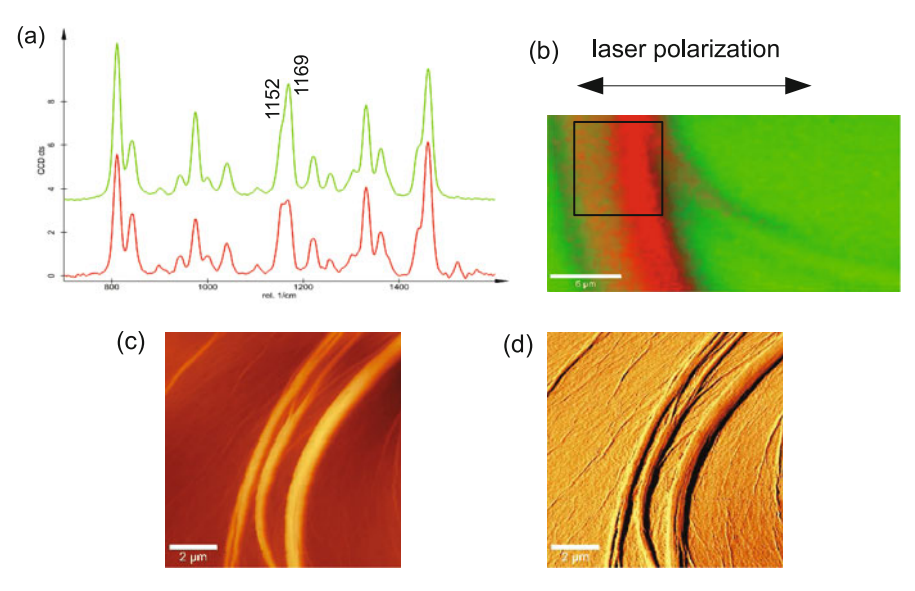


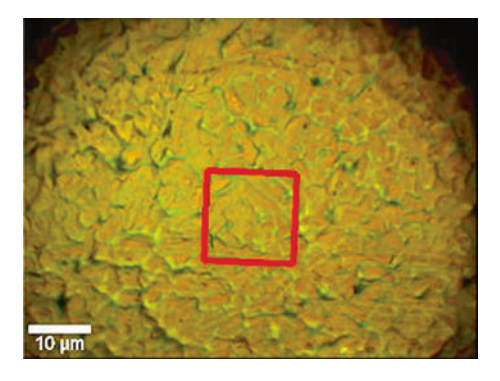
Fig. 11.5 Raman imaging of biaxially oriented polypropylene: Raman spectra (a), color-coded Raman image (b), AFM topography image (c), and AFM phase image (d). The scale bar in (b) is $6 \mu m$ and in (c) and (d) $2 \mu m$ long

laser (excitation wavelength $532\,\mathrm{nm}$) and a $100\times$ objective (NA = 0.9). The integration time per single spectrum was 0.1 s. From the 5000 individual spectra, two unique Raman spectra were calculated (Fig. 11.5a). The green spectrum is characteristic for polypropylene fibers oriented parallel to the laser polarization direction, (see Fig. 11.3a), whereas the red spectrum is characteristic for polypropylene fibers oriented perpendicular to the laser polarization direction. The color-coded Raman image (Fig. 11.5b) reveals the oriented fiber bundle. To prove the orientation of such fiber bundles, AFM (atomic force microscopy) measurements were performed on the sample area marked with a frame in Fig. 11.5(b). Figure 11.5(c) shows the topography of the BOPP film, whereas the simultaneously recorded phase image reveals the fiber bundle and the fine fibrillar structure of the BOPP film.

The simultaneously recorded phase image reveals much more details of the fine structure of the BOPP film compared to the Raman image. The oriented bundle seems much wider and oriented in a different direction in the Raman image due to the diffraction-limited resolution in all three volume directions. The phase image on the other hand is imaging only the surface topography.

Polypropylene films are commonly used as solid dielectrics in high voltage capacitors. Such films are produced by biaxially stretching unstretched molded polypropylene. The surface of such films has an efficiently roughened, fine uneven structure containing crater-like patterns or an isotropic and an anisotropic network structure, which is aligned in the extrusion direction. To obtain more detailed information about the fine structure of such foils, polarized Raman imaging can be

Fig. 11.6 Video image of a polypropylene film used as solid dielectric in capacitors. The *red frame* marks the area imaged with Raman imaging



employed. By using a polarization rotation (half-wave plate) a surface area can be analyzed using different laser polarization directions, thus determining the different preferential orientation of the spherulitic grains. Figure 11.6 shows the video image recorded on such a foil. The red square marks the area which was scanned for Raman imaging. The spectrometer was equipped with an 1800 grooves/mm grating. Over an area of $15\times15\,\mu\text{m}^2$, an array of 100×100 Raman spectra was recorded with an integration time of $0.1\,\text{s/spectrum}$.

The same area was first scanned with the laser polarization and analyzer both oriented horizontally to the x-axis of the image. In a second scan, the same area was scanned with the laser polarization and analyzer oriented both perpendicular to the x-axis of the image. The polarization-dependent Raman spectra of uniaxial isotactic polypropylene (Fig. 11.3) were used as basis spectra for the basis analysis of the recorded 2D spectral arrays [35]. Figure 11.7(a) shows the distribution of spherulitic structures which are oriented parallel (green) and perpendicular (red) to the laser polarization direction. By rotating the laser polarization direction and analyzer by 90° the image shown in Fig. 11.7(b) was recorded. In this case, spherulitic structures oriented parallel to the laser polarization direction are shown in yellow, whereas blue

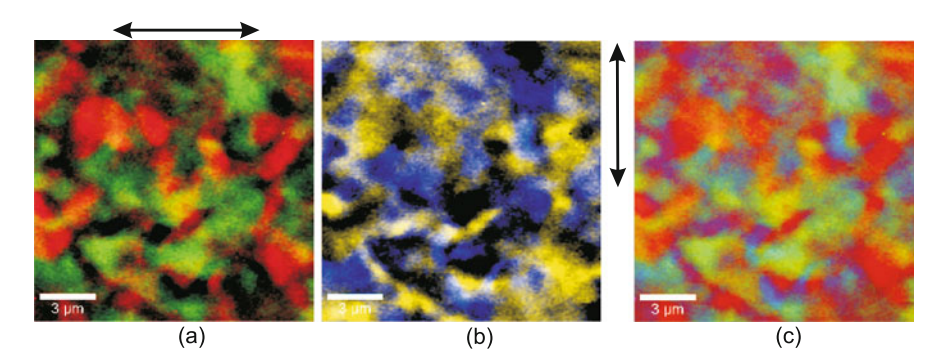


Fig. 11.7 Color-coded polarization-dependent Raman images of a polypropylene film used as solid dielectric in capacitors: Raman image of polypropylene oriented in parallel and perpendicular to the horizontal (**a**) and vertical (**b**) laser polarization direction and combined color-coded Raman image of all polarization directions

was used for perpendicularly oriented spherulitic structures. Figure 11.7(c) shows a color-coded image of the various grain orientations detected by using polarized confocal Raman imaging.

The predominant colors in Fig. 11.7(c) are red and green indicating that one measurement with polarized light is enough to characterize the orientation in such polymer films.

11.3 Raman Imaging of Polymer Blends

Polymer blends are designed to address the needs of different industries and in many cases the relationship between structure, morphology, and material properties is crucial for the optimization of material design. Since the beginning of the plastics industry it has been recognized that blending yields materials with property profiles superior to the features of the individual components. A polymer blend is a macroscopically homogeneous mixture of two or more different species of polymer which combine the useful properties of all of the constituents. The technology of blending is now advancing at a rapid pace. There has been progress in the understanding of the behavior of polymer blends, especially the thermodynamics and rheology [36, 37]. New blends are constantly being developed and characterized. The main parameters which influence the properties of a blend are the interface and the morphology. The morphology of a polymer blend indicates the size, shape, and spatial distribution of the component phases with respect to each other. The properties, such as mechanical, optical, rheological, dielectrical, and barrier properties, of polymer blends are strongly influenced by the type and granularity of the phase structure. A large variety of analytical methods are used to characterize the morphology of polymer blends. Raman imaging contributes to the analysis of multicomponent polymer systems by visualizing the distribution of individual components based on differences in the unique Raman spectra for different polymeric materials. Domains of different components in polymer blends are typically of a larger size. In many cases, they are formed during phase separation. Raman imaging provides real-space observation of different coarsening processes and allows direct quantification of phase volume fractions and the computation of domain interface curvatures of various morphologies. A direct assignment of image features to various polymer phases becomes available with a resolution down to 200 nm. Micro-phase separation patterns with spherical, cylindrical, lamellar, or micellar morphology, which are characterized by structural factors in the tens of nanometers range, can be analyzed by transforming the confocal Raman microscope into an AFM [35, 38].

In the following sections three different blends composed of immiscible polymers, which are at room temperature in either the rubbery or the glassy state, were investigated. For these studies, thin films of the polymer blends with a thickness of less than 100 nm were prepared by spin-coating solutions containing the polymers onto clean glass cover slides at 2000 rpm.

11.3.1 Raman Imaging of Thin Films of the Polymer Blend: Polystyrene (PS)- Ethyl-Hexyl-Acrylate (EHA)

In this section a polymer blend which consists at room temperature of the glassy-state polymer PS and the rubbery-state polymer EHA is described.

Figure 11.8(a) shows the Raman spectra of the pure blend components. Both PS (blue) and EHA (green) show characteristic band structures around 2800–3000 cm⁻¹, which are associated with C–H stretching and the peak at 1454 cm⁻¹ which is characteristic for C–H bending. EHA shows a Raman peak

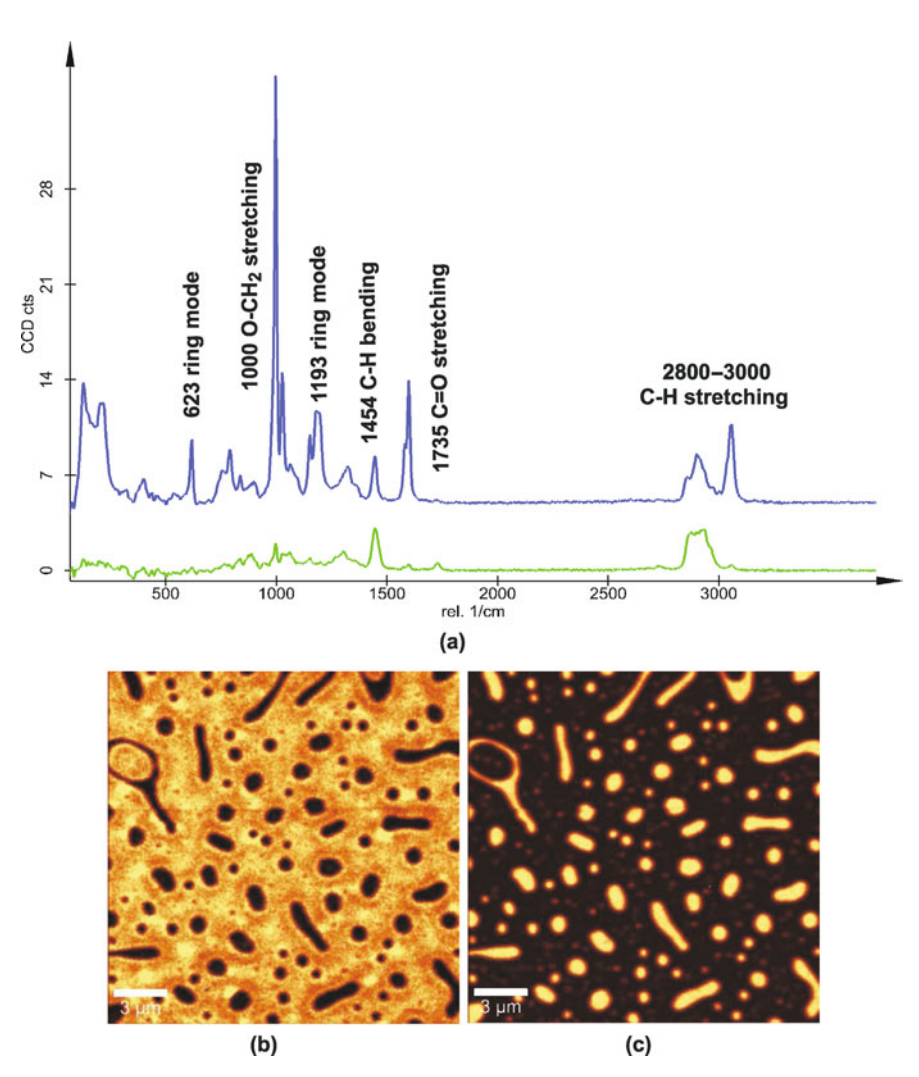


Fig. 11.8 Single Raman spectra of pure PS (blue spectrum) and EHA (green spectrum) (a), Raman image of EHA distribution (b), and Raman image of PS distribution (c)

at 1735 cm⁻¹ which is characteristic for C=O stretching, whereas PS shows the additional Raman bands associated with the benzene ring modes [39, 40]. These two spectra can be used for the basis analysis of 2D spectral arrays acquired from the polymer blend.

The variations in the Raman spectra of these two polymers make it possible to distinguish the various polymers from each other when they are blended. The blend of PS-EHA was scanned in Raman spectral imaging mode. Complete Raman spectra were recorded at every image pixel (200×200 spectra) with an integration time of 0.08 s/spectrum. To assign the different polymers in the film, the complete spectra of the two polymers were employed by using basis spectra analysis (see Chap. 4). The distribution of the EHA is shown in Fig. 11.8(b), whereas the distribution of PS is represented in Fig. 11.8(c). These two complementary Raman images show that PS forms islands surrounded by the EHA matrix. Both polymer phases wet the glass substrate.

High-resolution AFM images recorded on this film are shown in Fig. 11.9. The topography image (Fig. 11.9a) reveals that the PS islands are 40 nm higher than the surrounding EHA phase. The diameter of the PS islands range from 100 to 1500 nm. The simultaneously recorded phase image (Fig. 11.9b) shows a high phase contrast between the two materials. Brighter areas can be assigned to the harder (glassy) polystyrene, whereas the soft (rubbery) EHA appears darker. Within the EHA phase a netlike fine structure becomes visible in the phase image.

To determine the overall thickness of the thin film of the polymer blend, the film was scratched with a razor blade and imaged with AFM. Figure 11.10(a) shows the topography of the scratch and the corresponding height histogram of the image (Fig. 11.10b).

The measured height of the EHA phase of only 30 nm together with the focus spot size of 340 nm shows that a sample volume of less than $0.004~\mu m^3$ is enough to

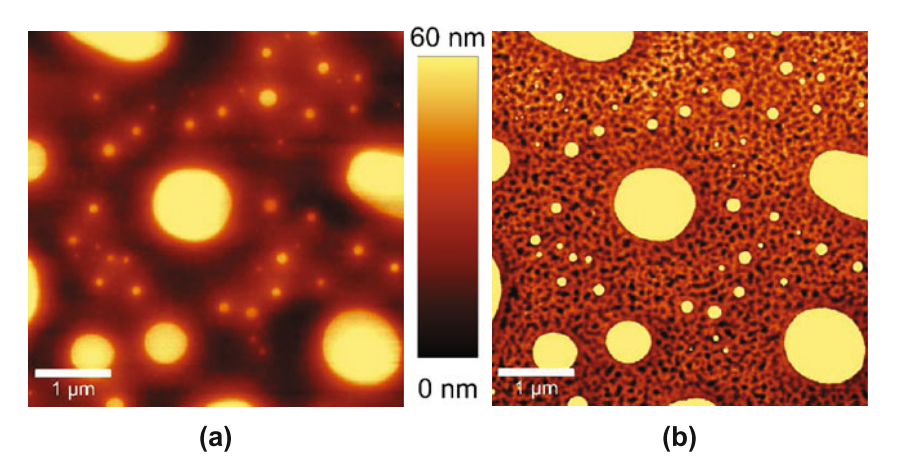


Fig. 11.9 High-resolution AFM AC mode image of the polymer blend PS-EHA: topography image (a) and simultaneously recorded phase image (b)

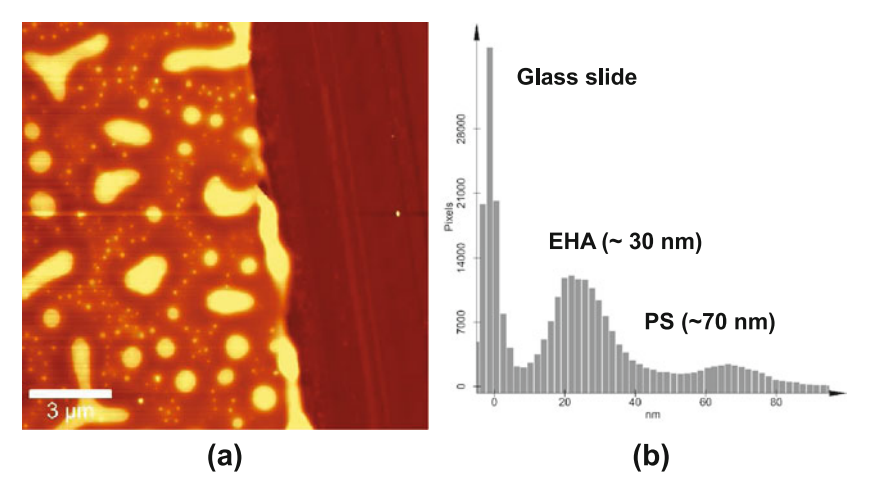


Fig. 11.10 AFM AC mode topography image of the scratched film of PS-EHA (a) and histogram of height distribution on the surface (b)

identify the chemical species with the confocal Raman microscope using integration times of less than 100 ms/spectrum.

11.3.2 Raman Imaging of Thin Films of the Polymer Blend Ethyl-Hexyl-Acrylate (EHA)-Styrene-Butadiene Rubber (SBR)

In this section a polymer blend consisting of two polymers, which are in the rubber phase at room temperature, is described. A 2D spectral array of 100×50 spectra was acquired from a sample area of $10 \times 5~\mu\text{m}^2$. From the 5000 recorded spectra, two distinct Raman spectra were calculated by using cluster analysis (see Chap. 4 in this book for a more detailed explanation). These spectra are represented in red and green in Fig. 11.11(a). The green spectrum shows the characteristic Raman bands of EHA (compare with green spectrum, Fig. 11.8a), whereas the red spectrum shows additional Raman bands at 1000 and 3060 cm⁻¹ and in the spectral range of $1635-1650~\text{cm}^{-1}$. The latter Raman bands are associated with C=C stretching and are characteristic for SBR [35]. The differential spectrum between the red and the green spectra is shown in blue in Fig. 11.11(a) and represents the unique Raman spectrum of SBR [35]. Figure 11.11(b) shows the Raman image of the distribution of the two detected species within the scanned surface area. The distribution of the pure EHA phase is represented in green and the red color denotes the presence of a mixed phase consisting of EHA and SBR.

To gain insight into the fine structure of the mixed phase consisting of EHA and SBR, high-resolution structural information is required. This can be obtained from high-resolution AFM images. In a previous study it could be shown that phase images recorded on thin films of pure SBR spin coated on glass substrates

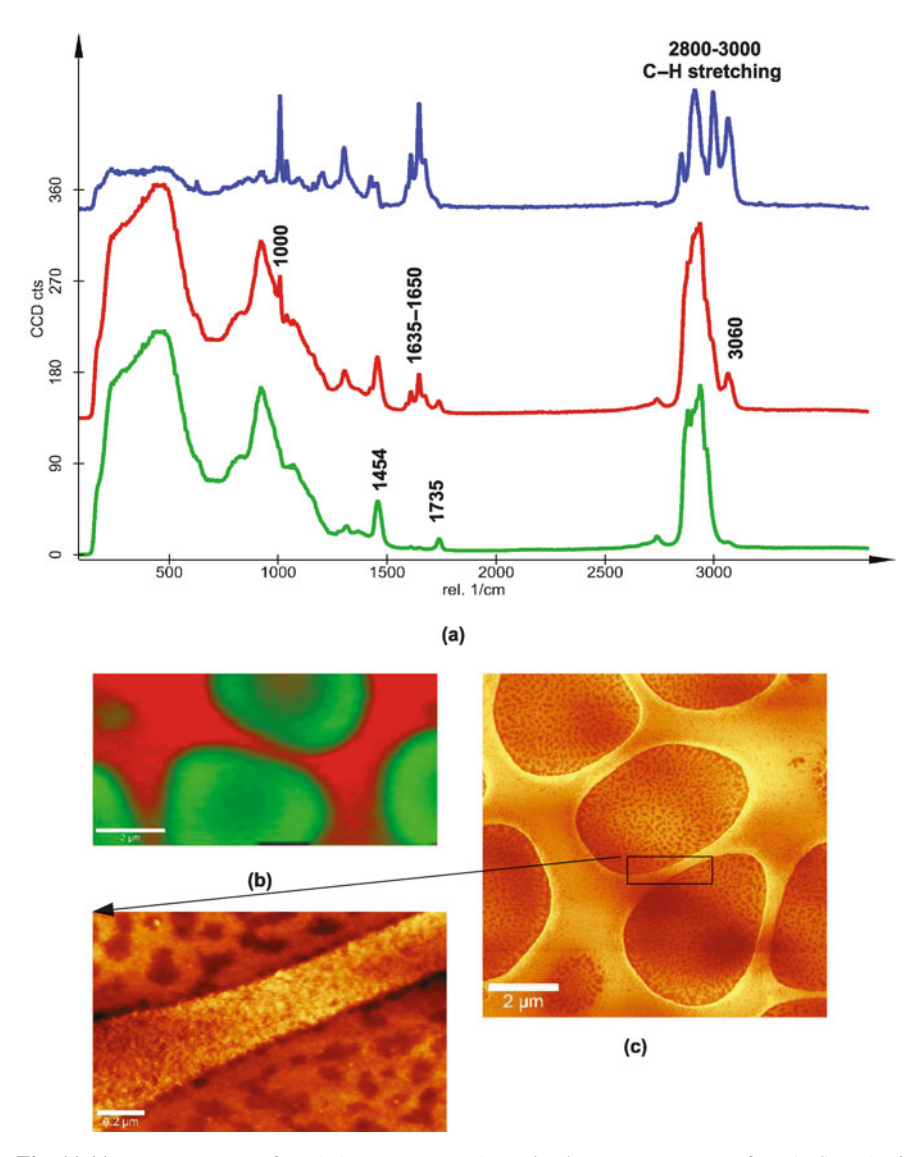


Fig. 11.11 Raman spectra of EHA (*green spectrum*), a mixed Raman spectrum of EHA+SBR (*red spectrum*), and the differential spectrum between *red* and *green* spectrum revealing the pure SBR Raman spectrum in *blue* (a), color-coded Raman image of the distribution of pure EHA and of the mixed phase EHA+SBR (b), and high-resolution AFM phase images of the polymer blend (c)

reveal a statistical distribution of the hard styrene blocks in the rubbery butadiene matrix [35]. The fine structure of pure EHA wetting the glass substrate is shown in Fig. 11.9(b).

AFM images recorded in AC mode on the polymer blend consisting of EHA and SBR reveal a two-level topography. The simultaneously recorded phase image

is shown in Fig. 11.11(c). The netlike structure, characteristic for EHA wetting the glass substrate, could be resolved in the topographic lower regions of the surface. This finding is in good agreement with the elliptic domains consisting of pure EHA found in the Raman image. The topographically elevated structure consisting of a large network appears featureless if a large area is scanned. The high-resolution AFM image obtained from a smaller scan area (see insert of Fig. 11.11c) reveals a grain-like fine structure in the topographically elevated structure, which is characteristic for SBR. The Raman image showed, however, that in these surface areas the two polymers SBR and EHA coexist, thus the SBR phase is formed on top of the EHA layer. By combining confocal Raman imaging with high-resolution AFM imaging, it could be shown that in this polymer blend only EHA is wetting the glass substrate. For this polymer blend only the combination of Raman and AFM imaging reveals the wetting and separation behavior of the two rubbery polymers without selective dissolution of one of the polymer phases.

11.3.3 Raman Imaging of Thin Films of the Polymer Blend PS-EHA-SBR

In this section a thin film of a three-component polymer blend is described, which at room temperature consists of the two rubbery-state polymers EHA and SBR and the glassy-state polymer PS.

A 2D spectral array of 128×128 spectra was acquired from a sample area of $20 \times 20 \, \mu m^2$ of this polymer film. The spectral array was analyzed using basis analysis. The Raman spectra shown in Fig. 11.12(a) were used as basis spectra. In the basis analysis technique, each measured Raman spectrum is fitted by a linear combination of a certain number of basis spectra (see also Chap. 4). A color-coded Raman image of the distribution of the three polymer phases is shown in Fig. 11.12(b). In this image, blue represents the distribution of PS while the green areas consist of pure EHA. Yellow denotes a mixed phase of EHA and SBR. This image confirms the previously observed phase separation processes: PS, the polymer in the glassy state at room temperature, and EHA, form an interface with the glass substrate, whereas the SBR is formed on top of the EHA phase.

High-resolution AFM images recorded from this blend show that PS is forming a topographically elevated rope-like structure, surrounded by SBR and EHA. A high-resolution AFM phase image (Fig. 11.12c) reveals the fine structures of the three blended polymers. The bright areas of this image can be associated with the hard PS-phase, whereas the dark red reveals the fine structure of EHA, the most adhesive component of the blend. The grain-like fine structure is found again in the SBR layer formed on top of the EHA phase.

A final evaluation of the structural arrangement of the various components of this blend is a confocal Raman depth scan. Figure 11.13 shows a color-coded confocal Raman depth scan performed on this three-component polymer blend. For this Raman image a 2D spectral array consisting of 100×50 complete Raman spectra

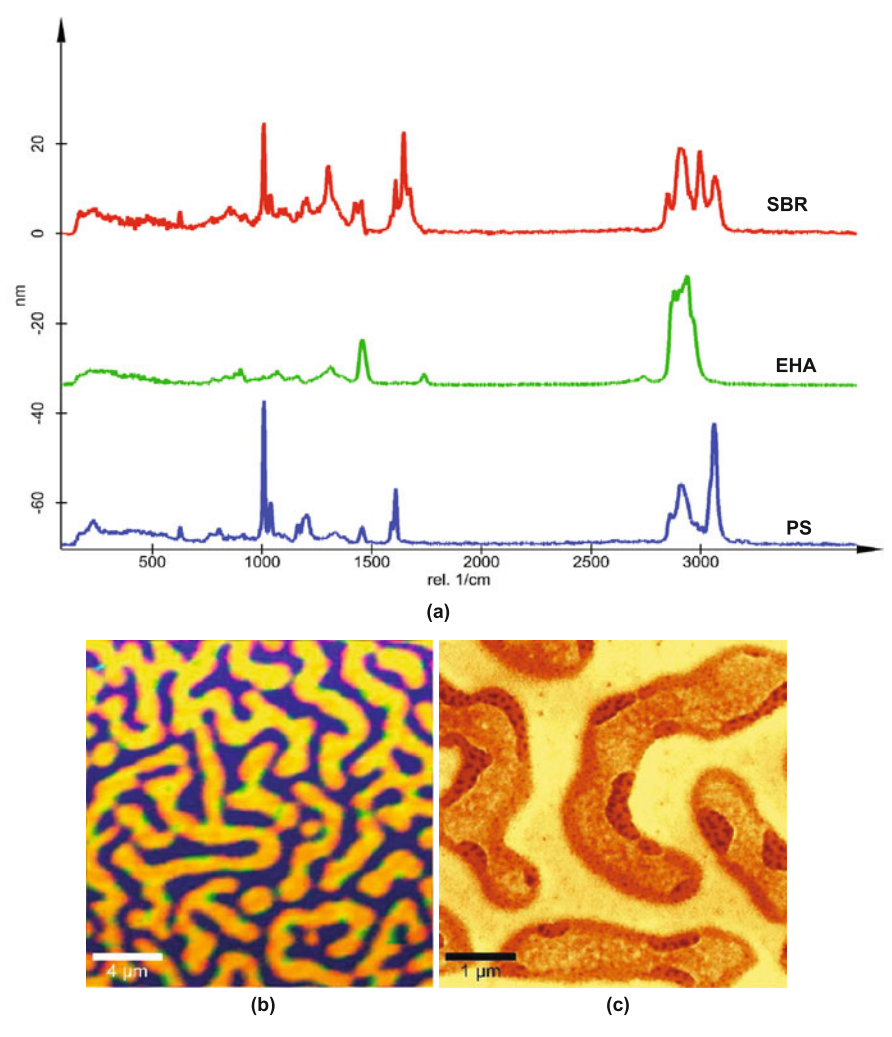


Fig. 11.12 Single Raman spectra of pure PS, EHA, and SBR used as basis spectra for the basis analysis of the 2D spectral array acquired from this sample (a), color-coded Raman image of the three-component polymer blend (b), and high-resolution AFM phase image of this polymer blend (c)

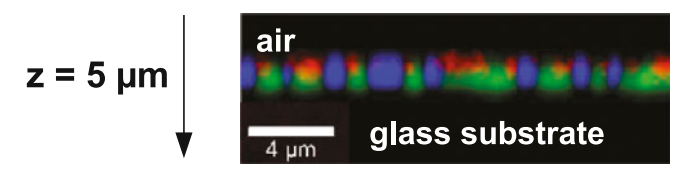


Fig. 11.13 Confocal Raman depth profile of the three-component polymer blend consisting of PS (*blue*), EHA (*green*), and SBR (*red*)

was recorded in a plane perpendicular to the surface, similar to a virtual section of the sample. The unique Raman spectra of the blend component (Fig. 11.12a) were used as basis spectra for the basis analysis software tool. Blue and green corresponding to PS and EHA, respectively, from this image form an interface with the glass substrate, whereas the red SBR phase is formed on top of the green EHA phase.

11.4 Polymer Coatings

Surfaces are coated to give them protection against a hostile environment, to enhance their appearance, or to impart specific properties to the surface. The desired effects can be achieved with coatings ranging from several micrometers to less than one micrometer in thickness. For some surfaces several layers are required to fulfill a specific task, in other cases a specific distribution of materials is needed. Establishing the chemical and morphological composition of a surface is therefore a vital step toward understanding its behavior. In the following, several examples of coatings will be presented.

11.4.1 Acrylic Paints

Alkyd and acrylics are used as binders in paints and coatings. These materials produce a shiny, hard finish that is highly water resistant. Of interest in studying this system are changes in the Raman spectra during the drying process of the paints and the distribution of the two phases within the paint. Figure 11.14 shows Raman spectra recorded from the alkyd phase before drying (a) and in the dry state of the paint (b). The decrease of the Raman bands at 1265 and 3012 cm⁻¹ (*cis*-C=C-H asymmetric stretching bands) and the *cis*-C=C stretch peak at 1656 cm⁻¹ are related to chemical changes during oxidation [41].

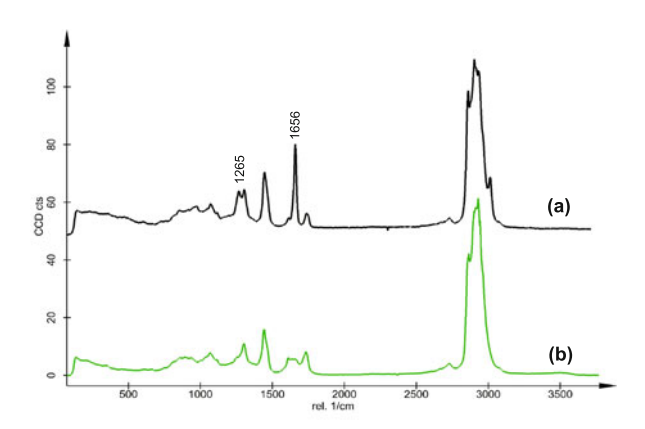


Fig. 11.14 Raman spectra of the alkyd phase before (**a**) and after (**b**) drying of the paint

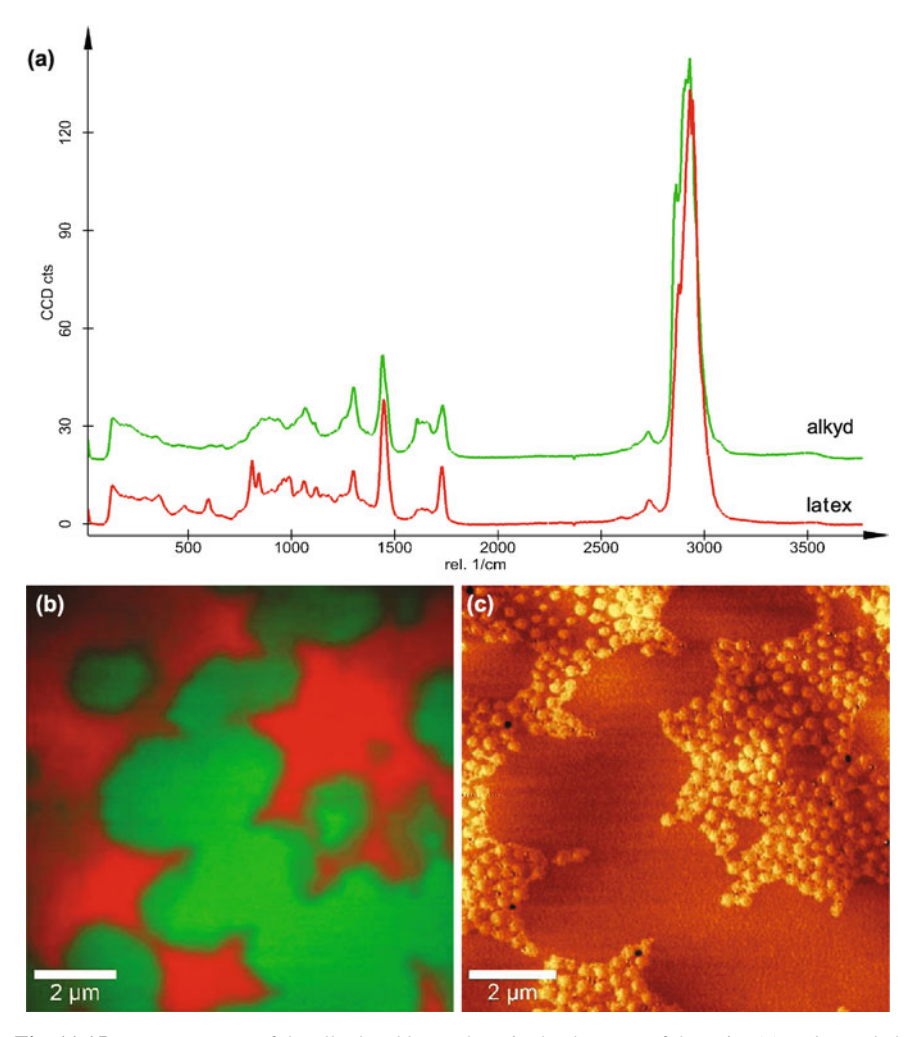


Fig. 11.15 Raman spectra of the alkyd and latex phase in the dry state of the paint (**a**), color-coded Raman spectral image of the paint surface (**b**), and AFM AC Mode phase image of the same sample area revealing the spherical latex particles (**c**)

Figure 11.15(a) shows the Raman spectra of alkyd and acrylic latex in their dry state. The small differences in the Raman spectra make it possible to distinguish the two phases in the emulsion. A Raman spectral image consisting of 200×200 spectra was recorded from a sample area of $10\times10~\mu m^2.$

The spectra from Fig. 11.15(a) were used as basis spectra for the basis spectra analysis of the recorded 2D spectral array. The resulting color-coded Raman image is presented in Fig. 11.15(b). This image indicates that large elliptic domains consisting of alkyd are surrounded by the acrylic latex phase. Fig. 11.15(c) shows the phase image of the dried paint, indicating the stiffer nature of the acrylic latex phase.

It also reveals the individual latex spheres, which are smaller than the diffraction limit (using an air objective) and are thus not resolved in the confocal Raman image. The diameter of the latex spheres range from 20 to 250 nm.

11.4.2 Adhesives

The use of multi-layered materials for adhesives is now a common practice. Confocal Raman depth scans provide insight into the layered structure of such polymers without any specific sample preparation.

As an example, Fig. 11.16 shows a confocal Raman depth scan performed on an adhesive paper. In this case two polymer layers were applied to the paper surface in order to fulfill the required tasks. The two polymers are immiscible and form a sharp interface (red and green) with the paper beneath (blue and yellow).

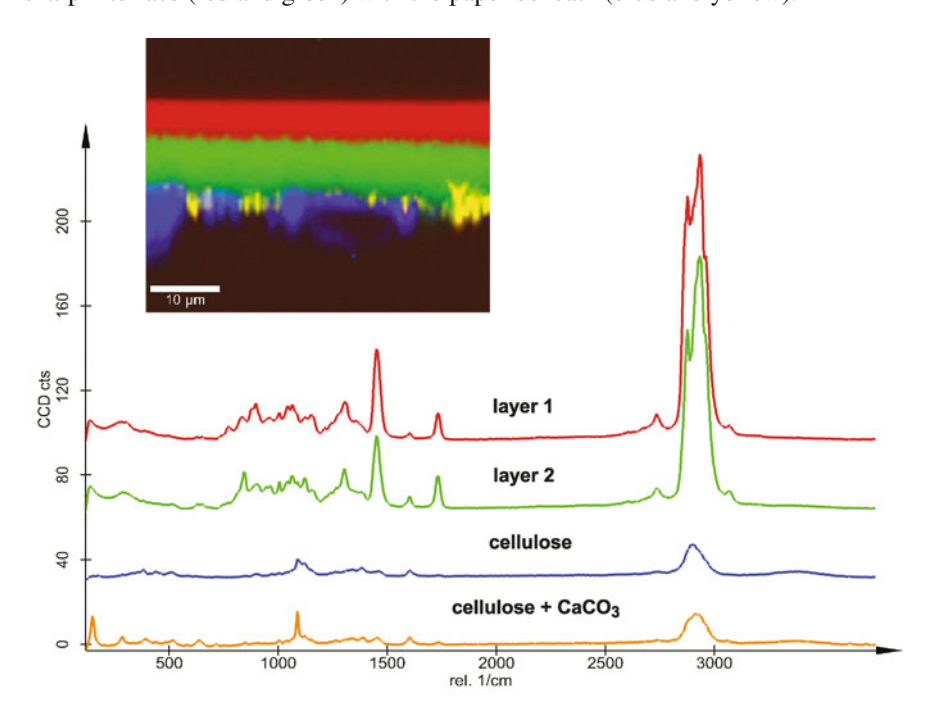


Fig. 11.16 Color-coded confocal Raman depth profile of adhesive polymeric layers on a paper substrate

11.5 Additives in Polymer Matrices

Nanomaterials are increasingly being used as additives to polymers to simultaneously enhance a variety of properties without sacrificing any qualities of the base polymer.

Additives of inorganic materials in solid form to polymer matrices have a great significance in plastics industry. They are used for a wide variety of purposes, e.g., anti-oxidants, stabilizers, fillers, and pigments. Anti-oxidants and stabilizers are added in small quantities to prevent degradation of the polymer when it is exposed to air, light, and heat. Fillers may be used simply either to produce a cheaper product or to improve the mechanical or electrical properties of the polymeric material. Confocal Raman microscopy allows the allocation of such fillers in the polymer matrix, leading to a better understanding of the properties of the materials. In the following, two examples of fillers are presented.

Fine metal powders and carbon black are commonly added to polymer matrices to improve the electrical, mechanical, or thermal properties of the polymers. Figure 11.17 shows a confocal Raman microscopy study of polypropylene with TiO₂ and carbon inclusions. An area of $30 \times 30~\mu\text{m}^2$ of the sample was scanned and a 2D array of 100×100 Raman spectra was acquired with an integration time of 100 ms spectrum. From this measurement four different spectra were evaluated using cluster analysis. These spectra are presented in Fig. 11.17(a). In addition to the orientation-dependent Raman spectra of polypropylene (blue and yellow spectra, Fig. 11.17a) the spectrum of TiO_2 (red) and the spectrum of amorphous carbon in an inorganic matrix (green) were extracted by the cluster analysis algorithm.

These spectra were used to evaluate the distribution of each component on the studied sample area using the basis analysis. The weighting factor resulting from the basis analysis denotes the presence of the species in a defined sample volume. Figure 11.17(b) shows the distribution of TiO_2 on the sample, whereas Fig. 11.17(c) shows the distribution of amorphous carbon. In Fig. 11.17(d) the color-coded Raman image of the distribution of polypropylene is presented. By overlaying the images described above and assigning each component the color of the corresponding Raman spectrum, the complete color-coded Raman image can be generated as shown in Fig. 11.17(d). From this image it can be clearly seen that the TiO_2 particles adhere to the different oriented polypropylene grains, whereas amorphous carbon forms large clusters with a diameter of up to 6 μ m.

Carbon nanotubes (CNTs) have physical properties that exceed those of commonly used materials. With a tensile strength eight times that of stainless steel and a thermal conductivity five times that of copper, CNTs are an obvious choice for creating a new class of composite materials. Their inclusion in a polymer or ceramic matrix holds the potential to enhance the host material's electrical, mechanical, or thermal properties by orders of magnitude, well above the performance possible with traditional fillers such as carbon black or ultra-fine metal powders.

Figure 11.18 shows the distribution of single-walled carbon nanotubes (SWC-NTs) in a polymer matrix. For this experiment a diode laser with a wavelength of 785 nm was employed for Raman imaging. An area of $20 \times 20 \ \mu m^2$ was scanned and a 2D array of 100×100 Raman spectra was acquired with an integration time of 200 ms spectrum. Figure 11.18(a) shows the three Raman spectra evaluated with cluster analysis. The Raman spectra of the polymer (red) and two different types of SWCNTs (blue and green) were detected. In this example, only SWCNTs show a Raman band in the spectral range $120{\text -}350\,\text{cm}^{-1}$. This Raman band arises from the coherent vibration of the carbon atoms in the radial direction, as if the tube

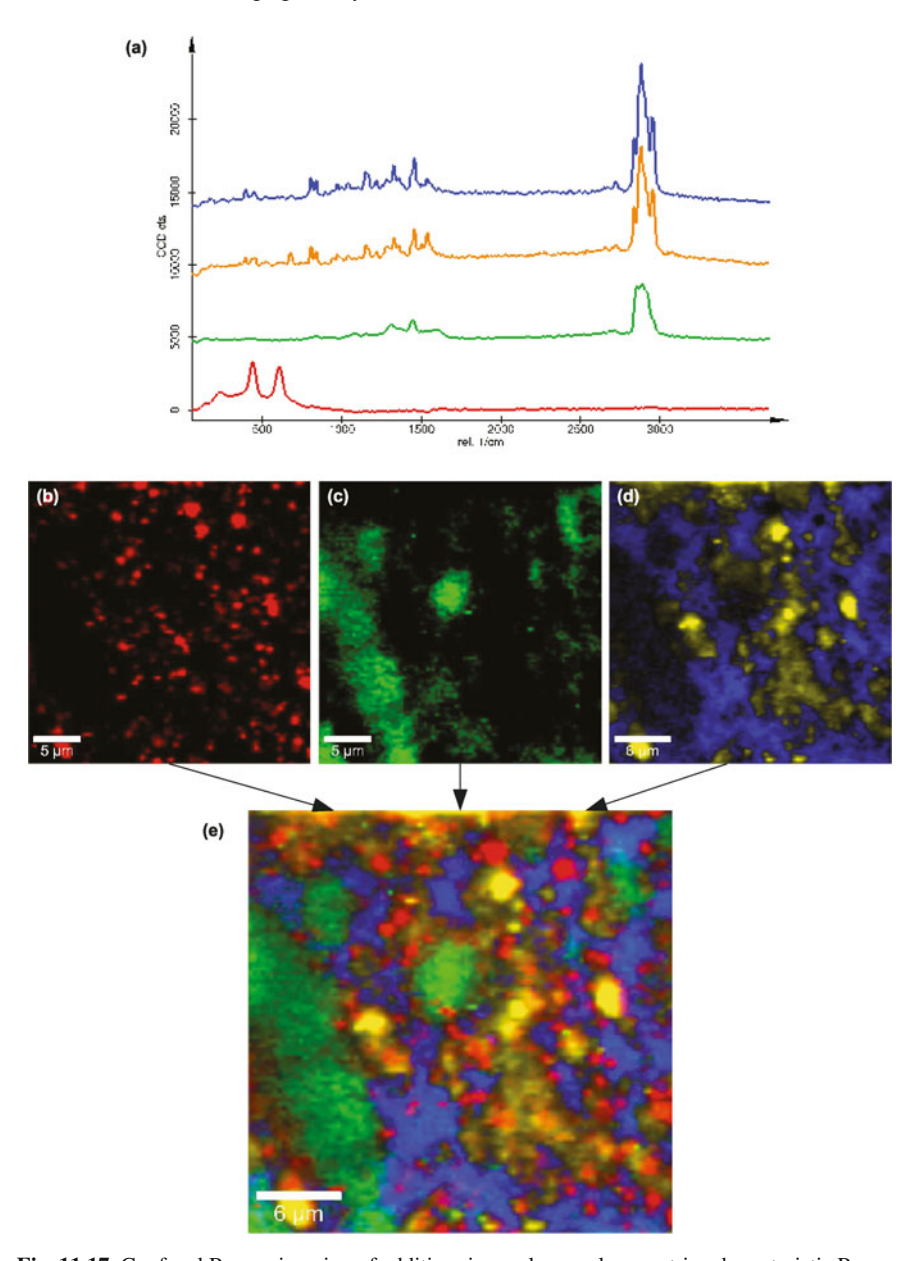


Fig. 11.17 Confocal Raman imaging of additives in a polypropylene matrix: characteristic Raman spectra evaluated from the 2D array of 10,000 spectra using cluster analysis: orientation-dependent PP Raman spectra (*blue and yellow*), Raman spectrum of amorphous carbon in organic matrix (*green*), and Raman spectrum of TiO_2 (*red*) (a), distribution of TiO_2 particles (b), distribution of amorphous carbon (c), distribution of PP (d), and color-coded Raman image of the analyzed surface area (e)

were breathing, and are known as radial breathing modes (RBM). These RBM frequencies (ω_{RBM}) are very useful to identify whether a given carbon material contains SWCNTs and for characterizing the nanotube diameter distribution (d_t) in the sample through use of the relation $\omega_{RBM} = A/d_t + B$, where the A and B parameters are determined experimentally [42, 43]. For typical SWCNT bundles, as expected in this polymer matrix, $A = 234 \,\mathrm{nm}\,\mathrm{cm}^{-1}$ and $B = 10 \,\mathrm{cm}^{-1}$ may be used. The two different ω_{RBM} found in this sample are at 258 and 267 cm⁻¹, corresponding to tube diameters of 0.96 and 0.91 nm, respectively. The distribution of these two types of SWCNTs is shown in Fig. 11.18(b). The SWCNTs with a diameter of 0.94 nm (green) appear as 2–4 μ m long rods, whereas the SWCNTs with a diameter of 0.91 nm appear much shorter (0.5–1 μ m).

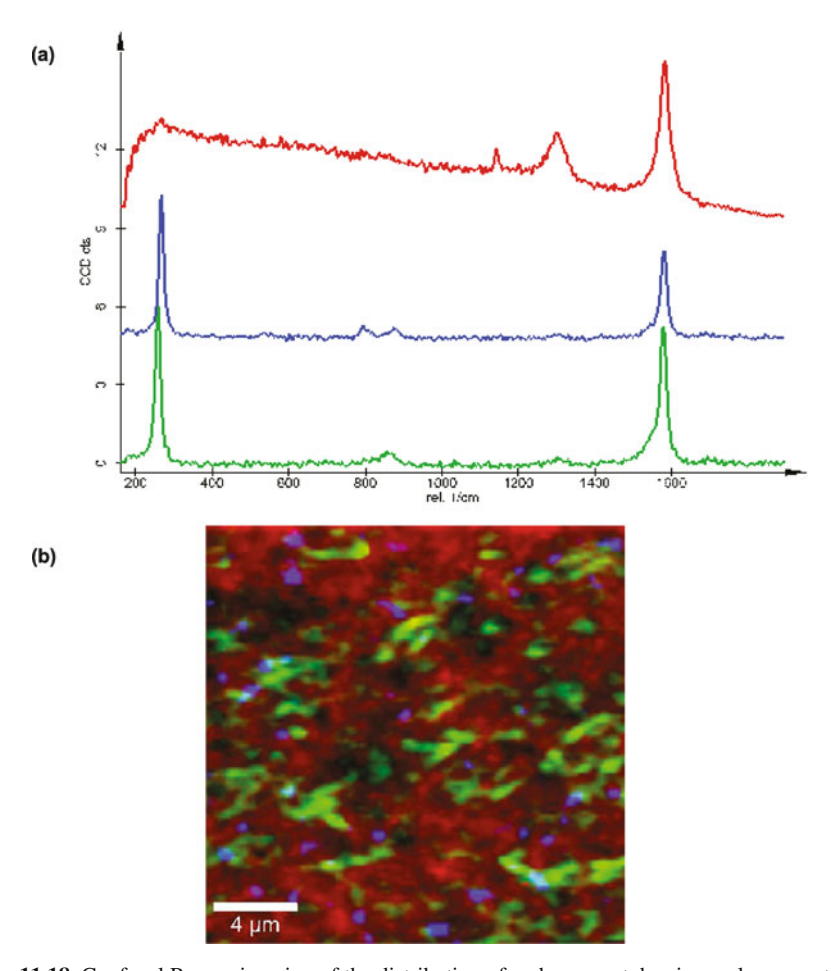


Fig. 11.18 Confocal Raman imaging of the distribution of carbon nanotubes in a polymer matrix: characteristic Raman spectra evaluated from the 2D array of 10,000 spectra using the cluster analysis tool of the WITec Project Plus software, polymer matrix (*red*), carbon nanotubes with different diameter (*blue, green*) (**a**) and color-coded Raman image of the analyzed surface area (**b**)

11.6 Summary

Confocal Raman microscopy is a powerful tool for the characterization of polymeric materials. It could be shown that Raman spectroscopy allows the identification of chemically distinct materials. In combination with a confocal microscope, the distribution of various polymer phases within a polymer matrix can be determined. As shown in Sect. 11.2, confocal Raman microscopy is sensitive to the orientation of long-chain polymeric materials, enabling the determination of orientation of fibers when the polarization direction of the excitation laser is known. Polymorphs of a polymer can be detected and their distribution on the sample visualized. In Sect. 11.3 the combination of confocal Raman microscopy and atomic force microscopy has been demonstrated in the studies of thin films of polymer blends. All studied blends showed a clear phase separation and although the analyzed films were very thin (<100 nm), the sensitivity of the confocal Raman microscope was still high enough to identify the chemical composition of the films with short integration times of 30–100 ms/spectrum.

Structural changes observed with AFM while imaging the polymer films can be linked with the chemical composition from Raman imaging, thus leading to the correlation between chemical composition data and the constructional morphology of the films. Furthermore, due to its confocal setup, the confocal Raman microscope can be used to determine the layered structure of polymer coatings without laborious sample preparation as shown in Sect. 11.4. Additionally, the detection of inorganic materials in a polymer matrix was demonstrated in Sect. 11.5.

Confocal Raman microscopy (especially in combination with AFM) allows the nondestructive characterization of heterogeneous materials. In combination with a suitable software package, chemical identification of sample volumes of only $0.004\,\mu\text{m}^3$ becomes available at integration times of less than $100\,\text{ms}$ spectrum.

References

- 1. W. Stocker, J. Beckmann, R. Stadler, J. Rabe, Macromolecules 29, 7502 (1999)
- N. Koneripalli, R. Levicky, F.S. Bates, J. Ankner, H. Kaiser, S.K. Satija, Langmuir 12, 668 (1996)
- 3. T.J. Morkved, H.M. Jaeger, Europhys. Lett. 40, 643 (1997)
- 4. T.S. McLean, B.B. Sauer, J. Polym. Sci. Part B 37, 85 (1999)
- 5. T. Zhong, D. Inniss, K. Kjoller, V. Ellings, Surf. Sci. 290, L688 (1993)
- 6. S.N. Magonov, V. Elings, M.H. Whangbo, Surf. Sci. 372, L385 (1997)
- 7. J. Tamayo, R. Garcia, Appl. Phys. Lett. **71**, 2394 (1997)
- 8. J. Tamayo, R. Garcia, Appl. Phys. Lett. 73, 2926 (1998)
- 9. R. Garcia, J. Tamayo, A. Paolo, Surf. Interface Anal. 27, 312 (1999)
- 10. J.P. Cleveland, B. Anczykowski, A.E. Schmid, V.B. Elings, Appl. Phys. Lett. 72, 2613 (1998)
- 11. W.W. Scott, B. Bhushan, Ultramicroscopy 97, 151 (2003)
- 12. G. Bar, Y. Thomann, R. Brandsch, H.J. Cantow, M.H. Whangbo, Langmuir 13, 3807 (1997)
- 13. S. Hild, O. Marti, F. Hollmann, B. Rieger, Eur. Polym. J. 40, 905 (2004)
- H.W. Siesler, K. Holland-Moritz, Infrared and Raman Spectroscopy of Polymers (Marcel Dekker, New York, NY, 1990)

- 15. H. Owen, D.E. Battery, M.J. Pelletier, J.B. Slater, SPIEE Proc. **260**, 2406 (1995)
- 16. E.D. Lipp, R.L. Grosse, Appl. Spectrosc. **52**, 42 (1998)
- 17. J.F. Aust, K.S. Booksh, M.L. Myrick, Appl. Spectrosc. **50**, 382 (1996)
- 18. T. Wilson, *Confocal Microscopy* (Academic, London, 1990)
- J.M. Chalmers, H.G.M. Edwards, J.S. Lees, D.A. Long, M.W. Mackenzie, H.A. Willis, J. Raman Spectrosc. 22, 613 (1991)
- 20. X. Wang, S. Michielsen, J. Appl. Polym. Sci 82, 1330 (2001)
- 21. A.S. Nielsen, D.N. Batchelder, R. Pyrz, Polymer **43**, 2671 (2002)
- 22. G.R. Strobl, W. Hagedorn, J. Polym. Sci. Polym. Phys. 16, 1181 (1978)
- 23. R. Mutter, W. Stille, G. Strobl, J. Polym. Sci. Pol. Phys. 31, 99 (1993)
- 24. P. Hendra, J. Vile, H.A. Willis, V. Zichy, Polymer 25, 785 (1984)
- 25. G. Keresztury, E. Foldes, Polym. Test **9**, 329 (1990)
- 26. E. Lamparska, V. Liegeois, O. Quinet, B. Champagne, ChemPhysChem 7, 2366 (2006)
- 27. V.K. Kuppa, J. in't Veld, G.C. Rutledge, Macromolecules 40, 5187 (2007)
- 28. K. Tashiro, S. Minami, G. Wu, M. Kobayashi, J. Polym. Sci. Polym. Phys. 30, 1143 (1992)
- J.C. Rodriguez-Cabello, J.C. Merino, T. Jawhari, J.M. Pastor, J. Raman Spectrosc. 27, 463 (1996)
- 30. L. Holliday, Structure and Properties of Oriented Polymers, Chap. 7 (Applied Science Publishers, London, UK, 1975)
- 31. S. Hild, A. Rosa, O. Marti, *Scanning Probe Microscopy of Polymers* (Oxford University Press, 1998), p. 110
- P. Schmidt, J. Dybal, J. Scudla, M. Raab, J. Kratochvil, K. Eichhorn, S.L. Quintana, J.M. Pastor, Macromol. Symp. 184, 107 (2002)
- 33. H. Tadokoro, H. Kobayashi, M. Ukita, K. Yasufuku, S. Murahashi, J. Chem. Phys. 42, 1432 (1965)
- 34. R.G. Snyder, J.H. Schachtschneider, Spectrochim. Acta 20, 853 (1964)
- 35. U. Schmidt, S. Hild, W. Ibach, O. Hollricher, Macromol. Symp. **230**(1), 133 (2005)
- L. Utracki, Encyclopaedic Dictionary of Commercial Polymer Blends (ChemTec Publishing, Toronto, 1994)
- 37. L. Utracki, *Polymer Blends Handbook* (Kluwer Academic, Dordrecht, 2002)
- 38. U. Schmidt, W. Ibach, J. Mueller, O. Hollricher, SPIE Proc. **6616**(1), 66160E (2007)
- 39. H. Kupsov, G.N. Zhizhin, Handbook of Fourier Transform Raman and Infrared Spectra of Polymers (Elsevier, Amsterdam, 1998)
- 40. G. Socrates, Infrared and Raman Characteristic Group Frequencies (Wiley, Chichester, 2001)
- 41. Z.O. Oyman, W. Ming, F. Micciche, E. Oostveen, J. van Haveren, R. van der Linde, Polymer 45, 7431 (2004)
- 42. M. Milnera, J. Kürti, M. Hulman, H. Kuzmany, Phys. Rev. Lett. 48, 1324 (2000)
- 43. A. Jorio, R. Saito, J.H. Hafner, C.M. Lieber, M. Hunter, T. McCluve, G. Dresselhaus, M.S. Dresselhaus, Phys. Rev. Lett. 86, 1118 (2001)

Chapter 12 Stress Analysis by Means of Raman Microscopy

Thomas Wermelinger and Ralph Spolenak

Abstract Raman microscopy provides the unique possibility to measure stresses in a fast and uncomplicated way in the sub-micrometer range. The maximal lateral resolution is determined by the laser wavelength. In a Raman spectrum of a deformed or strained material, peak positions are shifted relative to the peak positions of stress-free material. Quantifying these shifts allows the determination of sign and magnitude of internal stresses. Depending on the Raman tensor and therefore on the material's crystal structure, several components of the stress tensor can be measured. Hence, it is not always possible to analyze complicated stress states just by means of Raman microscopy without making adequate assumptions. For transparent Raman-active materials, 3D stress fields can be measured. This chapter will outline the principles of Raman stress measurements and present case studies on ceramics, semiconductors, and polymers.

12.1 Introduction

Over the past 20 years Raman microscopy has become a powerful tool for measuring mechanical stresses in the sub-micrometer range. Especially in the semiconductor industry the knowledge of mechanical stresses is a prerequisite for the production of reliable devices. Raman spectroscopy is currently the only laboratory method able to locally measure mechanical stresses on the micrometer length scale. Alternative methods, which either are based on large-scale facilities or are still in the development stages, include X-ray microdiffraction [1], convergent beam electron diffraction with a transmission electron microscope (TEM) [2], electron-induced Kossel diffraction with a scanning electron microscope (SEM) [3], or electron backscatter diffraction (EBSD) with an SEM [4]. All of these methods have two aspects in common: they all measure elastic strain in a crystalline material and require the knowledge of its elastic properties to convert strain into stress. All diffraction methods, independent of whether photons or electrons are the probe utilized, directly provide a measure of the lattice parameter of crystalline materials. Raman spectroscopy, on the other hand, is a spectroscopy technique which yields the energies of the phonon spectrum. In contrast to diffraction techniques which solely require crystal periodicity, Raman spectroscopy requires a material to be polarizable, which limits

the material's choice to ceramics, polymers, and semiconductors. Raman studies on metals [5] rely on the mechanical coupling of a Raman-active material to the metal and subsequent mechanical modeling. While Raman spectroscopy has traditionally been employed for studies of stress in microelectronic materials [6–10], strain measurements by Raman microscopy and the conversion to mechanical stress are currently being extended to other material's classes and applications. The following chapter thus focuses on the principles of strain measurements by Raman microscopy, its application to Si-based materials, and novel extensions.

12.1.1 Theoretical Background

Originally, Raman spectroscopy was used for analyzing and characterizing different compositions or phases, but the spectrum itself contains much more information. The Raman effect refers to the inelastic scattering of light due to its interaction with phonons or molecular vibrations. Strain due to mechanical stress affects the frequencies of the Raman-active phonons or molecular vibrations which lead to a shift of the Raman peak positions relative to the stress-free peak position [11]. As a simple metaphor one can compare the process to the tuning of a guitar string. The tuning changes the strain and the mechanical stress in the guitar string which leads to a change of the frequency of the vibration and therefore would also lead to a shift of the positions of the Raman peaks. In the following section we will explain the underlying theory of measuring the strain and show how to convert the results into stress. Different methods to measure mechanical stresses in materials with a cubic crystal structure such as silicon will be presented. The stress resolution of the method depends on the stress sensitivity of the Raman peak and the signal-to-noise ratio of the measured signal.

Only certain types of lattice vibrations give rise to Raman scattering. The Raman tensors show which phonons are Raman active and what kind of orientation these phonons have. The Raman tensor can be determined from the crystal structure of the material. According to Louden [12], silicon has three Raman tensors. In the crystal coordinate system x = [100], y = [010], and z = [001] they are

$$\Delta_1 = \begin{bmatrix} 0 & 0 & 0 \\ 0 & 0 & d \\ 0 & d & 0 \end{bmatrix}, \qquad \Delta_2 = \begin{bmatrix} 0 & 0 & d \\ 0 & 0 & 0 \\ d & 0 & 0 \end{bmatrix}, \qquad \Delta_3 = \begin{bmatrix} 0 & d & 0 \\ d & 0 & 0 \\ 0 & 0 & 0 \end{bmatrix}$$
(12.1)

where d is the component different from zero. These components define the intensity of a certain peak. In the case of silicon d is equal in all three tensors.

The total scattering intensity of the phonon modes (I) for a given geometry can be determined from the Raman tensors, Δ_j , and the polarization vector of the incident (e_i) and scattered (e_s) light and is given by

$$I = C \sum_{i} \left| e_{i} \cdot \Delta_{j} \cdot e_{s} \right|^{2} \tag{12.2}$$

where C is a constant. Measuring in a back-scattering mode from a (001) surface the incident as well as the scattered light beam is normal to the surface. In this case Δ_1 and Δ_2 correspond to scattering from the transverse optical phonons (TO), polarized along the x- or the y-axis, respectively. Δ_3 correlates to scattering from the longitudinal optical phonons (LO), polarized along the z-axis. Whether the phonon is longitudinal or transversal depends on the surface from which scattering is observed. Measuring in a back-scattering mode from a (100) surface, Δ_1 corresponds to the LO phonon [6]. The phonons are triply degenerated which means that they have all the same wave number of approximately $520\,\mathrm{cm}^{-1}$.

It follows from (12.2) that different modes can be measured depending on the orientation of the surface and the polarization direction of the light. Table 12.1 shows which of the modes can be obtained for a back-scattering experiment from a (001) surface, a (110) surface, or a $(11\overline{2})$ surface.

In a back-scattering configuration for a (001) surface only the longitudinal optical phonon mode is allowed regardless of the polarizations of the incident and the scattered light. In contrast to this, the back-scattering configuration of a (110) as well as a (11 $\bar{2}$) surface allows the excitation of all three Raman modes [8]. In these latter two cases the longitudinal and the transversal phonons can be measured independently from each other. Measuring from a (111) surface, all phonon modes are excited regardless of the polarization of the incident and the scattered light [13].

Polarization		Visible						
$e_{\rm i}$	$e_{\rm s}$	Δ_1	Δ_2	Δ_3				
Back sc	Back scattering from (001)							
(100)	(100)	_	_	_				
(100)	(010)	_	_	X				
$(1\bar{1}0)$	$(1\bar{1}0)$	_	-	X				
(110)	$(1\bar{1}0)$	_	_	_				
Back scattering from (110)								
$(1\bar{1}0)$	(001)	X	X	-				
$(1\bar{1}0)$	$(1\bar{1}0)$	_	-	X				
(001)	(001)	_	_	_				
Back scattering from (112)								
$(1\bar{1}0)$	(111)	X	X	_				
$(1\bar{1}0)$	$(1\bar{1}0)$	_	-	X				
(111)	(111)	X	X	X				

Table 12.1 Polarization selection rules for back scattering from a (001), a (110), or a (11\overline{2}) surface

12.1.2 Measuring in Conventional Back-Scattering Configuration

Strain caused by mechanical stress can influence the frequencies of the Raman mode [8, 11, 14, 15]. In the absence of strain, the triply degenerated phonons lead to a peak at $\omega_0 = 520 \, \mathrm{cm}^{-1}$. Strain changes the phonon vibrations and therefore can lift the

degeneracy of the Raman frequencies due to a symmetry reduction of the Raman tensors [8, 16]. This symmetry reduction causes splitting and shifting of the Raman peak. Ganesan et al. [11] showed that if strain is applied to a sample, the frequencies of the three optical phonon modes can be calculated by finding the eigenvalues, λ_j , j = 1, 2, 3, in the following equation:

$$\begin{vmatrix} p\varepsilon_{11} + q(\varepsilon_{22} + \varepsilon_{33}) - \lambda_1 & 2r\varepsilon_{12} & 2r\varepsilon_{13} \\ 2r\varepsilon_{21} & p\varepsilon_{22} + q(\varepsilon_{11} + \varepsilon_{33}) - \lambda_2 & 2r\varepsilon_{23} \\ 2r\varepsilon_{31} & 2r\varepsilon_{32} & p\varepsilon_{33} + q(\varepsilon_{11} + \varepsilon_{22}) - \lambda_3 \end{vmatrix} = 0 \quad (12.3)$$

where $p=-1.85~\omega_0^2$, $q=-2.31~\omega_0^2$, and $r=-0.71~\omega_0^2$ are the phonon deformation potentials (PDPs), which are material constants. ε_{ij} are the components of the strain tensor. The frequency of each mode in the presence of strain ω_j (j=1,2,3) of the strained crystal is related to the unstrained frequency, ω_0 by the following relationship:

$$\omega_j^2 = \omega_0^2 - \lambda_j \tag{12.4}$$

or, for the approximation of small strains [8]

$$\Delta\omega_j = \omega_j - \omega_0 \approx \frac{\lambda_j}{2\omega_0} \tag{12.5}$$

The polarization direction of each mode is given by the eigenvectors of (12.3).

The relation between the strain tensor ε in (12.3) and the stress tensor σ is given by Hooke's law:

$$\begin{cases}
\varepsilon_{11} \\
\varepsilon_{22} \\
\varepsilon_{33} \\
2\varepsilon_{23} \\
2\varepsilon_{13} \\
2\varepsilon_{12}
\end{cases} =
\begin{bmatrix}
s_{11} s_{12} s_{12} & 0 & 0 & 0 \\
s_{12} s_{11} s_{12} & 0 & 0 & 0 \\
s_{12} s_{12} s_{11} & 0 & 0 & 0 \\
0 & 0 & 0 s_{44} & 0 & 0 \\
0 & 0 & 0 & 0 s_{44} & 0 \\
0 & 0 & 0 & 0 & 0 s_{44}
\end{bmatrix}
\begin{pmatrix}
\sigma_{11} \\
\sigma_{22} \\
\sigma_{33} \\
\sigma_{23} \\
\sigma_{13} \\
\sigma_{12}
\end{cases}$$
(12.6)

where $s_{11} = 7.68 \times 10^{-2} \text{ Pa}^{-1}$, $s_{12} = -2.14 \times 10^{-12} \text{ Pa}^{-1}$, and $s_{44} = 12.7 \times 10^{-12} \text{ Pa}^{-1}$ are components of the elastic compliance tensor. This equation allows the calculation of the developing stresses from the measured strain. In the case of uniaxial stress along the [100] direction, (12.6) leads to the following nonzero components of the strain tensor: $\varepsilon_{11} = s_{11}\sigma_{11}$, $\varepsilon_{22} = s_{12}\sigma_{11}$, and $\varepsilon_{33} = s_{12}\sigma_{11}$. Solving (12.3) and (12.5) leads to the following results:

$$\Delta\omega_{1} = \frac{\lambda_{1}}{2\omega_{0}} = \frac{1}{2\omega_{0}}(ps_{11} + 2qs_{12})\sigma$$

$$\Delta\omega_{2} = \frac{\lambda_{2}}{2\omega_{0}} = \frac{1}{2\omega_{0}}[ps_{12} + q(s_{11} + s_{12})]\sigma$$

$$\Delta\omega_{3} = \frac{\lambda_{3}}{2\omega_{0}} = \frac{1}{2\omega_{0}}[ps_{12} + q(s_{11} + s_{12})]\sigma$$
(12.7)

For small strains one can assume that the Raman tensors do not change. According to Table 12.1 only the third Raman mode can be seen, when measuring in a back-scattering mode from a (001) surface. Therefore, only $\Delta\omega_3$ has a nonzero value. Similar to the uniaxial case, calculations can be performed assuming biaxial stress $(\sigma_{xx} + \sigma_{yy})$. Then an increase of the Raman frequency corresponds to compressive stress while a decrease of the Raman frequency indicates tensile stress.

The majority of substrates for silicon-based microelectronic devices have a (001) surface. As a consequence, the only measurable phonon is the longitudinal optical phonon and information is obtainable only from one parameter, namely for the out-of-plane component. As the stress tensor has six degrees of freedom, it is always necessary to make assumptions about the stress state. To show the importance of a realistic assumption for the stress tensor, three different stress states (hydrostatic, uniaxial along the x-axis, uniaxial along the z-axis) and their influence on the Raman signal are given [17]. In all three cases one supposes a Raman shift of 1 cm^{-1} . In the hydrostatic case, the corresponding values are

$$\sigma = -540 \begin{pmatrix} 1/3 & 0 & 0 \\ 0 & 1/3 & 0 \\ 0 & 0 & 1/3 \end{pmatrix} MPa$$
 (12.8)

while if one assumes a uniaxial stress along the x-axis, the value changes to

$$\sigma = -450 \begin{pmatrix} 1 & 0 & 0 \\ 0 & 0 & 0 \\ 0 & 0 & 0 \end{pmatrix} \text{MPa}$$
 (12.9)

and for uniaxial stress along the z-axis one gets

$$\sigma = -900 \begin{pmatrix} 0 & 0 & 0 \\ 0 & 0 & 0 \\ 0 & 0 & 1 \end{pmatrix} \text{MPa}$$
 (12.10)

The large differences among the values have an important consequence. Either the performed measurement is made on samples where the shape of the tensor is already well known, or one has to find a way to overcome the limitation of measuring only one phonon mode. In the following section we will not only explain how to measure stresses for the simple case where one phonon is excited but also show two different ways to overcome experimental limitations.

12.1.3 Off-Axis Raman Spectroscopy

The complete stress tensor for an arbitrary crystal orientation can be determined by tilting the incident beam away from the normal axis while polarizing the incident as well as the scattered beam [18, 19]. This experimental setup is called off-axis Raman

spectroscopy. One has to keep in mind that in this setup the laser is not focused and therefore the lateral resolution is low. So the method is suitable best for analyzing general stress states.

To detect all three Raman modes from a (001) surface of a silicon wafer, either the incident and/or the scattered light must have electric field components in all three x, y, and z directions to get signal from all three Raman tensors (see Sect. 12.1.2). As another requirement, incident and scattered light beams have to be polarized. If the incident light deviates from the surface normal, all three Raman modes are activated and can be measured. By adjusting the polarizer, one is able to vary the proportion of each mode to the total intensity signal. The correct experimental setup allows studying a selected phonon mode. Tuning the system allows one to determine all six components of the stress tensor.

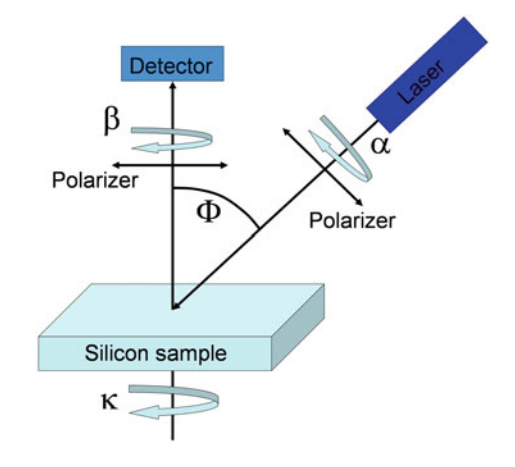
In the off-axis Raman spectroscopy it is important to define several experimental parameters, which have to be under direct experimental control. In the case described here four different angles have to be known. The angle between the incident laser and the surface normal Φ is the first important parameter. This angle allows the detection of all three phonon modes due to the nonzero z-component. The orientation of the incident light (α) as well as the scattered light (β) adjusted by a polarizer must be known. Finally, the orientation of the sample (κ) with respect to the incident light is also of high importance (see Fig. 12.1). Once the tilting angle (Φ) is fixed, all the other angles are adjusted to optimize the sensitivity of the apparatus

Due to the off-axis setup of the laser, (12.2) has to be adjusted. The final signal intensity at the detector from a given phonon mode can be expressed by the following equation:

$$I = C\left(d_k^H B d_k\right) \tag{12.11}$$

In this notation d_k is a pseudovector. Its components are the nonzero elements of the Raman tensor which only depend on the applied stress but not on the experimental

Fig. 12.1 Simplified schematic of an experimental setup for polarized off-axis Raman spectroscopy. α and β denote the orientation of the polarizer of the incident light and the scattered light, respectively. Φ is the tilting angle between the surface normal and the incident laser light. κ refers to the rotation angle of the silicon sample



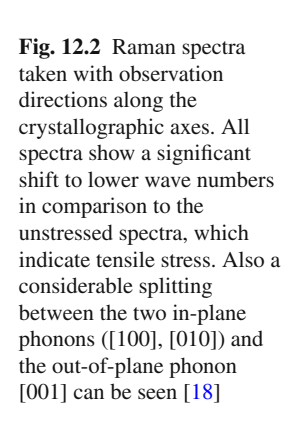
setup of the system. The superscript H denotes the complex-conjugate (Hermitian) transpose. B is the observation matrix which describes the directions of the vibrations. It depends only on the experimental setup of the measuring system and on the material properties, such as refractive index, but it does not depend on applied stress. C is a constant.

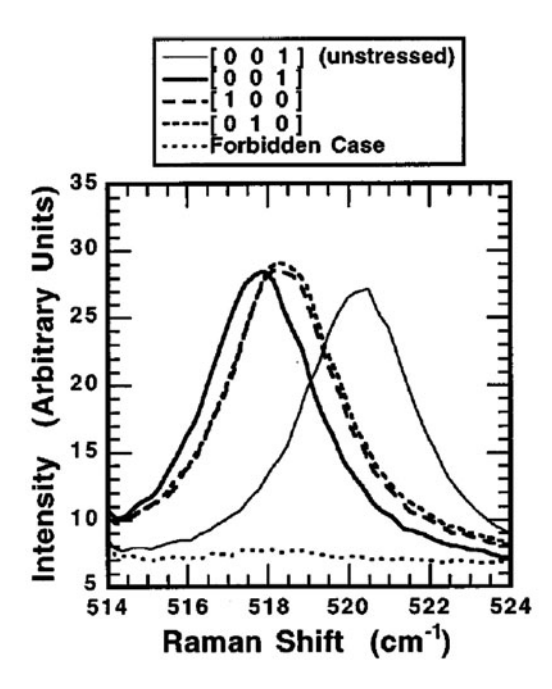
It is important to point out that in (12.11) the shape of the spectrum not only depends on the stress but is also a function of the experimental configuration, namely the observation directions given by the observation matrix B. B includes all the parameters which are under experimental control and must be calculated for every configuration $(\Phi, \alpha, \beta, \kappa)$. By adjusting these parameters, it is possible to selectively measure different phonon vibrations.

As an example, the Raman spectra measured on a silicon wafer with a (001) surface orientation under biaxial stress are shown in Fig. 12.2 [18].

The Raman measurements were taken parallel to the crystallographic axes. As one can see, it is possible to analyze different phonon vibrations in different observation directions. For visualizing the absolute shifts of the Raman peak position a spectrum from the unstressed wafer is plotted as well. The splitting between the two transversal optical phonons in the [100] and [010] direction and the longitudinal phonon in the [001] direction indicates biaxial stress in the wafer.

In conclusion one can say that polarized off-axis Raman spectroscopy is a characterization method which allows the analysis of the complete stress tensor of a silicon wafer. The largest drawback of the method is the lateral resolution. This problem can be overcome by implementing the method for micro-Raman spectroscopy.





12.1.4 Stress Tensor Analysis in Back-Scattering Raman Microscopy

We have seen that stress tensor analysis by means of Raman spectroscopy is generally possible, although the presented method does not provide local information about the stress state. To obtain local information about the stress is crucial for microelectronics, as it can be the origin of hillocks, voids, and cracks [20]. Therefore a method is required, which allows the measurement of stresses with a lateral resolution in the micrometer range or better. Bonera et al. presented a method to measure different components of the stress tensor with a spatial resolution of $1 \mu m$ by Raman spectroscopic technique [17, 21].

Equations (12.1) and (12.2) show that one obtains only information from the longitudinal optical phonon from an (001) surface in an ideal back-scattering experiment. The two transversal optical phonons are not excited. In this case, the electric field of the laser light is perpendicular to the surface normal (see Fig. 12.3a). If one uses an objective lens with a large numerical aperture (NA), all three phonons will be excited due to the fact that the incident laser light is no longer polarized perpendicular to the surface normal (Fig. 12.3b). The polarization vector also has a component in the *z*-axis. The higher the NA, the higher the intensity from the transversal optical phonons will be.

Polarizing the incident as well as the scattered light offers the possibility to measure all three phonon modes separately. Using the Porto notation, these three cases can be written as

$$z(y, y)\bar{z} \to \omega_1$$

$$z(x, x)\bar{z} \to \omega_2$$

$$z(y, x \otimes y)\bar{z} \to \omega_3$$
(12.12)

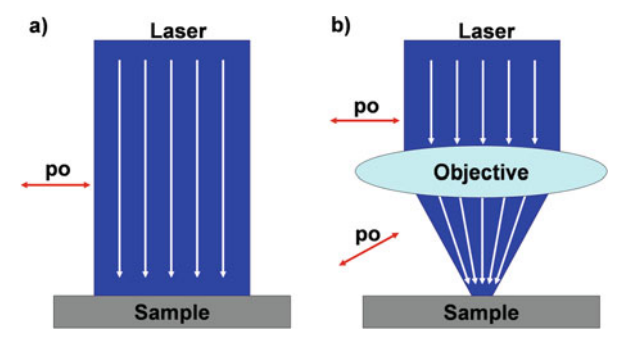


Fig. 12.3 (a) Ideal back-scattering configuration. The polarization (po) of the incident laser light is perpendicular to the surface normal. Only the LO phonon is excited. (b) Due to focusing the laser light the polarization vector (po) obtains a component parallel to the surface normal. Therefore all phonon modes are excited

In the Porto notation, the first symbol, z, defines the direction of the in-coming light, while the last symbol, \bar{z} , refers to the direction of the scattered light. The \bar{z} implies that the scattered light is rotated 180° with respect to z. The first parameter within the parentheses describes the polarization of the incident light, while the second symbol is the polarization direction of the scattered light. Equation (12.12) shows which experimental setup is required for measuring a certain phonon mode. To study ω_3 , which is the LO phonon, no polarizer is needed in the scattered beam. In this case, not only the LO phonon contributes to the total intensity, but also one of the TO phonons. However, in comparison to the intensity of the LO phonon the contribution of the TO phonon is negligible. Therefore, to get information from all three phonon vibrations, one has to measure the same region with all three different polarization states of (12.12). In an unstressed area, ω_1 , ω_2 , and ω_3 have the same frequency. In stressed areas, the three frequencies are shifted with respect to the unstrained case. The total amount of the shift of the corresponding frequency depends on the actual stress state.

To calculate the stress state, one has to assume that the angles of the unit cells of the crystal do not change and the unit cell remains orthogonal. This assumption results in all nondiagonal values of the stress tensor to vanish:

$$\sigma_{ij} = 0, \qquad i \neq j \tag{12.13}$$

In most cases this assumption is a simplification of the true stress state. Nevertheless, it allows one to measure three of the six components of the stress tensor instead of only one. It is convenient to split the stress tensor into a hydrostatic (σ_h) and a traceless (σ_t) component:

$$\sigma = \sigma_{\rm h} + \sigma_{\rm t} \tag{12.14}$$

Using (12.14) simplifies the secular matrix for the strained crystal (see (12.3)) to the following three linear equations:

$$\Delta\omega_{j} = \frac{(p+2q)(s_{11}+2s_{12})}{2\omega_{0}}\alpha' \cdot \sigma_{h} \cdot \alpha + \frac{(p-q)(s_{11}-s_{12})}{2\omega_{0}}\alpha' \cdot \sigma_{t} \cdot \alpha \quad (12.15)$$

where $\alpha = x, y$, and z; s_{11} and s_{12} are elements of the compliance tensor (see (12.6)); p and q are phonon deformation potentials. Equation (12.15) allows to determine the stress tensor with a lateral resolution depending on the wave length of the laser and the numerical aperture of the lens.

In conclusion, the above section presents a method to measure stress-induced Raman shifts from a silicon surface. The spatial resolution is in the sub-micrometer range. The method allows to measure different phonon polarizations which belong to different directions in space.

12.2 Case Studies

12.2.1 3D Raman Spectroscopy Measurements

Stresses and strains are important since they are related to material deformation and failures of devices. The detailed understanding of the stress fields can improve the design of applications to gain highest possible quality and mechanical durability. The most detailed analysis would be a full 3D characterization of the stress state in a material or device. However, at the moment only a few methods, such as 3D X-ray diffraction microscopy, are known to perform 3D measurements with a resolution at or below the micrometer range [22]. But few such systems are available worldwide. Therefore, only a few experiments have been performed to date. An alternative method at a laboratory scale is confocal Raman microscopy.

Sapphire is often used for pressure sensors or in applications for the electronics industry. Therefore it is important to understand the deformation behavior of sapphire single crystals. In this study a sapphire single crystal was used for measuring 3D stress fields around an indent with confocal Raman microscopy [23].

An indent from a Vickers microindentation was placed on the basal (0001) plane of a sapphire single crystal. The indent had a depth of about $0.5 \,\mu m$ and a diameter of about $4.5 \,\mu m$ (see Fig. 12.4). A confocal Raman microscope (WITec, CRM 200, wavelength: 442 nm) was used to measure the peak shifts around the indent. Due to the confocality of the microscope an exact 3D positioning of the focus spot is feasible [24]. The lateral resolution of the microscope is defined by the Rayleigh equation: $d = 1.22(\lambda_{Laser}/2NA)$ where λ_{Laser} is the wavelength of the laser and NA is the numerical aperture. In the case described here, the lateral resolution is 300 nm.

Figure 12.5 shows the Raman spectra of a sapphire single crystal measured in a back-scattering mode from the basal (0001) plane. The visible peaks at 380, 432,

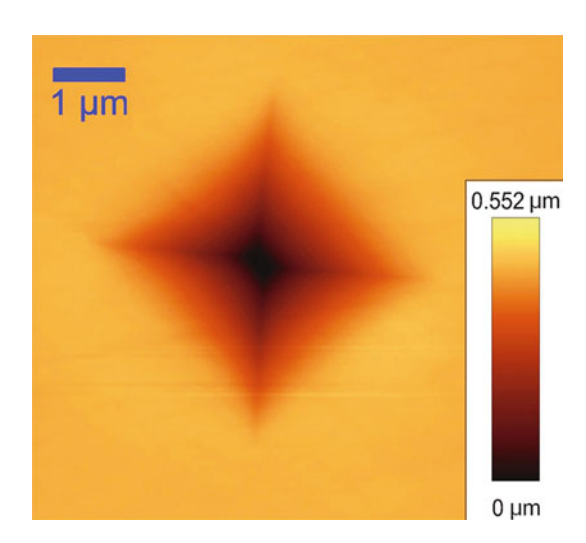
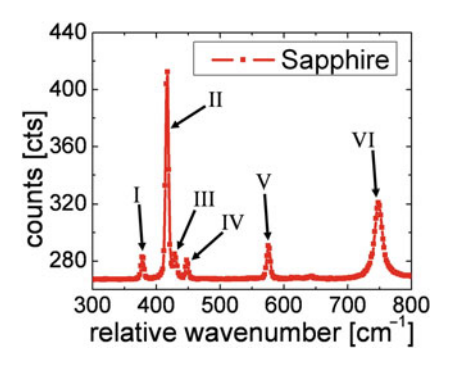


Fig. 12.4 AFM image of the Vickers microindent on the basal C(0001) plane of the Sapphire crystal. The diameter of the indent is about 4.5 μm

Fig. 12.5 Raman spectrum of a Sapphire single crystal. Arrows I, III, IV, V, and VI at 380, 432, 451, 578, and $751 \,\mathrm{cm}^{-1}$, respectively belong to E_g modes. The peak at $417 \,\mathrm{cm}^{-1}$ belongs to an A_{1g} mode



451, 578, and 751 cm⁻¹ belong to E_g modes while the peak at 417 cm⁻¹ belongs to an A_{1g} mode. With the exception of the peak at 378 cm⁻¹, which belongs to a phonon with an in-plane and out-of-plane component, all peaks belong to out-of-plane phonon vibrations.

Starting from the surface of the sapphire crystal, a stack of xy scans was taken at different z-positions. All measurements were made with the same x- and y-positions, changing only the z-coordinate by $0.4 \,\mu$ m between scans.

Figure 12.6 shows the shift of the peak at 417 cm⁻¹ around the indent starting from the surface of the single crystal down to 2.8 µm. The amount of the peak shift correlates directly to the residual stress. Bright colors correspond to compressive stresses whereas dark colors correspond to tensile stresses. While the indent has fourfold symmetry (see Fig. 12.4) the residual stress field around the indent shows a clear threefold symmetry.

The scans were performed in a back-scattering mode with a $100 \times$ objective with an NA of 0.9. Therefore, the lateral resolution was 300 nm. The scans had a size of

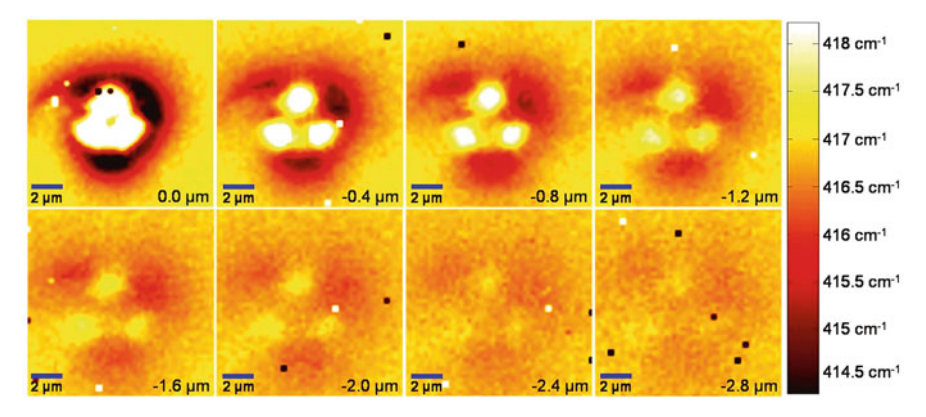


Fig. 12.6 Shift of the peak at $417\,\mathrm{cm^{-1}}$ wave numbers around the indent. High wave numbers correspond to compressive stress while low wave numbers correspond to tensile stress. The difference between maps is a distance of $0.4\,\mu\mathrm{m}$

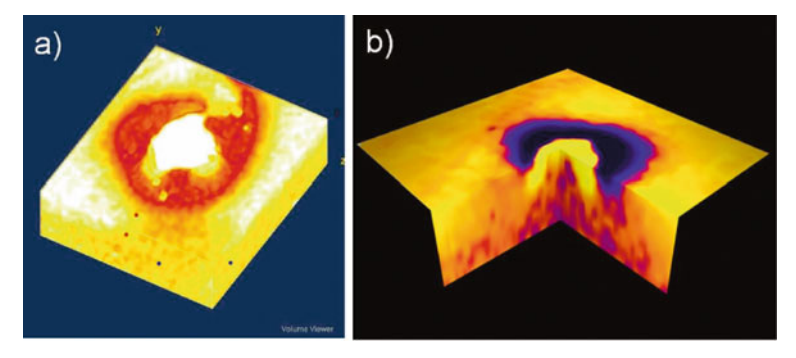


Fig. 12.7 The calculated 3D stress field around the indent. (a) Tensile stresses above a certain threshold are transparent. Only areas with compressive stresses or no stresses are visible in this volume $(12 \times 12 \times 4 \,\mu\text{m})$. (b) *Bright colors* indicate compressive stresses while *dark colors* correspond to tensile stresses $(20 \times 20 \times 2 \,\mu\text{m})$

 $12 \times 12 \,\mu\text{m}$ and consisted of 48×48 spectra. All the experiments were done with an integration time per spectra of $4.5 \, \text{s}$ using a 1800 grooves/mm grating.

From the stack of images it is possible to visualize the 3D stress field around the Vickers indent by using an image processing program such as imageJ [25]. Figure 12.7 shows the result of these calculations. However, as the peak at 417 cm⁻¹ belongs to an out-of-plane phonon vibration, only out-of-plane stresses are shown.

To understand why an indent with a clear fourfold symmetry leads to a residual stress field with a threefold symmetry one has to consider the deformation behavior of the material. In materials with a hexagonal crystal structure such as sapphire the c/a axis ratio of the unit cell defines the deformation behavior. Figure 12.8 shows the probability for activating a certain slip or twinning system as a function of the angle. The numbers refer to different deformation systems: "1" is a rhombohedral

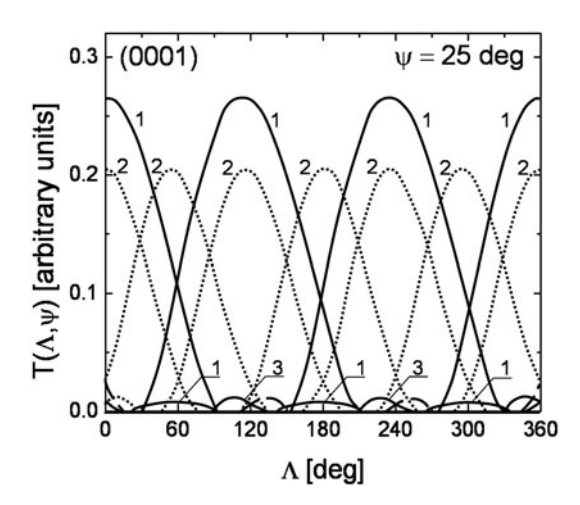


Fig. 12.8 Probability for activating a certain slip or twinning system, T, for all directions Λ around a spherical indent on the (0001) basal plane [26]

twinning system along the $\{0112\}$ plane, "2" belongs to a basal (0001) twinning system, and "3" denotes to a rhombohedral slip system along the $0\bar{1}\bar{1}2$ plane [26].

In this figure Λ describes an angle between the orientation of the indent and the orientation of the sapphire. The solid lines highlight the deformation systems which are activated in the particular experimental setup. According to Fig. 12.8, the dominating deformation systems involve threefold symmetry. Therefore it is reasonable to assume that the residual stress field will show a similar behavior.

The presented study demonstrated that the residual stress field is not solely influenced by the geometry of the indent. Although the Vickers indent shows fourfold symmetry the stress field shows a clear threefold symmetry. It could be shown that in a transparent sample such as sapphire the 3D stress field can be measured by means of confocal Raman microscopy, but only out-of-plane phonons could be measured. Therefore, relating this to the previous discussion little can be said about the stress tensor.

12.2.2 ZnO

As shown in the previous section, the confocal Raman microscopy makes it possible to calculate 3D stress fields. To get more information about the 3D stress field, it is important to measure different phonons corresponding to different directions. In the case of zinc oxide, two in-plane phonon vibrations which are perpendicular to each other can be measured.

As in the sapphire study, a single crystal was indented with a Vickers microindenter. In the case of the zinc oxide, the indent was placed on the sidewall of the crystal which was perpendicular to the basal plane. The indent (see Fig. 12.9a) had a diameter of about 7 μ m and a depth of about 1.6 μ m. Figure 12.9(b) shows a Raman spectra of zinc oxide (ZnO) taken from the sidewall of the sample. The electrical field of the incident laser light was parallel to the (0001)-axis of the crystal. Arrow II indicates the Raman peak at 378 cm⁻¹ which belongs to a phonon vibration of an A_1 mode polarized parallel to the (0001)-axis. Arrow III points to the Raman peak of an E_1 mode at 409 cm⁻¹ which corresponds to a phonon vibration polarized perpendicular to the *z*-axis [27]. As the phonons are perpendicular to each other, it is possible to analyze two components of the stress tensor. The peaks highlighted with arrows I and IV at 334 and 1149 cm⁻¹, respectively, belong to multiphonon processes.

Figure 12.10 shows the results of the Raman scans around the indent. The shifts of the Raman peaks at 378 and 409 cm⁻¹ are presented. High wave numbers correspond to compressive stress while low wave numbers correspond to tensile stresses. The low signal-to-noise ratio of the peak at 409 cm⁻¹ results in an image with much more noise than the image from the peak shift of the peak at 378 cm⁻¹. Nevertheless both scans show the same behavior; the residual stress field reveals a twofold symmetry.

As in the sapphire case, the twofold symmetry of residual stresses in zinc oxide can be explained by the deformation behavior. Zinc oxide has a wurtzite

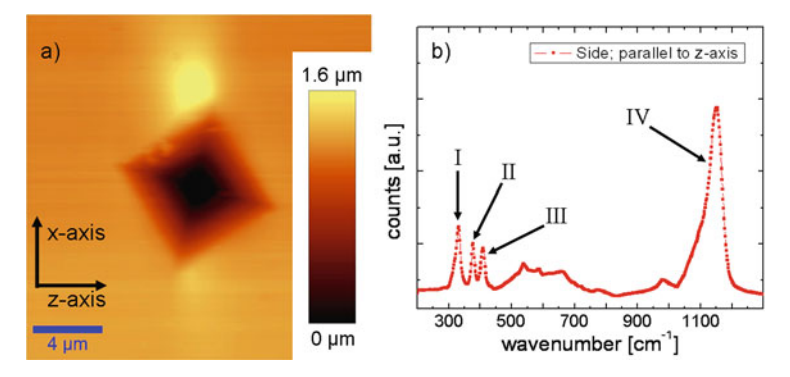


Fig. 12.9 (a) AFM image of the Vickers microindent on the sidewall of the zinc oxide crystal. The diameter of the indent is approximately $7\,\mu m$. (b) Raman spectra of ZnO taken from the sidewall of the crystal. The incident laser was polarized parallel to the *z*-axis of the crystal. The peaks highlighted with arrow II at $378\,\mathrm{cm^{-1}}$ and arrow III at $408\,\mathrm{cm^{-1}}$ are polarized parallel and perpendicular to the (0001)-axis, respectively. Arrow I at $334\,\mathrm{cm^{-1}}$ and arrow IV at $1149\,\mathrm{cm^{-1}}$ belong to multiphonon processes

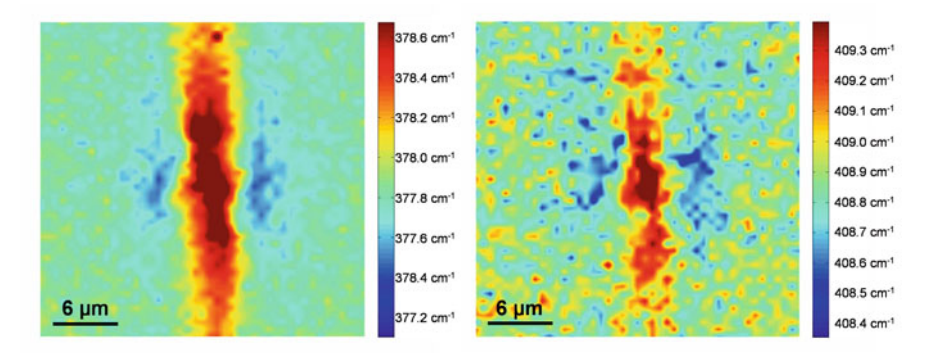
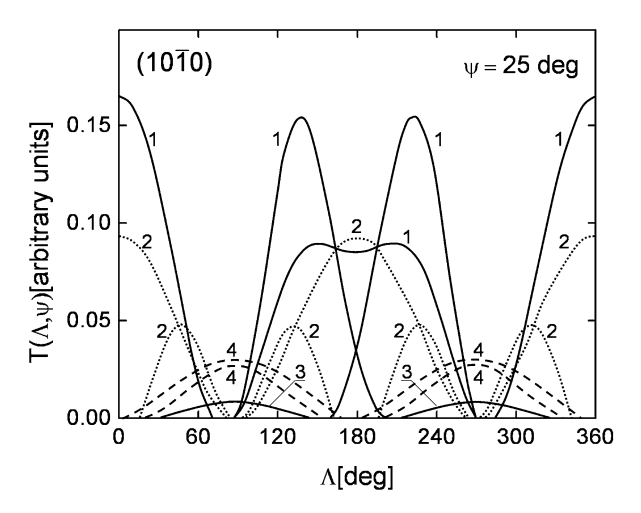


Fig. 12.10 Shift of the peaks at 378 and 409 cm⁻¹ around a microindent. High wave numbers correspond to compressive stresses while shifts to lower wave numbers indicate tensile stresses. The scan was taken at the surface of the sample

crystal structure which belongs to the group of hexagonal crystal systems [28, 29]. Although mechanism of plastic deformation in different hexagonal materials is never exactly equal the behavior still has some similarities. A comparable case of indentation on the ($10\bar{1}0$) plane of a sapphire single crystal showed that the plastic deformation exhibited a twofold symmetry (see Fig. 2.8) [26]. The numbers in Fig. 12.11 refer to different deformation systems: "1" is a rhombohedral twinning system along the {0112} plane, "2" belongs to a basal (0001) twinning system, "3" denotes a rhombohedral slip system along the { $12\bar{1}0$ }. All deformation systems are activated. Summing up the probability for activating certain slip or twinning systems lead to a twofold symmetry. As for sapphire, the twofold symmetry of the plastic deformation leads to the twofold symmetry of the residual stress field around the indent.

Fig. 12.11 Probability for activating a certain slip or twinning system, T, for all directions Λ around a spherical indent in sapphire on the (10 $\bar{1}0$) plane of a ZnO single crystal [26]. All deformation systems are activated



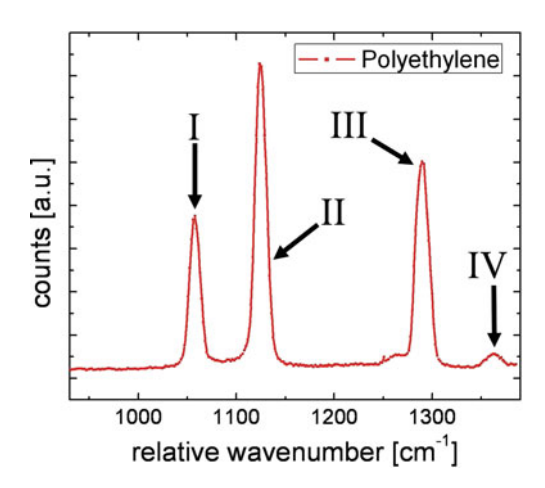
Manjon et al. [30] applied hydrostatic pressure to a zinc oxide crystal in a diamond anvil cell. They stated that the stress-induced shifts for the peaks at 378 and $409\,\mathrm{cm^{-1}}$ are 4.33 and $5.2\,\mathrm{cm^{-1}}$ GPa⁻¹, respectively. With these results it is possible to estimate the amount of the residual stresses in two directions which are perpendicular to each other. Taking the maximal peak shifts from the measurements leads to maximal residual stresses of $\pm 160\,\mathrm{MPa}$ parallel to the (0001)-axis and $\pm 90\,\mathrm{MPa}$ parallel to the (0001)-axis. Although the two directions are perpendicular to each other, neither of these directions have to correspond to the principle stress axis. Therefore, one cannot make any assumptions about shear stresses.

12.2.3 The Influence of Stress on the Peak Position of Polymers

So far we have described the influence of stress on the peak position of semiconductors (Si) and ceramics (sapphire and ZnO). But also the Raman peaks of materials other than ceramics and semiconductor are sensitive to applied stress and show similar effects [31–34]. In this section the stress-induced peak shift of polyethylene will be discussed.

Ultra-high molecular weight polyethylene (UHMWPE) thin films with different draw ratios were tested. The polyethylene was pre-oriented and stretched at an elevated temperature of 135°C to draw ratios of $\lambda = 20$, 40, and 50. A detailed description of the process is reported elsewhere [35]. The draw ratio is defined as the ratio of the unit length after the deformation, L to the initial unit length, L_0 : $\lambda = L/L_0$. The drawing leads to a preferred orientation of the polyethylene chains. The degree of the orientation after the stretching process has an influence on the mechanical properties such as the Young's modulus and the strain at breaking. For example, Young's modulus ranges from 40, 70, to 80 GPa for $\lambda = 20$, 40, and 50, respectively. Figure 12.12 shows a section of a Raman spectrum of polyethylene.

Fig. 12.12 Section of a Raman spectrum of polyethylene. The *arrows* indicate the following Raman peaks: I, v_{as} (C–C) asymmetric stretching mode at $1057 \, \text{cm}^{-1}$; II, v_s (C–C) symmetric stretching mode at $1123 \, \text{cm}^{-1}$; III, v_t (CH₂) twisting mode at $1291 \, \text{cm}^{-1}$; and IV, ω (CH₂) wagging mode at $1375 \, \text{cm}^{-1}$



The peak at 1057 cm⁻¹ belongs to an asymmetric stretching C–C vibration whereas the peak at 1123 cm⁻¹ corresponds to a symmetric stretching C–C vibration. One should note that the resulting peak at 1123 cm⁻¹ is the envelope of a "narrow" band and a "broad" band [33]. The peak at 1291 cm⁻¹ and the peak at 1375 cm⁻¹ belong to a twisting mode and a wagging mode of CH₂, respectively.

To see the influence of applied strain on the Raman spectra of polyethylene stress – strain measurements were carried out using a tensile testing machine. The tensile machine was mounted below a confocal Raman microscope (WITec, CRM 200, wavelength: 442 nm) to measure the Raman signal in situ. The strain was applied parallel to the direction of the drawing process.

Figure 12.13 shows the Raman shift as a function of applied strain for the polyethylene film made with a draw ratio of 50. Three different peaks were analyzed. For the peak at 1123 cm⁻¹, only the narrow band was analyzed as the broad band at the position did not influence the result. From the figure, one can see that the applied strain leads to a shift to lower wave numbers. Up to a strain of 2% the shift

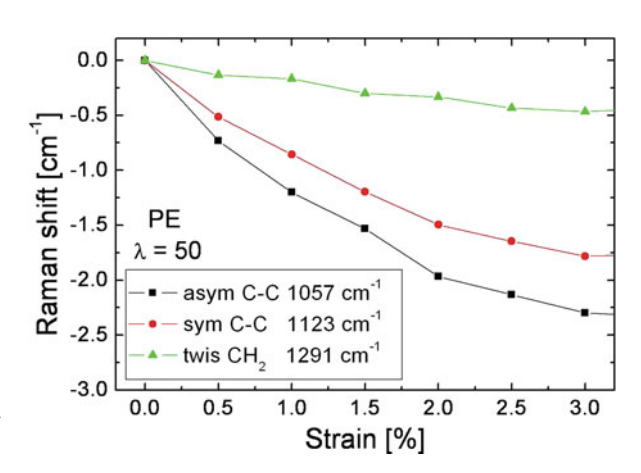


Fig. 12.13 Raman peak shift as a function of applied uniaxial strain for a polyethylene film with a draw ratio of 50

seems to be linear. For higher strains, the slopes of all three curves change. Furthermore, the three peaks show different strain dependencies. The peak at $1291~\rm cm^{-1}$ is only altered slightly and has a strain dependence of $0.16~\rm cm^{-1}/\%$. In comparison the peaks at 1123 and $1057~\rm cm^{-1}$ exhibit a strain dependence of 0.58 and $0.75~\rm cm^{-1}/\%$, respectively.

The reason for the different strain dependencies is the origin of the peaks. The peak at $1291\,\mathrm{cm}^{-1}$ belongs to a CH_2 wagging mode while the peak at $1057\,\mathrm{cm}^{-1}$ corresponds to a C–C molecule vibration, which is the backbone bond of the polyethylene. In a tensile experiment the stress is mainly applied on the back bond of the polymer. The C–H bonds of the polymer are like small side arms and are therefore much less affected by the stress.

Figure 12.14 shows the peak shift for the peak at $1057 \, \mathrm{cm}^{-1}$ for the draw ratios of $\lambda = 20$, 40, and 50 up to 5% strain. The peak corresponds to a C–C backbone vibration. All three samples show the same behavior. With increasing strain the peaks are shifted to lower wave numbers, but the slope of the peak shift strongly depends on the draw ratio of the film. The higher the draw ratio, the bigger is the slope of the sample.

Highly oriented polymers are assumed to consist of a number of anisotropic units with a uniform stress throughout the aggregate along the orientation axis [36]. Therefore, the macroscopic modulus can be expressed as

$$\frac{1}{E} = \frac{1}{E_c} + \frac{\langle \sin^2 \theta \rangle}{G} \tag{12.16}$$

where E is the macroscopic Young's modulus, E_c is the average chain modulus, G is the macroscopic shear modulus, and $\langle \sin^2 \theta \rangle$ is the mean value of orientation over the chain in the units about orientation axis. Equation (12.16) indicates that the deformation in highly orientated polymer films can be divided into a crystal stretching part (elongation of the polymer chains) and a rotation (shear deformation

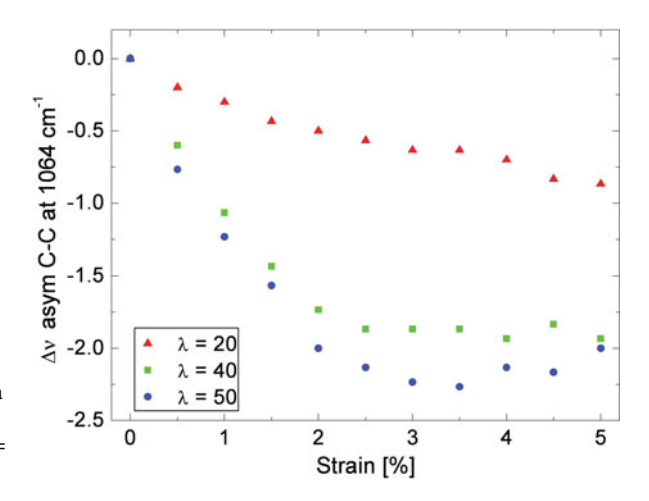


Fig. 12.14 Raman peak shift of the peak at $1057 \, \text{cm}^{-1}$ as a function of the strain for the three different draw ratios $\lambda = 20, 40, \text{ and } 50$

of small domains containing the chain segment). For high draw ratios the angle θ becomes small and therefore the portion of the rotation in (12.16) decreases. As a consequence, in highly orientated films applied strain or stress will strongly affect the elongation of the C–C backbone and therefore lead to a peak shift of the corresponding Raman peak. Maximal peak shifts could be obtained in polymer crystals where the chains are perfectly orientated and therefore θ becomes zero.

12.3 Discussion

Strain measurements by means of Raman microscopy have already been shown to be highly useful for applications in microelectronics and microsystems technology. In this application, the standard material is (100)-oriented single crystalline silicon, which is extremely well characterized in terms of mechanical and electronic properties. Also the phonon deformation potentials are well established. Currently, the application of strain measurements by Raman microscopy is being extended to further classes of materials. In these cases, phonon deformation potentials still need to be established. It is therefore important to investigate the advantages and drawbacks of this technique.

The advantages are

- High lateral resolution
- Depth resolution
- Available in laboratories at moderate cost
- Fast and easy data acquisition
- · High strain sensitivity

In contrast the disadvantages include

- Only certain classes of materials are Raman active
- Phonon deformation potentials are only available for a small set of materials
- Materials need to be transparent for 3D mapping
- Complete strain tensor is difficult to access
- Fluorescence may overshadow Raman peaks

In Table 12.2 the current technique is compared to other techniques for local strain measurements which are mostly based on diffraction. Electron diffraction is available in a laboratory environment, whereas X-ray diffraction requires synchrotron sources for spot sizes in the micrometer range.

The main advantage of Raman microscopy for strain measurements is its speed of acquisition and its ease of use. CBED requires extensive sample preparation and a TEM, Laue microdiffraction requires a synchrotron, which leaves only EBSD and a special Kossel technique which can be attached to SEMs. EBSD, however, has a poor strain resolution and the current state of the Kossel technique lacks automation. Raman microscopy is limited in terms of materials choice (polarizability) and needs the knowledge of phonon deformation potentials to allow for the conversion of peak shift into elastic strain. The conversion of strain into stress by Hooke's law is common to all methods. Complex strain states cannot currently be accessed by

	Raman	aman Electron diffraction X-r		X-ray micro	X-ray microdiffraction		
Chromatic		EBSD	CBED	Laue	Mono- chromatic	Kossel	
lateral resolution	300 nm	20 nm	5 nm	500 nm	50 nm	500 nm	
Depth resolution	500 nm	-	-	1 μm	-	-	
Ease of use	Lab based	SEM	TEM	Synchrot.	Synchrot.	SEM	
Strain resolution	10^{-4}	10^{-3}	10^{-4}	10^{-4}	10^{-4}	10^{-5}	
Time pixel	0.1 s	1 s	1 s	5 s	10 s	10 s	
Materials	Polarizable	_	Electron transparent	Single crystalline	Crystalline	Single crystalline	
Strain tensor components	1–3	2–5	2–5	5–6	1–2	6	

Table 12.2 Comparison of the Raman technique for stress measurement to comparable electron and X-ray diffraction-based techniques

Raman microscopy. This drawback will be overcome in the near future. With regard to lateral resolution, Raman microscopy is on the lower side for the methods compared. Here, two possibilities are viable. First, near-field optics could be employed to achieve resolutions below 100 nm. The issue with this option is that both near-field optics and the Raman effect strongly attenuate the primary signal and if used in conjunction leave just a few photons of signal to count. The other option is to locally enhance the signal by Plasmon resonances, e.g., by putting metallic nanoparticles of gold or silver in a focused beam [37–39].

In summary, Raman microscopy has been demonstrated to be a fast and relatively easy way to locally measure strains. With a well-developed experimental setup, more than one component of the strain tensor can be analyzed and certainly new materials will be analyzed in the future. Careful characterization of more materials that exhibit sharp Raman peaks in terms of the phonon deformation potential will enable strain measurements on more and more samples and make this technique useful for general local materials' stress analysis.

References

- N. Tamura, A. MacDowell, R. Spolenak, B. Valek, J. Bravman, W. Brown, R. Celestre, H. Padmore, B. Batterman, J.R. Patel, J. Synchrotron Radiat. 10, 137 (2003)
- 2. J. Nucci, S. Kramer, E. Arzt, C. Volkert, J. Mater. Res. 20, 1851 (2005)
- 3. J. Bauch, J. Brechbühl, H. Ullrich, G. Meinl, H. Lin, W. Kebede, Cryst. Res. Technol. **34**(1), 71 (1999)

- 4. R. Keller, A. Roshko, R. Geiss, K. Bertness, T. Quinn, Microelectron. Eng. 75(1), 96 (2004)
- 5. Q. Ma, S. Chiras, D. Clarke, Z. Suo, J. Appl. Phys. **78**(3), 1614 (1995)
- 6. I. Wolf, Semicond. Sci. Technol. 11, 139 (1995)
- 7. F. Cerdeira, C. Buchenauer, F. Pollak, M. Cardona, Phys. Rev. B 5(2), 580 (1972)
- 8. E. Anastassakis, A. Pinczuk, E. Burstein, F. Pollak, M. Cardona, Solid State Commun. 8, 1053 (1993)
- 9. G. Abstreiter, Appl. Surf. Sci. **50**(1–4), 73 (1991)
- V. Srikar, A. Swan, M. Unlu, B. Goldberg, S. Spearing, J. Microelectromech. Syst. 12(6), 779 (2003)
- 11. S. Ganesan, A. Maradudin, J. Oitmaa, Ann. Phys. **56**(2), 556 (1970)
- 12. R. Loudon, Adv. Phys. 13(52), 423 (1964)
- 13. S. Narayanan, S. Kalidindi, L. Schadler, J. Appl. Phys. **82**(5), 2595 (1997)
- 14. E. Anastassakis, E. Burstein, J. Phys. Chem. Solids **32**(2), 563 (1971)
- 15. E. Anastassakis, J. Phys. Chem. of Solids 32(2), 313 (1971)
- 16. I. Dewolf, H. Norstrom, H. Maes, J. Appli. Phys. **74**(7), 4490 (1993)
- 17. E. Bonera, M. Fanciulli, D. Batchelder, J. Appl. Phys. **94**(4), 2729 (2003)
- 18. G. Loechelt, N. Cave, J. Menendez, J. Appl. Phys. **86**(11), 6164 (1999)
- 19. G. Loechelt, N. Cave, J. Menendez, Appl. Phys. Lett. **66**(26), 3639 (1995)
- 20. S. Hu, J. Appl. Phys. **70**(6), R53 (1991)
- 21. E. Bonera, M. Fanciulli, D. Batchelder, Appl. Phys. Lett. **81**(18), 3377 (2002)
- H. Poulsen, S. Nielsen, E. Lauridsen, S. Schmidt, R.M. Suter, U. Lienert, L. Margulies, T. Lorentzen, D. Juul Jensen, J. Appl. Crystallogr. 34, 751 (2001)
- R. Nowak, T. Manninen, C. Li, K. Heiskanen, S. Hannula, V. Lindroos, T. Soga, F. Yoshida, JSME Int. J. Ser. A - Solid Mech. Mater. Eng. 46(3), 265 (2003)
- 24. T. Wermelinger, C. Borgia, C. Solenthaler, R. Spolenak, Acta Mater. 55(14), 4657 (2007)
- W. Rasband, Image Processing and Analysis, (National Institutes of Health: Bethesda, Maryland, USA, 1997–2007)
- R. Nowak, T. Sekino, K. Niihara, Philos. Mag. A Phys. Condens. Matter Struct. Defects Mech. Prop. 74(1), 171 (1996)
- 27. T. Damen, S. Porto, B. Tell, Phys. Rev. 142(2), 570 (1966)
- F. Decremps, J. Pellicer-Porres, A. Saitta, J. Chervin, A. Polian, Phys. Rev. B 65(9), 092101 (2002)
- 29. D. Mead, G. Wilkinson, J. Raman Spectrosc. **6**(3), 123 (1977)
- 30. F. Manjon, K. Syassen, R. Lauck, High Pres. Res. 22(2), 299 (2002)
- 31. K. Tashiro, G. Wu, M. Kobayashi, Polymer **29**(10), 1768 (1988)
- J. Moonen, W. Roovers, R. Meier, B. Kip, J. Polym. Sci. Part B Polym. Phys. 30(4), 361 (1992)
- 33. W. Wong, R. Young, J. Mater. Sci. 29(2), 510 (1994)
- 34. V. Mitra, W. Risen, R. Baughman, J. Chem. Phys. 66(6), 2731 (1977)
- 35. J. Lefèvre, Ultra-High-Performance Polymer Foils, Phd thesis, ETH Zurich, 2008
- 36. Y. Ward, R. Young, Polymer **42**(18), 857 (2001)
- 37. M. Moskovits, Rev. Mod. Phys. **57**(3), 783 (1985)
- 38. S. Nie, S. Emery, Science **275**(5303), 1102 (1997)
- L. Zhu, C. Georgi, M. Hecker, J. Rinderknecht, A. Mai, Y. Ritz, E. Zschech, J. Appl. Phys. 101(10), 104305 (2007)

A	Aperture angle, 6, 9, 10
Abberation function, 5	API, 166
Abbe, Ernst Karl, 2	API particles, 184
Abiogenic MMC formation, 128	Apoptosis, 158
Accumulations, 71	Aqueous alteration products, 120
Acquisition of spectra, 62	Asymmetric stretching C-C vibration, 274
Acrylic latex, 252	Atomic Force Microscopy (AFM), 172, 237,
Acrylics, 251	249
Active compound, 152	Atomic replacement, 124
Active drug delivery systems, 139	Attenuated total reflectance (ATR) objectives
Active pharmaceutical ingredients (API), 166	175
Active therapeutic coatings, 210	Augmented classical least squares method
Adhesive, 191	(aCLS), 212
Adhesive potential, 238	Australasian tektite field, 125
Aerogel, 118	Autofluorescence, 170
Aerosol, 189	Average spectra, 84
Ageing, 194	
Agglomerative clustering, 79	В
Albumin, 146	Backbone bond, 275
Aliphatic compound, 115	Back gate voltage, 105
Alkyd, 251, 252	Background, 71
Alkyl chain length, 212	Background subtraction, 61, 70, 86
Alpha-PbO ₂ -structured TiO ₂ , 125	Background suppression, 46
Alteration history, 119	Back scattered electrons (BSE), 171
Alteration history of minerals, 112	Backscattering configuration, 261, 266
Alteration veins, 113	Bacteria differentiation, 33
American Food and Drug Administration	Band structure, 102
(FDA), 157, 196	Basal (0001) twinning system, 271, 272
Amorphous, 215	Basis analysis, 57
Amorphous carbon, 254	Basis spectra, 82
Amorphous silica, 225, 234	Benzene ring modes, 246
Amphiphilic molecules, 153	Biaxially oriented polypropylene, 242
Ancient meteoritic materials, 124	Biaxial stress, 263, 265
Anisotropic units, 275	Binders, 251
Antenna, 35	Bioavailability, 178
Antibodies, 138	Biocompatibility, 203
Anti-oxidants, 254	Biodegradable
Anti-Stokes scattering, 24	matrix, 185
Antisymmetric stretch vibration, 25	polymer, 220

polymeric matrix, 178	Cell proteins, 138
polymeric nanocarriers, 157	Cells, 137
Biomass, 226	Cellular biology, 137
Biomolecules, 179, 232	Cellular components, 138, 145
Biopolymers, 179	Cellular metabolism, 159
Birefringence, 212, 214	Cellulose, 227
Blazing angle, 50	orientation, 225, 228, 230
Blending, 216	skeletons, 227
Boehmeria nivea, 227	Cell wall imaging, 228
Boltzmann-factor, 24	Cell wall layers, 225
Bond dipole, 24	Center of mass, 74
Bond polarizability, 24	Ceramics, 260
Breast cancer cell, 148	Ceramide, 158
Bright field microscopy, 170	Charge distributions, 105
Brillouin zone, 92	C-H bending, 246
Brine inclusions, 130	Chemical enhancement, 27, 37
Broadening, 75	Chemical imaging (CI), 165, 172, 173
BSE, 171	Chemical reaction, 83
Bulk microstructure, 116	Chiral vector, 91
Burst, 216	Chondrites, 130
	Chromite, 118
C	C-H stretching, 145, 148, 245
CaF ₂ substrates, 144	Cis-C=C stretch peak, 251
Cancer therapy, 152	Cis-C=C-H asymmetric stretching bands, 251
Carbon, 112, 254	Classical least squares (CLS), 179
Carbonaceous materials, 112, 116, 126	Clay minerals, 121
ancient terrestrial, 130	Clock voltage, 54
fossil, 130	Cluster, 142
Carbonaceous phases, 111	Cluster analysis, 75, 78, 82, 140, 247
Carbon allotropes, 92	CNTs
Carbon black, 254	(See also carbon nanotubes), 254
Carbon coating, 115	Coating, 214, 220, 251
Carbon metamorphism, 128	agents, 191
Carbon nanotubes, 91, 254	morphology, 210
metallic, 92	thickness, 205, 208
phonons, 92	Coesite, 121, 125
semiconducting, 92	Collection efficiency, 19, 44
Catheters, 203	Colouring agents, 191
Cation substitution, 124	Combination of various images, 84
CCD detector, 51	Cometary particles, 118
back-illuminated, 51	Common rock-forming minerals, 113
deep-depletion, 51	Complex-conjugate (Hermitian) transpose, 265
digitization noise, 53	Compliance tensor, 267
front-illuminated, 51	Composite materials, 254
QE curves, 51	Compositional variation, 68
quantum efficiency, 51	Compressive stress, 269, 271, 272
readout amplifier, 52	Computation time, 63
signal to noise ratio, 53	Condensed carbon phases, 113
CD95, 158	Conduction band, 95
C-D vibrations, 154	Confocal information depth, 59
Cell imaging, 145, 161	Confocal leaking, 114
Cellobiose, 226	Confocality, 45
Cell penetrating peptide, 156	Confocal microscope, 12
r	r

Confocal microscopy, 1	Defect-induced vibration, 93
Confocal pinhole size, 49	Deformation behavior, 268, 270, 272
Confocal Raman image, 64	Degenerated, 261
Confocal Raman microscope, 12	De-mixed, 86
Confocal setup	Depot systems, 178
mirror surface, 15	Depth resolution, 17, 18, 86
scattering point, 14	Depth scan, 253
Constant background, 70	Derivative, 69
Contamination, 114, 197	Detector function, 14
Content uniformity, 177, 191	Deuterium, 139, 154
Controlled drug delivery, 204	Devonian Rhynie Chert, 123
Control of sample damage, 119	Dexamethasone, 213, 215, 220
Core-shell structure, 186	1600-Dimensional space, 77
Correlation, 63, 64	Diamond, 92, 126
Cosmic ray removal, 61, 66, 86	Diamond anvil cell, 273
Cosmic rays, 141	Diamond paste, 114
Cost-benefit ratio, 181	Dichroic mirror, 48
C=O stretching, 246	Differential interference contrast (DIC), 170
Counterfeit identification, 169	
Counterstaining, 148	Differential scanning calorimetry (DSC), 168
Cracks, 266	Differentiation, 158
Cristobalite, 121	Diffraction limited, 181
Cross correlation plots, 78	Diffraction limited resolution, 242
Cross-section enhancement mechanisms, 27	Diffraction theory, 2
Cryo-fracture, 205	Digital Smoothing Polynomial, 69
Crystal lattice, 167	3-D intensity distribution, 5
Crystalline, 215	Dipole moment
Crystalline orientation, 120, 121	induced, 22
Crystallinity, 74	Disordered band, 126
Crystal matrix, 122	Dispersion characteristics, 50
Crystal orientation, 263	DISPO, 69
Crystal structure, 260	Distance calculation, 79
Crystallization, 240	Distribution of components, 85
Crystallographic axes, 265	Divisive clustering, 79
Crystallographic orientation, 120, 122	D-mode, 93, 94
CVD growth, 98	DNA, 33, 138, 144, 145
Cytoplasm, 146	Doping dependent line shift, 106
Czerny-Turner monochromator, 141	Doping fluctuations, 107
•	Double precision, 63
D	Double resonant process, 94
3-D analysis, 46	Double-resonant Raman scattering, 102
Dark spectrum, 71	3-D Raman spectroscopy measurements, 268
Data acquisition, 61, 62	Drawing process, 274
Data acquisition software, 64	Draw ratio, 273, 275
Data analysis, 61	Drug delivery systems, 152, 153
Data handling, 61	Drug eluting stent, 204, 205
Data presentation, 61	Drug/polymer coatings, 211
Data sets, 65	Drug polymorph, 211
Data stream, 62	Drug product formulation, 166
D band, 126	Dry powder inhaler, 190
Death receptor, 158	DSPC-d ₇₀ , 144, 154
Deep UV excitation, 33	3-D stress field, 270, 271
Defect mode, 94	3-D X-ray diffraction microscopy, 268
Defect mode, /T	5 12 1 1 1 1 1 1 1 1 1 1 1 1 1 1 1 1 1 1

Field distribution, 4, 9
Field enhancement, 27
Field geology studies, 130
Field of view (FOV), 176
Fillers, 254
Films over nanospheres, 38
Filters, 72
Fine structure, 249
Fingerprint region, 113, 145, 148
Finite conductance, 105
Fitting filters, 74
Fitting procedure, 83
Flavouring agents, 191
Fluid inclusions, 111, 129
Fluorescence, 33, 45, 71, 79, 180, 276
bleaching, 46
reduction of background, 45
time scale, 33
Fluorescence microscopy, 170
Fluorophore, 153
Foreign particulates, 196
Formation of minerals, 112
Forsterite, 123
Fossilized tree fern, 130
Fosterite, 120
Fourfold symmetry, 269
Fourier space filtering, 70
Franck-Condon point of absorption, 31
Freestanding sample geometry, 100
Fullerenes, 92
Fullerene soot, 116
Full vertical binning, 62
Functional coatings, 186
Fuzzy clustering, 81
Fuzzy c-means, 140
FWHM, 67, 74
G
Galilei, Galileo, 1
Gaussian, 74
Gaussian fit, 120
G band, 126
General stress states, 264
Geologic units, 112
Germ-line cells, 150
Glassy, 210
Glassy carbon, 128
Glassy state polymer, 245
Global illumination, 173
Global imaging, 45
γ-Globulin, 146
Glucopyranose rings, 227
Glucopyranose side chain, 227

Glucose sensor, 40	Hydrophilic gel, 204
Glycosidic linkages, 227	Hydrophilic polymer, 206
G'-mode, 93	Hydrostatic, 263
Goethite, 121	Hydrostatic component, 267
Gradients, 81	Hydrothermal systems, 128
Grain morphology, 124	Hygens, Christiaan, 1
Grain size, 121, 123	Hyperspectral, 65, 75, 82
Granule, 194	Hyperspectral unmixing, 140
Graphene, 91, 101	Hypodermal sterome, 234
crossover from the double to the single	,
layer, 105	I
doping domains, 106	
energy dispersion of, 101	IDWT, 69
FWHM of the D'-line, 103	Image contrast, 4, 86
identifying single-layer, 106	Image formation
indicator for single-layer, 104	coherent, 11
intensity of the G peak, 103	incoherent, 11
SFM, 103	for light scattering, 13
Graphite, 92	Raman scattering, 16
Graphitic band, 126	theory of, 11
Graphitic domain size, 131	Image generation, 62, 72
Graphitization grade, 128	Image masks, 81
Gratings, 50	Image scan, 65
Greens function, 10	Immiscible polymers, 244
Guanosine-5'-monophosphate, 32	Impact-altered mineralogy, 124
Gunflint microfossil, 126	Incoherent light scattering, 95
	Incubation time, 155
Н	Indent, 268
	Indirect DNA sensitivity, 40
Half-wave plate, 240 Halite/sylvite grains, 130	Industrial applications, 166
•	Inelastic scattering, 260
HCA, 139, 142	Infrared spectroscopy, 168
Heating trials, 119	Inhalation, 188
HeLa cell, 144, 145, 147, 159, 160	Inhalation particle, 182
Helical chain structure, 241	In-plane phonon vibrations, 271
Helmholtz-equation, 4	Integer, 63
Hemicelluloses, 226	Integrated circuits, 100
Hertzian dipole, 26, 35	Integrated intensity filter, 73
Hexagonal crystal, 270, 272	Integration time, 44
Hierarchical cluster analysis, 79,	Intensity, 65
139, 140, 142	Intensity distribution, 5
High resolution images, 63	Interface, 244
High resolution microscopy, 3	Intracellular drug delivery, 137
High through-put analysis, 169	Intracellular fusion processes, 157
High through-put screening (HTS), 169	Intraplane covalent bonds, 103
Hillocks, 266	Inverse discrete wavelet transformation, 69
Holographical beamsplitter, 48	Isotactic polypropylene, 240
Hooke's law, 262, 277	Isotactic tacticity, 239
Horsetail, 225, 232	
Humidity, 193	*
Huygens-Fresnel principle, 5	J
Hydrogel coating, 206	Janssen, Zacharias, 1
Hydrogels on glass, 207	Jarosite, 121
Hydrolysis, 186	Joint density of states, 95

K	Lumen, 232
Kasha's rule, 33	Luminesce, 125
Kataura plot, 96	Lysosomes, 150
Kerogenous material, 126	
Kirchhoff boundary conditions, 5	M
K-Means cluster analysis, 80, 86, 140	Macromolecular carbon, 126
•	Macroscopic modulus, 275
L	Magnetite, 119
α -Lactose monohydrate, 183	Magnification, 18
Laetia procera, 229	Manhattan, 79
Laser	Mantle-and-rim microstructure, 124
beam shape, 47	Mantle-derived fluids, 128
excitation power, 47	Martian aqueous alteration products, 121
frequency stability, 47	Mask output, 82
intensity stability, 47	Material properties, 244
line shape, 47	Matrix polysaccharides, 226
Laser beam damage, 116	Maturation, 150
Laser heating damage, 118	Maximum entropy filter, 69
Laser polarization, 241	MCF-7 cell, 144, 148
Laser power, 116	Mechanically abraded during polishing, 115
Laser power distribution, 117	Mechanical properties, 230
Laser wavelength, 47	Mechanical stress, 259
Latent crystal strain, 124	Median, 69
Latent strain, 121, 123	Medical devices, 203
Lateral resolution, 2, 14, 18, 47, 266	Memory space, 63
Latex spheres, 253	MER rovers, 132
Laue microdiffraction, 276	Metabolic intermediates, 150
Layering, 216	Metal colloids, 38
Lechatlierite, 121	Metallic nanosphere, 35
Lightning-rod-effect, 37	Metallic SWNTs, 95
Light scattering	Metal powders, 254
classical picture, 22	Metastable glass, 210
Lignified, 229	Meteorite chondrule, 121
Lignin distribution, 228	Meteorites, 113
LIME, 124	Method of stationary phase, 5
Limit of detection (LOD), 177	Microemulsion preconcentrates, 178
Linear combination, 76	Microfibril angle (MFA), 230
Linear Fit, 75	Microfibrillar, 226
Line imaging, 45	Micro-Raman spectroscopy, 44
Line scan, 65, 173	Microscope to Spectrometer coupling, 49
Lipid droplets, 232	Microscopy
Lipid rich regions, 149	confocal, 1
Liposomes, 153	high resolution, 3
Liposome structures, 157	optical, 1
Lippershey, Hans, 1	Microspectral SERS analysis, 39
Liquid binder, 191	Microstructure of a semicrystalline polymer,
Logical operators, 82	239
Long acting release (LAR) depots, 185–187	Mid infrared spectral imaging (MIRSI), 175
Longitudinal phonon, 261, 265	MIL 03346 martian meteorite, 121
Lorentzian, 67, 74, 75	Mineral birefringence, 114
Low pass filters, 68	Mineralogical context, 112, 126
LSP, 35	Mineralogy, 111
Lubricant, 189	Mineral phase chemical composition, 121
	=

Mineral phase imaging, 112, 120, 121	magnification, 18
Minimum integration time, 52	Observation matrix, 265
Mitochondria, 146, 149	Off-axis Raman spectroscopy, 263
Mitochondrial distribution, 140	Oil-alkane-water immersion, 89
Mitotracker ^(R) Green, 144	Oil-water-alkane immersion, 73, 80
Mixed phases, 80, 85	Oligopeptides, 179
Mixed spectra, 83	Olivine, 118, 120, 124
MMC, 126	Online evaluation, 81
Modified release pellets, 185	Oocytes, 151
Molecular polarizability, 22	Optical coordinates, 6
Molecular vibration, 238	Optical image formation
Monahans, 130	theory of, 2
Monochromatic reflectivity, 114	Optical microscopy, 1
Morphological characteristics, 239	Optical resolution, 7
Morphology, 244	Optical transitions, 98
Mouse oocyte, 150	Ordered and disordered polymer chains, 241
Moving average, 68, 71	± •
Multi-mode optical fiber, 49	Organic compounds, 114
Multiplex setups, 44	Orientation of grains, 122
Multi-spectral data sets, 62	Orientations of single crystals, 184
Multivariate data analysis, 72, 141	Origin of life, 112
Multivariate data methods, 86	Orthogonal subspace projection, 141
Multivariate image generation, 75	Oversampling, 181
Multivariate methods, 62, 141	Oxidation, 251
ividitivariate methods, 62, 141	Oxidation on heating, 118
N	D.
Nanocarrier systems, 137	P 251
Nanomaterials, 253	Paints, 251
Nanoparticle, 153, 155	Partial clustering method, 80
Nanoparticles, 38	Particle size distribution (PSD), 173
Nano-sized carrier systems, 157	Pauli exclusion principle, 105
Nanosphere lithography, 38	PBMA, 212, 213, 217, 218
Natural line width, 67	PCA, 76
Near infrared spectral imaging (NIRSI), 176	PDMA, 217, 218
Near infrared spectroscopy, 168	Peak broadening, 74
Ni islands, 98	Peak position, 74
NIR-FT, 227	Peak shift, 75, 268, 269, 275
NIRSI, 176	Peak width, 74
Noise-dominated data set, 78	Pectins, 226, 232–233
Noise sources, 52	Pellets, 185
Non-destructive mineral identification, 111	Peltier cooling, 52
Non-invasive labeling technique, 154	PEO-PCL-particles, 145
Non-linear background, 70	Peptides, 153
Non-orthogonal tight binding calculations, 96	Perinuclear region, 157
Nuclear region, 148	Perturbation theory, 29
Nucleic acids, 145	PET-PMMA polymer blend, 85, 89
Nucleus, 138, 152	Petrographic phase relationships, 123
Numerical aperture (NA), 44, 47, 180, 266,	Petrography, 111, 119
267	Pharmaceutical development, 165, 166
	Pharmaceutics, 211
0	Pharmacologically active compounds, 154
Objective, 89	Phase composition imaging, 123
achromatic, 1	Phase contrast, 246
choice of, 48	Phase image, 246

Phase separation, 217	Polypropylene, 239, 243, 254
PHMA, 214	Polysacharidic matrix polymers, 226
Phonon deformation potential, 267, 276	Polystyrene, 245
Phonon softening, 100	Poly(vinyl pyrrolidone), 209
Phosphate mineral, 121	Popigai impact structure, 125
Phospholipid, 146, 150, 154, 157	Porosity, 118
Photobleaching, 138	Porto notation, 266
Photosynthetically fixed carbon, 226	Powder mixture, 197
Physicotechnical properties, 167	Powder XRD (PXRD), 177
Pinhole	Power density, 100, 117
lateral position, 18	Poynting-vector, 7
Pinhole size, 13, 18	Precambrian Gunflint Chert, 131
Plant cell walls, 225	Preferred orientation, 273
Plant fibers, 227	Pre-processing, 61, 66
Plant tissue, 226	Pressure sensors, 268
Plasmon resonance, 36	Primary fluid inclusions, 113
Plasmons, 35	Principal component analysis, 75
Plastic deformation, 272	Prismatic slip, 272
PLGA, 221	Process Analytical Technology (PAT), 168
PMMA, 56, 66	Processing power, 80
Point detector, 43	Processor load, 74
Point-mapping, 173	Proliferation, 158
Point Spread Function (PSF), 10, 11	Proteins, 179
Polarizability	PS-EHA-SBR, 249
gradient of, 26	PS-PMMA, 84, 88
non-zero derivative, 24	Pseudo-hierarchical cluster tree, 80
quantum mechanical description of, 29	Pseudopolymorphs, 167
surface induced changes, 27	Pseudo-Voigt, 74
Polarizability tensor, 30, 183	effective, 12
Polarization, 183, 227, 228, 243	effective for detection, 14
macroscopic, 22	measurement of, 11
<u>*</u>	Pure component, 83
Polarization direction, 261, 267 Polarization of the electrical field, 8	Pure component spectra, 76, 144
	Pyrite grains, 112
Polarization plane, 120	Pyroxenes, 122
Polarization vector, 260, 266	
Polarized laser light, 230	Q
Polarized light microscopy, 170	Quadratric Fit, 75
Polarized off-axis Raman spectroscopy, 264	Quantum mechanical perturbation theory, 27
Polarized Raman spectra, 240	Quartz, 112, 118, 121, 123
Polyethylene, 273, 274	QUE 94366 carbonaceous chondrite, 120
Polyhexylmethacrylate, 214	QUE 94366 CV-type carbonaceous chondrite
Polymer blends, 244	121, 126
Polymer coating, 205, 251	_
Polymer diffusional layer, 215	R
Polymer matrix, 216	Radial breathing mode, 92, 93, 256
Polymer permeation, 114	Raman effect
Polymers, 126, 237, 238, 260, 273	surface-induced resonance, 37
Poly(methyl methacylate), 56	Raman emission
Polymorphic forms, 167	layer, 17
Polymorphism, 166	point, 16
Polymorphs, 211, 237	Raman enhancement mechanisms, 27
Polynomial background subtraction, 71	Raman information, 83
Polynomial baseline correction, 180	Raman instrumentation, 43

Raman mapping, 44	Sample damage, 116
Raman microscopes	Sample positioning, 63
developement of, 44	Sapphire, 268, 269
layout, 46	Savitzky-Golay, 69, 70
Raman mineralogy, 119	SBR, 249
Raman petrography, 124	Scanning electron microscopy (SEM), 171
Raman scattering, 23	Scattered Raman intensity, 25
frequency dependency, 22	Scattering geometry, 240
Raman scattering intensity, 47	Scattering point, 13
Raman signal optimization, 47	Schott, Otto, 2
Raman spectroscopy	Scouring rush, 232
introduction to, 21	Secondary cell walls, 226, 229
Raman tensors, 260	Secondary electrons (SE), 171
Raman thermal image, 100	Secondary oscillation, 26
Raman, C.V., 43, 183	Selected phonon mode, 264
Ramie, 227, 228	Selection rules, 24, 261
Rapamycin, 221	Selective average calculation, 81
Rayleigh equation, 268	Selective averaging, 81, 83
Rayleigh limit, 11	Selective excitation of chromophores, 31
Rayleigh scattering, 155	Self-assembling nanocarriers, 153
Ray-Tracing algorithm, 5	Semiconductors, 260
RBM, 92, 93, 256	Seneca, Lucius Annaeus, 1
Reabsorption of the scattered light, 33	SERRS, 37
Readout method, 67	SERS, 34
Readout noise, 52	SERS active substrates, 37
Readout register, 54	Sharp peak, 67
Reconstructed spectra, 78	Shear modulus, 275
Reduced carbon, 118	Shear stress, 273
Reference spectra, 70	β -Sheet protein, 145
Refractive index, 265	Shifting, 262
Relativistic particles, 91	Shift of Raman peak positions, 260
Renewable energy, 226	Shocked minerals, 124
Residual stress, 269, 271, 273	
Residual stress field, 271	Shock-formed phases, 125 Shock propagation vector, 124
Resolution, 268	Shock propagation vector, 124 Shot noise, 52
Resonance enhancement, 95	
Resonance Raman, 26, 31, 32, 138	Si, 88
Resonant Raman scattering, 28	Signal background, 71
Rhodamine derivative dye, 146	Signal to noise ratio, 31, 32, 51, 58, 78, 148
Rhombohedral slip system, 271, 272	Silanol groups, 234
Rhombohedral twinning system, 271, 272	Silicate glass, 121
Rhynie chert, 123	Silicon based microelectronic devices, 263
Ries meteorite impact crater, 125	Similarities, 79
RNA, 145, 179	Single crystal, 271
	Single molecule detection, 35
Row-nucleated structure, 240	Single-stranded RNA, 39
RRUFF, 121 Rubber phase, 247	Single-variant methods, 62
•	Single-walled carbon nanotubes, 254
Rubbery butadiene matrix, 248	SiO ₄ tetrathedra vibrational modes, 123
Rubbery state polymer, 245	Slip system, 270
a	Smearing, 68
S	Smoothing, 61, 68
Salt form, 166	S/N ratio, 83
Sample burning, 36	Soaking, 222

Software, 61	Symmetry reduction, 262
Spatial assignment, 86	Synchrotron, 276
Spatial coordinate, 65	Syndiotactic tacticity, 239
Spatial filtering, 141	Syringeability, 186
Specificity, 111	
Spectral cosmic ray removal, 67	Т
Spectral domain, 67	Tablet, 166, 177, 181
Spectral position, 65	Tablet coatings, 188
Spectra of components, 78	Tablet section, 192
Spectroscopic CCD camera, 62	Tablet surface, 193
Spherical aberrations, 209	Tangential mode, 93, 94
Spherical coordinates, 6	TAT peptide, 156
Spherulitic grains, 243	TATp-liposomes, 145
Spherulitic structure, 240	Temperature dependent phase transformations,
Splitting, 262, 265	170
Spray coating, 218	Temporal cosmic ray removal, 67
SsNMR, 168	Tensile stress, 269, 271, 272
Stabilizers, 254	Terahertz (THz) spectroscopy, 168
Stack, 269	Terrestrial explosion crater materials, 124
Stardust spacecraft, 118	Terrestrial impact craters, 124
Stents, 203	Therapeutic coatings, 203, 204
Stitching, 63	Thermal decomposition, 33, 48
Stokes scattering, 24	Thermal gravimetric analysis (TGA), 168
Strain, 74	Thermal history, 121
Strain dependence, 275	Thermal noise, 52
Strained crystal, 267	Thermar horse, 32 Thermography, 100
Strain measurements, 260	Thermography, 100 Thermoplastic polymer, 239
Strain tensor, 262	Thin sections, 114
Stray light suppression, 15	Threefold symmetry, 269
Strelley Pool formation, 112	Throughput, 46, 48
Stress analysis, 259	spectrometer, 49
Stressed tablets, 195	Tight binding energy model, 101
Stress induced peak shift, 267, 273	Tilting angle, 264
Stress state, 267	Time, 65
Stress tensor, 265, 271	Time-of-flight secondary ion mass
Structural orientation, 74	spectroscopy, TOF-SIMS, 173
Structure of carbon, 121	TiO ₂ , 254
Styrene blocks, 248	Tip-enhance Raman scattering, 39
Styrene-butadiene rubber, 247	TM-mode, 93, 94
Subbituminous (C) coal, 126	TOF-SIMS, 173, 175
Sub-cluster, 80	Toluca iron meteorite, 119, 126
Subspace, 77	
Sulfate minerals, 112	Topography image, 246
	Toxicology, 165
Sulfides, 118 Sum filter, 73	Traceless component, 267
Surface alteration, 115	Transistors, 100
Surface enhanced Raman scattering, 26, 34	Translational symmetry breaking, 105
	Transmission electron microscopy (TEM), 171
Surface irregularities, 114 Surface weathering products, 113	Transport vesicles, 150 Transport vesicles, 150 Transport vesicles, 150
Surface weathering products, 113	Transversal optical phonons, 261, 265
SWCNTs, 98–100, 254	Tridymite, 121
Swelling, 208 Symmetric stretching C. C. vibration, 274	Troilite, 119
Symmetric stretching C-C vibration, 274	Tube families, 97 Tupeble perrousband filter, 45
Symmetric stretch vibration, 24	Tunable narrowband filter, 45

Twinning system, 270	\mathbf{W}
Twofold symmetry, 271	Water content, 120
Two-layer coating, 218	Waterfall display, 65
,	Wave-like artifact, 71
**	Wavefunction
U	excited-state vibrational, 30
Ultra high molecular weight polyethylene	final ground-state, 30
(UHMWPE), 273	Wavelet decomposition, 69
Ultramicrotoming, 119	Wavelet transformation, 69, 72, 180
Uniaxial, 263	Wave vector, 6
Uniaxially drawn isotactic polypropylene film,	Weighted average, 68
240	Weighting factors, 83
Unit cell, 270	Wet granulation, 194
Univariate analysis, 72	Wetting, 248
Univariate image generation, 72	What Not to Do, 117
UV-resonance Raman spectroscopy, 33	White light images, 63
	Whitlockite, 121
\mathbf{V}	Wood, 226
Valence band, 95	Wood cells, 225
Vapor bubbles, 129	Wurtzite crystal structure, 272
Varying packing densities, 183	
Venus-specific mineralogy, 133	X
Vertex component analysis (VCA), 76, 139,	X-ray diffraction, 276
141, 142	X-ray fluorescence (XRF), 174
Vesicle-like inclusions, 149	X-ray microtomography (XMT), 172
Vesicles, 153	X-ray powder diffraction (XRPD), 168
Vesicles, 193 Vesicle structures, 154	*7
Vibrational states	Y
	Young's modulus, 273, 275
population of, 24 Violent indept 75, 76, 268, 270, 271	77
Vickers indent, 75, 76, 268, 270, 271	Z
Viscoelastic properties, 238	Zag, 130
Voids, 266	Zeiss, Carl, 2
Voigt, 74	Zinc oxide (ZnO), 271, 272